Geofluids

Nanoconfined Fluid Occurrence and Flow Behavior in Unconventional Gas/Oil Reservoirs

Lead Guest Editor: Zheng Sun
Guest Editors: Tao Zhang, Dong Feng, and Yu Pang

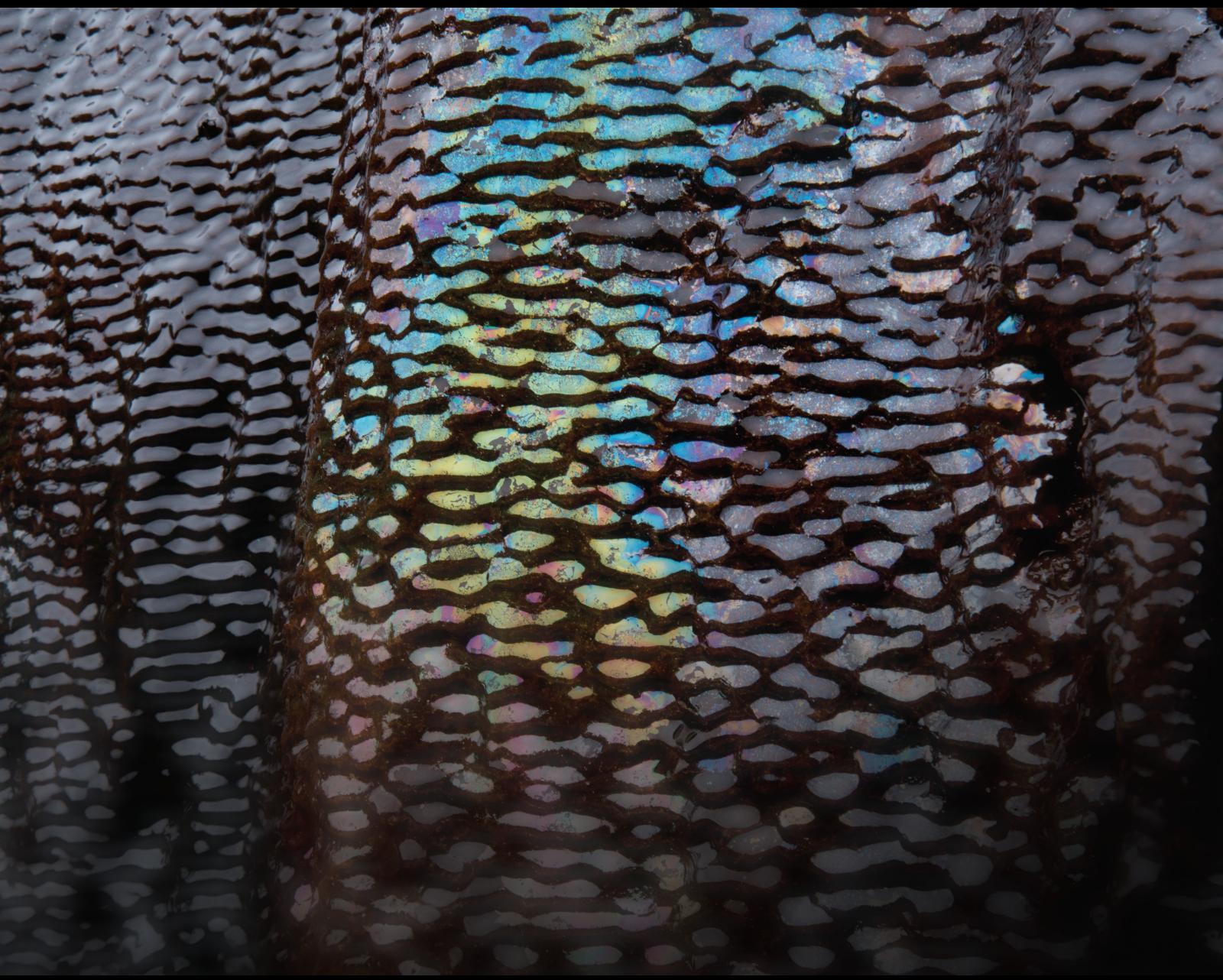

Nanoconfined Fluid Occurrence and Flow Behavior in Unconventional Gas/Oil Reservoirs

Geofluids

Nanoconfined Fluid Occurrence and Flow Behavior in Unconventional Gas/Oil Reservoirs

Lead Guest Editor: Zheng Sun
Guest Editors: Tao Zhang, Dong Feng, and Yu Pang

Chief Editor

Associate Editors

Academic Editors

Contents

Contents

Hindawi
Geofluids
Volume 2022, Article ID 2224321, 11 pages
https://doi.org/10.1155/2022/2224321

Research Article

Adaptability Study of Hot Water Chemical Flooding in Offshore Heavy Oilfields

Zenghua Zhang,[1,2] **Yi Jin**,[1,2] **Jian Zhang**,[1,2] **Engao Tang**,[1,2] **Zhijie Wei**,[1,2] **Dan Liang**,[1,2] **and Peihuan Li**[3]

[1]*State Key Laboratory of Offshore Oil Exploitation, Beijing 100028, China*
[2]*CNOOC Research Institute Co. Ltd., Beijing 100028, China*
[3]*China National Oil and Gas Exploration and Development Company Ltd. (CNODC), Beijing 100032, China*

Correspondence should be addressed to Zenghua Zhang; zhangzh20@cnooc.com.cn

Received 21 April 2022; Revised 31 August 2022; Accepted 5 October 2022; Published 17 November 2022

Academic Editor: Dong Feng

As a new heavy oil development technology, hot water chemistry flooding has great potential in offshore heavy oil fields development. In this paper, the adaptability of hot water chemical flooding was studied based on the typical model of offshore heavy oil fields. The main controlling factors affecting the hot water chemical flooding were analyzed and evaluated by single factor analysis. The technical boundary was established for offshore heavy oil fields. In addition, the hot water chemical flooding scheme was designed by a case study of a well group oilfield D. The results indicate that crude oil viscosity and well spacing have great influences on hot water chemical flooding performance. Hot water chemical flooding is favorable when the crude oil viscosity is between 300 and 1000 mPa·s and well spacing is around 200~400 m. The hot water chemical flooding scheme of the target well group results in 40.2×10^4 tons of incremental oil, and 6.3% of recovery factor being enhanced, which shows strong evidence that hot water chemical flooding enables great oilfield development performance.

1. Introduction

Heavy oil is one of the most important oil resources in the world and is widely distributed across the world. The reserves of heavy oil resources in China are also considerable [1]. The heavy oil resources with underground crude oil viscosity of 150~1000 mPa·s in the Bohai oilfield are of great percentage [2, 3]. At present, the heavy oil reservoirs in Bohai oilfield are mainly developed by conventional water flooding, which generally has poor development effect and low reserve recovery. They still have great potential to be extracted and produced [4–7].

The heavy oil reservoirs in Bohai oilfield have complex geological conditions, broken structures, and multiple oil-water systems with complex relationships [8–10]. It is characterized by large well spacing, irregular well pattern, high heterogeneity, deep burial, and consolidated reservoir cementation [11–13]. At the same time, offshore oil production is also affected by many factors such as platform space, service life, logistics resources, and the offshore environment [14–16]. The requirements for marine environmental protection and platform safety are also very strict. All these factors restrict the application of thermal recovery methods in offshore oilfields, which have been commonly adopted in onshore oilfields [17].

As a displacement method to enhance the recovery of heavy oil, hot water chemical flooding plays a role in the combination of physical and chemical effects [18–20]. The physical effect is mainly generated by heat, which is manifested in two aspects: (1) reducing the viscosity of the heavy oil by heating the reservoir and improving the mobility of heavy oil. The development performance gets improved with the adjusted mobility ratio and increased sweep efficiency; (2) heat can improve the microscopic displacement efficiency of heavy oil and enhance oil recovery. Chemical action is also mainly manifested in two aspects. (1) By

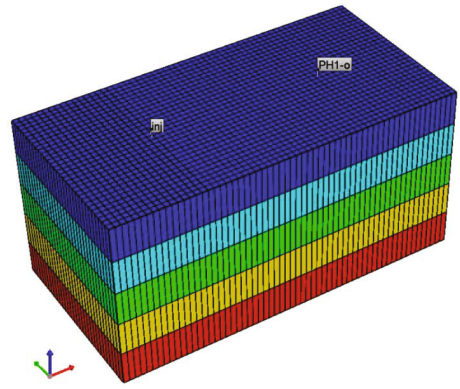

Figure 1: Meshing of the typical simulation model.

Table 1: Numerical simulation characterization of EOR mechanism for hot water chemical flooding.

EOR mechanism	Numerical simulation realization
Thermal viscosity reduction	Viscosity-temperature relation table at different temperatures
Displacement efficiency improvement by thermal method	High and low temperature relative permeability curve interpolation
Viscosity reduction by chemical agent	(1) the viscosity reduction rate of agent at different temperatures (2) by defining chemical reaction to generate oil with lower viscosity
Changing water phase viscosity to control mobility ratio	Nonlinear viscosity relation

Table 2: Results of water cut and recovery factor of 10 years production under different viscosity conditions.

Parameter	Value				
Oil viscosity/mPa·s	200	400	600	800	1000
Water cut/%	94.32	95.08	95.38	95.48	95.50
Recovery factor/%	14.66	11.73	10.15	9.06	8.21

adding chemical agents to the injected hot water, the viscosity of heavy oil gets reduced, thus improving the water-oil mobility ratio in the part of the reservoir that is not mainly affected by hot water. (2) The mobility ratio can be effectively controlled by adding the chemical agent with viscosifying effect, preventing the fingering and channeling effects. The synergistic effect manifests as the superposition of the mechanisms by injecting hot water and chemical agent to improve the water-oil mobility ratio, and finally increase the volumetric sweep efficiency and displacement efficiency [21, 22].

2. Study on the Influencing Factors of Hot Water Chemical Flooding for Offshore Heavy Oil Development

The offshore heavy oil development performance is mainly influenced by formation property, fluid property, and development factors. The numerical model is established based on the formation and fluid properties of oilfield D. Single factor analysis method is implemented to study the influence of crude oil properties, reservoir thermal physical properties, well spacing, and reservoir thickness on heavy oil development performance. Based on the sensitivity analysis, the technical boundary of hot water chemical flooding in offshore oilfield is determined.

2.1. Typical Simulation Model Build up for Offshore Heavy Oil Fields. CMG STARS module was used to establish a typical model for heavy oilfield to study the adaptability of hot water chemical flooding. The parameters of reservoir properties, fluid properties, thermophysical properties, relative permeability curve, and crude oil viscosity, as well as the viscosity-temperature curve, are established based on the general properties of Bohai heavy oilfields and laboratory experimental results. The total number of model grids is $61 \times 31 \times 5 = 9455$, and the grid size is $10\,\text{m} \times 10\,\text{m} \times 2\,\text{m}$. The model is a positive rhythm reservoir. The permeability of each layer is $3000 \times 10^{-3}\,\mu\text{m}^2$, $3500 \times 10^{-3}\,\mu\text{m}^2$, $4000 \times 10^{-3}\,\mu\text{m}^2$, $4500 \times 10^{-3}\,\mu\text{m}^2$, and $5000 \times 10^{-3}\,\mu\text{m}^2$. The model consists of one production well and one injection well, and it is shown in Figure 1. The characterization of the hot water chemical flooding mechanism in the numerical simulation model is shown in Table 1 [23–25].

Based on the water-flooding scheme, the numerical simulation study is carried out until the water cut reach 95%. In the simulation process, under different oil viscosity, the sensitivity analysis is limited to 10 years of production for the convenience of comparison. Water cut and recovery factor

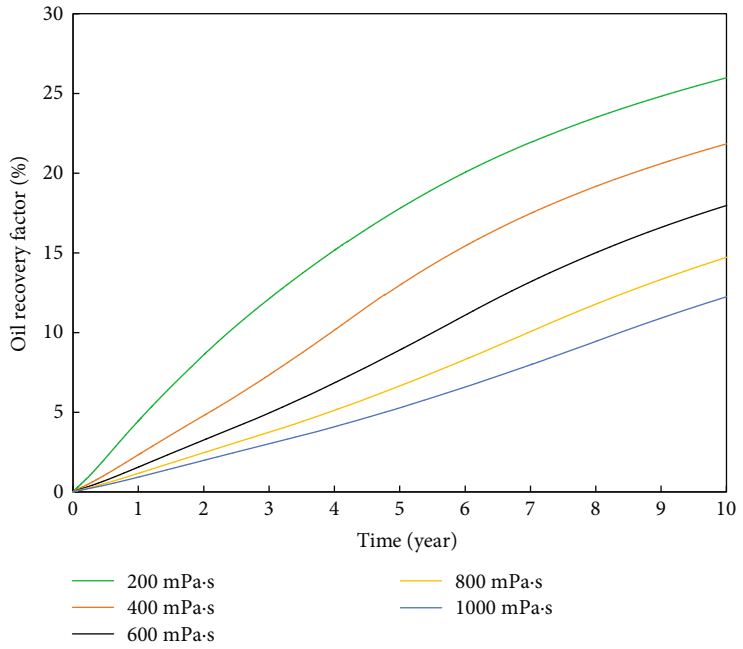

Figure 2: Recovery factors of hot water chemical flooding simulation with different oil viscosity.

Table 3: Influence of viscosity on the effect of different development methods.

Parameters	Recovery factor at different viscosity (%)					Maximum difference between recovery factor (%)
	200 mPa·s	400 mPa·s	600 mPa·s	800 mPa·s	1000 mPa·s	
10-year water flooding	14.66	11.73	10.15	9.06	8.21	6.45
10-year hot water chemical flooding	25.97	21.83	17.91	14.65	12.17	13.80

Table 4: Analysis table showing the influence of crude oil thermophysical properties on hot water chemical flooding performance.

The parameter types	Parameter	Range	Maximum difference between recovery factor (%)	Influence on hot water chemical flooding performance
Properties of crude oil	Compressibility/(1/kPa)	$1 \times 10 - 7 \sim 1 \times 10^{-6}$	0.03	Tiny
	Coefficient of thermal expansion/(1/°C)	$1 \times 10^{-4} \sim 1 \times 10^{-3}$	0.14	Tiny
	Coefficient of thermal conductivity/(J/m·day·°C)	$1 \times 10^{3} \sim 1 \times 10^{5}$	0.01	Tiny

of water-flooding scheme simulation with 10 years production are shown in Table 2.

2.2. Study on the Influencing Factors of Offshore Heavy Oil Reservoir Development. The permeability of offshore heavy oil reservoirs is generally greater than 2000 μm^2. The injectivity parameters can be continuously optimized and adjusted in the development process. Therefore, in this study, the influence of permeability and injectivity parameters on the effect of hot water chemical flooding is no longer considered. In this paper, the influences of formation property and fluid property on the performance of hot water chemical flooding are evaluated in terms of recovery factor.

2.2.1. Adaptability Study of Hot Water Chemical Flooding to Formation Crude Oil Properties. Firstly, the influence of crude oil viscosity on the development performance of hot water chemical flooding was analyzed. Crude oil viscosity was set to be 200, 400, 600, 800, and 1000 mPa·s. The simulation results are shown in Figure 2. It indicates that crude oil viscosity has a great influence on the recovery factor of 10 years of production by hot water chemical flooding. There is a maximum of 13.8% difference in recovery factor, and it can be seen in Table 3.

Secondly, the influence of the thermophysical properties of crude oil on the performance of hot water chemical flooding is studied. The numerical simulation results are shown in

Table 5: Analysis of the influence of rock thermal physical properties on hot water chemical flooding performance.

Parameter type	Parameter	Range	Maximum difference between recovery factor (%)	Influence on hot water chemical flooding performance
Rock property	Thermal capacity/(J/m^3·°C)	1×10^6 ~ 5×10^6	0	Tiny
	Compressibility/(1/kPa)	1×10^6 ~ 10×10^6	0.23	Tiny
	Coefficient of thermal expansion/(1/kPa)	1×10^{-7} ~ 50×10^{-7}	0	Tiny
	Coefficient of thermal conductivity/(J/m·day·°C)	0.5×10^5 ~ 5×10^5	0.26	Tiny

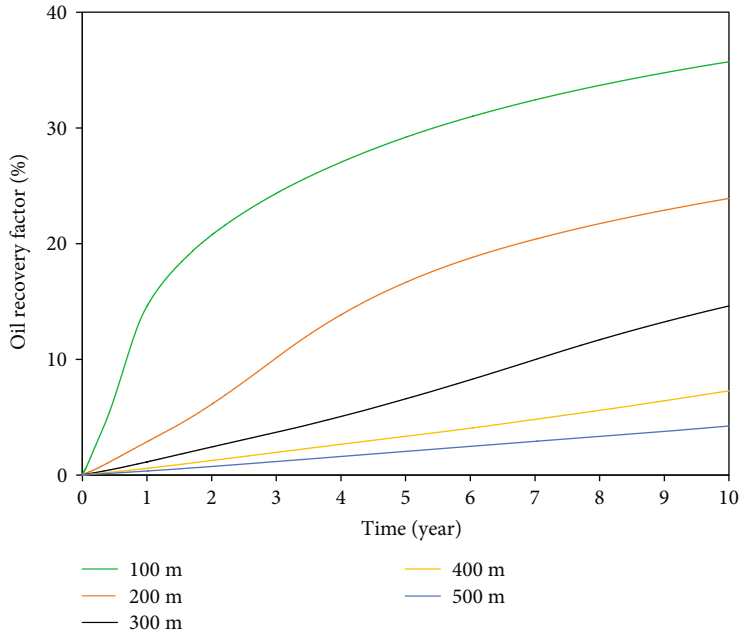

Figure 3: The influence of well spacing on the recovery factor of hot water chemical flooding.

Table 4. It can be seen that the compressibility coefficient, thermal expansion coefficient, and thermal conductivity coefficient of crude oil affect the recovery factor of hot water chemical flooding by 0.2% in the case of 10 years of hot water chemical flooding. Therefore, the influence of thermal physical parameters of crude oil on hot water chemical flooding can be ignored.

2.2.2. Adaptability Study of Hot Water Chemical Flooding to Thermal Physical Properties of Reservoir Rocks. In order to study the influence of thermophysical properties on the hot water chemical flooding performance, sensitivity studies are conducted. The rock thermal capacities were set to be 1.00×10^6, 2.58×10^6, and 5.00×10^6 J/m^3 · ∘C. The rock compressively coefficients were set to be 1×10^{-6}, 5×10^{-6}, and 10×10^{-6} 1/kPa. The rock thermal expansion coefficients were set to be 1×10^{-7}, 10×10^{-7}, and 50×10^{-7} 1/kPa. The thermal conductivity coefficients of rock were set to be 0.50×10^5, 1.63×10^5, and 5.00×10^5 J/m·day·°C. The results are shown in Table 5. It is indicated that the thermal capacity and thermal expansion coefficient of rock have little influence on the development performance, and the influence of rock compression coefficient and thermal conductivity coefficient on the recovery factor is less than 0.3%. The comprehensive analysis shows that the influence of rock thermal physical properties on the development performance can be ignored.

2.2.3. Adaptability Study of Hot Water Chemical Flooding to Well Spacing. Well spacing is an important factor that influences the recovery factor of offshore oilfield. Generally, offshore oilfield is usually developed with large spacing. The directional well spacing is typically 300 to 500 m, and 300 m after infill drilling. With this situation, it is necessary to evaluate the adaptability of hot water chemical flooding to well spacing [26, 27].

In the typical model, the well spacing is set to be 100 m, 200 m, 300 m, 400 m, and 500 m to study the influence of well spacing on the recovery factor of hot water chemical flooding development. According to the simulation results that shown in Figure 3, well spacing is an important factor affecting the final recovery factor. Under the hot water

Table 6: Influence of well spacing on the performance of different development methods.

Parameter	Recovery factor under difference well spacing					Maximum difference between recovery factor (%)
	100 m	200 m	300 m	400 m	500 m	
10-year water flooding	20.94	12.88	9.06	6.46	4.31	16.63
10-year hot water chemical flooding	35.74	23.95	14.65	7.30	4.26	31.48

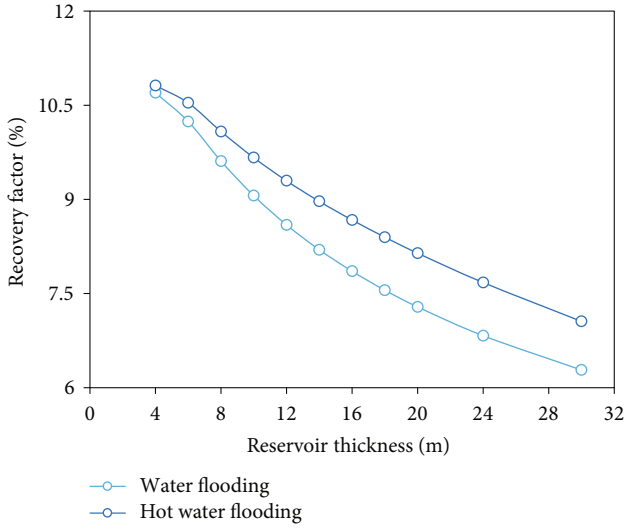

Figure 4: The influence of reservoir thickness on recovery factor of water flooding and hot water flooding.

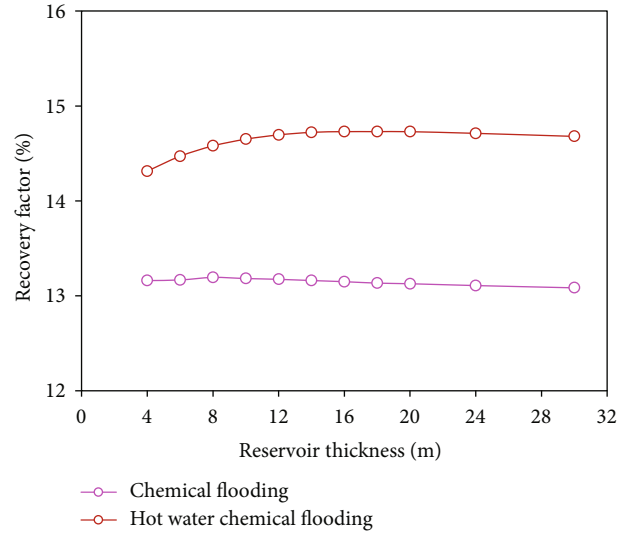

Figure 5: The influence of reservoir thickness on recovery factor of chemical flooding and hot water chemical flooding.

chemical flooding mode, the recovery factor of 100 m well spacing is 31.5% higher than that of 500 m well spacing. Details can be found in Table 6.

2.2.4. Adaptability Study of Hot Water Chemical Flooding to Reservoir Thickness. Reservoir thickness has different degrees of influence on different development methods. In the typical model, the reservoir thickness ranges from 4 m to 30 m. The influence of reservoir thickness on the development performance of hot water chemical flooding is studied. According to the simulation results shown in Figures 4 and 5, reservoir thickness has a great influence on the recovery factor under the water flooding and hot water flooding development modes, and the recovery factor decreases with the increase of reservoir thickness. The maximum difference of recovery degree under water flooding development mode is 4.4%, and the maximum difference of recovery factor under hot water flooding development mode is 3.8%. As for hot water chemical flooding, reservoir thickness has a certain influence on the recovery factor with the maximum recovery difference of 0.4%. While under the chemical flooding development method, the reservoir thickness has little influence. The maximum difference of recovery factor is only 0.1%. With the increase of thickness of heavy oil reservoir, chemical flooding or hot water chemical flooding can greatly improve the development effect compared with water flooding.

3. Study on the Adaptation Limit of Hot Water Chemical Flooding

Since reservoir thickness affects the hot water chemical flooding performance, it is believed that hot water chemical flooding also has certain adaptability to reservoir thickness in this paper. Therefore, based on the study, the influences of crude oil viscosity, spacing, and thickness on the hot water chemical flooding performance are further analyzed and evaluated using the single factor analysis method. Moreover, the contribution of thermal effect, chemical effect, and synergistic effect on the improvement of the final recovery factor of hot water chemical flooding under different parameters are quantitatively evaluated. Based on the synergistic effect index, the adaptation conditions of offshore heavy oil hot water chemical flooding are established. Three parameter settings in the typical model are shown in Table 7.

3.1. Study on Viscosity Limit of Formation Crude Oil. According to the simulation results, the contribution degree of the three oil incremental mechanisms to the recovery factor under different viscosity was plotted, and it is shown in Figure 6. The results indicate that the synergistic effect of hot water and chemical agents begins to appear when the viscosity of crude oil is greater than 200 mPa·s. When the viscosity of crude oil reaches 600 mPa·s, the contribution value reaches its maximum of 1.6%, and then decreases with the increase of viscosity. When the viscosity of crude oil is greater than 1000 mPa·s, the contribution value drops to

Table 7: Parameter settings in simulation model for hot water chemical flooding.

Factor	Level											
Viscosity/mPa·s	100	150	200	300	400	500	600	700	800	900	1000	1200
Thickness/m	2	4	6	8	10	12	14	16	18	20	24	30
Well spacing/m	100	150	200	250	300	350	400	450	500			

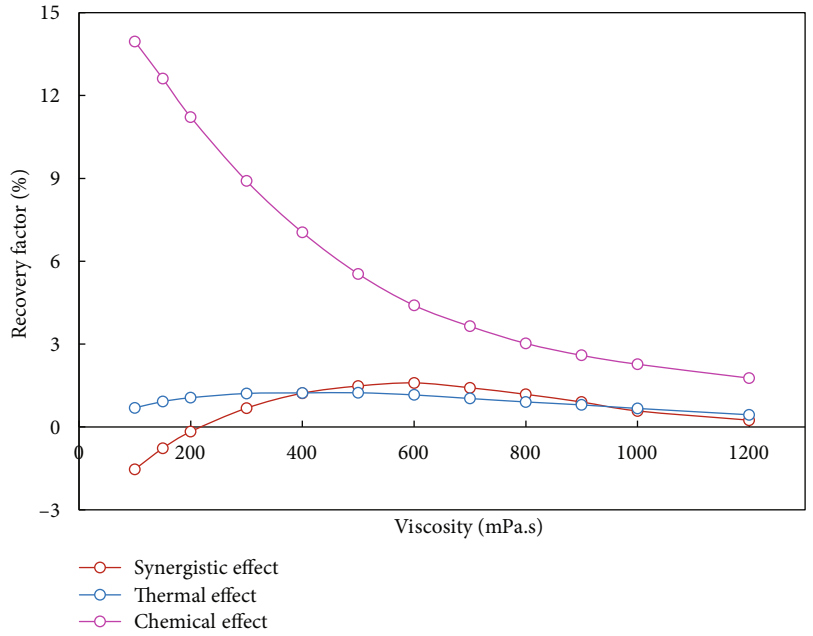

Figure 6: Contribution of oil incremental mechanism to the recovery factor of hot water chemical flooding under different viscosity.

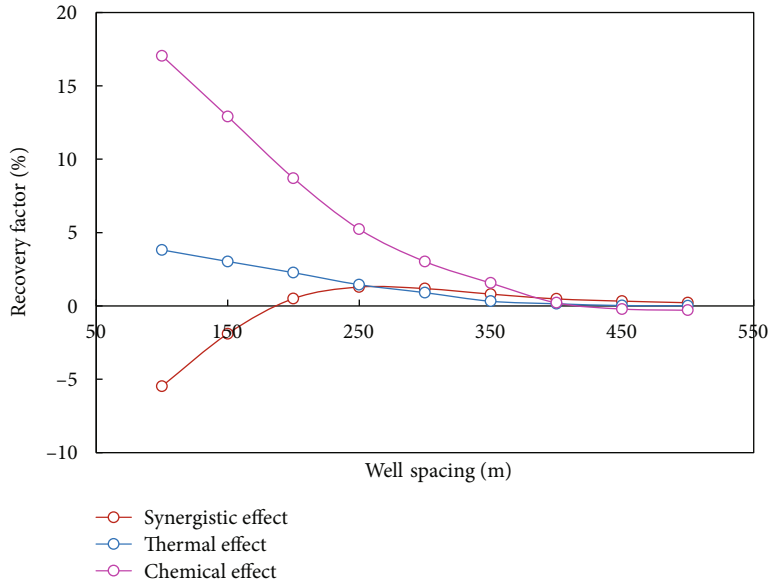

Figure 7: The contribution of three oil incremental mechanisms to the recovery factor of hot water chemical flooding under different well spacing.

0.5%. Taking the contribution value of 0.5% with synergistic effect as the technical boundary, the hot water chemical flooding is favorable when the crude oil viscosity is 300~1000 mPa·s. The recovery factors are improved by 3.5% ~ 10.8% compared with the water-flooding scheme, and the recovery is improved by 0.5% ~ 1.6% by synergistic

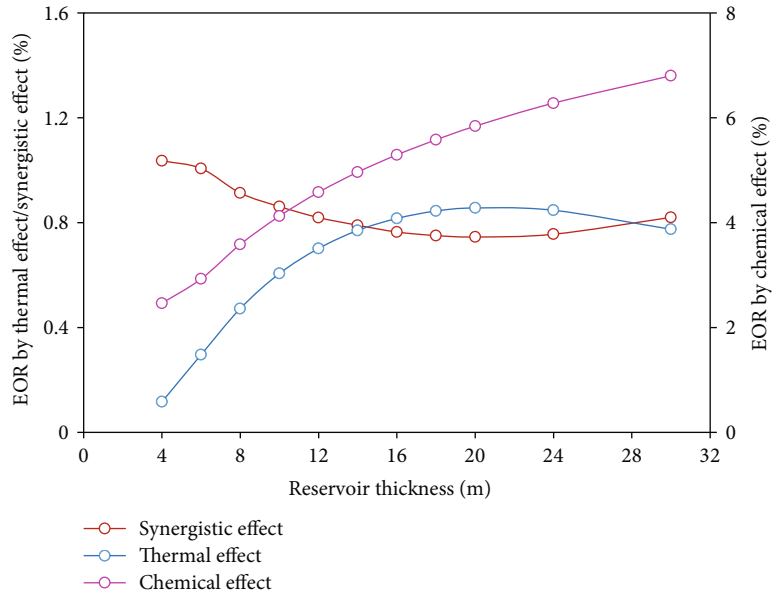

Figure 8: Contribution of three oil incremental mechanisms to the recovery factor of hot water chemical flooding under different reservoir thicknesses.

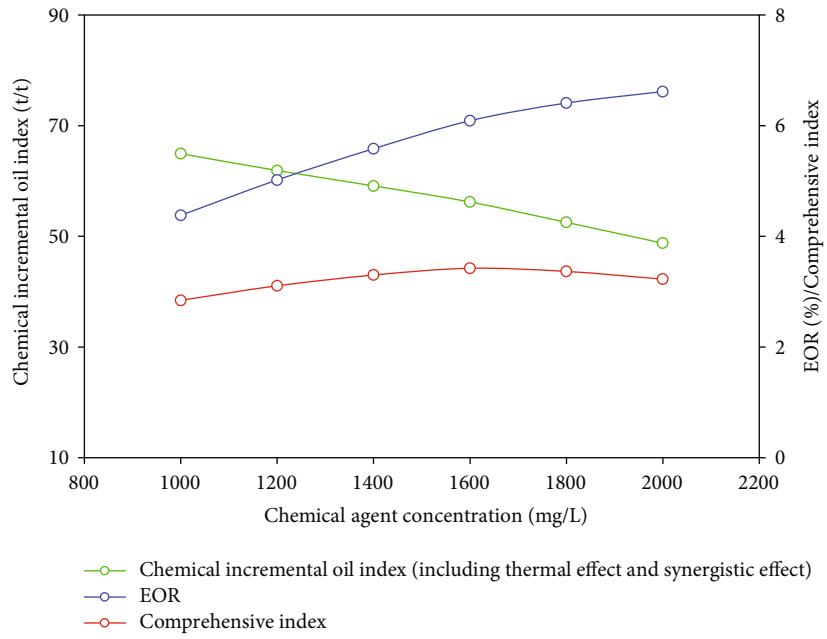

Figure 9: Optimization results of chemical agent concentration for hot water chemical flooding.

effect. The synergistic effect of hot water chemical flooding is the best when the viscosity of formation crude oil is 600 mPa·s.

3.2. Study on Well Spacing Limit. According to the simulation results, the contribution degree of the three oil incremental mechanisms to the recovery factor under different well spacing is plotted, and it is shown in Figure 7. The results show that when the well spacing is larger than 180 m, the synergistic effect begins to appear. When the well spacing is 300 m, the contribution of synergistic effect to the recovery degree reaches its peak of 1.2%, and then decreases to less than 0.5% when the well spacing is larger than 400 m. Similarly, taking the contribution value of 0.5% with synergistic effect as the technical boundary, the hot water chemical flooding is favorable when the well spacing is 200~400 m. The recovery factor of hot water chemical flooding is 0.9% ~ 11.5% higher than that of the water-flooding scheme. The synergistic effect improves the recovery by 0.5% ~ 1.3%. The synergistic effect of hot water chemical flooding is the best when the well spacing is 300 m.

3.3. Study on Reservoir Thickness Limit. According to the simulation results, the contribution degree of the three oil

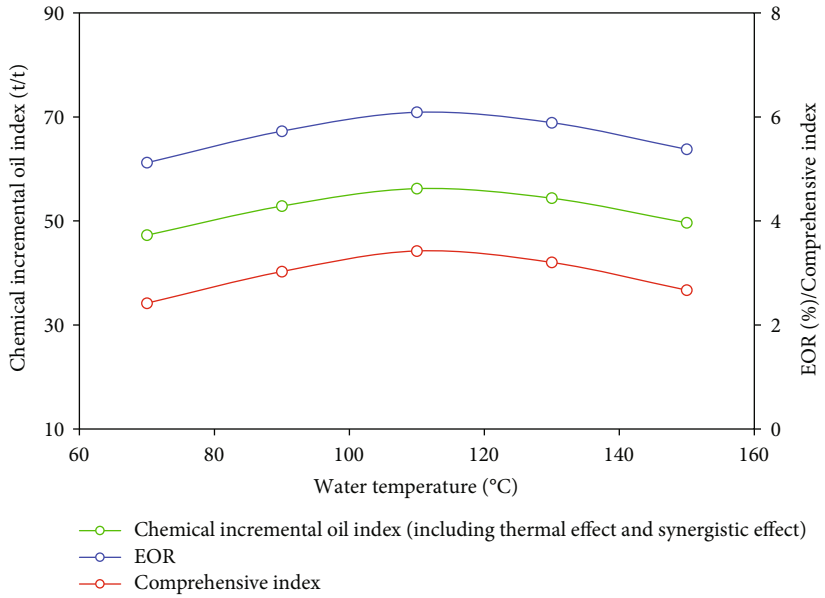

Figure 10: Optimization results of hot water injection temperature for hot water chemical flooding.

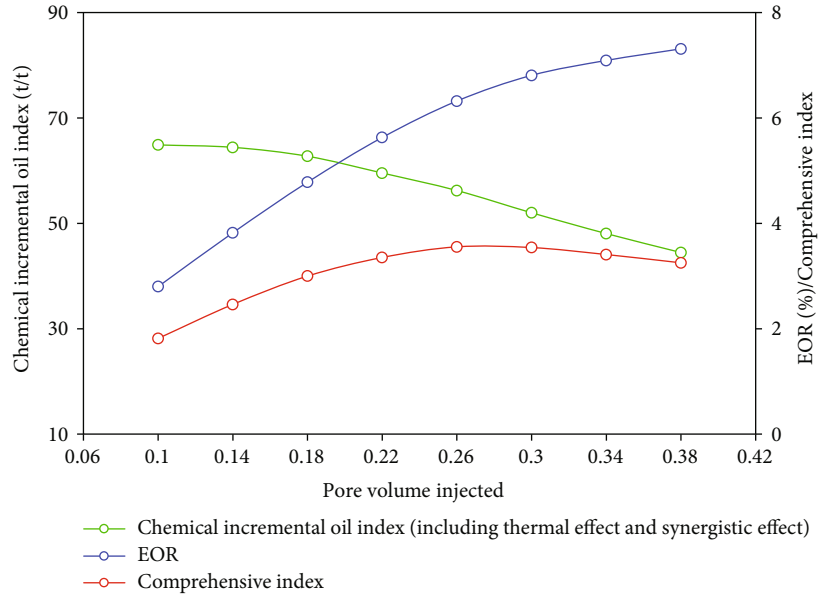

Figure 11: Optimization results of chemical agent injection volume for hot water chemical flooding.

incremental mechanisms to the recovery degree under different reservoir thicknesses is plotted in Figure 8. The research results show that with the increase of reservoir thickness, the synergistic effect of hot water chemical flooding decreases first and then increases. The main reason is that when the reservoir thickness is between 12 m and 24 m, the thermal effect and chemical effect have better effects on the development of heavy oil reservoirs, and the synergistic effect get reduced. As a whole, the synergistic effect can improve the recovery by 0.7% ~ 1%. Similarly, taking the contribution value of 0.5% with synergistic effect as the technical boundary, reservoir thickness has little limitation on the development of heavy oil with hot water chemical flooding. When the thickness of heavy oil reservoir reaches the technical boundary of the conventional development method, it is also suitable to carry out hot water chemical flooding.

4. Pilot Test Scheme Design of Hot Water Chemical Flooding in Bohai Oilfield D

Oilfield D is a layered structural reservoir, characterized by medium-shallow depth burial, large layer thickness, ultra-high porosity, and ultra-high permeability. The crude oil viscosity is 210~460 mPa·s, the average reservoir temperature is 57°C. The current comprehensive water cut is 88%, and

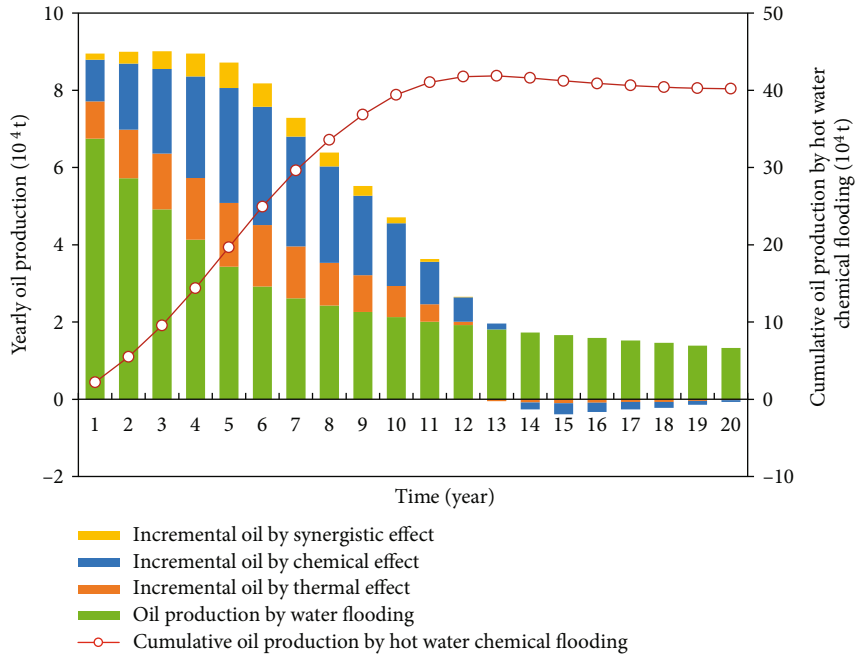

Figure 12: Recommended scheme indexes for hot water chemical flooding in pilot test area.

the recovery is 11%. Based on the adaptability analysis of hot water chemical flooding in offshore oil fields, it is favorable to carry out hot water chemical flooding. Through screening, the pilot test area of hot water chemical flooding is determined to be the 3 injection and 8 production well group, with the reserve of 6.36 million tons. At present, this well group adopts conventional water flooding development; therefore, the water-flooding scheme is taken as the basic scheme to study the oil incremental effect. On this basis, the parameters such as hot water temperature, chemical agent concentration, and chemical injection volume of hot water chemical flooding were optimized by taking EOR value, chemical incremental oil index, which is defined as incremented oil per ton of chemical agent injected and comprehensive index, which is defined as the EOR value times the chemical incremental oil index as the objective function, and the optimal scheme was finally offered.

4.1. Optimal Design of Injection Parameters. The numerical simulation of hot water chemical flooding is carried out to generate design samples for chemical agent concentration optimization. The results are shown in Figure 9. It can be seen from the figure that with the increase of chemical concentration, the EOR amplitude of hot water chemical flooding increases simultaneously, but the growth rate gradually decreases when the concentration exceeded 1600 mg/L. The comprehensive index reached its peak at 1600 mg/L, therefore the chemical agent concentration is recommended to be 1600 mg/L.

Similar process is conducted for temperature optimization. The optimization result of hot water injection temperature is shown in Figure 10. With the increase of hot water injection temperature, the EOR value of hot water chemical flooding increases first and then decreases. However, all indexes reach the peaks at 110°C, so 110°C is recommended as the injection temperature of hot water chemical flooding.

Finally, chemical agent injection volume optimization is carried out. As shown in Figure 11, with the increase of chemical agent injection volume, the EOR value of hot water chemical flooding increases, but the growth rate gradually decreases. The peak value of the comprehensive index occurs when the injection volume is 0.26 PV; consequently, the injection volume of chemical agent is recommended to be 0.26 PV.

4.2. Recommend Scheme. Based on the optimization results of injection parameters, the recommended scheme of the pilot test for hot water chemical flooding under optimal parameters was calculated. The concentration of chemical injection is 1600 mg/L, the temperature of hot water injection is 110°C, and the chemical agent injection volume is 0.26 PV (10 years). The chasing water flooding is implemented right after the end of hot water chemical flooding. As shown in Figure 12, compared with the conventional water flooding development, the recommended scheme yields 402,000 tons of cumulative incremental oil, among which the thermal effect contributes 31.6%, the chemical effect contributes 58.1% and the synergistic effect contributes 10.3%. The recovery factor increases by 6.3 percent. Therefore, from the perspective of oil incremental effect, under certain adaptation conditions, hot water chemical flooding can be used as a new technology for heavy oil development.

5. Conclusion

(1) As a new technology for heavy oil development, hot water chemical flooding can reduce the crude oil

viscosity through thermal and chemical effects, resulting in the improvements of oil-water mobility ratio and sweep efficiency. Under certain reservoir conditions, the synergistic effect of thermal effect and chemical effect can further improve the development performance of hot water chemical flooding

(2) It is found that crude oil viscosity and well spacing are important factors affecting the development performance of hot water chemical flooding. The hot water chemical flooding is favorable when the crude oil viscosity is 300~1000 mPa·s. Compared with the water-flooding scheme, the recovery factors are enhanced by 3.5% ~ 10.8%, from which the synergistic effect contributes 0.5% ~ 1.6%. The hot water chemical flooding is favorable when the well spacing is 200~400 m. Compared with the water-flooding scheme, the recovery factor is enhanced by 0.9% ~ 11.5%, where the synergistic effect contributes 0.5% ~ 1.3%. The synergistic effect of hot water chemical flooding achieve the best performance when the well spacing is 300 m

(3) The hot water chemical flooding scheme of the target well group results in 40.2×10^4 tons of incremental oil, and 6.3% of recovery factor being enhanced, which shows strong evidence that hot water chemical flooding enables great oilfield development performance

Data Availability

The data used to support the findings of this study are included within the article.

Conflicts of Interest

The authors declare that there is no conflict of interest regarding the publication of this paper.

Acknowledgments

This research was funded by the China National Offshore Oil Corporation (Project No: KJGG2021-0500).

References

[1] H. Huang, Z. Wang, and L. Yang, "Experimental simulation study on hot water/CO2 flooding efficiency of heavy oil in shallow reservoirs," *Petroleum and Natural Gas Chemical Industry*, vol. 46, no. 6, pp. 327–332, 2017.

[2] J. Wei, Q. Xu, and Y. Liu, "Discussion on steam injection assisted by viscosity reducer in heavy oil Wells," *Petrochemical Technology*, vol. 29, no. 7, pp. 52–54, 2022.

[3] H. Peihui, L. Haibo, H. Xu, C. Ruibo, Z. Yuwei, and L. Xiaoyang, "Alternative injection and its seepage mechanism of polymer flooding in heterogeneous reservoirs," in *SPE Asia Pacific Enhanced Oil Recovery Conference*, Kuala Lumpur, Malaysia, August 2015.

[4] W. Hao, "Discussion on hot water flooding technology for heavy oil in low permeability reservoirs," *Chemical Engineering and Equipment*, vol. 12, no. 3, pp. 82-83, 2017.

[5] Y. Wang, "Preliminary understanding of hot water flooding development in heavy oil block D," *Petro China*, vol. 3, no. 6, pp. 90–98, 2017.

[6] B. Sun, "Effect of temperature on relative permeability of heavy oil/hot water," *Journal of Southwest Petroleum University (Natural Science Edition)*, vol. 39, no. 2, pp. 99–104, 2017.

[7] D. Caili, Y. Qing, F. Xiqun et al., "Study and application of anionic and cationic polymers alternative injection for in-depth profile control in low permeability sandstone reservoir," in *SPE EUROPEC/EAGE Annual Conference and Exhibition*, Vienna, Austria, May 2011.

[8] M. Zhang, Y. Yang, Z. Wang, Y. Sun, X. Xing, and Z. Sun, "Comparison of microscopic oil displacement effects of heavy oil hot water flooding under different wettability conditions," *Science Technology and Engineering*, vol. 16, no. 26, pp. 195–199, 2016.

[9] J. Li, *Research on Heavy Oil Thermal/Chemical Flooding Technology*, China University of Petroleum, 2011.

[10] A. Li, "Experimental study on hot water flooding and thermochemical flooding of Cao 4 heavy oil in Le'an oilfield," *Oil and Gas Geology and Recovery*, vol. 18, no. 3, pp. 64–166, 2011.

[11] Y. Qin, Y. Wu, P. Liu, F. Zhao, Z. Yuan, and L. Liu, "Experimental study on the influence of temperature on oil-water relative permeability in heavy oil reservoirs," *Oil and Gas Geology and Recovery*, vol. 25, no. 4, pp. 121–126, 2018.

[12] X. Xie, X. Kang, and X. Zhang, "Evaluation method and application of chemical flooding potential in offshore heavy oil field," *China Offshore Oil and Gas*, vol. 28, no. 6, article 1673-1506, pp. 69–74, 2016.

[13] G. Wang, B. Liu, X. R. Wang, G. H. Zhang, and W. Zhang, "Influencing factors analysis and field test of water and polymer interference in offshore oilfields," *Petroleum Geology and Engineering*, vol. 34, no. 1, pp. 91–95, 2020.

[14] C. Qi, J. Li, and J. Jiang, "Injection-production parameters of multi-component thermal fluid huff and puff for offshore heavy oil research on multi-factor orthogonal optimization," *Special Oil and Gas Reservoirs*, vol. 19, no. 5, pp. 86–89, 2012.

[15] W. Zheng, X. Tan, and T. Wang, "A new method for determining steam huff and puff production in offshore heavy oil fields," *Xinjiang Petroleum Geology*, vol. 41, no. 3, pp. 344–348, 2020.

[16] M. Deniz and D. Birol, "Analytical solution of nonisothermal Buckley-Leverett flow including tracers," *SPE Reservoir Evaluation & Engineering*, vol. 11, no. 3, pp. 65–74, 2008.

[17] W. D. Pethrick, E. S. Sennhauser, and T. G. Harding, "Numerical modelling of cyclic steam stimulation in cold Lake oil sands," *Journal of Canadian Petroleum Technology*, vol. 27, no. 6, pp. 89–97, 1988.

[18] J. Yang, B. Jin, L. Jiang, and F. Liu, "An improved numerical simulator for surfactant/polymer flooding," in *SPE/IATMI Asia Pacific Oil & Gas Conference and Exhibition*, Nusa Dua, Bali, Indonesia, October 2015.

[19] Y. C. Su and T. L. Li, "Practice of development adjustment in offshore sandstone oilfield in high water cut stage," *China Offshore Oil and Gas*, vol. 28, no. 3, pp. 83–90, 2016.

[20] D. Wang, R. S. Seright, K. P. Moe Soe Let, K. Bhoendie, and W. R. Paidin, "Compaction and dilation effects on polymer

flood performance," in *SPE Europec featured at 79th EAGE Conference and Exhibition*, Paris, France, June 2017.

[21] Z. Wei and D. Zhang, "A fully coupled multiphase multicomponent flow and geomechanics model for enhanced coalbed-methane recovery and CO_2 storage," *SPE Journal*, vol. 18, no. 3, pp. 448–467, 2013.

[22] R. B. Cao, P. H. Han, and G. Sun, "Oil displacement efficiency evaluation of variable viscosity polymer slug alternative injection," *Oil drilling & Production Technology*, vol. 33, no. 6, pp. 88–91, 2011.

[23] J. Zhang, D. Liang, and X. D. Kang, "Research on hot water chemical flooding technology in offshore heavy oil fields," *China Offshore Oil Gas*, vol. 33, no. 5, pp. 71–80, 2021.

[24] H. Xu, *NB35-2 Heavy Oil Steam Huff and Puff Development Effect Evaluation Research*, China University of Petroleum (Beijing), 2016.

[25] H. Cao and K. Aziz, "Performance of IMPSAT and IMPSAT-AIM models in compositional simulation," in *SPE Annual Technical Conference and Exhibition*, San Antonio, Texas, September 2002.

[26] R. Courant, K. Friedrichs, and H. Lewy, "On the partial difference equations of mathematical physics," *IBM Journal of Research and Development*, vol. 11, no. 2, pp. 215–234, 1967.

[27] D. W. Zhao and I. D. Gates, "On hot water flooding strategies for thin heavy oil reservoirs," *Fuel*, vol. 153, pp. 559–568, 2015.

Hindawi
Geofluids
Volume 2022, Article ID 6399148, 10 pages
https://doi.org/10.1155/2022/6399148

Research Article

Evaluation of Reservoir Parameters and Well Productivity Based on Production Data: A Field Case in Xinjiang Oilfield, China

Rui Chen,[1] **Qiao Guo**,[2] **Jiaqi Li**,[1] **Yijun Zhang**,[1] **Wenpeng Bai**,[2] **Shiqing Cheng**,[2] **and Yang Wang**[2]

[1]*Research Institute of Engineering Technology, Xinjiang Oilfield Company, PetroChina, Karamay, Xinjiang 834000, China*
[2]*China University of Petroleum, Beijing, and State Key Laboratory of Petroleum Resources and Prospecting, Beijing, China*

Correspondence should be addressed to Yang Wang; petroyang@163.com

Received 8 March 2022; Revised 26 September 2022; Accepted 29 September 2022; Published 16 November 2022

Academic Editor: Qingquan Liu

The understanding of formation has always been a challenge for field development. In this paper, we evaluate the reservoir parameters and gas well productivity based on production data. The model of nonuniform conductivity of fractures in multistage fracturing horizontal wells (MFHW) is used to interpret the transient pressure data. Binomial and exponential deliverability equations and pressure dimensionless productivity formula are combined to evaluate the gas well productivity. After that, the key factors that influence gas well production are analyzed, and the gas rate vs. oil nozzle is presented. Results show that the fracture half-length and conductivity for high- and low-conductivity fractures, respectively, are obtained, apart from the reservoir pressure, permeability, skin factor, etc. The test time in each oil nozzle is recommended to extend to achieve stability and to obtain a more accurate absolute open flow potential. The findings of this study provides a guidance for the production data analysis of nonuniform conductivity of fractures in MFHW in the future work. And it can help for the better understanding of predicting gas production rates in MFHW.

1. Introduction

Rate and pressure are the most valuable data in the reservoir evaluation. No matter directly or indirectly, they are the inputs that needed in the all stages of production performance analysis [1–5]. Reservoir evaluation relies on amount of mathematical solutions of the flow equations for reservoir or well characterization, among which pressure transient analysis and well productivity evaluation are the most-often-used techniques in the petroleum engineering [6–9]. The main purpose of pressure transient analysis is to collect the shut-in pressure data under controlled well rate conditions to determine reservoir and fracture parameters and estimate reservoir size [10]. The productivity test is generally applied to evaluate the oil or gas well production capacity by changing the working system [11–14].

In a typical pressure transient analysis, pressure data is usually measured downhole (as close to the midreservoir as possible) while the flow rates are collected at surface. The pressure responses are generated by changing the production rates, and the pressure and its derivative data during a build-up (or falloff) period are analyzed to evaluate the reservoir features [15–18]. The pressure transient analysis starts during the 1950s and 1960s by Matthews and Russell [19]. In the early time, the pressure data is performed exclusively by hand with pencil and graph paper based on straight lines analysis [20, 21]. Starting in the late 1970s, more and more developments came from service companies. Type curve analysis was introduced by Bourdet and Gringarten [22], which marked the beginning of the end of manual analysis. Then, more complex models that consider different boundaries and reservoir types are proposed with the development of numerical techniques such as the Stehfest algorithm [23]. Since the introduction of pressure derivative curve proposed by Bourdet et al. [24, 25], pressure transient analysis has become a reliable tool and is accepted by researchers.

Derivatives have revolutionized pressure transient analysis by making it possible to identify different flow regimes from the slope of pressure and its derivative curves. After that, the power of pressure transient analysis is further enhanced with the introduction of deconvolution, which makes the analysis of variable-rate pressure data possible [26]. Gringarten et al. [27, 28] and Aluko et al. [29] described the pressure transient analysis is an inverse problem, which can be expressed as $I \rightarrow S \rightarrow O$, where the input "$I$" means the induced rate impulse; the output "O" is the measured pressure data, and the "S" represents the unknown reservoir system. To obtain the unknown reservoir system "S", we should identify the pressure responses by interpretation models [30–32].

Gas well production evaluation is the key of gas reservoir dynamic analysis ([33]; Wang et al. 2021). Unlike conventional production analysis for slightly compressible fluids, gas rate production considers two parts: (1) Forchheimier's flow equation, rather than Darcy's law, should be used to characterize the high-velocity flow of gas that flows in porous media [34]. Swift and Kiel [35] thought that the non-Darcy flow of gas flow results in an additional pressure drop near the wellbore. (2) Gas properties are highly pressure dependent, which leads to a highly nonlinear flow (Wang et al. 2021). From the 1920s to 1950s, some gas well production test methods, including back-pressure well test [36], isochronal well test [37], modified isochronal well test [38], and one-point method [39], were proposed, which were based on binomial methods for deliverability calculation. Binomial deliverability equation can better characterize the turbulent influence of gas flow, which is generally expressed as pressure, pressure-square, and pseudopressure method. With the binomial deliverability equation, the absolute open flow potential and the inflow performance relation curve can be obtained. Field engineers prefer to apply binomial pressure-square type to calculate gas well production. Chase and Alkandari [40] proposed a methodology to predict the gas productivity of fractured gas well by single-point test rather than the multipoint backpressure test. Wang et al. [41] presented a novel binomial equation that considers non-Darcy effects, and found that the non-Darcy effect affects high-permeability reservoirs more dramatically than the low-permeability reservoirs.

The model of nonuniform conductivity of fractures in MFHW is used to interpret the formation and fracture parameters with the transient pressure data, and it can obtain more accurate well test interpretation results. More importantly, the productivity evaluation is more in line with the actual situation of the formation. However, it requires higher quality of the build-up pressure data and production data.

2. Methodology

In this paper, we take a multifractured horizontal well in Xinjiang Oilfield as an example. Firstly, the pressure transient analysis method is described to interpret formation and fracture parameters. Secondly, the well productivity is evaluated by combining different approaches. Then, key influences factors on well production are analyzed, and finally the gas rate prediction in different working systems is presented. This work provides a clue to analyze the production data for exploratory wells. According to the main procedures, the general sketch of the problem under study and the workflow are presented in Figure 1.

3. Pressure Transient Analysis

Well SX161 is condensate gas well, located in Xinjiang Oilfield. It was subject to 11-stage fracturing, with a total fracturing fluid of 11992.80 m^3 and a total proppant of 675.90 m^3 from 6 August to 9 August 2021. It started to produce with natural energy from 15 August 2021. Then, the productivity well test was conducted with 5 oil nozzles: 5 mm, 6 mm, 7 mm, 8 mm, and 9.2 mm from 21 August to 3 September. After the productivity well test, it continued to produce by depletion from 4 September to 8 September. During 9 September to 18 September, this well was shut in to measure the build-up pressure. The pressure measurement history is presented in Figure 2.

The well is shut in to measure the build-up pressure data. The data points are smooth without any fluctuations by amplifying the well data, indicating the test data meets the analysis requirements. The pressure build-up speed is fast during the test period, with the pressure build up from 62.2 MPa to 66.61 MPa after 215.43 hours shut in. The pressure-derivative curve tends to a horizontal line after the wellbore-storage regime, which may be the vertical radial flow around the horizontal well. Then, the pressure and its derivative curves rise in parallel with 1/2 slope, indicating the linear flow regime that perpendicular to horizontal wellbore. Finally, there is a trend of horizontal radial flow at the end of the pressure-derivative curve.

The Saphir software (Kappa Workstation 5.20) is firstly applied to analyze the pressure response. The "Constant Wellbore + Horizontal fractured well + Homogeneous reservoir + Infinite boundary" model is selected to interpret the build-up pressure data. The pressure and its derivative matching curves are presented in Figure 3(a), and the interpretation results are shown in Table 1. Wellbore storage coefficient is 1.95 m^3/MPa. Reservoir permeability is 0.586×10^{-3} μm^2. Fracture skin factor is 0.29. Fracture half-length is 20.56 m. Initial reservoir pressure is 68.91 MPa.

In the actual field gas well development, the proppants may not be uniformly distributed, which results in the nonuniform flux density and fracture conductivity along the fractures. Meanwhile, the fluid is not produced in every section of horizontal wells (Figure 4). Based on this phenomenon, Qin et al. [42, 43] proposed an approach to investigate the nonuniform fluid production along horizontal wellbore. The pressure drop is caused by hydraulic fractures and horizontal well. The pressure drops caused by n horizontal sections are presented by superposition while the pressure drops caused by hydraulic fractures are derived by the superposition of continuous-vertical-plane sources. This model can diagnose the high production location and production rate, and the high-conductivity fracture length near the horizontal well and the low-conductivity fracture length far from the

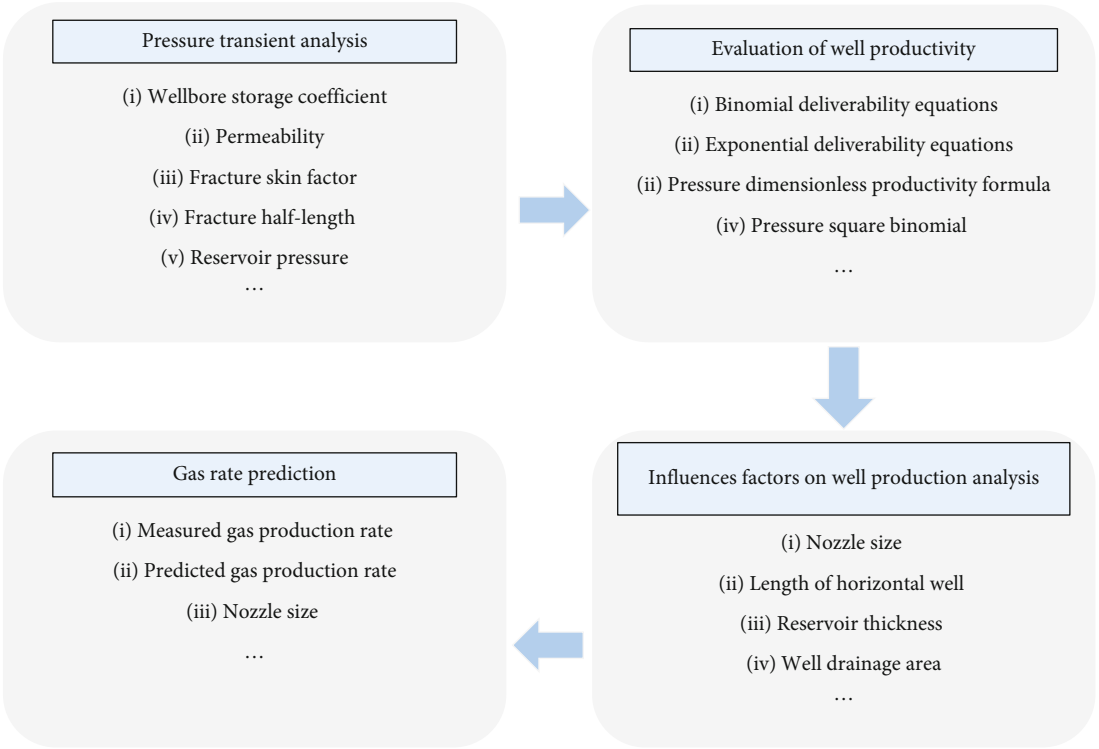

Figure 1: Workflow of the study.

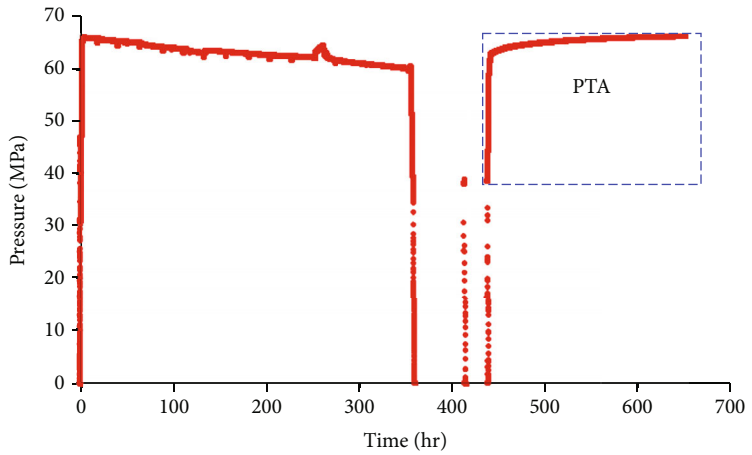

Figure 2: Pressure history of Well SX161.

horizontal well. Using the model of Qin et al., the pressure and its derivative matching curves are presented in Figure 3(b), and the interpretation results are shown in Table 1. Wellbore storage coefficient is 1.27 m^3/MPa. Reservoir permeability is 0.672×10^{-3} μm^2. Fracture skin factor is 0.75. Initial reservoir pressure is 68.21 MPa. However, compared with conventional model in Saphir, the fracture half-length is 16.8 m high-conductivity fracture and 53.1 m low-conductivity fracture. These values are closer to the fracturing design parameters, and demonstrates that the fracturing effect does not meet the expectation.

4. Well Productivity Analysis

The procedure for the gas well productivity test is to conduct a series of flow tests in different (generally more than 4) flow rates and measure the stabilized bottom-hole pressure data under each flow rates. For gas wells, the flow rate and bottom-hole pressure should satisfy the following relation [44]

$$p_R^2 - p_{wf}^2 = aq + bq^2, \quad (1)$$

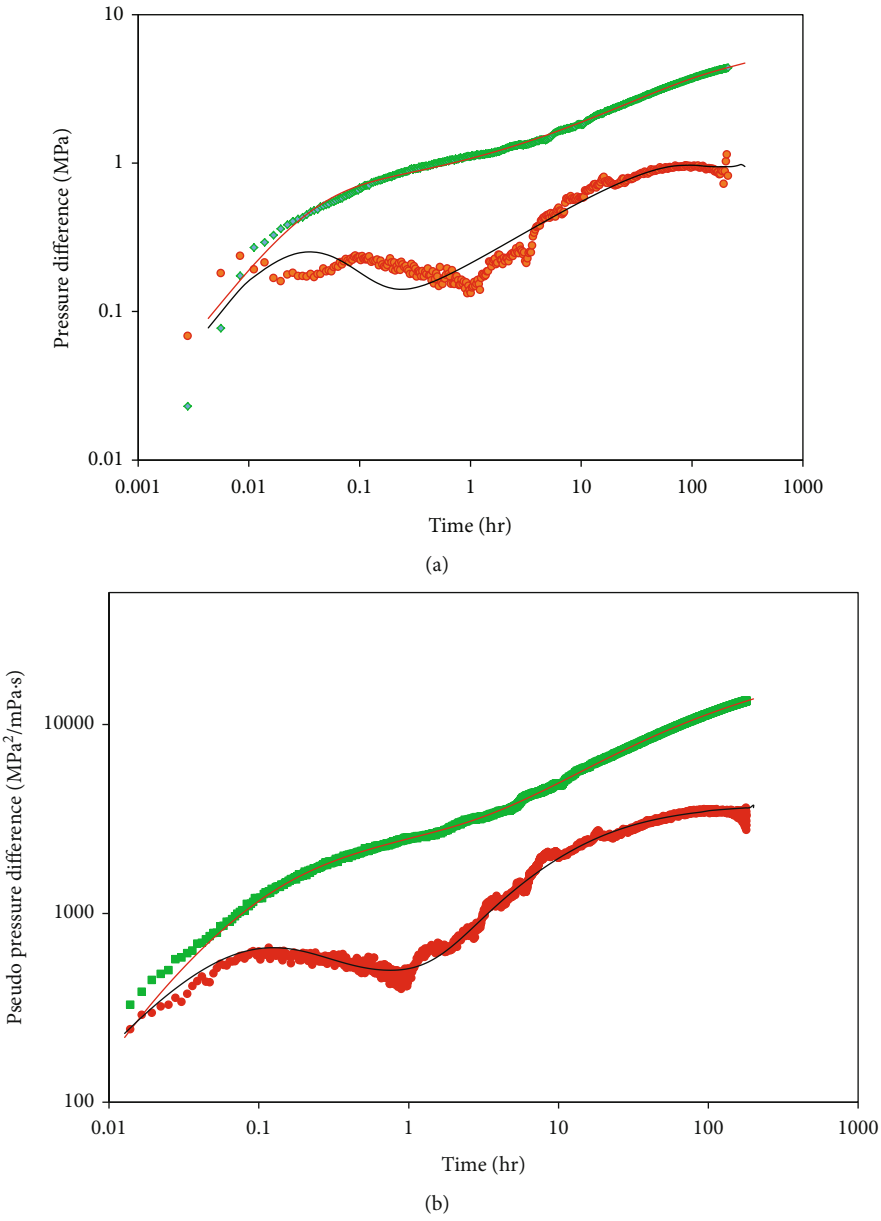

Figure 3: Comparison of pressure matching by Saphir and the model of Qin et al.

Table 1: Interpretation results between commercial software and the model of Qin et al.

	Saphir	Model of Qin et al.
Model	Constant wellbore Horizontal fractured well Homogeneous reservoir Infinite boundary	Constant wellbore Double-segment fracture Homogeneous reservoir Infinite boundary
Wellbore storage coefficient (m^3/MPa)	1.95	1.27
Permeability (10^{-3} μm^2)	0.586	0.672
Fracture skin factor	0.29	0.75
Fracture half-length (m)	20.56	16.8 + 53.1
Reservoir pressure (MPa)	68.91	68.21

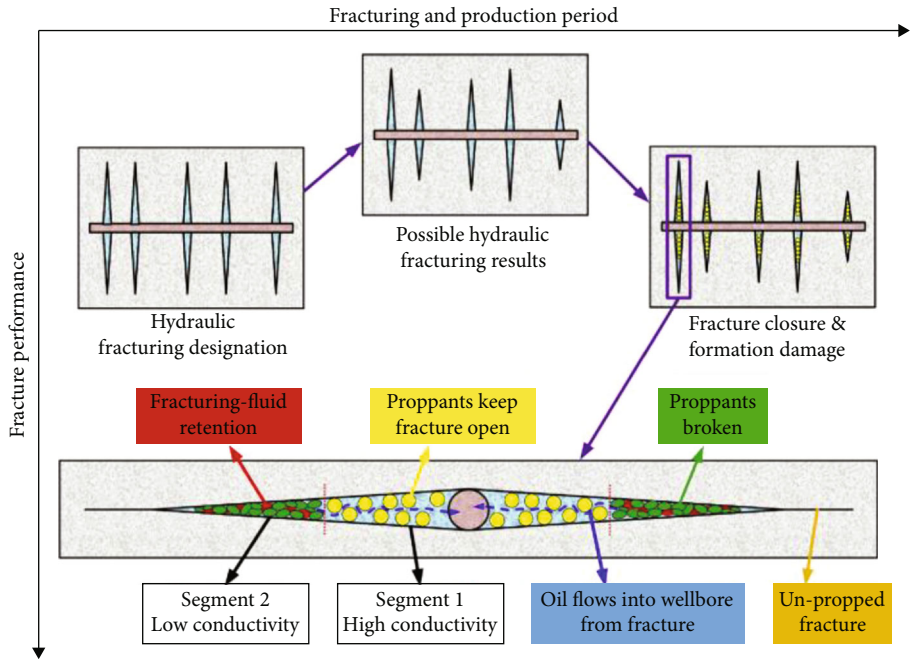

Figure 4: Fracture performance during different period [42].

Table 2: Measured data of productivity well test.

Oil nozzles (mm)	Bottom-hole pressure(MPa)	Gas rate (10^4m^3/d)	Oil rate (m^3/d)	Qt rate (10^4m^3/d)
5	67.217	2.535	26.05	2.829
6	66.45	3.758	37.38	4.179
7	65.265	6.2975	55.61	6.924
8	64.06	8.6358	79.02	9.526
9.2	62.87	13.44	122.16	14.817

where p_R is the average reservoir pressure, MPa. p_{wf} is the bottom-hole pressure, MPa. q is the gas rate, 10^4m^3/d. a is the laminar flow coefficient for gas wells. b is the turbulence coefficient for gas wells.

From Equation (1), we can obviously find that a plot of $p_R^2 - p_{wf}^2/q$ vs q has a linear relation with the intercept of a and slope of b. The plot applies to both linear flow and radial flow. Upon the a and b obtained, we can easily derive the absolute open flow of gas well.

$$q_{\mathrm{AOF}} = \frac{-b + \sqrt{b^2 + 4ap_R}}{2a}, \tag{2}$$

where q_{AOF} is the absolute gas flow rate of the well, 10^4m^3/d.

The measured pressure and rate for the Well SX161 is shown in Table 2. The reservoir pressure and the bottom-hole pressures in different oil nozzles are greater than the dew point pressure (57.12 MPa), indicating that the fluid flows in single phase under formation conditions. Two fluid types are used in the productivity evaluation: one is oil and gas equivalent, and the other one is single gas. In the oil and gas equivalent, the oil rate is converted into gas when evaluating the well's productivity. Three methods are applied here; the deliverability equations and the absolute gas flow potentials are presented in Table 3. We find that different methods yield different results.

It should be noted that the exponential productivity is a semiempirical formula, which has a high possibility of deviation in the interpretation results and is just used for double-check purpose. The pressure dimensionless productivity method is an empirical formula that commonly used in the industry, which may not be suitable for the productivity evaluation of the well in this field. Since the flow pressures and production rates in every system are not stable, it is recommended to extend the test time of every system to achieve stability in the next productivity test, to obtain the accurate absolute open flow potential, understand the productivity of single well, and guide the production allocation in the future.

There are many factors influencing the well productivity of horizontal well, including reservoir thickness, well drainage area, horizontal length, and so on. Joshi [45] proposed an equation to calculate the oil productivity of horizontal wells.

Table 3: Gas well production results by different methods.

Fluid type	Method	Equation	Absolute gas flow potential ($10^4 m^3/d$)
Oil and gas equivalent	Pressure square binomial	$p_R^2 - p_{wf}^2 = 0.0001 \times q + 0.3878 \times q^2$	144.22
	Exponential	$q = 0.02 \times \left(p_R^2 - p_{wf}^2\right)^{0.9834}$	111.35
	Pressure dimensionless productivity	$q/q_{max} = 1 - 0.202\left(p_{wf}/p_R\right) - 0.798\left(p_{wf}/p_R\right)^2$	80.64
Gas	Pressure square binomial	Negative slope	/
	Exponential	$q = 0.0148 \times \left(p_R^2 - p_{wf}^2\right)^{1.0155}$	99.41
	Pressure dimensionless productivity	$q/q_{max} = 1 - 0.202\left(p_{wf}/p_R\right) - 0.798\left(p_{wf}/p_R\right)^2$	78.21

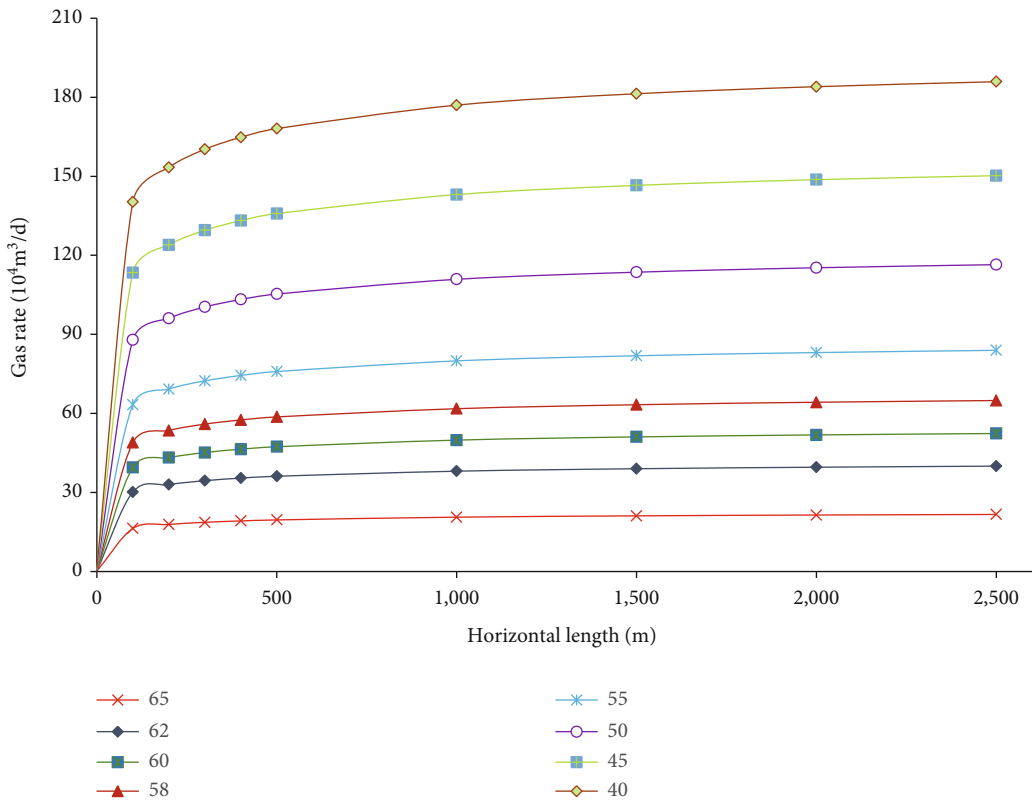

Figure 5: Relationship between gas rate and horizontal length in different bottom-hole-pressure.

$$q_g = \frac{kh\left(\psi_i - \psi_{wf}\right)}{1422T\left[\ln\left(r_{eh}/r'_w\right) - 0.75 + S\right]}, \tag{3}$$

where

$$r_{eh} = \sqrt{\frac{43560A}{\pi}}, \tag{4}$$

$$A = \frac{L(2b) + \pi y^2}{43560}, \tag{5}$$

$$r'_w = \frac{r_{eh}(L/2)}{x\left[1 + \sqrt{1 - (L/2x)^2}\right]\left[L/(2r_w)^{h/L}\right]}, \tag{6}$$

$$x = \left(\frac{L}{2}\right)\left[0.5 + \sqrt{0.25 + (2r_{eh}/L)^4}\right]^{0.5}. \tag{7}$$

q_g is the gas rate, $10^3 ft^3/d$. k is the permeability, $10^{-3}\,\mu m^2$. h is the fracture thickness, ft. ψ_i is the initial pseudopressure, psi^2/cp. ψ_{wf} is pseudo-bottom-hole-pressure, psi^2/cp. T is the reservoir temperature, R. S is the skin factor. r_{eh} is the drainage radius, ft. A is the drainage area, acre. L is the horizontal length, ft. x is the half of the major axis of the drainage ellipse,

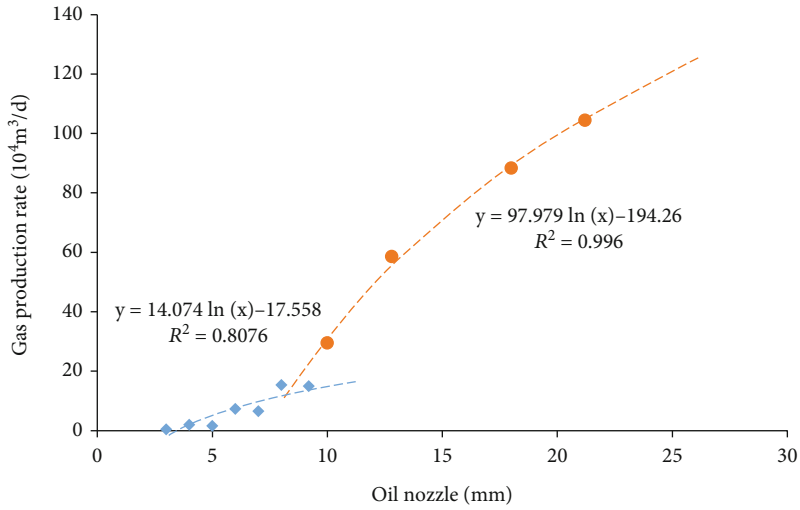

Figure 6: Correlation between gas well production rate and oil nozzle.

ft. y is the half the minor axis of the drainage ellipse, ft. r_w is the well radius, ft.

The horizontal section length of Well SX161 is 500 m. The half of the minor axis of the drainage ellipse is 100°m. Well radius is 0.06°m. Formation thickness is 17.16°m. Reservoir temperature is 126.8°C. Based on the interpretation result of pressure transient analysis, the skin factor is 0.99. The reservoir permeability is $5.641 \times 10^{-3} \circ \mu m^2$, and the reservoir pressure is 67.854°MPa. Applying Equations (3)–(7), we obtain the gas production rate with horizontal section length under different bottom-hole flow pressure conditions as shown in Figure 5.

We find that the gas production rate increases sharply with the increase of horizontal length firstly, then it turns to a slow upward trend. It reminds us that the oil increase rate decreases with the increase of horizontal length. The long horizontal section also adds the risk of water breakthrough and need more drilling cost. Therefore, it should balance the oil productivity and horizontal length. In addition, the gas production rate increases with the decrease of bottom-hole-pressure, as well acknowledged. Interestingly, the "inflection point", which signifies the turning point of oil well production increase rate, increases with the decrease of bottom-hole-pressure. Therefore, the long horizontal wells cannot give full play to its role of increasing production capacity under the pressure maintaining production condition. The horizontal length of Well SX161 is 500 m. If the oil field managers plan to amplify the pressure difference for the well production in the future, they are suggested to consider increasing the horizontal length, but no more than 1000 m as far as possible.

There are many methods to predict oil production, such as deliverability equations, rate transient analysis, empirical formula, nozzle size, and oil productivity regression. This well was tested twice for productivity, and the production rate grows greatly with the increase of oil nozzle. Therefore, it is necessary to know the production change rule and the key influence factors of the well, so as to facilitating the later production allocation guidance. Through analyzing the relationship between gas production and the oil nozzle (Figure 6), we find that

$$y = \begin{cases} 14.074 \times \ln(x) - 17.558 & r < 7.8\text{mm}, \\ 97.979 \times \ln(x) - 194.26 & r \geq 7.8\text{mm}. \end{cases} \quad (8)$$

Table 4 presents the comparison between measured gas rate and the predicted gas rate that estimated by equation *, which shows a great consistency. Based on the regression rule, the predicted gas production rates with the oil nozzles of 25 mm, 30 mm, and 35 mm, are estimated. It should be noted that the gas rate cannot always increase with the increase of oil nozzle.

Table 4: Comparison between measured and predicted gas production rate.

Oil nozzle (mm)	Measured gas production rate (10^4m^3/d)	Predicted gas production rate (10^4m^3/d)
4	2.46	1.95
5	2.42	5.09
6	8.08	7.65
7	7.01	9.83
8	15.82	11.71
9.2	15.30	13.68
10	28.90	31.34
12.8	58.67	55.53
18	88.60	88.94
21.2	104.66	104.97
25	—	121.12
30	—	138.99
35	—	154.09

5. Summary and Conclusions

In this paper, we investigate the pressure behavior of multi-fractured horizontal well and evaluate the gas well productivity based on a field case in Xinjiang Oilfield, China. Several conclusions are derived as follows:

(i) The formation and fracture parameters can be interpreted through production data. The fracture half-length is 16.8 m high-conductivity fracture and 53.1 m low-conductivity fracture can be obtained by the model of Qin et al., which provides an approach to evaluate the fracturing effect.

(ii) The gas well productivity is evaluated combining different methods. It is recommended to extend the test time in each nozzle to achieve stability in the next productivity test and to obtain the accurate absolute open flow potential.

(iii) The key factors that influence gas well productivity are analyzed; the nozzle size is the most important factor, followed by the length of horizontal wells, and the relation of gas rate and oil nozzle is obtained.

(iv) The predicted gas production rates with the oil nozzles of 25 mm, 30 mm, and 35 mm are estimated as $121.12 \times 10^4 m^3/d$, $138.99 \times 10^4 m^3/d$, and $154.09 \times 10^4 m^3/d$

Nomenclature

p_R: average reservoir pressure, MPa
p_{wf}: bottom-hole pressure, MPa
q: gas rate, $10^4 m^3/d$
a: laminar flow coefficient for gas wells
b: turbulence coefficient for gas wells
q_{AOF}: absolute gas flow rate of the well, $10^4 m^3/d$
q_g: gas rate, $10^4 m^3/d$
k: reservoir permeability, $10^{-3}\ \mu m^2$
h: fracture thickness, m
ψ_i: initial pseudo-pressure, $MPa^2/mPa{\cdot}s$
ψ_{wf}: pseudo-bottom-hole-pressure, $MPa^2/mPa{\cdot}s$
T: reservoir temperature, R
S: skin factor
r_{eh}: drainage radius, m
A: drainage area, m^2
L: horizontal length, m
x: the half the major axis of the drainage ellipse, m
y: the half the minor axis of the drainage ellipse, m
r_w: well radius, m.

Data Availability

The data used to support the findings of this study are included within the article. The data used to support the findings of this study are available from the corresponding author upon request.

Conflicts of Interest

The authors declare no conflicts of interest.

Acknowledgments

This work is supported by supported by the National Natural Science Foundation of China (52104049); the Strategic Cooperation Technology Projects of CNPC and CUPB (ZLZX2020-02). We gratefully acknowledge the financial support from Science Foundation of China University of Petroleum, Beijing (2462022BJRC004).

References

[1] B. A. Mohammad, D. Morteza, and Z. Sohrab, "Semi-analytical solution for productivity evaluation of a multi-fractured horizontal well in a bounded dual-porosity reservoir," *Journal of Hydrology*, vol. 581, article 124288, 2020.

[2] Y. Wang and L. F. Ayala, "Explicit determination of reserves for variable-bottomhole-pressure conditions in gas rate-transient analysis," *SPE Journal*, vol. 25, no. 1, pp. 369–390, 2020.

[3] Y. Wang, S. Cheng, K. Zhang et al., "A comprehensive work flow to characterize waterflood-induced fractures by integrating real-time monitoring, formation test, and dynamic production analysis applied to Changqing oil field, China," *SPE reservoir evaluation and engineering*, vol. 22, no. 2, pp. 692–708, 2019.

[4] C. Wei, Y. Liu, Y. Deng, S. Cheng, and H. Hassanzadeh, "Temperature transient analysis of naturally fractured geothermal reservoirs," *SPE Journal*, vol. 27, no. 5, pp. 2723–2745, 2022.

[5] C. Wei, Y. Liu, Y. Deng, S. Cheng, and H. Hassanzadeh, "Analytical well-test model for hydraulicly fractured wells with multiwell interference in double porosity gas reservoirs," *Journal of Natural Gas Science and Engineering*, vol. 103, article 104624, 2022.

[6] P. Jia, M. Ma, C. Cao, L. Cheng, H. Yin, and Z. Li, "Capturing dynamic behavior of propped and unpropped fractures during flowback and early-time production of shale gas wells using a novel flow-geomechanics coupled model," *Journal of Petroleum Science and Engineering*, vol. 208, no. 2022, article 109412, 2022.

[7] Z. Qu, B. Liu, and J. Zhang, "Study on polymer sweep radius and field application based on multi-layer and three-area composite well test," *Xinjiang Oil & Gas*, vol. 16, no. 4, pp. 66–69, 2020.

[8] C. Wei, S. Cheng, K. Tu et al., "A hybrid analytic solution for a well with a finite-conductivity vertical fracture," *Journal of Petroleum Science and Engineering*, vol. 188, article 106900, 2020.

[9] J. Zeng, J. Liu, W. Li, Y. K. Leong, D. Elsworth, and J. Guo, "Shale gas reservoir modeling and production evaluation considering complex gas transport mechanisms and dispersed distribution of kerogen," *Petroleum Science*, vol. 18, no. 1, pp. 195–218, 2021.

[10] H. Wu, Y. Jiang, and H. Liu, "Analysis on water breakthrough characteristics of edge bottom water composite reservoir in glutenite buried hill," *Xinjiang Oil & Gas*, vol. 17, no. 1, pp. 42–64, 2021.

[11] E. Sun, B. Li, and Q. Peng, "Method of productivity analysis for oil and water two-phase horizontal well during high water cut stage," *Xinjiang Oil & Gas*, vol. 15, no. 3, pp. 54–57, 2019.

[12] M. Wei, Y. Duan, M. Dong, Q. Fang, and M. Dejam, "Transient production decline behavior analysis for a multi-fractured horizontal well with discrete fracture networks in shale gas reservoirs," *Journal of Porous Media*, vol. 22, no. 3, pp. 343–361, 2019.

[13] S. D. Joshi, "Augmentation of well productivity with slant and horizontal wells (includes associated papers 24547 and 25308)," *Journal of Petroleum Technology*, vol. 40, no. 6, pp. 729–739, 1988.

[14] F. Wang, R. Gong, Z. Huang, Q. Meng, Q. Zhang, and S. Zhan, "Single-phase inflow performance relationship in stress-sensitive reservoirs," *Advances in Geo-Energy Research*, vol. 5, no. 2, pp. 202–211, 2021.

[15] Y. Wang, S. Cheng, K. Zhang, and L. F. Ayala, "Investigation on the transient pressure response of water injector coupling the dynamic flow behaviors in the wellbore, waterflood-induced fracture and reservoir: semi-analytical modeling and a field case," *International Journal of Heat and Mass Transfer*, vol. 130, pp. 668–679, 2019.

[16] C. Wei, S. Cheng, Y. Wang et al., "Practical pressure-transient analysis solutions for a well intercepted by finite conductivity vertical fracture in naturally fractured reservoirs," *Journal of Petroleum Science and Engineering*, vol. 204, article 108768, 2021.

[17] Y. Wu, L. Cheng, J. Killough et al., "Integrated characterization of the fracture network in fractured shale gas reservoirs–stochastic fracture modeling, simulation and assisted history matching," *Journal of Petroleum Science and Engineering*, vol. 205, article 108886, 2021.

[18] Y. Wu, L. Cheng, L. Ma et al., "A transient two-phase flow model for production prediction of tight gas wells with fracturing fluid-induced formation damage," *Journal of Petroleum Science and Engineering*, vol. 199, article 108351, 2021.

[19] C. S. Matthews and D. G. Russell, *Pressure Build-Up and Flow Tests in Wells*, Monograph Series, SPE, Dallas, 1967.

[20] A. S. Odeh and L. G. Jones, "Pressure drawdown analysis, variable-rate case," *JPT*, vol. 17, no. 8, pp. 960–964, 1965.

[21] J. E. Warren and P. J. Root, "The behavior of naturally fractured reservoirs," *Society of Petroleum Engineers Journal*, vol. 3, no. 3, pp. 245–255, 1963.

[22] D. P. Bourdet and A. C. Gringarten, "Determination of fissure volume and block size in fractured reservoirs by type-curve analysis," in *Paper presented at the SPE Annual Technical Conference and Exhibition*, Dallas, 1980.

[23] H. Stehfest, "Algorithm 368: numerical inversion of Laplace transforms D5," *Communications of the ACM*, vol. 13, no. 1, pp. 47–49, 1970.

[24] D. P. Bourdet and J. A. Ayoub, "Interpreting data in fractured reservoirs," *World Oil*, vol. 197, no. 5, pp. 77–87, 1983.

[25] D. P. Bourdet, T. M. Whittle, and A. A. Douglas, "A new set of type curves simplifies well test analysis," *World Oil*, vol. 196, no. 6, pp. 95–106, 1983.

[26] T. von Schroeter, F. Hollaender, and A. Gringarten, "Deconvolution of well test data as a nonlinear total least squares problem," in *Paper presented at the SPE Annual Technical Conference and Exhibition*, New Orleans, 2001.

[27] A. C. Gringarten, "From straight lines to deconvolution: the evolution of the state of the art in well test analysis," *SPE Reservoir Evaluation & Engineering*, vol. 11, no. 1, pp. 41–62, 2008.

[28] A. C. Gringarten, D. P. Bourdet, P. A. Landel, and V. J. Kniazeff, "A comparison between different skin and wellbore storage type-curves for early-time transient analysis," in *Paper presented at the SPE annual technical conference and exhibition*, Las Vegas, Nevada, 1979.

[29] L. Aluko, J. Cumming, and A. C. Gringarten, "Using deconvolution to estimate unknown well production from scarce wellhead pressure data," *Paper presented at the SPE annual technical conference and exhibition, virtual*, 2020, 2020.

[30] Y. Wang, S. Cheng, N. Feng et al., "Semi-analytical modeling for water injection well in tight reservoir considering the variation of waterflood - Induced fracture properties – case studies in Changqing oilfield, China," *Journal of Petroleum Science and Engineering*, vol. 159, no. 2017, pp. 740–753, 2017.

[31] Y. Wang, S. Cheng, F. Zhang et al., "Big data technique in the reservoir parameters' prediction and productivity evaluation: a field case in western South China sea," *Gondwana Research*, vol. 96, no. 2021, pp. 22–36, 2021.

[32] F. Zhang, S. Ma, and J. Zhang, "Derivation and application of generalized binomial productivity equation," *China Offshore Oil and Gas*, vol. 29, no. 6, pp. 87–91, 2017.

[33] J. Shi, J. Wu, Z. Sun, Z. H. Xiao, C. Liu, and K. Sepehrnoori, "Methods for simultaneously evaluating reserve and permeability of undersaturated coalbed methane reservoirs using production data during the dewatering stage," *Petroleum Science*, vol. 17, no. 4, pp. 1067–1086, 2020.

[34] X. Li, J. Liang, W. Xu, X. Li, and X. Tan, "The new method on gas-water two phase steady-state productivity of fractured horizontal well in tight gas reservoir," *Advances in Geo-Energy Research*, vol. 1, no. 2, pp. 105–111, 2017.

[35] G. W. Swift and O. G. Kiel, *The Prediction of Gas-Well Performance Including the Effect of Non Darcy Flow; JPT, 791; Trans., AIME*, 1962.

[36] H. R. Pierce and E. L. Rawlins, *The Study of a Fundamental Basis for Controlling and Gaging Natural-Gas Wells, Part 1-Computing the Pressure at the Sand in a Gas Well*, US Bureau of Mines, Washington DC, 1929.

[37] M. H. Cullender, "The isochronal performance method of determining the flow characteristics of gas wells," in *Paper presented at Petroleum branch fall meeting*, pp. 18–21, Dallas, Texas, USA, 1953.

[38] D. L. Katz, D. Cornell, and R. Kobayashi, *Handbook of Natural Gas Engineering*, McGraw-Hill Book Company, Inc, New York, 1959.

[39] H. Zhuang, *Dynamic Well Testing in Petroleum Exploration and Development*, Petroleum Industry Press, Beijing, 2009.

[40] R. W. Chase and H. Alkandari, "Prediction of gas well deliverability from just a pressure buildup or drawdown test," in *Paper presented at the SPE eastern regional meeting*, Pittsburgh, Pennsylvania, 1993.

[41] C. Wang, Z. P. Li, and F. P. Lai, "A novel binomial deliverability equation for fractured gas well considering non-Darcy effects," *Journal of Natural Gas Science and Engineering*, vol. 20, pp. 27–37, 2014.

[42] J. Qin, S. Cheng, Y. He et al., "An innovative model to evaluate fracture closure of multi-fractured horizontal well in tight gas reservoir based on bottom-hole pressure," *Journal of Natural Gas Science and Engineering*, vol. 57, pp. 295–304, 2018.

[43] J. Qin, S. Cheng, Y. He et al., "A novel well-testing model to analyze production distribution of multi-stage fractured horizontal well," *Journal of Natural Gas Science and Engineering*, vol. 59, pp. 237–249, 2018.

[44] L. G. Jones, E. M. Blount, and O. H. Glaze, "Use of short term multiple rate flow tests to predict performance of wells having turbulence," in *Paper presented at the SPE annual fall technical conference and exhibition*, New Orleans, Louisiana, 1976.

[45] S. D. Joshi, "Augmentation of well productivity using slant and horizontal wells," in *Paper presented at the SPE annual technical conference and exhibition*, New Orleans, Louisiana, 1986.

Hindawi
Geofluids
Volume 2022, Article ID 1293143, 13 pages
https://doi.org/10.1155/2022/1293143

Research Article

A Geocoupling Simulation Method for Fractured Reservoir Production

Xin Li,[1] **Zhengdong Lei**,[1] **Qinghui Zhang**,[2] **and Yuanqing Zhang**[3]

[1]*Research Institute of Petroleum Exploration and Development (RIPED), Beijing 100083, China*
[2]*Research Institute of Exploration and Development of Qinghai Oilfield Company, Dunhuang 736202, China*
[3]*Research Institute of Exploration and Development of Daqing Oilfield Company, Daqing 163412, China*

Correspondence should be addressed to Zhengdong Lei; leizhengdong@petrochina.com.cn

Received 8 April 2022; Revised 28 July 2022; Accepted 22 August 2022; Published 23 September 2022

Academic Editor: Bailu Teng

Reservoir simulation is critical to the design of reservoir development plan and has been extensively used. However, it is challengeable for to simulate the production process for fractured reservoirs, because of the fracture geometry and the fracture deformation. Specifically, three problems need to be solved. First, there is a lack of mathematical models that can predict the fracture deformation with acceptable precision. Second, the fracture deformation is stress-dependent; therefore, a geocoupled equation should be used to quantify the stress change, but the solution is extremely expensive. Third, the fracture geometries pose great challenges to traditional gridding techniques. This paper proposes a new geocoupling simulation method that is capable of modeling the complex fracture geometry as well as the fracture mechanical behavior. The geomechanical effects and the reservoir production performance are modeled through an implicit geocoupled model, which is developed based on the poro-mechanics theory. The fixed stress strategy is used to solve the geocoupled equations. Moreover, a comprehensive fracture modeling method is proposed, in terms of the fracture deformation model and the fracture gridding technique to model the fracture effects. Ultimately, this method is used to analyze two field-scale cases. The results demonstrate that this method exhibits good practicability and has practical significance for fractured reservoir development.

1. Introduction

In recent years, more and more attention has been attracted to fractured reservoirs. Actually, most unconventional reservoirs can be classified as fractured reservoirs. In fractured reservoir development, fracture is the major flow channel. Understanding the fracture effects on production is important, but is also extremely difficult. The reasons are:

1.1. Fracture Geometry. Fracture geometry is critical to reservoir simulation but is difficult to be integrated into the simulation algorithm [1]. On one hand, the geometry is irregular; on the other hand, the combined form of fracture networks is varied. As the properties of fractures are very different from those of the matrix, fractured reservoirs exhibit a high degree of heterogeneity. Describing the geometric features of fractures is challenging because the fractures exhibit various length scales and complex shapes. In a simulation, as the evolution of mechanical unknowns are not as dramatic as that of flow unknowns, the fracture geometry could be simplified in geomechanics simulation, but in flow simulation, the fracture geometry should be modeled explicitly. Traditionally, reservoir simulations use the dual-porosity dual permeability (DPDK) model [2] to model the fracture effects. DPDK treats the fractures and the matrix as two overlapped interacting continua. In a DPDK grid element, fractures are distributed in a predetermined pattern, and the transmissibility between fracture and matrix is derived accordingly. As the fractures are idealized in DPDK, the transmissibility is misrepresented in the case of large-scale fractures, making the application of DPDK limited in fractured reservoir simulation. Different from DPDK, both the discrete fracture model [3] (DFM) and the embedded discrete fracture model [4, 5] (EDFM) are capable of representing real fracture geometries. DFM is the most direct method because the fractures are modeled using grid

elements. Flow behaviors in fractures and between fractures and matrix are calculated using the grid transmissibility. The nature of DFM brings both advantages and disadvantages for DFM. The advantages are as follows: (1) the flux calculation method is simple and (2) the accuracy is high. The disadvantage is that the fidelity of fracture representation depends on the gridding technique; currently, the "X" shaped fractures could not be modelled. The limitation of DFM leads the development of the embedded discrete fracture model (EDFM). EDFM models fractures with virtual 2D polygon plates, which are inserted into the background grid. As the computational domains of the fractures and the matrix are different, the complicated gridding is not necessary in EDFM. The flow mass transfer between fractures and matrix is calculated using the non-neighboring connections (NNC). Three types of NNC are required in EDFM; they are as follows: (1) NNC between a fracture cell and its neighboring matrix grid block; (2) NNC between two cells of an individual fracture; and (3) NNC between two intersecting fractures. The detailed procedure using EDFM modeling fracture flow could be found in the work of Li [6].

1.2. Fracture Mechanic Behavior. In reservoir geomechanics simulation, the fracture mechanical deformation is modeled with a tailored constitutive model which is a superposition of fracture and matrix properties. The matrix can be treated as an elastic-plastic block, and the deformation could be calculated according to the elastic-plastic mechanics. However, fracture deformation is a complicated question because of the different stress-strain relationships between normal and shearing deformations [7]. For normal deformation, the constitutive relationship is monotonic and nonlinear. Researchers have proposed different empirical constitutive models [8–10] to describe the relationship. The most commonly used models are Shehata's model [11] and Bandis' model [12]. But for shear deformation, the constitutive relationships between shear stress and shear strain are not monotonic due to peak-shear strength [13]. Specifically, the fracture pre-peak deformation is usually assumed to be elastic, whereas the post-peak deformation is plastic [14]. Among the extant models, Barton's empirical model [15] is the most frequently utilized due to its simplicity and capability of predicting the shearing deformation of fractures with acceptable precision. Moreover, some theoretical models are based on the solid mechanics are proposed, and related works can be seen in Desai [16] and Amadei [17]. The most widely used theoretical model is Plesa's model [18], which is based on the theory of plasticity and contact mechanics. Currently, existing fracture constitutive models are still immature. Empirical models provide reasonable results in a predetermined range of stresses, but since the principles of energy conservation are not involved in such models, some nonphysical results may be produced when complex mechanical deformation processes are involved; moreover, because the model establishment is not based on a strict mathematical derivation, the robustness of empirical models cannot be guaranteed. Even through the theoretical model is more rigorous, the existing mechanics theory is not capable of modeling fracture behaviors in all aspects.

1.3. Geomechanics Simulation. Because of the importance of reservoir deformation, 3D mechanical calculation is necessary for fractured reservoir simulation. Two types of simulation methods, i.e., the continuum method and the discrete method, can be used. The finite difference method (FDM) discretizes the mechanical equations by replacing the partial derivatives with the numerical differences defined on neighboring grid points directly. Under preassigned initial/boundary conditions, the mechanical deformation can be obtained by solving the discrete equation. However, because of the complex geometry of the reservoir numerical domain, FDM may not be a suitable method. The finite element method (FEM) [19] which was first proposed in the early 1960s offers another choice. The advantages of FEM are its flexibility in modeling reservoir geometries and the convenience of dealing with complicated boundary conditions. To solve a problem, FEM also discretizes the target reservoir into many regular-shaped elements. The difference is that FEM does not discrete the equation directly, but set up the formulation in a weak form, and replaces the initial function with a set of trial functions for each subdomain. The discrete process for a FEM equation follows the law of energy conservation, so its results are more physical. In recent years, to improve the capacity of FEM in fractured reservoir applications, many corresponding developments have been proposed, such as the Generalized/eXtend Finite Element Method (GFEM), which is developed based on the partition of unity principle [20], the Virtual Element Method [21] (VEM), and the Boundary Element Method [22] (BEM). As reservoir simulation is for macroscale problems, the block-type discrete methods are also suitable. The most well-known and representative discrete method is the distinct element method (DEM) [23]. In the original framework of DEM, the solution strategy is explicit. Shi and Goodman further proposed an implicit solution strategy for DEM, which is also named the [24] discontinuous deformation analysis (DDA).

To integrate the geomechanical behaviors, the geomechanics equation and the flow equation should be coupled, and the coupling process would lead to a complex equation system. Three candidate solution schemes exist [25]: the loosely coupled scheme, the fully coupled scheme, and the sequentially coupled scheme. In loosely coupled scheme, the coupling is explicit. The geomechanical equation is solved every certain time step. Although this method saves computational costs compared to other coupling techniques, it is not rigorous and fails to capture some physical phenomena. In contrast, both fully coupled scheme and sequentially coupled scheme are implicit. Fully coupled scheme solves the governing equations of fluid flow and mechanics simultaneously at every time step. It is also unconditionally stable when the coupled problem is well-posed, but the computational cost can be prohibitively expensive. Sequential implicit scheme partitions the coupled problem into two subproblems, and the subproblems could be solved by different methods. The solution is identical to that calculated from the fully coupled scheme, but the computational cost is much less. The fixed stress splitting strategy [26] is an ideal sequential implicit scheme. It solves the flow sub-problem first with fixed volumetric stress. Kim et al. have shown that fixed-stress splitting exhibits excellent convergence properties for both single-phase and multiphase flow

problems [27]. From a pragmatic perspective view, fixed stress splitting is preferred to other schemes in geocoupled reservoir simulations.

This paper proposes a new geocoupled model for fractured reservoir simulation. The core idea of this model is that it emphasizes the effects of fractures and geomechanics simultaneously. The remainder of this paper is organized as follows: Section 2 presents the mathematical model for compositional flow and geomechanics. Section 3 describes the fracture model, including the fracture constitutive model, and the method to estimate fracture permeability. Section 4 proposes the fracture gridding technique, which includes the grid system and fracture modeling method. Section 5 first validates the accuracy of this model with two benchmark cases and then presents two large-scale cases to illustrate the applicability of this model. This work is concluded in Section 6 with a discussion of the advantages of this model.

2. Governing Equations

We treat that the solid computational domain and the fluid computational domain are overlapped. The governing equation of fluid flow is set up based on the theory of mass balance, and the governing equation of geomechanics is based on the theory of momentum conservation. Under the assumption of (1) quasi-static, (2) linear elastic, and (3) infinitesimal transformation, the governing equation for geomechanics can be written as

$$\begin{aligned} \mathrm{Div}(\mathbf{C}_{\mathrm{dr}} : \boldsymbol{\varepsilon} - b p_{\mathrm{E}} \boldsymbol{\delta}) + \left[\boldsymbol{\varphi}\rho_f + (\mathbf{1} - \boldsymbol{\varphi})\rho_s\right]\mathbf{g} = \mathbf{0}, \\ \boldsymbol{\varepsilon} = \frac{1}{2}(\mathbf{u}\nabla + \nabla\mathbf{u}), \end{aligned} \tag{1}$$

where Div(·) is the divergence operator; Cdr is the rank-4 elastic drained bulk modulus; $\boldsymbol{\varepsilon}$ is the strain tensor; b is the Biot coefficient; pE = Swpw + Sopo + Sgpg is the equivalent pore pressure; Sw, Sg, and So denote the saturation of water, gas, and oil, respectively; pw, pg, and po denote the pressure of water, gas, and oil phase, respectively; δ is the rank-2 identity tensor; ϕ is the true porosity; ρf = Swρw + Soρo + Sgρg is the fluid density; ρs is the rock density; g denotes gravity; and $\boldsymbol{u}$ is the displacement.

Related studies show that the phase transition behavior of underground fluid [28, 29] is very complex; therefore, we use the fully compositional flow model as the flow governing equations. The mass-balance equation for hydrocarbon component i is expressed in terms of the Eulerian derivative as

$$\begin{aligned} &\frac{\partial\left[\left(x_i S_{\mathrm{o}}\rho_{\mathrm{o}} + y_i S_{\mathrm{g}}\rho_{\mathrm{g}}\right)\phi\right] + \left[\left(x_i S_{\mathrm{o}}\rho_{\mathrm{o}} + y_i S_{\mathrm{g}}\rho_{\mathrm{g}}\right)\phi\right]\partial\varepsilon_{\mathrm{v}}}{\partial t} \\ &= \nabla\cdot\left[x_i\frac{\rho_{\mathrm{o}}k_{\mathrm{ro}}}{\mu_{\mathrm{o}}}k\left(\nabla p_{\mathrm{o}} - \rho_{\mathrm{o}}\vec{g}\right) + y_i\frac{\rho_{\mathrm{g}}k_{\mathrm{rg}}}{\mu_{\mathrm{g}}}k\left(\nabla p_{\mathrm{g}} - \rho_{\mathrm{g}}\vec{g}\right)\right] - q_i, \end{aligned} \tag{2}$$

where x_i and y_i are the mole fractions of component i in the oil and the gas phase, respectively; ε_{v} is the volumetric strain, which is the trace of the strain tensor $\boldsymbol{\varepsilon}$; μ_{o} and μ_{g} are the viscosity of oil and gas, respectively; k_{ro} and k_{rg} are the relative permeability of oil and gas, respectively; k is the absolute permeability; and q_i is the mole flow rate of component i from the grid to wells and/or boundaries. Owning to the Euler's form and the infinitesimal transformation, both the flow equation and the geomechanics equation can be discretized on static grids. From the consideration of efficiency and stability, fixed stress splitting and iteration is an ideal solution method for our model. This is also proven in the benchmark tests hereinafter. Li et, al. [3] proposed flow equation in terms of coupling terms for the fixed-stress splitting, which can be expressed as

$$\begin{aligned} \frac{\mathrm{d}m_i}{\mathrm{d}t} = N_{i,\mathrm{p}}\frac{\partial p}{\partial t} + N_{i,S_{\mathrm{w}}}\frac{\partial S_{\mathrm{w}}}{\partial t} + N_{i,S_{\mathrm{g}}}\frac{\partial S_{\mathrm{g}}}{\partial t} + N_{i,x_1}\frac{\partial x_1}{\partial t} \\ + N_{i,y_1}\frac{\partial y_1}{\partial t}\cdots + N_{i,x_{nc}}\frac{\partial x_{nc}}{\partial t} + N_{i,y_{nc}}\frac{\partial y_{nc}}{\partial t} + N_{i,\sigma}\frac{\partial \sigma_v}{\partial t}, \end{aligned} \tag{3}$$

where $N_{\alpha,\beta}$ is the coupling coefficient and subscripts α and β denote a component and a variable, respectively. For component i, they are

$$N_{i,\mathrm{p}} = D_c\left(S_{\mathrm{w}}\frac{\partial p_{\mathrm{w}}}{\partial p_{\mathrm{g}}} + S_{\mathrm{o}}\frac{\partial p_{\mathrm{o}}}{\partial p_{\mathrm{g}}} + S_{\mathrm{g}}\right) + x_i S_{\mathrm{g}}\phi\frac{\partial\rho_{\mathrm{g}}}{\partial p_{\mathrm{g}}} + y_i S_{\mathrm{o}}\phi\frac{\partial\rho_{\mathrm{o}}}{\partial p_{\mathrm{g}}}, \tag{4}$$

$$N_{i,\boldsymbol{S_w}} = D_c\left(S_{\mathrm{w}}\frac{\partial p_{\mathrm{w}}}{\partial S_{\mathrm{w}}} + S_{\mathrm{o}}\frac{\partial p_{\mathrm{o}}}{\partial S_{\mathrm{w}}}\right) + y_i\rho_{\mathrm{o}}\phi\frac{\partial S_{\mathrm{o}}}{\partial S_{\mathrm{w}}}, \tag{5}$$

$$N_{i,S_g} = D_c\left(S_w\frac{\partial p_w}{\partial S_g} + S_o\frac{\partial p_o}{\partial S_g}\right) + x_i\rho_g\phi + y_i\rho_o\phi\frac{\partial S_o}{\partial S_g}, \tag{6}$$

$$N_{i,x_i} = D_c\left(S_w\frac{\partial p_w}{\partial x_i} + S_o\frac{\partial p_o}{\partial x_i}\right) + S_g\rho_g\phi + x_i S_g\phi\frac{\partial\rho_g}{\partial x_i}, \tag{7}$$

$$N_{i,y_i} = D_c\left(S_w\frac{\partial p_w}{\partial y_i} + S_o\frac{\partial p_o}{\partial y_i}\right) + S_o\rho_o\phi + y_i S_o\phi\frac{\partial\rho_o}{\partial y_i}, \tag{8}$$

$$N_{i,\sigma} = \frac{\left(x_i S_{\boldsymbol{g}}\rho_{\boldsymbol{g}} + y_i S_{\boldsymbol{o}}\rho_{\boldsymbol{o}}\right)b}{K_{\boldsymbol{dr}}}, \tag{9}$$

where $D_{\boldsymbol{c}} = (x_i S_{\boldsymbol{g}}\rho_{\boldsymbol{g}} + y_i S_{\boldsymbol{o}}\rho_{\boldsymbol{o}})(((b-\phi)/K_{\boldsymbol{s}}) + (K_{\boldsymbol{s}}/K_{\boldsymbol{dr}}))$.

For the water phase, the coupling coefficients are as follows:

$$N_{\boldsymbol{w,p}} = D_{\boldsymbol{w1}}\frac{\partial p_{\boldsymbol{w}}}{\partial p_{\boldsymbol{g}}} + D_{\boldsymbol{w2}}\frac{\partial p_{\boldsymbol{o}}}{\partial p_{\boldsymbol{g}}} + \frac{b-\phi}{K_{\boldsymbol{s}}}S_{\boldsymbol{g}} + \frac{\rho_{\boldsymbol{w}}S_{\boldsymbol{w}}S_{\boldsymbol{g}}b^2}{K_{\boldsymbol{dr}}}, \tag{10}$$

$$N_{\boldsymbol{w},\boldsymbol{S_w}} = D_{\boldsymbol{w1}}\frac{\partial p_{\boldsymbol{w}}}{\partial S_{\boldsymbol{w}}} + D_{\boldsymbol{w2}}\frac{\partial p_{\boldsymbol{o}}}{\partial S_{\boldsymbol{w}}} + \rho_{\boldsymbol{w}}\phi, \tag{11}$$

$$N_{w,S_g} = D_{w1}\frac{\partial p_w}{\partial S_g} + D_{w2}\frac{\partial p_o}{\partial S_g}, \tag{12}$$

$$N_{w,x_i} = D_{w1}\frac{\partial p_w}{\partial x_i} + D_{w2}\frac{\partial p_o}{\partial x_i}, \tag{13}$$

$$N_{w,y_i} = D_{w1}\frac{\partial p_w}{\partial y_i} + D_{w2}\frac{\partial p_o}{\partial y_i}, \tag{14}$$

$$N_{w,\sigma} = \frac{\rho_w S_w b}{K_{dr}}, \tag{15}$$

where $D_{w1} = ((b-\phi)/K_s)S_w + (\rho_w S_w^2 b^2/K_{dr}) + S_w\phi\rho_w c_w$ and $D_{w2} = ((b-\phi)/K_s)S_o + (\rho_w S_w S_o b^2/K_{dr})$.

When two hydrocarbon phases coexist, the equation system is not closed. Equal fugacity equations and linear constraints for compositions and saturations should be added to the equation system to constrain the variable set:

$$f_i^{\mathrm{L}} - f_i^{\mathrm{V}} = 0, i = 1, \cdots, n_c, \tag{16}$$

$$\sum_{i=1}^{nc} x_i - 1 = 0, \tag{17}$$

$$\sum_{i=1}^{nc} y_i - 1 = 0, \tag{18}$$

$$S_w + S_g + S_o = 1. \tag{19}$$

Equations (3) to (19) describe the geocoupled compositional flow equation system, where the variable set is $\mathbf{u}, p_g, S_w, S_g, S_o, x_1, \cdots, x_{nc}, y_1, \cdots, y_{nc}$. The Peng-Robinson (PR) equation of state and the L.B.C. model are used to calculate the fluid property.

3. Fracture Deformation Model

3.1. Fracture Constitutive Model. We choose the Barton-Bandis model to estimate fracture's deformation because (1) Barton's model can model the deformation on normal and shear deformation simultaneously and (2) the experimental stress range of the Barton-Bandis model could cover that of our problem. The definition of a fracture's compliance follows the work of Bandis et al. [12] and is expressed in matrix form as

For a fractured rock mass, the compliance is is assumed to be linear-elastic and is the inverse of the element stiffness matrix; n_f is the number of fractures; and s_j is the fracture spacing.

$$\mathbf{C}_j = \mathtt{diag}\left(\mathtt{K}_n^{-1}, \mathtt{K}_s^{-1}, \mathtt{K}_s^{-1}\right), \tag{20}$$

where the normal and shear stiffness are defined as follows:

$$K_n = K_{ni}\left[1 - \frac{\sigma_n}{v_m K_{ni} + \sigma_n}\right]^{-2}; K_s = K_s^m\left(2 - \frac{\sigma_n}{USC}\right)\left(\frac{\sigma_n}{USC}\right), \tag{21}$$

where K_n is the normal stiffness; K_{ni} is the initial normal stiffness; σ_n is the effective normal stress; v_m is the maximum closure; K_s is the shear stiffness; K_s^m is the maximum shear stiffness; and USC is the dimensionless compressive strength of rock. K_{ni} and v_m are related to the joint roughness coefficient (JRC), joint compressive strength (JCS), and unstressed joint aperture a_0:

$$\mathtt{K}_{ni} = -7.15 + 1.75\,\mathtt{JRC} + 0.02\frac{\mathtt{JCS}}{\mathtt{a}_0}, \tag{22}$$

$$\mathtt{v}_m = -0.1023 - 0.0074\,\mathtt{JRC} + 1.135\left(\frac{\mathtt{JCS}}{\mathtt{a}_0}\right) - 0.251. \tag{23}$$

The definition of fracture compliance matrix describes the mechanical property of a fracture in its local coordinate system $[x', y', z']$. To construct a pseudo-continuum, the fracture compliance matrix should be transformed into the global coordinate system $[x, y, z]$, which accords with the coordinates of the solid and fluid zone. Equation (24) constitutes the final formulation of the transformation matrix $\boldsymbol{T}$:

$$\mathbf{T} = \begin{bmatrix} \cos(\mathtt{x'x})^2 & \cos(\mathtt{x'y})^2 & \cos(\mathtt{x'z})^2 & 2\cos(\mathtt{x'x})\cos(\mathtt{x'y}) & 2\cos(\mathtt{x'y})\cos(\mathtt{x'z}) & 2\cos(\mathtt{x'x})\cos(\mathtt{x'z}) \\ \cos(\mathtt{x'x})\cos(\mathtt{y'x}) & \cos(\mathtt{x'y})\cos(\mathtt{y'y}) & \cos(\mathtt{x'z})\cos(\mathtt{y'z}) & \cos(\mathtt{x'y})\cos(\mathtt{y'x}) + \cos(\mathtt{x'x})\cos(\mathtt{y'y}) & \cos(\mathtt{x'z})\cos(\mathtt{y'y}) + \cos(\mathtt{y'z})\cos(\mathtt{x'y}) & \cos(\mathtt{y'x})\cos(\mathtt{x'z}) + \cos(\mathtt{x'x})\cos(\mathtt{y'z}) \\ \cos(\mathtt{x'x})\cos(\mathtt{z'x}) & \cos(\mathtt{x'y})\cos(\mathtt{z'y}) & \cos(\mathtt{x'z})\cos(\mathtt{z'z}) & \cos(\mathtt{z'x})\cos(\mathtt{x'z}) + \cos(\mathtt{z'z})\cos(\mathtt{x'x}) & \cos(\mathtt{x'z})\cos(\mathtt{z'y}) + \cos(\mathtt{z'z})\cos(\mathtt{x'y}) & \cos(\mathtt{z'x})\cos(\mathtt{x'z}) + \cos(\mathtt{x'x})\cos(\mathtt{z'z}) \end{bmatrix}. \tag{24}$$

$$\boldsymbol{C}_t = \boldsymbol{C}_i + \sum_{j=1}^{n_f}\frac{1}{s_j}\boldsymbol{T}_j^{\mathrm{T}}\boldsymbol{C}_j\boldsymbol{T}_j, \tag{25}$$

where $\mathbf{C_t}$ is the resulting compliance of the fractured rock mass; $\mathbf{C_i}$ is the compliance of the intact rock matrix, which

3.2. Estimation of Fracture Permeability. In the ideal situation, in which a fracture only consists of two smooth and parallel plates, the hydraulic aperture is equal to the mechanical aperture, and thus the fracture permeability could be evaluated through the cubic law with respect to

the hydraulic aperture as follows:

$$k_f = k_{f,0} \cdot \frac{w_f^3}{w_{f,0}^3}, \tag{26}$$

where the subscript 0 denotes the reference state; k_f is the fracture permeability; and w_f is the hydraulic aperture. Due to the roughness of the two facing walls, the distribution of local apertures in a fracture is not uniform. For validity of the cubic law, this model employs Barton's empirical equation (Equation (27)) [30] to convert the mechanical aperture to the hydraulic aperture:

$$w_f = \begin{cases} a_m^2 JRC^{-2.5}, & \tau_h/\tau_p \le 0.75, \\ \sqrt{a_m} JRC_{mob}, & \tau_h/\tau_p > 0.75. \end{cases} \tag{27}$$

Consequently, the key to updating fracture permeability is estimating the mechanical aperture a_m, which can be expressed in terms of normal and shearing deformations:

$$a_m = a_0 - \Delta a_n + \tau_v, \tag{28}$$

where a_0 is the initial mechanical fracture aperture under zero effective stress; Δa_n is the change of fracture aperture due to the perturbation of normal effective stress; and τ_v is the shear induced dilation. Following Barton [31], Δa_n can be calculated as follows:

$$\Delta a_n = \begin{cases} -\frac{\sigma_n}{K_{ni}}, & \sigma_n \ge 0, \\ \left(\frac{1}{v_m} - \frac{K_{ni}}{\sigma_n}\right)^{-1}, & \sigma_n < 0. \end{cases} \tag{29}$$

The shear induced dilation τ_v is calculated using Asadollahi's model [32], in which the shear stress-dilation relationship comprises four stages: (1) linear elastic stage; (2) hardening stage; (3) softening stage; and (4) residual stage. The shear induced dilation is formulated as

$$\tau_v = \begin{cases} \left(\frac{2\tau_h^2}{3\tau_p} - \frac{\tau_h}{3}\right) \tan\left(JRC \cdot \lg\left(\frac{JCS}{\sigma_n}\right)\right), & \tau_h \le \tau_p, \\ \int_{\tau_p}^{\tau_h} \tan\left(JRC \cdot \left(\frac{JRC}{\sigma_n}\right)\left(\frac{\tau_p}{\delta}\right)0.381\right) d\tau + \tau_{v,p}, & \tau_h > \tau_p. \end{cases} \tag{30}$$

where τ is the shear displacement of fracture; τ_p is the peak shear displacement; and $\tau_{v,p}$ is the dilation displacement. τ_p and $\tau_{v,p}$ are both functions of joint roughness coefficient (JRC) and joint compressive strength (JCS):

$$\tau_p = 0.007 L^{0.45} \left(\frac{\sigma_n}{JCS}\right)^{0.34} \cos\left(JRC \cdot \lg\left(\frac{JCS}{\sigma_n}\right)\right), \tag{31}$$

$$\tau_{v,p} = \frac{1}{3}\tau_p \tan\left(JRC \cdot \lg\left(\frac{JCS}{\sigma_n}\right)\right). \tag{32}$$

It should be noted that the fracture permeability model is not unique in the geocoupled simulator. Equations (26) to (32) mostly follow the work of Barton [31], but other choices could exist. One advantage of the pseudo-continuum method is the flexibility in dealing with fracture geometries. Indeed, it is possible to use any empirical or tabular constitutive models for fractures.

4. Fracture Gridding Technique

For reservoirs with preexisting fractures, it is reasonable to treat the fractured block as a continuum, because the mechanical behavior of a fracture constitutes prior knowledge. By keeping the strain energy conservative, a fractured rock block can be represented as a pseudo-continuum [7], which exhibits the same mechanical behavior as the discontinuity. In particular, the mechanical property of the pseudo-continuum (fractured block) is obtained by summing the compliances of fractures and the intact rock.

In the flow problem, EDFM is used to model large-scale fractures, and DPDK is used to model small-scale fractures. The fracture deformation has two influences on the simulation process: the cumulative term calculation and the permeability updating. In the cumulative term calculation, the fracture deformation affects the calculation of material derivative and the volume strain distribution in DPDK model. In the calculation of flow term, the fracture deformation changes the permeability of fractures and then affects the calculation of fracture conductivity. In a geomechanical simulation, the constitutive properties of fractures directly affect the constitutive properties of fractured blocks. Based on the principle of strain energy balance, this section proposes the geomechanical discrete method of fractures, including the construction of equivalent continuous elements and the distribution method of fracture element deformation. The former is used to model the influence of fracture constitutive properties on element properties. The latter is used to distribute the volume strain and calculate the fracture conductivity.

The construction of an equivalent element is based on the conservation of strain energy. For an element, the energy conservation equation is

$$\left(\frac{V_f}{V_t}\boldsymbol{\varepsilon}_f + \frac{V_m}{V_t}\boldsymbol{\varepsilon}_m\right) = \left(\frac{V_f}{V_t}\mathbf{C}_f' + \frac{V_m}{V_t}\mathbf{C}_m\right) : \boldsymbol{\sigma}_B = \mathbf{C}_t : \boldsymbol{\sigma}_B = \boldsymbol{\varepsilon}_B, \tag{33}$$

where V is the volume and the footnotes f, m, and t denote the fracture, matrix, and the equivalent element, respectively. $\boldsymbol{\varepsilon}_B$ is the strain of the equivalent element; $\boldsymbol{\sigma}_B$ is the stress tensor of the equivalent element; and $\mathbf{C}_t$, $\mathbf{C}_f'$ and $\mathbf{C}_m$ are the compliance of equivalent element, fracture, matrix,

respectively. Hence, the $\mathbf{C}_t$ can be calculated as

$$\mathbf{C}_t = \frac{V_{fL}}{V_t}\mathbf{C}'_{fL} + \frac{V_{fS}}{V_t}\mathbf{C}'_{fS} + \frac{V_m}{V_t}\mathbf{C}_m, \tag{34}$$

where L and S represent large scale and small scale, respectively. It can be seen that the flexibility of the quasi-continuous element is equal to the weighted sum of the vol-

ume of the crack and the matrix. This equation assumes that the permeability of fracture and matrix are described in the same coordinate system, but in reality, the mechanical properties of fracture and matrix are often established in different coordinate systems, so it is necessary to combine the coordi-

$$\mathbf{T} = \begin{bmatrix} \cos(\angle x'x)^2 & \cos(\angle x'y)^2 & \cos(\angle x'z)^2 & 2\cos(\angle x'x)\cos(\angle x'y) & 2\cos(\angle x'y)\cos(\angle x'z) & 2\cos(\angle x'x)\cos(\angle x'z) \\ \cos(\angle x'x)\cos(\angle y'x) & \cos(\angle x'y)\cos(\angle y'y) & \cos(\angle x'z)\cos(\angle y'z) & \cos(\angle x'y)\cos(\angle y'x)+\cos(\angle x'x)\cos(\angle y'y) & \cos(\angle x'z)\cos(\angle y'y)+\cos(\angle y'z)\cos(\angle x'y) & \cos(\angle y'x)\cos(\angle x'z)+\cos(\angle x'x)\cos(\angle y'z) \\ \cos(\angle x'x)\cos(\angle z'x) & \cos(\angle x'y)\cos(\angle z'y) & \cos(\angle x'z)\cos(\angle z'z) & \cos(\angle z'x)\cos(\angle x'z)+\cos(\angle z'z)\cos(\angle x'x) & \cos(\angle x'z)\cos(\angle z'y)+\cos(\angle z'z)\cos(\angle x'y) & \cos(\angle z'x)\cos(\angle x'z)+\cos(\angle x'x)\cos(\angle z'z) \end{bmatrix}, \tag{35}$$

where $\angle\alpha\beta$ is the angle between local axis α and global axis β. Then, we can get the construction equation for the equivalent element:

$$\mathbf{C}_t = \sum_{j=1}^{n_{fL}} \frac{V_{fL,j}}{V_t}\boldsymbol{T}_j^T\mathbf{C}_{fL,j}\boldsymbol{T}_j + \sum_{i=1}^{n_{fS}} \frac{V_{fS,i}}{V_t}\boldsymbol{T}_i^T\mathbf{C}_{fS,i}\boldsymbol{T}_i + \frac{V_m}{V_t}\mathbf{C}_m, \tag{36}$$

where n_{fL} is the number of large fractures in the element and n_{fS} is the number of small fractures. In DPDK, small fractures are assumed to be uniformly distributed in the element at the same angle; they are equivalently treated as a change in porosity. In this case, the second item at the right end of the equation can be replaced by the following formula:

$$\sum_{i=1}^{n_{fS}} \frac{V_{fS,i}}{V_t}\boldsymbol{T}_j^T\mathbf{C}_{fS,i}\boldsymbol{T}_j = \frac{\phi_{fS}}{\phi_t}\boldsymbol{T}^T\mathbf{C}_{fS}\boldsymbol{T}. \tag{37}$$

In flow simulation, fracture and matrix are calculated separately. Therefore, it is necessary to decompose the deformation for fracture and matrix according to the deformation of the equivalent element, respectively. The deformation decomposition has two functions in the simulation. The first is to provide volume strain for the generation of the cumulative term in DPDK model. The second is to provide the stress state of fractures for the calculation of fracture permeability, so as to calculate the opening of fractures. The deformation distribution of equivalent elements is also based on the strain energy balance theory. The total deformation of the equivalent continuous element is the sum of the deformation of fracture and matrix:

$$\varepsilon_t V_t = \varepsilon_f V_f + \varepsilon_m V_m. \tag{38}$$

According to the energy conservation theory, the strain energy of an equivalent element meets the following condition in 1D situation:

$$K_{dr,t}(\varepsilon_{v,t})^2 V_t = K_{dr,f}(\varepsilon_{f,t})^2 V_f + K_{dr,m}(\varepsilon_{v,t})^2 V_m. \tag{39}$$

nate systems of the two. According to the space conversion principle of vector, the coordinate conversion matrix is

Then, the strain energy balance equation can be extended to

$$\underbrace{\left(K_{dr,f}V_f + K_{dr,m}\frac{V_f^2}{V_m}\right)}_{a}\varepsilon_f^2 + \underbrace{\frac{-2V_tV_f}{V_m}K_{dr,m}}_{c}\varepsilon_t\varepsilon_f + \underbrace{\left(K_{dr,m}\frac{V_t^2}{V_m} - K_{dr,t}V_t\right)}_{b}\varepsilon_t^2 = 0. \tag{40}$$

It can be concluded that when the quasi-continuous volume strain is known, the volume strain of crack and matrix are calculated as follows:

$$\varepsilon_f = \frac{\sqrt{((c^2/4a)(c^2/4a) - b)\varepsilon_t^2} - (c/2\sqrt{a})\varepsilon_t}{\sqrt{a}}. \tag{41}$$

It is obvious that

$$\sqrt{\left(\frac{c^2}{4a} - b\right)\varepsilon_t^2} = 0. \tag{42}$$

Therefore, the strain of crack and matrix can be calculated as follows:

$$\begin{aligned} \varepsilon_f &= -\frac{c}{2a}\varepsilon_t, \\ \varepsilon_m &= \frac{\varepsilon_t V_t - \varepsilon_f V_f}{V_m}. \end{aligned} \tag{43}$$

The stress calculation method under three-dimensional state of a fracture is

$$\boldsymbol{\sigma}_f = -\frac{c}{2a}\mathbf{D}_f\boldsymbol{\varepsilon}_t, \tag{44}$$

where D_f is the stiffness matrix of a fractured element in current state.

The governing equation system is linearized through the Newton-Raphson method. The coupling problem is solved through the fixed-stress splitting strategy, which solve the flow problem first with a fixed volumetric stress in one

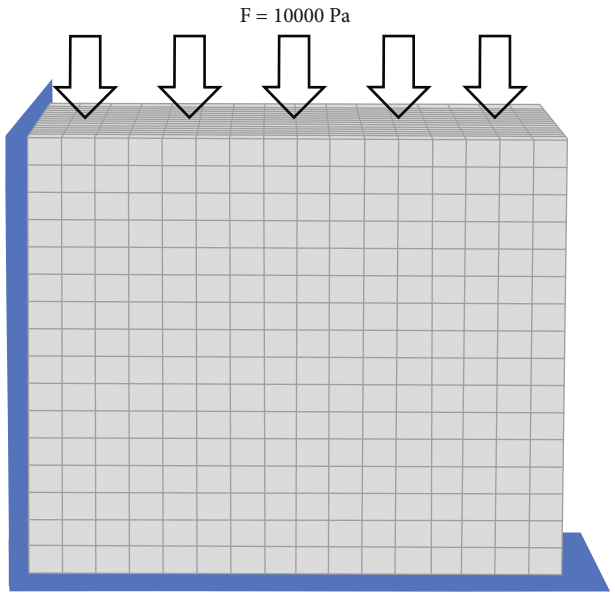

Figure 1: Illustration of Mandel's problem.

Table 1: Parameters for Case 2.

Variable	Value	Unit
Porosity	0.33	/
Permeability	15	mD
Rock density	2050.36	kg/m^3
Water density	1000	kg/m^3
Water viscosity	0.96	mPa·s
Poisson's ratio	0.4	/
Biot's coefficient	0.95	/
Young's modulus	1.0	GPa

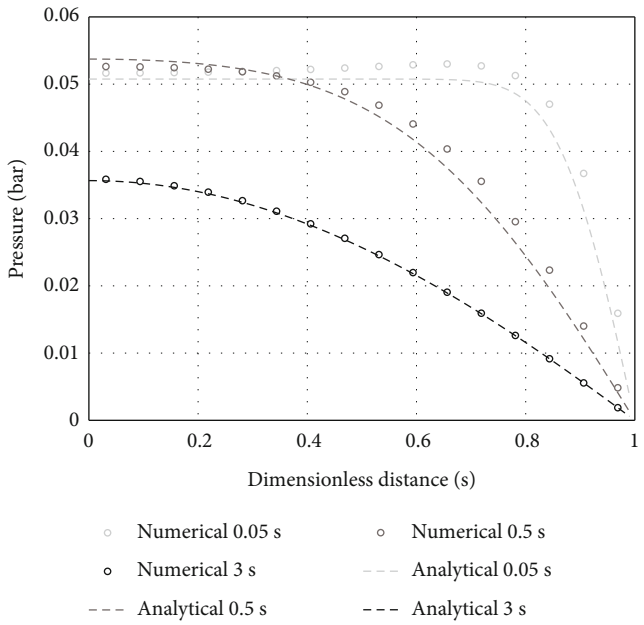

Figure 2: Pressure profile along the x-axis at 0.05 s, 0.5 s, and 3 s.

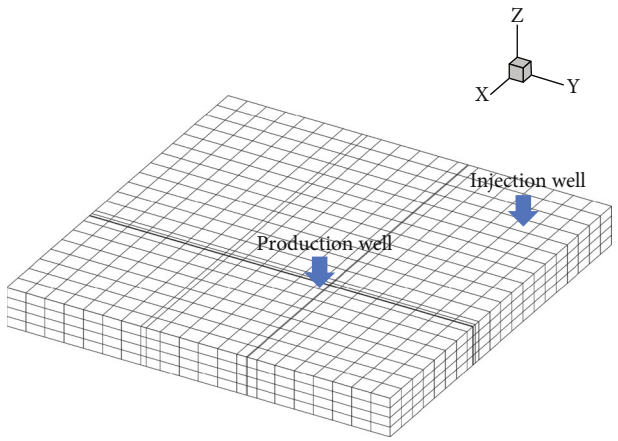

Figure 3: The geological model for Case 2.

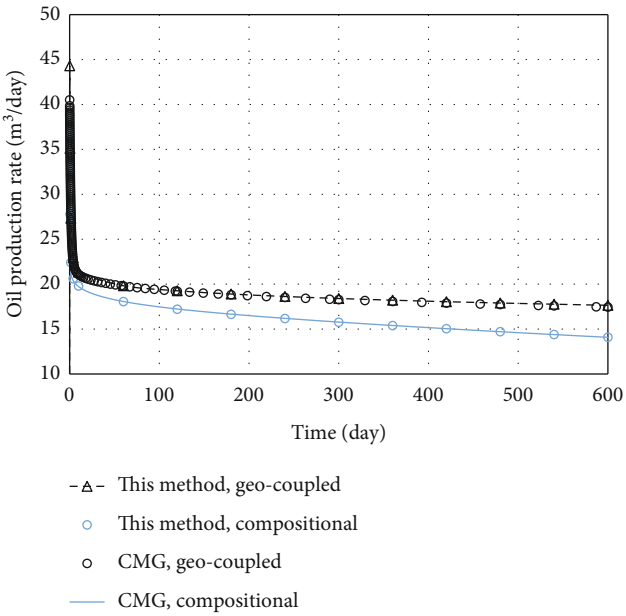

Figure 4: Comparison of oil production rate for Case 2.

iteration step. The fracture information is coupled with the governing equation system explicitly and is updated at the beginning of each time step. In each coupling step, the flow problem is solved first with the volumetric stress fixed; then, the geomechanical problem is solved with a frozen pressure. In the intermediate step, the displacement does not need to be calculated, because the mechanics problem is quasi-static.

5. Numerical Results

We show the validity and applicability of this model through some cases in this section. Case 1 is the Mandel's problem, which is widely used to validate the accuracy of geocoupled simulators. Case 2 is a reservoir with two fractures, which is set up to validate the accuracy of this method in dealing with fracture problems. Case 3 and Case 4 are two field-scale cases; they are set up to demonstrate the applicability of this method.

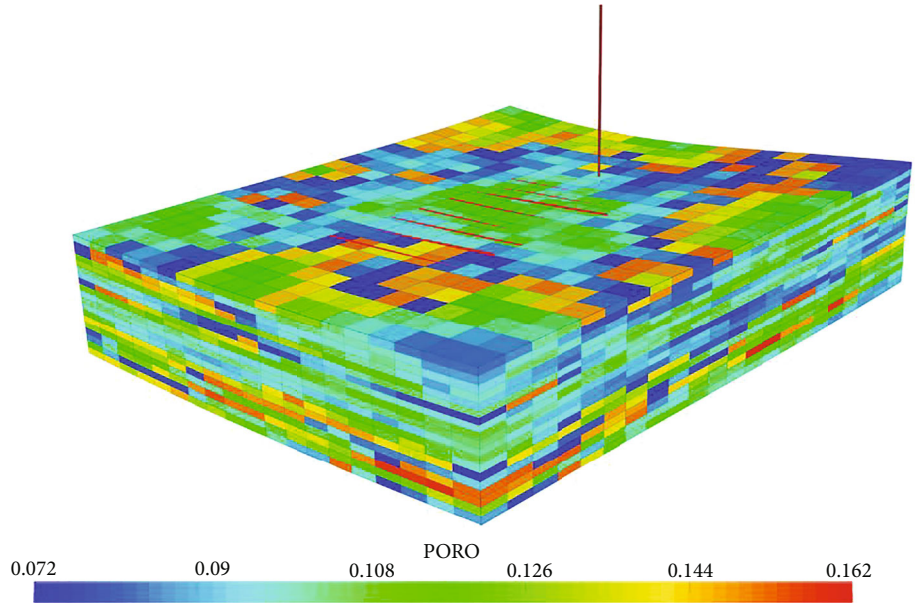

Figure 5: The geological model for Case 3.

Table 2: Parameters for Case 2.

Variable	Value	Unit
Fracture porosity	0.01	/
Matrix porosity	0.3	/
Fracture initial permeability	200	mD
Matrix initial permeability	0.12	mD
Young's modulus	30	GPa
Poisson's ratio	0.4	/
Biot's coefficient	0.95	/
Rock density	2050	Kg/m^3
Joint roughness coefficient (JRC)	10	/
Joint compressive strength (JCS)	250	Bar

Case 1. Mandel's problem. The physical model of this case is an infinitely long rectangular specimen sandwiched between two frictionless, rigid plates. Two lateral sides of the specimen are drained and traction-free. Initially, a force acts on the top surface, causing the Mandel-Cryer effect. The geometry set for Mandel's problem refers to Figure 1. The benchmark solution can be found in Goulet' work [33], and the numerical model is built using the parameters listed in Table 1. Because of the symmetry of the specimen, we only generate the numerical domain for a quarter of the specimen. The numerical solutions for pore pressure along the x-direction at various times are shown in Figure 2. It can be seen that the Mandel-Cryer effect is captured by this model. The solution from this model and the analytical solution are in good agreement.

Case 2. Comparison with CMG. Case 2 is a water-flooding problem in a rectangular reservoir. The reservoir size is 3000 m × 3000 m × 244 m. The traction is set to 32.9 MPa to face I+, J+, and K+, and the fixed displacement boundary condition is acted to face I-, J-, and K-. All sides are no-flow boundaries. The physical properties are listed in Table 1. Initially, the fluid pressure is 300 Bar, and the reservoir is oil-saturated. The grids are generated as shown in Figure 3. We set the initial oil production rate to 1589 m^3/d and the water injection rate to 476.96 m^3/d. We choose the CMG [34] as the benchmark simulator, which employs the explicitly coupled method to model the geocoupled problems. Figure 4 shows the comparison of the oil production rate and the water production rate. The result is outputted once when the solution reaches convergence. When the solution is not converged, the time step would be reduced, and the simulation would be rolled back. It can be seen that the results calculated by this model are very close to those of CMG, but because of the implicitly coupled strategy, the convergence of this method is better.

Case 3. Tight oil production.

Case 3 is a tight oil production problem, which contains a horizontal well that is 15 m long, with eight hydraulic fractures striking at different orientations. The stages 2, 4, and 6 are closed. The fractures are modeled using the EDFM method. The reservoir is discretized into 15084 grid cells, as shown in Figure 5. The geomechanical domain and the reservoir domain are identical. The top surface of the overburden is traction-free, and the bottom of the underburden is fixed. The vertical stress gradient is 20.5 kPa/m. The ratio between the maximum horizontal stress to the vertical stress is 0.9, and the ratio between the minimum horizontal stress to the vertical stress is 0.8. Initially, the fluid pressure is 155 Bar. Other physical properties of the case are listed in Table 2. The well is working under a constant bottom hole pressure (BHP) of 50 Bar.

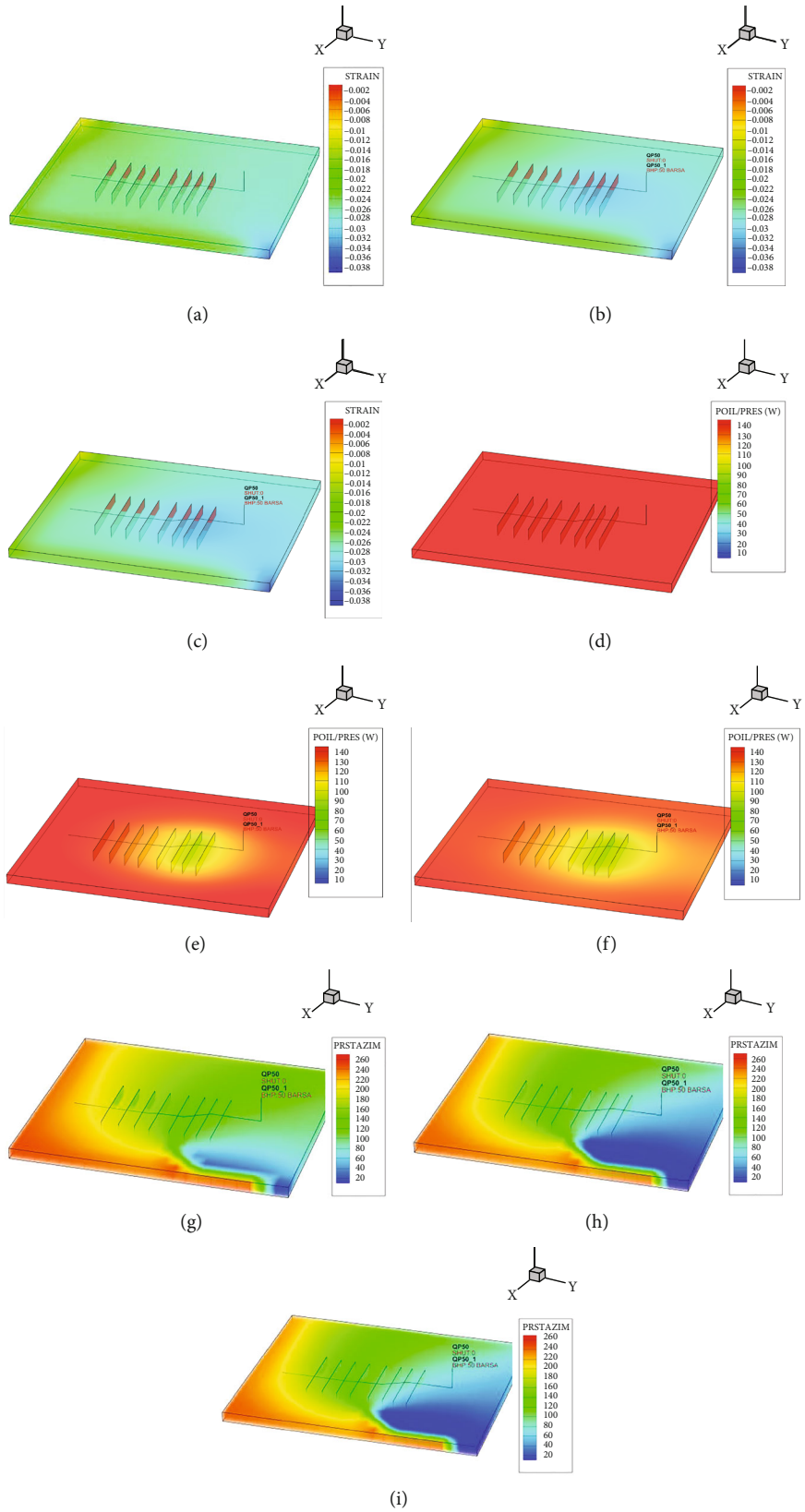

Figure 6: The simulation results of Case 3.

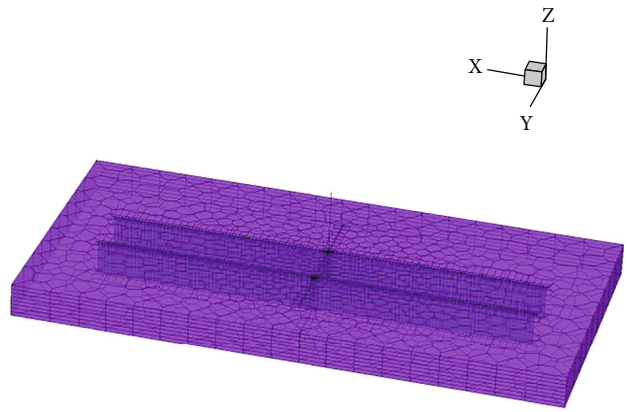

Figure 7: The geological model for Case 4.

Table 3: The fluid composition of Case 4.

Component name	Mole fraction	Critical pressure (Bar)	Critical temperature (K)	Mole weight	Critical volume m^3/kgmol
C1	78.17	46.4	190.7	16	0.0977
N2	0.55	33.9	126.2	28	0.089
C2	11.99	48.8	305.4	30	0. 147
C3	5.07	42.6	369.9	44	0. 202
CO2	0.55	73.9	304.2	44	0.0944
IC4	0.66	36.5	408.2	58	0.263
NC4	1.62	38	425.2	58	0.256
IC5	0.37	33.3	460.4	72	0.306
NC5	0.47	33.7	469.8	72	0.314
NC6	0.528	30.3	507.9	86	0.373
C7+	0.0055	27.8	589.2	114	0.463
C11+	0.0055	21.2	679.8	166	0.667
C15+	0.0055	16.6	760.2	230	0.92
C20+	0.0055	10.4	896.8	409	1.67

Figure 6 shows the simulation results; the simulation results of the initial state, the 1440th day, and the 2550th day are shown from left to right, from which we can see that the geomechanics affects the reservoir to a considerable degree. As the major flow channel, the fractures are critical to production. The volumetric strain and fluid pressure evolve mostly around the stimulated reservoir volume. Because of the press evolve, the difference between the maximum and minimum principal stress changes may affect the subsequent re-fracturing effect.

Case 4. Tight oil production: CO2 Huff-N-Puff.

Case 4 is designed to show the capability of this method in simulating the coupled geomechanics and compositional flow process in the presence of phase transition. As shown in Figure 7, the flow domain is a fractured reservoir with one horizontal well and two hydraulic fractures. Initially, the reservoir is oil-saturated, and the fluid composition is shown in Table 3. The reservoir fluid consists of fourteen pseudo hydrocarbon components, as shown in Table 2. The initial reservoir pressure is 250 Bar. The boundary conditions and physical properties used in this example are the same as those in Case 3. The schedule is from 0 to 1000 days, and the well is set to production with the bore pressure of 200 Bar; then, we start the Huff-N-Puff operation. The operation is implemented for 5 cycles; each cycle is 90 days, of which the first 30 days are the gas injection stage; and the daily gas injection is 800 m^3. After that, soak the well for 20 days and open for 40 days. Figure 8 compares the cumulative oil production under different conditions. It can be seen from the figure that the effect of geomechanics predicted from the geocoupled model is lower than that of the component model. After 1000 days of production, the production capacity of production wells was seriously insufficient. After the implementation of the Huff-N-Puff operation, the production capacity was effectively improved and the final cumulative production was increased by about 7.7%.

The main mechanism of the Huff-N-Puff operation is that it improves the fluidity of fluid by injecting light components while increasing the reservoir pressure. In the first 1000 days, the composition of the fluid is evenly distributed. The heterogeneous distribution is caused by the injection of

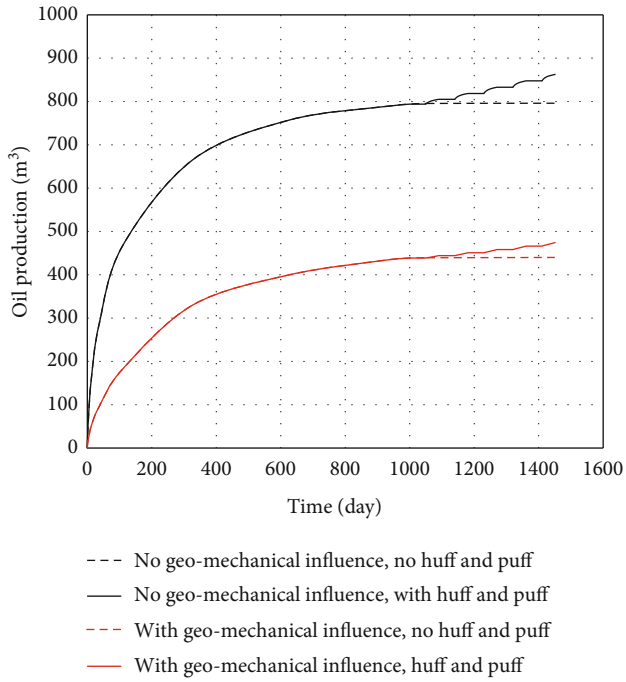

Figure 8: Comparison of cumulative production calculated with the two methods.

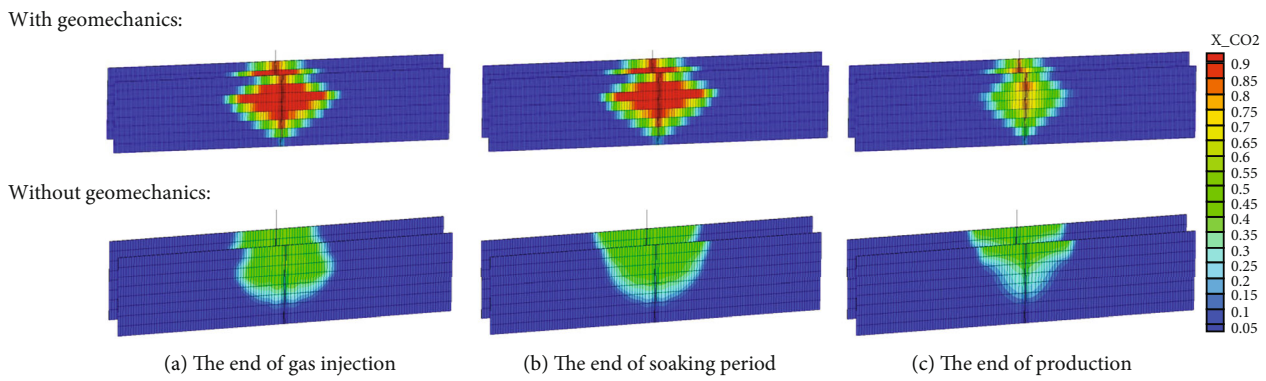

Figure 9: The concentration distribution for CO2.

CO2. Therefore, the reconstruction degree of reservoir fluid can be tracked according to the molar concentration of CO2. Figure 9 shows the carbon dioxide distribution simulated from the component model and the geocoupled model, respectively. From the fluid geocoupled model, it can be seen that after the CO2 injection, because the transverse permeability is much larger than the longitudinal permeability, it first improves the fluid of the perforated layer. After well soaking, due to its low molar mass, the component distribution is affected by buoyancy, resulting in its funnel-shaped distribution in the latter situation. In the geomechanical model, due to fracture closure behavior, the permeability of the fractured reservoir is low, and the fluid pressure is high. Therefore, the CO2 distribution predicted in the geocoupled model is smaller than that in the component model, and the concentration of CO2 in the distribution area is higher than that simulated in the component model.

6. Conclusion

In this work, a new geocoupled fractured reservoir model is proposed, which has the following advantages:

(1) Modeling the dynamic geomechanics field. Because of the implicit fully coupled model, the geomechanics field can be calculated and outputted in every time step. The geomechanics numerical field and the reservoir numerical field are identical

(2) Modeling the fracture deformation behaviors. The fracture treatment is a systematic work. In this work,

the fracture mechanical behaviors are modeled through Barton's model, and a novel fracture gridding technique, which is based on strain energy conservation, is proposed to integrate the fracture model into the simulation

We presented some numerical cases to demonstrate the accuracy and applicability of this model. Moreover, numerical cases show that this method is capable of dealing with some complicated problems, such as simulating the geocoupling process in the case of EDFM and DFM and coupling compositional flow and geomechanics. The practicality of this method makes it applicable for more complicated field problems.

Data Availability

The data used to support the findings of this study are available from the corresponding author upon request.

Conflicts of Interest

The authors declared no potential conflicts of interest with respect to the research, authorship, and/or publication of this article.

Acknowledgments

This work is partially funded by the National Natural Science Foundation of China (Grant No. 51974356).

References

[1] B. Bourbiaux, "Fractured reservoir simulation: a challenging and rewarding issue," *Oil & Gas Science & Technology*, vol. 65, no. 2, pp. 227–238, 2010.

[2] G. I. Barenblatt and Y. P. Zheltov, "Fundamental equations of filtration of homogeneous liquids in fissured rocks," *Soviet Physics Doklady*, 1960.

[3] X. Li, X. Li, D. Zhang, and R. Yu, "A dual-grid, implicit, and sequentially coupled geomechanics-and-composition model for fractured reservoir simulation," *SPE Journal*, vol. 25, no. 4, pp. 2098–2118, 2020.

[4] A. Moinfar, A. Varavei, K. Sepehrnoori, and R. T. Johns, "Development of a coupled dual continuum and discrete fracture model for the simulation of unconventional reservoirs," in *SPE reservoir simulation symposium*, OnePetro, 2013.

[5] A. Moinfar, A. Varavei, K. Sepehrnoori, and R. T. Johns, "Development of an efficient embedded discrete fracture model for 3D compositional reservoir simulation in fractured reservoirs," *SPE Journal*, vol. 19, no. 2, pp. 289–303, 2014.

[6] X. Li, D. Zhang, and S. Li, "A multi-continuum multiple flow mechanism simulator for unconventional oil and gas recovery," *Journal of Natural Gas Science and Engineering*, vol. 26, pp. 652–669, 2015.

[7] M. Nassir, *Geomechanical coupled modeling of shear fracturing in non-conventional reservoirs*, University of Calgary, 2013.

[8] A. Gens, I. Carol, and E. Alonso, "A constitutive model for rock joints formulation and numerical implementation," *Computers and Geotechnics*, vol. 9, no. 1-2, pp. 3–20, 1990.

[9] R. E. Goodman, *Methods of Geological Engineering in Discontinuous Rocks*, West Group, 1976.

[10] G. Swan, *Stiffness and associated joint properties of rocks. In conference on the application of rock mechanics to cut and fill mining: 01/06/1980-03/06/1980*, The Institution of Mining and Metallurgy, 1981.

[11] J. C. Sharp and Y. Maini, "Fundamental considerations on the hydraulic characteristics of joints in rock," in *Proceedings of the symposium of percolation through fissured rock*, Stuttgart, 1972.

[12] S. Bandis, A. Lumsden, and N. Barton, "Fundamentals of rock joint deformation," *International Journal of Rock Mechanics and Mining Sciences & Geomechanics Abstracts*, vol. 20, no. 6, pp. 249–268, 1983.

[13] Q. Lei, J. P. Latham, J. Xiang, and C. F. Tsang, "Polyaxial stress-induced variable aperture model for persistent 3D fracture networks," *Geomechanics for Energy and the Environment*, vol. 1, pp. 34–47, 2015.

[14] N. Barton and S. Bandis, "Effects of block size on the shear behavior of jointed rock," in *The 23rd US symposium on rock mechanics (USRMS)*, American Rock Mechanics Association, 1982.

[15] N. Barton, S. Bandis, and K. Bakhtar, "Strength, deformation and conductivity coupling of rock joints," *International journal of rock mechanics and mining sciences & geomechanics abstracts*, vol. 22, no. 3, pp. 121–140, 1985.

[16] C. S. Desai, K. L. Fishman, Y. Ma, D. Rigdy, and T. Kundu, *Constitutive Modelling of Joints under Cyclic Loading. Part 1. Modelling and Testing of Idealized Rock Joints*, Arizona Univ Tucson Dept of Civil Engineering, 1988.

[17] B. Amadei and S. Saeb, "Constitutive models of rock joints," *International Symposium on Rock Joints*, 1990.

[18] M. E. Plesha, "Constitutive models for rock discontinuities with dilatancy and surface degradation," *Mechanics of cohesive-frictional materials*, vol. 11, no. 4, pp. 345–362, 1987.

[19] O. C. Zienkiewicz, R. L. Taylor, and J. Z. Zhu, *The finite element method: its basis and fundamentals*, vol. 3, McGraw-hill London, 2005.

[20] V. Gupta, C. A. Duarte, I. Babuška, and U. Banerjee, "Stable GFEM (SGFEM): improved conditioning and accuracy of GFEM/XFEM for three-dimensional fracture mechanics," *Computer Methods in Applied Mechanics and Engineering*, vol. 289, pp. 355–386, 2015.

[21] M. F. Benedetto, S. Berrone, S. Pieraccini, and S. Scialò, "The virtual element method for discrete fracture network simulations," *Computer Methods in Applied Mechanics and Engineering*, vol. 280, no. 10, pp. 135–156, 2014.

[22] S. Mukherjee and Y. Liu, "The boundary element method," *International Journal of Computational Methods*, vol. 10, no. 6, article 1350037, 2013.

[23] P. A. Cundall and O. Strack, "The development of constitutive laws for soil using the distinct element method," *Numerical methods in geomechanics*, vol. 1, pp. 289–317, 1979.

[24] G. H. Shi and R. E. Goodman, "Two dimensional discontinuous deformation analysis," *International Journal for Numerical and Analytical Methods in Geomechanics*, vol. 9, no. 6, pp. 541–556, 1985.

[25] J. Kim, H. Tchelepi, and R. Juanes, "Stability and convergence of sequential methods for coupled flow and geomechanics: drained and undrained splits," *Computer Methods in Applied*

Mechanics and Engineering, vol. 200, no. 23-24, pp. 2094–2116, 2011.

[26] J. Kim, H. A. Tchelepi, and R. Juanes, "Stability and convergence of sequential methods for coupled flow and geomechanics: fixed-stress and fixed-strain splits," *Computer Methods in Applied Mechanics and Engineering*, vol. 200, no. 13-16, pp. 1591–1606, 2011.

[27] J. Kim, *Sequential methods for coupled geomechanics and multiphase flow*, vol. 71, Stanford University, 2010.

[28] L. Xiaoqi, F. Jichao, and J. Bingyu, "Interface properties in binary fluid using lattice Boltzmann method," *Frontiers in earth Science*, vol. 9, 2021.

[29] L. Xiaoqi, F. Jichao, and J. Bingyu, "Quantitative analysis of phase separation using the lattice Boltzmann method," *Frontiers in Earth Science*, vol. 9, 2021.

[30] N. Barton and V. Choubey, "The shear strength of rock joints in theory and practice," *Rock Mechanics*, vol. 10, no. 1-2, pp. 1–54, 1977.

[31] N. Barton, "The shear strength of rock and rock joints," *International Journal of Rock Mechanics and Mining Sciences & Geomechanics Abstracts*, vol. 13, no. 9, pp. 255–279, 1976.

[32] P. Asadollahi and F. Tonon, "Constitutive model for rock fractures: revisiting Barton's empirical model," *Engineering Geology*, vol. 113, no. 1-4, pp. 11–32, 2010.

[33] G. C. Goulet, "Validation and application of iterative coupling to poroelastic problems in bone fluid flow," *Bulletin of Applied Mechanics*, vol. 5, no. 17, pp. 6–17, 2009.

[34] Computer Modelling Group, *CMG, Version 2017.1*, Computer Modelling Group Ltd., Calgary, Alberta, Canada, 2017.

Hindawi
Geofluids
Volume 2022, Article ID 9420835, 10 pages
https://doi.org/10.1155/2022/9420835

Research Article

Characterization Method of Tight Sandstone Reservoir Heterogeneity and Tight Gas Accumulation Mechanism, Jurassic Formation, Sichuan Basin, China

Lin Jiang,[1] **Wen Zhao**,[1] **Benjian Zhang**,[2] **Chao Zheng**,[2] **Feng Hong**,[1] **and Jiaqing Hao**[1]

[1]*Research Institute of Petroleum Exploration and Development, PetroChina, Beijing 100083, China*
[2]*Research Institute of Petroleum Exploration and Development, Southwest Oilfield, PetroChina, Chengdu 610000, China*

Correspondence should be addressed to Wen Zhao; zhaow625@126.com and Benjian Zhang; zbjian@petrochina.com.cn

Received 6 April 2022; Revised 11 May 2022; Accepted 27 June 2022; Published 20 July 2022

Academic Editor: Chao-Zhong Qin

Although significant progress has been made in tight gas exploration and development, there is still a limited understanding of the gas accumulation mechanism in tight formation. The description of heterogeneity in the tight reservoir is still an obstacle during tight gas exploration. In this work, we will develop a 3D gas accumulation facility that can reflect the high temperature and pressure under the geological condition to simulate the gas accumulation process in the tight formation of the Jurassic Formation, Sichuan Basin. Both the physical experiment simulation and numerical simulation methods will be combined to reveal the mechanism of gas accumulation. The results show that (1) the permeability ratio can characterize the heterogeneity of tight reservoirs. Based on this parameter, petroleum geologists can understand the interlayer heterogeneity during fluvial deposition and predict the sweet spots of tight gas; (2) the permeability ratio relationship between hydrocarbon accumulation of the tight sandstone reservoir mainly manifests as long as there is the existence of the differential permeability and there will be differences in natural gas migration dynamics, so that the natural gas accumulates in pores and depends on the extent of source rock; and (3) although the difference between capillary force curves is at the core of the influence of the permeability ratio on the gas-bearing capacity of the "sweet spot" sand body, the permeability ratio is a parameter of practical engineering significance. This work adds new methods to tight gas formation heterogeneity characterization and sheds light on the mechanisms of hydrocarbon accumulation in tight formation.

1. Introduction

Heterogeneity is an important property of tight reservoirs; however, how to describe the reservoir heterogeneity has always puzzled petroleum geologists [1, 2]. Different from the tight gas deposited in North America, tight continental gas is widely distributed in China. Compared with marine sedimentary strata, continental sedimentary strata are more heterogeneous. As a Chinese petroleum geologist, Qiu [3] proposed a classification criterion for reservoir heterogeneity which gained him an excellent reputation. In this classification frame, reservoir heterogeneity is divided into three categories: (1) plane heterogeneity, which refers to the heterogeneity caused by the geometry, size, and continuity of a reservoir sand body, as well as the spatial variation of porosity and permeability within the sand body [4]; (2) intralayer heterogeneity, which is mainly used to characterize the changes of vertical reservoir properties in a single sand body and is a crucial geological factor controlling and affecting the sweep thickness of the vertical injection agent in a single sand body [5]; and (3) interlayer heterogeneity, which refers to the overall study of the vertical lithology and physical property differences among sand layers in a unit, belonging to the reservoir description of the scale of strata [6]. These three types of heterogeneity are widely used to describe reservoir heterogeneity. However, there are huge differences between tight sandstone reservoirs and conventional reservoirs. The heterogeneous description methods for conventional reservoirs have apparent limitations in the description process for tight sandstone gas reservoirs [7].

Especially for the fluvial tight sandstone gas in Sichuan Basin, people need a novel method that focuses on describing the heterogeneity of the tight sandstone reservoir in the study of the natural gas accumulation process.

Hydrocarbon accumulation simulation is an essential means of petroleum geology theory research. Since the 20th century, with the skyrocketing development of the hydrocarbon exploration theory, hydrocarbon accumulation simulation technology has also gained continuous success, from one-dimensional simulation to three-dimensional simulation [8, 9], from macroscopic basin simulation to microscopic molecular simulation [10], and from normal temperature and pressure simulation to high-temperature and pressure geological simulation [11]. The progress of hydrocarbon accumulation simulation technology also promotes the development and innovation of hydrocarbon migration and accumulation theory. The hydrocarbon accumulation simulation technology development can be divided into three stages: (1) the practical exploration stage from the early 20th century to the middle of the 20th century. In this stage, people mainly used simple physical simulation experiments to verify their theoretical hypotheses [12]. Petroleum geologists propose theoretical hypotheses, then design and build their experimental equipment to carry out experiments according to the mechanism of hydrocarbon migration and accumulation, and rely on the results to support their theoretical hypotheses [13, 14]; (2) from the middle of the 20th century to the end of the 20th century, people began to pay attention to the controlling effects of microscopic parameters such as interfacial tension and pore wettability [15, 16] and throat radius on hydrocarbon migration [17]. With the development of science and technology and petroleum and natural gas geological theory, people began to pay attention to microparameters such as wettability [18], interfacial tension, and pore-throat structure on oil and gas migration in the late 20th century. During this time, hydrocarbon accumulation simulation technology developed from macroscale to micro-scale [19, 20]. (3) The development and innovation stage from the 21st century to the present is also accompanied by the boom of unconventional resources and the birth of many new technologies and methods [21]. In the 21st century, more and more testing equipment and analytical instruments have been applied to petroleum geology. In this stage, people's simulation of the hydrocarbon accumulation process has changed from a normal temperature and pressure environment to a high-temperature and pressure environment closer to geological conditions [22]. With the rapid development of unconventional resources, the mechanism of oil and gas charging and hydrocarbon migration and accumulation at the micro- and nanoscale has become a core scientific issue in the theoretical study of tight oil and gas accumulation. At the same time, reservoir formation simulation technology has also been developed and many new technologies and methods have been applied in this field, such as online nuclear magnetic technology [23] and 3D CT imaging technology [24]. Similarly, with the rapid development of computer technology and algorithms and the digitization process of geological data, it is possible to simulate the process of hydrocarbon accumulation with multiscale, multidimensional, multifactor, large-scale, and whole-process dynamics. More and more numerical simulation methods have been applied to hydrocarbon accumulation simulation [25]. Oil and gas accumulation simulation technology promotes the study of oil and gas accumulation mechanisms and makes up for the lack of theoretical research. Especially in recent years, further breakthroughs have been made in the exploration and development of unconventional global resources.

However, there exist huge differences between conventional resources and unconventional resources; how to establish a set of physical and numerical tight sandstone gas accumulation simulation technology and method that can meet the conditions of underground temperature and pressure according to the characteristics of tight sandstone gas reservoir development becomes a critical technical problem to be solved. In this work, based on the geological background of the Jurassic Formation, Sichuan Basin, we will discuss the cause of the heterogeneity of tight reservoirs and study how to characterize the heterogeneity of tight reservoirs. The physical experiment simulation and numerical simulation will be combined to reveal the mechanism of tight gas accumulation.

The rest of this paper is organized as follows. In Section 2, the geological background of the Jurassic Formation, Sichuan Basin, will be introduced. The cause of heterogeneity of a tight reservoir and the study on how to characterize the heterogeneity of tight reservoirs will be discussed in Section 3. In Sections 4 and 5, the physical experiment simulation and numerical simulation will be combined to reveal the mechanism of tight gas accumulation. A case of field application will be presented in Section 7.

2. Geological Backgrounds

As a significant petroliferous basin, the Sichuan Basin is located at southwest China (Figure 1). The tectonic pattern of the Sichuan Basin is controlled by the alternating thrust and nappe activities of the Longmen Mountain, Micang Mountain-Daba Mountain, and Xuefeng Mountain orogenic belts, and the basin-mountain coupling processes of each depression belt in the basin are strongly staged and transferable.

The mid-late Triassic was the critical period for the tectonic system transformation of the middle and upper Yangtze block. The surrounding ocean basins were subducted and subducted until finally closed. With the closing of the Paleotethys ocean, the vast area of south China underwent large-scale marine backsliding and turned into continental deposition. During the Jurassic sedimentary period, the lacustrine delta and fluvial sedimentary system were mainly developed. The thrust-nappe activity in the Longmen Shan area began to weaken. In contrast, the Micang Mountain-Daba Mountain tectonic activity became intense, making the basin subsidence and sedimentary filling center gradually migrate from the front of Longmen Mountain in western Sichuan to the front of Micang Mountain-Daba Mountain in northern Sichuan.

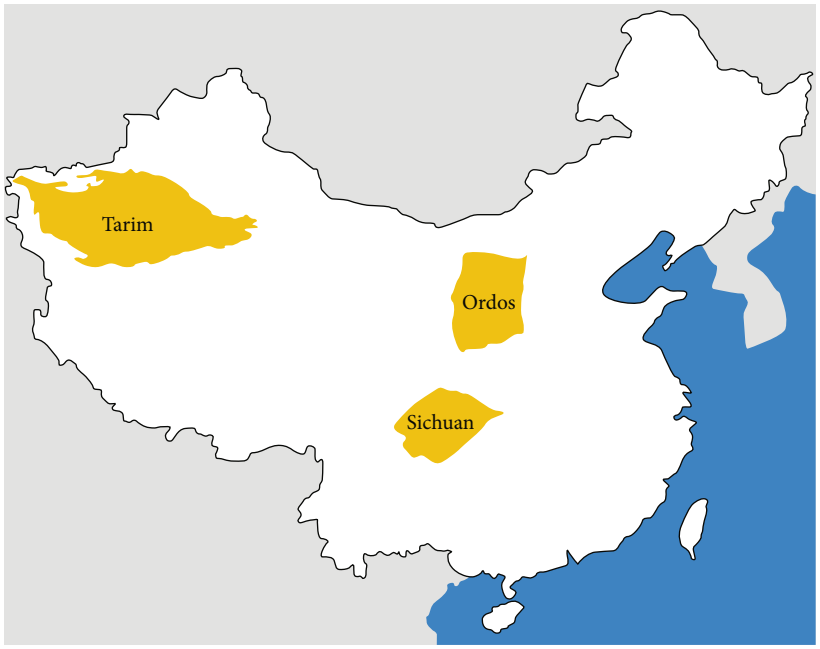

Figure 1: Map of the main sedimentary basins of China.

3. Characterization Method of Tight Sandstone Reservoir Heterogeneity

3.1. Heterogeneity Characteristics. Shaximiao Formation is a set of substantial thick purplish-red mudstone intercalated with the massive sand bodies, which is widely distributed in the basin. During the sedimentary period of the Shaximiao Formation, the detrital supply of Micang Mountain and Daba Mountain was strong, which controlled the provenance system of central Sichuan, and the piedmont provenance system of western Sichuan originated from Longmen Mountain. The channel sand reservoirs of Shaximiao Formation in the basin are well developed and affected by provenance, sedimentary microfacies, and diagenesis; the reservoirs have pronounced zoning and stratification.

The physical properties of different sand groups in different areas are characterized by low porosity-extremely low porosity and extremely low permeability-low permeability. The porosity ranges from 4% to 16%, with an average of 10.07%. Permeability ranges from 0.0018 to 191.338 mD, with an average of 3.45 mD. The fluvial sand group has firm heterogeneity and significant physical property difference between layers. The porosity of each sand group varies significantly from 7.11% to 14.58%. The permeability of each sand group varies greatly from 0.06 to 13.06 mD. Sedimentary microfacies mainly control the intralayer heterogeneity, and the interlayer heterogeneity is mainly controlled by diagenesis. Characterizing the heterogeneity of tight reservoirs and the predicting gas-bearing capacity have become a problem that people must face. This work will use the permeability ratio as a parameter to characterize the heterogeneity of tight reservoirs and discuss its relationship with gas saturation.

3.2. The Concept of the Permeability Ratio. Permeability ratio refers to the ratio of the maximum permeability to the minimum permeability of the rock, indicating the distribution range and difference in permeability [26]. The larger the permeability ratio is, the more substantial the heterogeneity of the reservoir pore space is. The closer to 1, the better the homogeneity of reservoirs.

The permeability ratio reflects the heterogeneity of the reservoir. Its geological meaning includes the following characteristics: (1) due to the influence of various geological processes of sandstone reservoir sedimentation, diagenesis, and later transformation, the permeability ratio varies; (2) the permeability ratio exists all the time; as long as there is heterogeneity in sandstone, the permeability ratio should be a relative concept; and (3) the permeability of sandstone reservoirs generally varies greatly, and there may be significant differences in different measurements of the same lithology. Therefore, the permeability ratio refers to the heterogeneity of rock, which is the characteristic of rock permeability caused by sedimentation, diagenesis, and later transformation. It is a relative concept and can be quantitatively characterized by the ratio of maximum permeability (K_{max}) and minimum permeability (K_{min}).

3.3. Formation of the Permeability Ratio. The permeability ratio essentially reflects the heterogeneity of rock. Primary and later reformations cause the differences in petrophysical properties. The main factors causing the heterogeneity of petrophysical properties are sedimentary environment and diagenesis.

3.3.1. Depositional Environment Difference. The sedimentary environment plays a vital role in the formation of permeability variety, which is mainly manifested in the variability of continental sedimentary facies. Mesozoic and Cenozoic continental

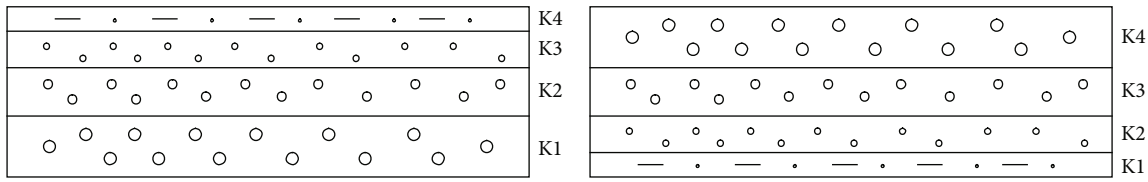

(a) Positive rhythm deposit (b) Negative rhythm deposit

Figure 2: A pattern of permeability differentials formed by sedimentation. (a) The positive rhythm deposit; (b) the negative rhythm deposit. In the positive rhythm deposit model, K1 > K2 > K3 > K4, and in the negative rhythm deposit model, K1 < K2 < K3 < K4.

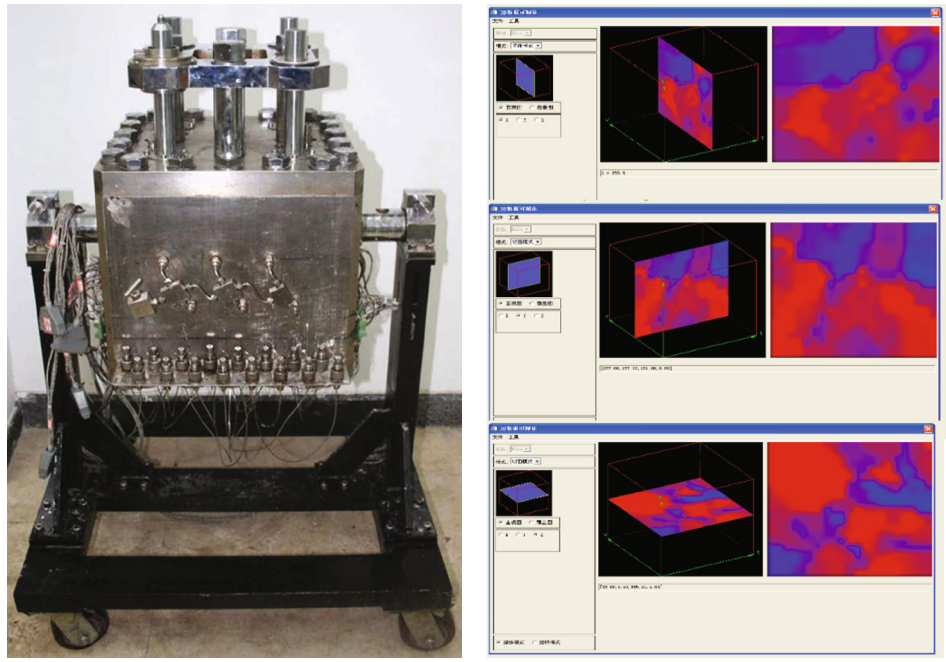

(a) 3D sandbox (b) Data acquisition software

Figure 3: 3D physical simulation facility and data acquisition software. (a) The main body of the 3D sandbox. (b) The distribution of fluids in the sandbox during the experiment process; the red represents the gas phase, and the blue represent the water phase.

sedimentary basins are mainly developed in tight sandstone gas reservoirs in China. Continental sedimentary systems include the alluvial fan system, river system, delta system, lake system, and swamp system, and each system has different sedimentary facies. Therefore, continental sedimentary patterns are variable both vertically and horizontally.

The permeability ratio caused by sedimentary facies can be different sedimentary systems or different sedimentary microfacies. In the longitudinal direction, the sedimentary phase transformation forms are positive rhythm deposition and antirhythm deposition. In the lateral direction, mainly sedimentary facies change, both of which can cause the heterogeneity of sandstone reservoirs in the longitudinal or transverse directions (Figure 2). Positive rhythmic sand is the common feature of various fluvial sedimentary sand bodies for rhythmic deposition. From the bottom to the top of the sandstone, the grain size changes from coarse to fine and the permeability changes from high to low. The permeability ratio in positive rhythm sand varies significantly due to different sedimentation.

3.3.2. Diagenetic Difference. Diagenesis controls the distribution of relatively high permeability zones. The formation has experimence a long period of sedimentation.

Compaction includes mechanicam compaction and pressolution. On the one hand, the pressure solution makes the particles contact more closely. On the other hand, the dissolved material precipitates to fill the intergranular pores or provides much silica for quartz enlargement and silica cementation, so the development of porosity and permeability of the clastic reservoir is more unfavorable. According to the experiment, the porosity loss of clastic rock can be divided into three levels. Class I is weak compaction, the clastic particles are point contact, and the porosity loss of clastic rock is 5%~10%. In class II, the clastic particle contact is linear contact or concave-convex contact and the porosity loss of clastic rock is 10%~15%. In class III, there is strong compaction, the clastic particles disappear obviously, and the porosity loss of clastic rock is 15%~30%. Diagenetic compaction and cementation also control the permeability ratio of clastic reservoirs. Without considering the later reservoir reconstruction, the compaction

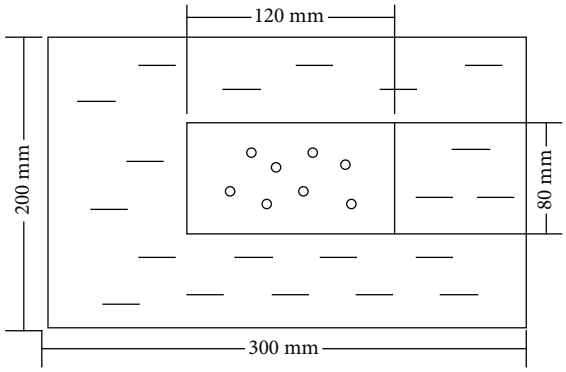

Figure 4: Sand filling model. The middle is a high-permeability sand body, surrounded by a low-permeability sand body.

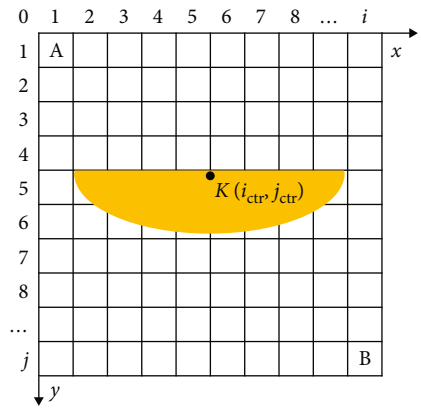

Figure 5: Schematic diagram of the simulation unit. The yellow means the sandstone with better porosity and permeability. The other white area near the yellow area means the sand with lower porosity and permeability [7].

and cementation increase with the increase of burial depth and the porosity and permeability of reservoirs tend to worsen. From the perspective of permeability difference, permeability becomes worse from shallow to deep and reservoirs in the same sedimentary environment also show heterogeneity in the longitudinal direction and there is permeability difference.

3.3.3. Late Reformation Origin. The formation of permeability difference is also caused by late reservoir transformation, leading to the existence of the same reservoir permeability difference. The later reformations are mainly dissolution and tectonism. Dissolution can increase the porosity and permeability of reservoirs. The favorable conditions are as follows: the depositional clastic rocks with coarser grain size and better porosity and permeability. There are many soluble substances in sandstone. Groundwater is acidic and has a specific flow rate. For example, clastic rock reservoirs in coal measures in China generally produce large numbers of organic acids and form an acidic formation water environment, which makes it challenging to form carbonate cementation in the early stage and is conducive to the development of intergranular micropores, thus contributing to porosity. Many tight sandstone gas reservoirs in China belong to coal measures.

The tectonic movement controls the sequence-sedimentary types and some diagenetic conditions and plays an indirect role in controlling the reservoir's physical properties; especially for fractured reservoirs, the structure is a direct control factor. Fractures and microfractures generated by structures can increase reservoir space and greatly improve permeability and serve as a significant channel for pore water transport. Fracture development can accelerate dissolution. Fractures have a great impact on reservoir and productivity in tight reservoirs, thus directly determining reservoir productivity.

The late structural transformation is mainly due to the extrusion of tectonic stress, the axial part of an anticline or the core of paleo-uplift is formed because of the fracture, and the permeability becomes better, often showing the characteristics of the axial wing permeability decreases, resulting in the existence of permeability level difference.

4. Physical Experiment Simulation of Tight Gas Accumulation

The experiment simulations of hydrocarbon migration and accumulation are mainly based on sandbox facilities. However, the typical sandbox experiment cannot restore the temperature and pressure conditions of the formation. In this section, we will develop a novel 3D sandbox facility that can restore the real reservoir's temperature and pressure condition.

4.1. Experimental Facility. The 3D sandbox experimental facility can be divided into two parts: the hardware part and the software part. Figure 3 shows both parts of the 3D physical sandbox simulation facility and date acquisition software.

Figure 3(a) shows the hardware part. The internal scale of the sandbox is $300 \times 300 \times 200$ mm; 128 electrodes and 12 temperature and pressure sensors are placed inside the sandbox. The sensors are uniformly distributed in the model in three dimensions to monitor the fluid migration and accumulation process. The electrode is in direct contact with the fluids in the sandbox, and the resistivity is used to determine whether the fluid at the vicinity of the measurement point is gas or water. The distribution characteristics of the fluid in the sandbox are obtained from the measurement point data of 128 electrodes.

There are significant differences in resistivity between the water and gas phases. Differences in resistivity will result in differences in the measured current value during the experiment. When the fluid near the measuring electrode is gas, the resistance measured is higher and the current measured is lower. When the fluid near the measuring electrode is water, the resistance measured is lower and the current measured is higher. Based on 128 measuring points we can obtain the fluid distribution characteristics of sandbox under high temperature and high pressure (Figure 3(b)).

4.2. Process of the Experiment. The primary process of the experiment is as follows.

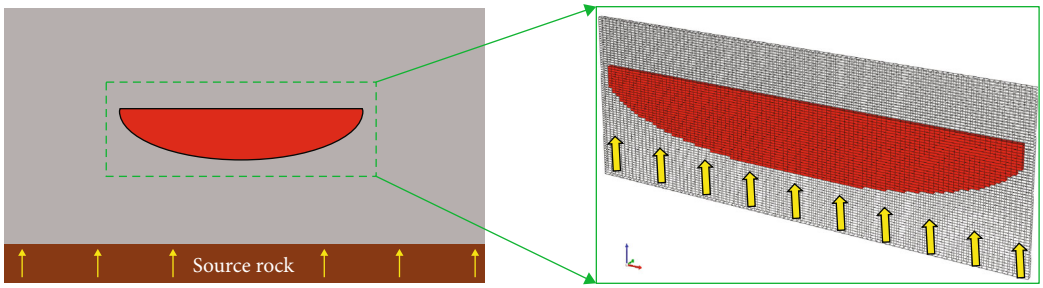

Figure 6: The numerical simulation process. The red means the center sand which has better porosity and permeability, the yellow means the gas, which migrate into the sand, and the size of cell is 0.5 m × 0.5 m [7].

Table 1: The properties of samples used in the capillary curve tests.

Sample	Porosity (%)	Permeability (mD)	Mercury injection curve (MIC)
No. 1	1.11	0.015	MIC-1
No. 2	3.69	0.028	MIC-2
No. 3	7.59	0.26	MIC-3
No. 4	10.31	2.62	MIC-4

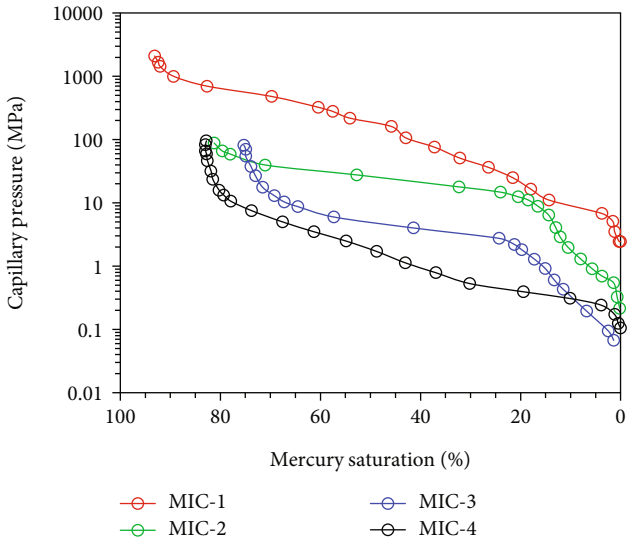

Figure 7: The capillary curves of four samples used in the numerical simulation process. The x-axis shows the injected mercury saturation, and the y-axis shows the capillary pressure. Through simple conversion, the pressure can be converted to capillary pressure in the presence of gas-water two-phase fluid.

Assemble equipment and install electrodes. Glass beads with different particle sizes were selected for experimental model filling. The electrodes of glass beads with different permeability were calibrated. Figure 4 shows the sand filling mode; the middle is a high-permeability sand body, surrounded by a low-permeability sand body.

The formation water is injected from the top cover of the mold by a dynamic injection system, and the sandstone body is compacted at the pressure of 9 MPa.

When the model is compacted, connect the electrode and pressure sensor circuit, move the whole model to the thermostat, and set the temperature of the thermostat at 90°C.

Run monitoring software, input physical experiment parameters, and start real-time data collection software.

The model was first saturated with water, and gas was injected from the bottom of the model at a stable pressure of 4.5 MPa for 13 days, and the experiment ended. The gas charging process is monitored in real time using the saturation measuring electrode. The phase distributions are given in Section 6.

As shown in Figure 4, in order to simulate the permeability heterogeneity of formation, the permeability of the middle permeability sand body is 300 mD and the permeability of the surrounded sand body is 100 mD, although the permeability of the physical model is higher than the actual tight formation. We want to use this model to simulate the permeability heterogeneity of formation, and this model can meet our requirements.

5. Numerical Simulation of Tight Gas Accumulation

In our previous work, we established a numerical simulation method for the tight gas reservoir; in this work, we will extend our previous work [7] and combine our numerical method with the physical experiment method in Section 4. Specific geological modeling methods and numerical simulation methods can be referred to our previously published literature. We only introduced the main methods and process of numerical simulation in this work. Figure 5 shows the schematic diagram of the numerical simulation unit, and the geological model is established as follows:

Assign coordinates to each grid in sequence (i, j).

Different sand bodies are numbered by the K value, and the top center of the central sand body is (i_{ctr}, j_{ctr}).

The control function formula (x, y, i_{ctr}, j_{ctr}) is used to describe the sand body morphology.

Judge whether the coordinate of any cell falls in the control formula. If it falls within the range of the sand body control formula, assign the value of the sand body to the cell. If the unit is not within the range of the control formula, the outer tight sandstone is assigned to the unit.

Table 2: Parameters for simulations.

	Parameters for center body			Parameters for surrounding sandstones		
	Porosity (%)	Permeability (mD)	MIC	Porosity (%)	Permeability (mD)	MIC
Simulation 1	3.69	0.028	MIC-2	1.11	0.015	MIC-1
Simulation 2	7.59	0.26	MIC-3	1.11	0.015	MIC-1
Simulation 3	10.31	2.62	MIC-4	1.11	0.015	MIC-1

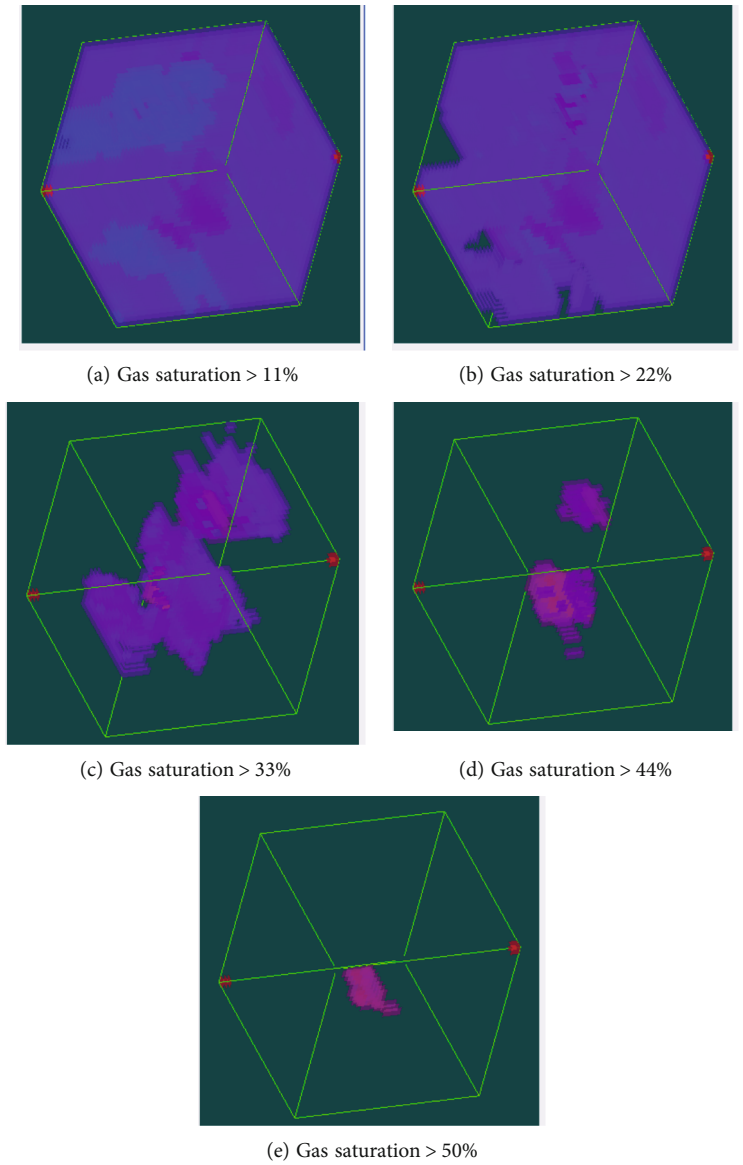

(a) Gas saturation > 11%

(b) Gas saturation > 22%

(c) Gas saturation > 33%

(d) Gas saturation > 44%

(e) Gas saturation > 50%

Figure 8: The gas saturation distribution of physical experiment simulation. From blue to red indicates a gradual increase in gas saturation. (a) Shows the gas saturation distribution, which is greater than 11%, and (e) omits the area with gas saturation of less than 55%.

After several cycles, each grid is assigned corresponding values to complete the resume of the geological model.

Figure 6 shows the numerical model used in this work which is similarly to the physical experiment model used in Section 4. This geological model is imported to the simulator CMG platform. Natural gas is charged from bottom to top. The red is the high-porosity and high-permeability sand body, and the gray part is the tight sandstone around the sand body. During the charging process, the natural gas from the source rock migrates to the sand body and accumulates in the sand body in the center.

During the numerical simulation process, the rock properties of the different sand bodies, such as porosity, permeability, and capillary curve, are from the natural rock sample of the

Table 3: Numerical simulation results.

	Pore volume of center sand body (m^3)	Gas saturation (%)	Reserve ($\times 10^4\ m^3$)
Simulation 1	3192.9	0.46	71
Simulation 2	5565.1	0.53	164
Simulation 3	8656.4	0.67	211

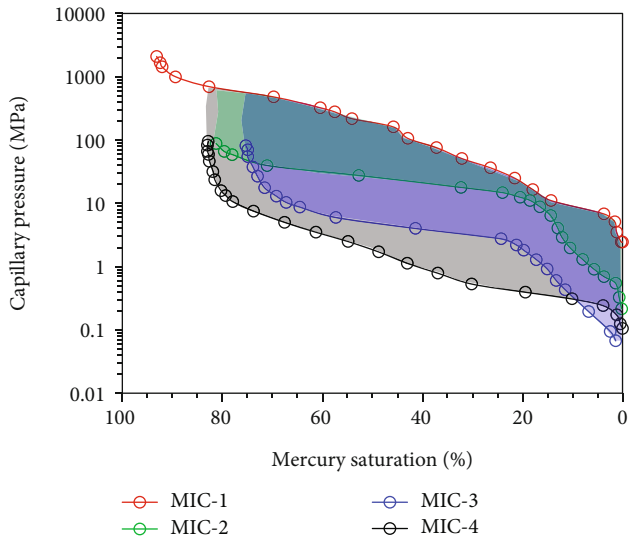

Figure 9: Capillary force curves for the four samples used in the simulations. As the surrounding rock, sample 1 has the highest capillary pressure of four samples and the other three capillary curves can enclose areas with the capillary curve of the surrounding rock. Three areas can be observed in this figure. Different colors distinguish them; the green area represents the capillary pressure difference between sample 1 and sample 2, which is used as the surrounding rock and center sandy body of simulation 1. The blue and the black areas represent simulation 2 and simulation 3.

tight formation. Table 1 shows the properties of four samples used in the numerical simulation process. The most crucial property of capillary curves is tested by the mercury injection method. Figure 7 shows the capillary curves of four samples used in the numerical simulation process. Through simple conversion, the pressure can be converted to capillary pressure in the presence of gas-water two-phase fluid.

Table 2 shows the used parameters for simulations in this work. During the numerical simulation process, sample 4 represents the surrounding rocks around the center sand body.

6. Results and Discussion

Figure 8 shows the results of the physical experiment simulation of Section 4. From blue to red indicates a gradual increase in gas saturation. The permeability difference of sandstone directly affects the gas-bearing property of tight sandstone reservoirs; the central sand body has the highest gas saturation. Heterogeneity is an essential feature of tight sandstone reservoirs. According to the understanding of the origin of permeability difference, the factors causing heterogeneity of tight sandstone reservoirs are original, mainly referring to the difference in permeability caused by the difference of sedimentary diagenesis, which is mainly reflected in the heterogeneity between layers. The other is the late transformation factor, which is the same sandstone reservoir, due to the late uneven dissolution, and structural fractures caused by the emergence of local high-permeability reservoirs, mainly manifested in the layer heterogeneity.

Due to the heterogeneity of tight sandstone, oil and gas migration and accumulation in sand bodies are different. During the migration of oil and gas in clastic reservoirs, the main driving forces are pressure and buoyancy. According to some scholars' research, the migration of natural gas in sandstone is mainly the function of buoyancy and capillary force.

Gas from the source rocks migrates into the capillary pore structure of the sandstone reservoir. Natural gas will accumulate under the barrier layer and accumulate into reservoirs if there is a barrier layer. In this process, the migration trend of natural gas is from the capillary pore structure to the conventional pore structure. The natural gas migration always migrates and accumulates along the reservoir with good porosity and permeability. For the heterogeneous sandstone with permeability difference, the oil and gas migration first points to the reservoir with good permeability.

Table 3 shows the results of the numerical simulation in Section 5. Compared to the physical simulation, the numerical simulation can simulate the high-temperature and pressure condition of actual formation and the reserve can be estimated in quantity. From simulation 1 to simulation 3, the permeability ratio becomes more extensive, which means that the heterogeneity of formation becomes stronger.

Figure 9 shows the capillary pressure difference between the center sand body and surrounding rock. The area enclosed by the capillary curves of the center sand body and surrounding rock shows the capillary pressure difference between the center sand body and surrounding rock. The larger the area is, the more significant the capillary pressure difference between the center sand body and surrounding rock, which represents that the more heterogeneous the formation is. As shown in Figure 9, the black area represents the capillary difference between sample 1 and sample 4; the green area represents the capillary difference between sample 1 and sample 2, and the black area is more extensive.

Through the abovementioned simulation and discussion, it can be observed that the difference in gas content caused by permeability level difference in simulations 1, 2, and 3 is, in essence, caused by the difference in capillary force between the center sand body and tight surrounding rock. In the charging process, when the natural gas enters the center sand body, the more significant the difference of capillary force between the center sand body and the tight

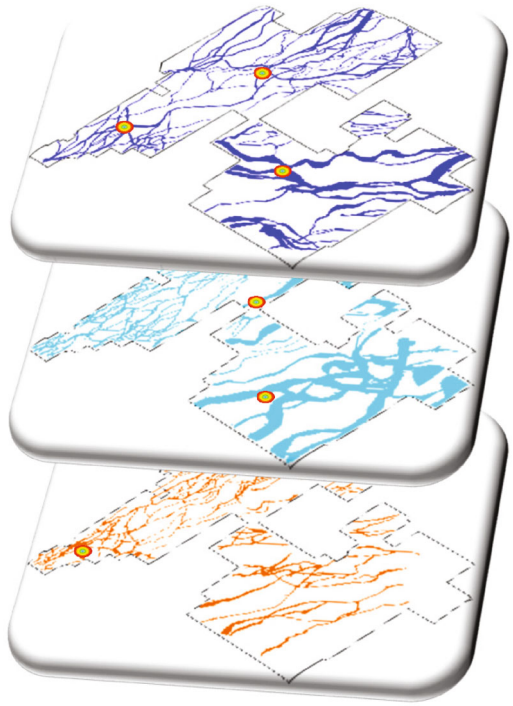

Figure 10: Multistage channel distribution model of Shaximiao Formation, Jurassic in the Sichuan Basin. Different colors indicate different periods.

surrounding rock, the easier the natural gas will accumulate in the "sweet spot" sand body. However, although the difference between capillary force curves is at the heart of the influence of permeability difference on the gas-bearing capacity of center sand, the parameter permeability difference is still of practical significance.

Generally, the lower the permeability, the greater the capillary force of the reservoir and the greater the permeability level difference can also reflect the more extraordinary capillary force difference between the center sand body and the tight surrounding rock. The permeability differential is much easier to obtain than the differential characterization of capillary forces. Some researchers used the permeability difference between the sweet spot and surrounding rock to judge the critical condition of gas accumulation. When the permeability difference is higher than the critical ratio, the gas is favorable to accumulate in the center sand body. If the ratio is less than the critical ratio, it becomes difficult for the gas to accumulate in the center sand body. The pore structure is complicated in the underground reservoir, so more attention should be paid to the capillary pressure difference between the sweet spot and surrounding rock to judge whether the gas can accumulate in the sweet spot.

The charging process of natural gas in sand bodies under different pore and permeability conditions. (1) When the natural gas generated from source rock enters tight sandstone, it must overcome the capillary force in the capillary pore structure to enter the reservoir; (2) the relatively high permeability of tight sandstone reservoir sand body (lens) capillary force primary does not exist; natrual gas migrates from sand body with low permeability to sand body with high permeability; natural gas accumulates in the upper area of sand body; (3) with the continuous charging of natural gas, the high-porosity and permeability sand body is filled with natural gas, forming a local gas-rich collective.

7. Field Application

The exploration of Jurassic tight gas in Sichuan Basin began in 1977 and went through three stages: gas generation exploration, lithologic gas exploration, and tight gas exploration and development stage.

(1) Early structural trap exploration stage (1977–1996). In this stage, petroleum geologists discovered the Daxingchang gas reservoir in southwest Sichuan

(2) Lithologic gas reservoirs in structural area stage (1997–2017). In this stage, Pingluoba, Yanjinggou, and Baima Temple gas reservoirs were found in southwest Sichuan, the Wubaochang gas reservoir was found in northeast Sichuan, and the Datachang gas reservoir in south Sichuan was discovered

(3) Tight gas exploration stage (2018–present). According to the abovementioned analysis, the essence of the gas accumulation in the tight formation is the heterogeneity of the reservoir. The permeability ratio can well describe the heterogeneity of the formation. Under the guidance of this geological theory, during the tight gas exploration stage, petroleum geologists discovered Qiulin and Bajiaochang multistage gas-bearing sand groups in central Sichuan; the PetroChina Company proved reserves of 9.462 billion cubic meters, and 17.686 billion cubic meters was submitted. The middle Sichuan Basin can be divided into 23 periods of channel sand groups from bottom to top longitudinally, and 13 periods are found to contain gas. Figure 10 shows the multistage channel distribution model of Jurassic in the Sichuan Basin. Different colors indicate different periods. The colorful points show the exploration wells with high production; they are located in the sand bodies, which have high permeability which has a higher permeability ratio

8. Conclusions

The permeability ratio can well characterize the heterogeneity of tight reservoirs. Based on this parameter, petroleum geologists can understand the interlayer heterogeneity during fluvial deposition and predict the sweet spots of tight gas.

The permeability ratio relationship between hydrocarbon accumulation of the tight sandstone reservoir mainly manifests as long as there is the existence of the differential permeability and there will be differences in natural gas migration dynamics, so that the natural gas accumulates in pores and depends on the extent of source rock.

The difference in gas saturation caused by the permeability ratio is caused by the difference in capillary force between the center sand body and the tight surrounding rock. The

permeability ratio is a parameter of practical engineering significance.

Data Availability

All supporting data can be found in the manuscript.

Conflicts of Interest

The authors declare that they have no conflicts of interests.

Acknowledgments

This work was supported by the CNPC Scientific Research and Technology Development Project "whole petroleum system theory and unconventional hydrocarbon accumulation mechanism" (2021DJ0101).

References

[1] R. Kadkhodaie-Ilkhchi, A. Kadkhodaie, R. Rezaee, and V. Mehdipour, "Unraveling the reservoir heterogeneity of the tight gas sandstones using the porosity conditioned facies modeling in the Whicher Range field, Perth Basin, Western Australia," *Journal of Petroleum Science and Engineering*, vol. 176, pp. 97–115, 2019.

[2] L. Huang, W. Zhou, H. Xu, L. Wang, J. Zou, and Q. Zhou, "Dynamic fluid states in organic-inorganic nanocomposite: implications for shale gas recovery and CO_2 sequestration," *Chemical Engineering Journal*, vol. 411, p. 128423, 2021.

[3] Y. Qiu, "Geological methodology of petroleum development (I)," *Petroleum Exploration and Development*, vol. 23, no. 2, pp. 43–47, 1996.

[4] P. Avseth, T. Mukerji, G. Mavko, and J. Dvorkin, "Rock-physics diagnostics of depositional texture, diagenetic alterations, and reservoir heterogeneity in high-porosity siliciclastic sediments and rocks—a review of selected models and suggested work flows," *Geophysics*, vol. 75, no. 5, p. 75A31-75A47, 2010.

[5] M. Venieri, S. J. Mackie, S. H. McKean et al., "The interplay between cm- and m-scale geological and geomechanical heterogeneity in organic-rich mudstones: implications for reservoir characterization of unconventional shale plays," *Journal of Natural Gas Science and Engineering*, vol. 97, article 104363, 2022.

[6] K. Alam, O. Abdullatif, A. El-Husseiny, and L. Babalola, "Depositional and diagenetic controls on reservoir heterogeneity and quality of the Bhuban Formation, Neogene Surma Group, Srikail Gas Field, Bengal Basin, Bangladesh," *Journal of Asian Earth Sciences*, vol. 223, p. 104985, 2022.

[7] W. Zhao, T. Zhang, C. Jia, X. Li, K. Wu, and M. He, "Numerical simulation on natural gas migration and accumulation in sweet spots of tight reservoir," *Journal of Natural Gas Science and Engineering*, vol. 81, p. 103454, 2020.

[8] W. Zhao, C. Jia, L. Jiang et al., "Fluid charging and hydrocarbon accumulation in the sweet spot, Ordos Basin, China," *Journal of Petroleum Science and Engineering*, vol. 200, p. 108391, 2021.

[9] W. Zhu, Y. Liu, Y. Shi, G. Zou, Q. Zhang, and D. Kong, "Effect of dynamic threshold pressure gradient on production performance in water-bearing tight gas reservoir," *Advances in Geo-Energy Research*, vol. 6, no. 4, pp. 286–295, 2022.

[10] W. Zhao, C. Jia, T. Zhang et al., "Effects of nanopore geometry on confined water flow: a view of lattice Boltzmann simulation," *Chemical Engineering Science*, vol. 230, p. 116183, 2021.

[11] L. Jiang, W. Zhao, J. Huang, Y. Fan, and J. Hao, "Effects of interactions in natural gas/water/rock system on hydrocarbon migration and accumulation," *Scientific Reports*, vol. 11, no. 1, pp. 1–13, 2021.

[12] M. J. Munn, "The anticlinal and hydraulic theories of oil and gas accumulation," *Economic Geology*, vol. 4, no. 6, pp. 509–529, 1909.

[13] W. C. Gussow, "Differential entrapment of oil and gas: a fundamental principle," *AAPG Bulletin*, vol. 38, no. 5, pp. 816–853, 1954.

[14] Z. Sun, B. Huang, K. Wu et al., "Nanoconfined methane density over pressure and temperature: wettability effect," *Journal of Natural Gas Science and Engineering*, vol. 99, p. 104426, 2022.

[15] B. Pan, Y. Li, H. Wang, F. Jones, and S. Iglauer, "CO2and CH4wettabilities of organic-rich shale," *Energy & Fuels*, vol. 32, no. 2, pp. 1914–1922, 2018.

[16] B. Pan, F. Jones, Z. Huang et al., "Methane (CH4) wettability of clay-coated quartz at reservoir conditions," *Energy & Fuels*, vol. 33, no. 2, pp. 788–795, 2019.

[17] R. Lenormand, E. Touboul, and C. Zarcone, "Numerical models and experiments on immiscible displacements in porous media," *Journal of Fluid Mechanics*, vol. 189, pp. 165–187, 1988.

[18] B. Pan, X. Yin, Y. Ju, and S. Iglauer, "Underground hydrogen storage: influencing parameters and future outlook," *Advances in Colloid and Interface Science*, vol. 294, p. 102473, 2021.

[19] X. Luo, "Simulation and characterization of pathway heterogeneity of secondary hydrocarbon migration," *AAPG Bulletin*, vol. 95, no. 6, pp. 881–898, 2011.

[20] B. Pan, T. Ni, W. Zhu et al., "Mini review on wettability in the methane–liquid–rock system at reservoir conditions: implications for gas recovery and geo-storage," *Energy & Fuels.*, vol. 36, no. 8, pp. 4268–4275, 2022.

[21] J. R. Boles, P. Eichhubl, G. Garven, and J. Chen, "Evolution of a hydrocarbon migration pathway along basin-bounding faults: evidence from fault cement," *AAPG Bulletin*, vol. 88, no. 7, pp. 947–970, 2004.

[22] D. Connolly, A. Lakhlifi, K. Rimaila et al., "Visualizing hydrocarbon migration pathways associated with the Ringhorne oil field, Norway: an integrated approach," *Interpretation*, vol. 10, no. 1, pp. SB27–SB37, 2022.

[23] T. K. Karamanos and G. M. Clore, "Large chaperone complexes through the lens of nuclear magnetic resonance spectroscopy," *Annual Review of Biophysics*, vol. 51, no. 1, pp. 223–246, 2022.

[24] M. Blunt, L. Kearney, A. Alhosani, Q. Lin, and B. Bijeljic, "Wettability characterization from pore-scale images using topology and energy balance with implications for recovery and storage," in *In SPE Annual Technical Conference and Exhibition*, OnePetro, 2021, September.

[25] Z. Chen, Q. Guo, C. Jiang et al., "Source rock characteristics and rock-eval-based hydrocarbon generation kinetic models of the lacustrine Chang-7 shale of Triassic Yanchang Formation, Ordos Basin, China," *International Journal of Coal Geology*, vol. 182, pp. 52–65, 2017.

[26] E. P. Weeks, "Determining the ratio of horizontal to vertical permeability by aquifer-test analysis," *Water Resources Research*, vol. 5, no. 1, pp. 196–214, 1969.

Hindawi
Geofluids
Volume 2022, Article ID 4145219, 18 pages
https://doi.org/10.1155/2022/4145219

Research Article

Prediction of the Control Effect of Fractured Leakage in Unconventional Reservoirs Using Machine Learning Method

Lei Pu,[1,2,3] **Jianjian Song**,[1,2,3] **Mingbiao Xu**,[1,2] **Jun Zhou**,[4] **Peng Xu**,[1,2,3] **and Shanshan Zhou**[1,2,3]

[1]*School of Petroleum Engineering, Yangtze University, Wuhan 430100, China*
[2]*Cooperative Innovation Center of Unconventional Oil and Gas, Yangtze University (Ministry of Education & Hubei Province), Wuhan, Hubei 430100, China*
[3]*Key Laboratory of Drilling and Production Engineering for Oil and Gas, Hubei Province, Wuhan Hubei, China 430100*
[4]*PetroChina Xinjiang Oilfield Development Company, Karamay, Xinjiang, China 834000*

Correspondence should be addressed to Jianjian Song; songjian629@yangtzeu.edu.cn
and Mingbiao Xu; xumingbiao@yangtzeu.edu.cn

Received 1 April 2022; Revised 25 May 2022; Accepted 3 June 2022; Published 24 June 2022

Academic Editor: Dong Feng

Bridging plugging is the most used method of plugging in unconventional oil reservoirs, and many factors affect the effect of bridging and plugging. Since the laboratory cannot simulate the actual leakage size of the lost formation and the corresponding leakage plugging process at the drilling site, the laboratory experiment results cannot reflect the actual leakage plugging construction effect. Aiming at the problem of frequent fracture leakage during drilling in Chepaizi block, Xinjiang, China, this paper proposes a set of machine learning methods based on a neural network. Three types of factors and 14 parameters with a strong correlation with the leakage control effect were screened out. Three categories of factors include construction parameters, choice of plugging material, and fluid properties of the carrier fluid. The training was carried out based on the collected field data, the appropriate activation function was set, and the deep well network structure was optimized. By improving the field plugging measures in the later period, the model was verified by these actual cases, and the results showed that the established model produced the highest R^2 of 0.974, has a good fit, and predicts well.

1. Introduction

In unconventional reservoir formations, leakage is one of the typical complex problems in the drilling process [1]. Faced with the problem of downhole leakage, improper treatment measures will lead to a low success rate of plugging, continuous leakage of drilling fluid, and an increase of lost working hours on-site and even further lead to wellbore scrapping (well abandonment) [2–3]. Carboniferous fractures are developed in the target layer of the Chepaizi block in Xinjiang, China, and loss of return and leakage frequently occurs during the drilling fluid process. Leakage control is a problem that has always plagued the site. Because the field engineer cannot understand the details of the underground lost formation, there is a problem of blindly plugging the leakage, which leads to the current situation of difficult one-time plugging. Frequent leakage problems cost a lot of construction time, and plugging construction takes 15% of the drilling cycle, which significantly increases the drilling cost and cannot meet the strategic needs of low-cost development [4–5].

The bridging plugging method is the most used in the construction of the Chepaizi block due to its simple construction process, low cost, and remarkable effect. Bridging and plugging materials are the key means to restore and enhance wellbore stress. The loss-stopping material establishes a dense, high-strength loss-stopping layer to balance the wellbore liquid column pressure, thereby preventing the propagation of fractures. Corrective borehole strengthening is a method to effectively improve the fracture

resistance of the rock formation by improving the formation closure stress and increasing the hoop stress in the near-wellbore area [6]. In this process, the quality of the plugging layer is related to various factors. Pump speed, pump pressure, the formula of bridging and plugging materials, and the viscosity of drilling fluid or particular plugging slurry will all affect the quality of the plugging layer. Poor quality plugging layer is the main reason for the failure of plugging [7–10].

Due to the significant difference between the actual situation of the leakage layer under the formation and the leakage channel simulated in the laboratory, there are certain limitations to the indoor fracture sealing experiment, and it is impossible to simulate the natural fractures in the formation, as well as the pumping displacement, and the pressure is also beyond the reach of laboratory equipment [11]. Laboratory experiments are lacking through the process of pumping the lost circulation slurry from the wellbore to the fracture. Therefore, according to laboratory experiments, it is often possible to obtain better effective plugging formulas, but the plugging process in the actual field still cannot play a good role. Since the laboratory experiment on the formulation of the plugging slurry is different from field plugging, the indoor plugging experiment method clearly understands the leakage channel [12–14]. However, the site's understanding of the underground leakage formation is vague. However, the loss dynamics, imaging logging data, and other methods have been adopted to infer the size of the leakage channel in the downhole lost formation. However, the cognition of downhole lost formation is limited within a specific range [15–18]. Therefore, it is not easy to choose a plugging method suitable for the site.

Machine learning methods are widely used in the exploration and development of the oil field. The large amount of data generated during the drilling process can solve practical problems in the field through machine learning. Pang et al. [19] extracted 22 comprehensive logging parameters from the drilling process and based on a set of deep learning mixed density network models, and they could reasonably predict the leakage problem. Gul and van Oort [20] avoided the pitfalls of manual measurement by establishing machine learning and deep learning to predict the filtration performance of water-based drilling fluids through fluid properties such as drilling fluid rheology, density, and temperature. Diaz et al. [21] used an artificial neural network to predict the permeability for nine drilling parameters obtained during drilling. Mahmoud et al. [22] compared three machine learning models, trained on 3,162 data sets of 6 (drilling parameters) and real-time prediction of formation lithology. Zhu Z et al. [23] predicted the settlement behavior of rod proppant in fractures through the artificial neural network, and the data set was from 588 practical laboratory experiments. Aiming at the advantages of machine learning methods in data processing, it can improve more accurate guidance for learning more data [24–26]. Machine learning methods seem to be able to replace the methods recommended by the experience of field engineers. These computationally intelligent methods can learn from the experience of plugging projects in this area and give more reasonable recommended methods [27].

According to the artificial neural network to estimate the most reasonable plugging formula, this study aims to evaluate the potential of using artificial neural networks to mine and analyze data from lost circulation plugging construction in the Chepaizi block, Xinjiang, China, and then build an intelligent model to predict lost circulation problems while drilling for the Carboniferous strata in the block. On-site technicians can use the construction effect of leakage to make quick and effective decisions in the face of leakage accidents.

2. The Theoretical Background of Fracture Plugging

2.1. The Missing Geological Conditions of the Chepaizi Block. The Chepaizi block is located on the northwestern margin of the Junggar Basin in Xinjiang, China. During the drilling process of the Chepaizi block, there were frequent leakages, mainly loss-of-return leakage; the loss time of front leakage was mainly distributed between 30 and 120 hours, and the potential leakage risk is high; the success rate of a single leakage plugging is low, and there are many cases of repeated leakage. The leakage situation in the Chepaizi block generally exists in the Carboniferous strata. The Carboniferous volcanic rock reservoirs in the Chepaizi area have developed fractures and have low pressure-bearing capacity. The Carboniferous volcanic rocks in the Chepaizi area have developed fractures, mainly oblique fractures, followed by low-angle fractures, accounting for 60.34% and 21.43% of the total number of observed fractures, respectively. Core observation shows that the core fracture length is 5-30 cm and the core fracture width is 0.1-0.6 mm.

The imaging images can identify fractures with different angles and filling degrees—Figure 1. The statistics of the Carboniferous imaging logging fractures in the Chepaizi area show that half-filled fractures and unfilled fractures account for 66% of the total number of identified fractures, with a high degree of effectiveness. High-angle fractures have the lowest filling degree, and low-angle fractures have the highest filling degree.

Taking well Che 482 in the Che 471 well area as an example, according to the characteristics reflected by the XRMI image data in Figure 2, the fracture types mainly include mesh fractures, oblique fractures, straight split fractures, induced fractures, filled-semifilled fractures, and microfractures. The Carboniferous fissures are related to the direction of faults and can be roughly divided into two groups, mainly near-EW-trending fissures (consistent with the average fault trend), followed by near-SN-trending fissures (consistent with the reverse fault trend).

2.2. Fracture Plugging Theory. Fracture leakage is one of the typically complex problems in the drilling process. There are currently two common solutions to plugging: active plugging and corrective plugging, depending on whether or not plugging occurs. In the process of actively strengthening the wellbore, the fracture tip is isolated from the wellbore pressure by the plugging material slurry, thereby preventing the expansion of the fracture. Corrective borehole strengthening is a method to effectively improve the fracture resistance of rock formations by improving the formation

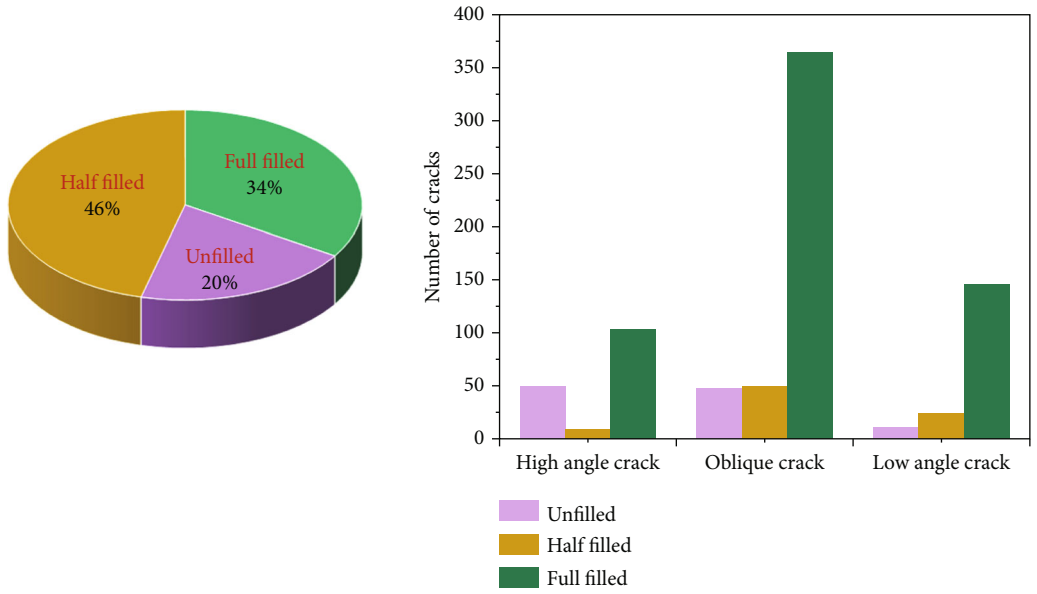

Figure 1: Characteristics of Carboniferous fractures in Chepaizi area.

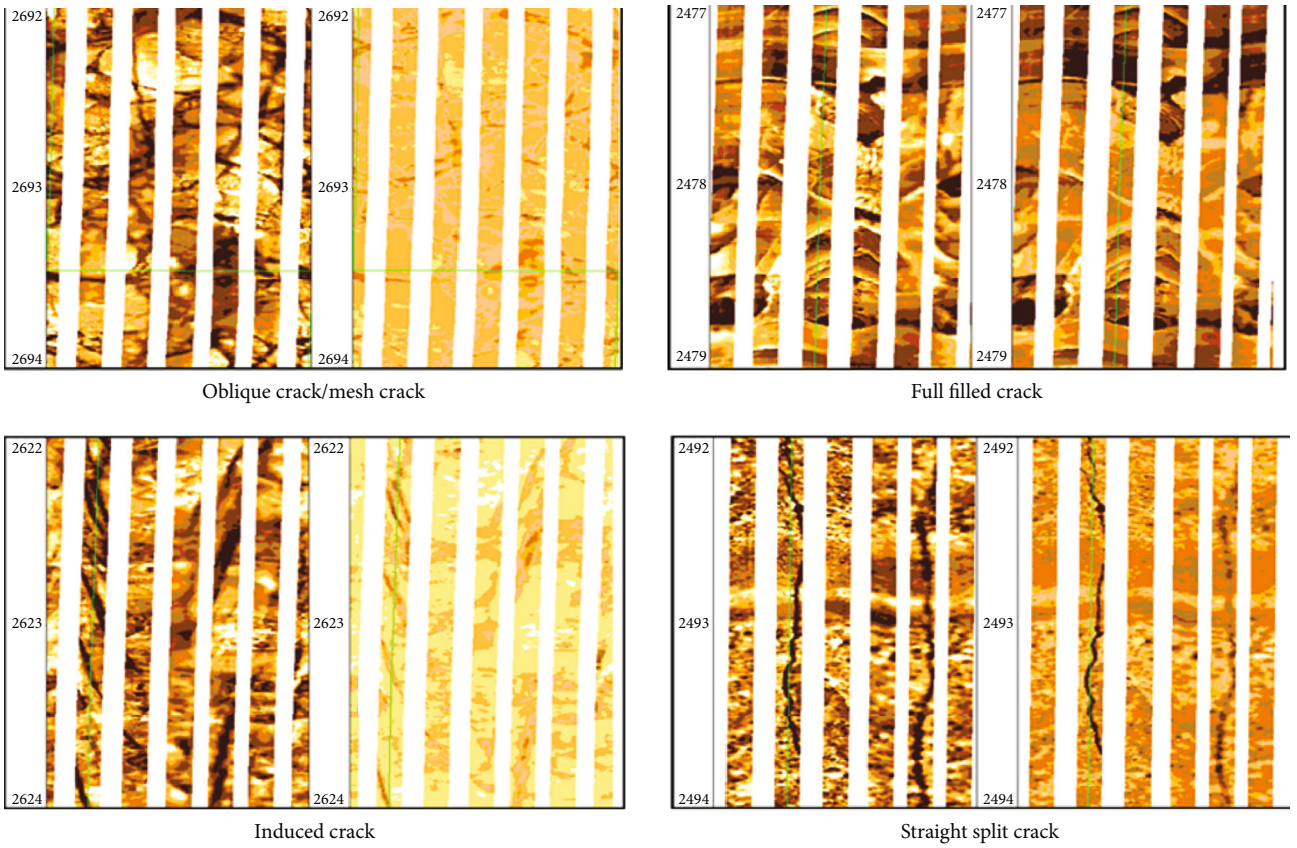

Figure 2: XRMI image characteristics of fractures in well Che 482.

closure stress and increasing the hoop stress in the near-wellbore area. The most common wellbore-strengthening theories are ring compression stress enhancement (stress cage) [28, 29], fracture propagation resistance (FPR) [30], and fracture closure stress (FCS) [31]. Figure 3 depicts the role of the plugging material in different wellbore-strengthening theories [32].

No matter which wellbore strengthening theory is adopted, it all involves the need to make the loss-stopping material be carried into the fracture so as to construct the

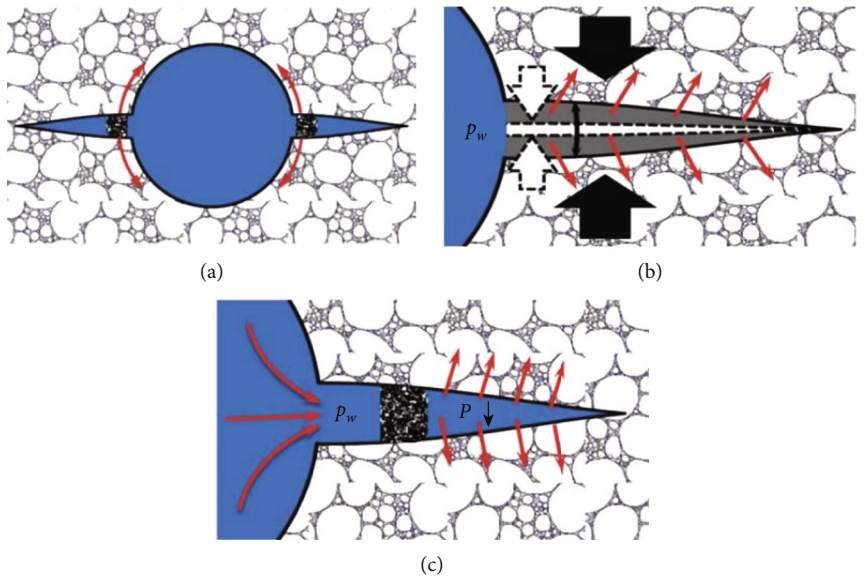

Figure 3: Common hypotheses related to mechanical wellbore strengthening. (a) Stress cage. (b) Fracture-closure stress. (c) Fracture-propagation resistance [32].

plugging zone. Loss-stopping materials are appropriately positioned within the fracture to isolate the pressure transfer in the fracture and increase the hoop stress in the near-wellbore region. This behavior is a complex process involving the migration behavior of particles in the fluid and the contact behavior between particles and particles and fractures.

The lost circulation material is carried into the fracture by drilling fluid or a particular lost circulation slurry. The behavior of fluid and particles in this transport process can be described by equations (1) and (2). According to the drilling fluid loss model in a single nonsite fracture established by Li et al. [33], for the non-Newtonian Heba drilling fluid, the flow velocity equation in the fracture is

$$V = \left(\frac{n}{2n+1}\right)\left(\frac{w}{2}\right)^{1+(1/n)}\left(\frac{1}{k}\right)^{1/n}\left(-\frac{d_p}{d_x} - \frac{2n+1}{n+1}\frac{2\tau_y}{w}\right)^{1/n}. \tag{1}$$

In the formula, n is the flow pattern index (dimensionless), K is the consistency coefficient (Pa▪s^n), τ_y is the dynamic shear force (Pa), P is the pressure (Pa) and w is the fracture width.

In the process of two-phase flow of the plugging material in the fluid, when the fluid in the fracture flows in a laminar flow state, the total drag force and drag force coefficients on the particles are equations (2) and (3), respectively:

$$F_d = C_D A_p \frac{\rho u^2}{2}, \tag{2}$$

$$C_D = \frac{24}{Re_p}, \tag{3}$$

where A_p is the surface area of the particle (cm^2), ρ is the density of the fluid, (g/cm^3), μ is the viscosity of the fluid (MPa▪s), and Re_p is the Reynolds number of the fluid.

Therefore, it can be found that the migration behavior of the plugging particles in the fluid is related to the density, size, and shape of the particles and the density, rheological properties, and velocity of the fluid. The particle size distribution of the plugging material has a significant impact on the fracture sealing efficiency. Whitfill [34] proposed that in fractures, the particle size distribution should be kept at about 50% of the fracture width, improving the bridging ability of the material between fractures. Alsaba et al. [35] also proposed a new standard; the D50 and D90 of the plugging material should be equal to or more excellent than 3/10 and 6/5 of the fracture width, respectively, which can effectively seal the fracture. In fact, different types of leakage-stopping materials have slightly different requirements for the particle size distribution of the leakage-stopping materials under the same fracture width. Therefore, before designing the particle size distribution of the leakage plugging material that is most suitable for fracture plugging, the type of leakage plugging material needs to be considered. This process needs to be determined through field plugging experience or some laboratory experiments.

2.3. Experimental Analysis of the Correlation Factors of the Missing Control Effect

2.3.1. Experimental Apparatus. Figure 4 is a schematic diagram of an experimental setup used to evaluate the plugging ability of the leakage plugging material to fractures. The device provides different pressures by pressurizing the fluid through a high-pressure nitrogen cylinder and can provide a maximum pressure of 10 MPa. The storage device of the plugging slurry contains a liquid level metering device that can measure the volume of the plugging slurry that is displaced into the fracture at each stage. The simulated fractures used were split using cores from the Carboniferous formation in the Chepaizi block. The advantage of this natural simulated fracture is that it can better simulate the roughness and bedding of the actual formation

fracture and the corresponding permeability. The length of the entire fracture is 20 cm. The front and rear ends of the clamping device containing simulated natural fractures are equipped with pressure sensors to record the pressure of the plugging slurry when it passes through the fracture. Once the leak-stopping material forms a good sealing layer in the fracture, the front-end pressure of the clamping device will rise rapidly. The pressure at this time represents the pressure that the sealing layer in the fracture can bear. The collection device of the plugging slurry can record the volume of the plugging slurry in the whole process. Finally, after the experiment is completed, the position of the plugging layer in the fracture can be measured by disassembling the natural simulated fracture device.

Based on the experience of on-site construction and laboratory experiments, we found that even if the plugging particles can form a suitable plugin for the fracture because the plugging position is close to the front end of the fracture or the fracture opening, it can withstand a high pressure. However, during the actual drilling process, due to the influence of downhole pressure fluctuations, the plugging layer at the fracture mouth fell off again, failing to plug. Therefore, to evaluate the effect of indoor leakage control more realistically, we evaluate the pressure-bearing capacity P (MPa) of the fracture sealing layer and measure the invasion depth L (cm) of the sealing layer in the fracture. These two aspects are used as the evaluation criteria for evaluating the sealing effect of the fracture.

2.3.2. Influence of Different Factors on the Effect of Plugging Experiments. The fracture size used in the fracture sealing experiment is a natural fracture with a size of 5 cm × 30 cm. The maximum applied pressure in the experiment is 8 MPa, and the carrier fluid used is the drilling fluid used in the field. The viscosity of the fluid is adjusted by adjusting the amount of the viscosifier. The displayed viscosity is the apparent viscosity of the drilling fluid. The original pumping pressure of the drilling fluid with the addition of lost circulation material was 1 MPa. The plugging material is the KZ-4 plugging particle, which is the most widely used KZ series plugging material in Chepaizi, with a particle size between 18 and 22 mm.

(1) Influence of the fluid properties of the carrier fluid on the leakage control effect

(2) Influence of pumping factors on leakage control effect

(3) Influence of plugging materials on the effect of leakage control

Through laboratory experiments, it is found that the effect of fracture loss control is not only related to the plugging material but also has a great relationship with the pumping pressure and fluid properties. Figure 5 shows that as the viscosity of the carrier fluid increases, the magnitude of the drag force exerted by the fluid on the particles increases. When the carried viscosity is greater than 30 MPa▪s, the plugging particles can be better carried to the fracture depth during the migration process, and the intrusion depth reaches 12 cm. The sedimentation velocity of the particles is also reduced, which avoids the increase in concentration caused by excessive accumulation and the formation of plugs at the fracture openings, which weakens the plugging quality. When the viscosity continues to increase, the penetration depth and pressure-bearing capacity no longer change. Figure 6 shows that with the increase of pumping pressure, although the pressure-bearing capacity can reach 8 MPa, the intrusion depth gradually decreases, from 12 cm to 1 cm. The reason is that when the particles and the particles and the wall are hindered, they cannot stay. The displacement speed of the particles also began to increase, and the particles could not enter into the fractures in a proper order, resulting in the chaos of the force chain between the particles and the fractures, and the fractures were blocked in advance. Figure 7 shows that when the concentration of particles is lower, at 10%, the particles cannot form a tight seal in the fracture. However, if the particle concentration is too high, it is not conducive to the displacement of the particles to the depth of the fracture.

Figure 8 shows the difference in the penetration depth of the formed plugging layer and the plugging state in different plugging experiments. Through experiments, it is found that the greater the invasion depth L (cm) of the plugging layer, the better the effect of the plugging layer and the greater the pressure it bears. However, during the experiment, when the pressure-bearing capacity reached the highest, there was a significant difference in the penetration depth. It shows that in the actual plugging process of on-site fractures, the leakage control effect of fractures has a significant relationship with the pumping parameters of construction, the properties, and concentrations of leakage plugging materials, and the properties of the fluid carried.

2.4. Determination of the Relevant Factors of the Leakage Control Effect of the Chepaizi Block. This study is to conduct machine learning on the leakage control effect of the Carboniferous fractured leakage formations in the Chepaizi block. The selection of data set types dramatically impacts the quality of machine learning. LCM particles are pumped into the reservoir section with the plugging slurry and enter the reservoir under the action of pressure difference. This process involves the interaction force between particles and fluids and between particles and fractures [36]. The suspending force and drag force generated by the fluid on the particles will obviously affect the suspension, bridging, and filling of the particles during the plugging process [37–38]. The particle size distribution and its own properties of LCM determine whether the "throat" of the fracture can be just plugged, so that the fracture channel can be converted into a porous channel [39]. Based on the results of laboratory experiments and the experience of on-site leakage accident handling, a large number of parameters on the site were screened, and three types of factors that had a strong correlation with the success rate of on-site leakage plugging were selected, namely, pumping parameters, type, and matching of plugging materials, the fluid properties of the carrier fluid.

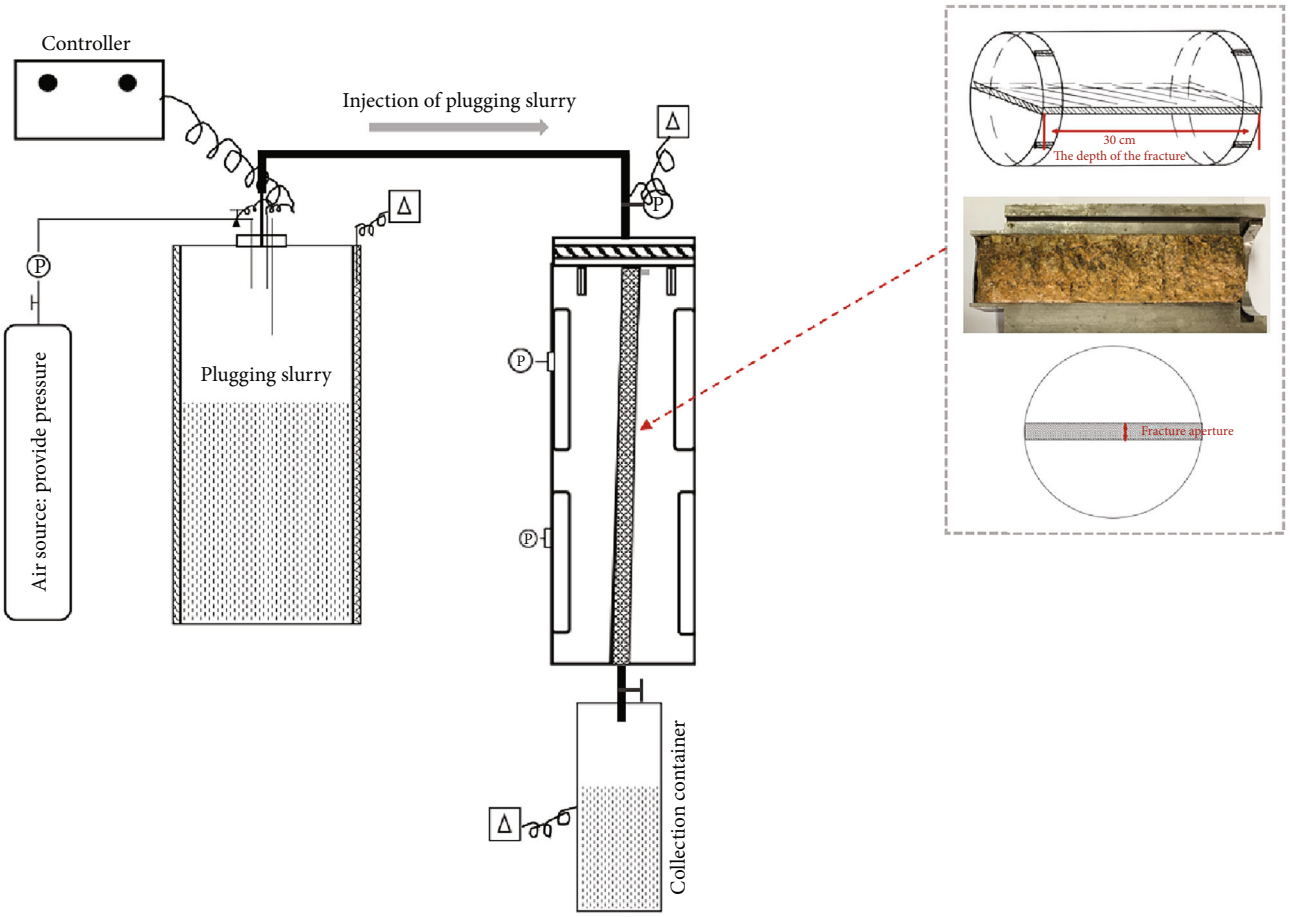

Figure 4: Indoor simulated natural fracture plugging an experimental device.

These three parameters can be further classified, and the same engineering factors can be divided into pumping displacement and maximum pumping pressure. The choice of the leakage-stopping material is the concentration of the leakage-stopping material and the type of the leakage-stopping material. The materials selected according to the type of on-site loss-stopping materials are KZ-3, KZ-4, KZ-5, walnut shell, vermiculite, comprehensive loss-stopping agent, and LWD-while-drilling agent. The fluid properties of the carrier fluid are divided into total volume, density, dynamic shear force, and funnel viscosity.

In the actual drilling process of the Carboniferous strata in the Chepaizi block, the leakage rate of each time has a certain difference. In fact, it is difficult to quantify the formation properties such as water swelling properties and heterogeneity. At the same time, we only study the leakage layer of the Carboniferous in this block, and other factors can be ignored, so the leakage velocity can be used as the description of missing stratigraphic characteristics. Finally, according to the parameters selected in the field, the field leakage control effect is defined. After each leakage plugging operation occurs, the actual leakage rate of the formation before and after the construction was compared. The leakage control effect is described in the form of a percentage, and the calculation formula is

$$E = 1 - \frac{V_{\text{initial}}}{V_{\text{after construction}}} \times 100\%. \tag{4}$$

In the formula, V_{initial} is the formation leakage rate before the plugging construction. The $V_{\text{after construction}}$ is the rate of formation leakage after on-site leakage plugging construction.

3. Artificial Neural Networks

When plugging the lost formation, the leakage control effect is affected by more than a dozen engineering parameters. When the information on the more than 400 times of plugging of more than 100 wells in the Carboniferous in this block is obtained after that, the neural network is applied to predict the leakage control effect of this block.

A neural network is a powerful tool for approximating unknown nonlinear functions [40], which helps solve different engineering problems and is now widely used in oil and gas exploration and development. The basic construction of a neural network is network construction, transfer function, and training method [41]. Neural networks build these

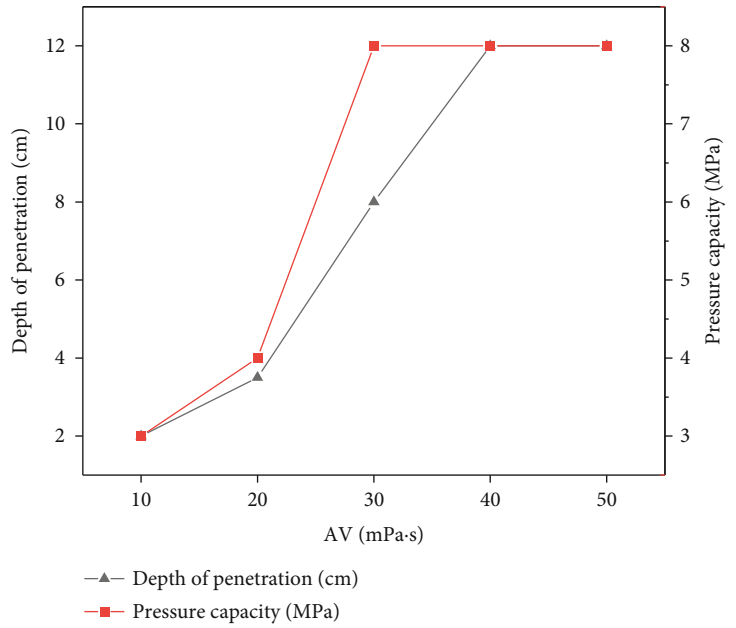

Figure 5: The effect of carrier fluid viscosity on the pressure-bearing capacity and invasion depth of the plugging layer.

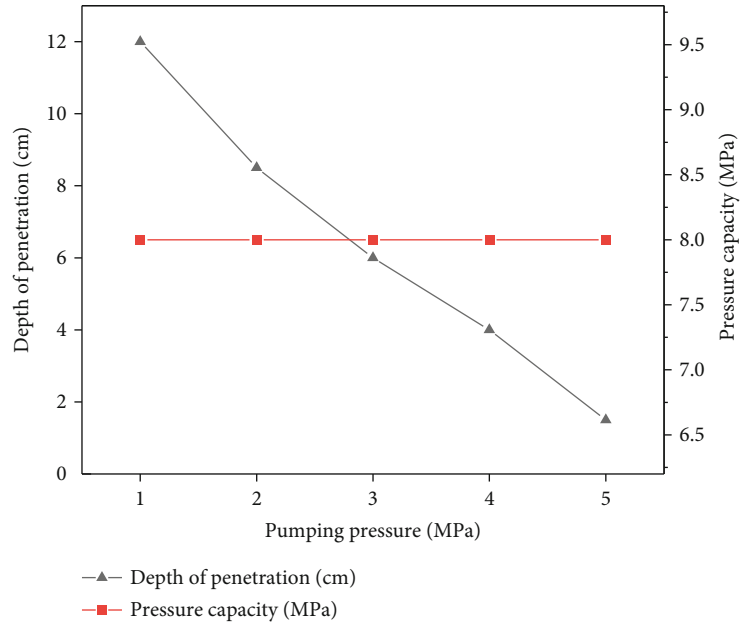

Figure 6: The effect of pumping pressure on the pressure-bearing capacity and invasion depth of the plugging layer.

network structures from neurons, including an input layer, an output layer, and one or more hidden layers. There is no connection between neurons in the same layer and forward connection between neurons in different layers [42]. The process of information propagation between neurons is divided into forwarding propagation and backpropagation. The output layer that does not get the expected value will say that the signal is transmitted back along with the originally connected node, and the desired goal is achieved by modifying the weight value.

We used logistic sigmoid and hyperbolic tangent transfer functions as activation functions. The logistic sigmoid and hyperbolic tangent transfer functions are considered to perform well for any problem involving fault diagnosis and feature classification. Logistic Sigmoid and hyperbolic tangent transfer functions are given by equations (5) and (6). Both functions are plotted in Figure 9. The model uses the Levenberg-Marquardt (LM) algorithm to find the extreme value of the function, which has the advantages of fast and efficient training and improving the convergence speed of

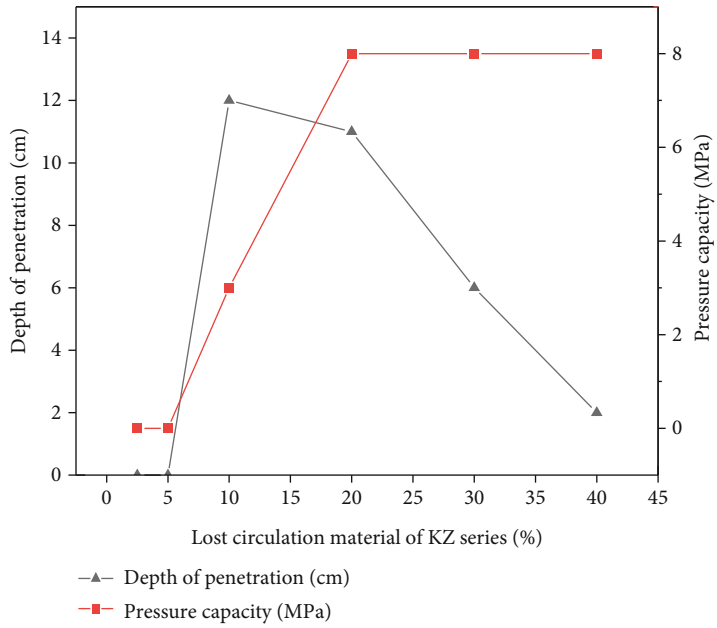

Figure 7: The effect of the concentration of the plugging material on the pressure-bearing capacity and invasion depth of the plugging layer.

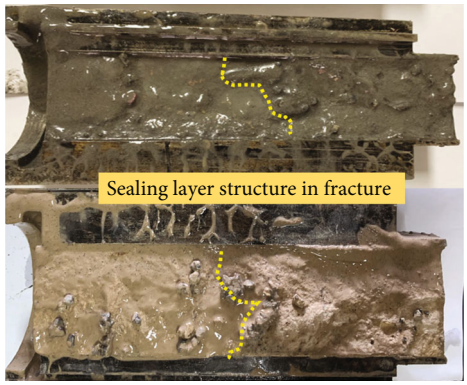

Figure 8: Experimental results of fracture plugging with different penetration depths.

ANN.

$$\text{Sigmoid}: \sigma(x) = \frac{1}{1 + e^{-x}}, \tag{5}$$

$$\text{Hyperbolic tangent}: \sigma(x) = \frac{e^{x} - e^{-x}}{e^{x} + e^{-x}}. \tag{6}$$

3.1. Data Collection and Preprocessing. Data sets play a crucial role in machine learning. A properly screened data set will improve the accuracy of predictions, while the introduction of redundant data sets will affect the prediction results. At the same time, the amount of data in the data set should be large enough to provide reliability for decision-making. In the 50 wells in the Chepaizi block, Xinjiang, China, fractured leakage occurred in different degrees in the Carboniferous strata, and each well had 3 to 5 fractured leakage behaviors, and each leakage plugging process took several times to block successfully. Therefore, according to the complex accident handling process in the drilling process recorded on the site, statistics and analyses are made about the on-site leakage plugging effect and various parameters in the actual construction process. Based on the empirical analysis of the on-site leakage plugging effect and the research on the relevant factors of the quality of the leakage plugging effect in the laboratory, this study selected the actual leakage rate on-site, the pump speed, and pump pressure during the construction process, and the matching and concentration of various types of leakage plugging materials. As well as the fluid properties (density, viscosity) of the carrier fluid as the data set used, these parameters are treated as independent variables. The leakage control effect is regarded as the dependent variable, and the leakage rate on-site will decrease to a certain extent after each leakage plugging construction. In order to digitize the leakage plugging effect on site, the actual leakage control effect is evaluated by taking the percentage reduction of the leakage rate before and after construction. When the on-site leakage plugging construction is completed, the leakage rate remains the same as before and does not decrease. At this time, the plugging quality is regarded as the worst, and 0% is used to represent the effect of this plugging construction. When the on-site leakage plugging construction is completed, the leakage rate decreases to 0, and the leakage plugging material smoothly enters the fracture to form a plugging layer to prevent the drilling fluid in the wellbore from leaking from the fracture again. At this time, the leakage control effect is the best, and the leakage rate decreases. The rate is 100%, and 100% is used to represent the effect of this plugging construction. In the 50 wells in the Chepaizi block, 450 cases (data sets) were collected.

In neural networks, high-valued data tends to increase the proportion of influence on the model, thus losing the features of low-valued data [43]. Therefore, it is necessary

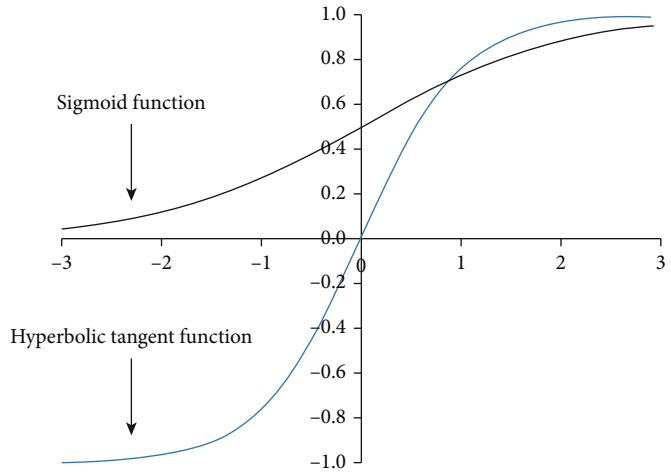

Figure 9: Schematic diagram of the hyperbolic tangent function and sigmoid function.

Table 1: Generated code for missing control-related parameters.

Column name	Overview	Code
Leak rate (m^3/h)	The rate of loss of drilling fluid during drilling	1
Displacement (m^3/h)	The rate at which the carrier fluid is pumped during the plugging process	2
Pumping pressure max (MPa)	The carrier fluid is pumped to the leakage layer, the pressure generated by the fluid at this time	3
Concentration (%)	The concentration of plugging particles in the overall plugging slurry	4
Addition of KZ-3 (t)	Plugging materials used in the field, mineral type granular plugging materials	5
Addition of KZ-4 (t)	Plugging materials used in the field, mineral type granular plugging materials	6
Addition of KZ-5 (t)	Plugging materials used in the field, mineral type granular plugging materials	7
Addition of walnut shell (t)	Plugging materials used on-site, plant-type granular plugging materials	8
Amount of vermiculite (t)	Leakage plugging materials used in the field, mineral type flaky leakage plugging materials	9
Amount of comprehensive plugging agent (t)	Composite leakage plugging material mixed with particles, flakes, and fibers	10
Addition amount of LWD agent (t)	Particle plugging material with particle size below 1 mm	11
Total addition (m^3)	The overall volume of carrier fluid	12
Density (g▪cm^3)	The density of carrier fluid	13
Funnel viscosity (s)	From the marsh funnel, indicating the viscosity of the drilling fluid	1 4
Actual blocking effect (%)	The ratio of the leakage velocity of the lost formation before and after the plugging construction	1 5

to normalize the data to avoid errors caused by the excessively large value range. Normalization of the data depends on the transfer function used to build the ANN.

When using logistic Sigmoid functions as the transfer function, with input and target data in the range (0, 1), use equation (7) to process the functions:

$$xn_i = \frac{(x_i - x_{\min})}{(x_{\max} - x_{\min})}. \tag{7}$$

Conversely, when using the TAANSIG transfer function, the input and target data are processed in the range (-1, 1) using

$$xn_i = \frac{2(x_i - x_{\min})}{(x_{\max} - x_{\min})} - 1. \tag{8}$$

Among them, xn_i represents the data set of plugging construction parameters after the standardization process is completed. x_i represents the original plugging construction parameter data set. $x_{\max}$ indicates the maximum value of the leakage plugging construction parameter data set, and $x_{\min}$ represents the minimum value of the leakage plugging construction parameter data set. Table 1 shows the generated codes for the relevant factors of the missing control effect.

Table 2: Statistical analysis and summary of sample data.

Types	Minimum	Maximum	Range	Arithmetic mean	Std. deviation	Skewness	Kurtosis
Leak rate (m^3/h)	3	100	9 7	51.37692	33.57244	0.430229	-1.35702
Displacement (m^3/h)	30	100.8	7 0.8	52.66154	18.32424	1.126849	1.879827
Pumping pressure max (MPa)	5	16	1 1	10.73077	2.739423	-0.02166	0.004141
Concentration (%)	0.05	0.3636	0.3136	0.109792	0.057074	3.442085	15.20886
Addition of KZ-3 (t)	0	2	2	0.461538	0.795698	1.350404	0.010491
Addition of KZ-4 (t)	0	2.5	2.5	0.942308	0.85852	0.238694	-1.44599
Addition of KZ-5 (t)	0	2.5	2.5	0.134615	0.510612	4.24259	18.6555
Addition of walnut shell (t)	0	3	3	1.923077	0.873678	-0.57641	-0.13565
Amount of vermiculite (t)	0	3	3	0.634615	0.915231	1.173339	0.043976
Amount of comprehensive plugging agent (t)	0	3	3	1.423077	1.080352	-0.17773	-1.36465
Addition amount of LWD agent (t)	0	2	2	0.134615	0.471448	3.500587	11.44695
Total addition (m^3)	11	80	69	55.42308	13.31042	-1.02063	3.95618
Density (g/cm^3)	1.15	1.25	0.1	1.221538	0.022819	-2.32647	5.916531
Funnel viscosity (s)	46	72	26	58.03846	9.500934	0.36903	-1.50663
Actual blocking effect (%)	0.1	1	0.9	0.596923	0.330102	0.280503	-1.75597

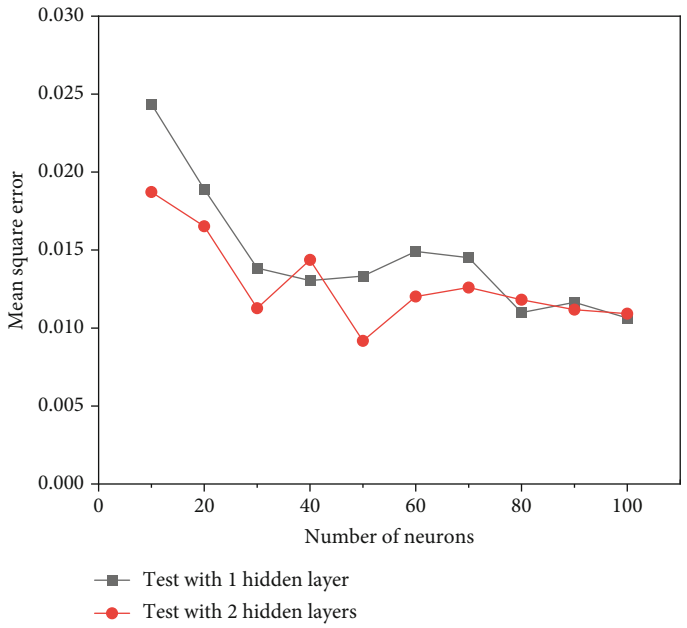

Figure 10: The MSE of an ANN model with different neurons and hidden layers (using the logistic Sigmoid functions).

Statistical analysis of the construction parameters and results of the plugging construction to determine the minimum value, maximum value, average value, range, standard deviation, skewness, and kurtosis of the data to be used. The data characteristics are shown in Table 2. We got a total of 4500 complete and valid data, including 22 data features.

3.2. Optimization and Evaluation of the Model. When using an artificial neural network, the statistical data set needs to be divided, and the standardized data set is randomly divided into a training data set and a test set. The training data set is used to tune the network weights and biases and compute gradients, and the test data set is used to test the developed model to evaluate its performance independently. The division ratio is related to the overall size of the data set. Based on the above, 80% of the data is used for training, and 20% is used for testing [44]. In the collected 450 sets of data sets, 360 sets of sample data are used for training, and 90 sets of sample data are used for testing. The training set and test set are suitable for the learning process, while the test set is used to test the ability of the model to achieve predictions.

This study used mean square error (MSE), mean absolute error (MAE), and coefficient of determination (R^2) as evaluation indicators. The formula is

$$\mathrm{MSE} = \frac{1}{n}\sum_{i}^{n}\left(P_{\mathrm{act}} - P_{\mathrm{pre}}\right)^2, \tag{9}$$

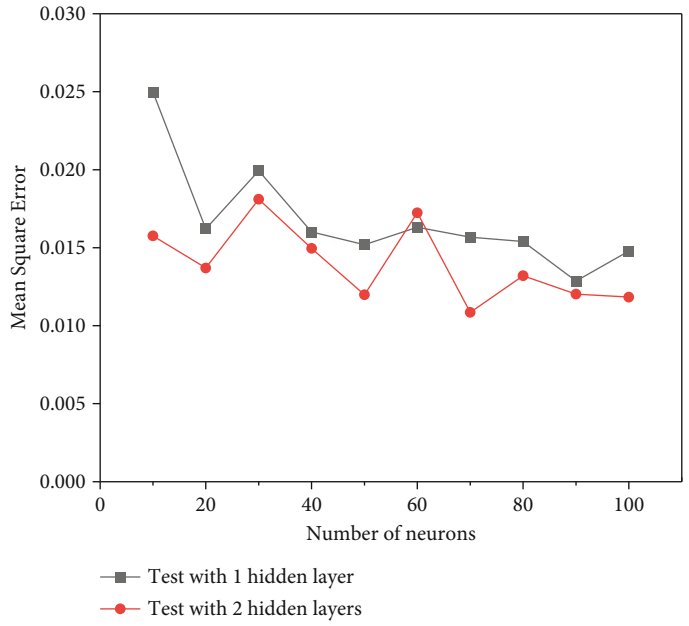

Figure 11: The MSE of an ANN model with different neurons and hidden layers (using the TASIG transfer function).

Table 3: Details of the developed artificial neural network architecture.

Feature	Value/model
Number of samples	450
Training algorithm	Levenberg-Marquardt algorithm
Hidden layer size	2L * 50N
Tolerance	1×10^{-6}
Maximum iteration	2000
Learning rate	0.07
Initial learning rate	0.01
Activation	Logistic sigmoid functions
Shuffle	TURE

$$\mathrm{MAE} = \frac{1}{m}\sum_{i=1}^{m}\left(P_{\mathrm{act}} - P_{\mathrm{pre}}\right), \tag{10}$$

$$R^2 = 1 - \frac{\sum_{i=1}^{n}\left(P_{\mathrm{act}} - P_{\mathrm{pre}}\right)^2}{\sum_{i=1}^{n}\left(P_{\mathrm{act}} - P_{\mathrm{ave}}\right)^2}. \tag{11}$$

In the above equation, y is the number of actually lost circulation solutions; $f(x)$ represents the number of correct simulated lost circulation solutions using machine learning methods; n is the total number of data types used for model evaluation. The proposed model has the highest sum R^2 and the lowest MSE, and MAE can be considered the best model.

4. Results and Discussion

4.1. The Architecture of ANN. The number of hidden layers, the number of neurons, and the transfer function are the key parameters that determine the accuracy of ANN, but there is no definite solution for the selection of ANN architecture. In order to find an ANN architecture suitable for this prediction model, it is necessary to conduct some experiments to determine the best configuration for ANN. Previous research has been done on the selection of the number of hidden layers and neurons, and some practical suggestions have been put forward. Boger and Guterman (1997) believed that hidden nodes should be at least as many as input nodes to capture 70%~90% of the features. Hecht-Nielsen proposed an empirical relationship between the number of computational hidden neurons and the number of input parameters, expressed in equation (11) [45]. Jiang et al. proposed a relational formula to determine the number of neurons in a multilayer hidden layer, and the relational formula is 12, where K, m_1, and m_2 are the number of neurons in the hidden layer, the number of input parameters, and the number of output parameters, respectively. m_3 is an empirical constant between 1 and 10 [46].

$$h = 2i + 1, \tag{12}$$

where h is the number of hidden neurons and i is the number of input parameters.

$$K = \sqrt{m_1 + m_2 + m_3}, \tag{13}$$

where K, m_1, and m_2 are the number of neurons in the hidden layer, the number of input parameters, and the number of output parameters, respectively. m_3 is an empirical constant between 1 and 10.

Based on the above features, we compare the prediction accuracy of each model by comparing the number of neurons in different hidden layers and the number of hidden layers. We control the number of neurons between 10 and 100. In order to control the complexity of the model and simplify the model, the number of hidden layers is set to 1

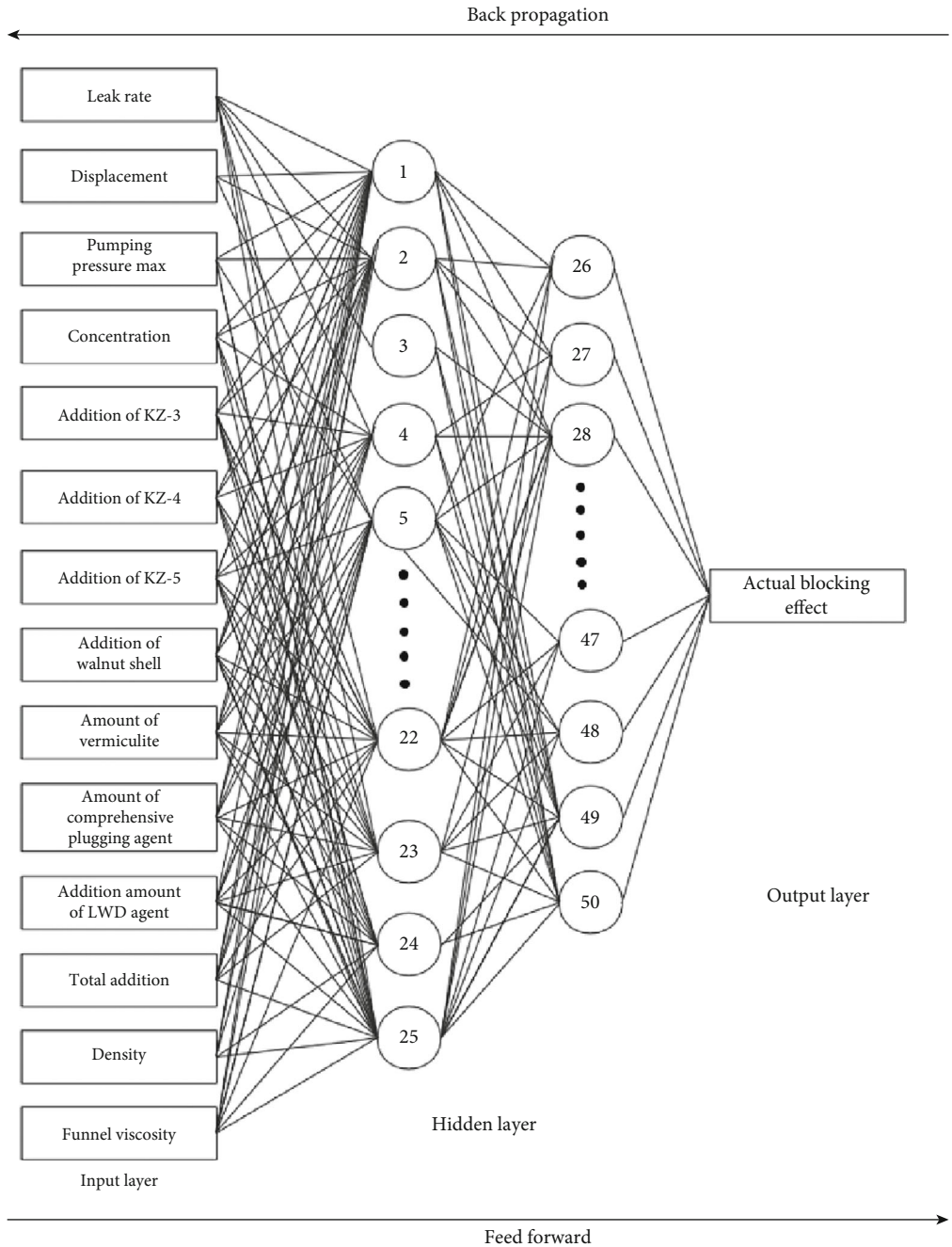

Figure 12: Topological structure of the ANN model established.

to 2 layers. Both TASIG and LOGSIG transfer functions were selected for testing. The prediction accuracy results obtained through different network structures are shown in Figures 10 and 11.

By changing the number of neurons in the hidden layer and the number of hidden layers, different transfer functions are used to analyze its impact on the performance of the model [47]. As shown in Figures 10 and 11, the ANN model's mean square error (MSE) varies with different model structures and is used to predict the effect of field leakage control.

With the increase in the number of neurons, the MSE of the ANN model shows a downward trend, and it can be found that the MSE of using two hidden layers is lower than that of using one hidden layer. When using logistic Sigmoid function s as the activation function of the hidden layer, as the number of neurons in the hidden layer continues to increase, the MSE gradually decreases, then increases, and then decreases again, until the number of neurons in the hidden layer reaches 80, and the MSE value of the model changes slightly. When the number of neurons is 50, the MSE is the lowest, which is 0.918%, and when using the TANSIG transfer function as the activation function, using two hidden layers, neurons with a quantity of 70 produced the best efficiency with an MSE of 1.08%. But an excessively high number of neurons have not been found to be more

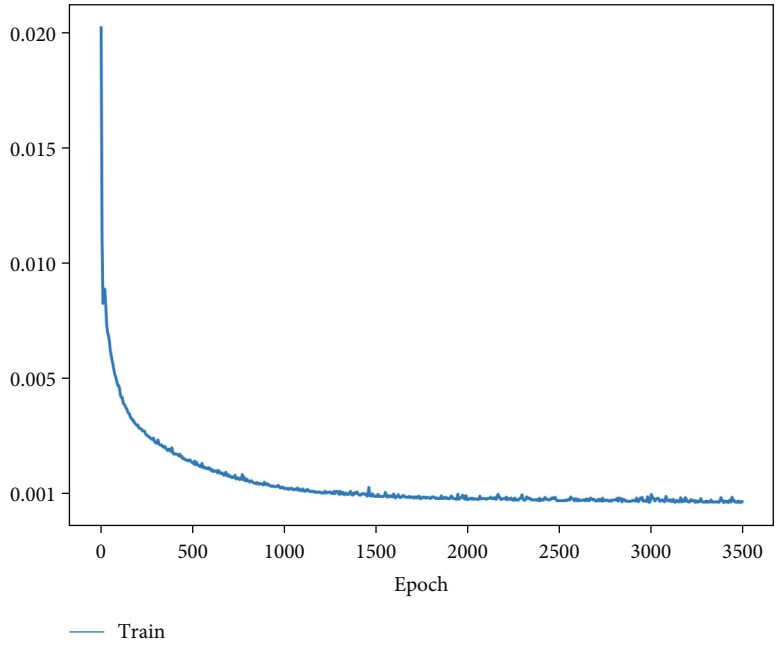

Figure 13: Variation of loss function during training and testing.

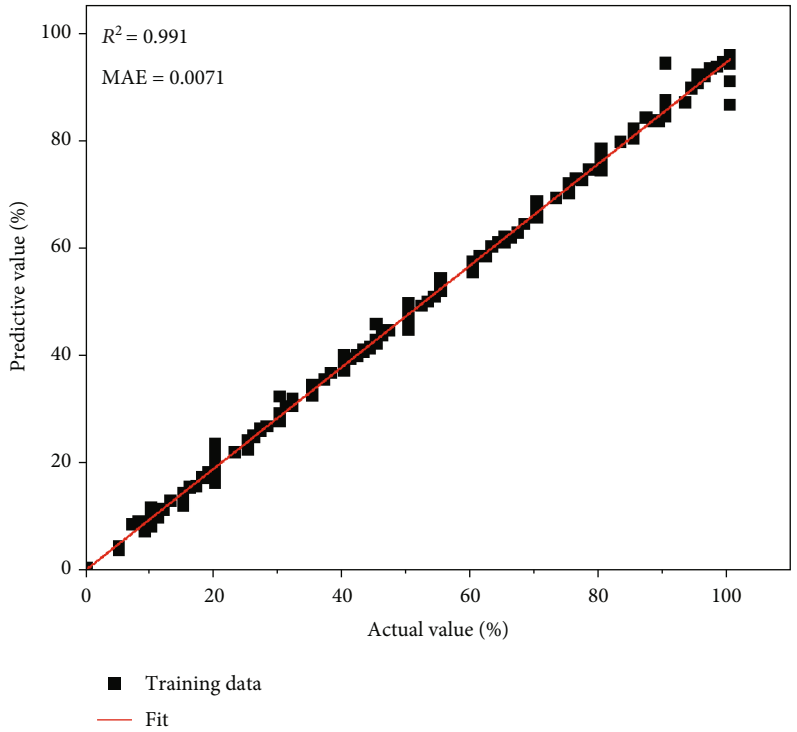

Figure 14: Model output and actual data: training data set.

efficient and can instead lead to higher error rates or longer convergence times, especially when training data is limited. The structure is simplified by comparing the prediction accuracy of the two structures and considering the reduction of the number of neurons as much as possible. The final selected ANN structure is shown in Table 3 and Figure 12.

4.2. Model Evaluation

4.2.1. Error Function. After determining the ANN model structure, input the data set. The mean square error (MSE) was chosen as the loss function. The error function decreases with increasing epochs during training and testing, as shown in Figure 13. After 2000 epochs, the loss function no longer

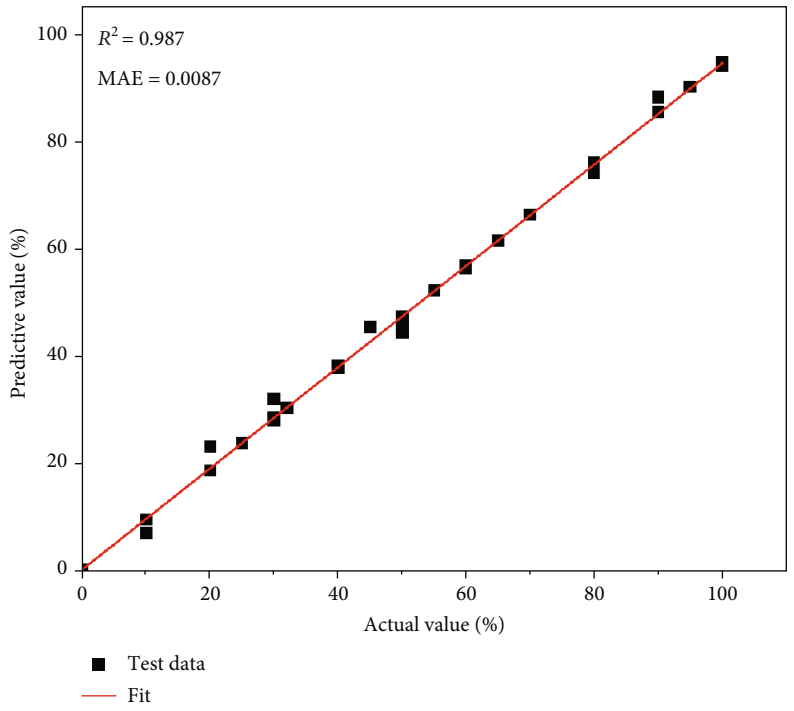

Figure 15: Model output and actual data: test data set.

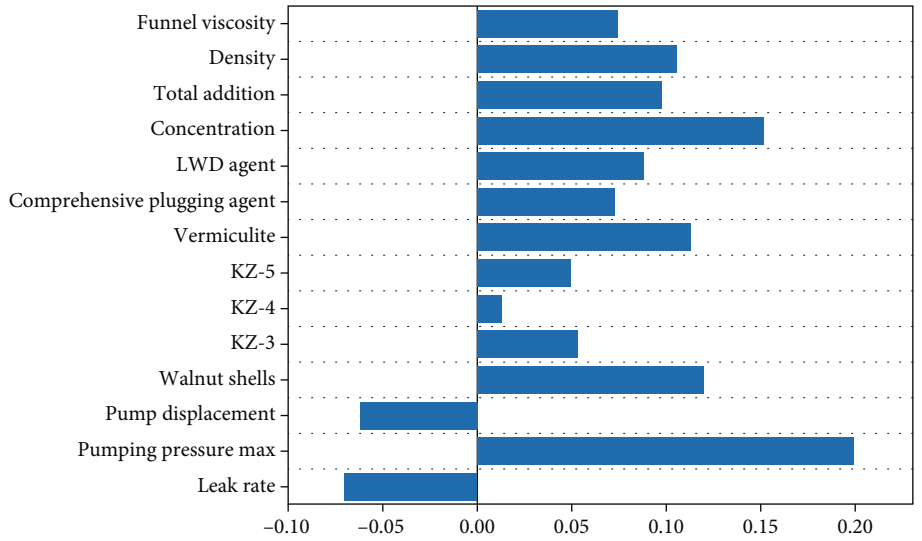

Figure 16: Correlation analysis between each characteristic data and the effect of missing control.

drops significantly and tends to stabilize. This means that the model does not need to increase the number of training times to improve its accuracy of the model.

4.2.2. Analysis of Accuracy. After selecting the best structure of the ANN, the accuracy of the model is characterized by the coefficient of determination R^2. Figures 14 and 15 show the difference between the predicted leaky control effect and the actual leaky control effect of the ANN model in the training and testing phases. The R^2 and MAE of the ANN model for the predicted target and the actual target for the training set were 0.991 and 0.0071, and the R^2 and MAE for the ANN model for the test data set using 20% of the data volume were 0.987 and 0.0087, which means that the model has high accuracy.

4.3. Correlation Analysis of Various Factors. The importance of individual features obtained from the model is shown in Figure 16. The figure shows the correlation of the maximum pumping pressure of the plugging slurry, the displacement, the formulation of the loss material, and the fluid properties of the carrier fluid on the actual loss control effect. The leakage size is considered to be negatively correlated with the leakage control effect. The more significant the leakage, the

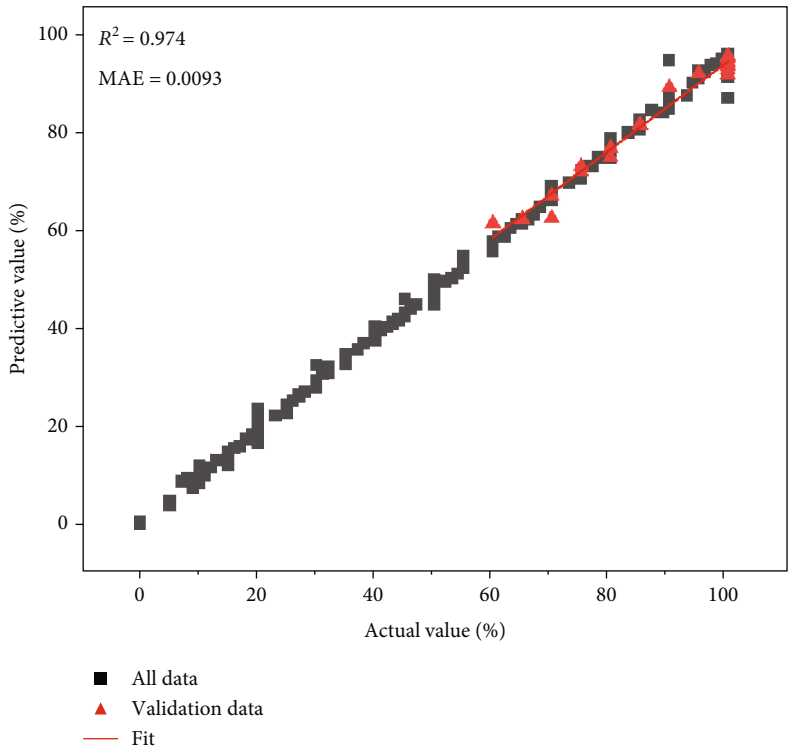

Figure 17: Validation of the model by the improved on-site leakage plugging case.

Table 4: Some real cases of fracture leakage plugging in Carboniferous strata in Chepaizi block.

Parameter	Well							
	A	B	C	D	E	F	G	I
Leak rate (m^3/h)	36	8	20	32.4	25	20	32.4	7.2
Displacement (m^3/h)	40.8	30	50.4	32.4	30	50.4	32.4	40.8
Pumping pressure max (MPa)	16	15	12	12	15	15	16	10
Concentration (%)	36	6	10	22.50	20	30	10	10
Addition of KZ-3 (t)	0	0	0	0	0	0	0	0
Addition of KZ-4 (t)	0	1.3	2	0	0	0	0	1
Addition of KZ-5 (t)	0	0	0	0	0	0	0	2
Addition of walnut shell (t)	2	0.5	3	3	2	3	2	0
Amount of vermiculite (t)	0	0	0	0	1	1	2	0
Amount of comprehensive plugging agent (t)	0	0	2	3	3	2	2	0
Addition amount of LWD agent (t)	2	0	0	3	0	3	0	0
Total addition (m^3)	11	30	60	40	30	30	60	30
Density (g▪cm^3)	1.21	1.1	1.22	1.14	1.21	1.22	1.13	1.14
Funnel viscosity (s)	50	49	52	48	52	53	53	45
Actual blocking effect (%)	100%	65%	100%	70%	90%	80%	95%	90%
ANN prediction (%)	9 9.81%	6 4.99%	9 7.63%	6 8.21%	9 2.08%	7 8.11%	9 6.12%	9 3.07%

worse the downhole plugging effect. In the plugging construction parameters, the size of the pumping displacement is negatively related to the plugging measures, and it is necessary to control the pumping displacement in the actual operation. The maximum pumping pressure has the strongest correlation with the leakage control effect, indicating that the maximum pumping pressure plays a great role in the leakage control effect. Among the leakage plugging materials, vermiculite and walnut shells have the most obvious effect. The irregular walnut shell has a higher friction coefficient with the fracture wall, which plays a better role in plugging in the fracture. The correlation strength of the concentration of the plugging material in the carrier fluid on the leakage control effect is second only to the maximum

pumping pressure. It shows that in the case of plugging construction implemented in Chepaizi block, the concentration of plugging materials needs to be further improved.

4.4. Data Verification of Actual Plugging Cases in the Field Using the ANN Model. Based on the analysis of the data by the model and the laboratory experiment research, further adjustments were made to the on-site leakage plugging formula system, and the corresponding construction parameters were adjusted at the same time. The plugging slurry is pumped into the lost formation with a displacement of 30~50 m^3/h in a low-displacement method, and the maximum pumping pressure is adjusted to more than 10 MPa to better squeeze the plugging slurry into the formation. At the same time, more flake materials vermiculite and walnut shells are used as plugging agents on site. At the same time, the concentration of the plugging material in the carrier fluid will further improve the leakage control effect of the field experiment.

Twelve times of plugging construction occurred in the following three wells. Use these 1 or 2 leak plugging construction data as a validation data set. Through the research on the actual leakage control effect in the field, as shown in Figure 17, it is found that the R^2 and MAE of the ANN model for the prediction target of the validation set and the actual target are 0.974 and 0.0093, indicating that the modified model has a good fit. Table 4 shows the detailed data of some cases after the improved plugging measures. After the adjustment of the plugging measures, the actual leakage control effect is greater than 65%, which has been dramatically improved compared with the previous one.

5. Conclusion

The prediction of the leakage control effect of the Carboniferous fractured leakage strata under the current leakage plugging construction measures in the Chepaizi block is studied by establishing the ANN model.

The experimental results show that the displacement pressure, the formulation of the plugging material, and the fluid properties of the carrier fluid play an important role in the leakage control effect of the fracture. In this study, through the analysis of on-site leakage plugging construction cases from a large number of construction parameters, a method for predicting the plugging effect of drilling site leakage plugging is proposed, and a set of ANN models with good accuracy is established.

The trained artificial neural network model can be well used to predict the performance of the plugging measures on the site of the subblocks of the car row. The trained model can produce predictions in seconds and is an excellent tool for evaluating the effectiveness of on-site leak plugging operations. In the subsequent 12 leakage accidents in three wells, the improved leakage plugging measures were applied, and the actual leakage control effect was obtained. Finally, the obtained data set is input into the model, which shows that the prediction results are in good agreement with the field application results, and the coefficient of determination $R^2 = 0.97408$.

This study provides a convenient and accurate way to effectively predict the effect of plugging measures in the Chepaizi block and provides help for the selection of reasonable construction parameters and optimal plugging slurry formulations. Due to different geological conditions and leakage reasons, the established model is only suitable for the Chepaizi subblock, and it still has certain limitations. In the future, we can try to collect more field data, and we can build a prediction model that can adapt to a wider range of blocks.

Data Availability

The [DATA TYPE] data used to support the findings of this study are available from the corresponding author upon request.

Conflicts of Interest

The authors declare that they have no conflicts of interest.

Authors' Contributions

Jianjian Song conceptualized the study and wrote, reviewed, and edited the manuscript. Lei Pu assisted the data curation, carried out formal analysis, and wrote the original draft. Lei Pu and Jun Zhou were responsible for methodology. Lei Pu and Shanshan Zhou contributed to the project administration. Jianjian Song and Jun Zhou were responsible for the resources. Jianjian Song and Mingbiao Xu supervised the study.

Acknowledgments

We would like to thank the Bakken Laboratory of Yangtze University for their support. At the same time, I would like to thank my friend Yuchen Zhang for her help. This research was supported by the Open Foundation of Cooperative Innovation Center of Unconventional Oil and Gas, Yangtze University (Ministry of Education and Hubei Province), No. UOGBX2022-02 and UOG2022-02.

References

[1] X. U. Chengyuan, J. Zhang, K. A. N. G. Yili et al., "Structural formation and evolution mechanisms of fracture plugging zone," *Petroleum Exploration and Development*, vol. 48, no. 1, pp. 232–242, 2021.

[2] L. Zhang, F. Zhou, W. Feng, M. Pournik, Z. Li, and X. Li, "Experimental study on plugging behavior of degradable fibers and particulates within acid-etched fracture," *Journal of Petroleum Science and Engineering*, vol. 185, article 106455, 2020.

[3] R. Li, G. Li, Y. Feng, X. Yang, Y. Teng, and Y. Hu, "Innovative experimental method for particle bridging behaviors in natural fractures," *Journal of Natural Gas Science and Engineering*, vol. 97, article 104379, 2022.

[4] Y. Feng, G. Li, and R. Li, "Influence of the lost circulation material injection method on the fracture plugging: a visualization experimental study," in *SPE/AAPG/SEG Unconventional Resources Technology Conference*, Austin, Texas, USA, July 2020.

[5] L. Zhang, Z. P. Li, F. P. Lai et al., "Integrated optimization design for horizontal well placement and fracturing in tight oil reservoirs," *Journal of Petroleum Science and Engineering*, vol. 178, pp. 82–96, 2019.

[6] L. Pu, P. Xu, M. Xu, J. Song, and M. He, "Lost circulation materials for deep and ultra-deep wells: a review," *Journal of Petroleum Science and Engineering*, vol. 214, article 110404, 2022.

[7] W. Sui, Y. Tian, Y. Zheng, and K. Dong, "Modeling temporary plugging agent transport in the wellbore and fracture with a coupled computational fluid dynamics–discrete element method approach," *Energy & Fuels*, vol. 35, no. 2, pp. 1422–1432, 2021.

[8] S. U. N. Jinsheng, B. A. I. Yingrui, R. Cheng et al., "Research progress and prospect of plugging technologies for fractured formation with severe lost circulation," *Petroleum Exploration and Development*, vol. 48, no. 3, pp. 732–743, 2021.

[9] G. Wang, C. Cao, X. Pu, and Z. Zhao, "Experimental investigation on plugging behavior of granular lost circulation materials in fractured thief zone," *Particulate Science and Technology*, vol. 34, no. 4, pp. 392–396, 2016.

[10] G. Wang, H. Du, and Z. Zhang, "Viscous behavior and wall slip of barite-weighted water-based drilling fluids containing a high particle fraction," *Journal of Petroleum Science and Engineering*, vol. 159, pp. 773–782, 2017.

[11] Y. Feng, G. Li, Y. Meng, and B. Guo, "A novel approach to investigating transport of lost circulation materials in rough fracture," *Energies*, vol. 11, no. 10, p. 2572, 2018.

[12] D. Feng, X. Li, X. Wang et al., "Water adsorption and its impact on the pore structure characteristics of shale clay," *Applied Clay Science*, vol. 155, pp. 126–138, 2018.

[13] X. Yan, Y. Kang, C. Xu, X. Shang, Z. You, and J. Zhang, "Fracture plugging zone for lost circulation control in fractured reservoirs: multiscale structure and structure characterization methods," *Powder Technology*, vol. 370, pp. 159–175, 2020.

[14] X. U. Chengyuan, Y. A. N. Xiaopeng, K. A. N. G. Yili, Y. O. U. Lijun, and J. Zhang, "Structural failure mechanism and strengthening method of fracture plugging zone for lost circulation control in deep naturally fractured reservoirs," *Petroleum Exploration and Development*, vol. 47, no. 2, pp. 430–440, 2020.

[15] J. I. A. Lichun, C. H. E. N. Mian, H. O. U. Bing, S. Zhen, and J. I. N. Yan, "Drilling fluid loss model and loss dynamic behavior in fractured formations," *Petroleum Exploration and Development*, vol. 41, no. 1, pp. 105–112, 2014.

[16] T. Zhang, F. Javadpour, Y. Yin, and X. Li, "Upscaling water flow in composite nanoporous shale matrix using lattice Boltzmann method," *Water Resources Research*, vol. 56, no. 4, article e2019WR026007, 2020.

[17] R. Albattat and H. Hoteit, "Modeling yield-power-law drilling fluid loss in fractured formation," *Journal of Petroleum Science and Engineering*, vol. 182, article 106273, 2019.

[18] M. B. Wang, Y. L. Guo, and W. Q. Chen, "Effect of solid particles on the lost circulation of drilling fluid: a numerical simulation," *Powder Technology*, vol. 363, pp. 408–418, 2020.

[19] H. Pang, H. Meng, H. Wang, Y. Fan, Z. Nie, and Y. Jin, "Lost circulation prediction based on machine learning," *Journal of Petroleum Science and Engineering*, vol. 208, article 109364, 2022.

[20] S. Gul and E. van Oort, "A machine learning approach to filtrate loss determination and test automation for drilling and completion fluids," *Journal of Petroleum Science and Engineering*, vol. 186, article 106727, 2020.

[21] M. B. Diaz, K. Y. Kim, H. S. Shin, and L. Zhuang, "Predicting rate of penetration during drilling of deep geothermal well in Korea using artificial neural networks and real-time data collection," *Journal of Natural Gas Science and Engineering*, vol. 67, pp. 225–232, 2019.

[22] A. A. Mahmoud, S. Elkatatny, and A. Al-AbdulJabbar, "Application of machine learning models for real-time prediction of the formation lithology and tops from the drilling parameters," *Journal of Petroleum Science and Engineering*, vol. 203, article 108574, 2021.

[23] Z. Zhu, X. Song, G. Li et al., "Prediction of the settling velocity of the rod-shaped proppant in vertical fracture using artificial neural network," *Journal of Petroleum Science and Engineering*, vol. 200, article 108158, 2021.

[24] I. Gomaa, S. Elkatatny, and A. Abdulraheem, "Real-time determination of rheological properties of high over-balanced drilling fluid used for drilling ultra-deep gas wells using artificial neural network," *Journal of Natural Gas Science and Engineering*, vol. 77, article 103224, 2020.

[25] G. Zhao, Y. Yao, L. Wang, C. D. Adenutsi, D. Feng, and W. Wu, "Optimization design of horizontal well fracture stage placement in shale gas reservoirs based on an efficient variable-fidelity surrogate model and intelligent algorithm," *Energy Reports*, vol. 8, pp. 3589–3599, 2022.

[26] L. Wang, Y. Yao, K. Wang, C. D. Adenutsi, G. Zhao, and F. Lai, "Data-driven multi-objective optimization design method for shale gas fracturing parameters," *Journal of Natural Gas Science and Engineering*, vol. 99, article 104420, 2022.

[27] A. K. Abbas, A. A. Bashikh, H. Abbas, and H. Q. Mohammed, "Intelligent decisions to stop or mitigate lost circulation based on machine learning," *Energy*, vol. 183, pp. 1104–1113, 2019.

[28] M. W. Alberty and M. R. McLean, "A physical model for stress cages," in *SPE annual technical conference and exhibition*, Houston, TX, USA, Sepetember 2004.

[29] R. Weijermars, "Stress cages and fracture cages in stress trajectory models of wellbores: implications for pressure management during drilling and hydraulic fracturing," *Journal of Natural Gas Science and Engineering*, vol. 36, pp. 986–1003, 2016.

[30] Z. Liu, M. Chen, and G. Zhang, "Analysis of the influence of a natural fracture network on hydraulic fracture propagation in carbonate formations," *Rock Mechanics and Rock Engineering*, vol. 47, no. 2, pp. 575–587, 2014.

[31] F. E. Dupriest, "Fracture closure stress (FCS) and lost returns practices," in *SPE/IADC Drilling Conference*, msterdam, The Netherlands, February 2005.

[32] C. Xu, Y. Kang, L. You, S. Li, and F. Chen, "High-strength, high-stability pill system to prevent lost circulation," *SPE Drilling & Completion*, vol. 29, no. 3, pp. 334–343, 2014.

[33] D. Li, S. Liu, Y. Kang, and Z. Hao, "Dynamic behavior of drilling fluid leakage in naturally# br# fractured formations," *Journal of Southwest Petroleum University (Science & Technology Edition)*, vol. 38, no. 3, p. 101, 2016.

[34] D. Whitfill, "Lost circulation material selection, particle size distribution and fracture modeling with fracture simulation software," in *IADC/SPE Asia Pacific Drilling Technology Conference and Exhibition*, Jakarta, Indonesia, August 2008.

[35] M. Alsaba, M. F. Al Dushaishi, R. Nygaard, O. M. Nes, and A. Saasen, "Updated criterion to select particle size distribution of lost circulation materials for an effective fracture sealing," *Journal of Petroleum Science and Engineering*, vol. 149, pp. 641–648, 2017.

[36] C. Lin, A. D. Taleghani, Y. Kang, and C. Xu, "A coupled CFD-DEM numerical simulation of formation and evolution of sealing zones," *Journal of Petroleum Science and Engineering*, vol. 208, article 109765, 2022.

[37] J. Zeng, H. Li, and D. Zhang, "Numerical simulation of proppant transport in hydraulic fracture with the upscaling CFD-DEM method," *Journal of Natural Gas Science and Engineering*, vol. 33, pp. 264–277, 2016.

[38] G. Wang, M. Dong, Z. Wang, T. Ren, and S. Xu, "Removing cuttings from inclined and horizontal wells: numerical analysis of the required drilling fluid rheology and flow rate," *Journal of Natural Gas Science and Engineering*, vol. 102, article 104544, 2022.

[39] G. Wang, Y. Huang, and S. Xu, "Laboratory investigation of the selection criteria for the particle size distribution of granular lost circulation materials in naturally fractured reservoirs," *Journal of Natural Gas Science and Engineering*, vol. 71, article 103000, 2019.

[40] V. D. Fachinotti, A. A. Anca, and A. Cardona, "Analytical solutions of the thermal field induced by moving double-ellipsoidal and double-elliptical heat sources in a semi-infinite body," *International Journal for Numerical Methods in Biomedical Engineering*, vol. 27, no. 4, pp. 595–607, 2011.

[41] D. A. Pandya, B. H. Dennis, and R. D. Russell, "A computational fluid dynamics based artificial neural network model to predict solid particle erosion," *Wear*, vol. 378, pp. 198–210, 2017.

[42] S. Smith, *Digital Signal Processing: A Practical Guide for Engineers and Scientists*, Elsevier, Amsterdam, Netherlands, 2013.

[43] M. T. Hagan, H. B. Demuth, and M. Beale, *Neural network design*, PWS Publishing Co, Boston, 1997.

[44] X. C. Zhang, J. G. Gong, and F. Z. Xuan, "A physics-informed neural network for creep-fatigue life prediction of components at elevated temperatures," *Engineering Fracture Mechanics*, vol. 258, article 108130, 2021.

[45] R. Hecht-Nielsen, "Theory of the backpropagation neural network," in *Neural Networks for Perception*, pp. 65–93, Academic Press, United States, 1992.

[46] Q. Jiang, R. Huang, Y. Huang et al., "Application of BP neural network based on genetic algorithm optimization in evaluation of power grid investment risk," *IEEE Access*, vol. 7, pp. 154827–154835, 2019.

[47] D. R. Baughman and Y. A. Liu, "Fundamental and practical aspects of neural computing," *Neural Networks in Bioprocessing and Chemical Engineering*, pp. 21–109, 1995.

Hindawi
Geofluids
Volume 2022, Article ID 5237534, 9 pages
https://doi.org/10.1155/2022/5237534

Research Article

Influence of Compositional Gradient Effect on Tight Condensate Gas Reservoir Development

Jing Chen,[1] **Xinmin Song**,[1] **Baozhu Li**,[1] **Xiaoli Luo**,[2] **Youjing Wang**,[1] **and Jinfang Wang**[1]

[1]*Research Institute of Petroleum Exploration & Development, PetroChina, Beijing 100083, China*
[2]*Southwest Oil & Gas Field Company, PetroChina, Chengdu, Sichuan 610041, China*

Correspondence should be addressed to Jing Chen; chenjingcycc@163.com

Received 6 April 2022; Revised 17 May 2022; Accepted 19 May 2022; Published 15 June 2022

Academic Editor: Zheng Sun

Condensate gas is a transition fluid between oil and gas, which is sensitive to the reservoir temperature and pressure. In condensate gas reservoir, especially in the moderate-giant one, fluid composition often varies with depth. This phenomenon has important influences on development. Anisothermal compositional gradient theory is used to analyze the main factors influencing the compositional gradient distribution to understand the basic regularities of the compositional variation with depth. Geothermal gradient, fluid composition, reservoir temperature, and reservoir pressure will affect the compositional gradient, of which geothermal gradient has the most direct and obvious influence. Furthermore, fluid model with compositional gradient was built in a tight condensate gas reservoir of the Middle East, and the influence of compositional gradient on dynamic performance is evaluated. The results show that the compositional gradient has a significant influence on the original gas in place, development strategy, central processing facilities, and so on. Therefore, compositional gradient requires more attention while exploiting moderate-giant condensate gas reservoirs in order to achieve more economical benefits.

1. Introduction

In the last decades, a large number of oil and gas reservoirs have been developed in the Middle East [1–7], including many transitional fluid reservoirs [8, 9], such as volatile reservoirs with high gas-oil ratio and rich condensate reservoirs. A common feature of these reservoirs is that the composition of the fluid changes with depth, a phenomenon known as compositional gradient effect. This phenomenon is particularly obvious in moderate-giant carbonate reservoirs and has an important impact on every link of oil-gas field development [7]. Previously, due to lack of understanding of the compositional gradient effect, this phenomenon was often ignored in the development of such critical reservoirs, resulting in poor recovery and economic benefits [8, 9].

As early as 1939, Sage and Lacey [10] pointed out that volatile oil reservoirs and condensate gas reservoirs rich in condensate are special reservoirs with component gradient distribution when discussing the phenomenon of component classification. However, it was not until the early 1980s that a large number of deep near-critical oil and gas reservoirs were found to have significant vertical compositional changes in the world that people paid more attention to this problem and proposed that the compositional gradient should be fully considered in the development of such reservoirs.

At present, some scholars at home and abroad have carried out many in-depth studies on the compositional gradient effect based on sage's research findings [11–16], but most of them focus on the composition variation with depth under isothermal conditions and there are few relevant literatures. Li [16] proposed to use isothermal compositional gradient model to show the distribution characteristics of fluid compositions and properties with depth. However, in some moderate-giant condensate reservoirs, reservoir temperatures increase with depth. The effect of reservoir temperature on compositional gradient cannot be ignored. In this paper, the anisothermal compositional gradient theory model is used to analyze the main factors affecting the distribution of compositional gradient and to evaluate its influence on the main links of oil and gas field development.

2. Anisothermal Compositional Gradient Theory Model

Before 1970s, Sage and Lacey [10] and Haase [17] proposed that in a gravitational field, when a multicomposition system is in real thermodynamic equilibrium, the system should be isothermal, and the sum of chemical and gravitational potentials of each composition in the system should be constant. In 1980, Schulte [18] proposed a calculation model of compositional gradient under the influence of gravity only based on the previous two scholars. With the additional term of gravity, the vertical equilibrium condition of a multicomposition system in the gravitational field can be expressed as

$$d\mu_i + M_i g dh = 0 \quad i = 1, 2, \cdots, n. \tag{1}$$

Both m_i and g are constant against h, and equation (1) can be rewritten as

$$\mu_i(h) - \mu_i\left(h^0\right) = M_i g\left(h - h^0\right); i = 1, 2, \cdots, n, \tag{2}$$

where n is the number of compositions in a system, i is the composition number, M_i is the molar mass of composition i, μ is the chemical potential of composition i, g is the gravitational acceleration, and h is the reservoir depth.

The relation between chemical potential μ and fugacity f_i of composition i is as follows:

$$\partial\mu_i = RT \ln f_i, \tag{3}$$

where R is the gas universal constant and T is the system temperature.

By combining equations (2) and (3), the fugacity relation equation of composition i at depth h and h^0 can be obtained:

$$\ln f_i^h - \ln f_i^{h^0} = \frac{M_i g\left(h - h^0\right)}{RT}. \tag{4}$$

The relation between fugacity f_i and fugacity coefficient φ_i is as follows:

$$\ln f_i = \varphi_i Z_i P, \tag{5}$$

where Z_i is the molar content of composition i in the system, and P is the system pressure.

Equation (4) is combined with equation (5), and the further deformation is

$$\ln\left(\varphi_i^h Z_i^h P^h\right) - \ln \varphi_i^{h^0} Z_i^{h^0} P^{h^0} = \frac{M_i g\left(h - h^0\right)}{RT}. \tag{6}$$

Equation (6) was applied to any composition i in the system, and there are n equations for the n-composition system, plus an additional equation, that is, the sum of the mole fraction values of all compositions in the system is 1:

$$\sum_{i=1}^{n} Z_i = 1. \tag{7}$$

Given the pressure P^{h^0} at depth h^0 and the composition content ($Z_i^{h^0}$, $i = 1, 2, \cdots, n$), the P^h and Z_i^h of each composition at depth h can be solved by using the $n + 1$ equations, where the fugacity coefficient φ_i can be obtained from the equation of state.

In fact, not very reservoirs have constant temperature. For thin reservoirs, the changes of reservoir temperature be ignored, but for thicker reservoirs, especially some moderate-giant carbonate reservoirs in the Middle East, temperature increases usually on the order of 0.02°C/m from top to bottom of the reservoir.

The changes of reservoir temperature need to be considered when solving the compositional gradient. In 2003, Pedersen and Lindeloff [19] proposed a compositional gradient calculation model under anisothermal conditions based on Haase's research.

Based on the irreversibility of the thermal process, the equation of molar compositions in the heat source with thermal gradient was established to solve this problem. The system is assumed to be in a steady state to simplify this problem. That means all composition fluxes were zero, the compositional gradient is assumed to be constant in time, and the effects of capillary force, composition convection and secondary migration are not considered. According to the equation (6), an additional term is added to express the influence of geothermal gradient, which also includes the average molecular weight M, the molecular weight M_i of all compositions, the partial molar enthalpy of the mixture $\tilde{H}$, and the partial molar enthalpy of composition $i\widetilde{H_i}$. A dynamic and stable system is established in the equilibrium of gravity and heat convection effect.

$$\begin{aligned} &\mathrm{RT}\ln\left(\varphi_i^h Z_i^h P^h\right) - RT \ln \varphi_i^{h^0} Z_i^{h^0} P^{h^0} \\ &\quad = M_i g\left(h - h^0\right) - M_i\left(\frac{H}{M} - \frac{\widetilde{H_i}}{M_i}\right)\frac{\Delta T}{T}; i = 1, 2, \cdots, n, \end{aligned} \tag{8}$$

where

$$\widetilde{H_i} = H_i^{ig} + \tilde{H}_i^{res}, \tag{9}$$

$$\tilde{H}_i^{res} = -RT^2 \frac{\partial \varphi_i}{\partial T}, \tag{10}$$

$$H = \sum_{i=1}^{n} Z_i \widetilde{H_i} = \sum_{i=1}^{n} Z_i H_i^{ig} + \sum_{i=1}^{n} Z_i \tilde{H}_i^{res}, \tag{11}$$

where H_i^{ig} is ideal gas enthalpy of composition i; $\tilde{H}_i^{res}$ is partial molar residual enthalpy of composition i.

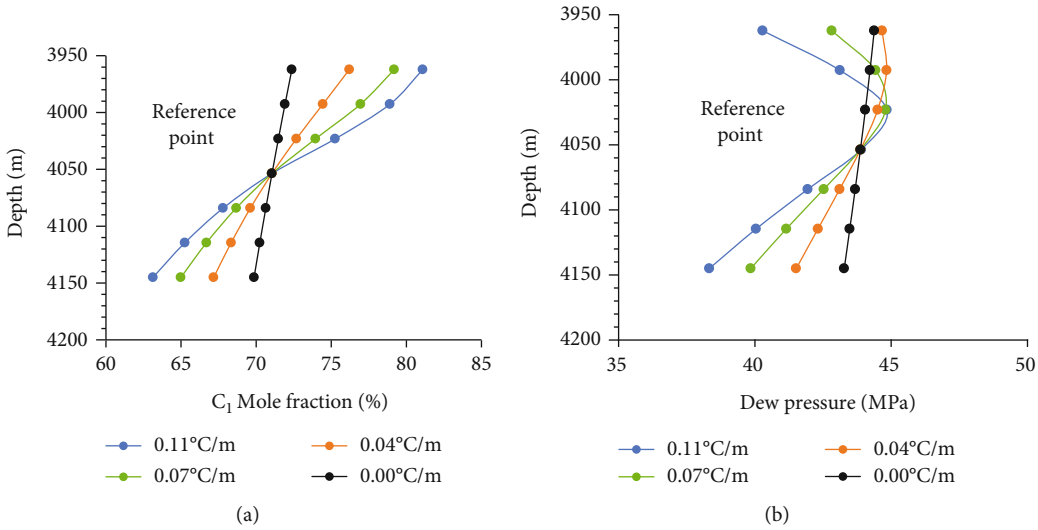

Figure 1: (a) Effect of geothermal gradient on compositional gradient. (b) Effect of geothermal gradient on dew point pressure.

When calculating the change of compositions with depth, an appropriate equation of state is firstly selected to obtain the vapor and liquid phase compressibility factors. And the equation of fugacity coefficient is applied to obtain the vapor and liquid phase fugacity coefficients of each composition [20–23]. Then, the compositions' fugacity coefficients, ideal gas enthalpy H_i^{ig}, and the compositional gradient are calculated according to equation (8). There is a trial calculation process in the solution process. The initial vapor-liquid ratio of composition i is preset to calculate the vapor and liquid fugidity coefficients under the equilibrium state. If they are equal, the trial calculation succeeds; if they are not equal, the initial setting value is returned to be modified. The calculation process must be repeated iteratively, usually completed by computer program.

3. Influence Factors of Compositional Gradient Distribution

Since the anisothermal compositional gradient model is built into the commercial software PVTsim, a multifunctional equation of state simulation software, it was used to analyze the influence factors of compositional gradient distribution by selecting SRK Peneloux equation of state, which has good adaptability to condensate gas and volatile oil. In this paper, the influence factors are divided into two categories: one is direct influence factors, such as gravity field and geothermal gradient, and the other is indirect influence factors, such as fluid composition, reservoir temperature, and reservoir pressure.

3.1. Geothermal Gradient. It can be deduced from the above equations that the most direct cause of the compositional gradient effect is the rebalancing of the chemical potential of each composition caused by gravity field and geothermal gradient. Therefore, the vertical compositional gradient effect and fluid properties will be different under different geothermal gradient. Taking the condensate gas sample as an example, C_1 and dew point pressure were taken as the observation objects (Figures 1(a) and 1(b)). When the local geothermal gradient is 0.00°C/m, only gravity differentiation plays a role in the compositional gradient, and the variation of fluid compositions within the thickness of 100 m was only about 1%. When the local geothermal gradient increases to 0.04°C/m, 0.07°C/m, and 0.11°C/m, respectively, the variation of fluid composition increases to 5%, 8%, and 10%. It can be seen that geothermal gradient is the most important factor leading to compositional gradient effect. Therefore, for reservoirs with large geothermal gradient, such as some ultrahigh temperature reservoirs, the compositional gradient effect has aroused great attention.

3.2. Fluid Composition. In order to investigate the influence of different fluid types on the distribution of compositional gradient under the same formation conditions, this paper selected three critical fluids, including volatile oil, rich condensate gas, and condensate gas, as the research objects. Composition data of fluid samples are shown in Table 1. Calculation results show that the contents of light compositions decrease, and the contents of heavy compositions increase in all three fluid samples with the increase of reservoir depth, especially C_1 and C_{7+}. The decrease of C_1 is almost equal to the increase of C_{7+} (Figure 2). The lighter fluid samples, the more obviously the fluid compositions change with depth. As shown in Figure 3, only C_1 and C_{7+} composition in the volatile oil obviously change with depth. For rich condensate of which fluid properties are lighter, composition $C_2 - C_6$ increase with depth, and their molar contents present obvious increasing trend. For condensate gas whose compositions are the lightest, the contents of $C_2 - C_6$ have the largest variation with depth, indicating that the lighter the fluid sample is, the more obvious the compositional gradient effect of the light composition is.

3.3. Reservoir Temperature. Taking rich condensate gas sample as an example, C_1 and dew point pressure are taken as

Table 1: Composition content of three fluid samples.

Composition	Volatile oil	Rich condensate gas	Condensate gas
N2	0.73	0.11	0.10
CO2	2.35	2.82	3.31
H2S	0.03	0.03	0.05
C1	57.71	71.06	81.52
C2	8.07	6.32	4.51
C3	5.45	3.71	2.10
iC4	1.05	0.76	0.44
nC4	2.66	1.76	0.88
iC5	1.05	0.79	0.44
nC5	1.21	0.91	0.50
C6	0.24	1.24	0.77
C7+	19.46	10.49	5.38

observation objects to study the compositional gradient effect and the variation of fluid properties of the same fluid at different reservoir temperatures. It can be seen from Figures 4(a) and 4(b) that the vertical fluid composition and fluid properties are different due to the different reservoir temperature at the reference depth. The higher the reservoir temperature is, the smaller the variation of fluid compositions and fluid properties is. It indicates that the increase of reservoir temperature will weaken the compositional gradient effect. Therefore, it can be seen that the fluid compositions and fluid properties vary with depth slightly in ultrahigh temperature reservoirs.

3.4. Reservoir Pressure. Reservoir pressure is one of the indirect factors affecting the distribution of fluid compositions and fluid properties with depth. The vertical fluid composition and properties are different due to the different reservoir pressure at the reference depth. As can be seen from Figures 5(a) and 5(b), the higher the reservoir pressure is, the weaker the vertical compositional gradient effect is, and the smaller the corresponding dew-point pressure changing with the depth is. Therefore, for reservoirs with high reservoir pressure, such as the deep buried reservoirs or ultrahigh pressure reservoirs, the compositional gradient effect will be weakened.

4. Typical Tight Condensate Gas Reservoir Development and Production Strategy

4.1. Brief Introduction of Gas Reservoir. S condensate gas reservoir located in the Middle East is a typical moderate-giant gas reservoir rich in condensate. The net pay of the reservoir is about 50 m, and the middle depth of reservoir is -4035 m. It belongs to a weak edge aquifer, low-porosity, and tight condensate gas reservoir with no stable buffer and good interlayer connectivity. Before this condensate gas reservoir was put into development, as shown in Figure 6 the original fluid samples were obtained from the high, middle, and low parts of the reservoir structure, and the gas-oil ratios were 1696 m^3/m^3, 754 m^3/m^3, and 445 m^3/m^3, respectively, showing obvious compositional gradient effect.

4.2. Original Gas in Place. The composition gradient effect results in the different composition in different reservoir depths, and the corresponding fluid parameters such as formation volume factor, dew point pressure, and gas-oil ratio also are great differences. The formation volume factor is one of the core parameters in the calculation of original gas in place. If the constant formation volume factor is used to calculate the original gas in place in oil reservoirs with obvious composition gradient, the calculated original gas in place will have obvious deviation from the actual value.

As shown in Figure 7, formation volume factor of the fluid in *S* tight condensate gas reservoir increases with the reservoir depth, from 0.0034 to 0.0049. Compared with the gas formation volume factor at -4035 m which is the middle depth of reservoir, the formation volume factor above -4035 m is smaller, while the formation volume factor below -4035 m is larger, with the maximum deviation ranges of -7% and 35%, respectively. If the formation volume factor at -4035 m is used to calculate the original gas in place of the entire condensate gas reservoir, the original gas in place of the reservoir above the -4035 m is smaller (blue shade in Figure 7), and the original gas in place below -4035 m is larger (red shade in Figure 7). *S* is a gently structured layered reservoir, most of the hydrocarbon is located above -4035 m. If the compositional gradient effect is neglected, that means the formation volume factor at -4035 m is used to calculate the original gas in place, and the surplus of the original gas in place below -4035 m cannot offset the shortage of original gas in place above -4035 m, resulting in the total original gas in place are about 5% smaller than the actual.

4.3. The Development Strategy. As shown in Figure 8, due to the compositional gradient effect, the fluid dew point pressure in the *S* tight condensate gas reservoir increases with depth, varying up to 2 MPa across the reservoir depth range. In the middle of the reservoir, the fluid became the rich condensate gas, and in the bottom of the reservoir, the fluid has developed from rich condensate to the volatile oil. So it can get better economic benefits to firstly develop the middle and lower part of the reservoir with more oil compositions. Therefore, the condensate gas reservoir adopts a development strategy of prioritizing the deployment of development wells in the structural wing and the perforation of the lower part of the reservoir. On the one hand, the gas cap expansion energy can maintain formation pressure, and the expansion energy of gas cap is used to maintain formation pressure, which is particularly important for tight gas condensate reservoirs. On the other hand, a large amount of high-quality condensate oil can be obtained quickly. However, due to the weak aquifer of the tight condensate gas reservoir and the high dew point pressure of fluid in the wing structure, it is necessary to carry out the pressure holding measures before the pressure at the bottom of the reservoir drops to the dew point pressure to avoid the impact of condensate banking on the overall recovery of the condensate gas reservoir.

The emphasis on the compositional gradient effect and such development strategy is very important for the tight condensate gas reservoir, because the reservoir property of

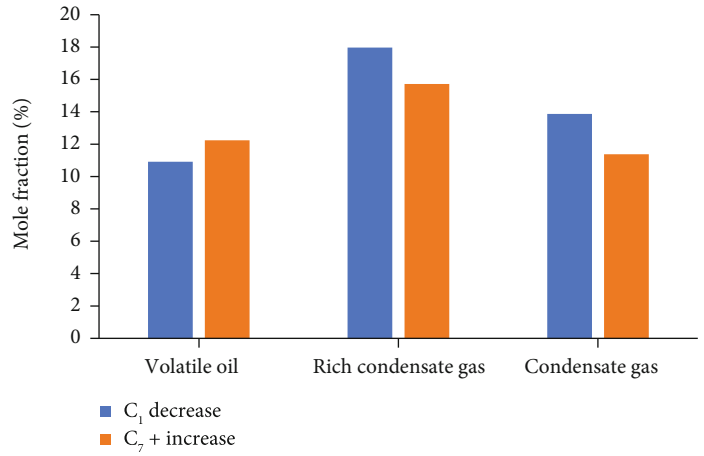

Figure 2: C_1/C_{7+} content variation with depth for different fluid samples.

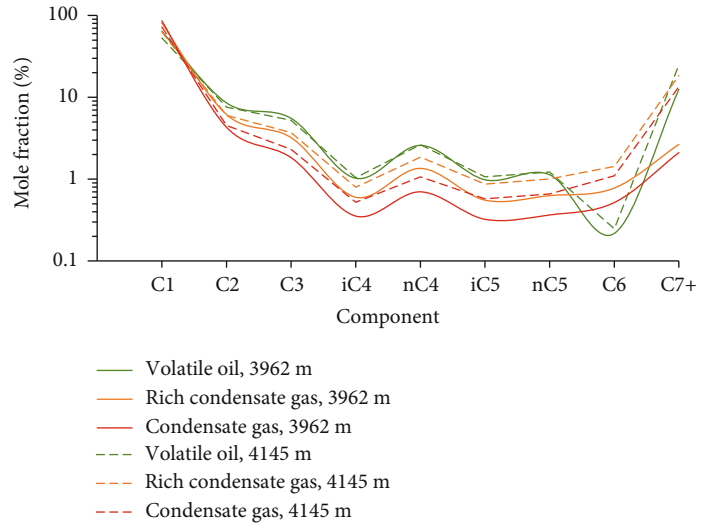

Figure 3: C_1/C_{7+} contents varying with depth for different fluid samples.

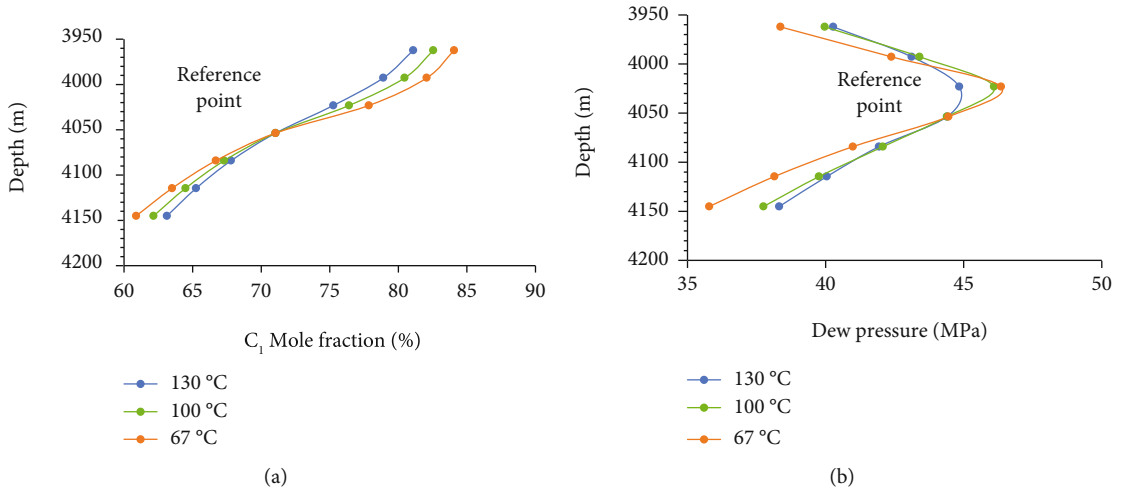

Figure 4: (a) Effect of reservoir temperature on compositional gradient. (b) Effect of reservoir temperature on dew point pressure.

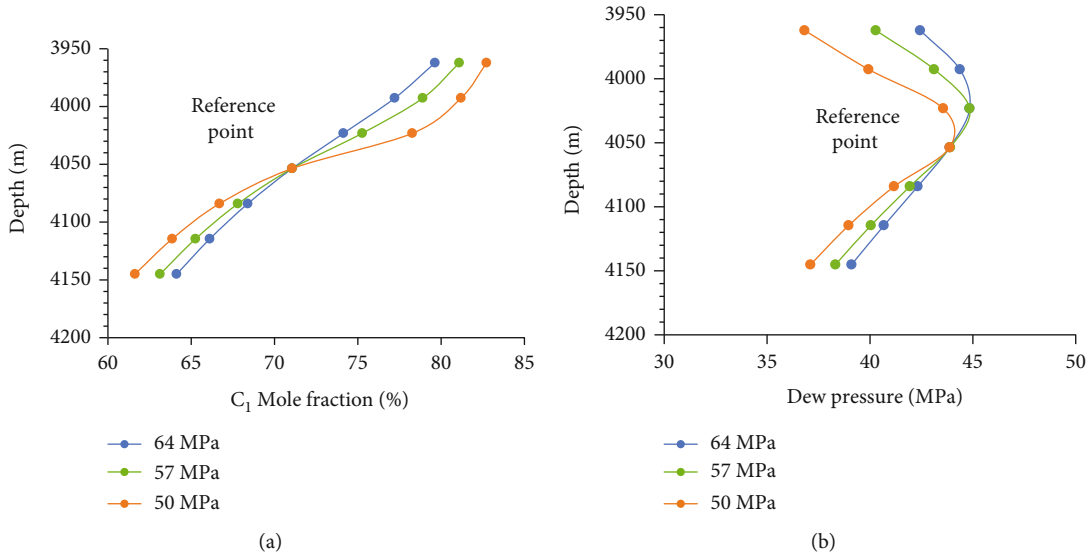

Figure 5: (a) Effect of reservoir pressure on compositional gradient. (b) Effect of reservoir pressure on dew point pressure of fluid.

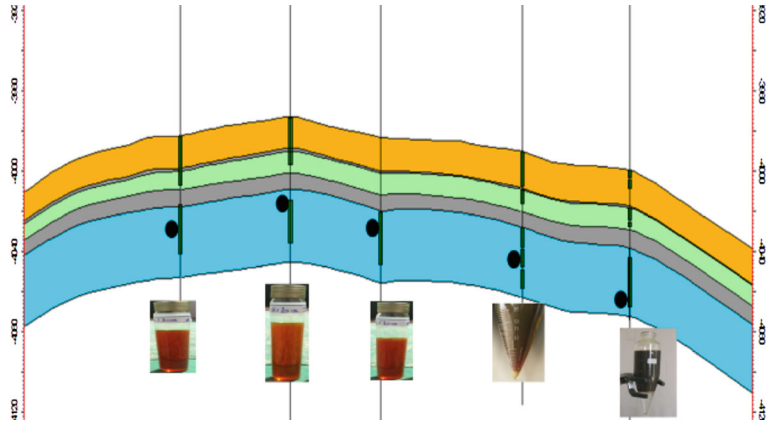

Figure 6: Sampling location of the original fluid in *S* tight condensate gas reservoir.

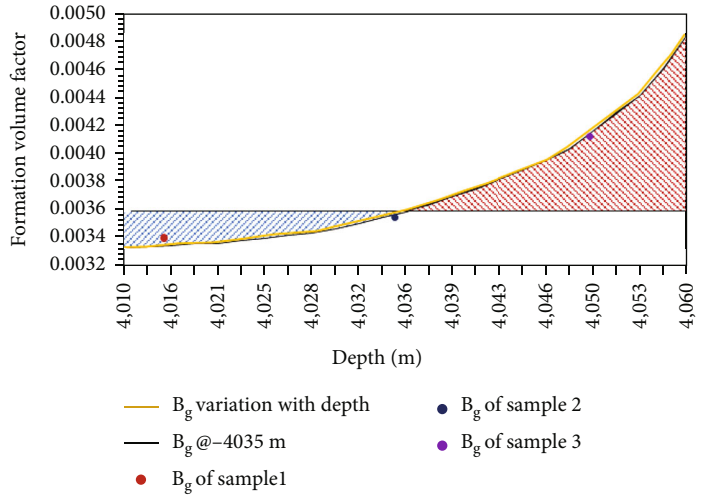

Figure 7: Formation volume factor of the original fluid in *S* condensate reservoir.

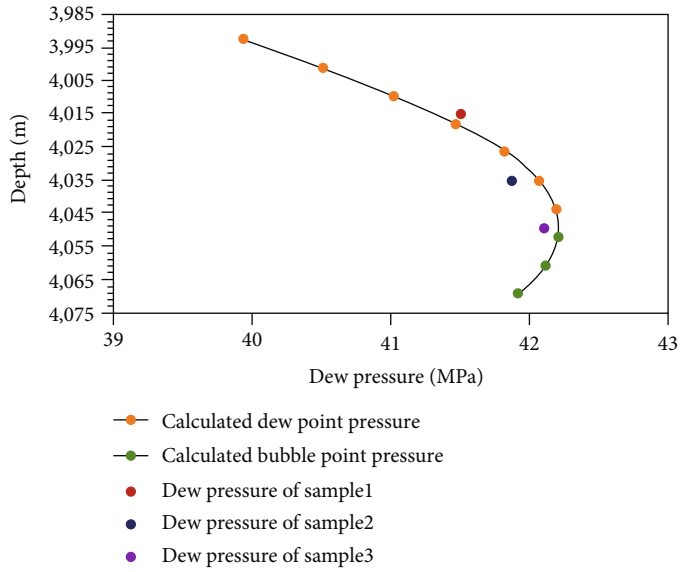

Figure 8: Dew point pressure of the original fluid in *S* condensate reservoir.

this type of condensate reservoir is very tight, and due to reservoir pressure lower than dew point pressure, the precipitation of condensate will seriously block the reservoir pores and the throats. This will cause the fluid to not flow smoothly in the reservoir, which in turn lead to a sharp reduction in recovery factor.

Thereby, it is necessary to consider the variation of oil/gas ratio and dew point pressure with depth caused by compositional gradient effect when developing development strategy, so as to achieve better development effect.

4.4. Surface Engineering Design. Compositional gradient effect also has great influence on oil and gas central processing facilities. The processing capacity of the oil and gas surface processing plants should be consistent with the subsurface production capacity. If the processing g capacity of the plants is too large, the economic benefit of the whole project will be adversely affected, while if it is too low, the production will be restricted. Therefore, the fluid properties and development steps of oil and gas reservoirs should be considered comprehensively in the construction of oil and gas central processing facilities.

As shown in Figure 9, the high, medium, and low gas/oil ratios in *S* condensate gas reservoir are 1696 m^3/m^3, 754 m^3/m^3, and 445 m^3/m^3, respectively. If the production gas/oil ratio of samples in middle depth is used in the design of the processing capacity of various plants in *S* condensate gas reservoir, it will lead to the situation that the surface plants cannot meet the production demand. In the early stages of development, production may be constrained by the ability of condensate processing units due to the priority of producing the condensate in the middle and lower parts of the reservoir. Also, in the middle and high part of the reservoir, as well as dissolved gas precipitation and other factors, the natural gas processing plant may not be able to handle all the produced gas,

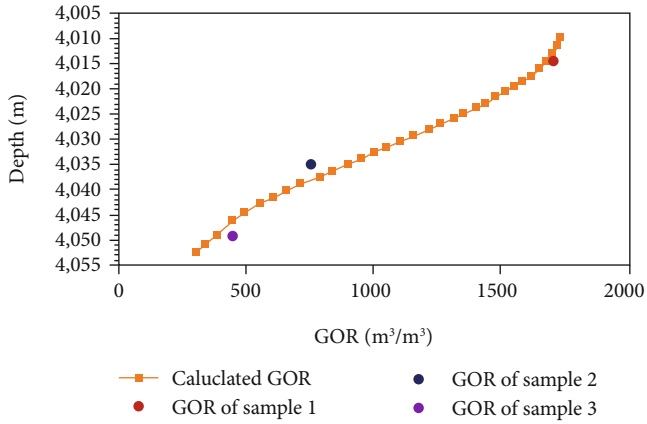

Figure 9: Gas oil ratio of the original fluid in *S* condensate reservoir.

resulting in production limit, which affects the development process and economic benefits of the whole project.

Therefore, in the development of a condensate gas reservoir with composition gradient effect, such as a condensate gas reservoir, before designing surface oil and gas processing facilities, on the one hand, original fluid samples at different depths should be obtained as much as possible for better understanding of reservoir fluids. On the other hand, in the preparation of the initial development plan, the integrated development strategy, zoning development or step by step production, or even combined with the surplus surface processing capacity of oil and gas in the adjacent oil and gas fields, should be adopted to improve the loading rate of processing facilities as much as possible to increase economic benefits.

5. Conclusion

Due to the influence of gravity field and geothermal gradient, transitional fluids such as condensate gas or volatile oil

always have compositional gradient effect, which is most obvious in moderate-giant reservoirs.

Geothermal gradient, fluid composition, reservoir temperature, and reservoir pressure all have varying degrees of influence on compositional gradient effect, and the geothermal gradient has the most direct and obvious influence. The larger the geothermal gradient is, the stronger the compositional gradient effect is. The larger the reservoir temperature and pressure are, the weaker the compositional gradient effect is. C_1/C_{7+} has the most obvious compositional gradient effect among all fluid compositions, and the increase of C_{7+} content is almost equal to the decrease of C_1 content.

Compositional gradient effect has important influence on the calculation of original gas in place, development strategy, surface engineering design, and so on. When an oil and gas field reservoir with compositional gradient effect is put into development in an all-round way, the original fluid samples at different depth should be taken as much as possible, so that a more clear understanding of reservoir fluid provides the solid material foundation for the entire development process and obtains maximum economic benefits.

Nomenclature

n: Number of compositions in a system
i: Composition number
M_i: Molar mass of composition i
μ_i: Chemical potential of composition i
g: Gravitational acceleration
h: Reservoir depth
R: Universal constant of the gas
T: System temperature
Z_i: Molar content of compositon i
P: System pressure
f_i: Fugacity of compositon i
φ_i: Fugacity coefficient of composition i
P^{h^0}: Pressure at depth h^0
$Z_i^{h^0}$: Composition i at depth h^0
P^h: Pressure at depth h
Z_i^h: Composition at depth h
M: Average molecular weight of the mixture
H_i^{ig}: Ideal gas enthalpy of composition i
$\tilde{H}_i^{res}$: Partial molar residual enthalpy of composition i
$\tilde{H}$: Partial molar enthalpy of the mixture
$\widetilde{H_i}$: Partial molar enthalpy of composition i.

Data Availability

The data used to support the findings of this study are included within the article.

Conflicts of Interest

The authors declare that there are no conflicts of interest regarding the publication of this paper.

Acknowledgments

This study was supported by CNPC science and technology project (kt2021-07-02).

References

[1] Z. Ningning, H. Dengfa, S. Yanpeng, and L. Haowu, "Distribution patterns and controlling factors of giant carbonate rock oil and gas fields worldwide [J]," *China Petroleum Exploration*, vol. 19, no. 6, pp. 54–65, 2014.

[2] L. Sun, Y. Yong, and B. Z. Li, "Classified evaluation methods and waterflood development strategies for carbonate reservoirs in the Middle East [J]," *Acta Petrolei Sinica*, vol. 43, no. 2, pp. 270–280, 2022.

[3] X. M. Song and Y. Li, "Optimum development options and strategies for water injection development of carbonate reservoirs in the Middle East," *Petroleum Exploration and Development*, vol. 45, no. 4, pp. 723–734, 2018.

[4] Y. L. Wang, X. M. Song, G. H. Wang et al., "Key technologies and practices for rapid and large-scale production increase in cooperation oil and gas fields of the Middle East [J]," *Acta Petrolei Sinica*, vol. 41, no. 12, pp. 1633–1642, 2020.

[5] L. Yisheng, L. Yuetian, and L. Changyong, "Division of flow units in thick carbonate reservoirs [J]," *Journal of Xi'an Shiyou University (Natural Sciene Edition)*, vol. 34, no. 2, pp. 104–111, 2019.

[6] H. Liu, Z. Tian, B. Liu, R. Guo, K. Shi, and Y. Ye, "Classification and prediction of giant thick strongly heterogeneous carbonate reservoirs in the Middle East area [J]," *Acta Petrolei Sinica*, vol. 40, no. 6, pp. 678–690, 2019.

[7] H. T. Sun, J. He, L. Wang, H. Q. Wang, and L. N. Guo, "Fracture characteristics of carbonate reservoirs in Asmari formation of a oil field in Iraq and its influence on reservoir development [J]," *Journal of Northeast Petroleum University*, vol. 44, no. 6, pp. 12–20, 2020.

[8] Y. C. Zhang, L. Yang, W. H. Gu et al., "Study on the variation law of gas oil ratio in gas injection development of deepsea volatile reservoirs and its application [J]," *China Offshore Oil and Gas*, vol. 31, no. 5, pp. 108-109, 2019.

[9] Y. C. Zhang, L. Yang, W. H. Gu, C. P. Dai, L. Deng, and Y. Ying, "Analysis on abnormal gas-oil ratio in condensate gas reservoir [J]," *Development Engineering*, vol. 31, no. 6, pp. 63–65, 2011.

[10] B. H. Sage and W. N. Lacey, "Gravitational concentration gradients in static columns of hydrocarbon fluids," *Transactions of AIME*, vol. 132, no. 1, pp. 120–131, 1939.

[11] F. Montel and P. L. Gouel, *Prediction of Compositional Grading in a Reservoir Fluid column*, SPE 14410, 1985.

[12] J. L. Greek and M. L. Schrader, *Reservoir: An Example of a Compositional Gradient from a Gravitational Field*, SPE14411, 1985.

[13] L. Hoier and C. H. Whitson, *Compositional grading-theory and practice*, SPE63085, 2000.

[14] H. Gurtis and U. Whison, *Compositional gradients in petroleum reservoirs [R]*, SPE 28000, 1994.

[15] J. H. Li, T. Jiang, and B. Liu, "Study on the compositon distribution of volatile oil reservoir [J]," *Xing Jiang Petroleum Geology*, vol. 31, no. 1, pp. 81–84, 2010.

[16] J. H. Li, T. Jiang, S. M. Chen, and W. M. Bao, "Numerical simulation of gas injection drive in volatile reservoirs with

compositional gradient [J]," *Journal of Petroleum and Gas*, vol. 34, no. 5, pp. 107–111, 2012.

[17] R. Haase, *Thermodynamik der Irreversiblen Prozesse*, Dietrich Steinkopff Verlag, Darmstadt, 1963.

[18] A. M. Schulte, *Compositional variations within a hydrocarbon column due to gravity*, SPE 9235, 1980.

[19] K. S. Pedersen and N. Lindeloff, *Simulations of compositional gradients in hydrocarbon reservoirs under the influence of a temperature gradient*, SPE 84364, 2003.

[20] A. Danesh, "PVT and Phase Behavior of Petroleum Reservoir Fluids [M]," in *Trans*, P. P. Shen and D. Han, Eds., Petroleum Industry Press, Beijing, 1991.

[21] S. L. Yang, J. Z. Wei, and R. Z. Jiang, *Physics of Petroleum Reservoirs [M]*, Petroleum Industry Press, Beijing, 2006.

[22] H. Q. Jiang, J. Yao, and R. Z. Jiang, *Fundamentals and Methods of Reservoir Engineering [M]*, China University of Petroleum Press, Beijing, 2006.

[23] P. C. Liu, *Fundamentals of Numerical Reservor [M]*, Petroleum Industry Press, Beijing, 2014.

Hindawi
Geofluids
Volume 2022, Article ID 1748605, 20 pages
https://doi.org/10.1155/2022/1748605

Review Article

Review of the Generation of Fractures and Change of Permeability due to Water-Shale Interaction in Shales

Kerui Liu,[1] Dangliang Wang,[1] James J. Sheng,[2] and Jianfeng Li[3]

[1]*China University of Mining & Technology (Xuzhou), School of Resources and Geosciences, China*
[2]*Texas Tech University, Lubbock, USA*
[3]*Xuzhou Coal Mining Group Corporation, China*

Correspondence should be addressed to Dangliang Wang; wangdangliang@cumt.edu.cn and James J. Sheng; james.sheng@ttu.edu

Received 7 March 2022; Accepted 11 May 2022; Published 13 June 2022

Academic Editor: Tao Chen

In shale development, water-based liquids are injected into the formations. In this process, water can interact with shales, especially with clay content. The interaction can lead to some phenomena, including clay swelling, reduction of mechanical properties of shales and fractures, generation and propagation of fractures, particle detachment, and permeability change. All the phenomena can impact productivity during the development, thereby impacting our investment and return on investment (ROI). So far, many researchers have put their time and efforts into this topic, and many articles have been published. However, some discrepancies still exist in shale reservoirs regarding the role of the interaction between water and shale, especially the impact of clay swelling. Some believe that clay swelling causes formation damage, mainly impairing shale permeability. Others state that fractures can be induced because of clay swelling, leading to the enhancement of shale permeability. So far, few articles have reviewed the various views on this interaction. Additionally, the relationship between each phenomenon is not discussed. In this paper, we try to draw a clear picture of water-shale interaction by reviewing the published studies, mainly focusing on experimental methodology and experimental results. Based on the review, we summarized the influencing factors as well as the mechanisms about the formation of fractures and change of permeability due to water-shale interaction. In water-shale interaction, the induced fractures are generated by the combined effects from clay swelling, reduction of mechanical properties of shales and fractures, and stress anisotropy. Shale permeability can be enhanced if the generated fractures can form an effective flow channel. However, if the generated fractures cannot serve as an effective flow channel, shale permeability will be impaired by clay swelling, water blocking, stress-sensitive, etc.

1. Introduction

The unconventional resource is becoming more and more important in the USA. The unconventional oil from tight oil reservoirs is estimated to exceed 12 million barrels per day [1]. Shale is an important resource in unconventional plays. Lots of companies have great interests and invest plenty of resources into developing shale. Shale is low permeable; hydraulic fracturing is the key to improve shale productivity [2]. Water is the major component of the fracturing fluid [3], and less than 10% of fracturing fluids are recovered [4]. Besides, aqueous solutions, working as EOR methods, are injected into shale plays to enhance oil recovery [5] Once aqueous solutions are injected into shales, water can interact with shale, which cause clay swelling, changing of mechanical properties of shales, and changing of petrophysical properties, thereby impacting oil productivity and oil recovery.

Clay swelling commonly occurs in water-shale interaction. It is widely accepted that clay swelling causes the impairment of formation permeability in conventional reservoirs [6–8]. However, many experimental results show that clay swelling can induce fractures in shales [9–15]. The generated fractures may result in permeability enhancement. No articles thoroughly explain the role of water-shale interaction in the development of shales so far. This paper was aimed at filling this research gap by summarizing the research results and analyzing the impacting factors.

Changing of mechanical properties of shales and fractures is another result of water-shale interaction. Due to water imbibition, the strength of shale can be weakened [16–18]; thus, fractures can be induced more easily. Besides, water-shale interaction can weaken the mechanical properties of fractures [19–23]. Studies show that stress intensity factor, crack extension force, and subcritical fracture growth index (SCI) can be impacted by clay swelling and water-shale interaction [19, 20]. The change in the mechanical properties of fractures is beneficial for fracture generation, as well. However, no articles have summarized those changes and discussed the effect of those changes in water-rock interaction.

Water-shale interaction can alter the permeability dramatically by the generation of fractures [12, 24, 25], particle detachment [11, 12], plugging of flow channels [26], and pore spaces [6], as well as water blocking [24]. We review previous works on the effect of water-shale interaction on permeability change in this paper. The experimental methodologies that were used in the published articles are discussed. The advantages and disadvantages of those experimental methodologies are analyzed. Besides, the relationship between the generated fractures, particle detachment, and permeability change is stated. The factors that could influence particle detachment and permeability change are summarized.

The rest of this paper is extended in four parts: Part 2 briefly introduces the characteristics of shales, clay minerals, and clay swelling. Part 3 discusses the role of water-shale interaction in fracture generation and the possible mechanisms. Part 4 discusses the role of water-shale interaction in permeability change and the possible mechanisms. Part 5 concludes this paper and provides a further experimental approach.

2. Characteristics of Shale, Clay Minerals, and Clay Swelling

2.1. Characteristics of Shales. Shale belongs to sedimentary rock and is most abundant on earth [27]. Shale is characterized as layered, fissile fine-grained, heterogeneous, and anisotropic. Shale's mineralogical composition controls the lithological properties of shale [28]. The typical minerals that are usually found in shales include clay minerals, quartz, feldspars, and carbonates [29, 30]. Organic matter is also a common component for shales [31, 32]. Clay minerals form the load-bearing framework in shales [33, 34]. Clay minerals are the key factor in the water-shale interaction and will be detailed discussed in Subsection 2.2. Shale has a low permeability, ranging from nano-Darcy to micro-Darcy [35, 36]. To accurately evaluate the permeability of shales is difficult. Many factors can impact permeability, like porosity, fluid viscosity, grain size and shape, and tortuosity [37]. Natural fractures and beddings largely exist in shales [38–40]. Therefore, laboratory-measured permeability underestimates the reservoir permeability in shales [41]. How to accurately measure the permeability of shales is an interesting topic and worthy to put efforts on. In this review paper, we will only focus on the change of permeability due to water-shale interaction.

2.2. Clay Minerals in Shales and Clay Swelling. Clay is a layered silicate mineral called phyllosilicate. Typically, clays are fine crystalline particles with two-dimensional arrays of silicon/oxygen tetrahedra or aluminum (or magnesium)/oxyhydroxy octahedra. There are five sorts of clays: illite, montmorillonite, chlorite, kaolinite, and attapulgite [42]. Most often, based on properties, crystal structure, and capacity to accommodate water within clay structure, clay minerals are divided into three main groups: smectite, illites, and kaolinite [43]. Montmorillonite is included in the smectite family [44]. Based on the swelling potential, smectite, illite, and kaolinite are marked as high, moderate, and low swelling potential clays [43]. The swelling potential is the potential volume change for clay minerals. Clay mineralogy plays the most important role in volume change, even in small fractions [45]. Clay can expand up to 20 times its original volume [46].

The process by which clay minerals in shale absorb water is called clay hydration [47]. For most studies, clay hydration is clay swelling. Simply put, clay swelling is the result of increased space between the layered structure of clay minerals and the adsorbed cations [48, 49]. Clay swelling consists of two stages: intracrystalline swelling and osmotic swelling [49]. The hydration of exchangeable cations in the interlayer space leads to internal crystallization, resulting in enhanced space between the clay layers (as shown in Figure 1). Concentration differences between ions in solution and ions in the space between clay layers cause osmotic swelling (shown in Figure 2).

Clay swelling can be affected by initial water content, adsorbed water, clay fraction, and confining pressure. Swelling occurs only when the water balance inside the shale is disturbed when it is in contact with the fluid. Studies show that dry shales are more reactive to water than water-saturated shales [50, 51]. The initial water content in shales can influence swelling rate as well as swelling potential. A study by Chenevert [52] showed that the swelling rate decreased sharply with increasing water absorption time. The highest expansion rates were recorded in the first few hours. Studies conducted by Al-Mhaidib and Al-Shamrani [53] and Sabtan [54] showed that swelling volume and swelling ratio decreased with increasing initial water content. Gomez-Gutierrez et al. [55] stated that the more water adsorbed, the larger the swelling volume, which was supported by Bryson et al. [56]. For here, the samples were not confined. Sabtan [54] measured the free swelling potential for 30 clay shale samples with different clay fraction. In his study, swelling volume increased as the clay fraction increased. A similar trend was achieved by Gomez-Gutierrez et al. [55] and Bryson et al. [56]. Confining pressure could negatively influence the swelling volume of clay minerals [57]. To combine those influencing factors, Lyu et al. [58] developed an MLR model to predict clay swelling. The relationship between swelling potential (S), water content (W), clay fraction (C), and confining pressure (P) can be expressed as $S = 30.0247 - 0.274W + 0.0455C - 9.1778 \log(P)$.

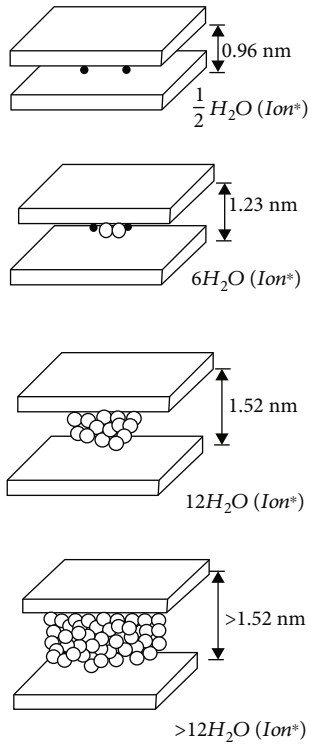

Figure 1: Schematic illustration of intracrystalline expansion of sodium montmorillonite: the interlayer space is expanding due to the hydration of exchangeable cations in the presence of water [49].

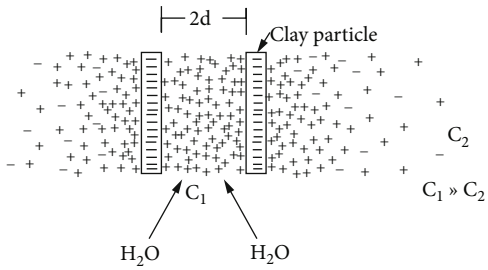

Figure 2: Illustration of osmotic swelling of the clay particle [49].

The temperature could influence clay swelling, as well. Wang et al. [59] and Huang et al. [60] employed a temperature range from −10°C to 23°C to investigate the swelling of shales. Their results showed that when the temperature is lower than 10°C, the expansion potential of shale decreases with the increase of temperature. The temperature could positively influence the swelling volume of shales when the temperature was higher than 10°C. Li et al. [61] studied the effect of temperature change on fracture generation in water-shale interaction. They compared the CT images for the tests under 80°C with those under 20°C. They found that fractures were more likely to develop in the tests using 80°C. The combined effects from high temperature and water-shale interaction led to the propagation of fractures. Additionally, as cool water is injected into hot formations, the water-cooling effect can induce fractures by the increase in pore pressures and the shrinkage of formations [62, 63]. The thermal effect is beneficial to the generation of fractures in water-shale interaction. However, so far, no experiments have been conducted to support this statement when samples are under stress anisotropy.

The types and concentrations of salts in water-based liquids also have an impact on clay swelling. The ions of Na^+, K^+ can influence the clay swelling. KCl is a commonly used swelling inhibitor [64, 65]. Wong [18] used water and brine (1% NaCl solution) to test the swelling potential of La Biche shale samples. He found that clay swelled more in the water when compared with brine.

3. The Influence of Water-Shale Interaction on Fracture Formation and Propagation

This section introduces the experimental methodologies and results related to fracture formation and propagation due to water-shale interaction. The interaction-induced fractures and the testing conditions are discussed. Based on those experimental results, the mechanisms about the role of water-shale interaction in fracture formation and propagation are discussed.

3.1. Induced Fractures in Experimental Studies. To study the interaction between water and shale, spontaneous imbibition tests were carried out. Figure 3 shows the imbibition tests performed by Morsy and Sheng [66]. Other researchers conducted the similar tests [9, 66–75]. From their results, the imbibition process was controlled by capillary actions, osmotic fluid flow, and clay minerals. To represent the imbibed water, the weight difference was used in most tests. Dehghanpour et al. [9] conducted imbibition tests for samples from five different shale formations. In their tests, they compared the imbibition profiles of oil and brines. The brine intake of all samples was significantly higher than the oil intake of the same samples. Besides, they found that excess water intake was due to water adsorption by clay minerals by comparing the inhalation profiles of oil and brine with oil intake. The water-shale interaction-induced microfractures even disintegration were observed in their tests. Samples from Fort Simpson had the highest clay content; therefore, disintegration was observed; samples from Otter Park had the least clay content, and only microfractures were observed. Figure 4 shows the generated fractures in the tests which were conducted by Morsy et al. [71] and Morsy and Sheng [66]. From their results, clay swelling can induce fractures. The above results indicate the following: (1) clay content is the main reason for the water uptake in the tests; (2) clay swelling can generate fractures in the imbibition tests; and (3) whether or not disintegration can occur is related to the amount of clay content in the samples. However, those tests were conducted without any restrains, and the mechanisms behind the generation of fractures were not discussed in these studies.

To examine the role of confining pressure in fracture generation because of clay swelling, several researchers introduced confining pressure into their tests [11, 25, 76–79]. In their tests, a core holder capable of holding the core sample and a pump for applying confining pressure are required. Figure 5 shows a schematic diagram of the

Figure 3: Imbibition tests from Morsy and Sheng [66].

device used by Bin et al. [76] and Wang et al. [25]. In their tests, the sample can imbibe water from the open ends of the core holder.

To observe the generated fractures, a CT scanner was employed by Bin et al. [76] and Wang et al. [25]. The general test procedure is that (1) the core samples are scanned before the tests; (2) the sample is placed in the core holder and exposed to confining pressure for imbibition tests; and (3) after imbibition tests, pressures are released, and the samples are scanned again to observe the generated fractures. For this experimental methodology, elastic strain energy is stored inside the samples as long as the confining pressure is applied. The release of confining pressure can result in a sudden release of strain energy, thereby causing the generation of fractures or even the failure of samples [80–82]. In their tests, it is hard to tell whether the fractures are generated by water-shale interaction or the sudden release of strain energy. It is better to monitor the process of the generation and propagation of fractures when the water imbibition tests are running under confining pressures. Two methods were employed: (1) first is monitoring the pressure change in the tests [11]. In their tests, A shale sample is exposed to a designed upstream pressure of water under confining pressure. Downstream pressure is maintained at atmospheric pressure. The upstream pressure is recorded. A pressure drop can be achieved if the fractures are generated. (2) Second is using an X-ray core holder system [77–79]. Figure 6 shows the schematic of the apparatus in their tests. CT images are achieved without releasing the confining pressure. In these ways, the effect of the sudden release of strain energy on fracture generation can be eliminated.

Bin et al. [76] and Wang et al.'s [25] results show that fractures were induced and developed (shown in Figure 7). In Bin et al.'s [76] results, fractures grow and connect to form complex fracture networks (shown in Figure 7(a)). In Wang et al.'s [25] tests, both isolated and connected fractures were observed on the CT images. In both studies, the reason for the generated fractures was clay swelling due to water-shale interaction. However, based on the description of their experimental procedures, both studies dried the cores and scanned the samples to get the CT images. Once the confining pressure is released, the CT scanning cannot accurately show the welling induced fractures. The effect of the sudden release of confining pressure, which caused the sudden release of strain energy inside the samples, cannot be differentiated from the effect of clay swelling. Therefore, it is difficult to identify whether the generated fractures were caused by clay swelling or by the sudden release of confining pressure. In Bin et al.'s [76] study, another set of tests was performed to characterize the distribution of pore-fracture structures in the samples during imbibition testing. The distribution of T_2 spectra was analyzed. The longer the transversal relaxation time, the larger the size of the pore-fracture structure should be. From Figure 8, the peak value of the transversal relaxation time increased in their tests, which means the size of the pore-fracture structure increased due to water-shale interaction. Combined with the results from CT images and those from the T_2 spectra, it is found that under the action of confining pressure, the expansion of clay can produce fractures.

Roshan et al. [11] explored the underlying mechanism of water uptake by using partially saturated samples to conduct tests. Free and confined water imbibition tests were done. For the confined test, a shale sample was placed under confining pressure of 1000 psi. The sample was exposed to distilled water by upstream pressure of 500 psi for 40 h. Figure 9 shows the induced fracture in the test. The fracture was formed by taking a longer time under confining pressure when compared with the tests without restrain. They stated that the formation of fractures under confining pressure is due to the decrease in the mechanical strength of the rock and the swelling of the clay. Besides, they indicated that this fracture was formed along with weak structures (beddings and laminations).

By comparing the results from Bin et al. [76], Wang et al. [25], and Roshan et al. [11], we can see that fractures can be generated due to the effect of water-shale reaction in shales under confining pressure. However, the formation of such fractures may take a longer time. The main factor that can contribute to the generation of such fractures is clay swelling. Other factors, like the degradation of the mechanical strength of shale, can also be beneficial for fracture generation in water-shale interaction.

Zhang and Sheng [77, 78] and Zhang et al. [79] employed CT images to observe fractures. Isotropic confining pressure was applied in their tests. Samples from Mancos shale formation were used. The constant pore pressure (0.03 MPa) was used for all the tests, and confining pressure (0.1 MPa, 2.0 MPa, and 20.0 MPa) was applied for the tests. Figure 10 shows the CT images from Zhang and Sheng [78]. They observed that at lower confining pressures, the samples developed more fractures. The generated fractures under confining pressures could close and reopen, which means the generation of the fractures was largely impacted by water-shale interaction and the applied confining pressure. Besides, Zhang and Sheng [78] found that swelling strain decreased due to confining pressure. The larger the confining pressure, the more the swelling strain was reduced. Ewy and Stankovic [83] reached similar results: increasing confining pressure leads to a decrease in swelling. Sufficient confining pressure could prevent clay swelling from occurring. A threshold confining pressure exists. Above this threshold, swelling decreases with the increasing confining

Figure 4: (a) Barnett shale sample after one week of spontaneous imbibition in distilled water [71]. (b) Imbibition testing results from Morsy and Sheng [66].

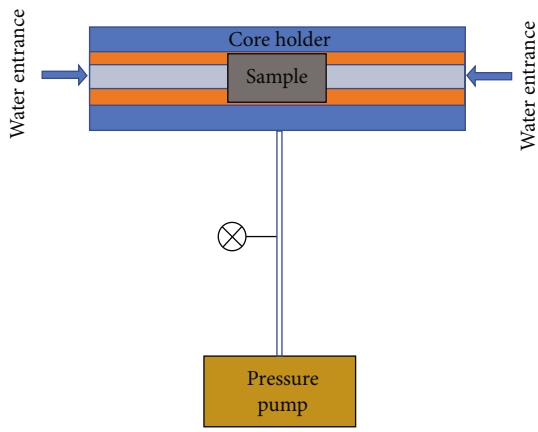

Figure 5: The schematic of the apparatus that was used by Bin et al. [76] and Wang et al. [25] to conduct imbibition tests with confining pressure.

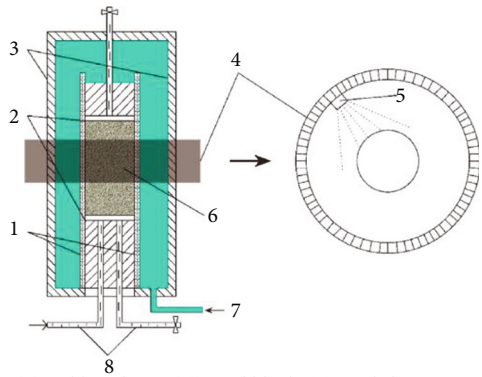

(1) Rubber sleeve; (2) Load block; (3) Steel sleeve;
(4) CT scanner; (5) X-ray source; (6) Shale core;
(7) Fluid for confining pressure application;
(8) Test solution injected into shale.

Figure 6: The CT scanner and X-ray core holder that were used by Zhang and Sheng [77, 78] and Zhang et al. [79].

pressure or is prevented by confining pressure completely. The threshold for confining pressure changes from shale to shale. In conclusion, in water-shale interaction, confining pressure has a negative impact on fracture formation.

In fracture formation, stress anisotropy plays a positive role. Liu and Sheng [10], Liu and Sheng [12], and Liu et al. [13] investigated the role of clay swelling in fracture formation in shales with stress anisotropy. In their tests, stress anisotropy is applied using anisotropic core support. The schematic of the test system is shown in Figure 11. The results indicate that clay swelling and stress anisotropy can facilitate the fracture initiation and development when shales meet water. More fractures can be formed with larger stress anisotropy (shown in Figure 12).

Liu and Sheng [10] also observed the dynamic changes of the generated fractures in water-shale interaction under stress anisotropy. They and Zhang and Sheng [78] reached the same conclusions: (1) water-shale interaction does have a positive effect on fracture formation for samples; (2) fractures can be induced much easier in water-shale interaction when samples are under stress anisotropy.

3.2. The Influencing Factors for the Generation of Fractures in Shales. Wang et al. [84] found that clay mineral types and fractions are critical for water-shale interaction. Shale reacts with water stronger with more clay minerals. Clay swelling can change the stress distribution, leading to a stress concentration around fracture tips, thus causing the fractures to grow. This statement is supported by the simulation work done by Liu et al. [13]. Clay swelling can cause the redistribution of the stress in the models. Stress concentration was observed around the generated fractures to cause the generation and propagation of the fractures.

Natural fractures are everywhere in shales [39, 40, 85]. Natural fractures are suspected as a factor in productions in shales. Additionally, natural fractures serve as the sites for fracture creation and propagation in shales [10, 39, 86, 87]. The locations of natural fracture also can impact the fracture formation and distribution [86]. Natural fractures can facilitate the formation and growth of new fractures in water-shale interaction (shown in Figure 13).

Bedding and lamination are ubiquitous in shales [40]. Roshan et al. [11] observed that the induced fracture was formed along with the bedding (shown in Figure 9). Moradian et al. [88] also observed that if the bedding directions are 60° and 90°, fractures with bedding directions were dominant. This result is same as the results from Liu and Sheng [10] and Makhanov et al. [68]. Water absorption parallel to the lamination is higher than perpendicular to the same lamination [89]. The enhancement of the imbibition rate was caused by the generation of fractures. This observation indicated that lamination was beneficial for the generation of fractures in water-shale interaction. By those results, bedding and lamination is another positive factor to influence the generation and propagation of fractures in water-shale interaction.

Organic matter is a common component in shales [32, 90]. Xue et al. [91] conducted water imbibition tests under

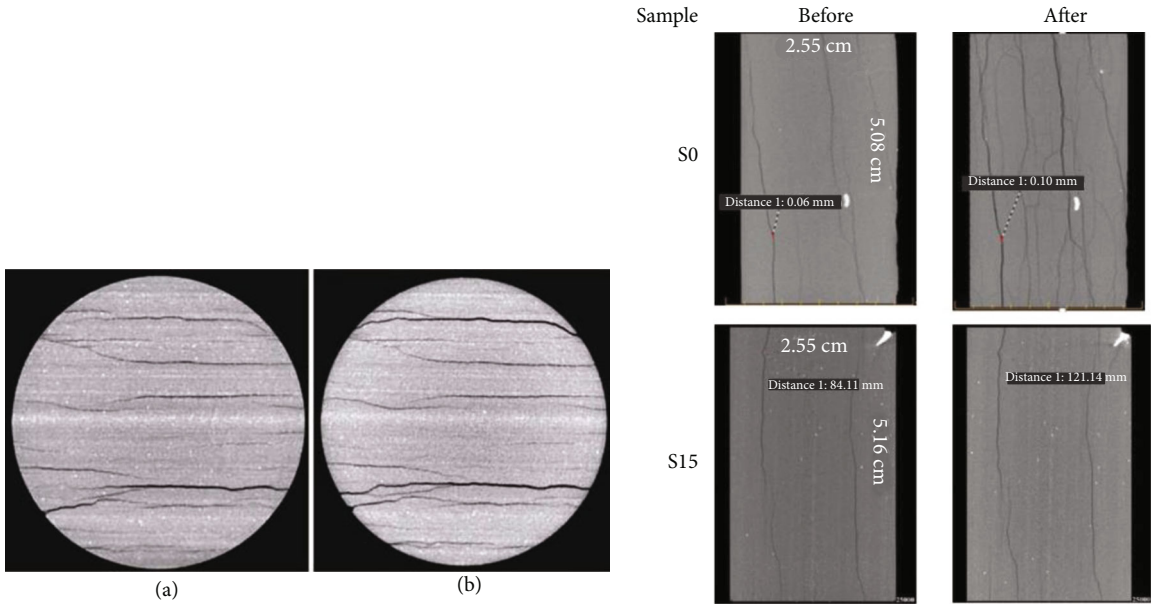

Figure 7: (a) Fracture generated and propagated in Bin et al.'s [76] tests. (b) Fracture generated and propagated in Wang et al.'s [25] tests.

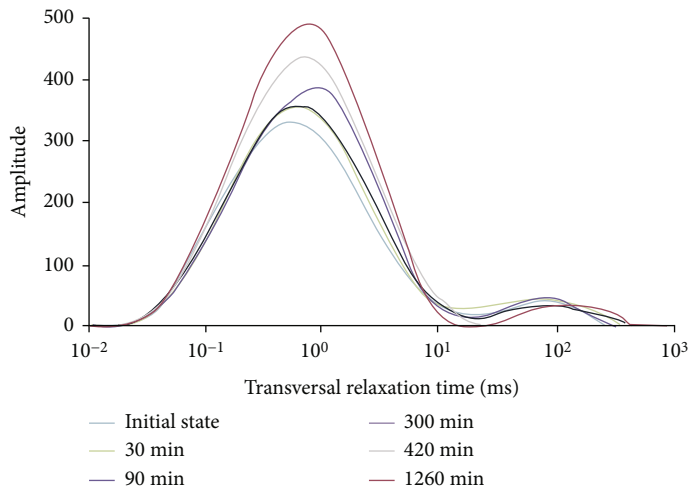

Figure 8: T_2 spectra of one sample during water-shale interaction in Bin et al.'s [76] tests.

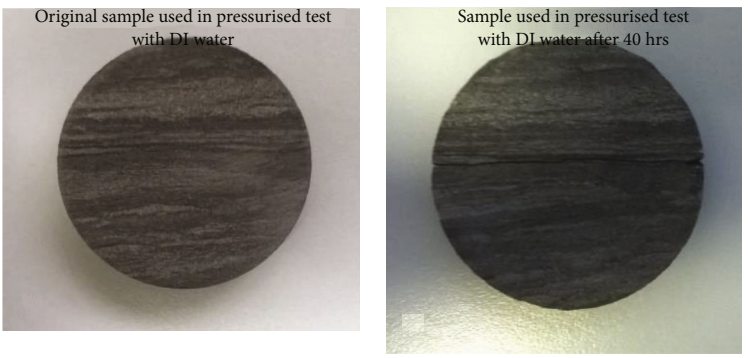

Figure 9: Testing results from [11].

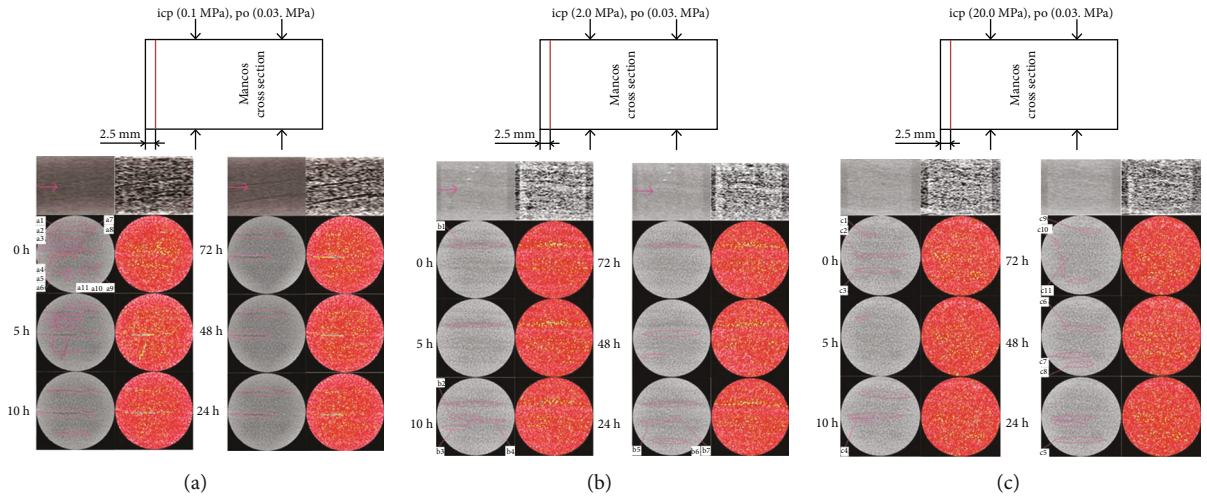

FIGURE 10: CT images of Mancos shale samples at different confining pressures. ICP means confining pressure. PO means injected fluid pressure or pore pressure [78].

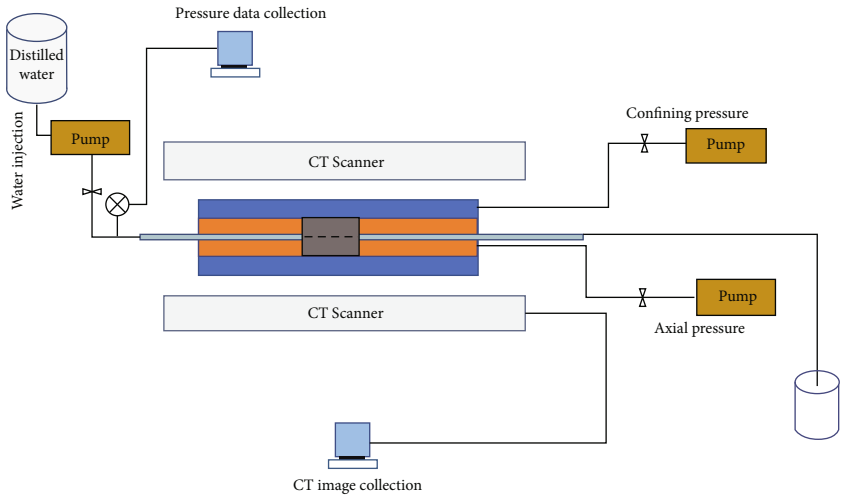

FIGURE 11: The schematic of the test system (Liu and Sheng [10] and Liu and Sheng [12].

atmospheric conditions. They found that the generation of fractures mainly occurred in the areas between organic matter and inorganic minerals. The cohesion between the mineral particles could be weakened after the water-shale interaction. The nonclay mineral particles are exfoliated to form inorganic pores, which gradually develop into microfractures between the nonclay mineral particles and the clay mineral particles.

Li et al. [92] observed that microfractures were generated along with the interfaces between organic and inorganic matter as well as between different components. Similar results were observed by Wang et al. [84]. Organic matter can provide space for fracture development caused by clay swelling and capillary pressure [93]. Organic matter is another positive factor for the generation and propagation of fractures in water-shale interaction.

3.3. Change of Shale's Mechanical Properties due to Water-Shale Interaction. The mechanical properties of shales and fractures are changed because of water-shale interaction. The elasticity, hardness, and strength of shales are deteriorated, which is termed as "shale softening." The properties of fractures, like fracture conductivity, stress intensity factor (K_c), crack extension force (G_c), and subcritical fracture growth index (SCI), are reduced.

Shale's mechanical strength can be weakened under the effect of water-shale interaction [16–18]. Cheng et al. [16] compared the shale strength of dry and water-saturated samples. The results indicated that the compressive strength, Young's modulus, and the anisotropy of the water-saturated samples were reduced compared to the results of the dry samples (as shown in Figure 14). The average compressive strength of water-saturated samples was 28.9% lower than that of the dry samples, with a maximum decrease of 54% for water-saturated samples. Likewise, the mean and maximum reductions in Young's modulus of the water-saturated samples were 26.1% and 62%, respectively. Two reasons why we need to compare Young's modulus are as follows: (1) the brittleness of shales can be used to determine the ability to be fractured of the shales [94], and brittleness is

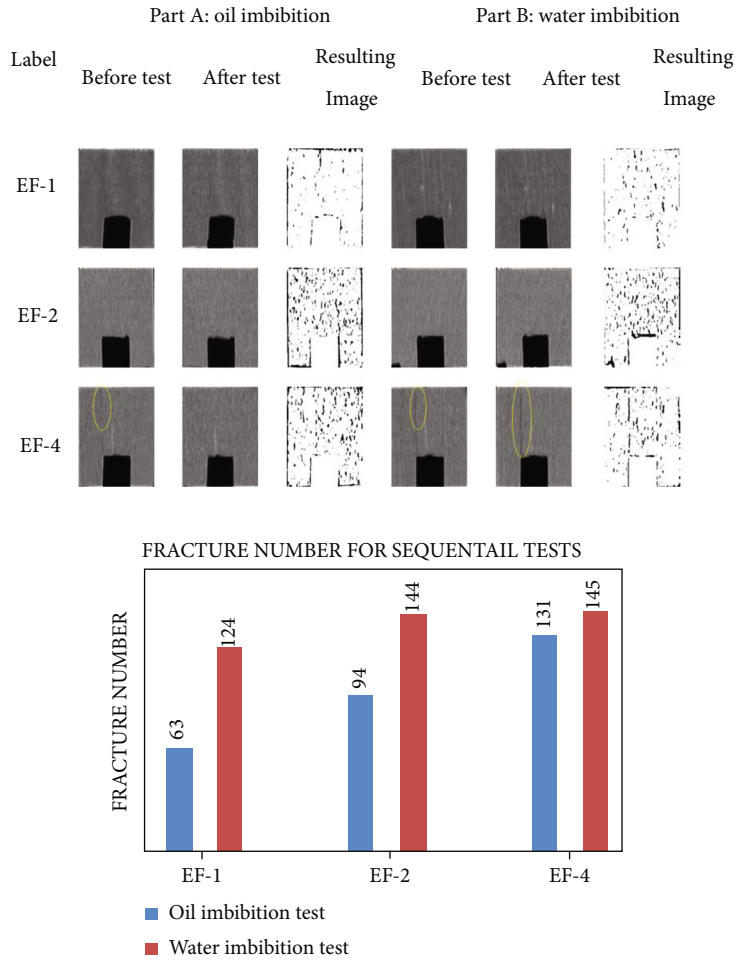

Figure 12: Results from Liu and Sheng [10].

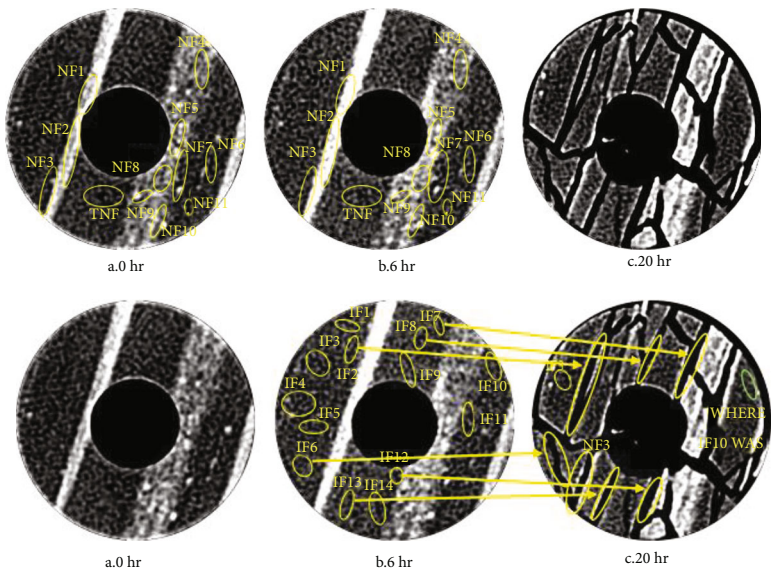

Figure 13: Results for EF-6. The testing condition was 1350 psi axial and 500 psi confining pressure [10].

a function of Young's modulus. The shale is more brittle with a higher Young's modulus. Brittle shale has a higher potential for fracture initiation and propagation and the formation of a complex fracture network than ductile shale. (2) Decreased Young's modulus leads to deterioration of fracture conductivity [95]. Once the compressive strength of

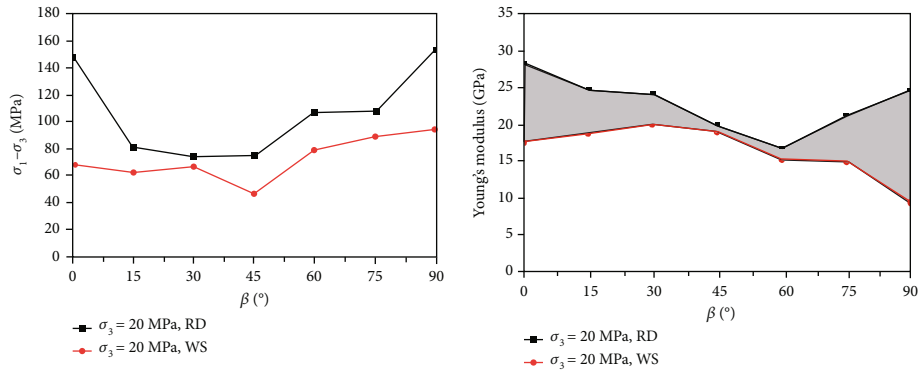

(a) (b)

FIGURE 14: (a) Comparison of the compressive strength of the dry (RD) and water-saturated (WS) samples from Cheng et al. [16]. (b) Comparison of Young's modulus of the dry (RD) and water-saturated (WS) samples from Cheng et al. [16].

the shales is weakened by water-shale interaction, it is easier to meet the failure criterion and fractures could develop in shales. The results from Wong [18] indicated that Young's modulus decreased with increasing swelling. Besides, the behavior of shale under larger swelling was like a ductile material. Similar results were achieved by Yang et al. [96]. Talal [17] compared the effect of Na^+, K^+, Ca^{2+} on the compressive strength of shales. The results indicated that K^+ had a strengthening effect on shale strength, while Na^+ and Ca^{2+} ions had a weakening effect on shale strength. Akrad et al. [95] measured Young's modulus of shales before and after exposure to 2% KCl slickwater and freshwater. The results showed that potassium ion (K^+) caused the reduction of Young's modulus of shales, no matter it was "soft" mineral with Young's modulus below 30 GPa or "hard" mineral with Young's modulus above 30 GPa. The highest reduction occurred in Eagle Ford shale (70%), which resulted in a 39% loss in fracture conductivity. 52% of the reduction was observed for Bakken shale, causing a 14% loss in fracture conductivity. For these two shales, high calcite (77%) and low clay content (8% for Eagle Ford and 4% for Bakken) were measured. For the clay-rich samples, like Lower Bakken (clay content of 47%) and Haynesville (clay content of 57%), a lesser decrease was observed in Young's modulus (22% for Lower Bakken and 6% for Haynesville), resulting in a lesser reduction in fracture conductivity (5% for Lower Bakken and 1% for Haynesville). These results indicated that clay swelling might not cause permeability impairment as bad as assumed. The reduction of fracture conductivity was also reported by Pedlow and Sharma [97] and Jansen et al. [98]. Li et al. [92] examined the effect of water-shale interaction on the tensile strength of shales. Tensile strength is critical for predicting fracture initiation and growth. The smaller the tensile strength, the easier the fractures can be generations. As shown in Figure 15, as the water content increases from 4.45% to 11.7%, the water-shale interaction reduces the tensile strength by 4.4% to 51.7%, which means that fractures are more likely to develop due to the decrease in tensile strength. In conclusion, the change of the mechanical properties of shales due to water-shale interaction can facilitate fracture generation in shales.

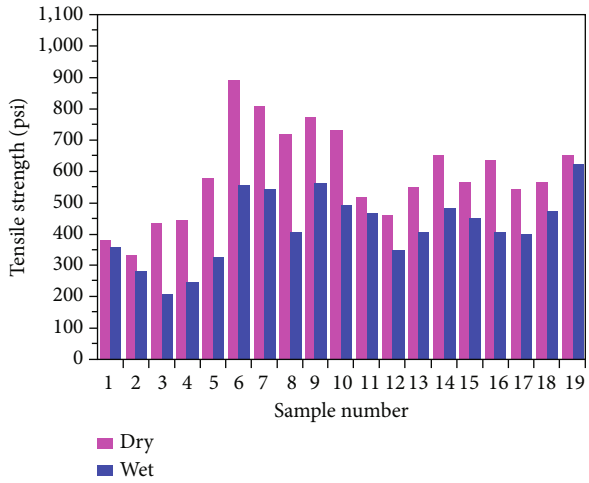

FIGURE 15: Comparison of the tensile strength of dry and wet Eagle Ford samples from Li et al. [92].

The properties of fractures are affected by water-shale interaction. Based on the equilibrium law, stress intensity factor (K_c) or crack extension force (G_c) has a critical value. Once those values are reached or exceeded, the fracture can propagate [99]. As stress corrosion occurs, fracture can develop when the K or G is far below the critical values, which is known as subcritical fracture growth [99]. Stress corrosion means that the strained Si-O bonds at crack tips are more reactive to environmental agents than the unstrained bonds of crystalline silicates because of the reduced strain-induced overlap of atomic orbitals [99]. A weakened state is produced due to strained bond-environmental agent reaction, resulting in that the bonds can be broken at a lower stress than the unstrained bonds. A general expression to represent the weakening effect of silicate and quartz in water is proposed as the following [100–104]:

$$\mathrm{H-O-H+[-Si-O-Si-]} \rightleftarrows \mathrm{[-Si-OH\cdot HO-Si-]} \quad (1)$$

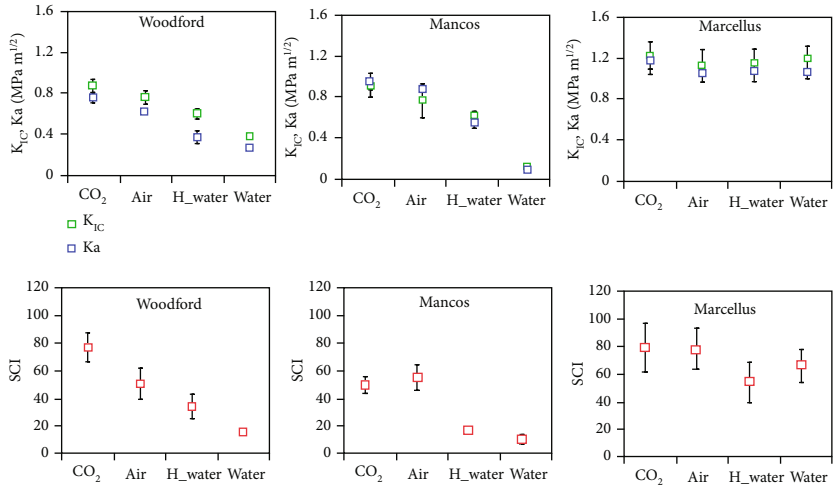

Figure 16: Testing results from Chen et al. [19].

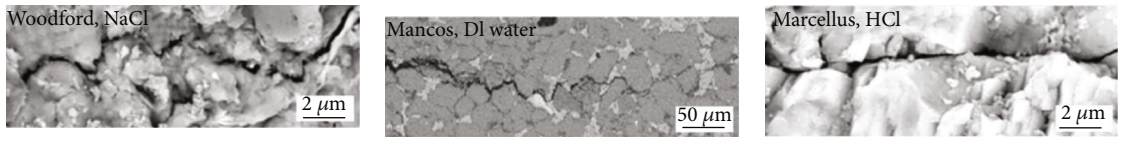

Figure 17: Fracture traces by SEM in Chen et al. [20].

It is first-order chemical reaction when strong Si – O bonds hydrolyze to weaker hydrogen-bonded hydroxyl groups attached to silicon atoms. Thus, water-shale interaction can result in stress corrosion.

Chen et al. [19] investigated the change of fracture mechanical properties in clay-rich shales under water-shale interaction. Their results (shown in Figure 16) indicated that even at low smectite content, clay-rich shales had a strong water-weakening effect, resulting in a 54% reduction in fracture toughness and 77% reduction in subcritical fracture growth index for water-saturated samples. The carbonate-rich shale barely had water-weakening effects. Besides, K_{IC} for wet samples was reduced by more than 50% compared to dry samples for clay-rich shales. For samples without clay minerals [105], K_{IC} dropped less than 20% with increasing water saturation. The reduction in subcritical fracture growth index in clay-rich samples could reach 77%, while the reduction in subcritical fracture growth index for samples without clay minerals was negligible or less than 50% [21–23].

Their findings suggest that water-shale interactions lead to the weakening of the subcritical fracture properties of clay-rich shale, which may lead to subcritical fracture growth and failure more prone to clay-rich shale than clay-poor shale.

Chen et al. [20] conducted comparison work for Woodford shale, Mancos shale, and Marcellus Shale with different temperatures, pH, and varying fluid salinities. The generated fractures were traced by scanning electron microscopy (SEM) (shown in Figure 17). The clay fabrics and grain boundaries are shown in Figure 18.

It can be seen from Figure 17 that intergranular fractures are generated in the clay-rich shale, forming zigzag traces at the grain scale. As can be seen in Figure 18, clay fabrics and grain boundaries and pits are observed on the fracture surfaces of the Woodford and Mancos Shales (red arrows in Figures 18(b) and 18(d)). The fracture trace observations were compared with the clay structure and grain boundaries, and the fractures were formed by clay swelling.

According to Chen et al. [19], Chen et al. [20], Nara et al. [21, 22], and Waza et al. [23], two points are reached: (1) clay swelling is primarily responsible for the generation of the fractures in water-shale interaction; (2) the reduction in stress intensity factor (K_c), crack extension force (G_c), and subcritical fracture growth index (SCI) can facilitate the generation and propagation of fractures in water-shale interaction. However, those tests were conducted without restrains.

Through the comparison, the degradation of mechanical properties of shales and fractures due to water-shale interaction has a positive effect on the generation of fractures in shales.

3.4. Mechanisms about the Generation and Development of Fractures in Water-Shale Interaction. The initiation of swelling-induced fractures is due to swelling pressure [106], which is the difference in the hydrostatic pressure of the water inside and outside of the clay membrane. Once the swelling pressure is large enough, it can break the natural cementation of shale and allow the generation of swelling-induced fractures. A similar explanation is stated by Steiger [107] which suggests that interactions between water and

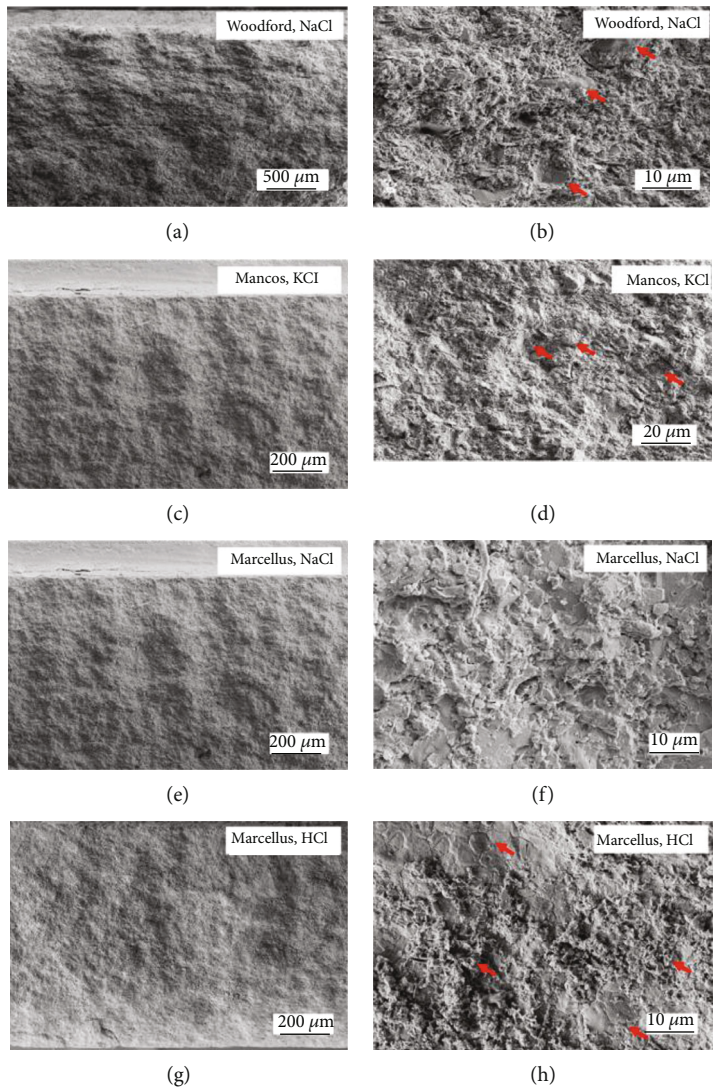

Figure 18: Fracture surfaces in the tests conducted by Chen et al. [20].

silicate surfaces or cations provide the driving force, causing water adsorption and swelling until separation between crystallites occurs, leading to the disintegration of unconfined shale. However, it is still controversial that if the own effect of swelling stress is large enough to initiate fractures under confined conditions. Xu et al. [108] measured the swelling stress under confining conditions. The measured stress was less than 100 psi (0.69 MPa). However, the measurements from Nuesch et al. [109] showed that swelling stress could reach 682 psi (4.7 MPa). No studies have evidence to show that fractures can be directly induced by the only effect of clay swelling under confined conditions. More efforts are needed to answer this question.

The fractures induced by the water-shale interaction under stress conditions are more likely caused by the combined effects from clay swelling, reduction of mechanical properties of shales and fractures, and stress conditions. The initiation of fractures can be triggered by clay swelling through the formation of new pores and microfractures. Meanwhile, clay swelling can induce nonuniform stress, resulting in the local stress concentration around fractures. The reduction of mechanical properties of shales and fractures can facilitate the generation of fractures by lowering the fracture mechanical properties. Fractures can propagate under the combined effect of clay swelling, stress anisotropy, shale, and reduced mechanical properties of fractures. The characteristics of shale natural fractures, bedding, and organic and inorganic matter interface can be used as the place for the generation of induced fractures. In this process, clay swelling, redistribution of stress, and the reduction of mechanical properties of shales and fractures are caused by water-shale interaction. Therefore, water-shale interaction is critical in the formation of fractures under stress conditions. However, new experimental methodology or even new apparatus is needed to quantitatively reflect the contribution of water-shale interaction in the generation of fractures in shales.

Another mechanism that may induce fractures in water-shale interaction is mechanical failure. The mechanical failure is caused by increased pore pressure caused by the

imbibition of fluids. Makhanov et al. [110] found that although oil had no affinity for absorption in clays, some microfractures still were created with oil adsorption. This result revealed that the pore pressure due to fluid imbibition reduced the effective stress and thus created fractures. This kind of fractures is generated by mechanical failure of samples. A similar conclusion was reached by Santos et al. [51]. However, it is difficult to tell the amount and importance of the fractures caused by mechanical failure due to fluid imbibition. Besides, it is hard for us to separately study the effect of mechanical failure due to fluid imbibition in water-shale interaction. The reason is that once the fluid is imbibed into samples, the fractures caused by fluid-shale interaction and fractures caused by the mechanical failure may occur at the same time, and we cannot tell whether the fractures are caused by the interaction or mechanical failure.

4. The Change of Permeability due to Water-Shale Interaction

In this part, the permeability change due to water-shale interaction in the experiments is summarized. Based on those experimental results, the mechanisms about the change of permeability due to water-shale interaction are analyzed.

4.1. Experimental Methodologies That Were Used and the Experimental Results. Most researchers believe that water-shale interaction causes formation damage, mainly permeability impairment in shales; however, many studies showed that induced fractures were formed in water-shale interaction. Unlike conventional reservoirs, enhancing oil productivity in shales mainly relies on the conductivity of fractures, even though the conductivity of such induced fractures is lower than that of propped fractures in hydraulic fracturing [98, 111]. The matrix permeability and conductivity of natural fractures can be damaged due to the interaction between water and shale, especially clay swelling [47, 112]; however, shale permeability can be enhanced by the induced fractures [9, 11, 24]. What is the final effect on permeability change is an interesting question.

Based on the methodology, the permeability tests can be divided into two types: gas permeability measurement during water imbibition and pressure monitor during water imbibition. The gas permeability measurement during water imbibition was popularly used by lots of researchers [6, 24, 25, 75, 77]. The general testing procedure is the following: the sample is exposed to water-based fluid initially. After a certain period, the sample is removed from the fluid and the gas permeability is measured. Then, the sample is resumed to the fluid to continue the imbibition test. For this method, this procedure may be repeated several times to achieve the gas permeability for different time spots in the fluid imbibition tests. In the studies from Aksu et al. [6], Shen et al. [24], and Zhou et al. [75], they did not mention clean the samples before measuring permeability. In Wang et al. [25], they dried the core samples before measuring permeability. In Zhang and Sheng [77], they vacuumed the sample before measuring the permeability. This methodology can quantitatively reflect the effective gas permeability change in the tests. However, gas permeability cannot truly represent absolute permeability in shales. Besides, different methodologies are employed to measure shale permeability [113]. Pressure monitor during water imbibition was not as widely used as gas permeability measurements [11, 12]. For this methodology, the upstream pressure or pressure difference is monitored in the tests. The increase of pressure can reflect the enhancement of shale permeability; otherwise, the impairment of shale permeability can be shown by the decrease of pressure. This methodology can indirectly and qualitatively reflect the change of shale permeability. However, it is still unsolved to quantitatively reflect the change of shale permeability in the tests. Permeability is a function of multiple factors, like stress, pore throat, pore size, and liquid viscosity. This research gap needs to be filled.

Shen et al. [24] measured the permeability change in water imbibition tests for sandstones and shales. The pulse-decay permeability methodology was used to measure samples' permeability. Before they conducted imbibition tests, permeability for dry samples was measured. Then, the imbibition tests were conducted. After a certain period of imbibition tests, the imbibition cells were removed from the imbibition liquid, and permeability tests were conducted as soon as the cells were removed. Figure 19 shows the permeability change vs. the increased water content in their tests. In the early stage, the decrease of shale permeability (Y1, Y2, and Y3) was due to the reduction of effective flow channel caused by water blocking and stress sensitivity. It means that the applied stress conditions have an impact on the permeability change [24]. At the middle stage, samples' permeability (Y1, Y2, and Y3) increased due to the generation and propagation of new induced fractures caused by clay swelling. Shale permeability (Y1, Y2, and Y3) decreased, at the last stage, which is due to water blocking and stress sensitivity. A failure occurred in the sample Y4, resulting in a permanent increase in the sample's permeability. The failure was caused by clay swelling. They stated that the three critical factors to control shale permeability are clay swelling, stress sensitivity, and water blocking. Whether the permeability can be increased depends on the comparison of these three factors.

Shales' wettability, hydration stress, and permeability change in slickwater treatment are studied by Yuan et al. [114]. The testing methodology is similar to Shen et al.'s [24]. The permeability was damaged by the narrowed flowing channels due to clay swelling at the beginning of the test. Under the effect of swelling stress and capillary pressure, fractures were induced. However, the fractures are not interconnected to form effective flow channels. Therefore, the contribution from these fractures to permeability was negative. As water-shale interaction continues, fractures propagated and interconnected because of the increased hydration stress and wettability change. Thus, shale permeability was recovered and even higher than the original value. A pressure build-up method was used by Zhou et al. [75] to measure the samples' gas permeability. They stated that matrix permeability and fracture permeability were

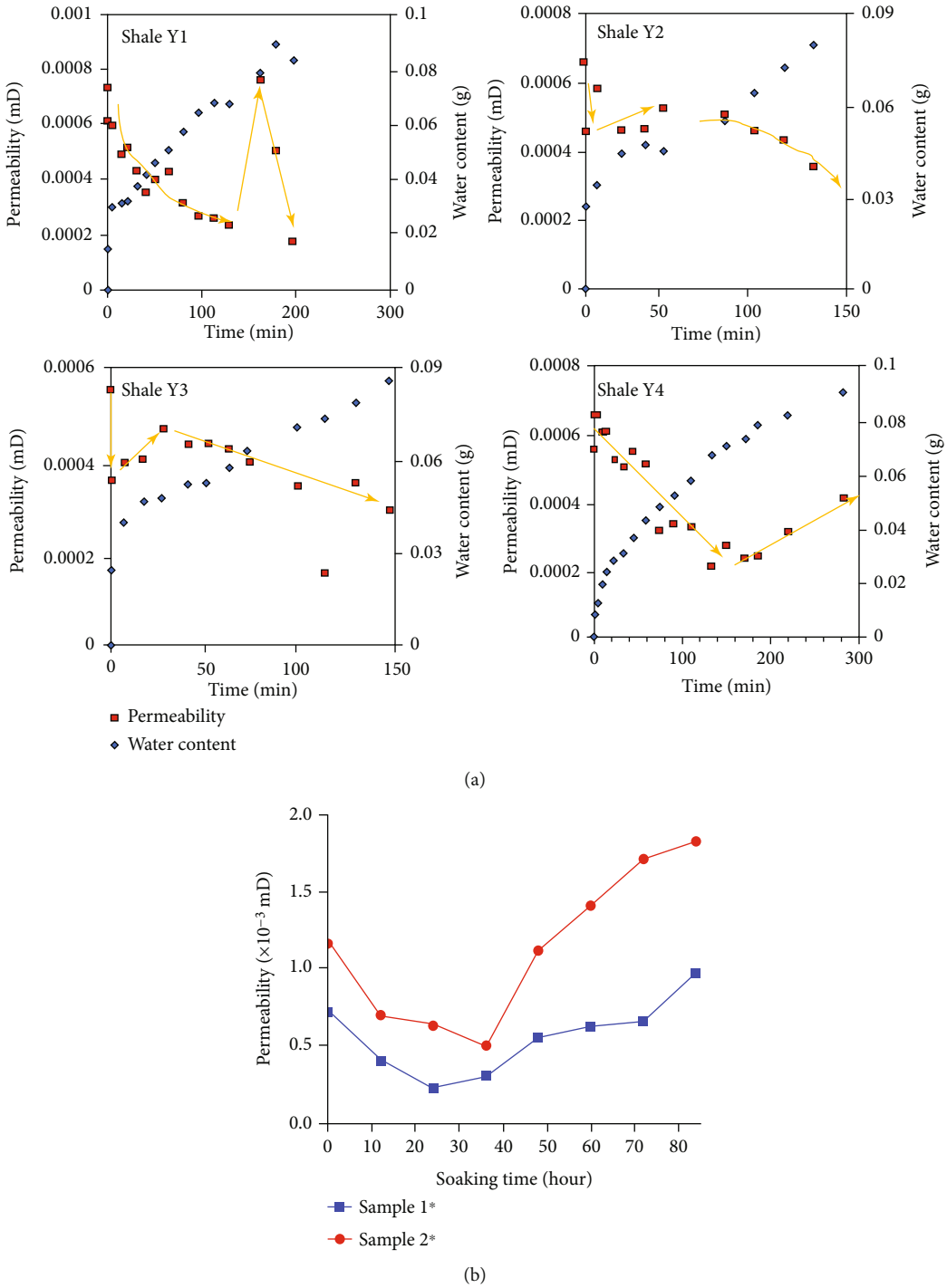

FIGURE 19: (a) Change of shales' permeability in water imbibition tests [24]. (b) Change of shales' permeability in water imbibition tests [114].

decreased due to clay swelling and water blocking. Besides, they observed that the samples' permeability could be increased due to the generation of microfractures. In the pictures provided by them, the generated microfractures propagated through the core samples and formed an effective flow channel, thereby increasing the sample's permeability. All the above three studies used effective gas permeability to represent the change of shale permeability. However, it is widely accepted that gas permeability is higher than liquid permeability [115–117]. Moreover, no accurate formula was proposed to represent the gas and liquid permeability correlations for various shales. The measured gas permeability cannot correctly represent the permeability change in water-shale interaction.

Roshan et al. [11] conducted a test under confining pressure (1000 psi). In the test, the injection pressure is 500 psi

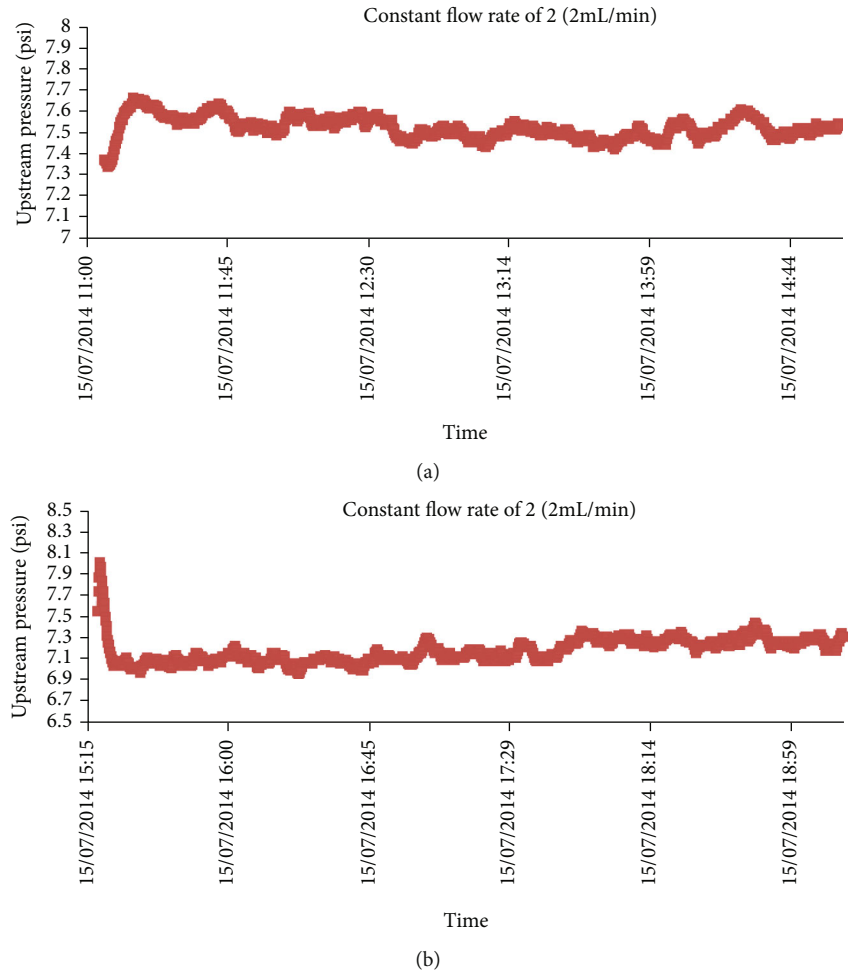

Figure 20: Upstream pressure curve from Roshan et al. [11].

and the injected fluid is DI water. The upstream pressure was recorded. No pressure change was observed until a fracture was generated (shown in Figure 9). Similarly, in their permeability test, they recorded the change of the upstream pressure in the imbibition test with the downstream pressure at atmospheric conditions. Figure 20 shows the pressure curve from their test. In the test using 10 wt.% NaCl solution, the upstream pressure was almost constant, whereas, in the test using DI water, the pressure changed from 8 psi to 7 psi. After close observation of the tested sample, they found that particle detachment by clay swelling occurred and caused this pressure drop.

To study permeability change due to water-shale interaction, one set of experiments was performed by Liu and Sheng [12]. In their tests, the upstream pressure was monitored to represent the change of permeability. Figures 21 and 22 show the experimental results.

From Figure 22, pressure data decreased once fractures were generated or propagated. Multiple fractures were generated and interconnected to form flow channels and cause the failure of the sample, resulting in the permanent recovery of shale permeability. In another test, an isolated fracture was generated and did not form an effective flow channel for DI water; thereby, the pressure increased in the test. The results indicated that if the fractures are isolated and could not form an effective flow channel, the fractures did not contribute to the recovery of shale permeability. However, once the fractures form effective flow channels, shale permeability can be recovered. It is seen from Figure 22 that particle detachment occurred on the artificial fracture surface. The detached particles were washed away by the DI water, enhancing the shale permeability.

4.2. Mechanisms about Permeability Change due to Water-Shale Interaction. From those studies, shale permeability can be enhanced if the generated fractures can form an effective flow channel. However, if the generated fractures cannot serve as an effective flow channel, shale permeability will be impaired by clay swelling, water blocking, stress-sensitive, etc. Gas permeability cannot be used to represent the permeability change in water-shale interaction. Pressure monitor cannot quantitatively show the permeability change in water-shale interaction. It is unsolved to quantitatively reflect permeability change by water-shale interaction. More efforts are needed.

Particle detachment affects permeability changes. The permeability of the shale can be increased when the separated particles can be washed away from the shale. Grain

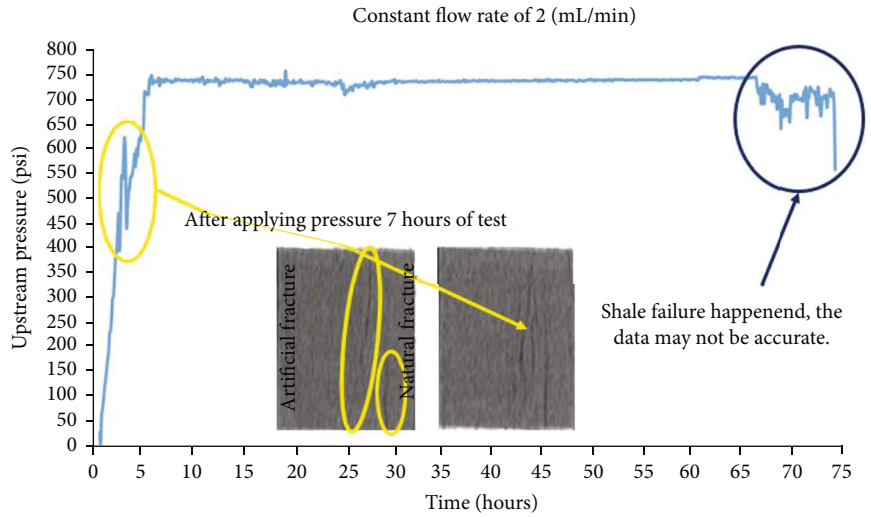

Figure 21: One testing result from Liu and Sheng [12].

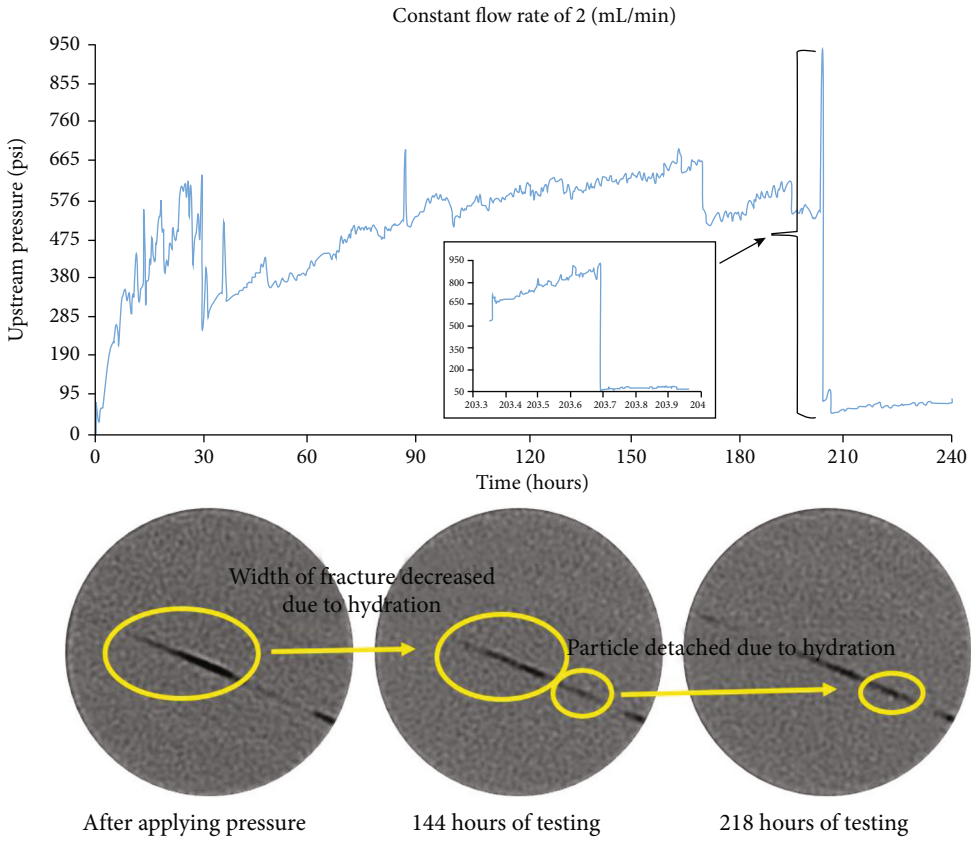

Figure 22: Another testing result from Liu and Sheng [12].

detachment can lead to pore or pore-throat plugging problems, thereby impairing shale permeability. Mohan et al. [118] found that kaolinite and muscovite are more easily detached from the shale surface when swelling occurs. The effects of pH, ion exchange, and brine salt concentration can affect particle separation. Higher pH, lower ionic strength, and low salinity can facilitate separations [119–123]. Whether particle detachment is beneficial to shale permeability depends on whether the detached particles can be transported from the shale.

5. Concluding Remarks

Water-shale interaction is a complex phenomenon. This reaction can cause clay swelling, reduction of mechanical properties of shales, generation and propagation of fractures,

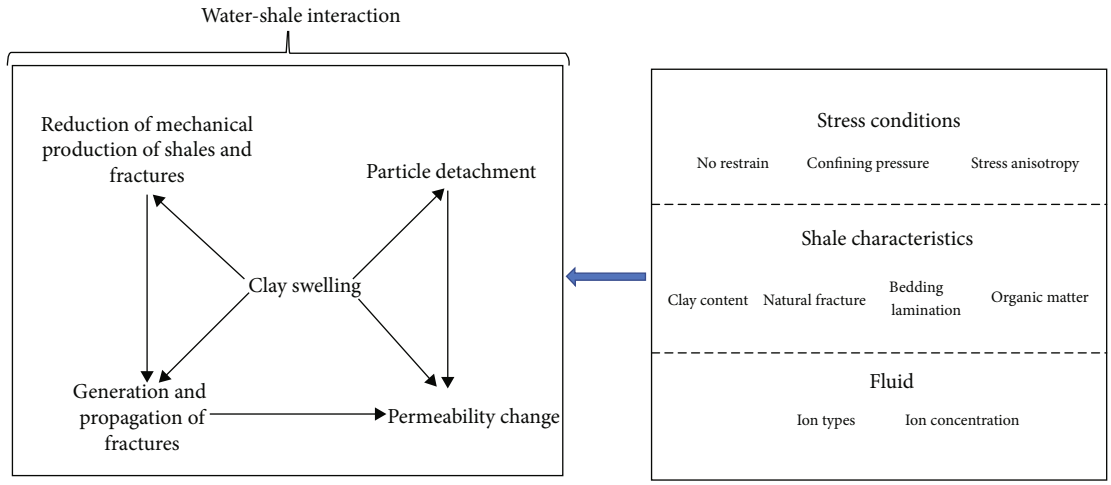

Figure 23: Phenomena appearing in water-shale interaction, the impact between these processes, and the other influencing factors.

particle detachment, permeability change, etc. Other conditions, like stress condition, shale characteristics, and reacting fluid, could influence the reaction. Figure 23 summarizes these phenomena and the relationship between each other.

Clay swelling is the key phenomenon occurring in water-shale interaction. Clay swelling can trigger the generation of fractures, cause the detachment of particles, influence the magnitude of the reduction of mechanical properties of shales and fractures, and impact permeability change. Experiments showed that fracture can be generated in water-shale interaction. The most likely mechanism for the generation of fractures in water-shale interaction is that the induced fractures are generated by the combined effects from clay swelling, reduction of mechanical properties of shales and fractures, and stress anisotropy. However, other mechanisms can induce fractures as well, like the swelling pressure, the mechanical failure caused by the imbibition of water. Whether clay swelling can directly induce fractures under stress conditions is still questionable. To answer this question, a new experimental methodology and apparatus are needed. Ideally, the process of the generation of clay swelling inducing fractures under stress conditions should be monitored and captured in the reaction between water and shale. The effect of clay swelling and stress conditions should be separated. Measuring gas permeability cannot accurately reflect the permeability change by water-shale interaction. Using liquid to measure the liquid permeability is difficult because of the injectivity issue in low permeable shales. Pressure monitoring can qualitatively reflect permeability change in shales. However, it is better to quantitatively reflect the permeability change in water-shale interaction under stress anisotropy. More efforts are needed.

Data Availability

Data are available by contacting the authors.

Additional Points

Highlight. (i) Water-shale interaction can cause clay swelling, change of mechanical properties of shales, generation of fractures, and permeability change. (ii) Fractures are generated by the combined effects from clay swelling, reduction of mechanical properties of shales and fractures, and stress anisotropy. (iii) Both the induced fractures and particle detachment can impact shale permeability. (iv) Stress condition, shale characteristics, and the reacting fluid could influence water-shale interaction.

Conflicts of Interest

The authors declare that they have no conflicts of interest.

Acknowledgments

This work is supported by the National Key Research and Development Program of China (No. 2019YFC1805400) and the Fundamental Research Funds for the Central Universities (No. 2020ZDPY0201).

References

[1] F. Aloulou and T. Cook, "Tight oil expected to make up most of U.S. oil production increase through 2040," 2017, https://www.eia.gov/todayinenergy/detail.php?id=29932.

[2] J. B. Curtis, "Fractured shale-gas systems," *AAPG Bulletin*, vol. 86, no. 11, pp. 1921–1938, 2002.

[3] J. D. Arthur, B. Bohm, and M. Layne, *Hydraulic fracturing considerations for natural gas wells of the Marcellus shale*, ALL Consulting, LLC, Tulsa, Oklahoma, 2009.

[4] M. E. Mantell, "Recycling and reuse of produced water to reduce freshwater use in hydraulic fracturing operations," in *Summary of the technical workshop on water acquisition modeling: Assessing impacts through modeling and other means*, U.S. Environmental Protection Agency, Washington, D.C., 2013.

[5] J. J. Sheng, *Enhanced Oil Recovery Field Case Studies*, Gulf Professional Publishing, 2013.

[6] I. Aksu, E. Bazilevskaya, and Z. T. Karpyn, "Swelling of clay minerals in unconsolidated porous media and its impact on permeability," *GeoResJ*, vol. 7, pp. 1–13, 2015.

[7] D. H. Gkay and R. W. Rex, "Formation damage in sandstones caused by clay dispersion and migration," in *Clays and Clay Minerals*, pp. 355–366, Berkeley, California, 1966.

[8] M. J. Wilson, L. Wilson, and I. Patey, "The influence of individual clay minerals on formation damage of reservoir sandstones: a critical review with some new insights," *Clay Minerals*, vol. 49, no. 2, pp. 147–164, 2014.

[9] H. Dehghanpour, Q. Lan, Y. Saeed, H. Fei, and Z. Qi, "Spontaneous imbibition of brine and oil in gas shales: effect of water adsorption and resulting microfractures," *Energy & Fuels*, vol. 27, no. 6, pp. 3039–3049, 2013.

[10] K. Liu and J. J. Sheng, "Experimental study of the effect of stress anisotropy on fracture propagation in Eagle Ford shale under water imbibition," *Engineering Geology*, vol. 249, pp. 13–22, 2019.

[11] H. Roshan, S. Ehsani, C. E. Marjo, M. S. Andersen, and R. I. Acworth, "Mechanisms of water adsorption into partially saturated fractured shales: an experimental study," *Fuel*, vol. 159, pp. 628–637, 2015.

[12] K. Liu and J. J. Sheng, "A new experimental methodology to investigate water adsorption into shale under stress anisotropy conditions," in *SPE Liquids-Rich Basins Conference-North America*, Society of Petroleum Engineers, 2019.

[13] K. Liu, J. J. Sheng, and Z. Zhang, "A simulation study of the effect of clay swelling on fracture generation and porosity change in shales under stress anisotropy," *Engineering Geology*, vol. 278, p. 105829, 2020.

[14] K. Liu and J. J. Sheng, "Experimental study of the effect of temperature change in water-shale interaction on fracture generation and permeability change in shales under stress anisotropy," in *55th US Rock Mechanics/Geomechanics Symposium*, One Petro, 2021.

[15] K. Liu and J. J. Sheng, "Experimental study of the effect of water-shale interaction on fracture generation and permeability change in shales under stress anisotropy," *Journal of Natural Gas Science and Engineering*, vol. 100, article 104474, 2022.

[16] J. Cheng, Z. Wan, Y. Zhang, W. Li, S. S. Peng, and P. Zhang, "Experimental study on anisotropic strength and deformation behavior of a coal measure shale under room dried and water saturated conditions," *Shock and Vibration*, vol. 2015, Article ID 290293, 13 pages, 2015.

[17] A. B. Talal, "A novel experimental technique to monitor the time-dependent water and ions uptake when shale interacts with aqueous solutions," *Rock Mechanics and Rock Engineering*, vol. 46, no. 5, pp. 1145–1156, 2013.

[18] R. C. K. Wong, "Swelling and softening behaviour of La Biche shale," *Canadian Geotechnical Journal*, vol. 35, no. 2, pp. 206–221, 1998.

[19] X. Chen, P. Eichhubl, J. E. Olson, and T. A. Dewers, "Effect of water on fracture mechanical properties of shales," *Journal of Geophysical Research: Solid Earth*, vol. 124, no. 3, pp. 2428–2444, 2019.

[20] X. Chen, P. Eichhubl, J. E. Olson, and T. A. Dewers, "Salinity, pH, and temperature controls on fracture mechanical properties of three shales and their implications for fracture growth in chemically reactive fluid environments," *Geomechanics for Energy and the Environment*, vol. 21, article 100140, 2020.

[21] Y. Nara, K. Morimoto, T. Yoneda, N. Hiroyoshi, and K. Kaneko, "Effects of humidity and temperature on subcritical crack growth in sandstone," *International Journal of Solids and Structures*, vol. 48, no. 7-8, pp. 1130–1140, 2011.

[22] Y. Nara, H. Yamanaka, Y. Oe, and K. Kaneko, "Influence of temperature and water on subcritical crack growth parameters and longterm strength for igneous rocks," *Geophysics Journal International*, vol. 193, no. 1, pp. 47–60, 2013.

[23] T. Waza, K. Kurita, and H. Mizutani, "The effect of water on the subcritical crack growth in silicate rocks," *Tectonophysics*, vol. 67, no. 1-2, pp. 25–34, 1980.

[24] Y. Shen, H. Ge, M. Meng, Z. Jiang, and X. Yang, "Effect of water imbibition on shale permeability and its influence on gas production," *Energy & Fuels*, vol. 31, no. 5, pp. 4973–4980, 2017.

[25] Q. Wang, C. Lyu, and D. R. Cole, "Effects of hydration on fractures and shale permeability under different confining pressures: an experimental study," *Journal of Petroleum Science and Engineering*, vol. 176, pp. 745–753, 2019.

[26] S. Tangparitkul, A. Saul, C. Leelasukseree, M. Yusuf, and A. Kalantariasl, "Fines migration and permeability decline during reservoir depletion coupled with clay swelling due to low-salinity water injection: an analytical study," *Journal of Petroleum Science and Engineering*, vol. 194, article 107448, 2020.

[27] F. T. Mackenzie and R. M. Garrels, *Evolution of Sedimentary Rocks*, Norton, New York, 1971.

[28] F. R. Sattler and D. A. Barnes, "Geological characterization and assessment of confining layer potential of the Upper Ordovician Utica shale, Michigan Basin, USA," in *Paleozoic Stratigraphy and Resources of the Michigan Basin*, G. M. Grammar, W. B. Harrison, and D. A. Barnes, Eds., vol. 531, pp. 35–54, Geological Society of America, USA, 2018.

[29] D. M. Wang, Y. M. Xu, D. M. He, J. Guan, and O. M. Zhang, "Investigation of mineral composition of oil shale," *Asia-Pacific Journal of Chemical Engineering*, vol. 4, no. 5, pp. 691–697, 2009.

[30] D. H. Yaaton, "Mineral composition of the average shale," *Clay Minerals Bulletin*, vol. 5, no. 27, pp. 31–36, 1962.

[31] J. W. De Leeuw and C. Largeau, "A review of macromolecular organic compounds that comprise living organisms and their role in kerogen, coal, and petroleum formation," in *Organic Geochemistry*, M. H. Engel and S. A. Macko, Eds., vol. 11 of Topics in Geobiology, pp. 23–72, Springer, Boston, MA, 1993.

[32] A. C. Hutton, A. J. Kantsler, A. C. Cook, and D. M. McKirdy, "Organic matter in oil shales," *The APPEA Journal*, vol. 20, no. 1, pp. 44–67, 1980.

[33] M. H. Bhuiyan, M. I. Kolstø, and R. M. Holt, "Effects of stress and strain on wave velocities in compacted sand-kaolinite and kaolinite-smectite," in *73rd EAGE Conference and Exhibition incorporating SPE EUROPEC 2011*, p. 238, European Association of Geoscientists & Engineers, 2011.

[34] E. Fjar, R. M. Holt, A. M. Raaen, and P. Horsrud, *Petroleum Related Rock Mechanics*, Elsevier, 2008.

[35] M. E. Best and T. J. Katsube, "Shale permeability and its significance in hydrocarbon exploration," *The Leading Edge*, vol. 14, no. 3, pp. 165–170, 1995.

[36] A. Salama, M. F. E. Amin, K. Kumar, and S. Sun, "Flow and transport in tight and shale formations: a review," *Geofluids*, vol. 2017, Article ID 4251209, 21 pages, 2017.

[37] J. Cui, Q. Sang, Y. Li, C. Yin, Y. Li, and M. Dong, "Liquid permeability of organic nanopores in shale: calculation and analysis," *Fuel*, vol. 202, pp. 426–434, 2017.

[38] J. F. Gale and J. Holder, "Natural fractures in some US shales and their importance for gas production," *Geological Society, London, Petroleum Geology Conference Series*, vol. 7, no. 1, pp. 1131–1140, 2010.

[39] J. F. Gale, S. E. Laubach, J. E. Olson, P. Eichhubl, and A. Fall, "Natural fractures in shale: a review and new observations," *AAPG Bulletin*, vol. 98, no. 11, pp. 2165–2216, 2014.

[40] M. Mokhtari, B. T. Bui, and A. N. Tutuncu, "Tensile failure of shales: impacts of layering and natural fractures," in *SPE Western North American and Rocky Mountain Joint Meeting*, Society of Petroleum Engineers, 2014.

[41] C. M. Bethke, "Modeling subsurface flow in sedimentary basins," *Geologische Rundschau*, vol. 78, no. 1, pp. 129–154, 1989.

[42] H. van Olphen, *Clay Colloid Chemistry*, John Wiley & Sons Inc, New York City, 2nd edition, 1977.

[43] P. C. Kariuki, T. Woldai, and F. Van Der Meer, "Effectiveness of spectroscopy in identification of swelling indicator clay minerals," *International Journal of Remote Sensing*, vol. 25, no. 2, pp. 455–469, 2004.

[44] H. H. Murray, "Traditional and new applications for kaolin, smectite, and palygorskite: a general overview," *Applied Clay Science*, vol. 17, no. 5-6, pp. 207–221, 2000.

[45] K. H. Head, *Manual of Soil Laboratory Testing*, Pentech Press, London, 1992.

[46] J. H. Park, H. J. Shin, M. H. Kim et al., "Application of montmorillonite in bentonite as a pharmaceutical excipient in drug delivery systems," *Journal of Pharmaceutical Investigation*, vol. 46, no. 4, pp. 363–375, 2016.

[47] H. Singh, "A critical review of water uptake by shales," *Journal of Natural Gas Science and Engineering*, vol. 34, pp. 751–766, 2016.

[48] E. J. Hensen and B. Smit, "Why clays swell," *The Journal of Physical Chemistry B*, vol. 106, no. 49, pp. 12664–12667, 2002.

[49] F. T. Madsen and M. Müller-Vonmoos, "The swelling behaviour of clays," *Applied Clay Science*, vol. 4, no. 2, pp. 143–156, 1989.

[50] H. Santos and S. A. B. da Fontoura, "Concepts and misconceptions of mud selection criteria: how to minimize borehole stability problems?," in *SPE Annual Technical Conference and Exhibition*, Society of Petroleum Engineers, 1997.

[51] H. Santos, S. A. B. da Fontoura, A. Gupta, and J. C. Roegiers, "Laboratory tests for wellbore stability in deepwater, Brazil," in *Latin American and Caribbean Petroleum Engineering Conference*, Society of Petroleum Engineers, 1997.

[52] M. E. Chenevert, "Shale alteration by water adsorption," *Journal of Petroleum Technology*, vol. 22, no. 9, pp. 1141–1148, 1970.

[53] A. I. Al-Mhaidib and M. A. Al-Shamrani, "Influence of swell on shear strength of expansive soils," in *Advances in Unsaturated Soil, Seepage, and Environmental Geotechnics*, pp. 160–165, Melbourne, Australia, 2006.

[54] A. A. Sabtan, "Geotechnical properties of expansive clay shale in Tabuk, Saudi Arabia," *Journal of Asian Earth Sciences*, vol. 25, no. 5, pp. 747–757, 2005.

[55] I. C. Gomez-Gutierrez, L. S. Bryson, and T. C. Hopkins, "Correlations between geotechnical properties and the swell behavior of compacted shales," in *Geo-Frontiers 2011: Advances in Geotechnical Engineering*, pp. 4119–4128, Dallas, Texas, United States, 2011.

[56] L. S. Bryson, I. C. Gomez-Gutierrez, and T. C. Hopkins, "Development of a new durability index for compacted shale," *Engineering Geology*, vol. 139-140, pp. 66–75, 2012.

[57] M. A. Al-Shamrani and A. W. Dhowian, "Experimental study of lateral restraint effects on the potential heave of expansive soils," *Engineering Geology*, vol. 69, no. 1-2, pp. 63–81, 2003.

[58] Q. Lyu, P. G. Ranjith, X. Long, Y. Kang, and M. Huang, "A review of shale swelling by water adsorption," *Journal of Natural Gas Science and Engineering*, vol. 27, pp. 1421–1431, 2015.

[59] Z. W. Wang, S. L. Huang, and R. C. Speck, "Swelling behavior of shales in cold regions," *Journal of Cold Regions Engineering*, vol. 8, no. 1, pp. 21–34, 1994.

[60] S. L. Huang, R. C. Speck, and Z. Wang, "The temperature effect on swelling of shales under cyclic wetting and drying," *Pergamon*, vol. 32, no. 3, pp. 227–236, 1995.

[61] Z. Li, Y. Duan, Y. Peng, M. Wei, and R. Wang, "A laboratory study of microcracks variations in shale induced by temperature change," *Fuel*, vol. 280, article 118636, 2020.

[62] P. Fakcharoenphol, S. Charoenwongsa, H. Kazemi, and Y. S. Wu, "The effect of water-induced stress to enhance hydrocarbon recovery in shale reservoirs," *SPE Journal*, vol. 18, no. 5, pp. 897–909, 2013.

[63] P. A. Siratovich, I. Sass, S. Homuth, and A. Bjornsson, "Thermal stimulation of geothermal reservoirs and laboratory investigation of thermally-induced fractures," *GRC Transactions*, vol. 35, pp. 1529–1535, 2011.

[64] C. L. G. Amorim, R. T. Lopes, R. C. Barroso et al., "Effect of clay-water interactions on clay swelling by X-ray diffraction," *Nuclear Instruments and Methods in Physics Research Section A: Accelerators, Spectrometers, Detectors and Associated Equipment*, vol. 580, no. 1, pp. 768–770, 2007.

[65] O. F. Joel, U. J. Durueke, and C. U. Nwokoye, "Effect of KCL on rheological properties of shale contaminated water-based MUD (WBM)," *Global Journals Inc.(USA)*, vol. 12, no. 1, 2012.

[66] S. Morsy and J. J. Sheng, "Imbibition characteristics of the Barnett shale formation," in *SPE Unconventional Resources Conference*, Society of Petroleum Engineers, 2014.

[67] F. Liang, J. Zhang, H. H. Liu, and K. M. Bartko, "Multiscale experimental studies on interactions between aqueous-based fracturing fluids and tight organic-rich carbonate source rocks," in *SPE Kingdom of Saudi Arabia Annual Technical Symposium and Exhibition*, Society of Petroleum Engineers, 2018.

[68] K. Makhanov, H. Dehghanpour, and E. Kuru, "An experimental study of spontaneous imbibition in Horn river shales," in *SPE Canadian unconventional resources conference*, Society of Petroleum Engineers, 2012.

[69] S. S. Morsy, J. J. Sheng, and M. Y. Soliman, "Improving hydraulic fracturing of shale formations by acidizing," in *SPE Eastern Regional Meeting*, Society of Petroleum Engineers, 2013.

[70] S. Morsy and J. J. Sheng, "Effect of water salinity on shale reservoir productivity," *Advances in Petroleum Exploration and Development*, vol. 8, no. 1, pp. 9–14, 2014.

[71] S. Morsy, A. Gomaa, and J. J. Sheng, "Imbibition characteristics of Marcellus shale formation," in *SPE Improved Oil Recovery Symposium*, Society of Petroleum Engineers, 2014.

[72] S. Morsy, A. Gomaa, and J. J. Sheng, "Improvement of eagle ford shale formations water imbibition by mineral dissolution and wettability alteration," in *SPE Unconventional Resources Conference*, Society of Petroleum Engineers, 2014.

[73] S. Morsy, J. J. Sheng, A. M. Gomaa, and M. Y. Soliman, "Potential of improved waterflooding in acid-hydraulically-fractured shale formations," in *SPE Annual Technical Conference and Exhibition*, Society of Petroleum Engineers, 2013.

[74] L. L. Wang, G. Q. Zhang, S. Hallais, A. Tanguy, and D. S. Yang, "Swelling of shales: a multiscale experimental investigation," *Energy & Fuels*, vol. 31, no. 10, pp. 10442–10451, 2017.

[75] Z. Zhou, H. Abass, X. Li, and T. Teklu, "Experimental investigation of the effect of imbibition on shale permeability during hydraulic fracturing," *Journal of Natural Gas Science and Engineering*, vol. 29, pp. 413–430, 2016.

[76] Q. I. A. N. Bin, Z. H. U. Juhui, Y. A. N. G. Hai et al., "Experiments on shale reservoirs plugs hydration," *Petroleum Exploration and Development*, vol. 44, no. 4, pp. 652–658, 2017.

[77] S. Zhang and J. J. Sheng, "Effects of salinity and confining pressure on hydration-induced fracture propagation and permeability of Mancos shale," *Rock Mechanics and Rock Engineering*, vol. 50, no. 11, pp. 2955–2972, 2017.

[78] S. Zhang and J. J. Sheng, "Effect of water imbibition on fracture generation in Mancos shale under isotropic and anisotropic stress conditions," *Journal of Geotechnical and Geoenvironmental Engineering*, vol. 144, no. 2, 2018.

[79] S. Zhang, J. J. Sheng, and Z. Shen, "Effect of hydration on fractures and permeabilities in Mancos, Eagleford, Barnette and Marcellus shale cores under compressive stress conditions," *Journal of Petroleum Science and Engineering*, vol. 156, pp. 917–926, 2017.

[80] Z. Liu, J. Shao, W. Xu, and Y. Meng, "Prediction of rock burst classification using the technique of cloud models with attribution weight," *Natural Hazards*, vol. 68, no. 2, pp. 549–568, 2013.

[81] S. P. Singh, "Burst energy release index," *Rock Mechanics and Rock Engineering*, vol. 21, no. 2, pp. 149–155, 1988.

[82] J. Zhou, X. Li, and H. S. Mitri, "Evaluation method of rockburst: state-of-the-art literature review," *Tunnelling and Underground Space Technology*, vol. 81, pp. 632–659, 2018.

[83] R. T. Ewy and R. J. Stankovic, "Shale swelling, osmosis, and acoustic changes measured under simulated downhole condition," *SPE Drilling & Completion*, vol. 25, no. 2, pp. 177–186, 2010.

[84] Y. Wang, X. Liu, L. Liang, and J. Xiong, "Experimental study on the damage of organic-rich shale during water-shale interaction," *Journal of Natural Gas Science and Engineering*, vol. 74, article 103103, 2020.

[85] A. Ougier-Simonin, F. Renard, C. Boehm, and S. Vidal-Gilbert, "Microfracturing and microporosity in shales," *Earth-Science Reviews*, vol. 162, pp. 198–226, 2016.

[86] Q. Lei, J. P. Latham, J. Xiang, and C. F. Tsang, "Role of natural fractures in damage evolution around tunnel excavation in fractured rocks," *Engineering Geology*, vol. 231, pp. 100–113, 2017.

[87] W. Wang, J. E. Olson, M. Prodanović, and R. A. Schultz, "Interaction between cemented natural fractures and hydraulic fractures assessed by experiments and numerical simulations," *Journal of Petroleum Science and Engineering*, vol. 167, pp. 506–516, 2018.

[88] Z. Moradian, A. Seiphoori, and B. Evans, "The role of bedding planes on fracture behavior and acoustic emission response of shale under unconfined compression," in *51st US Rock Mechanics/Geomechanics Symposium*, American Rock Mechanics Association, 2017.

[89] E. Ghanbari and H. Dehghanpour, "Impact of rock fabric on water imbibition and salt diffusion in gas shales," *International Journal of Coal Geology*, vol. 138, pp. 55–67, 2015.

[90] M. F. Romero-Sarmiento, J. N. Rouzaud, S. Bernard, D. Deldicque, M. Thomas, and R. Littke, "Evolution of Barnett shale organic carbon structure and nanostructure with increasing maturation," *Organic Geochemistry*, vol. 71, pp. 7–16, 2014.

[91] H. Xue, S. Zhou, Y. Jiang, F. Zhang, Z. Dong, and W. Guo, "Effects of hydration on the microstructure and physical properties of shale," *Petroleum Exploration and Development*, vol. 45, no. 6, pp. 1146–1153, 2018.

[92] H. Li, B. Lai, H. H. Liu, J. Zhang, and D. Georgi, "Experimental investigation on Brazilian tensile strength of organic-rich gas shale," *SPE Journal*, vol. 22, no. 1, pp. 148–161, 2017.

[93] L. Yang, H. Ge, Y. Shen et al., "Imbibition inducing tensile fractures and its influence on in-situ stress analyses: a case study of shale gas drilling," *Journal of Natural Gas Science and Engineering*, vol. 26, pp. 927–939, 2015.

[94] J. Du, L. Hu, J. N. Meegoda, and G. Zhang, "Shale softening: observations, phenomenological behavior, and mechanisms," *Applied Clay Science*, vol. 161, pp. 290–300, 2018.

[95] O. M. Akrad, J. L. Miskimins, and M. Prasad, "The effects of fracturing fluids on shale rock mechanical properties and proppant embedment," in *SPE Annual Technical Conference and Exhibition. Society of Petroleum Engineers*, OnePetro, Denver, Colorado, USA, 2011.

[96] Z. Yang, L. Wang, G. Zhang, and C. Ho, "Micromechanical characterization of fluid-shale interactions via nanoindentation," in *SPE Asia Pacific Hydraulic Fracturing Conference*, Society of Petroleum Engineers, 2016.

[97] J. Pedlow and M. Sharma, "Changes in shale fracture conductivity due to interactions with water-based fluids," in *SPE Hydraulic Fracturing Technology Conference*, Society of Petroleum Engineers, 2014.

[98] T. A. Jansen, D. Zhu, and A. D. Hill, "The effect of rock mechanical properties on fracture conductivity for shale formations," in *SPE Hydraulic Fracturing Technology Conference*, OnePetro, 2015.

[99] B. K. Atkinson, *Fracture Mechanics of Rock*, Elsevier, 2015.

[100] B. K. Atkinson, "A fracture mechanics study of subcritical tensile cracking of quartz in wet environments," *Pure and Applied Geophysics*, vol. 117, no. 5, pp. 1011–1024, 1979.

[101] B. K. Atkinson and P. G. Meredith, "Stress corrosion cracking of quartz: a note on the influence of chemical environment," *Tectonophysics*, vol. 77, no. 1-2, pp. T1–T11, 1981.

[102] R. J. Martin, "Time-dependent crack growth in quartz and its application to the creep of rocks," *Journal of Geophysical Research*, vol. 77, no. 8, pp. 1406–1419, 1972.

[103] C. H. Scholz, "Static fatigue of quartz," *Journal of Geophysical Research*, vol. 77, no. 11, pp. 2104–2114, 1972.

[104] M. V. Swain, J. S. Williams, B. R. Lawn, and J. J. H. Beek, "A comparative study of the fracture of various silica

modifications using the Hertzian test," *Journal of Materials Science*, vol. 8, no. 8, pp. 1153–1164, 1973.

[105] Y. Nara, K. Morimoto, N. Hiroyoshi, T. Yoneda, K. Kaneko, and P. M. Benson, "Influence of relative humidity on fracture toughness of rock: implications for subcritical crack growth," *International Journal of Solids and Structures*, vol. 49, no. 18, pp. 2471–2481, 2012.

[106] L. Ji and T. Geehan, "Shale failure around hydraulic fractures in water fracturing of shale gas," in *SPE Unconventional Resources Conference Canada*, Society of Petroleum Engineers, 2013.

[107] R. P. Steiger, "Fundamentals and use of potassium/polymer drilling fluids to minimize drilling and completion problems associated with hydratable clays," *Journal of Petroleum Technology*, vol. 34, no. 8, pp. 1661–1670, 1982.

[108] M. Xu, A. Gupta, and H. Dehghanpour, "How significant are strain and stress induced by water imbibition in dry gas shales?," *Journal of Petroleum Science and Engineering*, vol. 176, pp. 428–443, 2019.

[109] R. Nuesch, F. T. Madsen, and W. Steiner, "Long time swelling of anhydritic rocks: mineralogical and microstructural evaluation," in *8th ISRM Congress*, International Society for Rock Mechanics and Rock Engineering, 1995.

[110] K. Makhanov, A. Habibi, H. Dehghanpour, and E. Kuru, "Liquid uptake of gas shales: a workflow to estimate water loss during shut-in periods after fracturing operations," *Journal of Unconventional Oil and Gas Resources*, vol. 7, pp. 22–32, 2014.

[111] X. Weng, V. Sesetty, and O. Kresse, "Investigation of shear-induced permeability in unconventional reservoirs," in *49th US Rock Mechanics/Geomechanics Symposium*, American Rock Mechanics Association, 2015.

[112] T. Zhou, S. Zhang, L. Yang, X. Ma, Y. Zou, and H. Lin, "Experimental investigation on fracture surface strength softening induced by fracturing fluid imbibition and its impacts on flow conductivity in shale reservoirs," *Journal of Natural Gas Science and Engineering*, vol. 36, pp. 893–905, 2016.

[113] R. Feng, S. Chen, S. Bryant, and J. Liu, "Stress-dependent permeability measurement techniques for unconventional gas reservoirs: review, evaluation, and application," *Fuel*, vol. 256, article 115987, 2019.

[114] B. Yuan, Y. Wang, and Z. Shunpeng, "Effect of slick water on permeability of shale gas reservoirs," *Journal of Energy Resources Technology*, vol. 140, no. 11, 2018.

[115] J. Behnsen and D. R. Faulkner, "Water and argon permeability of phyllosilicate powders under medium to high pressure," *Earth*, vol. 116, no. B12, 2011.

[116] Q. Duan and X. Yang, "Experimental studies on gas and water permeability of fault rocks from the rupture of the 2008 Wenchuan earthquake, China," *Science China Earth Sciences*, vol. 57, no. 11, pp. 2825–2834, 2014.

[117] A. A. Moghadam and R. Chalaturnyk, "Laboratory investigation of shale permeability," in *SPE/CSUR Unconventional Resources Conference*, Society of Petroleum Engineers, 2015.

[118] K. K. Mohan, H. S. Fogler, R. N. Vaidya, and M. G. Reed, "Water sensitivity of sandstones containing swelling and non-swelling clays," in *Colloids in the Aquatic Environment*, pp. 237–254, Elsevier, 1993.

[119] J. A. Bergendahl and D. Grasso, "Mechanistic basis for particle detachment from granular media," *Environmental Science & Technology*, vol. 37, no. 10, pp. 2317–2322, 2003.

[120] J. Bergendahl and D. Grasso, "Prediction of colloid detachment in a model porous media: thermodynamics," *AICHE Journal*, vol. 45, no. 3, pp. 475–484, 1999.

[121] H. H. Murray, "Chapter 2 structure and composition of the clay minerals and their physical and chemical properties," in *Developments in Clay Science*, H. H. Murray, Ed., vol. 2, pp. 7–31, Elsevier, 2006.

[122] H. Roshan, M. A. Q. Siddiqui, K. Regenauer-Lieb, A. Lv, A. Hedayat, and M. Serati, "Digital multiphysics interferometry: a new approach to study chemo-thermo-hydro-mechanical interactions in geomaterials," in *52nd US Rock Mechanics/Geomechanics Symposium*, American Rock Mechanics Association, 2018.

[123] Y. Zhuang, X. Liu, H. Xiong, and L. Liang, "Microscopic mechanism of clay minerals on reservoir damage during steam injection in unconsolidated sandstone," *Energy & Fuels*, vol. 32, no. 4, pp. 4671–4681, 2018.

[124] H. Dehghanpour, H. A. Zubair, A. Chhabra, and A. Ullah, "Liquid intake of organic shales," *Energy & Fuels*, vol. 26, no. 9, pp. 5750–5758, 2012.

[125] T. Engelder, L. M. Cathles, and L. T. Bryndzia, "The fate of residual treatment water in gas shale," *Journal of Unconventional Oil and Gas Resources*, vol. 7, pp. 33–48, 2014.

[126] P. Fakcharoenphol, B. Kurtoglu, H. Kazemi, S. Charoenwongsa, and Y. S. Wu, "The effect of osmotic pressure on improve oil recovery from fractured shale formations," in *SPE Unconventional Resources Conference*, Texas, USA, 2014.

[127] H. Roshan, A. Z. Al-Yaseri, M. Sarmadivaleh, and S. Iglauer, "On wettability of shale rocks," *Journal of Colloid and Interface Science*, vol. 475, pp. 104–111, 2016.

[128] H. Roshan, M. S. Andersen, H. Rutlidge, C. E. Marjo, and R. I. Acworth, "Investigation of the kinetics of water uptake into partially saturated shales," *Water Resources Research*, vol. 52, no. 4, pp. 2420–2438, 2016.

Hindawi
Geofluids
Volume 2022, Article ID 1549003, 18 pages
https://doi.org/10.1155/2022/1549003

Research Article

Nanoconfined Gas Flow Behavior in Organic Shale: Wettability Effect

Shan Wu,[1] **Xiaorui Wang**,[2] **Ying Yu**,[3] **Yao Yu**,[3] **Liang Zhang**,[4] **and Ran Mao**[5]

[1]*School of Chemical Engineering and Technology, China University of Mining and Technology, Xuzhou 221116, China*
[2]*Longdong Shale Oil Development Project Department, Changqing Oilfield Company, CNPC Qingyang, Gansu 745100, China*
[3]*No.7 Oil Production Plant of PetroChina Changqing Oilfield Branch, Gansu 745100, China*
[4]*Huabei Oil Communication Co. Ltd., Renqiu, Hebei 062552, China*
[5]*The Fourth Oil Extraction Plant of Petrochina Huabei Oilfield Company, Langfang, Hebei 065000, China*

Correspondence should be addressed to Shan Wu; wushan_cumt@163.com

Received 24 March 2022; Revised 4 May 2022; Accepted 11 May 2022; Published 27 May 2022

Academic Editor: Keliu Wu

A clear understanding of nanoconfined gas flow behavior in shale gas reservoirs is beneficial for its efficient development. Nanopores in the shale gas reservoirs are characterized by complex surface chemistry and composition, as well as affinity, while their impact on methane flow has not been investigated comprehensively before. In light of current research status, this article proposes a simple yet robust theoretical model, incorporating bulk-gas flow flux and surface diffusion of adsorption gas. In particular, wettability effect, indicating the influences of the shifted critical properties and adsorption thickness, is captured as well. In this article, gas physical attributes, such as gas compressibility factor and gas viscosity, are modified under the nanoconfinement effect and wettability effect, and also the variation of effective pore size, induced by surface wettability, is considered. Notably, wettability effect in this article is described by using a macroscopic form, surface contact angle, facilitating the model applicability. In addition, both the bulk-gas flow model and surface-diffusion model, developed in this research, are able to achieve excellent agreements compared with the existed documents, clarifying the reliability of the proposed model. Meanwhile, key role of wettability effect on nanoconfined gas flow behavior, especially for surface diffusion of adsorption gas, is demonstrated. Results show that (a) the gas flux in small nanopores may exceed that in large nanopores, due to the predominant role of surface diffusion, while pore size is less than 10 nm; (b) the absence of real gas effect will lead to inaccurate characterization of nanoconfined gas flow capacity, and the magnitude can reach 7% for pore size of 5 nm and will enlarge with further pore size shrinkage; (c) wettability effect governs the total gas flux when pore size is less than 10 nm, while its impact will be greatly mitigated when pore size is greater than 50 nm. This article provides a comprehensive investigation to shed light on surface wettability on gas flow behavior through nanopores.

1. Introduction

It is always an urgent issue to ensure the energy supply around the world, providing the basic guarantee for the development of human beings [1, 2]. Up to date, with the rapid depletion of conventional fossil energy, encompassing oil reservoirs, coal, and natural gas, some brilliant ideas are raised up to meet the increasing energy need, such as the wind energy, solar energy, and unconventional oil/gas energy [3–5]. Notably, although the unconventional oil/gas energy belongs to fossil energy, its geological reserve is dozens greater than regular oil/gas reservoirs [6–8], presenting the favorable potential to become the alternative energy in the years to come. In this research, emphasis is put on shale gas reservoirs, a member of unconventional gas reservoirs, which are characterized by diversity of nanopores, ultralow permeability, and huge reserves. Due to its ultralow permeability, generally spanning from several to hundreds of nano-Darcy [9–11], the economic development of shale gas reservoirs was extremely challenging for a relatively long period. And, thanks to the invention of multistage hydraulic fracturing technology, a couple of high-conductivity

artificial fractures can be constructed in shale reservoirs [12, 13], dramatically advancing the gas flow capacity in the target formation. After that, the successful development of shale gas reservoirs has achieved. However, according to the typical production performance for shale gas wells, the gas production rate undergoes rapid decline at the initial production stage and then keeps stable at the middle and late stage [14–16]. From the acknowledged theory, regarding the production data analysis, the gas production rate at early stage depends on the fracture conductivity, while it heavily depends on reservoir inherent permeability at middle or late stage. Also, it should be noted that the period of middle and late production stage is far longer than the early stage. As a result, in order to have a clear image of production behavior at middle or late stage, one is supposed to have a clear knowledge of essential flow capacity in shale. However, because of the complexity exerted by nanoscale molecular interactions, the gas flow behavior in shale nanopores still remains vague. Other than that, the surface properties of nanopores [17–19], including composition, affinity, and structure, may affect microscopic interactions, further aggravating the complexity. Accordingly, precise characterization of nanoconfined gas flow behavior is helpful to explain gas production performance at middle or late production, and the motivation of this article is to address this issue.

Apart from the natural fractures, shale rock can be regarded as the nanoscale porous media. Moreover, shale matrix possesses the dual-wettability feature [20–22], including organic matter, presenting a strong attraction force on gas molecules, and the inorganic matter, presenting a strong attraction force on water molecules. It is the dual-wettability property that the gas-water distribution mode [23, 24] in shale becomes complex, as well as interesting. In the primary state, as for the organic matter in shale, due to the repulsive force exerted by organic-pore surface, the existence of water molecules in organic nanopores is hard. In addition, strength of the repulsive force will increase with the increasing thermal maturity. Notably, there exist two gas phase storage modes, including the adsorption gas, with thickness of a molecular diameter, and bulk-like gas. Also, a great deal of efforts has been devoted to investigating gas adsorption behavior [25–27], demonstrating that the adsorption phase density can be 2~5 times that of bulk-gas density. Actually, the bulk-like gas phase in the nanoscale organic nanopores is different with bulk gas, as its behavior is influenced by the interactions induced by pore surface, while the bulk gas is free of surface interactions. As a result, with the intention of capturing gas flow behavior through organic nanopores, one must shed light on the adsorption gas flow mechanism and bulk-like gas flow mechanism simultaneously. As for the inorganic nanopores, the surface mineral composition [28–30], such as quartz, feldspar, and chlorite, has strong affinity towards water molecules; therefore a thin water film takes place, with the thickness of several nanometers. The stabilization of water film in inorganic nanopores is heavily dependent on environmental humidity, pressure, and temperature, and its accurate characterization is crucial for reserve estimation and production prediction. As the adsorption positions are occupied by water molecules in inorganic nanopores, there exists only the bulk-gas phase. From the aforementioned context, it can be inferred that the gas flow behavior in organic nanopores shows dramatic difference compared with that in inorganic nanopores; both cannot be described by regular formulas for bulk gas. In this article, we focus on gas flow behavior inside organic nanopores, consisting of bulk-like gas and adsorption gas. Nanoconfined gas flow capacity has been studied by the previous excellent contributions; the Knudsen number [31–34], defined as the ratio of mean free path to pore size, is utilized to quantify the nanoconfinement impact. When Knudsen number falls below 0.001, gas flow behavior can be characterized by the classic no-slip NS (Navier-Stokes) equation [35, 36], as the flow mechanism is continuum flow. And, the flow mechanism becomes slip flow, in which the molecules at the boundary gain mobility, when Knudsen number ranges from 0.001 to 0.1. Notably, the slip flow can also be properly described by NS equation by modifying the boundary conditions, and the parabolic relationship, in terms of the gas velocity streamline, remains valid. Applicability of the NS equation breaks down when the Knudsen number is far beyond 0.1, corresponding to the transition flow and free molecular flow. In order to cover the entire range of Knudsen number, efforts have been performed, and a series of theoretical models have been proposed. Additionally, in terms of flow mechanism of adsorption gas, the surface diffusion, a special mechanism apparently different from the above bulk-gas flow mechanisms, is considered as a suitable approach to explain the adsorption gas flow behavior. Based on the surface diffusion theory, the mobility of adsorption gas is mainly driven by concentration gradient, regarding the adsorption gas content. In light of this point, some models are proposed to describe nanoconfined gas flow in organic matter, coupling bulk-like gas flow mechanism and surface diffusion of adsorption gas. However, it remains in serious debate on the way to couple the above different flow mechanisms, and also the existence of surface diffusion in shale gas reservoirs is still questionable. Hence, the accurate characterization of gas flow capacity through organic nanopores is still challenging. Furthermore, considering the predominant role of organic matter on shale gas production performance, properly solving this issue is fairly urgent.

Multiple approaches, including molecular dynamics (MD), numerical methods (such as LBM and PNM), and theoretical models, have been applied to shed light on nanoconfined methane flow behavior. As for the MD method [37, 38], its applicability is heavily dependent on powerful computational performance, and its simulation duration is generally limited to several nanoseconds. As a result, although the MD method is well-acknowledged as the precise characterization regarding microscopic fluid behavior, it remains hard to be a frequently utilized method, due to its high expense and complex construction process of molecular systems. Using molecular dynamics, Zhang et al. investigated the impact of nanopore geometry [39], including the cylindrical and conical nanopores, on gas transport through inorganic nanopores. With the help of MD method, Sun et al. [40] constructed shale organic nanopores by utilizing kerogen molecules and studied methane flow capacity in the

constructed nanopores [41]. Yu et al. performed in-depth analysis upon gas flow characteristics by the use of MD [42], and a unified analytical model was proposed for organic and inorganic nanopores. After that, Yu et al. (2020) continued their research, and shed light on the roughness impact on nanoconfined gas flow. Wang et al. (2021) provided a comprehensive review on gas adsorption/diffusion in shale nanopores [43], highlighting the necessity of MD simulation in this research domain. In addition to MD method, LBM is a kind of numerical methods, suitable for microscopic fluid characterization. Notably, the reliability of LBM method roots in the continuum hypothesis, leading to its inherent deficiency that LBM fails to reproduce flow behavior once the Knudsen number is beyond 10 [44–46]. Zhao et al. utilized LBM method to simulate shale gas production performance, considering gas adsorption impact [47]. Due to the excellent computational efficiency, LBM method was also widely used to reveal nanoconfined water flow and nanoconfined gas-water two-phase flow. Particularly, the LBM method can serve as the promising upscaling method to link pore-scale fluid flow mechanism and that in porous media. Moreover, Huang et al. studied methane phase behavior in nanopores [48], accounting for the surface-molecule interactions as well as gas adsorption, elaborating the vapor-liquid coexistence feature. It should be highlighted that the MD and LBM method are regarded as the approaches for pore-scale fluid modeling methods, regardless of the upscaling aspect of LBM method. As a result, there exists an evident knowledge gap to characterize fluid flow in porous media. In order to address this issue properly, PNM, pore network modeling, is raised up, coupling the pore connectivity and overall conductivity [49–51]. Evidently, PNM cannot be utilized to investigate the pore-scale fluid flow behavior. Javadpour et al. reviewed gas flow models upon shale gas reservoirs, presenting the robustness of PNM describing gas flow capacity through nanoscale porous media [52]. Song et al. firstly constructed multiscale PNM in accordance with low-resolution and high-resolution SEM images, and then macroscopic parameter, permeability, was predicted by using PNM and compared with laboratory experimental results [53]. Yi et al. focused on the extraction of pore network [54], regarding shale gas samples. In particular, pore size and throat length in Yi's PNM can alter with pressure, different with existed contributions. In addition to the aforementioned methods, the theoretical model, possessing the analytical formulas and clear applicability preconditions, is also a robust approach to explore nanoconfined gas flow. Comparing with MD, LBM, or laboratory experiments, the advantage of theoretical model is free of numerical simulation complexity and measurement errors caused by apparatus. Also, formulas in the established theoretical model have clear physical meanings, facilitating the understanding of the model and subsequent modifications [55–57]. As mentioned in the above text, the shale rock, composed of organic matter and inorganic matter, is a typical dual-wettability porous media. To the current knowledge, the theoretical models have paid little attention to wettability effect on nanoconfined gas flow. Javadpour et al. revealed the existence of nanopores in shale and proposed a theoretical model [58], combining the continuum flow and Knudsen flow, to characterize gas flow capacity in nanopores. Then, with the development success of shale gas/oil reservoirs, the theoretical investigations, in terms of fluid behavior in nanopores, become heat. The investigations can be roughly divided into two categories, the first one is modifying the boundary conditions for the slip flow [59, 60] and the other one is weight superposition of several gas flow mechanisms [61, 62]. To sum, the wettability effect has not received due attention at this point, while its impact cannot be neglected particularly at nanoscale. Hence, there is an evident knowledge gap to figure out shale gas transport behavior under wettability effect. In this article, a robust theoretical model, putting emphasis on wettability effect, is proposed, expecting to shed light on surface wettability on gas flow in organic nanopores.

The whole paper content is arranged based on the following way. At first, the physical model, presenting the organic nanopore in shale, is introduced, highlighting the wettability effect on adsorption phase and flow behavior. Then, formulas, capturing the wettability effect on shifted critical properties, the adsorption phase thickness, and the methane viscosity, are provided. Then, the formulas, describing nanoconfined flow behavior, are modified by coupling the wettability effect. As a result, the model for gas transport through the organic nanopore, considering wettability effect, is developed. The clarification upon the reliability of the proposed model is presented in Section 4. After that, concrete gas flow behavior is investigated and discussed in Section 5. Finally, several conclusions are drawn.

2. Physical Model

In this article, attempts are implemented to reveal the gas flow behavior at nanopore scale, highlighting the impact induced by surface wettability. To the current knowledge that multiple nanoconfined mechanisms have been properly addressed, the consideration of surface wettability distinguishes this research from previous contributions. Therefore, the underlying reason, for surface wettability altering gas flow capacity, is the key issue in this work. At first, the physical meaning or process, demonstrating the wettability impact, needs to be clarified. At bulk condition, in compliance with the classic theory for phase variation, the gas behavior is mainly governed by intermolecular interactions, indicating the collisions between massive gas molecules. Notably, collision between fluid molecules and surface takes place inevitably, which however can be neglected at bulk condition. Related equations of state [63–65], such as PR-EOS and RK-EOS, root in the intermolecular interactions and can reproduce bulk-fluid phase behavior with high accuracy, claiming the little impact from the surface at bulk condition. With pore size shrinkage, the space volume, available for gas molecules, undergoes reduction. As a result, the quantity, suggesting the frequency of intermolecular collisions, declines rapidly. In the meanwhile, there still exist the molecule-surface interactions, keeping nearly unchanged no matter at bulk condition or in the narrow pores. Therefore, on the basis of the above analysis content, the frequent

surface-molecule interactions in narrow pores are expected. Particularly, the surface impact may play the dominant role determining fluid behavior in nanopores. In the other words, when pore size shrinks from several micrometers, denoting the bulk condition, to nanometers, and denoting the shale nanopores in this article, the surface impact, suggesting the interaction force imposed on the gas molecules, cannot be neglected and becomes a predominant role. Thus, the evident difference between the gas behavior in bulk condition and that in the nanoconfined condition is the relative strength of the surface-molecule interactions.

Following the above analysis, it is attractive to put in-depth investigation on key factors, affecting the relative strength of surface-molecule interactions in nanopores. In this article, the surface wettability effect, generally described as the macroscopic contact angle, is the research emphasis. Although dramatic efforts are devoted to studying nanoconfined gas flow behavior, the wettability impact has not been revealed at this point. As depicted in Figure 1, the fluid distribution characteristics under diverse surface wettability are presented. Fluid molecules in nanopores can be categorized as adsorption phase, which is close to surface with a thickness of 1~3 molecular diameters [66, 67], and bulk-like phase away from the surface. As for nanopores with strong affinity, fluid molecules, belonging to adsorption phase, increase a lot, which are highlighted in green in Figure 1(a). From the left side to the right side, the adsorption molecules decline with decreasing surface affinity, as a result of the weak attraction force upon gas molecules. Therefore, the gas flow behavior will be altered due to the wettability impact; from the fluid distribution feature in Figure 1, it is evident that surface diffusion in nanopores with strong affinity will be stronger than that with weak surface affinity. Also, bulk-phase flow capacity will weaken due to the shrinkage of pore size, caused by the occupation of adsorption molecules. Accordingly, wettability effect will make a difference upon nanoconfined gas flow behavior, including both surface diffusion for adsorption molecules and bulk-like gas flow, which however has not received due attention. This article performs attempt to study this issue, focusing on gas flow capacity through organic nanopores considering different surface contact angles.

3. Model Establishment

This article focuses on the wettability effect on gas flow behavior through organic nanopores. Notably, the wettability effect is captured by coupling the shift of critical properties as well as adsorption thickness in the gas transport model. In detail, the shifted critical properties are utilized to evaluate gas viscosity and density, further affecting the bulk-like gas flow behavior. Meanwhile, the adsorption phase thickness is considered while calculating surface diffusion. Following this way, the transport model is modified by considering the wettability effect.

3.1. Wettability Effect on Shifted Critical Properties. The gas critical properties will shrink under nanoconfinement space [68, 69], inherently caused by the strong surface-molecule interaction. Similar with pore size, the surface affinity can also change the strength of surface-molecule interaction, as depicted in Figure 1. As a result, the critical property can be correlated with surface wettability. Feng et al. proposed a simple formula [70], elaborating the relationship between surface contact angle, macroscopic form of surface wettability, and fluid critical properties. Reliability of the formula is verified well, as it can reproduce nanoconfined fluid critical properties and achieve excellent match against experimental data or simulation results. Also, the formula demonstrates that the methane critical property, including critical temperature and pressure, can be described as a function of pore size and surface contact angle. Also, Feng et al. (2021) pointed out that nanopore geometry is also an influential factor upon critical properties, suggesting the decreasing degree of critical properties in the cylindrical nanopores will be severer than that in slit nanopores.

$$\frac{T_{cb} - T_c}{T_{cb}} = \frac{P_{cb} - P_c}{P_{cb}} = \frac{\xi}{m} \times 0.65 \ln\left(\frac{180}{\theta}\right), \tag{1}$$

where T_{cb} and P_{cb} are methane critical temperature and critical pressure at bulk state, respectively; T_c and P_c are nanoconfined critical temperature and critical pressure, respectively; θ denotes the surface contact angle, degree; ξ is a constant, related to nanopore geometry, which is equal to 0.56 for cylindrical nanopores; and m denotes the representative pore size, defined as the ratio of realistic pore radius to methane molecular diameter.

It can be inferred from Equation (1) that methane critical properties are correlated with pore size and surface contact angle at the same time. In addition, in the case of the large m, indicating that the pore size is far beyond methane diameter, the nanoconfined critical properties will approach the bulk value, regardless of the wettability impact. Notably, the wettability effect, in terms of the critical properties, becomes evident once the pore size decreases into nanoscale. As a result, it highlights the urgency to consider the wettability effect when investigating nanoconfined methane behavior. Based on Equation (1), nanoconfined methane critical properties can be calculated over a wide range of pore size and surface contact angle.

3.2. Adsorption Methane Thickness. In this article, we put emphasis on the organic nanopores in shale, inherently possessing the attraction force on methane molecules. Thus, unlike bulk-state methane molecules, freely distributed in space, the adsorption phenomenon, indicating methane molecules adhering on the surface, takes place in nanopores. In this way, the molecules in nanopores are divided into two categories, involving of the adsorption phase and bulk-like phase. The adsorption phase will inevitably occupy the space close to the surface, leading to the decline of effective pore size. Thus, the adsorption phase thickness is the key parameter, requiring to be quantified. In the meantime, there are different transport mechanisms for adsorption phase and bulk-like methane; therefore, the quantification of adsorption thickness contributes to the model establishment for gas transport through organic nanopores.

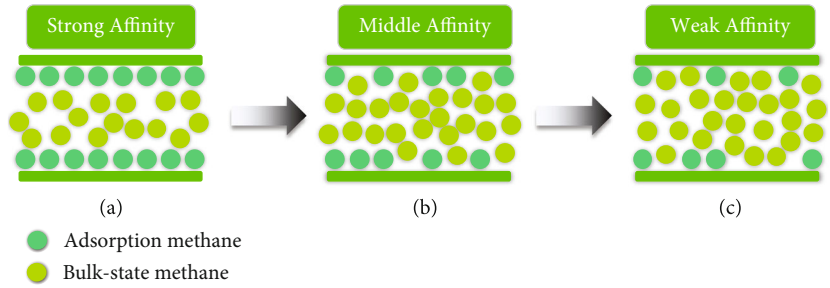

Figure 1: Fluid molecular distribution and flow characteristics: (a) Strong affinity; (b) Middle affinity; (c) Weak affinity.

Zhang et al. developed a robust correlation formula to characterize the adsorption thickness in nanopores [71]; its applicability covers the majority of common fluids, including methane, carbon dioxide, and oil with carbon number ranging from 3 to 10. The formula suggests that the adsorption phase thickness is not only related to the inherent molecular size, but also the pore size. The decrease of pore size will result in strong attraction force, induced by surface, upon molecules, further leading to the climb of adsorption thickness. Concrete correlation formula is given below.

$$h_{ad} = \frac{\chi}{\ln(r/\sigma)} + \delta \cdot \frac{\sigma}{r}, \tag{2}$$

where h_{ad} denotes the adsorption phase thickness, m; χ and δ denote the empirical coefficients for the correlation, dimensionless; r denotes the nanopore radius, m; and σ denotes the molecular diameter, and it equals to 0.38 nm for methane.

$$\chi = -8.314 \times 10^{-14} M^2 + 2.047 \times 10^{-11} M + 3.086 \times 10^{-11}, \tag{3}$$

$$\delta = -6.3565 \times 10^{-14} M^2 + 3.1550 \times 10^{-11} M - 5.8538 \times 10^{-10}, \tag{4}$$

where M is the methane molecular weight per mol, which is 16 g/mol here.

Notably, the formula fails to capture the wettability impact on adsorption thickness. Inferred from Equation (1), the methane phase behavior will be fairly close to the nanoconfined methane once the surface contact angle approaches 180°, indicating that adsorption phenomenon disappears at a super-weak surface affinity condition. In the other words, the adsorption thickness tends to decline with increasing surface contact angle and becomes zero when contact angle reaches 180°. However, the formula for the adsorption thickness at this point cannot reproduce the above scenario, evidently conflict with the Equation (1) and its underlying simulation results, experimental observations. In this regard, we correlate the model, raised by Zhang et al. (2019), with the wettability impact, characterized by surface contact angle.

$$h_{ad} = \left(\frac{\chi}{\ln(r/\sigma)} + \delta \cdot \frac{\sigma}{r}\right) \times \left(1 - \frac{\theta}{180}\right), \tag{5}$$

where θ denotes the surface contact angle, degree.

On the basis of Equation (5), the decline relationship between the surface wettability and adsorption phase thickness can be captured, which keeps in compliance with Equation (1). Therefore, the theoretical background of Equation (5) is more solid than the original Equation (2), suffering the deficiency of not considering the surface wettability impact. Notably, the correlation of wettability on adsorption thickness indeed lacks necessary verification efforts and may produce uncertainty. Also, as mentioned above, consideration of wettability impact in this article is the first attempt to the knowledge, and the developed formula can capture the general variation principle between the surface contact angle and adsorption phenomenon. Thus, although Equation (5) fails to achieve the accurate characterization of adsorption thickness, it has fairly solid scientific basis and is suitable for investigation and discussion at the primary stage. It is important to admit that this technical part may result in error, and some improvements are urgent in the future. Due to the existence of adsorption phase thickness, the effective pore size for bulk-gas flow becomes the primary pore size subtracting the adsorption thickness.

$$r_{eff} = r - h_{ad}. \tag{6}$$

3.3. Bulk-Gas Flow Behavior. Gas flow capacity in the organic nanopore is contributed by two parts, involving of the bulk-gas flow and surface diffusion of adsorption molecules. In terms of the first part, bulk-gas flow behavior is closely related to the Knudsen number, characterizing the frequency of fluid-surface collisions, which is defined as the ratio of mean free path to nanopore radius.

$$Kn = \frac{\lambda}{r_{eff}}, \tag{7}$$

where Kn denotes the Knudsen number, dimensionless and λ denotes the gas free path, nm. Notably, the free path is

heavily dependent on gas viscosity [72, 73], which has the following calculation formula.

$$\lambda = \frac{\mu}{P}\sqrt{\frac{\pi ZRT}{2M}}, \tag{8}$$

where μ denotes the gas viscosity, cp; Z denotes the gas compressibility, dimensionless; R denotes the gas universal constant, which is equal to 8.314 J/mol/K; and P denotes the surrounding pressure, Pa.

The gas viscosity can be described as a function of pressure and temperature, and its change law is well characterized by the following equation [74].

$$\mu = \mu_{atm}\left[1 + \frac{A_1}{T_r^5}\left(\frac{P_r^4}{T_r^{20} + P_r^4}\right) + A_2\left(\frac{P_r}{T_r}\right)^2 + A_3\left(\frac{P_r}{T_r}\right)\right], \tag{9}$$

$$P_r = \frac{P}{P_c}, \tag{10}$$

$$T_r = \frac{T}{T_c}, \tag{11}$$

where λ_{atm} denotes the gas viscosity at the standard condition, suggesting the temperature is 293 K and pressure is 0.1 MPa; P_r and T_r denote the reduced pressure and reduced temperature, respectively; and A_1, A_2, and A_3 are empirical coefficients, which are assigned as 7.9, 9.0×10^{-6}, and 0.28, respectively.

Inferred from Equations (9) ~(11), in terms of the calculation of gas viscosity, the dependence on methane critical properties is demonstrated. The methane critical properties, including Tc and Pc, are altered under the nanoconfinement effect and wettability impact simultaneously, as described in Section 3.1, and the methane viscosity is also affected by wettability effect. Therefore, the critical properties, utilized for the calculation of gas viscosity, are the nanoconfined critical properties in Equation (1), instead of that in bulk state. In this way, the gas viscosity under the wettability impact can be calculated.

Utilizing the simulation tool as well as theoretical analysis, Karniadakis et al. [75] developed a robust formula for gas transport through cylindrical nanopores [75], covering the Knudsen number over 10; however, the wettability impact has not been considered. Thus, the model, proposed by Karniadakis et al. [75], can be regarded as a desirable start point and will become a more powerful investigation approach to explore microscopic gas behavior, by taking care of the wettability impact. Also, on the basis of Wu et al. [76], the Knudsen number for typical shale gas reservoirs ranges from 0.0002 to 6 and, therefore, falls in the application scope of Karniadakis et al. [75] research.

$$J_{\text{bulk}} = \frac{r_{eff}^2 PM}{8\mu RT}(1 + \alpha Kn)\left(1 + \frac{4Kn}{1 - bKn}\right)\frac{dP}{dl}, \tag{12}$$

$$\alpha = \alpha_o \frac{2}{\pi}\tan^{-1}\left(\alpha_1 Kn^{\beta}\right), \tag{13}$$

where J_{bulk} denotes the gas mass flux through the nanopore, kg/m^2/s; b is the empirical coefficient, dependent on the boundary condition, which is assigned as -1 in this article; and α_o, α_1, and β are coefficients for describing gas rarefication impact, which are assigned as 1.19, 4, and 0.4, respectively.

In order to facilitate the evaluation of transport capacity, the conductance, the ratio of gas mass flux to pressure difference, is provided. Notably, in Equation (14), the shrinkage of effective pore size, induced by the adsorption phase thickness, is considered in r_{eff}, and also variation of gas viscosity and Knudsen number manifest the wettability impact.

$$C_{bulk} = \frac{r_{eff}^2 PM}{8\mu RT}(1 + \alpha Kn)\left(1 + \frac{4Kn}{1 - bKn}\right). \tag{14}$$

Meanwhile, real gas effect, denoting that inherent methane molecular volume cannot be overlooked, is coupled in Equation (8). Then, the developed Equation (14) represents the bulk-gas transport conductance in a nanopore. In order to extend its applicability, further work can be devoted to upscaling the pore-scale investigation to nanoscale porous media.

3.4. Surface Diffusion Behavior. Different from the bulk-gas transport behavior, driven by displacement pressure, the mobility of the adsorption molecule is governed by surface diffusion, driven by molecular concentration gradient. At the equilibrium state, the adsorption molecules hop from the adsorption region to the bulk-like region, and the exchange velocity is the same. In the case of a nanopore with a displacement pressure, indicating that the pressure at the inlet is higher than that at the exit, the molecular concentration at the inlet is greater than that at the exit. For the adsorption phase, the concentration gradient takes place, resulting in the adsorption molecules moving from the inlet to the exit. The above physical process is the surface diffusion, on the basis of the analysis, which is closely related to pressure and surface coverage, a key factor representing the ratio of realistic adsorption amount to the maximum value. Wu et al. have established a model for surface diffusion [77], correlating the diffusion capacity with pressure difference, neglecting the capillary pressure between the vapor phase and adsorption phase.

$$J_{\text{surf}} = D_s \frac{C_{sc}}{P}\frac{dP}{dl}, \tag{15}$$

where J_{surf} denotes gas mass flux contributed by surface diffusion, kg/m^2/s; D_s^o is the diffusion coefficient, while gas coverage factor is zero, m^2/s; and C_{sc} denotes the gas concentration, derived from the single-layer adsorption assumption, kg/m^3.

$$C_{sc} = \frac{4\phi M}{\pi\sigma^3 N_A}, \tag{16}$$

Table 1: The basic parameters to reproduce the bulk-like gas flow behavior.

Contributors	Method	Material	Pressure	*Kn* range	Contact angle[#]
Loyalka and Hamoodi [82]	LBM	/	Low pressure	$10^{-3} \sim 10$	30°
Tison [83]	Experiments	Stainless steel tube	0.1 ~ 400 KPa	Entire range	60°

[#]Contact angle information is not available in previous references; its determination relies on the surface material, fluid type, and fitting results comprehensively.

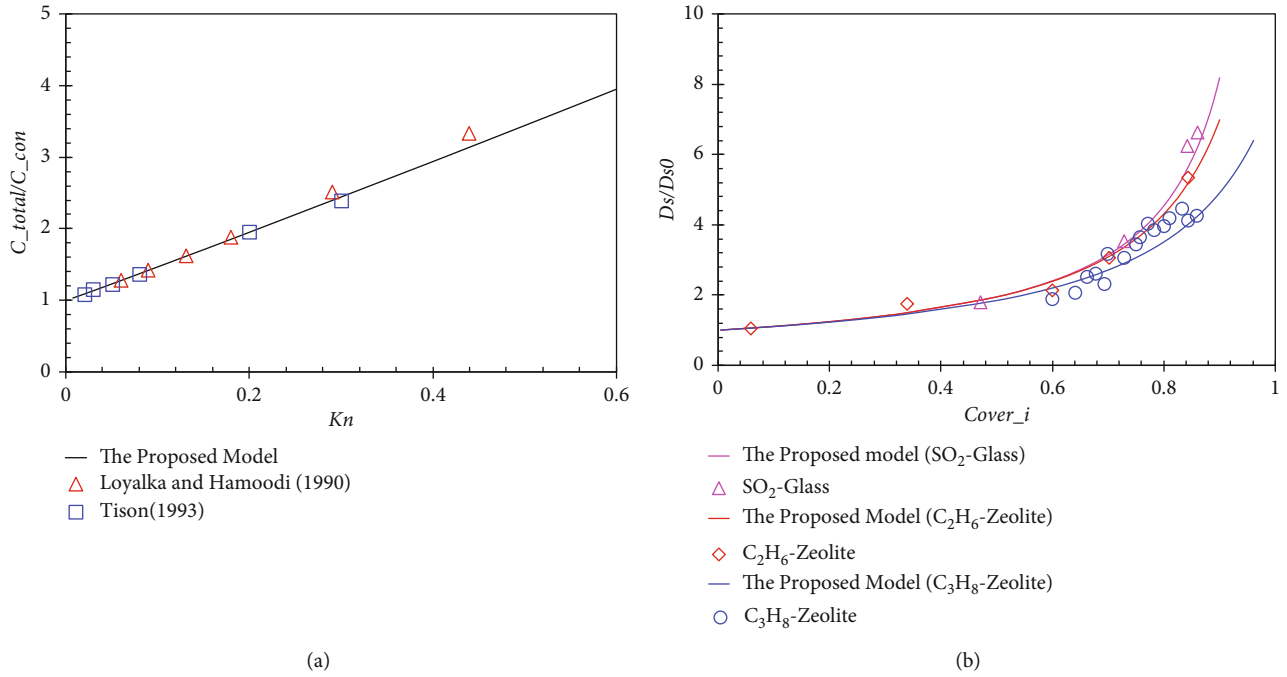

(a) (b)

Figure 2: The verification of the proposed model: (a) the bulk-gas flow model utilizing the ratio of nanoconfined gas conductance and that for no-slip NS equation; (b) the surface diffusion model utilizing the diffusion coefficient ratio.

$$D_s^o = 8.29 \times 10^{-7} T^{0.5} \exp\left(-\frac{\Delta H^{0.8}}{RT}\right), \tag{17}$$

$$D_s = D_s^o \frac{(1-\phi) + (\kappa/2)\phi(2-\phi) + \{H(1-\kappa)\}(1-\kappa)(\kappa/2)\phi^2}{(1-\phi+(\kappa/2)\phi)^2}, \tag{18}$$

$$H(1-\kappa) = 0, \kappa > 1, \tag{19}$$

$$H(1-\kappa) = 1, \kappa \le 1, \tag{20}$$

$$\kappa = \frac{\kappa_b}{\kappa_m}, \tag{21}$$

where D_s denotes the diffusion coefficient under a specified gas coverage, m^2/s; Φ denotes the gas coverage factor, dimensionless; κ_m denotes the molecular potential for forward migration, m/s; and κ_b denotes the molecular potential for blockage, m/s. Notably, the κ is assigned as 0.5, and isosteric adsorption heat at zero coverage ($\triangle H$) is 1.6×10^4 J/mol.

The precondition for the above formulas is the single-layer adsorption assumption [78, 79], suggesting that the surface will be fully occupied with the thickness of a molec-

Table 2: The basic parameters to reproduce the surface diffusion.

Gas type	Surface	κ	Temperature	Contact angle[#]
SO_2 [84]	Glass	0	288 K	12°
C_2H_6 [85]	Zeolite	0.2	323 K	15°
C_3H_8 [86]	Zeolite	0.3	323 K	20°

Contact angle information is not available in previous references; its determination relies on the surface material, fluid type, and fitting results comprehensively.

Table 3: The basic parameters for nanoconfined gas transport investigation.

Parameter	Symbol	Unit	Value
Gas type	CH_4	/	/
Molecular weight	M	g/mol	16
Langmuir pressure	P_L	MPa	2
Ratio for surface diffusion	κ	/	0.5
Adsorption heat when Φ is 0	$\triangle H$	J/mol	16000
Pore size	r	nm	2~100
Contact angle	θ	°	0~180
Pressure	P	MPa	0.1~50

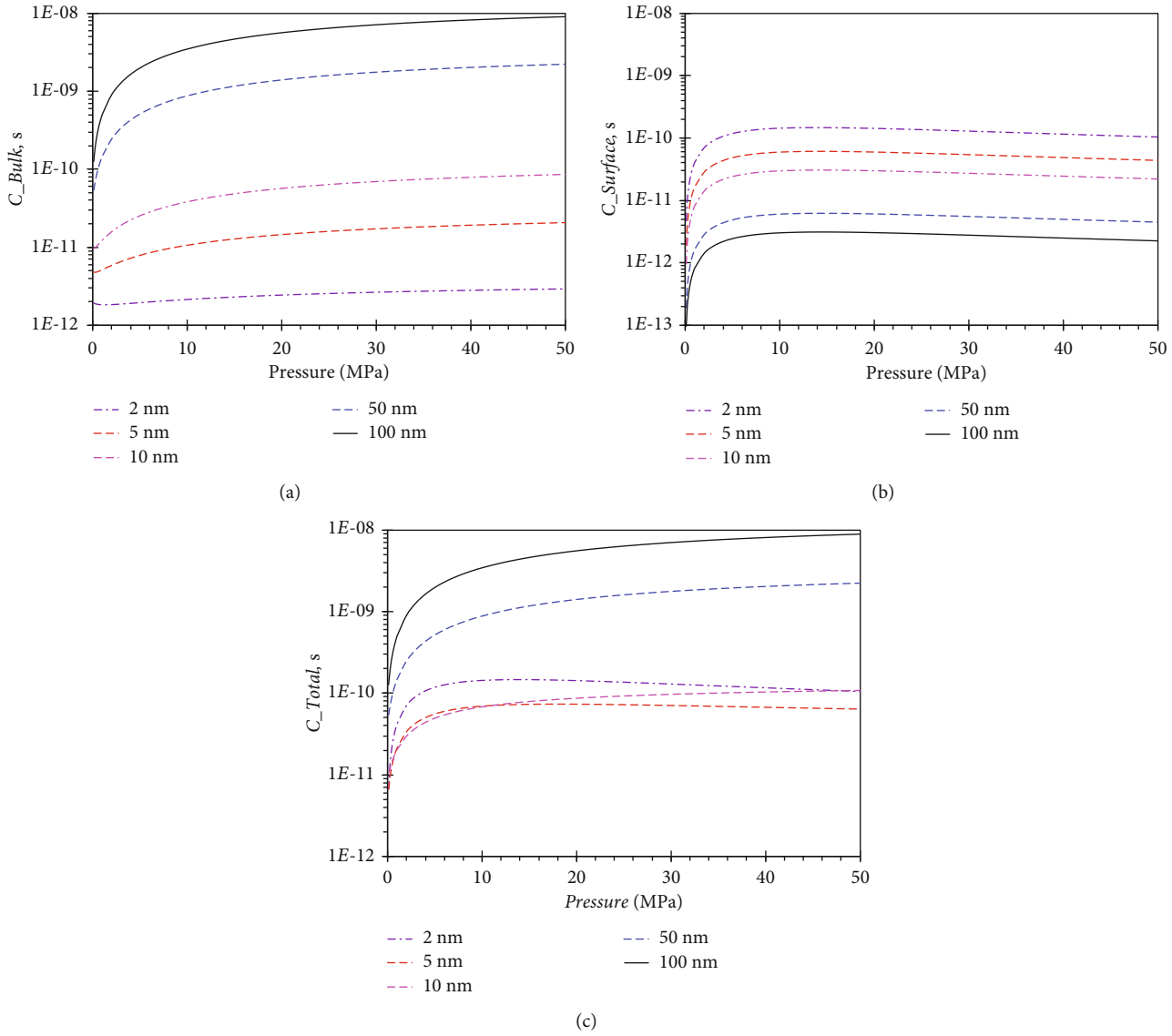

Figure 3: Nanoconfined gas flow behavior in the organic nanopore: (a) Bulk-like gas transport behavior; (b) Surface diffusion of adsorption molecules; (c) Total gas conductance.

ular diameter, when the gas coverage approaches 1. Notably, in this article, the adsorption phenomenon is correlated with surface wettability; thus, the gas coverage, with the definition of current adsorption amount to the maximum amount, is related to the surface contact angle. In Section 3.2, focusing on the calculation of adsorption thickness, thickness, obtained from the formula, will always be smaller than a methane molecular diameter; therefore, the single-layer assumption holds during the model establishment. Then, the traditional gas coverage was described as a function of pressure; however, the wettability effect is considered in this article.

$$\phi = \frac{P/Z}{P_L + P/Z} \times \frac{h_{ad}}{\sigma}. \tag{22}$$

Similarly, to facilitate the upcoming comparison, the gas mass flux is transformed as the conductance, which is provided below.

$$C_{\text{surf}} = D_s \frac{C_{sc}}{P}. \tag{23}$$

3.5. Total Nanoconfined Flow in Organic Pores. Coupling the bulk-like gas conductance and surface diffusion, the total gas flow capacity through an organic nanopore can be evaluated. In this article, an area-average concept is utilized to couple both two flow mechanisms. The concept has been widely applied in the nanoconfined fluid flow theory, like the evaluation of nanoconfined water viscosity and identification of adsorption fluid molecules. Also, some research efforts for nanoconfined gas behavior have achieved good results under the concept. The main

discrepancy between this work and previous contributions is the consideration of wettability impact. As stated and derived in the aforementioned context, the adsorption phase thickness, the gas viscosity, and adsorption coverage are all related to surface contact angle. As a result, the research can be regarded as the previous contributions incorporating surface wettability impact. In sum, the area-average concept is doable to handle this issue.

$$C_{\text{total}} = \left(1 - \frac{h_{ad}}{r}\right)^2 C_{\text{bulk}} + \left(1 - \left(1 - \frac{h_{ad}}{r}\right)^2\right) C_{\text{surf}}, \quad (24)$$

where C_{total} is the gas flow capacity through a specified organic nanopore, s.

The adsorption thickness is a function of pressure and will decline with a decreasing pressure when the other conditions remain unchanged. Thus, the alteration of the weight coefficients for C_{bulk} and C_{surf} happens, demonstrating the nanoconfined flow capacity always change with pressure. This phenomenon highlights the research value for the efficient development of shale gas reservoirs, as the proposed model can capture the change principle of the realistic gas flow capacity under the depressurization process of shale gas reservoirs. Besides, in terms of the realistic development process [80, 81], the pore radius will experience the shrinkage impact, induced by the stress dependence, and the enlarge impact, exerted by the matrix shrinkage. However, in this article, the potential factors, upon original pore size, are not coupled at this point. The proposed model can be further modified by taking care of these factors in the future. This work focuses on the wettability effect on pore-scale gas flow performance.

4. Model Validation

Before the proposed model can be utilized to investigate gas flow in organic nanopores, its reliability requires careful examination. As described in Section 3, the proposed model consists of two components, including the bulk-gas model and a diffusion model for adsorption molecules. Notably, the wettability effect, in the form of surface contact angle, is incorporated in both bulk-gas model, as well as the surface diffusion model. To current knowledge, experimental results are hard to identify whether the mass flux contributions from the bulk gas or adsorption gas and so does the molecular simulation. In this regard, the above two models are verified separately in this article.

As for the proposed bulk-gas model, the enhance factor, describing the enhancement degree of gas flow rate under the nanoconfinement effect, has the definition as the ratio of conductance calculated by the proposed bulk-gas model to that evaluated by no-slip NS equation. In accordance with the definition, the enhance factor can be obtained, which is a function of Knudsen number. Loyalka and Hamoodi [82] and Tison [83] have provided fruitful data for the nanoconfined bulk-gas flow, with the help of advanced numerical method and laboratory experiments. Detailed basic data collected from the previous documents is tabulated in Table 1. Notably, in this part, the surface diffusion is neglected, and then the C_{total} is degenerated from Equations (24) to (14). C_{con} denotes the gas conductance based on the no-slip NS equation, and the formula for enhance factor is provided.

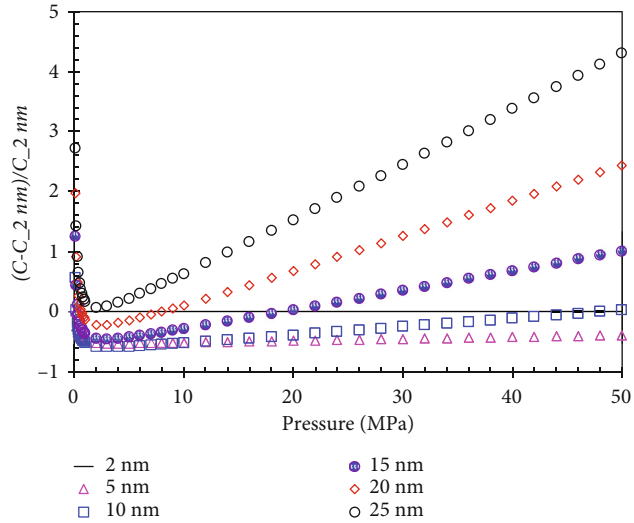

Figure 4: Comparison of total gas flux at a specified pore size to that of 2 nm.

$$C_{\text{total}}/C_{con} = \frac{r_{eff}^2}{r^2}(1 + \alpha Kn)\left(1 + \frac{4Kn}{1 + Kn}\right). \quad (25)$$

As depicted in Figure 2(a), it can be demonstrated that the proposed bulk-gas model is able to achieve good agreements with existed simulation results and experimental data. Also, based on the relationship between gas conductance and Knudsen number, it can be inferred that the gas rarefaction, induced by the nanoconfinement impact, plays a positive role for gas transport capacity. Concrete underlying mechanisms will be specified in the following discussion part. As for the proposed surface diffusion model, the ratio of diffusion coefficient at a given gas coverage to that at zero gas coverage is used. Similarly, relevant data is collected from the previous references, in which gas type includes SO_2, C_2H_6, and C_3H_8, and detailed information is presented in Table 2.

It can be observed from Figure 2(b) that the proposed model for surface diffusion can reach a good match with the actual recorded value. The surface diffusion becomes evident with the increase of gas coverage, and the enhancement amplitude also climbs with the increasing gas coverage. As the surface diffusion is a unique mechanism for gas-flux contribution, comparing with the gas flow through conventional pores, the nanoconfined gas flow capacity strengthens dramatically. Thus, the difference, between nanoconfined gas behavior and bulk gas, arises in both the bulk-like gas flow and surface diffusion. With the intent of capturing gas flow behavior in the organic nanopore, one should take care

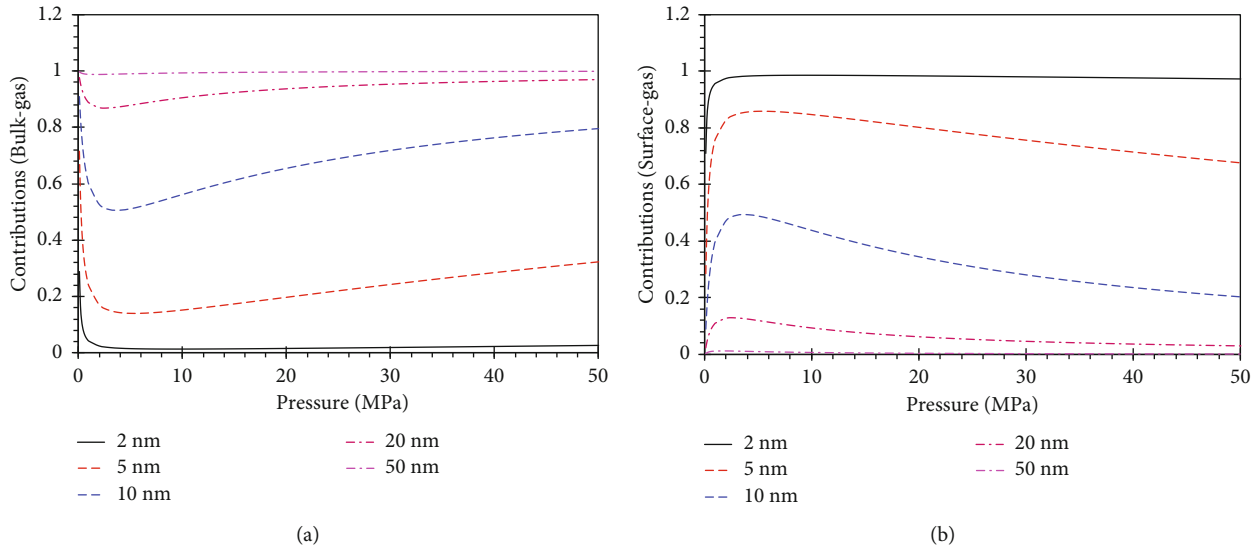

Figure 5: Contributions to the total gas conductance: (a) Bulk-like gas; (b) Adsorption gas molecules.

of both the bulk-like gas transport model and surface diffusion model.

5. Results and Discussion

After clarifying the reliability of the proposed model, it is sensible to shed light on gas flow behavior in the organic nanopore, with the help of the above research efforts. Actually, previous contributions have been performed to investigate the issue; however the wettability effect, denoting the surface affinity to methane molecules and becoming more evident in a nanoscale space, has received little attention. In this article, we focus on the wettability effect on the gas flow behavior, looking forward to enriching relevant knowledge about shale gas flow mechanisms. Some basic parameters are provided in Table 3, facilitating the analysis upon influential factors.

5.1. Nanoconfined Flow Conductivity. To date, the discrepancy between the nanoconfined gas flow behavior and that in bulk state has been widely reported. Intuitively, the discrepancy stems from the shrinkage of pore scale, suggesting the pore size influence. A general knowledge in terms of the role of pore size is urgent. Five sets of pore size are utilized here, including 2 nm, 5 nm, 10 nm, 50 nm, and 100 nm, covering the entire pore size range of the organic shale nanopores. And, in this part, the surface contact angle remains unchanged as 30°, and the other parameters are used from Table 3. As depicted in Figure 3, the nanoconfined gas flow behavior over the pressure, ranging from 0.1 to 50 MPa, is presented. In the case of bulk-like gas, the conductance increases with the increasing pressure. The greater methane density, under the higher pressure, is supposed to take responsible for this phenomenon. Also, the high-pressure atmosphere will mitigate the methane free path, resulting in small Knudsen number; therefore, the molecules at boundary may lose mobility. As a result, the high-pressure atmosphere can impair the gas conductance, regardless of the enhance effect based on the methane density. Meanwhile, at a specific pressure, bulk-gas conductance has a positive correlation with pore size. However, the gas conductance, contributed by surface diffusion, has a negative correlation with pore size. It is because the volume-weight coefficient for adsorption gas becomes greater with the decline of pore size. For example, as the adsorption phase thickness falls in a small range, as inferred from Equation (5), the volume-weight coefficient for surface diffusion in 2 nm will far beyond that in 100 nm. In addition, from Figure 3(b), for a specific pore size, the conductance will increase rapidly at first and then become stable with the increasing pressure. The first stage for rapid increase is mainly attributed by the dramatical increase of diffusion coefficient (D_s) as well as gas concentration (C_{sc}), and both are sensitive to the variation of pressure.

After analyzing the flow behavior of bulk-like gas and adsorption molecules separately, the total gas conductance, directly manifesting the gas flow capacity in the organic nanopore, is presented in Figure 3(c). It can be observed that the pore size has little impact on the general variation feature between the gas conductance and pressure; gas flow capacity always has a positive relationship with increasing pressure. In order to achieve a clear image about total gas conductance, for the pressure ranging from 0.1 to 50 MPa, it is surprising to find that total conductance in 5 nm and 10 nm is less than that in 2 nm. Also, in Figure 4, the total gas conductance in 15 nm and 20 nm is less than 2 nm in the pressure range of 0.1~20 nm and 0.1~8 MPa, respectively. Based on the traditional theory, the greater pore size corresponds to the stronger gas flow capacity, while the nanoconfined gas flow behavior can alter the above perspective. The phenomenon can be attributed to the role of surface diffusion, which is dominant in nanopores with pore size less than 5 nm. It should be noted that the traditional theory roots in the bulk-gas flow mechanism and overlooks the surface

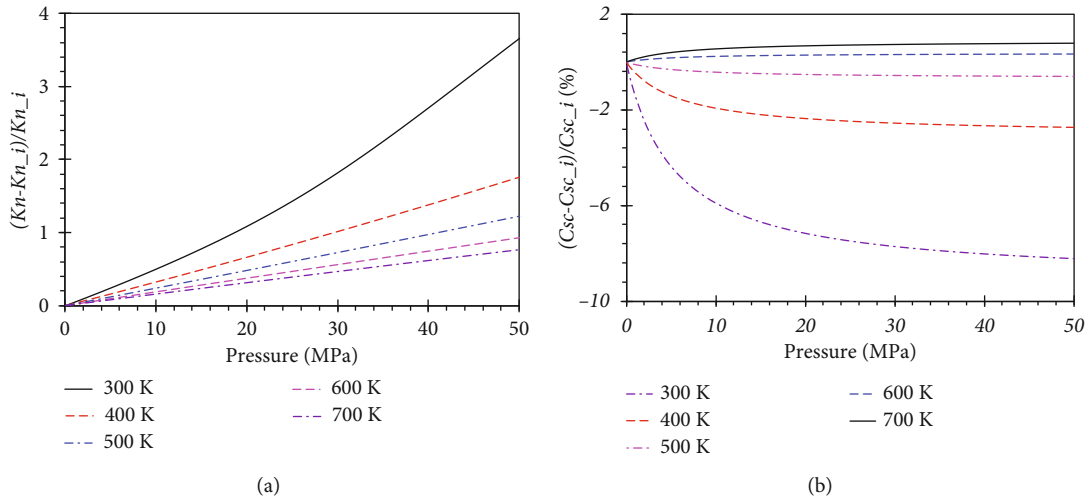

Figure 6: Variation of key parameters caused by real gas effect: (a) Kn; (b) Gas concentration.

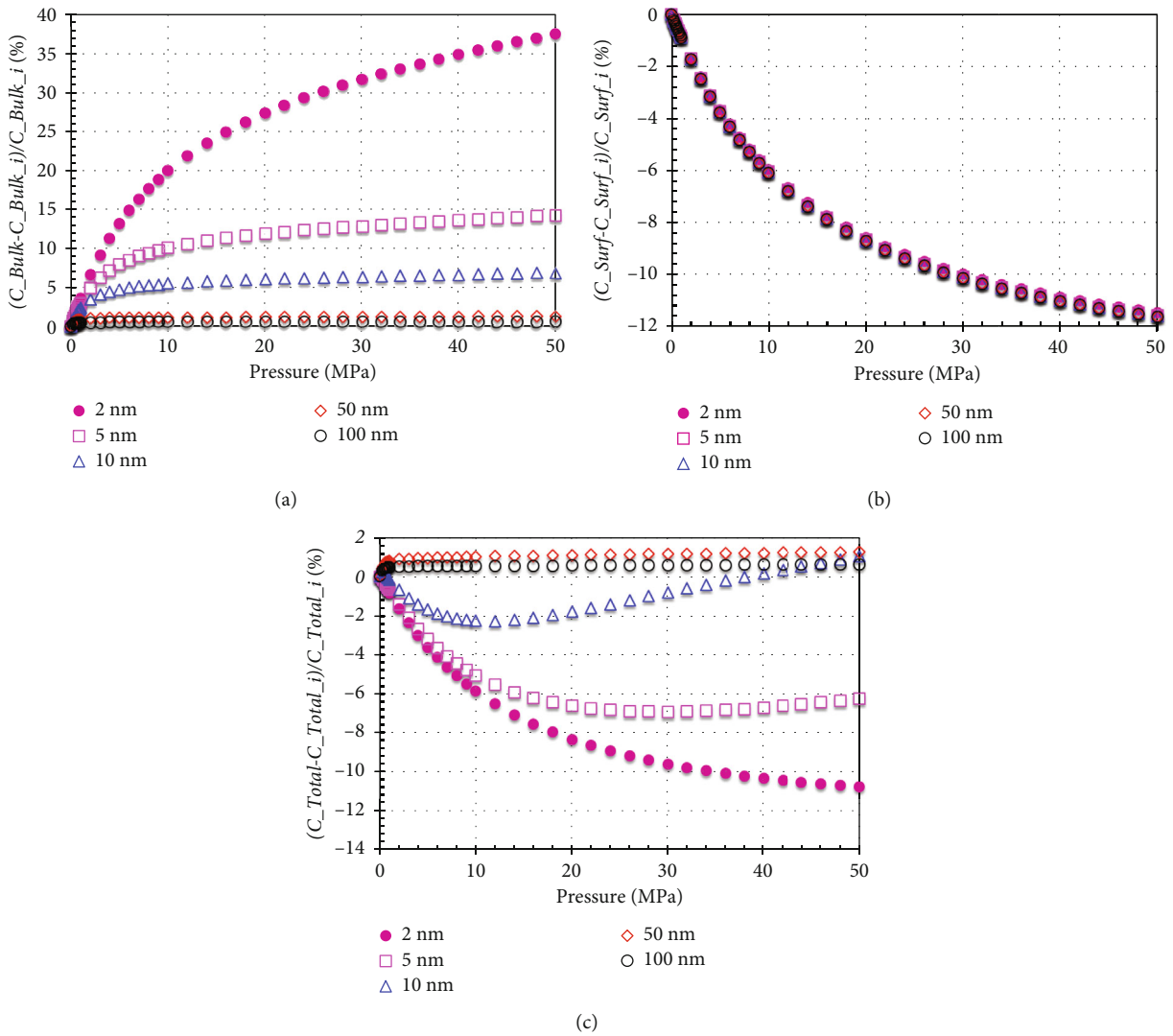

Figure 7: Deviation caused by the real gas effect: (a) Bulk-like gas conductance; (b) Surface diffusion; (c) Total gas conductance.

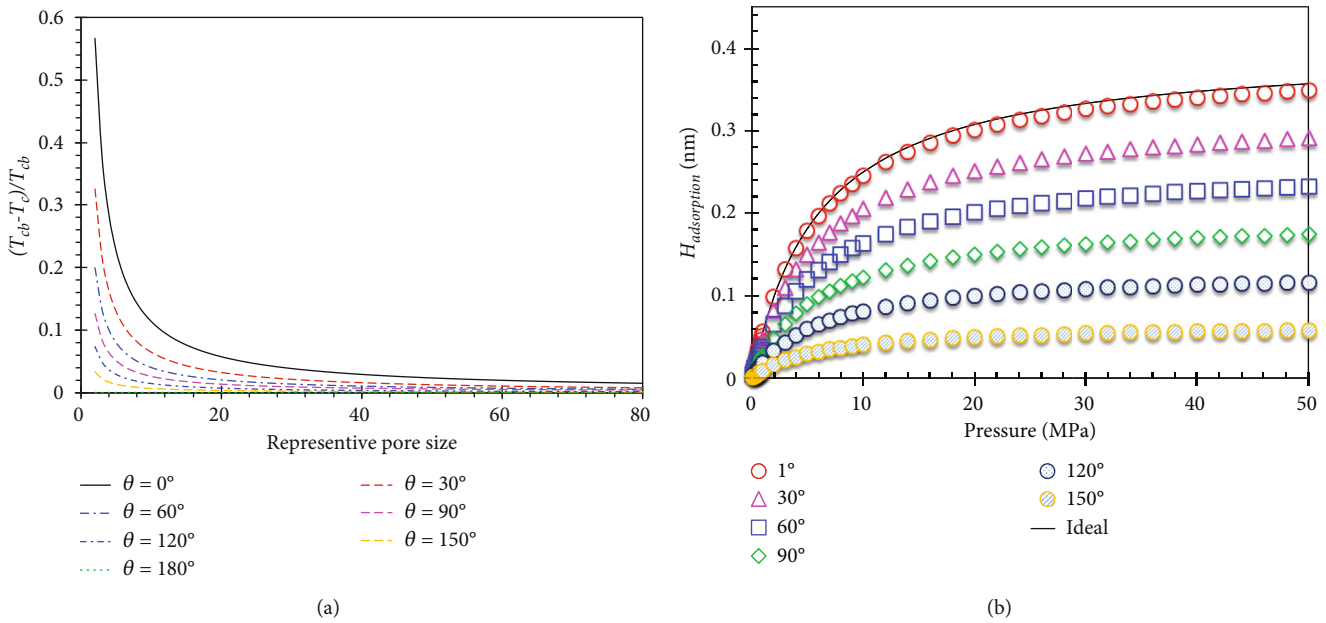

Figure 8: The variation of key parameters caused by wettability impact: (a) Critical properties; (b) Adsorption phase thickness.

diffusion. Thus, although the gas conductance in small pores, contributed by bulk gas, is less than that in large pores, the gas conductance, contributed by surface diffusion, may drastically enhance gas flow capacity and allow gas conductance in small pores greater than that in the large pores. The observation is helpful to understand shale gas production behavior in field.

The contributions of bulk-like gas and adsorption molecules are presented in Figure 5. It can be concluded that surface diffusion is dominant for pore size less than 5 nm and bulk-gas flow mechanism becomes the prominent contributor for pore size larger than 50 nm. When pore size falls in the range of 5~50 nm, the relative strengths of bulk-gas flow mechanism and surface diffusion are heavily dependent on pressure. The contribution of bulk-gas conductance will decrease first and then increase stable. On the contrary, the contribution of surface diffusion will increase first and then decrease stable. It is the variation feature that the gas conductance in small pores can exceed that in large pores. Thus, the gas flow capacity through nanopores may be underestimated based on the current theory, and the surface diffusion contribution cannot be neglected for small nanopores.

5.2. Real Gas Effect. In realistic shale organic nanopores, the atmosphere pressure can reach as high as 50 MPa. And, the gas molecules cannot be considered as ideal gas under this condition, as frequency of intermolecular collision climbs a lot, and intermolecular distance becomes comparable to molecular diameter. Associated influence will arise by considering the molecular inherent diameter, such as the variation of gas viscosity and compressibility, as well as MFP, which is called as real gas effect. For previous pieces of research efforts in biological or physical scope, due to the small atmosphere pressure, gas molecules are widely regarded as the real gas effect. However, the assumption appears to break down for shale gas reservoirs. Notably, for ideal gas, the gas viscosity (μ) remains unchanged as the gas viscosity at the standard condition (μ_{atm}), regardless of alteration of pressure and temperature. And the idea gas compressibility (Z) is always 1. In the following comparison, the original symbol with an additional i suggests the physical parameter for ideal gas assumptions. The other parameters are used from Table 3.

Similar to the verification section, the bulk-gas flow mechanism and surface diffusion are investigated separately. In Figure 6(a), the Knudsen number for real gas can reach as great as 3 times that of ideal gas. Also, the magnitude increases with the increasing pressure. Notably, the discrepancy, induced by real gas effect, upon Knudsen number disappears, while the pressure approaches 0.1 MPa. This phenomenon meets the above analysis that the real gas behavior can be regarded as the same as ideal gas under low pressure. Therefore, the bulk-gas flow capacity will be underestimated, while the real gas effect is not considered. At a specified pressure, the real gas effect will be mitigated by enhancing temperature. As for the surface diffusion, the gas concentration is utilized to shed light on the real gas effect. In the case of temperature less than 500 K in Figure 6(b), the gas concentration will decline with the increasing pressure, and the magnitude can reach as great as 8%. In contrast, when temperature exceeds 500 K, the gas concentration will show a slightly increase trend. The above phenomenon is mainly caused by the dependency of natural gas compressibility on surrounding temperature.

With the intent of quantifying the real gas effect, the concrete deviation is calculated and presented in Figure 7. As depicted in Figure 7(a), due to the existence of real gas effect, gas conductance will be enhanced, and the magnitude can reach 15% when pore size is equal to 5 nm. Notably, the magnitude will be greatly mitigated in large nanopores, and

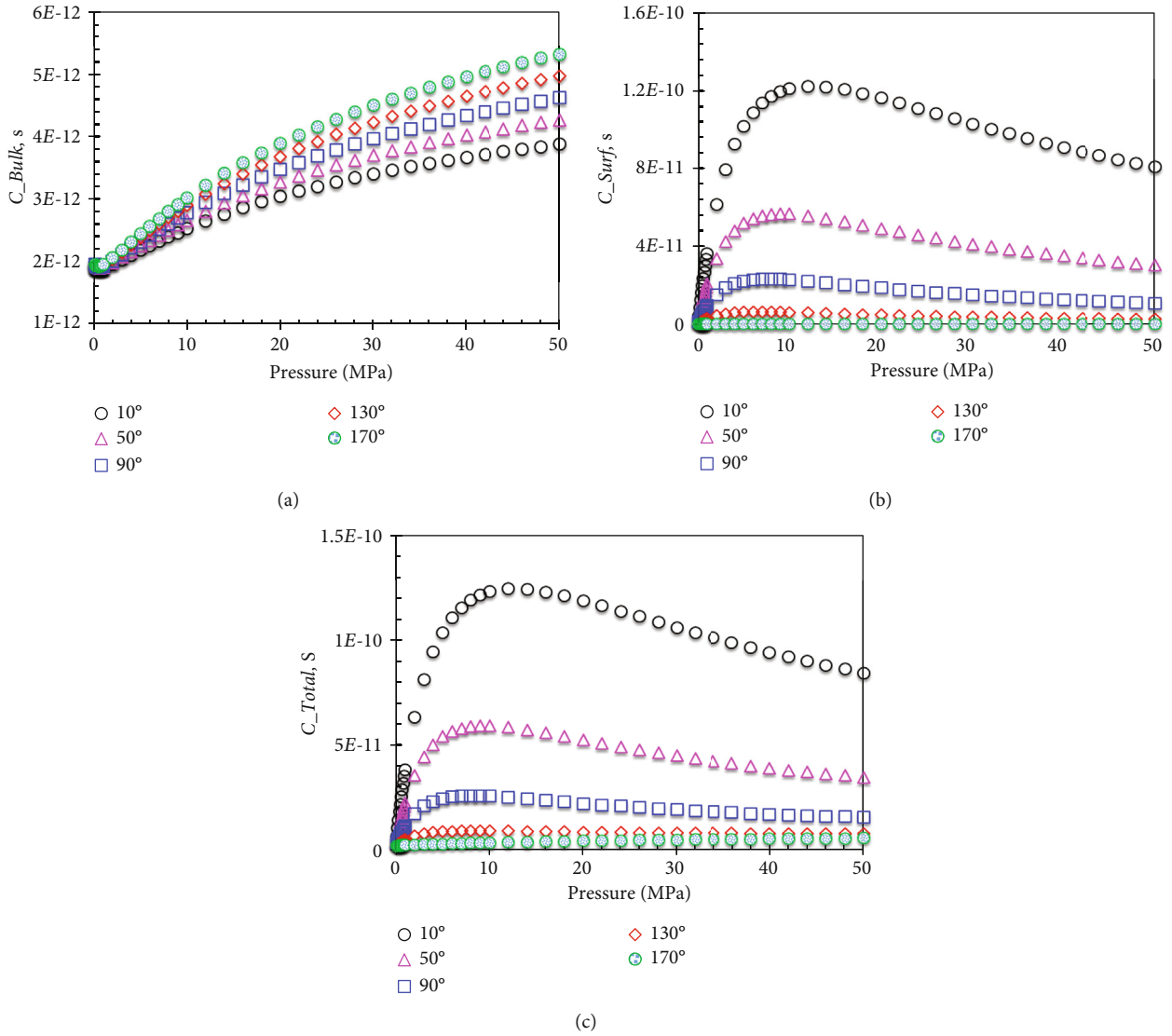

Figure 9: Wettability impact on gas transport through organic nanopore when pore size is equal to 2 nm: (a) Bulk-like gas conductance; (b) Surface diffusion; (c) Total gas conductance.

it will be close to zero for pore size beyond 50 nm. As for surface diffusion in Figure 7(b), the gas conductance shows a negative relationship with regard to pressure, indicating that real gas effect indeed impairs the contributions from surface diffusion. The relationship is insensitive to the variation of pore size. In Figure 7(c), combining the bulk-like gas flow mechanism and surface diffusion, the negative correlation between pressure and total gas conductance holds when pore size is less than 10 nm. However, when pore size exceeds 50 nm, the gas conductance will increase with increasing pressure. The relative contribution of gas flow mechanisms, presented in Figure 5, can be used to elucidate the issue. For small nanopores, the prominent factor, in terms of the total gas conductance, is surface diffusion and turns to be bulk-like gas flow for large nanopores. As a result, the total conductance will show the negative correlation with increasing pressure, keeping in line with the surface diffusion, and show the positive correlation, keeping in line with the bulk-like gas conductance.

5.3. Wettability Effect. In shale, the surface affinity for organic nanopores is diversity, relying on the surface composition and pore size, as well as physical structure. Also, shale is a highly-developed heterogeneous porous media across thousands of geological years [87, 88]. There exists a variety of kerogen molecular types, known as the basic components for shale organic nanopores, as well as a wide range of thermal maturity, which will result in different surface wettability upon shale gas. Also, considering the mineral composition in the organic nanopores, particularly at the low-maturity period, the surface contact angle is set to fall in the range of 0~180°. The other parameters are used in Table 3.

In this article, the wettability effect is represented by the methane critical properties and adsorption phase thickness, both which are heavily dependent on the surface contact angle. As depicted in Figure 8(a), the critical temperature will decline with the pore size shrinkage. Also, at a specified pore size, strong surface affinity corresponds to the large

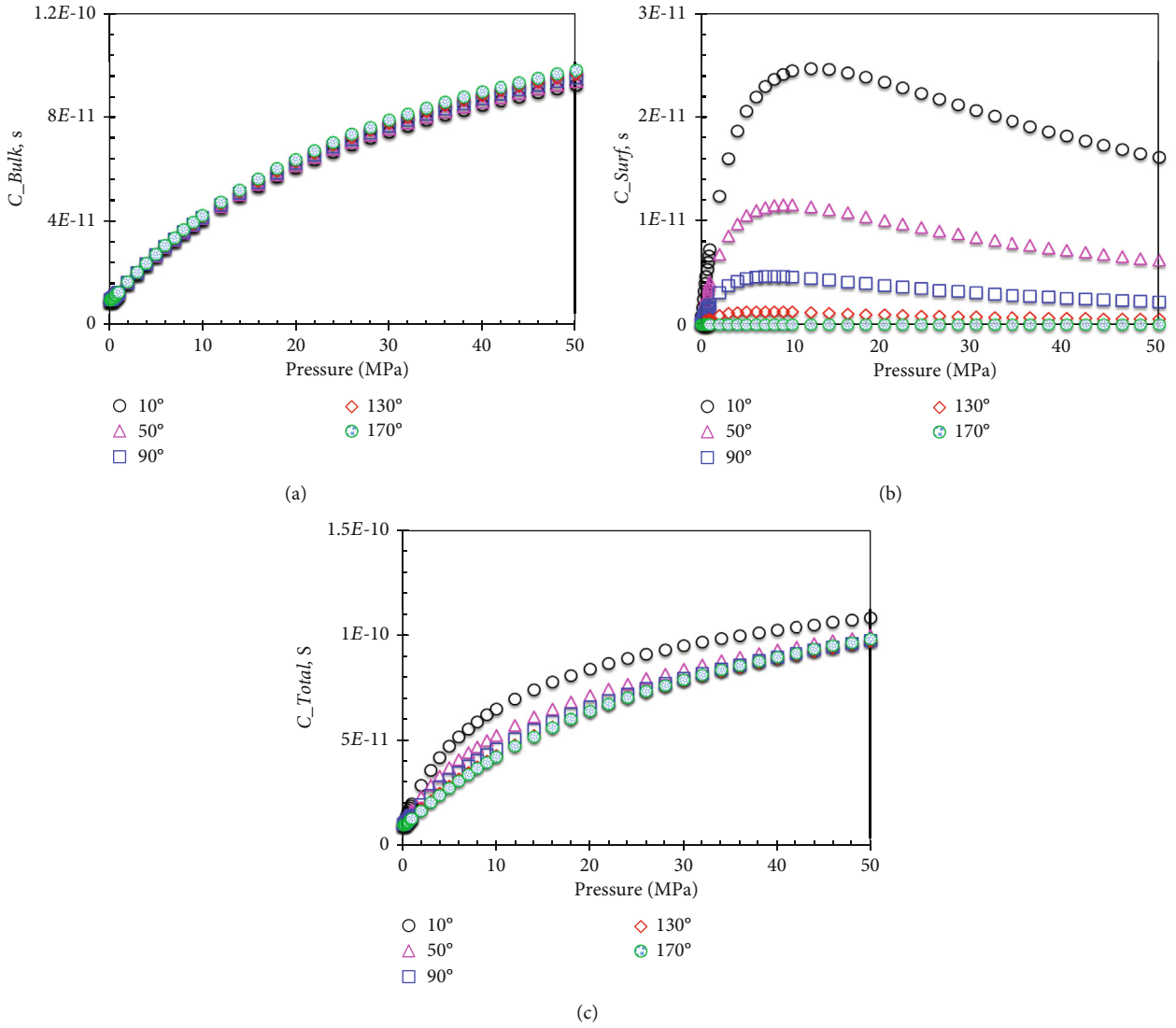

Figure 10: Wettability impact on gas transport through organic nanopore when pore size is equal to 10 nm: (a) Bulk-like gas conductance; (b) Surface diffusion; (c) Total gas conductance.

decreasing magnitude, manifesting the influence of strong interactions between surface and molecules. In Figure 8(b), the adsorption phase thickness versus surface contact angle is presented. As for the strong surface affinity, the adsorption thickness will approach the ideal gas. And the adsorption phenomenon will disappear for extreme weak surface affinity, imposing a repulsive force upon the methane molecules near the surface.

As for small nanopores with pore size of 2 nm, the wettability effect on gas conductance, contributed by bulk-like gas and adsorption gas, is quantified. In Figure 9(a), it can be found that bulk-gas conductance will decrease while the surface affinity strengthens. Similarly, Figure 9(b) denotes the variation feature of surface diffusion versus pressure, indicating that the gas conductance, contributed by surface diffusion, will enhance with strong surface affinity. After comparison, it can be concluded that the deviation of bulk-gas conductance caused by surface wettability is smaller than the surface diffusion. Hence, wettability impact has minor influence on the bulk-gas flow mechanism and major influence on the surface diffusion. Furthermore, on the basis of Figure 9(c), the tendency of total gas conductance versus pressure is close to that for surface diffusion, which is caused by the dominant role of surface diffusion in small nanopores.

When pore size becomes 10 nm, the overall impact, induced by surface wettability, on gas conductance changes. In Figure 10(a), the tendency is the same with that in Figure 9(a); however, the discrepancy caused by the surface wettability becomes smaller, comparing with that in 2 nm. It demonstrates that the wettability impact on bulk-gas flow behavior will become weak with the increasing pore size. Additionally, wettability effect on surface diffusion remains unchanged, comparing with that in 2 nm, as presented in Figure 10(b). In the meanwhile, the total conductance versus pressure shows dramatic difference with that in 2 nm, which can be explained by the relative contributions, presented in Figure 5. The wettability impact has little influence on

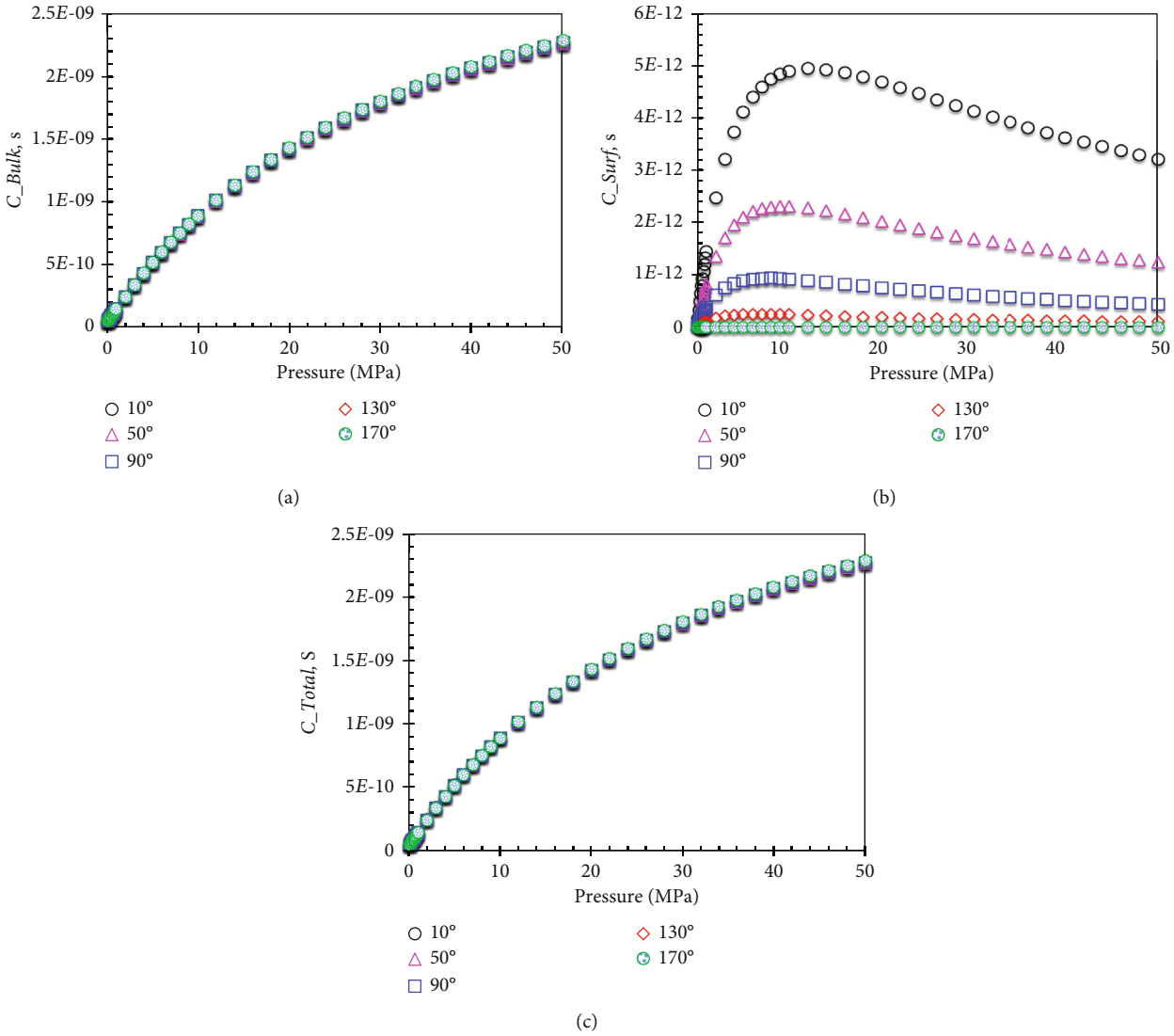

FIGURE 11: Wettability impact on gas transport through organic nanopore when pore size is equal to 50 nm: (a) Bulk-like gas conductance; (b) Surface diffusion; (c) Total gas conductance.

bulk-gas flow behavior in large nanopores, and mainly affects the surface diffusion. Thus, the total gas conductance versus pressure will approach that for surface diffusion in 2 nm and approach the bulk-like gas flow mechanism when pore size is beyond 10 nm.

Regularity of nanoconfined flow behavior in the organic nanopore with pore size of 50 nm is presented in Figure 11, demonstrating the correctness of the aforementioned analysis. In the large nanopore, the total conductance and bulk-like gas conductance share the same variation feature, regardless of the wettability effect on surface diffusion. As a result, in the case of the total gas flow capacity, the wettability effect has little impact when pore size is beyond 50 nm, while it cannot be neglected when pore size is less than 10 nm. Accordingly, the wettability impact has the applicability scope, suggesting the upper limit of pore size is 10 nm, which is in line with the surface diffusion. In light of the fact that massive shale organic nanopores have pore size less than 10 nm, thus the wettability impact is worthy of consideration for precise flow behavior characterization.

6. Conclusions

(1) A robust model for gas flow through the shale organic nanopore is developed, coupling surface wettability into both bulk-gas flow model, as well as surface diffusion model. Key factors, induced by surface wettability and pore size shrinkage, are considered properly, including the critical property shift, gas viscosity variation, and adsorption phase thickness

(2) Gas conductance, contributed by bulk-gas flow mechanism, has a positive relationship with pore size; however that from surface diffusion has the opposite trend. The gas flux in small nanopores may exceed that in large nanopores, due to the predominant role of

surface diffusion while pore size is less than 10 nm. Absence of real gas effect will lead to inaccurate characterization of nanoconfined gas flow capacity, the magnitude can reach 7% for pore size of 5 nm

(3) The wettability impact has little influence on bulk-gas flow behavior and mainly affects the surface diffusion. Wettability effect governs the total gas flux when pore size is less than 10 nm, while its impact will be greatly mitigated when pore size is greater than 50 nm. The wettability impact has the applicability scope, and its upper limit of pore size is 10 nm

Data Availability

Data is available on request.

Conflicts of Interest

The authors declare that they have no conflicts of interest.

Acknowledgments

We acknowledge China University of Mining & Technology for the permission to publish this work.

References

[1] P. Mastropietro, P. Rodilla, and C. Batlle, "Emergency measures to protect energy consumers during the Covid-19 pandemic: a global review and critical analysis," *Energy Research & Social Science*, vol. 68, p. 101678, 2020.

[2] J. Millward-Hopkins, J. K. Steinberger, N. D. Rao, and Y. Oswald, "Providing decent living with minimum energy: a global scenario," *Global Environmental Change*, vol. 65, p. 102168, 2020.

[3] Z. Sun, B. Huang, K. Wu et al., "Nanoconfined methane density over pressure and temperature: wettability effect," *Journal of Natural Gas Science and Engineering*, vol. 99, p. 104426, 2022.

[4] T. Wang, S. Tian, G. Li, L. Zhang, M. Sheng, and W. Ren, "Molecular simulation of gas adsorption in shale nanopores: a critical review," *Renewable and Sustainable Energy Reviews*, vol. 149, p. 111391, 2021.

[5] V. Ş. Ediger, J. V. Bowlus, and A. F. Dursun, "State capitalism and hydrocarbon security in China and Russia," *Energy Strategy Reviews*, vol. 38, p. 100725, 2021.

[6] T. Fang, Y. Zhang, B. Ding, Y. Yan, and J. Zhang, "Static and dynamic behavior of CO2 enhanced oil recovery in nanoslits: effects of mineral type and oil components," *International Journal of Heat and Mass Transfer*, vol. 153, p. 119583, 2020.

[7] Y. Pang, X. Hu, S. Wang, S. Chen, M. Y. Soliman, and H. Deng, "Characterization of adsorption isotherm and density profile in cylindrical nanopores: modeling and measurement," *Chemical Engineering Journal*, vol. 396, p. 125212, 2020.

[8] J. Xu, K. Wu, S. Yang et al., "Real gas transport in tapered non-circular nanopores of shale rocks," *AICHE Journal*, vol. 63, no. 7, pp. 3224–3242, 2017.

[9] H. Song, M. Yu, W. Zhu et al., "Numerical investigation of gas flow rate in shale gas reservoirs with nanoporous media," *International Journal of Heat and Mass Transfer*, vol. 80, pp. 626–635, 2015.

[10] Q. Zhang, Y. Su, W. Wang, M. Lu, and G. Sheng, "Gas transport behaviors in shale nanopores based on multiple mechanisms and macroscale modeling," *International Journal of Heat and Mass Transfer*, vol. 125, pp. 845–857, 2018.

[11] Y. Yin, Z. G. Qu, and J. F. Zhang, "Multiple diffusion mechanisms of shale gas in nanoporous organic matter predicted by the local diffusivity lattice Boltzmann model," *International Journal of Heat and Mass Transfer*, vol. 143, p. 118571, 2019.

[12] P. Yu, D. Dempsey, and R. Archer, "A three-dimensional coupled thermo-hydro-mechanical numerical model with partially bridging multi-stage contact fractures in horizontal-well enhanced geothermal system," *International Journal of Rock Mechanics and Mining Sciences*, vol. 143, p. 104787, 2021.

[13] Z. Sun, B. Huang, Y. Liu et al., "Gas-phase production equation for CBM reservoirs: interaction between hydraulic fracturing and coal orthotropic feature," *Journal of Petroleum Science and Engineering*, vol. 213, p. 110428, 2022.

[14] Y. Miao, X. Li, Y. Zhou et al., "A new rate-transient analysis model for shale gas reservoirs coupled the effect of slip flow and surface diffusion," *International Journal of Heat and Mass Transfer*, vol. 124, pp. 1–10, 2018.

[15] J. Zhao, D. Fu, Y. Li, Y. Jiang, W. Xu, and X. Chen, "REV-scale simulation of gas transport in shale matrix with lattice Boltzmann method," *Journal of Natural Gas Science and Engineering*, vol. 57, pp. 224–237, 2018.

[16] H. Wang, L. Chen, Z. Qu et al., "Modeling of multi-scale transport phenomena in shale gas production – a critical review," *Applied Energy*, vol. 262, p. 114575, 2020.

[17] H. Gao, J. Wang, X. Chen et al., "Nanoconfinement effects on thermal properties of nanoporous shape-stabilized composite PCMs: a review," *Nano Energy*, vol. 53, pp. 769–797, 2018.

[18] A. Fatah, Z. Bennour, H. B. Mahmud, R. Gholami, and M. Hossain, "Surface wettability alteration of shales exposed to CO2: implication for long-term integrity of geological storage sites," *International Journal of Greenhouse Gas Control*, vol. 110, p. 103426, 2021.

[19] I. W. R. Saputra, O. Adebisi, E. B. Ladan, A. Bagareddy, A. Sarmah, and D. S. Schechter, "The influence of oil composition, rock mineralogy, aging time, and brine pre-soak on shale wettability," *ACS Omega*, vol. 7, no. 1, pp. 85–100, 2021.

[20] M. R. Yassin, H. Dehghanpour, J. Wood, and Q. Lan, "A theory for relative permeability of unconventional rocks with dual-wettability pore network," *SPE Journal*, vol. 21, no. 6, pp. 1970–1980, 2016.

[21] B. Ghanbarian, F. Liang, and H. H. Liu, "Modeling gas relative permeability in shales and tight porous rocks," *Fuel*, vol. 272, p. 117686, 2020.

[22] Z. Sun, S. Wang, H. Xiong, K. Wu, and J. Shi, "Optimal nanocone geometry for water flow," *AICHE Journal*, vol. 68, no. 3, p. e17543, 2022.

[23] K. Wang, K. Ye, B. Jiang, H. Li, and Y. Tan, "The mechanism of gas-water extraction in micro- and nanoscale pores in shale gas reservoirs: based on gas-water interactions," *Chemical Engineering Science*, vol. 248, p. 117259, 2022.

[24] J. Li, X. Li, X. Wang et al., "Water distribution characteristic and effect on methane adsorption capacity in shale clay," *International Journal of Coal Geology*, vol. 159, pp. 135–154, 2016.

[25] C. R. Clarkson, N. Solano, R. M. Bustin et al., "Pore structure characterization of North American shale gas reservoirs using

USANS/SANS, gas adsorption, and mercury intrusion," *Fuel*, vol. 103, pp. 606–616, 2013.

[26] D. R. Sandoval, W. Yan, M. L. Michelsen, and E. H. Stenby, "Modeling of shale gas adsorption and its influence on phase equilibrium," *Industrial & Engineering Chemistry Research*, vol. 57, no. 17, pp. 5736–5747, 2018.

[27] Z. Sun, B. Huang, Y. Li, H. Lin, S. Shi, and W. Yu, "Nanoconfined methane flow behavior through realistic organic shale matrix under displacement pressure: a molecular simulation investigation," *Journal of Petroleum Exploration and Production Technology*, vol. 12, no. 4, pp. 1193–1201, 2022.

[28] L. Huang, W. Zhou, H. Xu, L. Wang, J. Zou, and Q. Zhou, "Dynamic fluid states in organic-inorganic nanocomposite: implications for shale gas recovery and CO_2 sequestration," *Chemical Engineering Journal*, vol. 411, p. 128423, 2021.

[29] S. Jribi, T. Miyazaki, B. B. Saha et al., "Equilibrium and kinetics of CO_2 adsorption onto activated carbon," *International Journal of Heat and Mass Transfer*, vol. 108, pp. 1941–1946, 2017.

[30] E. Fathi and I. Y. Akkutlu, "Multi-component gas transport and adsorption effects during CO_2 injection and enhanced shale gas recovery," *International Journal of Coal Geology*, vol. 123, pp. 52–61, 2014.

[31] K. Wu, Z. Chen, X. Li et al., "Flow behavior of gas confined in nanoporous shale at high pressure: real gas effect," *Fuel*, vol. 205, pp. 173–183, 2017.

[32] S. Yang, K. Wu, J. Xu, J. Li, and Z. Chen, "Roles of multicomponent adsorption and geomechanics in the development of an Eagle Ford shale condensate reservoir," *Fuel*, vol. 242, pp. 710–718, 2019.

[33] R. Li, Z. Chen, K. Wu, X. Hao, and J. Xu, "An analytical model for water-oil two-phase flow in inorganic nanopores in shale oil reservoirs," *Petroleum Science*, vol. 18, no. 6, pp. 1776–1787, 2021.

[34] X. Wang, J. Chen, D. Ren, and Z. Shi, "Role of gas viscosity for shale gas percolation," *Geofluids*, vol. 2020, 10 pages, 2020.

[35] M. Dejam, "Advective-diffusive-reactive solute transport due to non-Newtonian fluid flows in a fracture surrounded by a tight porous medium," *International Journal of Heat and Mass Transfer*, vol. 128, pp. 1307–1321, 2019.

[36] M. Dejam, H. Hassanzadeh, and Z. Chen, "Semi-analytical solution for pressure transient analysis of a hydraulically fractured vertical well in a bounded dual-porosity reservoir," *Journal of Hydrology*, vol. 565, pp. 289–301, 2018.

[37] S. Wang, Q. Feng, F. Javadpour, M. Zha, and R. Cui, "Multiscale modeling of gas transport in shale matrix: an integrated study of molecular dynamics and rigid-pore-network model," *SPE Journal*, vol. 25, no. 3, pp. 1416–1442, 2020.

[38] H. Wang, Z. Qu, Y. Yin, J. Bai, and B. Yu, "Review of molecular simulation method for gas adsorption/desorption and diffusion in shale matrix," *Journal of Thermal Science*, vol. 28, no. 1, pp. 1–16, 2019.

[39] L. Zhang, C. Liu, Q. Li, S. Wang, S. Cai, and E. Huo, "Shale gas transport through the inorganic cylindrical and conical nanopores: a density gradient driven molecular dynamics," *International Journal of Heat and Mass Transfer*, vol. 183, p. 122126, 2022.

[40] Z. Sun, X. Li, W. Liu, T. Zhang, M. He, and H. Nasrabadi, "Molecular dynamics of methane flow behavior through realistic organic nanopores under geologic shale condition: pore size and kerogen types," *Chemical Engineering Journal*, vol. 398, p. 124341, 2020.

[41] Z. Sun, B. Huang, S. Yan et al., "Nanoconfined methane thermodynamic behavior below critical temperature: liquid–vapor coexistence curve under wettability effect," *Industrial & Engineering Chemistry Research*, vol. 61, no. 14, pp. 4971–4979, 2022.

[42] H. Yu, J. Fan, J. Xia, H. Liu, and H. Wu, "Multiscale gas transport behavior in heterogeneous shale matrix consisting of organic and inorganic nanopores," *Journal of Natural Gas Science and Engineering*, vol. 75, p. 103139, 2020.

[43] H. Yu, H. Xu, J. Fan, F. Wang, and H. Wu, "Roughness factor-dependent transport characteristic of shale gas through amorphous kerogen nanopores," *The Journal of Physical Chemistry C*, vol. 124, no. 23, pp. 12752–12765, 2020.

[44] T. Zhang, X. Li, X. Wang et al., "Modelling the water transport behavior in organic-rich nanoporous shale with generalized lattice Boltzmann method," *International Journal of Heat and Mass Transfer*, vol. 127, pp. 123–134, 2018.

[45] J. Huang, F. Xiao, C. Labra, J. Sun, and X. Yin, "DEM-LBM simulation of stress-dependent absolute and relative permeabilities in porous media," *Chemical Engineering Science*, vol. 239, p. 116633, 2021.

[46] M. Sheikholeslami, "Influence of magnetic field on Al_2O_3-H_2O nanofluid forced convection heat transfer in a porous lid driven cavity with hot sphere obstacle by means of LBM," *Journal of Molecular Liquids*, vol. 263, pp. 472–488, 2018.

[47] J. Zhao, J. Yao, L. Zhang, H. Sui, and M. Zhang, "Pore-scale simulation of shale gas production considering the adsorption effect," *International Journal of Heat and Mass Transfer*, vol. 103, pp. 1098–1107, 2016.

[48] J. Huang, X. Yin, M. Barrufet, and J. Killough, "Lattice Boltzmann simulation of phase equilibrium of methane in nanopores under effects of adsorption," *Chemical Engineering Journal*, vol. 419, p. 129625, 2021.

[49] G. Cao, M. Lin, W. Jiang et al., "A statistical-coupled model for organic-rich shale gas transport," *Journal of Petroleum Science and Engineering*, vol. 169, pp. 167–183, 2018.

[50] B. L. Liu, A. Suzuki, and T. Ito, "Effect of capillary force on performance of shale rock fracturing," *53rd US Rock Mechanics/Geomechanics Symposium*, 2019, New York City, June 2019, 2019.

[51] G. Sheng, H. Zhao, Y. Su et al., "An analytical model to couple gas storage and transport capacity in organic matter with noncircular pores," *Fuel*, vol. 268, p. 117288, 2020.

[52] F. Javadpour, H. Singh, A. Rabbani, M. Babaei, and S. Enayati, "Gas flow models of shale: a review," *Energy & Fuels*, vol. 35, no. 4, pp. 2999–3010, 2021.

[53] W. Song, J. Yao, K. Zhang, H. Sun, and Y. Yang, "The impacts of pore structure and relative humidity on gas transport in shale: a numerical study by the image-based multi-scale pore network model," *Transport in Porous Media*, pp. 1–25, 2021.

[54] Z. Yi, S. Hu, S. Wu, J. Ma, J. Gao, and Y. Yuan, "Pore network extraction for shale gas flow in nanoporous media," *Marine and Petroleum Geology*, vol. 126, p. 104896, 2021.

[55] Z. Sun, J. Shi, K. Wu et al., "Transport capacity of gas confined in nanoporous ultra-tight gas reservoirs with real gas effect and water storage mechanisms coupling," *International Journal of Heat and Mass Transfer*, vol. 126, pp. 1007–1018, 2018.

[56] R. Xu, M. S. Prodanović, and C. J. Landry, "Simulation of gas adsorption and capillary condensation in shale Nanopores using lattice Boltzmann modeling," in *SPE/AAPG/SEG Unconventional Resources Technology Conference*, Houston, Texas, USA, July 2018.

[57] Z. Song, Y. Song, J. Guo, Z. Zhang, and J. Hou, "Adsorption induced critical shifts of confined fluids in shale nanopores," *Chemical Engineering Journal*, vol. 385, p. 123837, 2020.

[58] F. Javadpour, D. Fisher, and M. Unsworth, "Nanoscale gas flow in shale gas sediments," *Journal of Canadian Petroleum Technology*, vol. 46, no. 10, 2007.

[59] B. Hu and J. G. Wang, "A lattice Boltzmann simulation on the gas flow in fractal organic matter of shale gas reservoirs," *Journal of Petroleum Science and Engineering*, vol. 210, p. 110048, 2022.

[60] Y. Li, P. Dong, and D. Zhou, "A dynamic apparent permeability model for shale microfractures: coupling poromechanics, fluid dynamics, and sorption-induced strain," *Journal of Natural Gas Science and Engineering*, vol. 74, p. 103104, 2020.

[61] Z. Liehui, S. Baochao, Z. Yulong, and G. Zhaoli, "Review of micro seepage mechanisms in shale gas reservoirs," *International Journal of Heat and Mass Transfer*, vol. 139, pp. 144–179, 2019.

[62] S. Zhan, Y. Su, Z. Jin, W. Wang, and L. Li, "Oil-water two-phase flow behavior in shale inorganic nanopores: from molecule level to theoretical mathematical model," in *Unconventional Resources Technology Conference*, December 2020.

[63] N. Sobecki, C. Nieto-Draghi, A. Di Lella, and D. Y. Ding, "Phase behavior of hydrocarbons in nano-pores," *Fluid Phase Equilibria*, vol. 497, pp. 104–121, 2019.

[64] C. Herdes, C. Petit, A. Mejia, and E. A. Muller, "Combined experimental, theoretical, and molecular simulation approach for the description of the fluid-phase behavior of hydrocarbon mixtures within shale rocks," *Energy & Fuels*, vol. 32, no. 5, pp. 5750–5762, 2018.

[65] S. Luo, J. Lutkenhaus, and H. Nasrabadi, "A framework for incorporating nanopores in compositional simulation to model the unusually high GOR observed in shale reservoirs," *SPE Reservoir Simulation Conference*, 2019, Galveston, Texas, USA, 2019, 2019.

[66] X. Zheng, B. Zhang, H. Sanei et al., "Pore structure characteristics and its effect on shale gas adsorption and desorption behavior," *Marine and Petroleum Geology*, vol. 100, pp. 165–178, 2019.

[67] K. Zeng, P. Jiang, Z. Lun, and R. Xu, "Molecular simulation of carbon dioxide and methane adsorption in shale organic nanopores," *Energy & Fuels*, vol. 33, no. 3, pp. 1785–1796, 2019.

[68] K. Zhang, L. Liu, and G. Huang, "Nanoconfined water effect on CO2 utilization and geological storage," *Geophysical Research Letters*, vol. 47, no. 15, p. e2020GL087999, 2020.

[69] K. Zhang, N. Jia, S. Li, and L. Liu, "Quantification and evaluation of thermodynamic miscibility in nanoconfined space," *Industrial & Engineering Chemistry Research*, vol. 58, no. 11, pp. 4609–4624, 2019.

[70] D. Feng, S. Bakhshian, K. Wu et al., "Wettability effects on phase behavior and interfacial tension in shale nanopores," *Fuel*, vol. 290, p. 119983, 2021.

[71] K. Zhang, N. Jia, and L. Liu, "CO2 storage in fractured nanopores underground: phase behaviour study," *Applied Energy*, vol. 238, pp. 911–928, 2019.

[72] J. Xie, M. K. Borg, L. Gibelli, O. Henrich, D. A. Lockerby, and J. M. Reese, "Effective mean free path and viscosity of confined gases," *Physics of Fluids*, vol. 31, no. 7, article 072002, 2019.

[73] D. Chai, Z. Fan, and X. Li, "A new unified gas-transport model for gas flow in nanoscale porous media," *SPE Journal*, vol. 24, no. 2, pp. 698–719, 2019.

[74] M. He, Y. Zhou, B. Chen et al., "Effect of pore structure on slippage effect in unsaturated tight formation using pore network model," *Energy & Fuels*, vol. 35, no. 7, pp. 5789–5800, 2021.

[75] G. Karniadakis, A. Beskok, and N. Aluru, *Microflows and Nanoflows: Fundamentals and Simulation*, Springer Science & Business Media, 2006.

[76] K. Wu, Z. Chen, X. Li, C. Guo, and M. Wei, "A model for multiple transport mechanisms through nanopores of shale gas reservoirs with real gas effect-adsorption-mechanic coupling," *International Journal of Heat and Mass Transfer*, vol. 93, pp. 408–426, 2016.

[77] K. Wu, X. Li, C. Wang, W. Yu, and Z. Chen, "Model for surface diffusion of adsorbed gas in nanopores of shale gas reservoirs," *Industrial & Engineering Chemistry Research*, vol. 54, no. 12, pp. 3225–3236, 2015.

[78] W. Pang and Z. Jin, "Ono-Kondo lattice model for propane multilayer adsorption in organic nanopores in relation to shale gas," *Fuel*, vol. 235, pp. 158–166, 2019.

[79] G. Sheng, Y. Su, F. Javadpour et al., "New slip coefficient model considering adsorbed gas diffusion in shale gas reservoirs," *Energy & Fuels*, vol. 34, no. 10, pp. 12078–12087, 2020.

[80] S. Alafnan, A. Awotunde, G. Glatz, S. Adjei, I. Alrumaih, and A. Gowida, "Langmuir adsorption isotherm in unconventional resources: applicability and limitations," *Journal of Petroleum Science and Engineering*, vol. 207, p. 109172, 2021.

[81] S. Huang, Y. Wu, L. Cheng, H. Liu, Y. Xue, and G. Ding, "Apparent permeability model for shale gas reservoirs considering multiple transport mechanisms," *Geofluids*, vol. 2018, 18 pages, 2018.

[82] S. K. Loyalka and S. A. Hamoodi, "Poiseuille flow of a rarefied gas in a cylindrical tube: solution of linearized Boltzmann equation," *Physics of Fluids A*, vol. 2, no. 11, pp. 2061–2065, 1990.

[83] S. A. Tison, "Experimental data and theoretical modeling of gas flows through metal capillary leaks," *Vacuum*, vol. 44, no. 11-12, pp. 1171–1175, 1993.

[84] E. R. Gilliland, R. F. Baddour, G. P. Perkinson, and K. J. Sladek, "Diffusion on surfaces. I. Effect of concentration on the diffusivity of physically adsorbed gases," *Industrial and Engineering Chemistry Fundamentals*, vol. 13, no. 2, pp. 95–100, 1974.

[85] Y. T. Yeh, *Diffusion and Adsorption of Gases in Molecular Sieves (PhD Diss.)*, State University of New York, Buffalo, 1989.

[86] D. M. Ruthven and K. F. Loughlin, "Correlation and interpretation of zeolitic diffusion coefficients," *Transactions of the Faraday Society*, vol. 67, pp. 1661–1671, 1971.

[87] D. Liu, H. Ge, Y. Shen, H. Liu, and Y. Zhang, "Experimental investigation on imbibition characteristics of shale with highly developed bedding fractures," *Journal of Natural Gas Science and Engineering*, vol. 96, p. 104244, 2021.

[88] M. Arif, M. Mahmoud, Y. Zhang, and S. Iglauer, "X-ray tomography imaging of shale microstructures: a review in the context of multiscale correlative imaging," *International Journal of Coal Geology*, vol. 233, p. 103641, 2021.

Hindawi
Geofluids
Volume 2022, Article ID 2339395, 10 pages
https://doi.org/10.1155/2022/2339395

Research Article

Effect Evaluation of Nanosilica Particles on O/W Emulsion Properties

Guanzheng Qu,[1] **Jian Su**,[2] **Tao Shi**,[3] **Rui Guo**,[4] **and Jiao Peng**[5]

[1]*School of Petroleum Engineering, Xi'an Shiyou University, Xi'an 710065, China*
[2]*Drilling and Production Technology Research Institute of Liaohe Oilfield, Panjin 124000, China*
[3]*No. 8 Oil Production Plant, Changqing Oilfield, CNPC, Xi'an 710018, China*
[4]*Directional Well Service Branch, Bohai Drilling Engineering Company Limited, CNPC, Tianjin 300457, China*
[5]*School of Aeronautics, Northwestern Polytechnical University, Xi'an 710072, China*

Correspondence should be addressed to Guanzheng Qu; quguanzheng@126.com

Received 15 February 2022; Revised 9 May 2022; Accepted 10 May 2022; Published 24 May 2022

Academic Editor: Tao Zhang

O/W emulsion reinforced by nanosilica particle has good application in hydrocarbon development. However, there are few reports on the influence of nanosilica particles on the oil-water interface of O/W emulsion. The effect of nanosilica particles on the interfacial properties of O/W emulsion was indirectly investigated by measuring the interfacial properties between aqueous dispersion of nanosilica particles and kerosene, and the properties of O/W emulsion reinforced by nanosilica particle were studied. The results showed that the aqueous dispersion of nanosilica particles could significantly reduce the interface tension (with kerosene) by more than 50%, and the interface tension between the aqueous dispersion and kerosene decreased with the increase in nanosilica content. The aqueous dispersion of nanosilica particles could significantly change rock wettability. When the content of nanosilica particles increased from 0.1% to 0.7%, the contact angle decreased from 44.89° to 27.62°. The surface tension of O/W emulsion prepared by the aqueous dispersion of nanosilica particles and kerosene was among 25 mN/m~30 mN/m. The contact angle was also particularly small, with an average of about 20.00°, a minimum of 12.50°. The salts had little effect on the interface tension of emulsions but had a significant influence on the contact angle and its stability. Magnesium salt could reduce the three-phase contact angle and increase the hydrophilic properties of O/W emulsion, while calcium salt had the opposite effect. Calcium salt and magnesium salt could reduce the stability of the emulsion, and calcium salt had a greater influence. The oil-water stratification adding either calcium salt or magnesium salt was about 1 day~3 days earlier than that without salts. In the experiment, when the content of nanosilica particles was among 0.3%~0.7%, the viscosity of O/W emulsion increased with the increase in nanosilica particles. When the content was 0.9%, the viscosity suddenly decreased, and the extent of reduction was about 21.7%. The findings of this study can help for better understanding the application of nanosilica particles in O/W emulsion, giving some suggestions for the application of nanoparticles in hydrocarbon development.

1. Introduction

With the increasing depletion of hydrocarbon resources and the increasingly prominent contradiction between supply and demand, it has always been the hot issue to dig the development potential of the reservoir after water flooding and further improve both the utilization degree of the reservoir and the resource recovery in the field of hydrocarbon resource development [1–4]. Therefore, various methods have been used in the attempt to improve oil recovery [5–9]. Fracturing and acidizing are two mainly recommended methods for reservoir stimulation, and the role of the stimulation techniques is to improve the seepage capacity of the reservoir and reduce the seepage resistance [10, 11]. For conventional low-permeability reservoirs, they can accelerate the production rate, and for ultra-low-permeability

reservoirs such as shale and tight sandstone reservoirs, it can help to improve the ultimate recovery [12–14]. The chemical flooding has always been the most commonly employed techniques for enhancing oil recovery [15–18], such as surfactant flooding, polymer flooding, alkali flooding, emulsion flooding, and various chemical combination flooding. The mechanism of enhancing oil recovery by chemical flooding has two aspects: increasing sweep efficiency and enhancing oil displacement efficiency. Besides, CO_2 flooding and foam flooding are also widely applied for enhancing oil recovery [19, 20] and their mechanism is similar to that of chemical flooding.

Among them, emulsion flooding is one of the most important methods to enhance oil recovery [21, 22] and shows a good application further in enhanced oil recovery after water flooding. Meanwhile, studies have shown that in situ emulsification of crude oil is also an important means to enhance oil recovery, especially for heavy oil reservoirs [23–26]. Besides, there are also reports on the application of emulsion combined with carbon dioxide or foam to enhance oil recovery [27, 28].

As an oil-water composite system, O/W emulsion has good application in both adjusting the flow profile of reservoir fluid and improving the fluid sweep coefficient. Besides, in recent years, with the development of nanotechnology and the integration of interdisciplinary approaches, nanotechnology has been gradually applied to various fields of reservoir development, showing good applications [29–32].

Nanotechnology is the design and application of engineered or naturally occurring nanoparticles with the order of 1-100 nm to accomplish specific purposes [33–35]. Nanoparticles possess two unique properties of ultrasmall particle size and ultra-high-specific surface area. And material properties are sized dependent at the nanoscale; therefore, nanoparticles can be engineered to contain specific optical, magnetic, interfacial, thermal, electrical, or chemical properties to perform specific functions. Combined together, these unique properties allow nanoparticles to be used for many purposes in the oilfield. Nanosilica, nanoalumina, nanotitanium dioxide, nanoferric oxide, and nanocopper oxide are all the nanomaterials used in the development of hydrocarbon resources [36–38], and they are served in various aspects such as drilling fluid filtration reduction [39, 40], cementing [41, 42], temperature sensor and thermal conductivity improvement [43], slow release of surfactant [44], tracer, foam, and emulsion stability improvement [45–49], fracturing fluid performance improvement [50, 51], EOR, and oily sewage treatment [37, 38, 52, 53], achieving good results. Besides, the retention and adsorption of nanoparticles in porous media and their influence on fluid transportation are also reported [54–59]. Most of the above reports on the application of nanoparticles in hydrocarbon development are about nanosilica particles. And nanosilica particles are widely favored in reservoir development due to their wide source and high cost performance.

In the reports on the emulsion stabilized by nanoparticles, it was mainly about the effect of emulsion on enhancing oil recovery with the synergies of nanoparticles. However, there were few reports especially on the effect of nanoparticles on the interfacial properties of O/W emulsion.

However, it is very important to study the effect of nanosilica particles on the oil-water interface properties of O/W emulsion for understanding the mechanism of nanosilica particles strengthening O/W emulsion, and it can provide reference for the application of nanoparticles in hydrocarbon development.

The previous reports were mostly about the application of nanosilica particles in oil and gas development, and there are no reports about the effect of nanosilica particles on oil-water interface properties of O/W emulsion. In the O/W emulsion system, nanosilica particles tend to adsorb on the oil-water interface due to the difference between oil and water, changing the interfacial properties, so as to change the properties of O/W emulsion.

Therefore, it is of great significance to study the effect of nanosilica particles on the oil-water interface of emulsion. However, there are no methods or means to directly determine the interfacial properties of O/W emulsion currently. In order to study the effect of nanosilica particles on O/W emulsion, the O/W emulsion interface reinforced by nanosilica particles is regarded as the interface between the aqueous solution of nanosilica particle and the oil phase. The oil-water interfacial properties of the O/W emulsion are approximately characterized by measuring the interfacial properties between the two phases. And the general sketch of the study is shown in Figure 1.

This method has some certain limitations. Since the homogeneous O/W emulsion reinforced by nanosilica particle is regarded as two phases—the aqueous solution of nanosilica particles and oil phase, this method can only qualitatively analyze the influence of nanosilica particles on the interfacial properties of O/W emulsion. It is necessary to explore other experimental methods to accurately describe the distribution of nanosilica particles in the O/W emulsion system and the influence of nanosilica particles on the oil-water interfacial properties in O/W emulsion. Besides, the study is only carried out with the temperature 30°C, without investigating the effect of other temperatures.

In the study, different concentrations of nanosilica aqueous solution and O/W emulsion reinforced by nanosilica were firstly prepared, respectively. Then, the surface tension of nanosilica aqueous solution, the interfacial tension between nanosilica aqueous solution and kerosene, and the contact angle of nanosilica aqueous solution were investigated with different concentrations of nanosilica. After that, the effects of nanosilica particles on the stability and viscosity of O/W emulsion were investigated. Finally, the effects of salt content on the stability of O/W emulsion reinforced by nanosilica and the properties of O/W emulsion reinforced by nanosilica in the presence of sodium ions and magnesium ions were also investigated. Totally, the experimental procedure can be summarized as shown in Figure 2.

2. Laboratory Experiments

2.1. Experimental Apparatus and Chemicals. Experimental apparatus mainly include an SFZL-A automatic surficial/interfacial tensiometer, balance, blender, HWY-10 thermostat

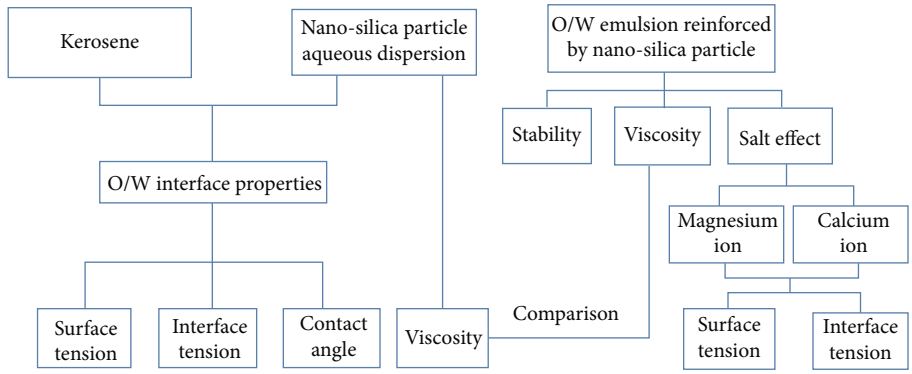

Figure 1: The general sketch of the study.

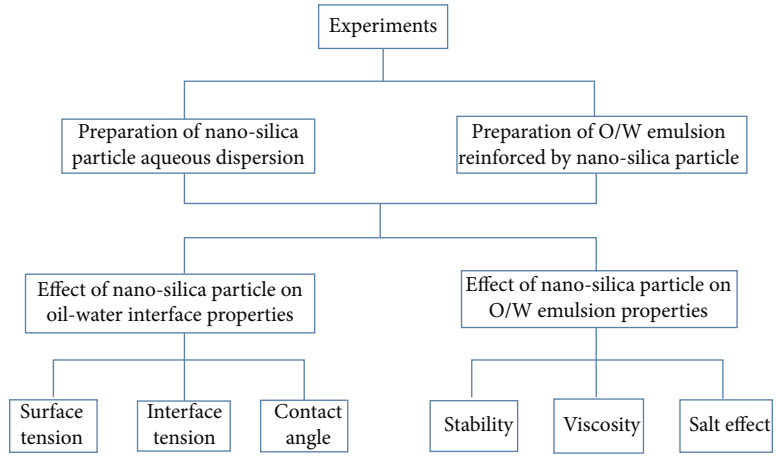

Figure 2: The flowchart of the experiments.

water bath, JGW-360a contact angle meter, rotary viscometer, etc.

The main chemicals used in the experiment are nanosilica particles (mean particle size 20 nm), emulsifier FC, distilled water, kerosene, calcium chloride, magnesium chloride, etc.

2.2. Experimental Methods

2.2.1. Preparation of O/W Emulsion. Firstly, nanosilica particles and emulsifier FC were added to the beaker, and then, the mixture was diluted with distilled water to the required concentration. The nanosilica particles and emulsifier were fully dispersed in distilled water by stirring for 5 minutes in a constant speed blender. Then, kerosene was added to the beaker and stirred at a high speed for 20 minutes in a constant speed blender to obtain O/W emulsion reinforced by nanosilica particles.

2.2.2. Effect of Nanosilica Particles on Oil-Water Interface Properties. The nanosilica particles were added into distilled water and fully stirred, so that the nanosilica particles were fully dispersed in distilled water, and the aqueous dispersion of nanosilica particles was obtained. The interface properties between nanosilica particle dispersion and kerosene were evaluated by using the SFZL-A automatic surficial/interfacial tensiometer and JGW-360a contact angle meter, and the effect of nanosilica particles on the oil-water interface properties was quantified.

2.2.3. Effect of Nanosilica Particles on O/W Emulsion Properties. O/W emulsions reinforced by different contents of nanosilica particles were prepared, and the stability, rheological properties, and salt resistance of O/W emulsions with nanosilica particles were evaluated. The main instruments included the NDJ-85 rotary viscometer and HWY-10 thermostat water bath.

3. The Experiment Result Analysis

3.1. Effect Evaluation of Nanosilica Particles on Interface Properties. The oil-water interface has a direct impact on the emulsion properties; however, the oil-water interface properties of O/W emulsion cannot be directly measured and characterized. Interface tension and contact angle are two commonly recommended parameters to characterize the interface properties. So considering the adsorption of nanosilica particles on the oil-water interface, the interface tension and contact angle between the aqueous dispersion of nanosilica particles and kerosene were measured, and the effect of the nanosilica particle adsorption on the oil-water interface properties of the emulsion was indirectly quantified by interface tension and contact angle.

3.1.1. Surface Tension of Aqueous Dispersion with Nanosilica Particles. The aqueous dispersions of nanosilica particles with the contents of 0.1%, 0.3%, 0.5%, 0.7%, and 0.9% were prepared, respectively. The surface tension of aqueous dispersions with different contents of nanosilica particles was measured, and the surface tension of distilled water was used as a reference to clarify the effect of nanosilica particles on the surface tension of aqueous dispersion. In order to ensure the accuracy of the measurements, the surface tension was measured several times and their average was taken as the value of surface tension. The specific results are shown in Figure 3.

It could be obtained from Figure 3 that the surface tension of aqueous dispersion with nanosilica particles showed the explicit trend of declining with the increase in nanosilica particle content. When the content of nanosilica particles was among 0.1%~0.5%, the surface tension decreased rapidly. When the content of nanosilica particles was about 0.5%, the surface tension decreased with the increase in the nanoparticle contents. While the content of nanosilica particles was 0.9%, the surface tension reached the minimum, 54.33 mN/m.

The nanosilica particles in the aqueous dispersion tended to be gradually adsorbed on the surface of the dispersion, with the influence of the interfacial difference between the dispersion and the air, and the adsorption amount increased with the content of nanosilica particle increasing, thus reducing surface tension of the aqueous dispersion.

3.1.2. Interface Tension between Aqueous Dispersion of Nanosilica Particles and Kerosene. The aqueous dispersions of nanosilica particles with the contents of 0.1%, 0.3%, 0.5%, 0.7%, and 0.9% were prepared, respectively, and the interface tensions between aqueous dispersions with different contents of nanosilica particles and kerosene were measured.

The interface tension between water and kerosene was taken as the reference, and the specific results are shown in Figure 4. The interface tension between aqueous dispersion of nanosilica particles and kerosene decreased rapidly and fluctuated slightly with the increase in nanosilica particle content. Overall, there was little difference in interfacial tension between aqueous dispersion with different silica contents and kerosene, and the interface tension between them fluctuated in the range of 17 mN/m~19 mN/m, which was significantly less than that between kerosene and water (40.26 mN/m).

The nanosilica particles in aqueous dispersion were adsorbed on the oil-water interface due to the difference in properties at the oil-water interface, which played a role in reducing the interface tension. Moreover, the ability of nanosilica particles to reduce the interface tension was related to their adsorption capacity. As solid particles, the adsorption capacity of nanosilica particles on the oil-water interface was limited, so the adsorption capacity on the interface had reached saturation with small content of nanosilica particles. Therefore, the ability to reduce the interface tension no longer increased with the increase in nanosilica particle content.

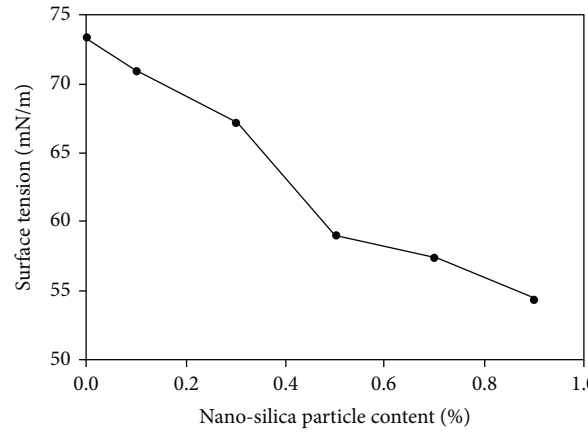

Figure 3: Relationship between nanosilica particle content and surface tension.

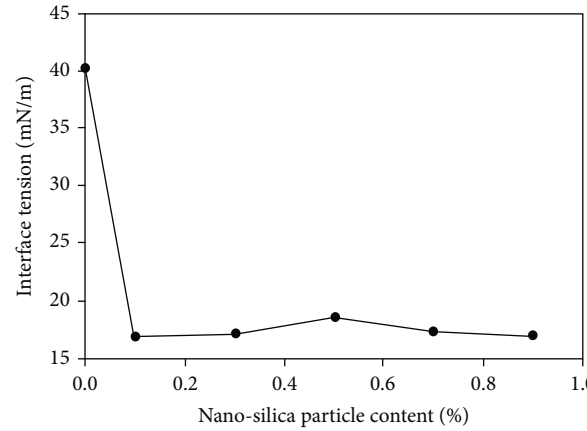

Figure 4: Relationship between nanosilica particle content and interface tension.

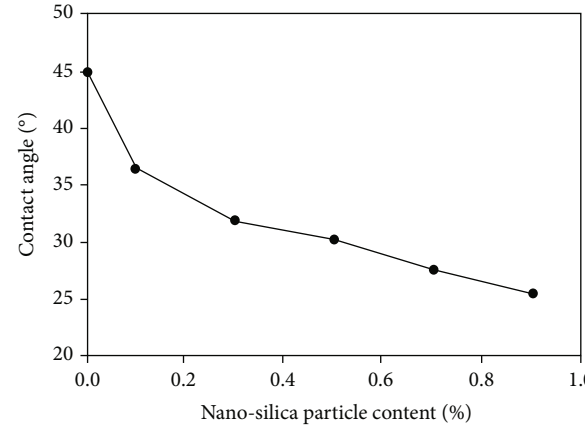

Figure 5: Relationship between nanosilica particle content and contact angle.

3.1.3. Contact Angle of Aqueous Dispersions with Nanosilica Particles. The contact angles of aqueous dispersion with different contents of nanosilica particle were measured, and the specific results are shown in Figure 5.

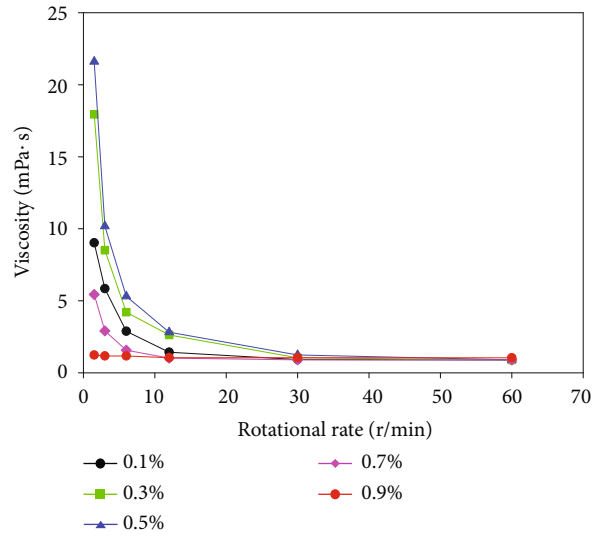

Figure 6: Shear thinning of nanosilica particle aqueous dispersion.

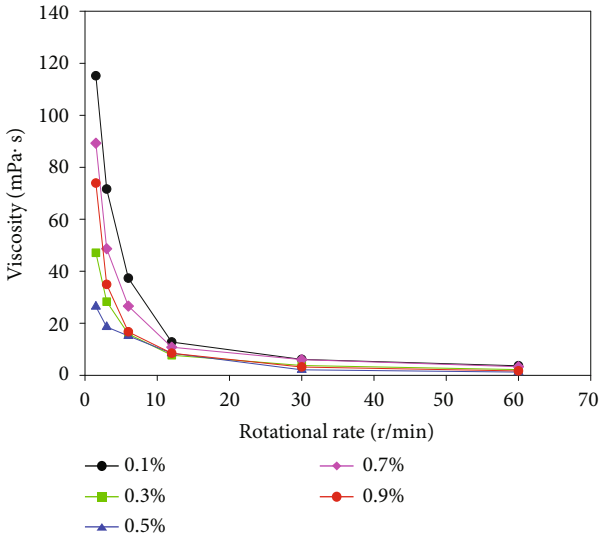

Figure 7: Relationship between the rotational rate and emulsion viscosity.

It could be seen from Figure 5 that with the increase in nanosilica particle content, the contact angle of aqueous dispersion with nanosilica particles showed a declining trend. When the content of nanosilica particles was 0.9%, the contact angle reached the minimum, about 25.56°. Since the measured contact angle is the angle between nanosilica aqueous dispersion and air on the interface of the glass slide and the main components of nanosilica particles and glass slide are basically the same, the adsorption amount of nanosilica particles on the surface of the glass slide increased with the increase in their content, and their adsorption capacity on the interface of aqueous dispersion and air was limited. Therefore, the three-phase contact angle increased with the increase in nanosilica particle content.

Figure 6 shows the relationship between the rotational rate and the viscosity of nanosilica particle aqueous dispersion at temperature 30°C. And the curves of different colors represented different contents of nanosilica particles. The aqueous dispersion of nanosilica particle had the significant phenomenon of shear dilution, and the viscosity decreased rapidly with the increase in rotational speed. The rotational rate of 30 r/min was the critical rate; when the rotational rate was less than 30 r/min, the viscosity of different nanosilica aqueous dispersions decreased rapidly with the increase in the rotational rate. In the study, when the content of nanosilica particle was 0.5%, the viscosity of O/W emulsion was maximum, followed by that of 0.3%, 0.1%, 0.7%, and 0.9%. When the content of nanosilica particle was 0.9%, the viscosity of O/W emulsion remained basically constant, and the rotational rate had little effect on the viscosity. Then, when the rotational rate was greater than 30 r/min, the viscosity of O/W emulsion was basically stable and no longer varied with the rotational rate, and the viscosity difference among O/W emulsions with different contents of nanosilica particle was small. And the viscosity of nanosilica particle aqueous dispersions was different when the content of nanosilica particle changed.

3.2. Effect Evaluation of Nanosilica Particles on O/W Emulsion Properties. After the effect of nanosilica particles on the interface properties of O/W emulsion was obtained, the stability, viscosity, and salt resistance of O/W emulsion reinforced by nanosilica particles were also systematically evaluated. And all the O/W emulsions in the study were prepared with the volume ratio between oil and water being 3 : 7.

3.2.1. Effect of Nanosilica Particles on Emulsion Stability. The O/W emulsions with the content of nanosilica particle among 0.1%~0.9% were prepared, and the effect of nanosilica particle on the stability of O/W emulsion was investigated. As a solid medium, nanosilica particles could adsorb on the oil-water interface to stabilize O/W emulsion. The observation period was ten days. During the first two days, the O/W emulsions were observed every two hours, and on the third day to the tenth day, the O/W emulsions were observed every half day. And after ten days, the O/W emulsions reinforced by nanosilica particle were still evenly distributed and had good stability, without stratification or precipitation. The nanosilica particles adsorbed on the interface of O/W emulsion could form a network structure, and the composite structure could improve the stability of the interface film, thereby improving the stability of the emulsion. The stability of the emulsion increased with the increase in nanoparticle content.

3.2.2. Effect Evaluation of Nanosilica Particles on the Viscosity of O/W Emulsion. The relationship between the rotational rate and the viscosity of O/W emulsion reinforced by nanosilica particles is shown in Figure 7, and the viscosity was measured at temperature 30°C. The curves of different colors in Figure 7 represented the different contents of nanosilica particles. The viscosity of O/W emulsion decreased as the rotational rate increased, and when the rotational rate was greater than 30 r/min, the viscosity of O/W emulsion

with different contents of nanosilica particles was almost the same. However, when the rotational rate was less than 30 r/min, O/W emulsion with different contents of nanosilica particles showed the phenomenon of shear thinning. The viscosity of O/W emulsion was not positively correlated with the content of nanosilica particles, and it showed that the emulsion with the content of nanosilica particle 0.1% had the highest viscosity, followed by that with the content of nanosilica particle 0.7%, 0.9%, and 0.5%, and when the content of nanosilica particle was 0.3%, O/W emulsion had the lowest viscosity. The viscosity difference between emulsions was related to the content of nanosilica particle, its adsorption capacity on O/W interface, adhesion state, and emulsion particle size, and it was a complicated process.

3.2.3. Viscosity Comparison between Aqueous Dispersion and O/W Emulsion. The rotational rate of 12 r/min was adopted to measure the viscosity of the aqueous dispersion of nanosilica particles and O/W emulsion reinforced by nanosilica particles, and the content of nanosilica particles in both aqueous dispersion and O/W emulsion was 0.1%, 0.3%, 0.5%, 0.7%, and 0.9%, respectively. Besides, the viscosity of aqueous dispersion without nanosilica particles was taken as the reference. As shown in Figure 8, the viscosity of aqueous dispersion with nanosilica particles was a little higher than that without nanosilica particles, and with the content of nanosilica particles increasing, the viscosity of aqueous dispersion with nanosilica particles showed the trend of increasing firstly and then decreasing. And when the content of nanosilica particles was 0.5%, the viscosity of the aqueous dispersion reached the maximum, 2.82 mPa·s. When the content of nanosilica particles was 0.7%, the viscosity of the aqueous dispersion reached the minimum, 1.02 mPa·s, almost the same as that without nanosilica particles, and was about one-third of that with the content of nanosilica particles 0.5%. The viscosity difference between different aqueous dispersions was due to the uneven distribution of nanosilica particles in the dispersion.

The viscosity of O/W emulsion reinforced by nanosilica particles was obviously higher than that of aqueous dispersion while the content of nanosilica particles was the same. As for the O/W emulsion reinforced by nanosilica particles, when the content of nanosilica particles was 0.1%, the viscosity of O/W emulsion reached the maximum, 12.77 mPa·s. However, when the content of nanosilica particles was 0.3%, the viscosity of O/W emulsion reached the minimum, 7.71 mPa·s. When the content of nanosilica particles was higher than 0.3%, the viscosity showed the trend of increasing firstly and then decreasing. When the content of nanosilica particles was 0.1%, there were no enough nanosilica particles to stabilize O/W emulsion, so the system was unstable and the viscosity showed much higher. When the content of nanosilica particles increased, the O/W emulsion tended to be stable and the emulsion particles tended to be smaller, showing an increase in viscosity. And when the content of nanosilica particles was 0.9%, the nanosilica particles were excessive, and the equilibrium of the system was disturbed, showing a decrease in viscosity.

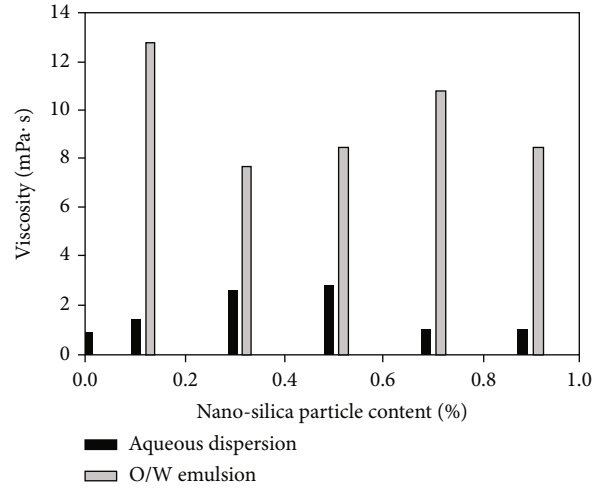

Figure 8: Viscosity comparison between aqueous dispersion and O/W emulsion.

3.2.4. Effect Evaluation of Salt Content on the Performance of O/W Emulsion Reinforced by Nanosilica Particles. From the above experimental evaluation, the stability and viscosity properties of O/W emulsion with the content of nanosilica particles 0.7% were better than those with other content, and it could significantly reduce both interface tension and contact angle. So during the evaluation, the content of nanosilica particles in O/W emulsion was chosen as 0.7%.

(1) Effect of Salt on Emulsion Stability. As for the effect of salt on the stability of emulsion, both magnesium salt and calcium salt were used to study their effects on the stability of emulsion, and the salt contents were selected as 0.008 mol/L, 0.010 mol/L, and 0.020 mol/L, respectively. The observation period was ten days, and during the first two days, the O/W emulsions were observed every two hours, and on the third day to the tenth day, the O/W emulsions were observed every half day.

After ten days of observation, the O/W emulsion was slightly transparent in the beaker with the magnesium salt content of 0.020 mol/L, followed by the magnesium salt content of 0.010 mol/L. Therefore, it could be found that the magnesium salt has the negative effect on the stability of O/W emulsion, and the higher the content of magnesium salt, the greater the effect on the stability of the emulsion. However, on the whole, the emulsion with different contents of magnesium salts still had good stability. With regard to the effect of calcium ion, it was found that with the increase in calcium ion, more transparent liquid was separated from the upper layer of O/W emulsion. By ten days, there were about 4 mm height precipitates in the beaker when the content of calcium ion was 0.020 mol/L, and there were obvious floccules in the stratification part. Therefore, calcium ion also had a certain inhibitory effect on the stability of O/W emulsion, and the effect was positively correlated with calcium ion content. On the whole, the effect of calcium salt on the stability of O/W emulsion was higher than that of magnesium salt.

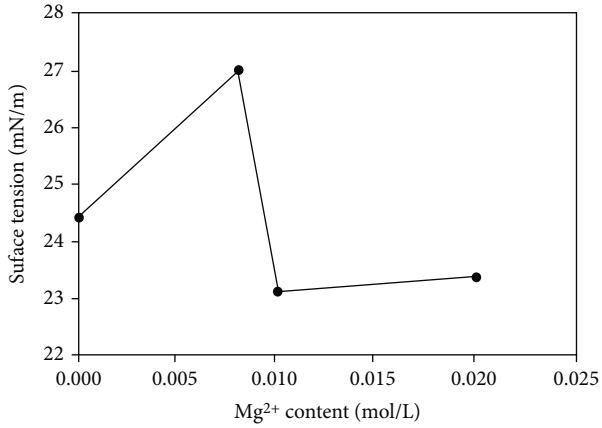

Figure 9: Relationship between Mg^{2+} content and emulsion surface tension.

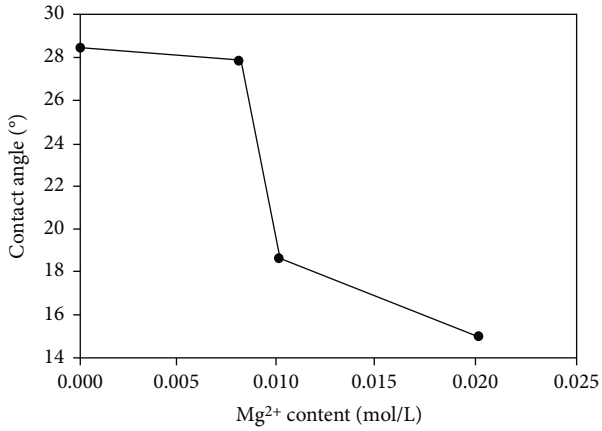

Figure 10: Relationship between Mg^{2+} content and emulsion contact angle.

The addition of inorganic salts was conducive to reducing the charge number of the interface film, compressing the thickness of the double layer, reducing the repulsion between the emulsion droplets, and facilitating the coalescence, thus effectively accelerating the demulsification of emulsions. The demulsification efficiency was related to the ionic valence state and the radius of hydrated ions.

(2) Magnesium Ion (Mg^{2+}). During the evaluation, the contents of Mg^{2+} were chosen as 0.008 mol/L, 0.010 mol/L, and 0.020 mol/L, respectively, and the effects of Mg^{2+} on surface tension, contact angle, and the stability of O/W emulsion reinforced by nanosilica particles were studied.

As shown in Figure 9, generally, with the increase in Mg^{2+} content, the surface tension of O/W emulsion reinforced by nanosilica particles first increased and then decreased and stabilized. When Mg^{2+} content was 0.008 mol/L, the viscosity of O/W emulsion reached the maximum, about 26.99mN/m. When Mg^{2+} content increased from 0.008 mol/L to 0.010 mol/L, the surface tension of O/W emulsion decreased greatly. After Mg^{2+} content was greater than 0.010 mol/L, the surface tension showed a stable trend.

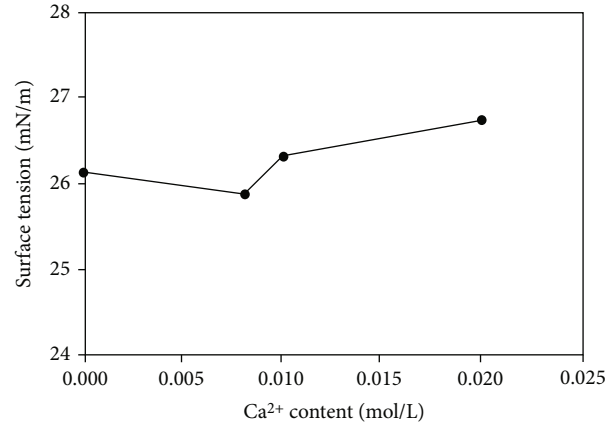

Figure 11: Relationship between Ca^{2+} content and emulsion surface tension.

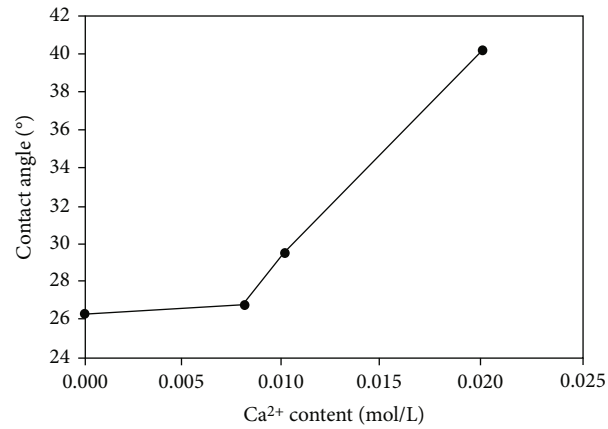

Figure 12: Relationship between Ca^{2+} content and emulsion contact angle.

As shown in Figure 10, with the increase in Mg^{2+} content, the contact angle of O/W emulsion reinforced by nanosilica particles generally showed a decreased trend, and Mg^{2+} content of 0.010 mol/L was taken as the critical point; when Mg^{2+} content was greater than 0.010 mol/L, the decreased amplitude was a little greater.

(3) Calcium Ion (Ca^{2+}). For the convenience of comparison, the content of Ca^{2+} in the experiment should correspond to the content of Mg^{2+}, and the contents of Ca^{2+} were chosen as 0.008 mol/L, 0.010 mol/L, and 0.020 mol/L, respectively. The evaluation parameters were also the same, namely, surface tension, contact angle, and emulsion stability, respectively.

As shown in Figure 11, with the increase in Ca^{2+} content, the surface tension of O/W emulsion reinforced by nanosilica particles generally showed the trend of decreasing firstly and then increasing and being stable, which almost showed the opposite trend of the effect of Mg^{2+}. The surface tension of O/W emulsion reinforced by nanosilica particles affected by Ca^{2+} was limited to 26 mN/m~27 mN/m, whose fluctuation was much smaller than that affected by

Mg^{2+}. It showed that the surface tension of O/W emulsion was related to not only ion content but also ion type.

As shown in Figure 12, the contact angle of O/W emulsion reinforced by nanosilica particles generally increased with the content of Ca^{2+} increasing. When Ca^{2+} content was 0.020 mol/L, the contact angle was about 1.5 times that without Ca^{2+}. Ca^{2+} content of 0.010 mol/L was taken as the critical point; when Ca^{2+} content was greater than 0.010 mol/L, the contact angle increased rapidly with the increase in Ca^{2+} content. However, while Ca^{2+} content was less than 0.010 mol/L, the contact angle increased slowly with the increase in Ca^{2+} content. So, as the content of Ca^{2+} increased, the hydrophobicity of O/W emulsion increased gradually.

4. Summary and Conclusions

(1) The aqueous dispersion of nanosilica particles could significantly reduce the interface tension (with kerosene), and the extent of reduction was more than 50%. In terms of reducing the interface tension, the interface tension was 17.02 mN/m when the content of nanosilica particles was 0.9%. And the interface tension was 16.96 mN/m while the content was 0.1%. The decrease in interface tension was not positively correlated with the content of nanosilica particles

(2) The aqueous dispersion of nanosilica particles could significantly change rock wettability. When the content of nanosilica particles increased from 0.1% to 0.7%, the contact angle decreased from 44.89° to 27.62°, showing a strong hydrophilic property. The relationship between contact angle and the content of nanosilica particles was not linear

(3) The surface tension of O/W emulsion reinforced by nanosilica particles was among 25 mN/m~30 mN/m, which was at a low value. The contact angle was also very small, with the average of about 20.00° and a minimum of 12.50°, showing a strong hydrophilic property

(4) The salts had little effect on interface tension of O/W emulsion reinforced by nanosilica particles but had a significant effect on the contact angle and stability of O/W emulsion. In the experiment, magnesium salt could reduce the three-phase (O/W emulsion, air, and glass slip) contact angle and increase the hydrophilic properties of O/W emulsion, while calcium salt had the opposite effect

(5) Both calcium salt and magnesium salt could reduce the stability of O/W emulsion reinforced by nanosilica particles. The stability of O/W emulsion without either calcium salt or magnesium salt was about 10 days, but the oil-water stratification adding either calcium salt or magnesium salt was about 1 day~3 days earlier than that without salts; besides, calcium salt had a greater impact on the stability of O/W emulsion

(6) When the nanosilica particle content was among 0.3%~0.7%, the viscosity of O/W emulsion increased with the increase in nanosilica particle content. When the content of nanosilica particles was 0.9%, the viscosity suddenly decreased, and the maximum extent of reduction was 21.7%

Data Availability

The data used to support the findings of this study are available from the corresponding author upon request.

Conflicts of Interest

The authors declare that they have no conflicts of interest.

Acknowledgments

The study was funded by the Natural Science Basic Research Program of Shaanxi (2019JQ-488) and Youth Program of National Natural Science Foundation of China (51804255).

References

[1] M. T. G. Janssen, R. M. Pilus, and P. L. J. Zitha, "A comparative study of gas flooding and foam-assisted chemical flooding in Bentheimer sandstones," *Transport in Porous Media*, vol. 131, no. 1, pp. 101–134, 2020.

[2] S. Park, E. S. Lee, and W. Sulaiman, "Adsorption behaviors of surfactants for chemical flooding in enhanced oil recovery," *Journal of Industrial & Engineering Chemistry*, vol. 21, pp. 1239–1245, 2015.

[3] J. E. Parra, G. A. Pope, M. Mejia, and M. T. Balhoff, "New approach for using surfactants to enhance oil recovery from naturally fractured oil-wet carbonate reservoirs," in *SPE Technical Conference & Exhibition*, Dubai, UAE, 2016.

[4] Z. Wu, H. Liu, and X. Wang, "3D experimental investigation on enhanced oil recovery by flue gas coupled with steam in thick oil reservoirs," *Energy & Fuels*, vol. 32, no. 1, pp. 279–286, 2018.

[5] K. Babu, N. Pal, V. K. Saxena, and A. Mandal, "Synthesis and characterization of a new polymeric surfactant for chemical enhanced oil recovery," *Korean Journal of Chemical Engineering*, vol. 33, no. 2, pp. 711–719, 2016.

[6] H. Gao, H. Lai, J. Zhang, and Q. Xue, "Effects of bacterial cell density and alternating microbial- and enzymolysis-enhanced oil recovery on oil displacement efficiency," *Chemical Engineering Journal*, vol. 327, pp. 28–38, 2017.

[7] L. Sierra, L. East, M. Y. Soliman, and D. Kulakofsky, "New completion methodology to improve oil recovery and minimize water intrusion in reservoirs subject to water injection," *SPE Journal*, vol. 16, no. 3, pp. 648–661, 2011.

[8] D. Yin, Y. Q. Li, and D. F. Zhao, "Utilization of produced gas of CO_2 flooding to improve oil recovery," *Journal of the Energy Institute*, vol. 87, no. 4, pp. 289–296, 2014.

[9] H. M. Zaid, N. R. A. Latiff, N. Yahya, H. Soleimani, and A. Shafie, "Application of electromagnetic waves and dielectric nanoparticles in enhanced oil recovery," *Journal of Nano Research*, vol. 26, pp. 135–142, 2013.

[10] T. Guo, S. Zhang, Z. Qu, T. Zhou, Y. Xiao, and J. Gao, "Experimental study of hydraulic fracturing for shale by

stimulated reservoir volume," *Fuel*, vol. 128, no. 14, pp. 373–380, 2014.

[11] N. Khan, J. Pu, C. Pu et al., "Comparison of acidizing and ultrasonic waves, and their synergetic effect for the mitigation of inorganic plugs," *Energy & Fuels*, vol. 31, no. 10, pp. 11134–11145, 2017.

[12] F. Medeiros, B. Kurtoglu, E. Ozkan, and H. Kazemi, "Analysis of production data from hydraulically fractured horizontal wells in shale reservoirs," *SPE Reservoir Evaluation & Engineering*, vol. 13, no. 3, pp. 559–568, 2010.

[13] M. Salah, M. El-Sebaee, and T. Batmaz, "Channel fracturing technology-a paradigm shift in stimulation of tight reservoir and unlock production potential," in *79th EAGE Conference and Exhibition 2017- SPE EUROPEC*, Paris, France, 2017.

[14] M. Wu, M. Ding, J. Yao, C. Li, Z. Huang, and S. Xu, "Production-performance analysis of composite shale-gas reservoirs by the boundary-element method," *SPE Reservoir Evaluation & Engineering*, vol. 22, pp. 238–252, 2019.

[15] B. Al-Shakry, B. S. Shiran, T. Skauge, and A. Skauge, "Enhanced oil recovery by polymer flooding: optimizing polymer injectivity," in *SPE Kingdom of Saudi Arabia Annual Technical Symposium and Exhibition*, Dammam, Saudi Arabia, 2018.

[16] M. S. Kamal, I. A. Hussein, and A. S. Sultan, "Review on surfactant flooding: phase behavior, retention, IFT, and field applications," *Energy & Fuels*, vol. 31, no. 8, pp. 7701–7720, 2017.

[17] I. I. Demikhova, N. V. Likhanova, A. E. Moctezuma, J. R. Hernandez Perez, O. Olivares-Xometl, and I. V. Lijanova, "Improved oil recovery potential by using emulsion flooding," in *SPE Russian Oil & Gas Exploration & Production Technical Conference & Exhibition*, Moscow, Russia, 2014.

[18] H. Zhong, T. Yang, H. Yin, J. Lu, K. Zhang, and C. Fu, "Role of alkali type in chemical loss and ASP-flooding enhanced oil recovery in sandstone formations," *SPE Reservoir Evaluation & Engineering*, vol. 23, no. 2, pp. 431–445, 2020.

[19] J. Wang, Y. Zhang, and J. Xie, "Influencing factors and application prospects of CO2 flooding in heterogeneous glutenite reservoirs," *Scientific Reports*, vol. 10, no. 1, 2020.

[20] Y. Zhang, Y. Wang, F. Xue et al., "CO_2 foam flooding for improved oil recovery: reservoir simulation models and influencing factors," *Journal of Petroleum Science & Engineering*, vol. 133, pp. 838–850, 2015.

[21] B. Ding, Q. Sang, Z. Nie et al., "An improved study of emulsion flooding for conformance control in a heterogeneous 2D model with lean zones," *SPE Journal*, vol. 26, no. 5, pp. 3094–3108, 2021.

[22] X. Zhou, F. M. AlOtaibi, M. S. Kamal, and S. L. Kokal, "An experimental study on oil recovery performance using in situ supercritical CO_2 emulsion for carbonate reservoirs," in *Abu Dhabi International Petroleum Exhibition & Conference*, Abu Dhabi, UAE, 2020.

[23] C. C. Ezeuko, J. Wang, and I. D. Gates, "Investigation of emulsion flow in steam-assisted gravity drainage," *SPE Journal*, vol. 18, no. 3, pp. 440–447, 2013.

[24] M. Mojarad and D. Hassan, "Analytical modeling of emulsion flow at the edge of a steam chamber during a steam-assisted-gravity-drainage process," *SPE Journal*, vol. 21, no. 2, pp. 353–363, 2016.

[25] H. K. Sarma, B. B. Maini, and K. Jha, "Evaluation of emulsified solvent flooding for heavy oil recovery," *Journal of Canadian Petroleum Technology*, vol. 37, no. 7, pp. 55–62, 1998.

[26] J. Wang and M. Dong, "Simulation of O/W emulsion flow in alkaline/surfactant flood for heavy oil recovery," *Journal of Canadian Petroleum Technology*, vol. 49, no. 6, pp. 46–52, 2009.

[27] L. Cui and M. Bourrel, "Selection of CO_2-soluble surfactants for CO_2 foam/emulsion in hot and salty carbonate reservoirs," in *RDPETRO 2018: Research and Development Petroleum Conference and Exhibition*, Dhabi, UAE, 2018.

[28] A. Emadi, M. Sohrabi, S. A. Farzaneh, and S. Ireland, "Experimental investigation of liquid-CO_2 and CO_2-emulsion application for enhanced heavy oil recovery," in *EAGE Annual Conference & Exhibition incorporating SPE Europec*, London, UK, 2013.

[29] R. Hasannejad, P. Pourafshary, A. Vatani, and A. Sameni, "Application of silica nanofluid to control initiation of fines migration," *Petroleum Exploration and Development*, vol. 44, no. 5, pp. 850–859, 2017.

[30] Q. Sun, Z. Li, S. Li, L. Jiang, J. Wang, and P. Wang, "Utilization of surfactant-stabilized foam for enhanced oil recovery by adding nanoparticles," *Energy & Fuels*, vol. 28, no. 4, pp. 2384–2394, 2014.

[31] Y. Kazemzadeh, B. Dehdari, Z. Etemadan, M. Riazi, and M. Sharifi, "Experimental investigation into Fe_3O_4/SiO_2 nanoparticle performance and comparison with other nanofluids in enhanced oil recovery," *Petroleum Science*, vol. 16, no. 3, pp. 112–124, 2019.

[32] I. Kim, A. J. Worthen, M. Lotfollahi, K. P. Johnston, D. A. DiCarlo, and C. Huh, "Nanoparticle-stabilized emulsions for improved mobility control for adverse-mobility waterflooding," in *SPE Improved Oil Recovery Conference*, Tulsa, Oklahoma, USA, 2017.

[33] A. K. Alhuraishawy, R. S. Hamied, H. A. Hammood, and W. H. AL-Bazzaz, "Enhanced oil recovery for carbonate oil reservoir by using nano-surfactant: part II," in *SPE Gas & Oil Technology Showcase and Conference*, Dubai, UAE, 2019.

[34] H. A. Hammood, A. K. Alhuraishawy, R. S. Hamied, and W. H. AL-Bazzaz, "Enhanced oil recovery for carbonate oil reservoir by using nano-surfactant: part I," in *SPE Gas & Oil Technology Showcase and Conference*, Dubai, UAE, 2019.

[35] H. C. Lau, M. Yu, and Q. P. Nguyen, "Nanotechnology for oilfield applications: challenges and impact," in *Abu Dhabi International Petroleum Exhibition & Conference*, Abu Dhabi, 2016.

[36] O. A. Alomair, K. M. Matar, and Y. H. Alsaeed, "Experimental study of enhanced-heavy-oil recovery in Berea sandstone cores by use of nanofluids applications," *SPE Reservoir Evaluation & Engineering*, vol. 18, no. 3, pp. 387–399, 2015.

[37] G. Dordzie and M. Dejam, "Enhanced oil recovery from fractured carbonate reservoirs using nanoparticles with low salinity water and surfactant: a review on experimental and simulation studies," *Advances in Colloid and Interface Science*, vol. 239, article 102449, 2021.

[38] S. O. Olayiwola and M. Dejam, "A comprehensive review on interaction of nanoparticles with low salinity water and surfactant for enhanced oil recovery in sandstone and carbonate reservoirs," *Fuel*, vol. 241, pp. 1045–1057, 2019.

[39] O. Mahmoud, H. A. Nasr-El-Din, Z. Vryzas, and V. C. Kelessidis, "Using ferric oxide and silica nanoparticles to develop modified calcium bentonite drilling fluids," *SPE Drilling & Completion*, vol. 33, no. 1, pp. 12–26, 2018.

[40] M. Rashidi, A. Sedaghat, B. Misbah, M. Sabati, and K. Vaidyan, "Use of SiO2 nanoparticles in water-based drilling fluids for

improved energy consumption and rheology: a laboratory study," *SPE Journal*, vol. 26, no. 6, pp. 3529–3543, 2021.

[41] R. Qalandari, A. Aghajanpour, and S. Khatibi, "A novel nanosilica-based solution for enhancing mechanical and rheological properties of oil well cement," in *SPE Asia Pacific Oil and Gas Conference and Exhibition*, Brisbane, Australia, 2018.

[42] A. K. Santra, P. Boul, and X. Pang, "Influence of nanomaterials in oilwell cement hydration and mechanical properties," in *SPE International Oilfield Nanotechnology Conference and Exhibition*, Noordwijk, The Netherlands, 2012.

[43] M. M. Tawfik, "Experimental studies of nanofluid thermal conductivity enhancement and applications: a review," *Renewable & Sustainable Energy Reviews*, vol. 75, pp. 1239–1253, 2017.

[44] A. W. Alsmaeil, A. Enotiadis, M. A. Hammami, and E. P. Giannelis, "Slow release of surfactant using silica nanosized capsules," *SPE Journal*, vol. 25, no. 6, pp. 3472–3480, 2020.

[45] C. Carpenter, "Gelled emulsions of CO2, water, and nanoparticles," *Journal of Petroleum Technology*, vol. 66, no. 7, pp. 135–137, 2014.

[46] M. Khajehpour, R. Etminan, J. Goldman, F. Wassmuth, and S. Bryant, "Nanoparticles as foam stabilizer for steam-foam process," *SPE Journal*, vol. 23, no. 6, pp. 2232–2242, 2018.

[47] E. Neubauer, R. E. Hincapie, T. Clemens, and M. Cornelius, "Selection of nanomaterials as emulsion stabilizers in alkali-polymer EOR of high-TAN number oil," in *SPE Improved Oil Recovery Conference*, 2020.

[48] R. Singh and K. K. Mohanty, "Foams stabilized by in-situ surface activated nanoparticles in bulk and porous media," *SPE Journal*, vol. 21, no. 1, pp. 121–130, 2016.

[49] T. Uetani, J. Kai, T. Hitomi, H. Seino, K. Shimbori, and H. Yonebayashi, "Experimental investigation of crude-oil emulsion stability: effect of oil and brine compositions, asphaltene, wax, toluene insolubles, temperature, shear stress, and water cut," *SPE Production & Operations*, vol. 35, pp. 320–334, 2020.

[50] M. F. Fakoya and S. N. Shah, "Effect of silica nanoparticles on the rheological properties and filtration performance of surfactant-based and polymeric fracturing fluids and their blends," *SPE Drilling & Completion*, vol. 33, no. 2, pp. 100–114, 2018.

[51] W. Li, J. Liu, J. Zeng et al., "A critical review of the application of nanomaterials in frac fluids: the state of the art and challenges," in *SPE Middle East Oil and Gas Show and Conference*, Manama, Bahrain, 2019.

[52] L. Corredor, B. Maini, and M. Husein, "Improving polymer flooding by addition of surface modified nanoparticles," in *SPE Asia Pacific Oil and Gas Conference and Exhibition*, Brisbane, Australia, 2018.

[53] J. Theurer, O. Ajagbe, J. Osorio et al., "Removal of residual oil from produced water using magnetic nanoparticles," *SPE Journal*, vol. 25, no. 5, pp. 2482–2495, 2020.

[54] L. Hendraningrat, L. Shidong, and O. Torsœter, "A glass micromodel experimental study of hydrophilic nanoparticles retention for EOR project," in *SPE Russian Oil and Gas Exploration and Production Technical Conference and Exhibition*, Moscow, Russia, 2012.

[55] L. Hendraningrat, S. Li, and O. Torsæter, "Effect of some parameters influencing enhanced oil recovery process using silica nanoparticles: an experimental investigation," in *SPE Reservoir Characterisation & Simulation Conference & Exhibition*, Abu Dhabi, UAE, 2013.

[56] S. Li and O. Torsæter, "Experimental investigation of the influence of nanoparticles adsorption and transport on wettability alteration for oil wet Berea sandstone," in *SPE Middle East Oil & Gas Show & Conference*, Manama, Bahrain, 2015.

[57] M. Alaskar, M. Ames, S. Connor et al., "Nanoparticle and microparticle flow in porous and fractured media-an experimental study," *SPE Journal*, vol. 17, no. 4, pp. 1160–1171, 2012.

[58] A. Zamani, B. Maini, and P. P. Almao, "Propagation of nanocatalyst particles through Athabasca sands," *Journal of Canadian Petroleum Technology*, vol. 52, no. 4, pp. 279–288, 2011.

[59] T. Zhang, M. J. Murphy, H. Yu et al., "Investigation of nanoparticle adsorption during transport in porous media," *SPE Journal*, vol. 20, no. 4, pp. 667–677, 2015.

Hindawi
Geofluids
Volume 2022, Article ID 4488032, 18 pages
https://doi.org/10.1155/2022/4488032

Research Article

Sedimentary Characteristics and Evolution Controlling Factors of Platform Margin Reef-Shoal: A Case Study of Upper Carboniferous-Middle Permian in Wushi Area, Tarim Basin

Ke Sun,[1] **Huixi Lin**,[1] **Guanmin Wang**,[2] **Qinghua Chen**,[2] **and Jibiao Zhang**[1]

[1]*Sinopec Petroleum Exploration and Production Research Institute, Beijing 100083, China*
[2]*School of Geosciences, China University of Petroleum (East China), Qingdao 266580, China*

Correspondence should be addressed to Ke Sun; sunke@s.upc.edu.cn

Received 24 March 2022; Accepted 18 April 2022; Published 11 May 2022

Academic Editor: Zheng Sun

Upper Carboniferous-Middle Permian platform margin reef-shoal reservoirs are one of the most important exploration targets for the northwestern margin of Tarim Basin. In order to obtain a clear understanding of the controlling factors for the platform margin reef-shoal development, field outcrops in the Wushi area, northwestern margin of Tarim Basin had been studied in this article by field measurements, thin section identification, carbon and oxygen isotope testing, and ancient provenance analysis. Studies have shown that the platform margin reefs in the Wushi area were dominated by algae reefs, and the platform margin shoals are dominated by bioclastic shoals and gravel shoals. The characteristics of algal bind inside grains were common. During the Zhaerjiake period, interbedded reefs and shoals were the main type, and platform marginal reefs were of the progressive type. During the Balediertage period, huge thick platform margin reefs were the main type, and the platform margin reefs were of accretion-weak progressive type. The development controlling factors of the platform margin reef-shoal are mainly relative sea-level change, palaeosource, and paleogeomorphy. Relative sea-level changes controlled the development characteristics and superposition mode of the platform margin reef-shoal; there were two sides of the influence of the palaeosource on the platform margin reef-shoal; the paleogeomorphology controlled the development position and spreading scale of platform margin reef-shoal. In the covering area, the platform margin reef-shoal reservoirs adjacent to the fault zone and with large sedimentary thickness might have a good prospect for hydrocarbon exploration.

1. Introduction

Reef-shoal reservoirs play an important role in carbonate reservoirs and are prone to form high-yield oil and gas fields with huge reserves, such as Ghawar oil field in Saudi Arabia, Zertan oil field in Libya, and Old Golden Lane oil field in Mexico [1]. In recent years, with major breakthroughs in reef-shoal facies oil and gas fields of Upper Ordovician Lianglitage Formation in Tarim Basin, Triassic Changxing Formation, and Feixianguan Formation in Sichuan Basin, such as Tazhong I gas field, Puguang gas field, and Yuanba gas field, the research interest of reef-shoal facies is increasing [2–6]. Studies show that the favorable area of reef-shoal body in Tarim Basin is $1.58 \times 104\,km^2$, and the amount of oil and gas resources is more than $1.5 \times 109\,t$, indicating its huge exploration potential [7]. As one of the important exploration targets in Tarim Basin, the Carboniferous-Permian reef-shoal reservoirs have been found in Tazhong area (Tahe 1 well and Tazhong 4 well) [8]. However, in the northwestern margin of Tarim Basin, the Carboniferous-Permian is buried deeply in the covering area, and no exploration wells have been drilled into the target layer. Therefore, field outcrop research of platform margin reef facies is of great significance for hydrocarbon exploration. Many previous studies have been carried out on the platform margin reef-shoal facies of the Carboniferous-Permian in the northwestern margin of Tarim Basin. Based on the outcrop research in Keping area, Zhang believed that the platform margin reef-shoal in the northwestern margin of Tarim was mainly developed in Late Carboniferous to Early

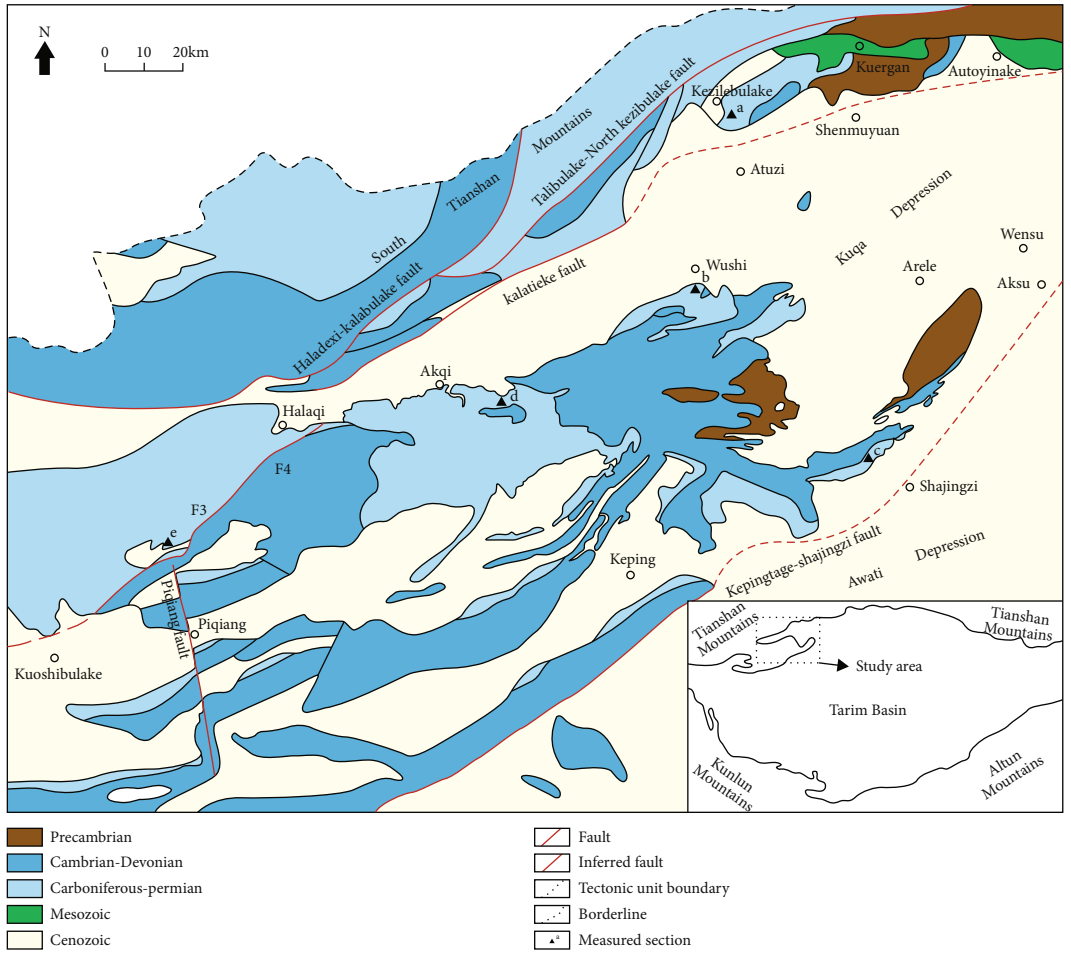

Figure 1: Location and stratigraphic distribution in Wushi area, northwestern of Tarim Basin. (a) Kezilebulake. (b) South of Wushi. (c) Sishichang. (d) Sepabayi. (e) Aoyibulake.

Permian, and the reef-building organisms were mainly blue-green algae [9]. Deledaer further studies suggested that the stable transgression of Late Carboniferous to Early Permian was the basis for the large-scale development of carbonate platforms and platform margin reef-shoals [10]. Based on the study of Kangkelin Formation in the Western Tarim Basin, Wang proposed that sea-level fluctuation and palaeo-topography controlled the migration of reef-shoals, and the sedimentary background of platform margin reef-shoal was carbonate gentle slope model [8]. Through a systematic study of Permian reef limestone in the northwestern margin of Tarim Basin, Luo believed that the progradational reef with huge thickness reflected that the growth rate of reef body matched the rate of reef base [11]. It can be seen that researchers have studied the sedimentary characteristics, spatial and temporal distribution, migration mechanism, and sedimentary model of platform margin reef-shoals [8–11], but the sedimentary differences and controlling factors of platform margin reef bank in different periods and tectonic positions are not discussed. This problem affects the understanding and exploration evaluation of platform margin reef-shoal facies development law. Taking the upper Carboniferous-Middle Permian in Wushi area as an example, this paper systematically studies the large sedimentary differences of the platform margin reef-shoal in different periods and different tectonic positions. On this basis, the evolution controlling factors and exploration potential of platform margin reef-shoal in are discussed, via stable isotope test, Fluorescent thin section observation, reservoir porosity, and permeability test. The research results of this paper can provide reference for the hydrocarbon exploration of platform margin reef-shoal in Tarim Basin.

2. Geology Settings

Wushi area is located in the northwest margin of Tarim Basin, connected with the southern Tianshan orogenic belt by the Kalatieke fault to the north, and connected with the Awati Depression and Bachu Uplift by the Kepingtage-Shajingzi fault to the south, and connected with Aksu area in the east and Piqiang area in the west (Figure 1). Tectonically, Wushi area is located between Tarim block and southern Tianshan orogenic belt. Since the Late Devonian, the Yili-Central Tianshan Block first collided with the eastern Tarim Block. In the Carboniferous, southern Tianshan ocean closed from east to west in a scisscis-type manner until the southern Tianshan ocean closed [12]. From Late Carboniferous to Early Middle Permian, the northwestern

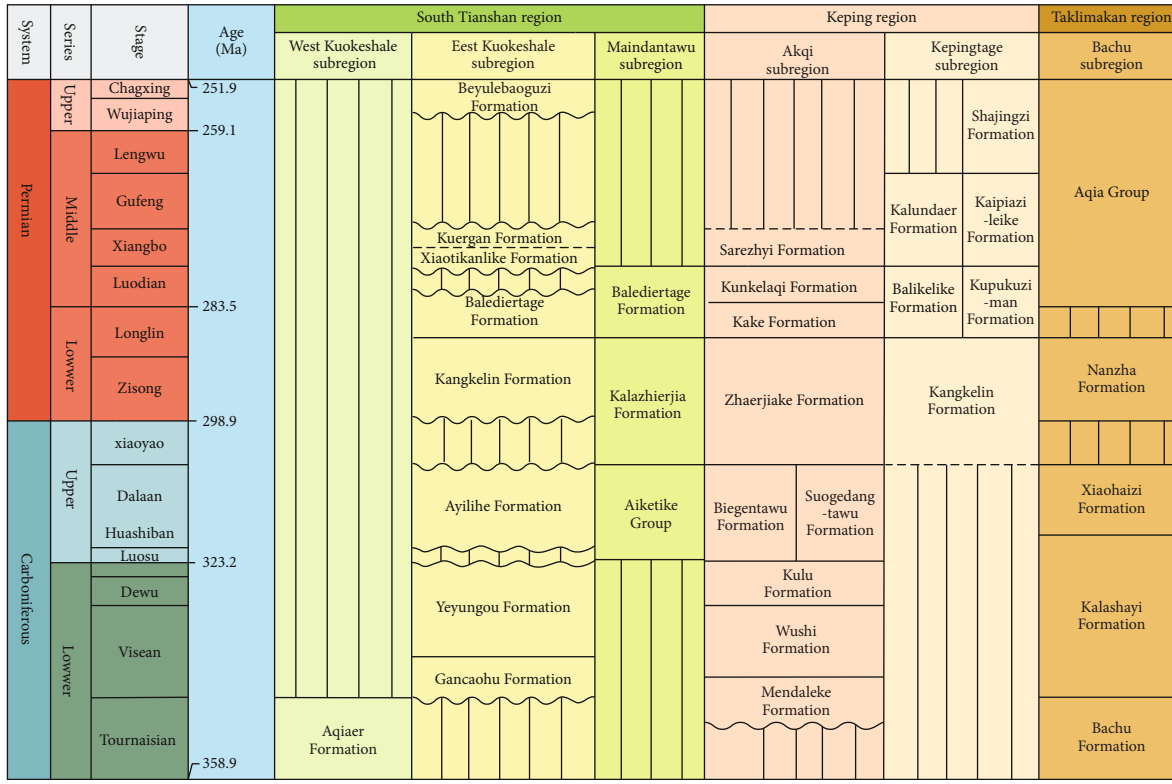

(a)

Figure 2: Continued.

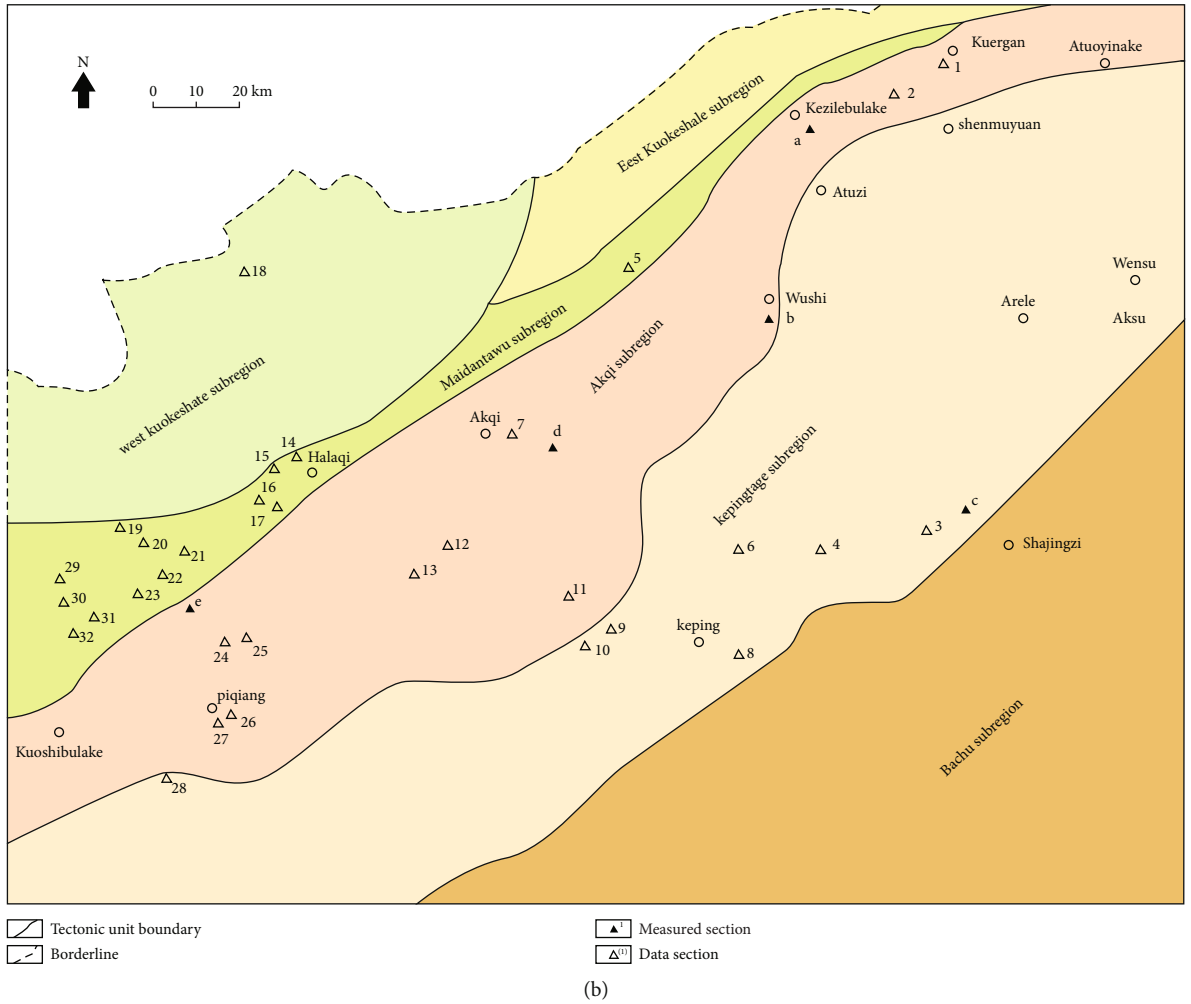

(b)

Figure 2: Stratigraphic division and regionalization scheme of Carboniferous-Permian in Wushi area, northwestern of Tarim Basin. (a) Kezilebulake. (b) South of Wushi. (c) Sishichang. (d) Sepabayi. (e) Aoyibulake. (1) Kuergan; (2) Shenmuyuan; (3) Kaipaiziruike; (4) south slope of Yinganshan; (5) Kekeyumusu; (6) Tongguzibu; (7) north bridge of Tuoshihan; (8) Xiaoerbulake; (9) Subashi-I; (10) Subashi-II; (11)Tikeliketage-Qiudayisayi; (12) Kake; (13) Muziduke; (14) Halaqi-I; (15) Halaqi-II; (16) Bijingtawu-I; (17) Bijingtawu-II; (18) Keleikesu river valley; (19) north slope of Kalatieke Mountain-I; (20) north slope of Kalatieke Mountain-II; (21)Yiqike; (22) south foothills of Kalatieke-I Yimugantawu; (23) Huoshibulake; (24) Kekebukesan Mountain-I; (25) Kekebukesan Mountain-II; (26) west of Piqiang Mountain; (27) Kekebukesan Mountain-III; (28) Yimugantawu; (29) Kutiereke-I; (30) Kutiereke-II; (31) foothill of Kalatieke Mountain-II; and (32) Kutiereke-III.

margin of Tarim Basin did not build mountains strongly immediately after the closure of the southern Tianshan ocean basin, but still developed a foreland remnant basin opening westward [13, 14]. The platform margin reef-shoal in Wushi area was developed in this tectonic background. After the Middle Permian, the late Tianshan movement led the revival of the southern Tianshan orogenic belt, and the strong compressional nappe closed the residual basin. The Wushi area started the molasite evolution stage of the foreland basin. After that, Yanshanian, Indosinian, and Himalayan movement caused multiple thrust nappe and strike-slip, which further complicated the distribution of Carboniferous-Permian in Wushi area.

Because the distribution of Carboniferous-Permian in Wushi, Keping, and Aheqi is relatively stable (Figure 1), a systematic stratigraphic framework has been established [15, 16]. Wushi area can be divided into 3 stratigraphic regions and 6 stratigraphic subregions (Figure 2). According to section, the platform reef-shoal facies was mainly developed during Late Carboniferous-Middle Permian in Kepingtag, Aheqi, and Maidantawu stratigraphic regions. Kangkelin Formation ($(C_2\text{-}P_1)\ k$), Zarjake Formation ($(C_2\text{-}P_1)\ z$), Kalazhierjia Formation ($(C_2\text{-}P_1)\ kl$), Balediertage Formation ($P_{1\text{-}2}b$), and Kunkelaqi Formation ($P_{1\text{-}2}k$) were involved (Figure 2(a)). In order to facilitate understanding, Zhaerjiake period and Balediertage period are adopted in the following paper when the sedimentary characteristics of platform margin reef-shoal in different periods are described.

3. Materials and Methods

3.1. Materials. The samples in this study are from 5 Carboniferous-Permian sections (section a–e) in Wushi

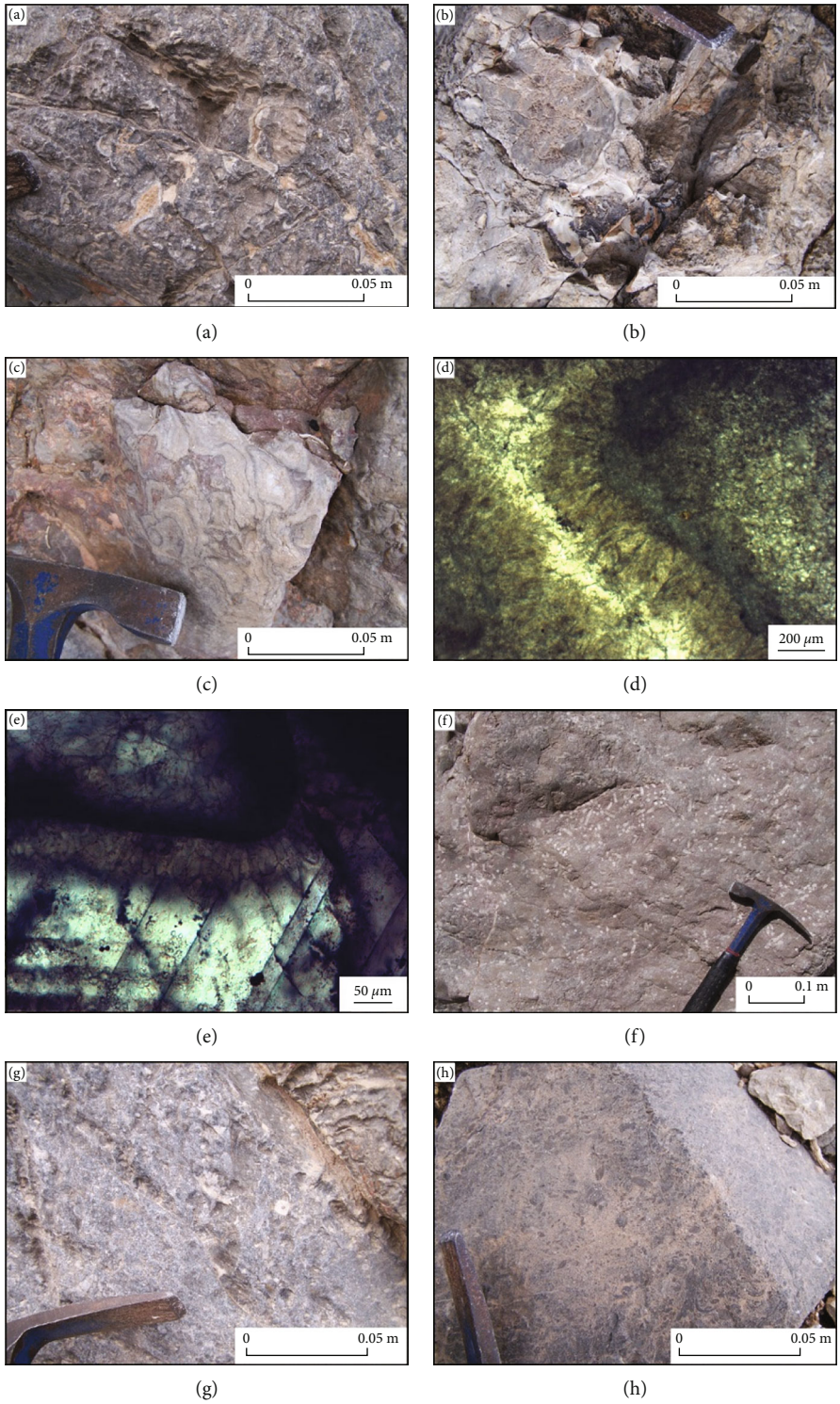

Figure 3: Continued.

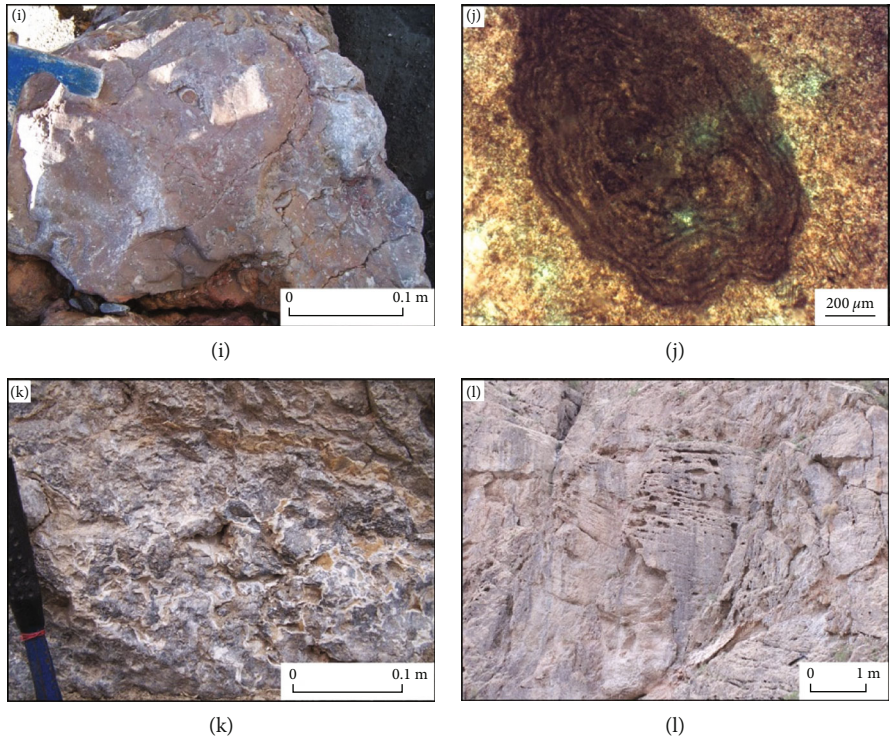

FIGURE 3: Outcrops and microscope photos of platform margin reef-shoal facies in Wushi region. (a) Algal bonded reef limestone, Zhaerjiake Formation, section e. (b) Algal bonded reef limestone, Kunkelaqi Formation, section d. (c) Algal bonded reef limestone, Balediertage Formation, section a. (d) Bonding layer in algal bonded reef limestone, Kunkelaqi Formation, section e. (e) Two stage carbonate filler in algal bonded reef limestone, Balediertage Formation, section a. (f) Crinoid micrite limestone, Balediertage Formation, section a. (g) Bioclastic micritic limestone, Zhaerjiake Formation, section e. (h) Bioclastic limestone, Zhaerjiake Formation, section d. (i) Bioclastic micrite limestone, Balediertage Formation, section a. (j) Algal clast micrite limestone, Kunkelaqi Formation, section e. (k) Algal bonded calcirudite, Zhaerjiake Formation, section e. (l) Bioclastic gravel-bearing arenaceous limestone, Balerdiertage Formation, section a.

area, northwestern of Tarim Basin (Figure 1). Based on detailed field outcrops observation, 171 rock samples were collected in total. Through hand specimens and microscopic observation, 33 samples were used for stable isotope analysis, 18 samples were used for reservoir porosity and permeability test, and 3 samples were used for fluorescent thin section observation.

3.2. Experimental Method

3.2.1. C and O Isotope Analysis. The C and O isotopic content of seawater varies with the sedimentary environment, and these changes are recorded in syn-sedimentary carbonate rocks. C and O isotope content has been widely used to study regional and global relative sea-level change [17–20]. C and O isotope analysis of carbonate rocks mainly adopts phosphoric acid method which is widely used by laboratories. The experimental method is that carbonate minerals react with 100% phosphoric acid at a specific temperature to release CO_2, and the C and O isotope content of carbonate can be determined by measuring the C and O isotope of CO_2.

The detailed experimental process is as follows. (1) Under the condition of high vacuum, the carbonate rock sample is subjected to constant temperature reaction with 100% phosphoric acid, in which the limestone part is fully reacted at $(25.0 \pm 0.1)^{\circ}$C for 24 hours, and the dolomitic part fully reacts at $(50.0^{\circ}C \pm 0.1)$ for 72 hours. (2) The generated water is separated by freezing method to collect CO_2, and then, the CO_2 is sent to the stable isotope mass spectrometer (MAT-252) for obtaining C and O isotope content.

In order to facilitate the comparison with other C and O isotope test results, the test results are expressed by the thousandth difference of the isotope ratio between the test value and the standard sample (Pee Dee Belemnite) value, $\delta^{13}C_{PDB}$, and $\delta^{18}O_{PDB}$.

3.2.2. Reservoir Porosity and Permeability Test. Helium gas is an inert gas, not easy for chemical reaction, and can effectively inhibit the gas effect. Using helium gas as the test medium not only does not pollute the sample, but also ensures high test accuracy. Therefore, helium gas is used as the medium in this experiment. POROPDP-200 apparatus is used to test the porosity and permeability of the sample.

Reservoir porosity test consists of four steps. (1) Set the temperature to $200 \pm 2^{\circ}$C, and put the sample into the constant temperature drying oven until completely drying (test dry weight less than 0.001 g); (2) after cooling to room temperature, the samples were loaded into the sample chamber, and the pressure in the standard chamber filled with gas and equilibrium state was recorded, respectively; (3) the rock skeleton volume can be calculated according to Boyle's law,

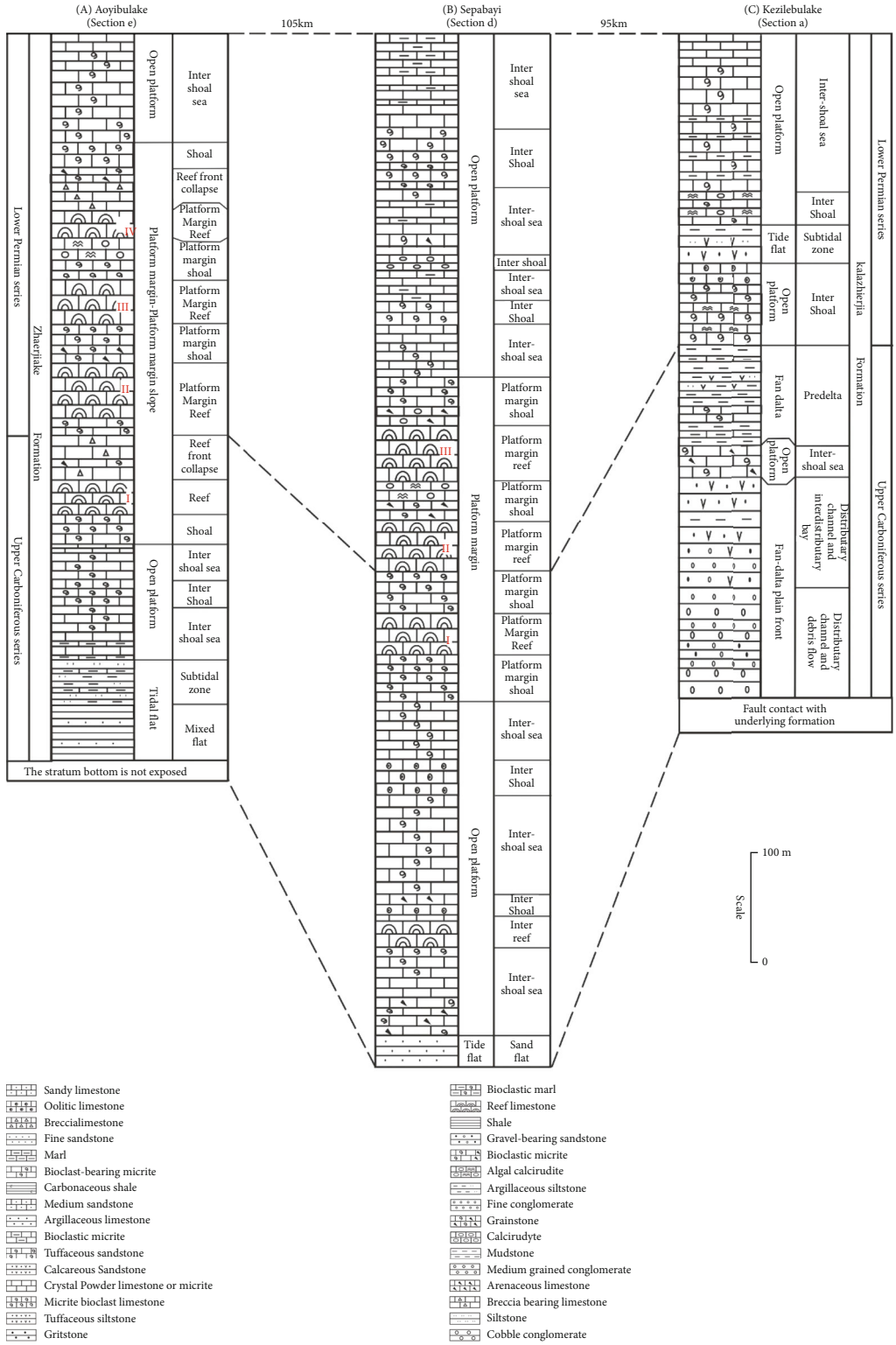

Figure 4: Stratigraphic histogram of Zhaerjiake period in Wushi region, northwestern of Tarim Basin.

and the total volume of rock can be measured by powder accumulation method; and (4) calculate the sample porosity.

Reservoir permeability test consists of three steps. (1) Set the temperature to $200 \pm 2^{\circ}C$, and put the sample into the constant temperature drying oven until completely dried (test dry weight less than 0.001 g); (2) after cooling to room temperature, the samples are loaded into the sample chamber; (3) increase the confining pressure, pass the gas to test the flow rate, and record the gas flow rate through the sample per unit time and the pressure value above and below the sample; and (4) calculate the sample permeability.

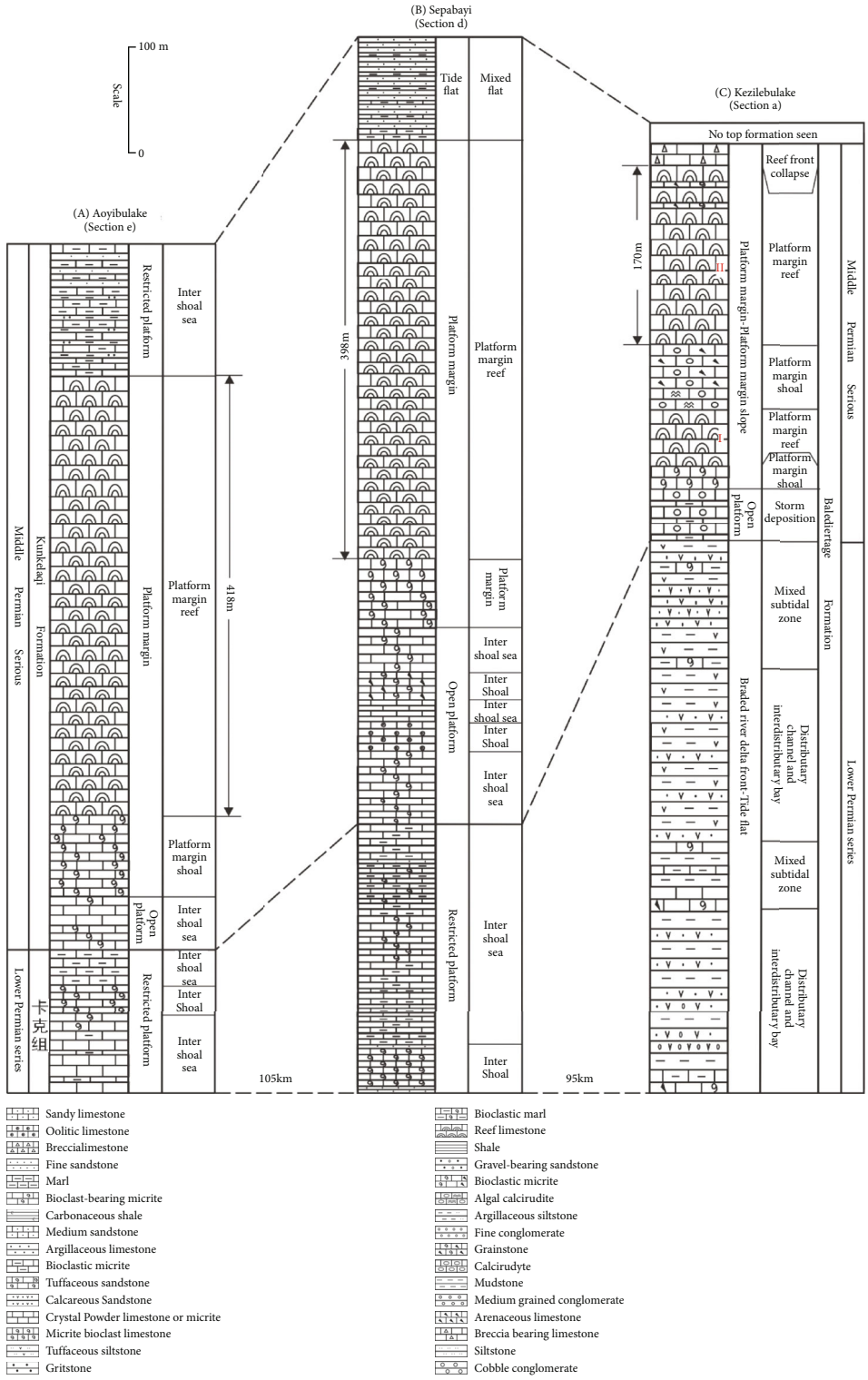

Figure 5: Stratigraphic histogram of Baledietage period in Wushi area, northwestern of Tarim Basin.

3.2.3. Fluorescent Thin Section Observation. Hydrocarbons and other organic matter contents in rocks glow in different colors under UV excitation. With the increase of the maturity of petroleum components, the fluorescence wavelength will shorten. Therefore, hydrocarbon properties can be inferred by fluorescence color and luminance.

ORTHOLUX-II fluorescence microscope is used in this experiment; the experimental process is as follows: (1) through the thin section observation, the suitable carbonate samples for fluorescent examination should be selected; (2) make the selected samples into fluorescent thin section; and (3) through the fluorescent thin section observation,

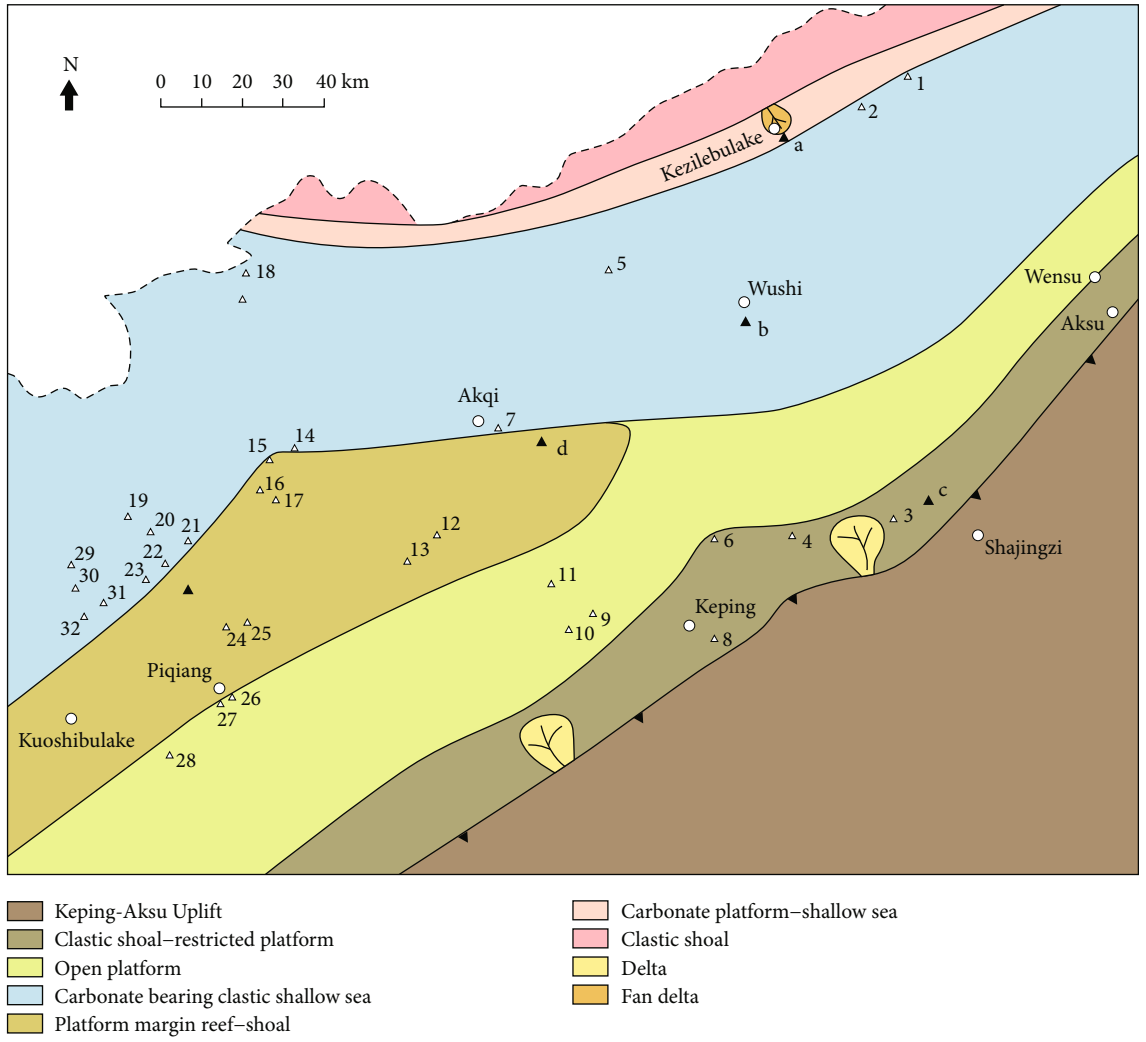

Figure 6: Sedimentary facies distribution of Zhaerjiake period in Wushi region (section names are shown in Figure 2).

describe the color, brightness, and distribution characteristics of hydrocarbon fluorescence.

4. Results

4.1. Lithologic Characteristics

4.1.1. Platform Margin Reef. The platform margin reef in Wushi area was mainly composed of boundstone and skeleton boundstone, followed by bafflestone. The boundstone was mainly grayish black, grayish white and grayish red thick to massive algal bound reef limestone (Figures 3(a) and 3(b)). The reef-building organisms are dominated by algae. The algae fossils had native characteristics, accounting for more than 70% of the reef-building organisms, and a few sponges and grid bryozoan skeletons were occasionally seen. The reef attached organisms included crinoids, cephalopods, and brachiopods in algal bound reef limestone. The skeleton boundstone were mainly sponge-algal bound reef limestone. The sponge skeleton was filled with bioclastic and grayish red micrite, and sparite-bounding layers was curved and around the skeleton (Figure 3(c)). Through microscopic observation, it was found that the algae bonding layer developed along the edge of carbonate grain (Figure 3(d)). Some dense algal bound reef limestones had strong diagenesis, and two-stage cementation characteristics could be seen (Figure 3(e)). The bafflestone was mainly brown crinoid micrite limestone, with crinoid stem content of 40%~70%, and the maximum diameter of crinoid stem was about 5 mm. Some crinoids were elongated, reflecting the weak hydrodynamic conditions behind the reef (Figure 3(f)).

4.1.2. Platform Margin Shoal. The platform margin shoal in Wushi area was mainly composed of bioclastic shoal and gravel shoal, followed by sand gravel shoal. The lithology of bioclastic shoal was gray, gray-black, gray-red bioclastic limestone, or bioclastic micritic limestone. Bioclastic types included crinoids, abrasives brachiopods, bivalves, algae, foraminifera, skink, and crinoids. The bioclastic content of some bioclastic limestones could reach more than 60%, reflecting shallow water high-energy environment (Figures 3(g)–3(j)). Gravel shoals had the characteristics of algae binding, which might be the transition type from shoal to platform margin reef. The lithology of gravel shoal was

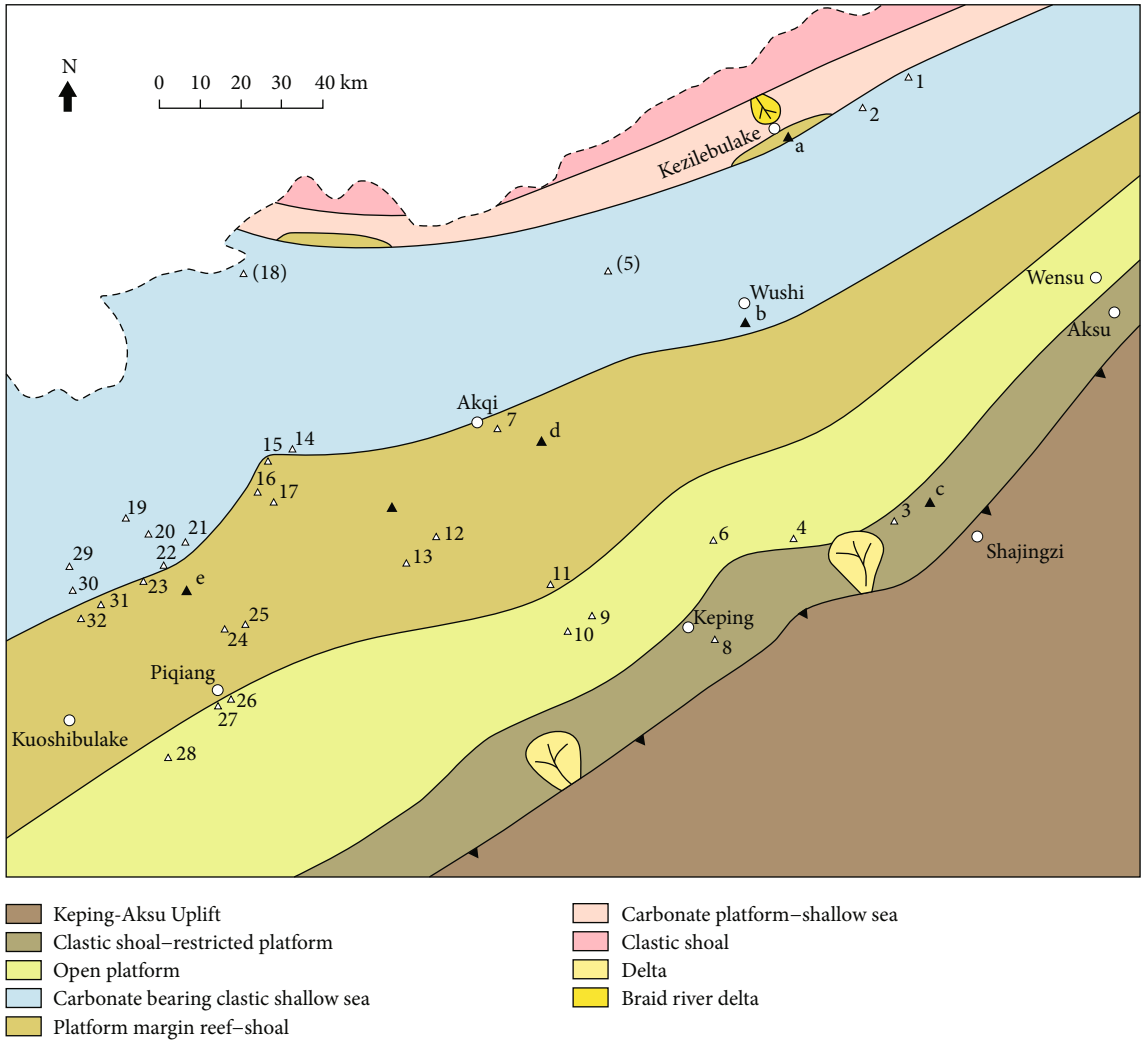

Figure 7: Sedimentary facies distribution of Balediertage period in in Wushi region (section names are shown in Figure 2).

light gray and grayish red algae bonded calcirudite. The gravels were well sorted, subangular, and subround, and the gravel diameter was 2-5 cm. Bright crystal cementation among gravels and local residual pores was filled with brown micritic, and secondary pores were easily formed by weathering and leaching along the algal cavity (Figure 3(k)). The lithology of sand gravel shoal was gray-brown bioclastic-gravel-bearing arenaceous limestone with crossbedding lamina, and beaded dissolution holes developed along structural fractures or bedding (Figure 3(l)).

4.2. Sedimentary Sequence

4.2.1. Zhaerjiake Period. There are 4 reef-forming cycles of Zhaerjiake Formation in Aoyibulake section (Figure 4(a)). In each cycle, the single-layer reef limestone thickened upward and was a prograding reef. In cycle I, the thickness of reef was 32 m. The thickness of reef base was 28 m, which was sparry bioclastic limestone. The sedimentary sequence of bioclastic-bearing sparry limestone-bioclastic sparry limestone-algal bonded reef limestone could be seen vertically. In cycle II, the thickness of reef limestone was 63 m. The reef base was 56 m thick. The sedimentary sequence of slump breccia limestone-crinoid micritic limestone-algal bonded reef limestone can be seen vertically. The thickness of reef limestone in cycle III is 40 m. The thickness of reef base was 35 m. The sedimentary sequence of grainstone, sparry bioclastic limestone, and algal bonded reef limestone was developed vertically. In cycle IV, the thickness of reef limestone was 25 m. The reef base was 39 m. The reef cover was collapsed rock rich in deformed micritic lamina, 26 m thick, which vertically consisted of bioclastic limestone-algal bonded gravel limestone-algal bonded reef limestone-breccia-bearing micritic limestone-granular micritic limestone sedimentary sequence. At the top of the platform margin shoal and upper open platform formed a sedimentary sequence consisted of bioclastic limestone-bioclastic micrite-bioclastic micrite limestone-micrite, reflected the deepening of water body during Zhaerjiake period.

There are 3 reef-forming cycles of Zhaerjiake Formation in Sepabayi section (Figure 4(b)). In each cycle, the single-layer reef limestone had the characteristics of upward thickening and the number of layers increased, and it was a progradation reef. In cycle I, the thickness of reef limestone was

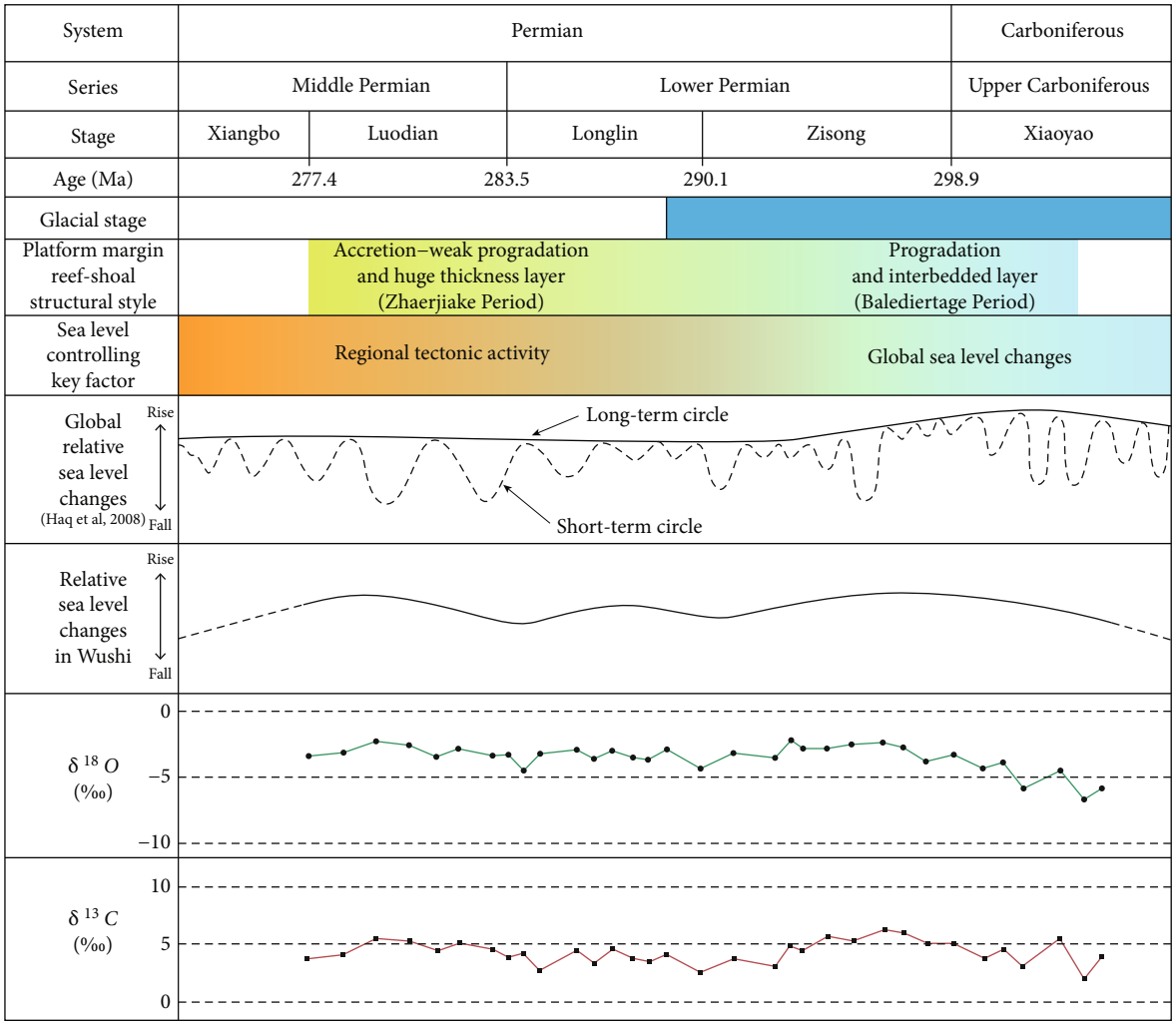

Figure 8: Developmental controlling factors of Carboniferous-Permian reef and shoal in Wushi area.

38 m, and the thickness of reef base was 35 m. The thickness of reef limestone in cycle II was 47 m, and the thickness of reef base was 38 m. The sedimentary sequences of bioclastic micritic limestone-bioclastic limestone-algal bonded reef limestone developed vertically in cycle I and II. The thickness of reef limestone in cycle III was 51 m, and the thickness of reef base was 43 m. The sedimentary sequence of grainstone-algal bonded gravel limestone-algal bonded reef limestone was developed vertically. The shoal facies reef cap on the top and the intershoal sea consisted of bioclastic sand gravel limestone-bioclastic micritic limestone–bioclastic-bearing micritic limestone-micritic limestone. It reflected the deepening of water body at the end of reef formation period.

4.2.2. Balediertage Period. The Kunkelaqi Formation developed a huge thickness reef-forming cycle in the Aoyibulake section (Figure 5(a)). The accumulative thickness of massive algal reef limestone is 418 m, and the thickness of single-layer reef limestone is nearly equal or slightly increased upward. The thickness of dense single-layer reef limestone at the top could reach more than 20 m, with accretion and weak progradation characteristics. The lithology of underlying platform margin shoal was bioclastic micritic limestone and formed the reef base with a thickness of 77 m. The lithology of overlying restricted platform was argillaceous limestone and marl intercalated with argillaceous siltstone or fine sandstone, which formed the reef cover. The clastic rock intercalated with marl became coarser and thicker upward, reflecting that the water body became shallower in the late stage of reef formation.

The huge thick reef-forming cycle was developed in the Kunkelaqi Formation of Sepabayi section (Figure 5(b)). The accumulative thickness of massive reef limestone was 418 m. The thickness of single reef limestone was nearly equal or slightly increased upward. The maximum thickness of reef limestone at the top was more than 15 m, which was aggradation-weak progradation type reef. The underlying bioclastic micritic limestone of platform margin shoal formed the reef base, with a thickness of 65 m. The overlying tidal flat facies marl, mudstone, and fine sandstone constituted the reef cover. The content of sandstone in the reef cover increased upward and the number of layers increased, reflecting that the water body became shallower in the late stage of reef formation.

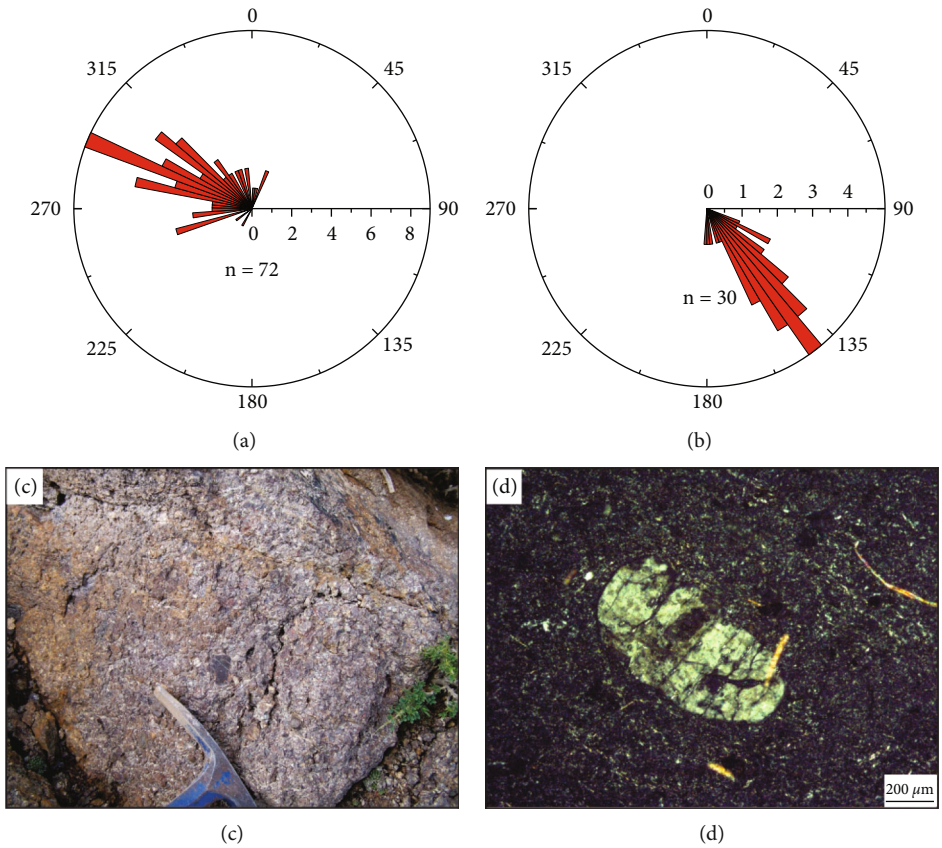

Figure 9: Sandstone laminae occurrence rose diagrams and proximal clastic photos. (a) Sandstone laminate attitude rose diagram, Kangkelin Formation, Sishichang section. (b) Sandstone laminate attitude rose diagram, Balediertage Formation, Kezibulake section. (c) Volcanic breccia, Balediertage Formation, Kezibulake section. (d) Tuff, cross-polarized light, Balediertage Formation, Kezibulake section.

There are 2 reef-forming cycles in the Balediertage Formation of Kezilebulake section (Figure 5(c)). In cycle I, the thickness of platform margin reef was 53 m. The monolayer reef was accretion reef, and the thickness of reef base was 22 m. Vertically, it formed the sedimentary sequence of crinoid micrite limestone-sponge algae bonded reef limestone. In cycle II, the thickness of reef body was 170 m, which increased upward slightly, with aggradation-weak progradation characteristics. The base thickness of shoal facies reef was 62 m. The sedimentary sequence of algal bound gravelly limestone-bioclastic gravelly sandy limestone-spongy algal bound reef limestone developed vertically. The top colluvial facies reef cap was a medium thick grain micritic limestone containing reef breccia.

In conclusion, interbedded platform margin reefs and shoals were mainly developed in Wushi area during Zhaerjiake period, and the platform margin reef was mainly progradation type. The reef-forming cycles suggested frequent relative sea-level fluctuations. In the Balediertage period, the development of extremely thick platform margin reef was dominant, and the accumulated thickness of reef limestone showed a decreasing trend (418 m-398 m-170 m) from west to east (Figure 5). Platform margin reef was accretion and progradation type, which was obviously different from the interbedded reef-shoal of Zhaerjiake Formation. The few reef-forming cycle might be related to the long-term stable rise of relative sea level.

4.3. Plane Distribution Characteristics

4.3.1. Zhaerjiake Period. The palaeogeographic pattern in Wushi area during the Zharjiak period showed that the residual marine basin was sandwiched between the Keping-Aksu Uplift and the southern Tianshan orogenic belt. The northwest margin of Tarim had the characteristics of basement landform of "low in the West and high in the East". With the rise of regional sea level in the Late Carboniferous, the seawater invaded from west to east, making the uplift area of the Early Carboniferous submerged. With the continuous expansion of carbonate sedimentary range, wide and gentle carbonate platforms are developed in the northern margin of Keping-Aksu Uplift, while narrow and long carbonate platforms are developed in the top of the south Tianshan orogenic wedge. From northeast to southwest, the study area successively developed clastic rock shore facies, carbonate platform carbonate-shallow marine facies, clastic rock shallow marine facies, platform margin reef-shoal facies, open platform facies, and clastic rock shore-limited platform facies (Figure 6).

According to the shore facies, tidal flat facies and restricted platform facies developed in Kangkelin Formation of Sishichang section; the seawater had invaded near Shajingzi-Keping line at this time. In the Piqiang area in the southwest, the platform margin reef-shoal facies began

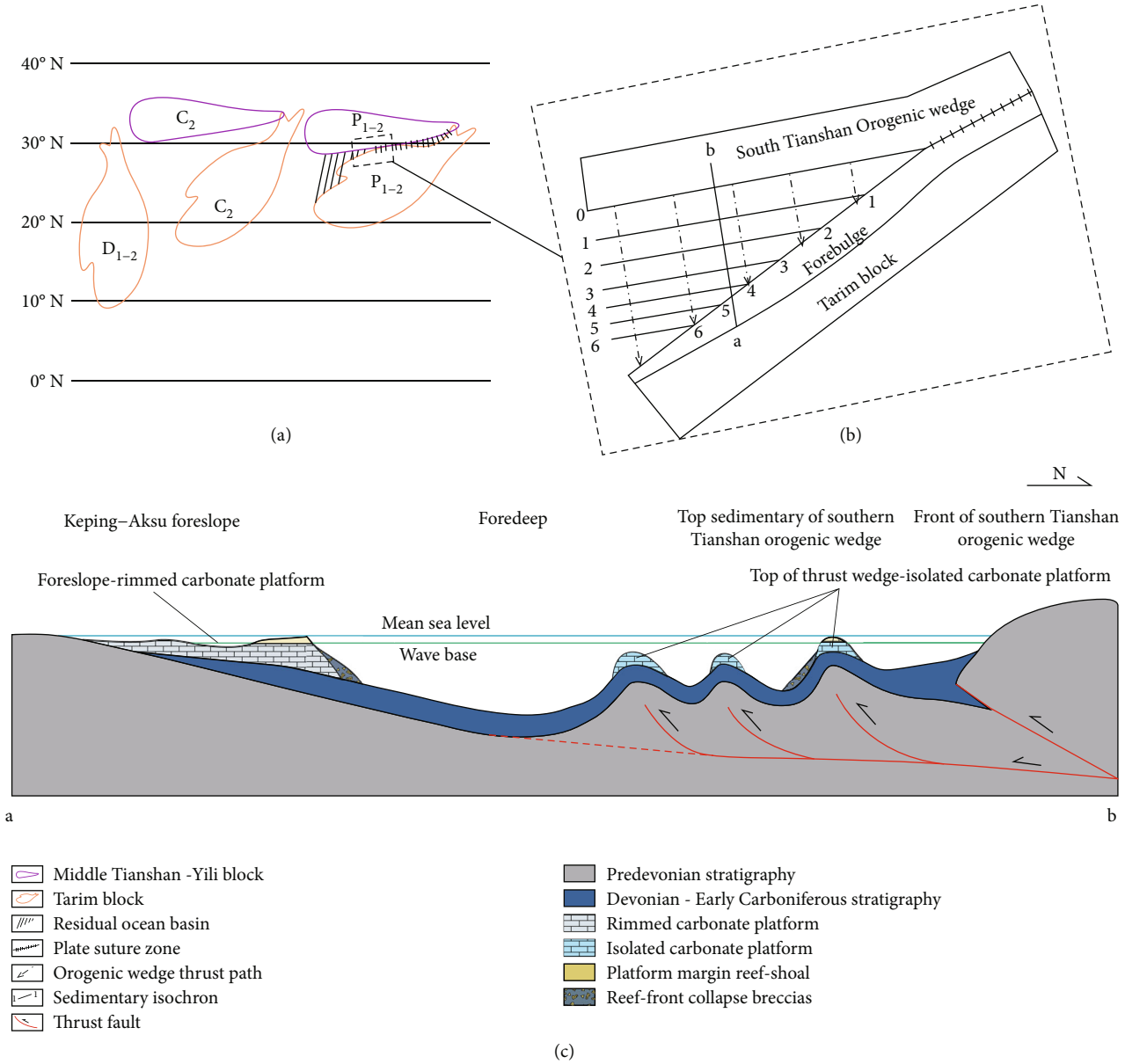

Figure 10: Late Paleozoic plate tectonic setting, closure model of residual sea basin and paleogeomorphology section diagram in northwestern of Tarim Basin.

to develop along the front slope of Keping-Aksu Uplift. The reef-shoal body was distributed in a strip in the northeast direction, and the width of the facies belt in the northeast direction reduced. According to the lithofacies of the control sections, the platform margin reef-shoal could extend to the northeast at least near Aheqi. The extension length of the whole facies belt was at least about 200 km, and the overlapping width was about 30-50 km (Figure 6).

4.3.2. Balediertage Period. The palaeogeomorphology in Wushi area during Balediertage period basically inherited Zhaerjiake period. The range of clastic rocks in the foredeep was obviously smaller than that in the early stage. The open platform, limited platform, and clastic rock shore facies in the northern margin of Keping-Aksu Uplift retreated slightly (Figure 7). However, the sedimentary range of the platform margin was slightly expanded, which might be related to the high carbonate deposition rate in the platform margin. The control sections are located at the easternmost edge of the platform margin reef-shoal facies, the distance between Tikeliketage-Qiudayisayi section (section (11)) and Sepabayi (section d) was 38 km. In the former section, the thickness of the platform margin reef of Kunkelaqi Formation was 200-300 m [11], while the measured thickness of the latter section, the Kunkelaqi Formation reached 398 m (Figure 5(b)), indicating that the platform margin reef-shoal facies still had at least 38 km overlapping width in the east of Aheqi.

According to the distribution of sedimentary facies, it was inferred that the platform margin reef-shoal of

Table 1: Physical analysis data of platform margin reef-shoal reservoirs in Wushi area.

Section	Formation	Sample	Porosity (%)	Permeability (mD)	Sedimentary facies	Lithology	Evaluation results
e	Kunkelaqi	C1004	4.21	3.740	Platform margin reef	Reef limestone	II
e	Kunkelaqi	C1006	3.63	1.310	Platform margin reef	Reef limestone	II
e	Kunkelaqi	C1009	1.14	0.082	Platform margin reef	Reef limestone	III
e	Kunkelaqi	C1010	0.56	0.036	Platform margin shoal	Bioclastic limestone	III
e	Zhaerjiake	C1012	3.42	2.550	Platform margin shoal	Bioclastic limestone	II
e	Zhaerjiake	C1015	0.89	0.033	Platform margin reef	Reef limestone	III
e	Zhaerjiake	C1016	0.51	0.028	Platform margin shoal	Grain limestone	III
e	Zhaerjiake	C1019	0.97	0.077	Platform margin reef	Reef limestone	III
d	Kunkelaqi	C1119	1.56	0.074	Platform margin reef	Reef limestone	III
d	Kunkelaqi	C1115	0.77	0.039	Platform margin reef	Reef limestone	III
d	Kunkelaqi	C1113	0.64	0.038	Platform margin shoal	Bioclastic limestone	III
d	Zhaerjiake	C1111	0.83	0.072	Platform margin shoal	Bioclastic limestone	III
d	Zhaerjiake	C1109	1.28	0.063	Platform margin reef	Reef limestone	III
d	Zhaerjiake	C1101	1.84	0.051	Platform margin shoal	Grain limestone	III
a	Balediertage	C1308	3.32	1.680	Platform margin reef	Reef limestone	II
a	Balediertage	C1312	2.81	1.950	Platform margin reef	Grain limestone	II
a	Balediertage	C1313	0.72	0.023	Platform margin reef	Reef limestone	III
a	Balediertage	C1323	0.92	0.027	Platform margin reef	Reef limestone	III
a	Balediertage	C1326	1.36	0.081	Platform margin shoal	Bioclastic limestone	III

Bladiertage stage might penetrate the whole area, and the distribution area was the largest (Figure 7). In the northern part of Wushi area, small platform margin reef-shoal with discrete distribution began to develop at the top of the south Tianshan mountains thrust wedge. Under the influence of paleogeomorphology and near provenance, the platform margin reef-shoal could be transformed into braided river delta front laterally (Figure 7).

5. Discussion

5.1. Controlling Factors on Development of Platform Margin Reef-Shoal

5.1.1. Relative Sea-Level Change. Reef-shoal is sensitive to paleowater depth changes, and its development characteristics and superimposed patterns are a direct response to changes in relative sea level [21]. Relative sea-level rise and fall is a joint response of global sea-level fluctuation and regional tectonic activity, which is especially important for foreland deposits [22]. In order to determine the influence of relative sea-level fluctuation on the evolution of platform margin reef and shoal, C and O isotope tests were carried out on 33 samples collected from the Aoyibulake section. The sea-level change curves were plotted in combination with sedimentary facies changes. By comparing the relationship between relative sea-level changes in Wushi region and global sea-level changes [20], it can be seen that the trend of sea-level change in Wushi area was basically consistent with that of global sea-level change in Zhaerjiake period (Xiaoyao period-Zisong period), which was in a continuous rising state. Sedimentary and provenance records of the Lower Permian in the Sishichang section indicate that there was no large-scale uplift of the southern Tianshan mountains before at least the Early Permian Zinsong (Asselian) period [23, 24]. Therefore, the relative sea level during the Zhaerjiake period was mainly controlled by global sea-level changes (Figure 8). During this period, tectonic activity was weak, the basin basement subsidence driven by sedimentary load was slow, and the relative sea level rose slowly. At this time, the sedimentation rate of platform margin reef was slightly higher than that of the relative sea-level rise. Therefore, progradational platform margin reef developed along the slope of the front of Keping-Aksu Uplift. On the other hand, the secondary glaciation-interglacial cycle caused frequent sea-level fluctuations due to the Gondwana III glacial event (about 307~289 Ma) [25]. The frequent fluctuation of sea level led to the alternating reef-forming cycle and shoal-forming cycle, so the platform margin reef and shoal showed an interbedded structure (Figure 4). Balediertager period (Longlin-Luodian stage), Wushi area, existed significant difference with the global relative sea-level change; tectonic activity might gradually became the main control factors of relative sea level (Figure 8) and continental rise tectonic flexure basin basement subsidence, along with the steady rose in relative sea level, while the relative sea-level rise rate close to or slightly below the platform margin reef sedimentary rate. Therefore, accretion-weak prograding reef mainly developed. In addition, the basement subsidence caused a stable rise in relative sea level, and the single reef-forming cycle was long, resulting in the development of extremely thick platform margin reefs (Figure 5). During the Kalendar stage, regional regression led to the rapid decline of relative sea level, and the shallow water led to the rapid extinction of platform margin reefs and shoals.

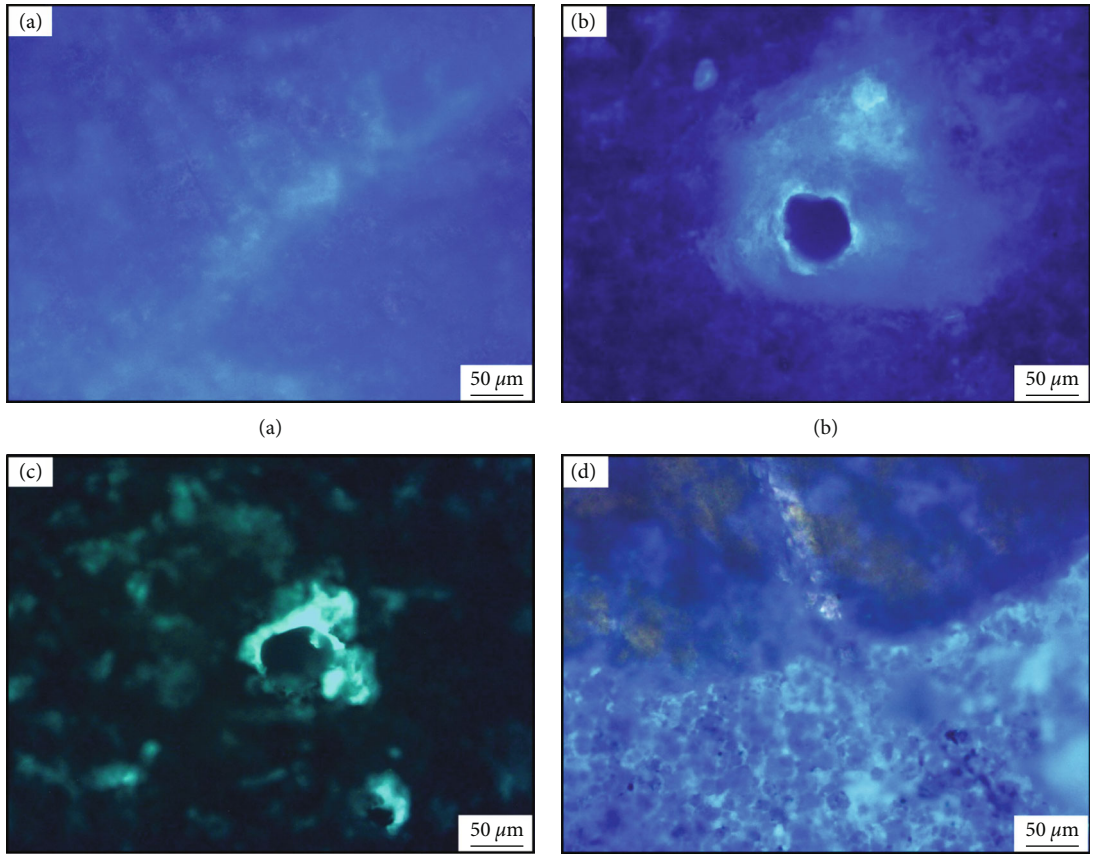

Figure 11: Fluorescence phenomenon of the platform margin reef-shoal reservoir under the fluorescence microscope. (a) Fluorescence of calcite cement veins, C1001, Kunkelaqi Formation, section e. (b) Fluorescence of calcite cement dissolution pore, C-1001, Kunkelaqi Formation, section e. (c) Fluorescence of calcite cement dissolution pore, C1006, Kunkelaqi Formation, section e. (d) Fluorescence of two-phrase carbonate fillings, C1322, Balediertage Formation, section a.

5.1.2. Palaeosource. The accumulation of siliceous clasts from orogenic wedges or cratons leads to mixing of carbonate and siliceous clastic deposits or to the termination of carbonate deposits [26]. Some researchers believe that terrigenous clastic deposition far away from the mainland is the most fundamental controlling factor for the formation of carbonate platform [27]. Therefore, studies have shown that in a high-nutrient environment with a small amount of remote siliceous debris injection, corals adapted to a high cleanliness and low-nutrient environment are gradually replaced by algae and sponges that prefer a high-nutrient environment [28]. In other words, the input of a small amount of siliceous debris is beneficial to the development of algal reefs. Therefore, there are two sides to the influence of the source of antiquities on the development of platform margin reef and shoal. No terrigenous coarse debris was found in the Zarjak, Kakak, and Kunklaqi formations in the Aoyibulake and Serpapayi sections (Figures 3 and 4). The rose diagram of the Conklin Formation sandstone laminate occurrence in Sishichang section shows that the main direction of the palaeocurrent is NW (Figure 9(a)), indicating that the provenance came from the Tarim Craton in the south. Guo [24] further demonstrated that the clastic rock components and heavy mineral assemblages in the Kangklin Formation reflect stable tectonic setting, and the detrital zircon dating of sandstone revealed that the provenance was mainly from the paleouplift within the Tarim block [24, 29]. Therefore, the platform margin reef-shoal located in the slope of the front edge of Keping-Aksu Uplift belongs to the remote source type, and a small amount of siliceous fine debris input could promote the large-scale development of algal reef. In contrast, the rose pattern of sandstone laminate occurrence in the Baledilta Formation showed a SSE direction of paleocurrenic flow, indicating that the provenance came from the southern Tianshan polycyclic orogenic belt in the north (Figure 9(b)). The sandstone detrital model of the Kalazhierjia Formation in the western section of Maidantawu subregion also indicates that the provenance is mainly from the multicycle orogenic belt [30]. Near source coarse clastic deposition of fan delta and braided river delta developed under carbonate platform of Kalazhierjia Formation and Balediertage Formation in Kezibulake section (Figure 4 and Figure 5), among which volcanic breccia and tuff all reflect the characteristics of near source (Figures 9(c) and 9(d)). Therefore, the coarse clastic from the southern Tianshan orogenic belt was easy to be imported into the platform margin of the slope in front of the orogenic wedge. The mixed sedimentation restricted

the growth and expansion of platform margin reef-shoal to a certain extent.

5.1.3. Paleogeomorphy. The relatively high palaeogeomorphology in the basin is prone to reef-shoal facies, and the high productivity of carbonate in the reef-shoal region promotes the palaeogeomorphology difference [31, 32]. During Devonian to Carboniferous, the Middle Tianshan-Yili block and Tarim block collided continuously (Figure 10(a)). On the one hand, the northern margin of Tarim block developed giant foreuplift inherently on the basis of Keping-Aksu Uplift due to tectonic flexural action (Figure 10(b)). On the other hand, extrusion resulted in the development of a series of fault-spreading folds parallel to the orogenic belt in the southern Tianshan thrust wedge top zone (Figure 10(c)), which constituted the relatively high part of the Paleozoic paleogeomorphology in the area. Controlled by scissor-type closure, there was still a west-opening residual marine basin in the northwestern margin of Tarim Basin from Late Carboniferous to Middle Permian [14]. During the Zhaerjiake period, the platform margin reef-shoal began to develop along the high slope of the front slope of Keping-Aksu Uplift. Due to the low basement topography and smooth seawater circulation in the southwest (Piqiang area), the platform margin reef-shoal was characterized by large-scale and continuous distribution (Figure 6 and Figure 10(c)). The topographic elevation of the uplifted basement became steeper, the sea basin became narrower, the seawater circulation became worse, and the facies zone became narrower. At the same time, in the front of the southern Tianshan orogenic belt, isolated platforms began to develop on the wedge top underwater anticline with suitable water depth (Figure 10(c)). During the Balerdiertage period, because of the deflection of the southern Tianshan orogenic wedge, the paleogeomorphic conditions suitable for the development of platform margin reef-shoal might have appeared in the northeast slope of the Keping-Aksu Uplift. And the platform margin reef-shoal extended further to the northeast. On the side of the orogenic wedge of the southern Tianshan mountains, because of the scale limitation of the anticline, the platform margin reef-shoal developed in the isolated platform was difficult to form belts. The isolated platform margin reef-shoal is characterized by small-scale and discrete distribution (Figure 7 and Figure 10(c)).

5.2. Exploration Potential of Platform Margin Reef-Shoal. According to the classification standard of Paleozoic carbonate reservoir rocks in Keping area [33], the quality evaluation of the Upper Carboniferous to Middle Permian platform margin reef-shoal reservoirs in Wushi area was medium (II) to poor (III) (Table 1). The porosity of platform margin reef-shoal reservoir was 0.72%~4.2%, and the permeability was $0.023 \sim 3.74 \times 10^{-3}$ mD. The porosity of platform edge shoal reservoir was 0.56%~3.4%, and the permeability was $0.028 \sim 2.55 \times 10^{-3}$ mD. There was no significant correlation between reservoir physical property and sedimentary facies type and lithology. Thin sections showed that the primary pores of the reservoir were mostly cemented in the later stage (Figure 3(e)), and the deviation of reservoir physical property might be related to the strong diagenesis in later stage.

Previous studies had shown that the reef limestone and micritic limestone of the Lower Permian-Middle Permian were intermediate-good source rocks themselves, but the outcrops were mainly low-mature source rocks (R_o is 0.42%~1.15%), which may be due to the lack of overlying Cenozoic cap rocks [33]. The huge thick tidal flat mudstone in Kalundaer Formation was stable and could be used as a regional cap rock. The oil-source correlation showed that the oil seedlings of Balikelike Formation exposed near Piqiang were from the source rocks of this formation [34]. The C isotope correlation reveals that oil and gas migrated at a short distance, and the oil seedlings should be self-generated and self-stored [33].

By fluorescence thin sections observation, the blue and blue-green fluorescence was significant along the calcite cement vein and near the dissolution hole of the reservoir. This phenomenon showed that after the formation of cement, oil and gas migration and accumulation did occur along fractures or dissolution holes and caves (Figure 11). In fact, several samples with medium physical properties came from the Aoyibulake and Kezilebulake sections adjacent to the fault zone (Figure 1). This might be due to the development of rock fractures near the fault zone, and the deep hydrothermal solution was also easy to migrate and dissolve. Although the physical properties of platform margin reef-shoal reservoirs were poor, their huge distribution scale made up for this defect to a certain extent. To sum up, in the covered area, the platform margin reef-shoal reservoirs adjacent to the fault zone and with large sedimentary thickness might have good hydrocarbon exploration prospects.

6. Conclusions

(1) The platform margin reefs in the Wushi area were dominated by algae reefs, and the platform margin shoals are dominated by bioclastic shoals and gravel shoals. The characteristics of algal bind between grains were common

(2) During the Zhaerjiake period, interbedded reefs and shoals were the main type, and platform marginal reefs were of the progressive type. During the Balediertage period, huge thick platform margin reefs were the main type, and platform margin reefs were of accretion-weak progressive type

(3) The development controlling factors of the platform margin reef-shoal are mainly relative sea-level change, palaeosource, and paleogeomorphy. Relative sea-level changes controlled the development characteristics and superposition mode of the platform margin reef-shoal; there were two sides of the influence of the palaeosource on the platform margin reef-shoal; the paleogeomorphology controlled the development position and spreading scale of platform margin reef-shoal

(4) In the covering area, the platform margin reef-shoal reservoirs adjacent to the fault zone and with large sedimentary thickness might have a good prospect for hydrocarbon exploration

Data Availability

Data are available on request.

Conflicts of Interest

The authors declare that there is no conflict of interest regarding the publication of this paper.

Acknowledgments

This research was funded by the National Natural Science Foundation of China (No. U19B6003).

References

[1] Z. Zhao, "Types, accumulation models and exploration concepts of marine carbonate reservoirs," *Petroleum Exploration and Development*, vol. 35, no. 6, pp. 692–703, 2008.

[2] G. H. Wu, Q. M. Li, B. S. Zhang, L. S. Dong, Y. G. Zhang, and H. Q. Zhang, "Structural characteristics and exploration fields of no. 1 faulted slope break in Tazhong area," *Acta Petrolei Sinica*, vol. 26, no. 1, pp. 27–30, 2005.

[3] J. Y. Gu, X. Y. Zhang, P. Luo, Z. Luo, and H. Fang, "Development characteristics of organic reef-bank complex on Ordovician carbonate platform margin in Tarim Basin," *Oil & Gas Geology*, vol. 26, no. 3, pp. 277–283, 2005.

[4] Y. Ma, "Generation mechanism of Puguang gas field in Sichuan basin," *Acta Petrolei Sinica*, vol. 28, no. 2, pp. 9–14, 2007, 21.

[5] C. Zou, C. Xu, Z. Wang et al., "Geological characteristics and forming conditions of the platform margin large reef-shoal gas province in the Sichuan Basin," *Petroleum Exploration and Development*, vol. 38, no. 6, pp. 641–651, 2011.

[6] W. Zhao, A. Shen, J. Zhou, X. wang, and J. Lu, "Types, characteristics, origin and exploration significance of reef-shoal reservoirs: a case study of Tarim Basin, NW China and Sichuan Basin, SW China," *Petroleum Exploration and Development*, vol. 41, no. 3, pp. 257–267, 2014.

[7] J. F. Han, C. H. Sun, Z. Y. Wang, Y. G. Ji, H. Li, and J. Chen, "Superimposed compound karst model and oil and gas exploration of carbonate in Tazhong uplift," *Earth Science*, vol. 42, no. 3, pp. 410–420, 2017.

[8] L.-D. Wang, B.-S. Yu, Y.-W. Zhang, and J.-J. Miao, "Sedimentary facies and model of Kangkelin age, western Tarim Basin," *Petroleum Exploration and Development*, vol. 33, no. 6, pp. 707–712, 2006.

[9] Z. Zhang, S. Wu, Z. Gao, S. L. Xiao, and Bahatehan, "Research on sedimentary model from Late Carboniferous to Early Permian epoch in Kalpin region, Xinjiang," *Xinjiang Geology*, vol. 1, pp. 9–20, 1983.

[10] Deledaer, "Sedimentary system of Carboniferous-Permian of western Tarim," *Xinjiang Geology*, vol. 14, no. 4, pp. 350–357, 1996.

[11] J. H. Luo, Z. C. Che, X. Y. Zhou, Y. Li, J. L. Li, and J. Y. Zhang, "Spatio-temporal distribution and its oil-gas significances of Permian reef limestones on the northwestern margin of the Tarim basin," *Geological Review*, vol. 53, no. 5, pp. 577–585, 2007.

[12] M. B. Allen, B. F. Windley, and C. Zhang, "Palaeozoic collisional tectonics and magmatism of the Chinese Tien Shan, central Asia," *Tectonophysics*, vol. 220, no. 1-4, pp. 89–115, 1993.

[13] B. F. Han, G. Q. He, X. C. Wang, and Z. J. Guo, "Late Carboniferous collision between the Tarim and Kazakhstan–Yili terranes in the western segment of the South Tian Shan Orogen, Central Asia, and implications for the northern Xinjiang, western China," *Earth-Science Reviews*, vol. 109, no. 3-4, pp. 74–93, 2011.

[14] Y. Zou, Z. Xing, and Z. Xu, "Evolution of sedimentary basins in Tarim during Neoproterozoic-Paleozoic," *Earth Science*, vol. 39, no. 8, pp. 1200–1216, 2014.

[15] Z. Zhou, *The Strata of Tarim Basin*, Science Press, Beijing, 2001.

[16] C. Jia, S. Zhang, and S. Wu, *Tarim Basin and Surrounding Strata [M]*, Science Press, Beijing, 2004.

[17] A. H. Knoll, J. M. Hayes, A. J. Kaufman, K. Swett, and I. B. Lambert, "Secular variation in carbon isotope ratios from Upper Proterozoic successions of Svalbard and East Greenland," *Nature*, vol. 321, no. 6073, pp. 832–838, 1986.

[18] J. L. Banner and G. N. Hanson, "Calculation of simultaneous isotopic and trace element variations during water-rock interaction with applications to carbonate diagenesis," *Geochimica et Cosmochimica Acta*, vol. 54, no. 11, pp. 3123–3137, 1990.

[19] E. L. Grossman, T. E. Yancey, T. E. Jones et al., "Glaciation, aridification, and carbon sequestration in the Permo- Carboniferous: the isotopic record from low latitudes," *Palaeogeography, Palaeoclimatology, Palaeoecology*, vol. 268, no. 3-4, pp. 222–233, 2008.

[20] B. U. Haq and S. R. Schutter, "A chronology of Paleozoic sea-level changes," *Science*, vol. 322, no. 5898, pp. 64–68, 2008.

[21] X. Zhu, D. Zhong, X. Yuan et al., "Development of sedimentary geology of petroliferous basins in China," *Petroleum Exploration and Development*, vol. 43, no. 5, pp. 820–829, 2016.

[22] Z. Zhao, "Indicators of global sea-level change and research methods of marine tectonic sequences: take Ordovician of Tarim Basin as an example," *Acta Petrolei Sinica*, vol. 36, no. 3, pp. 262–273, 2015.

[23] Z. Sun, S. Wang, H. Xiong, K. Wu, and J. Shi, "Optimal nanocone geometry for water flow," *AICHE Journal*, vol. 68, no. 3, article e17543, 2022.

[24] C. Guo, J. Gao, and Z. Li, "Depositional and provenance records of Lower Permian sandstones from Sishichang area, northwestern Tarim Basin: implication for tectonic evolution," *Earth Science*, vol. 43, no. 11, pp. 4149–4168, 2018.

[25] M. C. Rygel, C. R. Fielding, T. D. Frank, and L. P. Birgenheier, "The magnitude of Late Paleozoic glacioeustatic fluctuations: a synthesis," *Journal of Sedimentary Research*, vol. 78, no. 8, pp. 500–511, 2008.

[26] S. L. Dorobek, "Synorogenic carbonate platforms and reefs in foreland basins: controls on stratigraphic evolution and platform/reef morphology," *Special Publications*, vol. 52, pp. 127–147, 1995.

[27] J. Gu, F. Ma, and L. Ji, "Types, characteristics and main controlling factors of carbonate platform," *Journal of Palaeogeography*, vol. 11, no. 1, pp. 21–27, 2009.

[28] N. R. Watts and R. Riding, "Growth of rigid high-relief patch reefs, mid-Silurian, Gotland, Sweden," *Sedimentology*, vol. 47, no. 5, pp. 979–994, 2000.

[29] Z. Sun, B. Huang, Y. Liu et al., "Gas-phase production equation for CBM reservoirs: interaction between hydraulic fracturing and coal orthotropic feature," *Journal of Petroleum Science and Engineering*, vol. 213, p. 110428, 2022.

[30] B. Jing, J. H. Luo, and Z. C. Che, "Evolution of the Carboniferous-Permian Foreland Basin and Hydrocarbon Prospects in the Northwestern Margin of the Tarim Basin," *Tech. Rep., Research Institute of Exploration and Development*, PetroChina Tarim Oilfied Company, 2006.

[31] Z. Sun, B. Huang, Y. Li, H. Lin, S. Shi, and W. Yu, "Nanoconfined methane flow behavior through realistic organic shale matrix under displacement pressure: a molecular simulation investigation," *Journal of Petroleum Exploration and Production Technologies*, vol. 12, no. 4, pp. 1193–1201, 2022.

[32] C. Lin, H. Yang, J. Liu et al., "Paleostructural geomorphology of the Paleozoic central uplift belt and its constraint on the development of depositional facies in the Tarim Basin," *Science in China*, vol. 52, no. 6, pp. 823–834, 2009.

[33] W. Xia, Y. Yang, G. Zhang et al., "Comprehensive research report on petroleum geology in paleozoic to cenozoic outcrop areas from Aksu to Keping," Exploration and Development Research Institute of Tarim Oilfield Branch, Exploration and Development Research Institute of Dianqiangui Oilfield Branch, 2002.

[34] Z. Sun, B. Huang, K. Wu et al., "Nanoconfined methane density over pressure and temperature: wettability effect," *Journal of Natural Gas Science and Engineering*, vol. 99, p. 104426, 2022.

Hindawi
Geofluids
Volume 2022, Article ID 2197001, 12 pages
https://doi.org/10.1155/2022/2197001

WILEY | Hindawi

Research Article

Numerical Simulation of Choke Size Optimization in a Shale Gas Well

Jianfa Wu, Xuefeng Yang, Yunting Di, Peiyun Li, Jian Zhang, and Deliang Zhang

PetroChina Southwest Oil & Gasfield Company, Chengdu 610000, China

Correspondence should be addressed to Yunting Di; dyt87797@petrochina.com.cn

Received 13 January 2022; Accepted 24 March 2022; Published 6 May 2022

Academic Editor: Zheng Sun

To optimize the flowback system of shale gas horizontal wells after fracturing and to maximize the production capacity of gas wells, pipe flow and flowback models of shale gas multistage fractured horizontal wells were established based on the actual geological engineering conditions and the fracture parameters inverted from automatic history matching by combining experimental and numerical simulation methods. Optimization of the maximum choke size, reasonable opening choke size, replacement stages, and choke replacement frequency were studied. The research results show that the larger the production pressure difference in the early period, the higher the initial gas production rate but the easier the migration of proppant and the higher its stress sensitivity, which increases the permeability damage and weakens the reservoir recovery ability. Thus, the fracture conductivity gets worse and the later gas production rate and liquid production rate get lower. Specifically, the research results mainly include the following: (1) The laboratory experiment results show that the effective stress exceeding 19 MPa caused a proppant breakage and embedding phenomenon, leading to difficult recovery from reservoir permeability damage. Therefore, the maximum production pressure difference corresponding to the single-well maximum choke size shall not exceed 19 MPa. (2) A small opening choke size of a shale gas well is superior to the large one, and according to the numerical simulation, the choke size of 3 mm is recommended to be the reasonable opening choke size. (3) Under the drainage and production systems of replacing the choke size from small to large, the simulation results indicate that the production effect under the drainage and production systems of increasing the choke size incrementally stage by stage with an increase in amplitude of 1 mm is much better than that under the drainage and production systems of increasing the choke size by skipping the stage. (4) When the choke size is increased stage by stage, the research results indicate that the optimal duration of each grade of choke size is 3 days, beyond which, the increase of EUR will not be remarkable. The application of the proposed fine choke system research method in Well-CN001 indicates that the influence amplitude of the reasonable choke system on the daily gas production of Well-CN001 is in the range of 65.96%–121.67% and that on single-well EUR increase amplitude in 20 years is in the range of 5.2%–22.27%. The research results provide technical support for understanding the influence of different choke systems on the productivity of shale gas wells and optimizing the reasonable drainage and production systems of shale gas wells after fracturing.

1. Introduction

Shale gas reservoirs typically require large-scale volume fracturing to be economically viable. Upwards of 10,000 cubic meters of fracturing fluid is injected into a formation, making the flowback process particularly important. The amounts of fluid filtration, conductivity of hydraulic fractures, and subsequent development of the wells are impacted. Therefore, the selection of the optimal choke size is a key part of the design of drainage and production systems, which determine whether gas well productivity can be achieved.

The drainage and production systems currently applied on site are quite different. Chokes are generally between 3 mm and 13 mm and are replaced from large to small or small to large, with varying replacement frequencies. Some scholars believe that the use of large chokes at the beginning makes the fracturing fluid flow back as soon as possible, reducing the damage from fracturing fluid to the reservoir, such as water lock damage and clay expansion. Meanwhile,

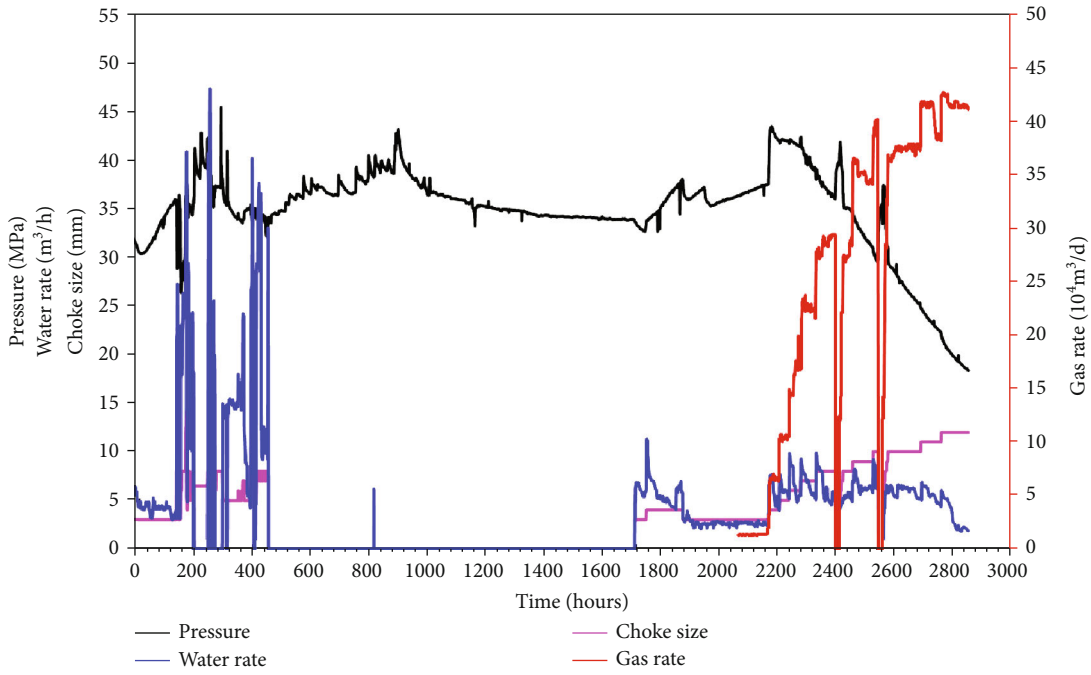

Figure 1: Well-CN001 drainage and production-test curve.

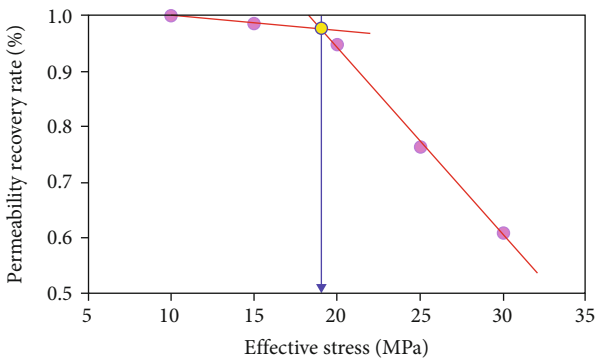

Figure 2: Permeability recovery curve under different effective stress conditions.

many scholars prefer gradually enlarging the choke, so as to prevent the embedding and reflux of proppant and improve the fracture conductivity. The advantage of adopting the choke system is usually related to the protection of fracture conductivity, which is related to stress sensitivity. Miller et al. and Quintero and Devegowda [1–2] believe that fluid production from the reservoir reduces the pore pressure and increases the net effective stress. The increase of stress leads to the decrease of fracture conductivity, including hydraulic fracture and natural fracture. Wilson et al., Lerza et al., Rojas and Lerza, and Rodriguez and Maldonado [3–6] believe that excessive production pressure difference in the early stage of shale gas well drainage and production damages fracture stress sensitivity seriously. Fractures are the main gas production channels in shale reservoirs, so the production under smaller pressure difference in the early period is quite important to protect fracture conductivity and optimize the EUR.

The choke system affects the flowback rate and production of shale gas wells. Numerical simulation and production data analysis have been used to study the postfracture choke system of shale gas wells. Liu et al. [7] studied the size selection of the blowout choke by establishing the two-dimensional filtration and fracture-forced closure model of fracturing fluid and the proppant reflux model of the shale gas well. However, in the study, the selection range of the choke size is only between 3.5 mm and 6.5 mm and only one choke size is selected without considering the change of the choke size in the same model. Han et al. [8] used numerical simulation and experimental analysis to study various backflow influencing factors, but it is mainly mechanism research and lacks the combination with the flowback system. Wijaya and Sheng [9] analyzed a large number of the flowback data of shale gas wells in a particular area but lacked theoretical support and could not accurately represent the formation. Some early studies tried to predict the impact of the choke system on final recoverable reserves; however, due to the prediction methods, there were no consistent results. Some researchers believe that the choke system can improve the EUR, while others believe that the choke system cannot significantly affect the recovery efficiency and also hurts the net present value (NPV). For example, Tripoppoom et al. [10] simulated the production situations of the Haynesville Oilfield by means of numerical simulation, which indicated that the choke system could improve the 30 years' EUR by 28%.

The choke system is considered to be better able to protect the fracture conductivity in the early stage of shale gas well, so as to reach the goal of improving gas well's EUR. In the early literatures, however, no consistent conclusion is reached on whether the choke system is really beneficial to EUR. At present, the formulation of the drainage and

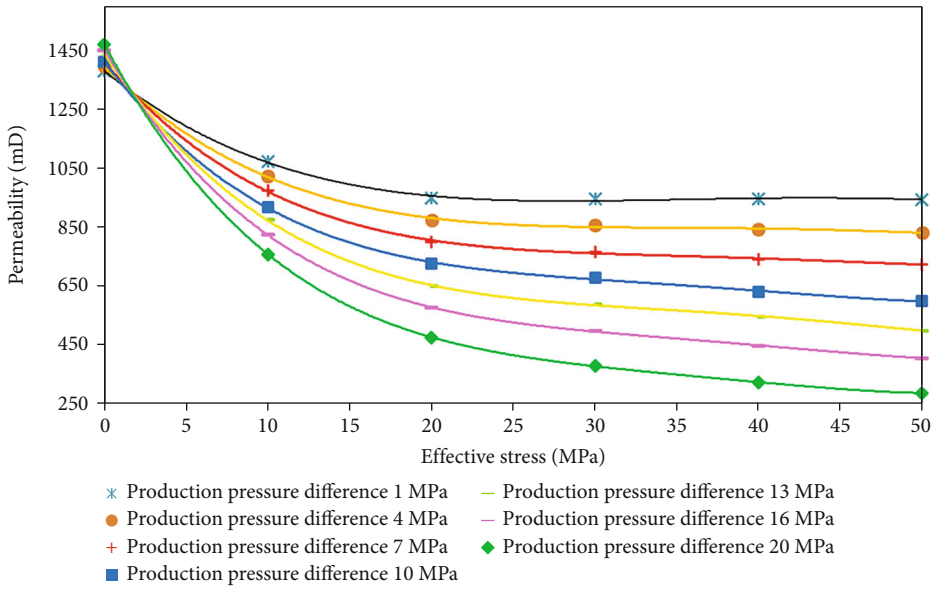

Figure 3: Permeability curve under different production pressure difference and effective stress conditions.

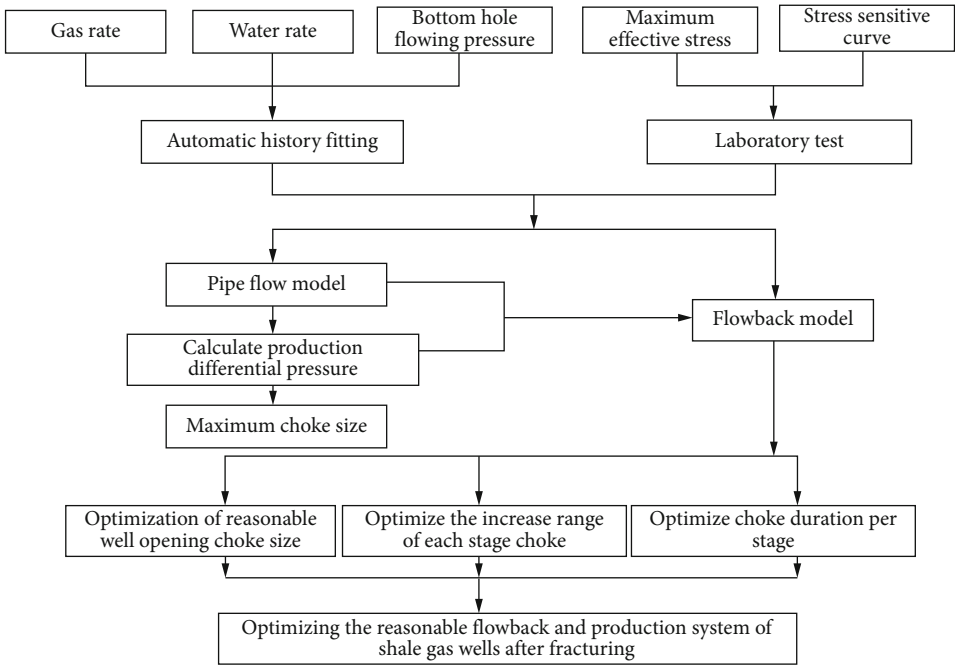

Figure 4: Workflow chart for optimizing choke system of shale gas well.

production system of shale gas well mainly depends on field experience and statistical analysis, there has been no basis for selecting the reasonable flowback control parameter and especially choke size and replacement timing, and there is lack of theoretical researches on reasonable drainage and production system. Based on literature research, the impact of the choke system on gas well EUR is unclear, highlighting the importance of this study. These studies did not conduct sufficient uncertainty analysis of their results, leading to different conclusions. The previous studies only used one reservoir model, but there are many uncertainties in the volume characteristics of the reformed reservoir, including relative permeability, capillary pressure curve, stress sensitivity, and fracture and matrix water saturation, which is considered to be the main reason for different conclusions. In this paper, a set of research methods for optimizing the choke system in the flowback stage after fracturing of a shale gas well are innovatively developed by adopting the method of combining numerical simulation and laboratory experiment. Different from the previous researches, this paper carries out numerical simulation from the perspective of mechanism and then combines the results with the production, so as to form the choke system which can be used to guide field production. It is concluded that the selection of the

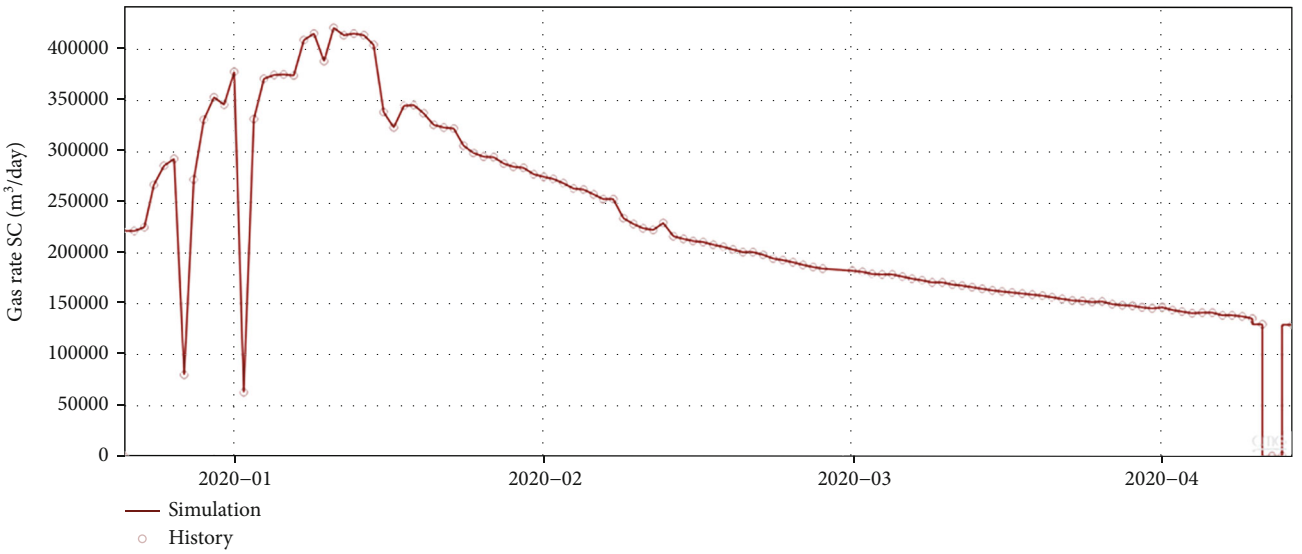

Figure 5: Daily gas production fitting diagram.

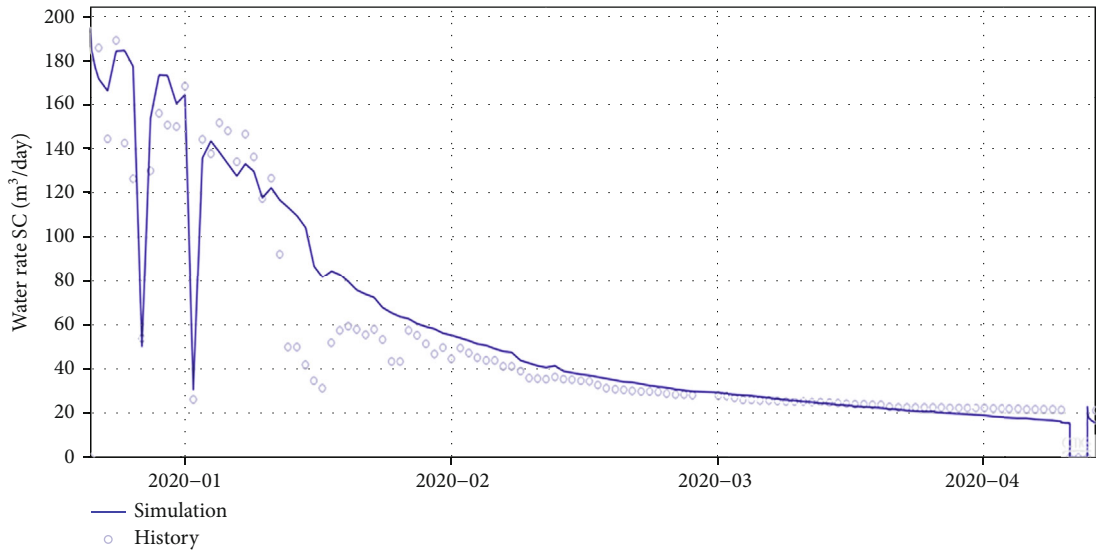

Figure 6: Daily liquid production fitting diagram.

reasonable choke size, replacement mode, replacement frequency, and increasing stages in the flowback process of shale gas wells is of important significance to the optimization of gas well drainage and production systems and lays a theoretical base for the formulation of a reasonable flowback system of a shale gas well.

2. Background

The drainage and production systems of "Well plugging–Controlled drainage–Step-by-step amplification–Adjustment and stability" are adopted in the shallow shale gas wells of southern Sichuan Basin according to experience, and then, the test production rate is obtained according to the test specification to evaluate the productivity of gas wells. However, refined drainage and production systems have not been established and the selection of on-site choke systems is still based on experience. There is no theoretical basis for the formulation of a detailed choke system such as optimal well opening choke size, maximum choke size, duration of different chokes, and increased choke ranges at each level. Additionally, a series of problems occurred in the drainage and production stages, affecting the productivity of the wells (Figure 1).

Due to the lack of theoretical support, on-site drainage and production systems are mostly determined by experience, causing the following problems. (1) During drainage and production, the well is shut due to certain reasons and the choke size is adjusted back and forth, affecting the productivity of the gas well; (2) the size of choke is too large at the start of production, resulting in the rapid decline of casing pressure and the backflow and embedding of the proppant; (3) the maximum choke size of a single well cannot be determined, and the use of too large a choke leads to

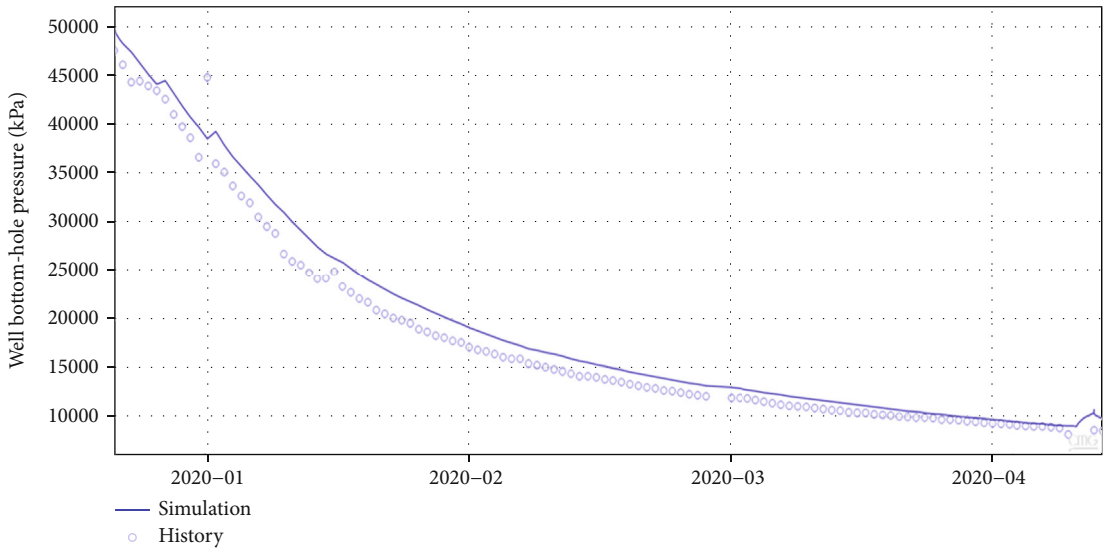

Figure 7: Bottom hole flow pressure fitting diagram.

Table 1: The inversion results of Well-CN001 fracture parameters.

Uncertain parameter	Min value	Max value	*P*50 value
Fracture height (m)	5	20	12.7
Fracture half-length (m)	70	180	85.4
Fracture conductivity (md·m)	20	70	29
Fracture water saturation	0.6	0.8	0.713
Fracture width (m)	0.07	0.1	0.09
HF efficiency	0.6	0.9	0.696

serious sand production in the gas well, affecting the conductivity of supporting fractures and the smoothness of wellbore flow channels; and (4) the duration of each level of choke is uncertain. The duration of each level is as short as a few hours and as long as more than 10 days, and it is defined only by experience.

2.1. Research on Stress Sensitivity of Hydraulic Fractures. Due to the artificial fractures in the fracturing transformation of a shale gas reservoir, the proppant will be embedded and broken and will migrate during drainage and production, creating stress sensitivity within the reservoir. With changes in the drainage and production systems and effective stress, the fracture permeability will decrease irreversibly, affecting the EUR of shale gas wells. Conducting stress sensitivity tests on artificial fractures in shale reservoirs under various production pressure differential conditions and then quantitatively evaluating the impact of artificial fractures on shale, proppant embedding, damage, migration, and permeability will provide support for determining an optimal choke system. The cores of *Longyi* $_1^1$ *and Longyi* $_1^2$ layers were selected for artificial fracture experiments and stress sensitivity experiments on shale artificial fracture permeability under different pressure change modes and different production pressure differentials.

When the effective stress acting on the core decreases, pressure within the reservoir recovers. The permeability recovery rate of artificial fractures in shale was analyzed and studied when the effective stress decreased. According to the results of the indoor experiment (Figure 2), with the gradual increase and decrease of the initial effective stress, the damage of the reservoir in the initial stage gradually decreases, the recovery ability of the reservoir gradually increases, and the increase range of the recovery rate first increases and then decreases. The relationship between effective stress and permeability recovery rate has an inflection point at the effective stress of 19 MPa, i.e., the permeability recovery rate at this point is high (95%), and the maximum increase in recovery rate (18%) occurs. Then, continuing to reduce the initial effective stress, the permeability recovery rate is 98% and the recovery rate increases rapidly from 18% to 3%, i.e., the protection increase of the reservoir is not obvious. When the effective stress exceeds 19 MPa, the proppant is apparently broken and embedded and the reservoir permeability damage is difficult to recover from.

Experiments of artificial fracturing and sand laying in shale yielded permeability stress sensitivity curves of artificial fracture under different production pressure differentials. The experiments exhibited significant differences in the permeability sensitivity of artificial fractures in shale with different production pressure differentials. The greater the production pressure difference is, the greater the decline of fracture permeability will be (Figure 3). The stress sensitivity curves of different production pressure differences obtained from this research are the basis for the optimization numerical simulation of drainage and production systems based on the choke size.

2.2. Determination Method of the Optimal Choke System. Based on the experimental data, a set of detailed numerical simulation methods for choke system optimization was established in this study (Figure 4). Through a series of processes, the optimal choke system of a single well was determined.

The method is as follows.

(1) The fracture parameters of shale gas wells are inversed by automatic history fitting technology

(2) Based on the actual geological engineering parameters and inversion fracture parameters, the flowback and pipe flow models more in line with the actual production are established and the production differential pressures corresponding to different choke sizes of a single well are calculated

(3) The stress sensitivity curves under various production pressure differentials obtained from the experiments are applied to the flowback model, and different scenarios are designed to study the numerical simulation of the choke size optimization of a single well

(4) In the numerical model established by the combination of experiment and numerical simulation, the optimization of the maximum choke size, well opening choke size, choke increase range, and choke duration of each stage are performed

This method makes the numerical simulation process closer to the actual drainage and production process of shale gas wells. Thus, the simulation results are more accurate, solving the problem that the on-site drainage and production systems are formulated only by experience and providing theoretical support for guiding the formulation of on-site optimum drainage and production systems of shale gas wells.

2.3. Automatic History Fitting of Well-CN001. An early flowback model on Well-CN001 established the fracturing situation based on actual geological conditions, fracturing engineering parameters, and automatic history fitting results. After fracturing the well, the shape and volume of fractures were still unclear and it was difficult to accurately characterize fractures. Historical fitting uses production performance data to narrow the results and obtain optimal reservoir and fracture parameters. However, the conventional history fitting process is cumbersome and complex, so it is difficult to obtain representative fitting results efficiently and accurately. Automatic history fitting can solve this problem. Herein, the ability of an embedded discrete fracture (EDFM) to deal with complex fractures is used, combined with the Markov chain Monte Carlo inversion algorithm (MCMC) [10], and through artificial intelligence neural network automatic sampling machine learning, the automatic history fitting of three parameters, i.e., daily gas production, bottom hole pressure, and daily liquid production, is realized for Well-CN001 (Figures 5–7). Finally, the inversion of key fracture parameters of Well-CN001 includes effective fracture height, fracture length, conductivity, cluster effectiveness, and fracture water saturation. The inversion results of relevant fracture parameters are shown (Table 1).

2.4. Establishment of the Pipe Flow Numerical Model and Solution of Production Pressure Difference in the Shale Gas Well. The wellbore pipe flow model of the shale gas well is used to calculate the production differential pressure corresponding to different choke sizes of a single well and combine surface measures with formation flow conditions. The wellbore pipe flow model incorporates the fluid component model, inflow performance relationship model, flow correlation selection, and choke flow model. The establishment of the pipe flow model is based on the actual data of Well-CN001 (Figure 8). The depth of wellbore casing is 4,946 m, the inner diameter is 150 mm, and the outer diameter is 170 mm. The length of the completion section is 1,500 m, the number of perforation sections is 25, and the fracture parameters are inversed by automatic history fitting. The fluid components in the component model include water, methane, ethane, and carbon dioxide. The Peng–Robinson equation of the state and Pedersen viscosity calculation model are used. The IPR model adopts a trilinear transient model suitable for horizontal wells. The Baker–Jardine correlation suitable for the gas–water two-phase flow in horizontal wells is adopted as the flow correlation. The choke flow model includes a choke connecting the wellhead, a production pipeline, and a sink (Figure 9).

Herein, the optimization of the choke size in the post pressure flowback process of a shale gas well is based on

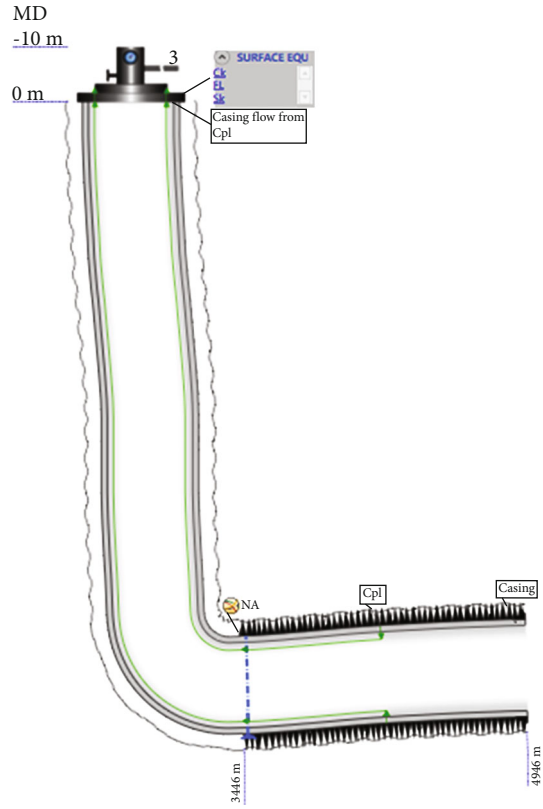

Figure 8: Schematic of Well-CN001 wellbore model.

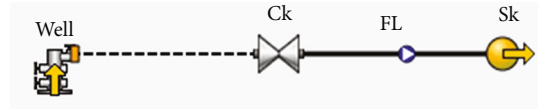

Figure 9: Schematic of Well-CN001 mouth flow model.

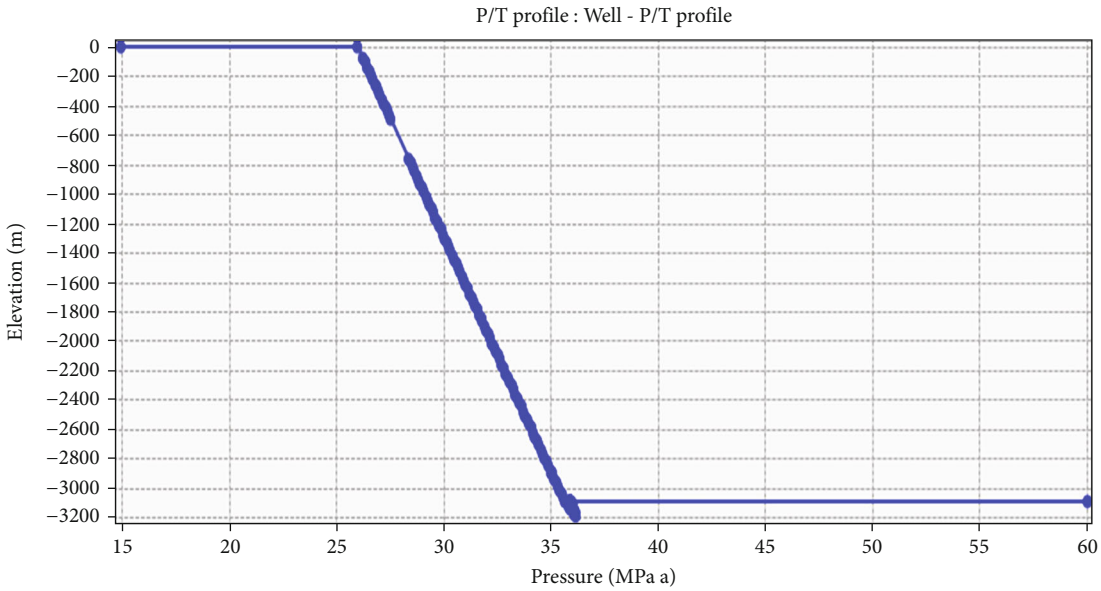

Figure 10: 12 mm choke size wellbore pressure profile.

Table 2: Production pressure difference corresponding to different choke sizes of Well-CN001.

Choke size (mm)	3	4	5	6	7	8	9	10	11	12
Production pressure difference (MPa)	1.1	3.5	4.5	9.0	12.7	16.2	19.0	21.1	23	24.0

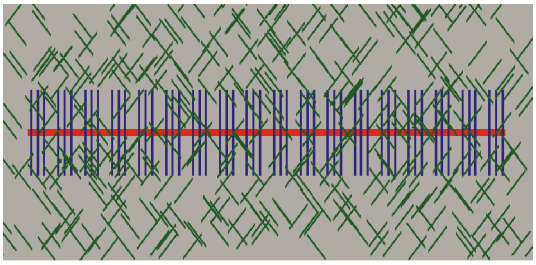

Figure 11: Schematic of numerical model of Well-CN001.

the calculation of production pressure difference corresponding to the choke size. Based on the pipe flow model established by the pipe flow calculation software, the production differential pressures corresponding to different choke sizes of Well-CN001 are determined. The size range of oil choke is 3 mm–12 mm, which is the common size of oil choke on site, and the formation pressure is 60 MPa. The wellbore pressure profile under different choke size systems is obtained through simulation, and the production differential pressure is calculated. The wellbore pressure profile calculated using a 12 mm choke size is shown (Figure 10). According to the model calculation results, the production differential pressures corresponding to different choke sizes of Well-CN001 are shown (Table 2).

2.5. Well Flowback Numerical Model. The numerical model of shale gas well flowback includes the matrix system and the fracture system (Figure 11). The establishment of the fracture system adopts the new-generation embedded discrete fracture EDFM simulation technology, which is more flexible than the local grid encryption technology. The fracture is directly embedded into the matrix grid, which can effectively reduce the number of grids and improve the calculation efficiency. The entire flowback model considers the characteristics of shale adsorption and desorption and the stress-sensitive effect of fractures, and the parameter setting is combined with the geological conditions, engineering parameters, and automatic history fitting results of actual wells. The relevant parameters of the model are shown (Table 3). The model assumes that the flow is a gas-water two-phase flow. It starts to simulate after the gas phase is stable and ignores the capillary force.

The flowback models consider the stress sensitivity under different choke sizes, i.e., the stress sensitivity curves corresponding to different production pressure differentials are designed. In the subsequent simulation study on the choke system, 41 numerical models are designed on the basis of this model and each of them sets the production pressure difference according to the choke size and then selects the corresponding stress sensitivity curve to carry out simulation calculation.

2.6. Optimization of the Maximum Choke Size. For a single well, the maximum choke size with relatively small impact on fracture conductivity is determined based on proppant reflux, embedding, and crushing. The production pressure difference corresponding to different choke sizes of Well-CN001 is calculated by the pipe flow model. According to the theory obtained from the stress sensitivity experiment of the shale artificial fracture, when the effective stress exceeds 19 MPa, the permeability damage of the artificial

Table 3: The relevant parameters of the Well-CN001 model.

Grid characteristics	pa Grid number Grid size	$263 \times 107 \times 1$ $10 \times 20 \times 20$	Fraction m
	Shale reservoir characteristics		
	Reservoir thickness	20	m
	Shale matrix porosity	0.06	Fraction
	Shale matrix permeability	0.0001	md
	Initial water saturation	30	%
	Rock compressibility coefficient	4.35×10^{-7}	Kpa
	Initial reservoir temperature	110	°C
	Formation pressure	60	MPa
	Fracture characteristics		
	Number of fracturing sections	25	
	Average section length	60	m
	Number of perforation clusters	3	
	Fracture height	12.8	m
	Fracture half-length	84.3	m
	Fracture width	0.097	m
	Fracture permeability	308.7	md
	Fracture cluster efficiency	0.702	Fraction

fracture is difficult to recover. Combined with the results of the two, the corresponding choke size of the well when the production pressure difference is about 19 MPa is the maximum choke size of the well. The maximum choke size is 9 mm (Figure 12). In the follow-up study, the choke replacement mode and replacement frequency are optimized and the maximum choke size simulated is set to 9 mm.

2.7. Optimization of the Well Opening Choke Size. Currently, the commonly used choke size of shale gas wells is between 3 mm and 13 mm. To study the influence of the well opening choke size on the early flowback process, since the maximum choke size of Well-CN001 is 9 mm, through the established shale gas well flowback numerical model, the initial choke size is between 3 mm and 9 mm, and then, the step-by-step increase range is 1 mm to the maximum choke size of 9 mm. The duration of each stage of choke is three days; 9 mm choke is used in the production stage under the total production time of 20 years and 3 months. The stress-sensitive curves corresponding to different choke sizes and different production differential pressures have been obtained through experiments. In the numerical simulation process, different choke sizes are set according to the experimental results and different stress-sensitive curves are used for the simulation calculation to improve the calculation accuracy.

The smaller the opening choke size is, the higher the initial daily gas production and peak daily gas production

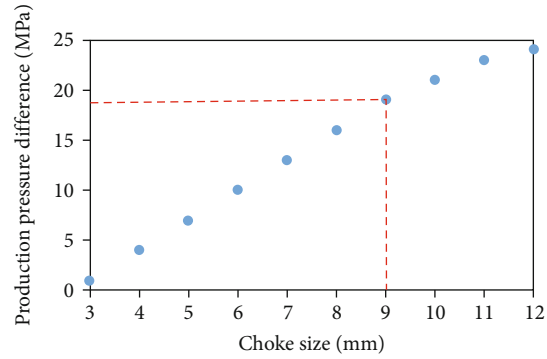

Figure 12: Maximum choke size under limited production differential pressure of Well-CN001.

within 3 months is but the daily gas production in the middle and late stages is lower (Figure 13). The initial choke size of 3 mm is 65.96% higher than the daily gas production on the 90th day of the initial choke size of 9 mm. With the increase of the opening choke size, the flowback rate and EUR in 20 years of production are lower and the reduction range gradually increases (Figure 14). The initial choke size of 3 mm is 13.19% higher than the EUR of the initial choke size of 9 mm. At the beginning, large choke flowback is adopted with the higher production pressure difference and the higher initial gas production. However, the proppant is more likely to migrate, causing high stress sensitivity and permeability damage, weakening the reservoir recovery ability and the fracture conductivity. The gas production and liquid production reduce in the later stage. Therefore, it is better to choose a small well opening choke size. The optimal well opening choke size of Well-CN001 is 3 mm (Figure 15).

2.8. Optimize the Increase Range of Each Stage Choke. The choke size and replacement stages in the early flowback process are also important factors affecting the productivity of shale gas wells. Herein, the choke size is simulated from 3 to 9 mm, the duration of each stage is five days, and the increase range of each stage is 1 mm, 2 mm, 3 mm, and 4 mm. In the simulation, different stress sensitivity curves are used under different choke sizes, 9 mm choke is used in the production stage, and the total production time is 3 months and 20 years.

Under the condition of constant choke duration, the smaller the increase of the choke size at each stage, the lower is the initial daily gas production and peak gas production in three months but the flowback rate daily gas production is larger in the middle and later stages (Figure 16). The daily gas production of each stage increased using 1 mm is 121.67% higher than that of the 90th day with an increase of 4 mm. With the increase of the size of each stage choke, the flowback rate and the EUR are lower in 20 years of production and the decrease rate increases (Figures 17–18). The increase of 1 mm per stage is 22.27% higher than the 20-year EUR with an increase of 4 mm. The smaller the increase of the choke size at each stage, the smaller the production differential pressure at the same time. This means that the permeability stress sensitivity of the shale artificial fracture is

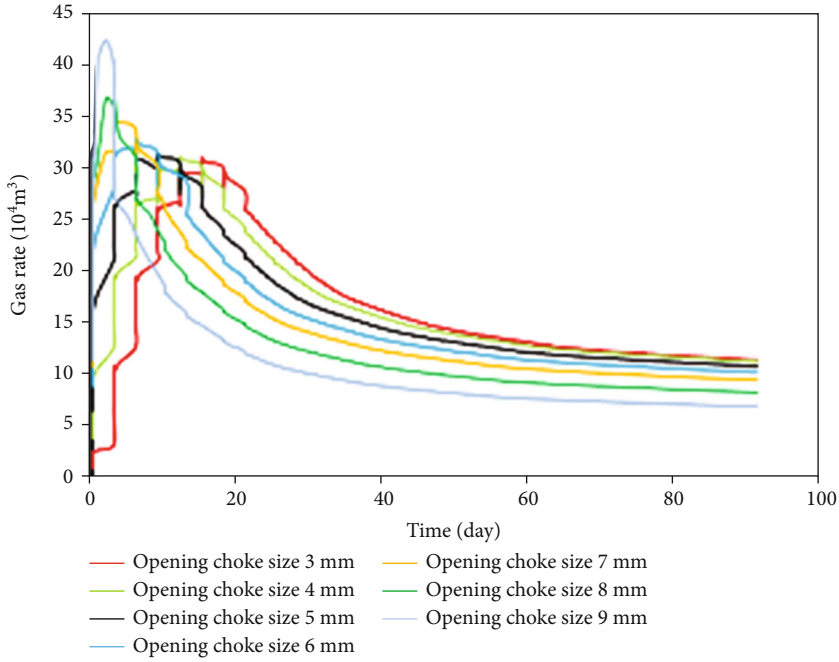

Figure 13: Comparison curve of daily gas production in three months with different choke replacement methods.

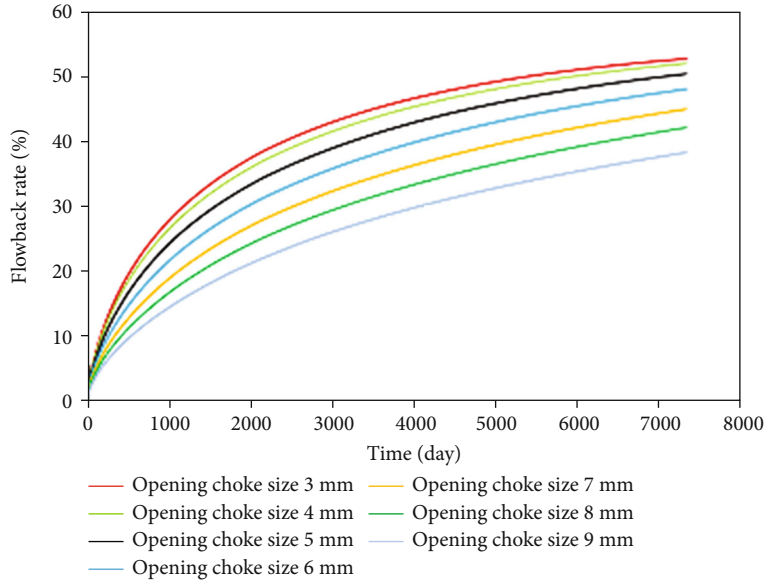

Figure 14: Comparison curve of 20-year flowback rate of different choke replacement methods.

weaker, providing favorable channels for later gas flow. Therefore, within the maximum choke size range, it is wise to increase the choke size by 1 mm at each stage rather than by 2 mm or larger, which is more helpful to improve the productivity of shale gas wells.

2.9. Optimize Choke Duration per Stage. The duration of each choke level is a specific research on the choke system. Through the established flowback model, the choke size is simulated from 3 to 9 mm, the increase range of each stage is 1 mm, and the duration of each stage is 1 day, 2 days, 3 days, 4 days, and 5 days. In the simulation, different stress sensitivity curves are used under different choke sizes; 9 mm choke is used in the production stage, and the total production time is 3 months and 20 years.

When the replacement stage of the choke size is 1 mm, the longer the duration of the choke size of each stage, the lower the daily gas production in the initial stage within three months, but the daily gas production is higher in the middle and later stages. When the duration is higher than three days, the increase of daily gas production decreases (Figure 19). The duration of each choke stage is five days, which is 90.19% higher than the daily gas production on the 90th day with a duration of one day. When the duration

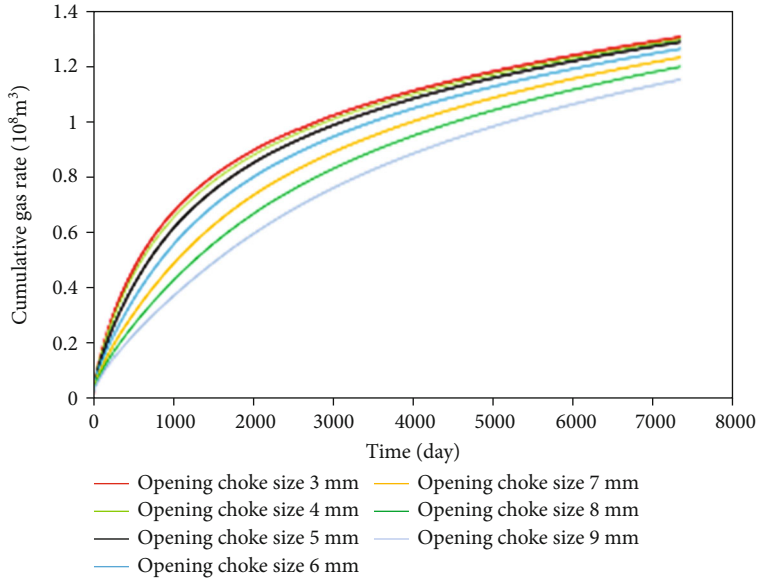

Figure 15: Comparison curve of 20-year cumulative gas production of different choke replacement methods.

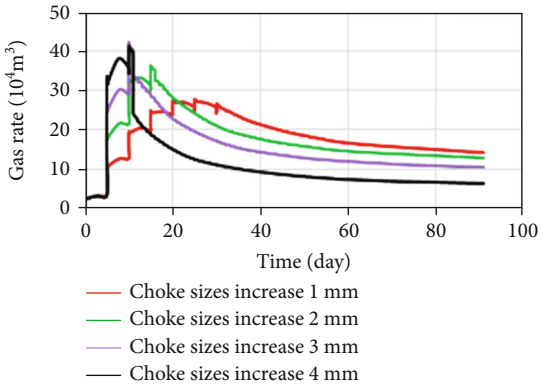

Figure 16: Comparison curve of daily gas production in three months for different choke size increase.

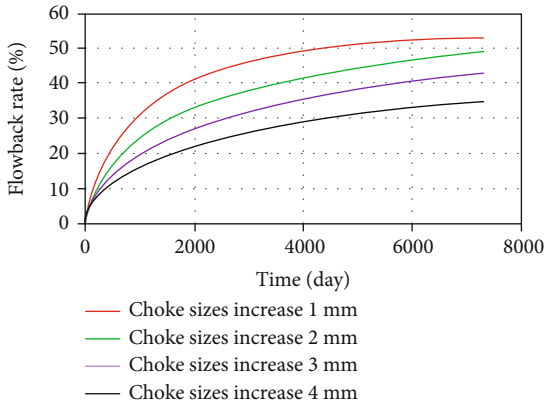

Figure 17: Comparison curve of 20-year flowback rate of different choke size increase.

of the choke size of each stage is less than three days, the 20-year flowback rate and EUR increase with the increase of duration. When the duration of the choke size at each stage

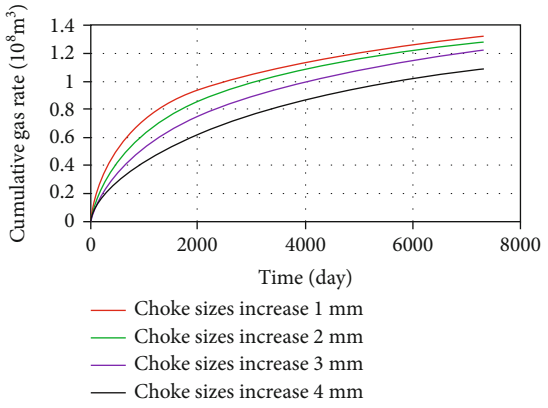

Figure 18: Comparison curve of 20-year cumulative gas production of different choke size increase.

is higher than three days, the flowback rate and EUR change slightly (Figure 20). The duration of each stage choke is five days, which is 5.2% higher than the 20-year EUR with a duration of one day. The longer the small choke size lasts, the smaller the early production differential pressure and the smaller the initial gas production is. The stress sensitivity becomes low, which can reduce the early fracture closure damage, helping to improve the fracture conductivity. Under the smaller initial reservoir damage, it is favorable to the increase of medium- and long-term cumulative gas production of a single well. With the increase of the duration of each level of choke, the time of drainage and production stage also increase. The increase of the overall drainage and production time leads to the longer retention time of the fracturing fluid in the reservoir and affects the production effect of gas wells. Therefore, it is better to keep the duration of each level of choke long. Therefore, under the condition that the choke size is increased step by step and the duration of each choke is the same, the optimal duration of each choke size is three days.

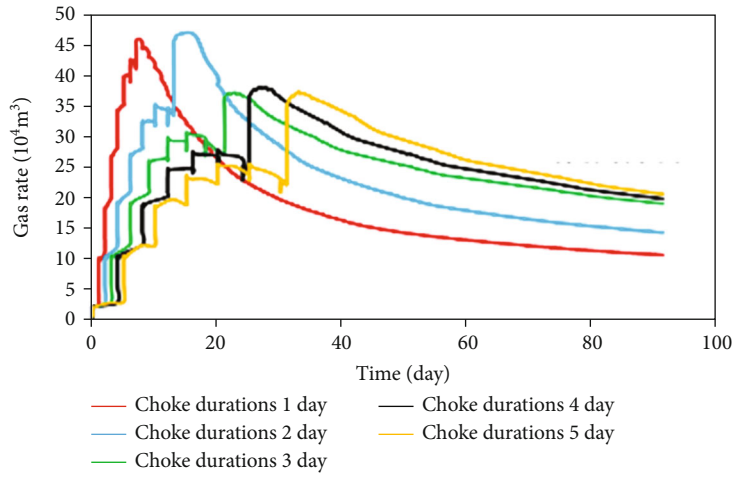

Figure 19: Comparison curve of daily gas production of three months with different choke durations.

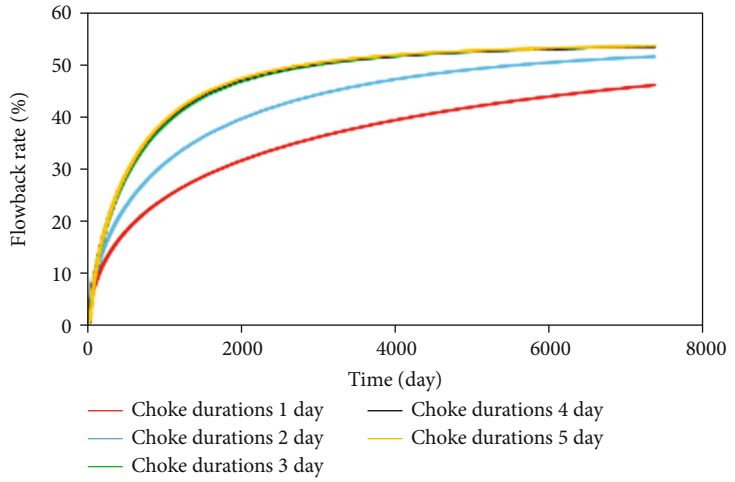

Figure 20: Comparison curve of 20-year flowback rate of different choke durations.

2.10. Limitation. In this paper, existing numerical simulation software are used to carry out numerical simulation analysis on the flowback of shale gas wells but they are limited in the simulation of shale imbibition and hydration and can hardly simulate shale imbibition and hydration. In the whole life cycle of a shale gas well, the variation of reservoir permeability caused by imbibition and hydration still has an influence on the result, which needs further researches.

3. Conclusion

(1) With the gradual decrease of the initial effective stress, the damage of the reservoir in the initial stage is weakened, the recovery ability of the reservoir is enhanced, and the increase range of the recovery rate initially increases and then decreases. When the effective stress exceeds 19 MPa, the proppant is apparently broken and embedded, which makes the reservoir permeability damage recovery more difficult. Therefore, the optimal maximum choke size of different shale gas wells is determined when the production differential pressure does not exceed 19 MPa

(2) Through the application of the refined choke system research method established in this paper to Well-CN001, the impact of different choke systems on the third month daily gas production of Well-CN001 is 65.96%–121.67% and the impact on the 20-year EUR of a single well is 5.2%–22.27%

(3) The higher the initial gas production is, the larger the early production pressure difference will be but the proppant is more likely to migrate and its stress sensitivity becomes high. The permeability damage increased and the reservoir recovery ability becomes lower if the fracture conductivity and the gas and liquid production decreased in the later stages. Therefore, the smaller the opening choke size of shale gas well is, the better it is. The common opening choke size can be 3 mm. Within the maximum choke size range, the increase range of the choke size at each stage is preferably 1 mm. When the choke size is

increased stage by stage, the optimal duration of each choke size is three days

Data Availability

The original contributions presented in this study are included in the article and further inquiries can be directed to the corresponding author(s).

Conflicts of Interest

The authors declare that the research was conducted in the absence of any other commercial or financial relationships that could be construed as potential conflicts of interest.

Acknowledgments

This work was financially supported by The Research On Improvements Of The Producing Degree In Shale (kt2021-11-02), The Major Technical Field Test Project of PetroChina (2019F-31-02), and the Science and Technology Cooperation Project of the CNPC-SWPU Innovation Alliance (2020CX020202). The research is supported by the PetroChina Southwest Oil & Gasfield Company.

References

[1] R. S. Miller, M. Conway, and G. Salter, "Pressure-dependent permeability in shale reservoirs implications for estimatedultimate recovery," in *Paper AAPG Search and Discovery 90122©2011 Presented at the AAPG Hedberg Conference*, Austin, Texas, December 2010.

[2] J. Quintero and D. Devegowda, "Modelling based recommendation for choke management in shale wells," in *Unconventional Resources Technology Conference. Society of Exploration Geophysicists, American Association of Petroleum Geologists, Society of Petroleum Engineers. URTEC-2154991-MS. URTEC-2015-2154991*, 2015.

[3] K. Wilson, I. Ahmed, and K. MacIvor, "Geomechanical modeling of flowback scenarios to establish best practices inthe midland basin horizontal program," *Unconventional Resources Technology Conference. Society of ExplorationGeophysicists, American Association of Petroleum Geologists, Society of Petroleum Engineers. URTEC-2448089-MS*, 2016.

[4] A. Lerza, D. Rojas, and B. Liang, "Defining the optimal drawdown strategy in the Vaca Muerta formation," in *Unconventional Resources Technology Conference*, Society of Exploration Geophysicists, American Association of Petroleum Geologists, Society of Petroleum Engineers. URTEC-2880115-MS, 2018.

[5] D. Rojas and A. Lerza, "Horizontal well productivity enhancement through drawdown management approach in Vaca-Muerta shale," in *SPE Canada Unconventional Resources Conference*, Society of Petroleum Engineers, 2018, SPE-189822-MS.

[6] A. Rodriguez and F. Maldonado, "Evaluating pressure drawdown strategy for hydraulically fracture shale gascondensate producers," in *SPE Oklahoma City Oil and Gas Symposium*, p. SPE-195235-MS, Society of Petroleum Engineers, 2019.

[7] L. Naizhen, L. Ming, and Z. Shicheng, "Flowback pattern of shale gas well after fracturing," *Natural Gas Industry*, vol. 3, pp. 50–54, 2015.

[8] H. Huifen, L. Wang, Q. He et al., "Flowback pattern and control parameter optimization of shale gas well," *Petroleum Drilling and Production Process*, vol. 40, pp. 253–260, 2018.

[9] N. Wijaya and J. J. Sheng, "Effect of choke management in optimizing shale-oil production with models of different recovery driving mechanisms," in *SPE Annual Technical Conference and Exhibition*, 2020.

[10] S. Tripoppoom, W. Yu, K. Sepehrnoori, and J. Miao, "Application of assisted history matching workflow to shale gas well using EDFM and neural network-Markov chain Monte Carlo algorithm," *Paper URTeC 2019-659, presented at the unconventional resources technology conference*, 2019, Denver, Colorado, USA, July 2019, 2019.

Hindawi
Geofluids
Volume 2022, Article ID 5993701, 11 pages
https://doi.org/10.1155/2022/5993701

Research Article

Transient Pressure Behavior of a Horizontal Well in a Naturally Fractured Gas Reservoir with Dual-Permeability Flow and Stress Sensitivity Effect

Guiqin Wang, Rui Zhang, and Liangliang Cui

School of Petroleum and Environmental Engineering, Yan'an University, Yan'an 716000, China

Correspondence should be addressed to Guiqin Wang; guiqin1990@126.com

Received 28 February 2022; Accepted 11 April 2022; Published 30 April 2022

Academic Editor: Zheng Sun

Dual-permeability flow and stress sensitivity effect are two fundamental issues that have been widely investigated in transient pressure analysis for horizontal wells. However, few attempts have been made to simulate the combined effects of dual-permeability flow and stress-dependent fracture permeability on the pressure transient dynamics of a horizontal well in a naturally fractured gas reservoir. In this approach, an analytical model is proposed to integrate the complexities of pressure-dependent PVT properties, dual-permeability flow behavior, and stress-dependent fracture permeability characteristics. The nonlinearity of the mathematical model is weakened by using Pedrosa's transform formulation. Then, the Laplace integral transformation and separation of variables are applied to solve the model. Based on the solution of the mathematical model, a series of new-type curves are drawn to make a precise observation of different flow regimes. The main differences between the proposed model and the traditional models are discussed, and the effects of the permeability modulus of fractures, storability ratio, interporosity flow factor, and skin factor on transient pressure response are also examined. The results show that there are obvious differences in transient pressure dynamic curves between the proposed model and traditional models. The stress sensitivity effect plays a significant role in the intermediate flow period and the late-time pseudoradial flow period. The dual-permeability flow behavior mainly affects the early transient and interporosity flow stages. The proposed model can accurately simulate the transient pressure behaviors of a horizontal well in a naturally fractured gas reservoir with a dual-permeability flow and stress sensitivity effect. The novel model can be used to interpret pressure signals with accurate matching results and more reasonable interpreted parameters.

1. Introduction

Transient pressure analysis of a horizontal well in a naturally fractured gas reservoir is greatly affected by fracture seepage parameters and stress-dependent fracture permeability. For naturally fractured reservoirs, the fractures are always with heterogeneities [1, 2]. An experimental study on fracture stress sensitivities proves that stress-dependent fracture permeability significantly affects the transient pressure response [3]. So, it is pretty essential to propose a comprehensive model to capture the transient behavior of horizontal wells in naturally fractured gas reservoirs.

Because it is often impossible to describe the complex fractures precisely, continuum models are proposed to capture the flow behavior of this kind of reservoir. Much research has been done on theoretical models of vertical wells in naturally fractured reservoirs. Barenblatt et al. [4] proposed a classic double-porosity and single-permeability model to study vertical well production in porous media reservoirs. This model assumes that a naturally fractured reservoir is composed of two completely overlapping continua, porous matrix, and fractures. Warren and Root [5] expanded Barenblatt et al.'s approach to cover the independent physical properties of fracture and matrix. In their model, naturally fractured formation is formed by matrix blocks, which is separated by uniform and orthogonal fractures. Besides, the pseudosteady-state interporosity flow is firstly adopted to simulate mass transfer between fracture

and matrix systems. After that, Kazemi et al. [6], de Swaan [7], Raghavan and Ohaeri [8], Serra et al. [9], Jalali and Ershaghi [10], Wu and Pruess [11], Bui et al. [12], Wu et al. [13], Kuchuk et al. [14], Jia et al. [2], and Wang et al. [15] proposed their own dual-media model for naturally fractured reservoirs with the consideration of transient interporosity flow behavior. These models assume that the fracture system is the only flow pathway directly connected with wellbore by ignoring the flow from the matrix system to the wellbore. Because the dual-porosity and single-permeability model is no longer applicable in naturally fractured reservoirs, a great deal of work have instead been directed at using dual-porosity and dual-permeability models [14, 16–18] to describe the flow behavior, which assumes that both the fracture and matrix systems are the flow pathway directly connected with the wellbore, also considered the pseudosteady-state and transient-state interporosity flow between matrix and fracture systems. However, most of the models ignored the effect of the stress-dependent fracture permeability on transient pressure response. Although a great deal of work has been done on theoretical models of naturally fractured gas wells considering stress sensitivity of fracture permeability, most of them are restricted to the dual-porosity and single-permeability flow problem [3, 15, 19–21].

In recent years, horizontal wells have been increasingly applied to some naturally fractured gas reservoirs. Research on the transient pressure behavior of this kind of well has become increasingly popular among engineers [22–30]. However, transient pressure analysis for horizontal wells is commonly performed assuming that permeability for natural fractures remains constant, which might not be physically applicable for stress-sensitive reservoirs. Besides, dual-permeability flow is seldom considered in their models. In general, the big challenge of analyzing the transient pressure response of a horizontal well is that the dual-permeability flow behavior and stress-dependent fracture permeability should be all incorporated in the mathematical models.

This paper presented a novel semianalytical model to examine the combined effects of dual-permeability flow behavior and stress-dependent fracture permeability on the transient pressure response of a horizontal well in a naturally fractured gas reservoir. The nonlinearity of the governing equations caused by the stress sensitivity of fracture permeability is eliminated using Pedrosa's [31] transform formulation. With Laplace transform and separation of variables, we got the analytical solution of the mathematical model. A series of new transient pressure dynamic curves are drawn to observe different flow regimes based on the solution. Then, differences between the proposed model and traditional models are discussed and the effects of some critical parameters on transient pressure response are also analyzed with the proposed model.

2. Methodology

2.1. Model Assumption. As shown in Figure 1, the naturally fractured gas reservoir is composed of fracture and matrix systems and the physical properties of the two systems are

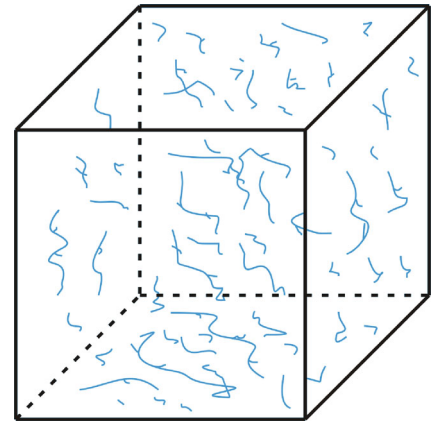

Figure 1: Schematic of naturally fractured reservoir.

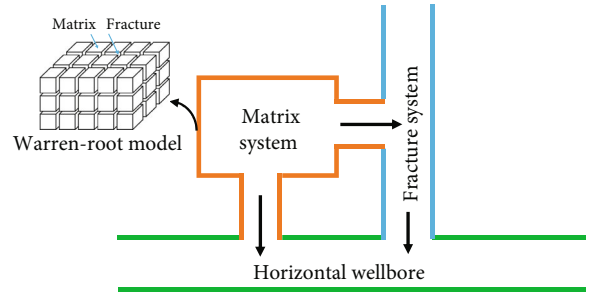

Figure 2: Dual-porosity and dual-permeability flow scheme.

independent. A radial cylindrical dual-porosity and dual-permeability medium reservoir is considered in which a single horizontal well is located at the center, completely penetrating the formation. The matrix/fracture flow is schematically described in Figure 2. In this study, the proposed model assumes that both the fracture and matrix systems are the flow pathway directly connected with the wellbore and fluids in the fracture and matrix systems first flow into the horizontal wellbore, followed by the matrix-fracture interporosity flow. Some simplifying physical model assumptions for the derivation of the governing equation are listed as the horizontal well produced with the constant production rate in a naturally fractured gas reservoir. The external boundaries of the top and bottom are assumed to be closed, and the lateral boundary is assumed to be infinite. The matrix-fracture interporosity flow in the reservoir is described by the pseudosteady-state model [5, 25, 26]. Fluid flow follows the law of Darcy seepage, and stress-dependent fracture permeability is considered. Also, capillary and gravity forces are neglected to simplify the model.

2.2. Mathematical Model. The PVT properties, such as fluid viscosity and volume factor of the gas phase, are quite sensitive to formation pressure. In this section, the pseudopressure transformation is used to capture pressure-dependent PVT properties and reduce the nonlinearity of governing differential equations. The definitions of pseudopressure and pseudotime are given by

$$\psi_j = 2\int_0^p \frac{p}{\mu_g Z}dp, \quad j = f, m,$$
$$t_a = \int_0^t \frac{\mu_{gi}c_{ti}}{\mu_g(p)c_t(p)}dt, \tag{1}$$

where p is the pressure, MPa; ψ_f is the pseudopressure of the fracture, MPa^2/(mPa·s); ψ_m is the pseudo pressure of the matrix, MPa^2/(mPa·s); t is the time, h; t_a is the pseudotime; μ_g is the gas viscosity, mPa·s; c_t is the total compressibility coefficient, MPa^{-1}; and Z is the gas compressibility factor.

To describe the degree of stress sensitivity and its influence to fracture permeability, the concept of pseudopermeability modulus γ_f is defined as [19, 26]

$$\gamma_f = \frac{1}{k_f}\frac{\partial k_f}{\partial \psi_f}. \tag{2}$$

Equation (2) can be further written as

$$k_f = k_{fi}e^{-\gamma_f(\psi_i - \psi_f)}, \tag{3}$$

where k_f is the permeability of fracture, mD; k_{fi} is the initial permeability of fracture, mD; ψ_i is the initial pseudopressure, MPa^2/(mPa·s); and γ_f is the pseudopermeability modulus of the fracture, (mPa·s)/MPa^2.

To establish and solve the model, a radial cylindrical system (r) is used to describe the flow of the fracture and matrix system. With consideration of the dual-porosity and dual-permeability flow behavior and stress-dependent fracture permeability, the governing differential equation of the complex system can be described as follows:

For the fracture system,

$$\frac{\partial^2\psi_f}{\partial r^2} + \frac{1}{r}\frac{\partial\psi_f}{\partial r} + \gamma_f\left(\frac{\partial\psi_f}{\partial r}\right)^2 + \frac{k_{fvi}}{k_{fhi}}\left[\frac{\partial^2\psi_f}{\partial z^2} + \gamma_f\left(\frac{\partial\psi_f}{\partial z}\right)^2\right] + \alpha\frac{k_m}{k_{fhi}}\left(\psi_m - \psi_f\right) = e^{\gamma_f(\psi_i-\psi_f)}\frac{\phi_f\mu_g c_{tf}}{3.6k_{fhi}}\frac{\partial\psi_f}{\partial t}. \tag{4}$$

For the matrix system,

$$\frac{\partial^2\psi_m}{\partial r^2} + \frac{1}{r}\frac{\partial\psi_m}{\partial r} + \frac{k_{mv}}{k_{mh}}\frac{\partial^2\psi_m}{\partial z^2} - \alpha\frac{k_m}{k_{mh}}\left(\psi_m - \psi_f\right) = \frac{\phi_m\mu_g c_{tm}}{3.6k_{mh}}\frac{\partial\psi_m}{\partial t}. \tag{5}$$

For the initial condition,

$$\psi_f\Big|_{t=0} = \psi_m|_{t=0} = 0. \tag{6}$$

In the inner boundary condition,

$$\lim_{\varepsilon\longrightarrow 0}\left[\lim_{r\longrightarrow 0}\frac{4\pi h}{\mu_g\varepsilon}\int_{z_w-\varepsilon/2}^{z_w+\varepsilon/2}\left(k_{mh}r\frac{\partial\psi_m}{\partial r} + k_{fhi}e^{-\gamma_f(\psi_i-\psi_f)}r\frac{\partial\psi_f}{\partial r}\right)dz\right] = \frac{p_{sc}TZ}{pT_{sc}}q_{sc}, |z - z_w| \le \frac{\varepsilon}{2}. \tag{7}$$

The top and bottom boundaries are assumed to be closed and given by

$$\left.\frac{\partial\psi_m}{\partial z}\right|_{z=0} = \left.\frac{\partial\psi_f}{\partial z}\right|_{z=0} = 0,$$
$$\left.\frac{\partial\psi_m}{\partial z}\right|_{z=h} = \left.\frac{\partial\psi_f}{\partial z}\right|_{z=h} = 0 \tag{8}$$

The lateral boundary condition is assumed to be infinite and expressed as

$$\lim_{r\longrightarrow\infty}\psi_m = \lim_{r\longrightarrow\infty}\psi_f = \psi_i, \tag{9}$$

where c_{tf} is the total compressibility of the fracture, MPa^{-1}; c_{tm} is the total compressibility of the fracture, MPa^{-1}; h is the reservoir thickness, m; k_{fhi} is the initial horizontal permeability of the fracture, mD; k_{fvi} is the initial vertical permeability of the fracture, mD; k_{mh} is the horizontal permeability of the matrix, mD; k_{mv} is the vertical permeability of the matrix, mD; p is pressure, MPa; p_{sc} is the pressure at standard condition, MPa; q_{sc} is the surface gas production rate, 10^4 m^3/d; r is the radial distance, m; T is temperature, K; T_{sc} is the temperature at standard condition, K; z is the vertical distance from the bottom, m; z_w is the vertical distance of the horizontal well from the bottom, m; ε is a variable in the z direction, m; ϕ_f is the porosity of fracture; ϕ_m is the porosity of the matrix; and α is the geometric shape factor of matrix block, m^{-2}.

To make the equations homogeneous, some dimensionless variables are defined and tabulated in Table 1. Taking the dimensionless variables into equations (4)–(9), one can obtain the dimensionless differential equations.

For the fracture system,

$$\kappa\left\{\frac{\partial^2\psi_{fD}}{\partial {r_D}^2} + \frac{1}{r_D}\frac{\partial\psi_{fD}}{\partial r_D} - \gamma_{fD}\left(\frac{\partial\psi_{fD}}{\partial r_D}\right)^2 + \frac{1}{h_D^2}\left[\frac{\partial^2\psi_{fD}}{\partial {z_D}^2} - \gamma_{fD}\left(\frac{\partial\psi_{fD}}{\partial z_D}\right)^2\right]\right\} = e^{\gamma_{fD}\psi_{fD}}\left[\omega_f e^{-2S}\frac{\partial\psi_{fD}}{\partial t_D} + \lambda_{mf}e^{-2S}\left(\psi_{fD} - \psi_{mD}\right)\right]. \tag{10}$$

Table 1: Definitions of the parameters used in this work.

Parameters	Symbol	Definition
Dimensionless pseudopressure of the fracture	ψ_{fD}	$\psi_{fD} = \left(\left(78.489\left(k_{mh} + k_{fhi}\right)h\right)/Tq_{sc}\right)\left(\psi_i - \psi_f\right)$
Dimensionless pseudopressure of the matrix	ψ_{mD}	$\psi_{mD} = \left(\left(78.489\left(k_{mh} + k_{fhi}\right)h\right)/Tq_{sc}\right)\left(\psi_i - \psi_m\right)$
Dimensionless vertical distance	z_D	$z_D = z/h$
Dimensionless pseudotime	t_D	$t_D = \left(\left(3.6\left(k_{mh} + k_{fhi}\right)\right)/\left(\mu {r_w}^2\left(\phi_m C_{mt} + \phi_f C_{\mathrm{ft}}\right)\right)\right)t_a$
Dimensionless reservoir thickness	h_D	$h_D = \left(h/r_w e^{-S}\right)\sqrt{\left(k_{fhi}/k_{fpi}\right)}$
Dimensionless radial distance	r_D	$r_D = r/r_w e^{-S}$
Dimensionless wellbore storage coefficient	C_D	$C_D = C_s/\left(6.2832\left(\phi_f C_{\mathrm{ft}} + \phi_m C_{mt}\right)hr_w^2\right)$
Dimensionless pseudopermeability modulus	γ_{fD}	$\gamma_{fD} = \left(Tq_{sc}/78.489k_{fhi}h\right)\gamma_f$
The permeability ratio of the fracture system to the sum of the fracture and matrix system	κ	$\kappa = k_{fhi}/\left(k_{fhi} + k_{mh}\right)$
Capacitance coefficient of the fracture	ω_f	$\omega_f = \phi_f C_{\mathrm{ft}}/\left(\phi_f C_{\mathrm{ft}} + \phi_m C_{mt}\right)$
Interporosity flow factor of matrix system into the fracture system	λ_{mf}	$\lambda_{mf} = \alpha_m k_{mh} r_w^2/\left(k_{fhi} + k_{mh}\right)$

For the matrix system,

$$(1-\kappa)\left(\frac{\partial^2\psi_{mD}}{\partial {r_D}^2} + \frac{1}{r_D}\frac{\partial\psi_{mD}}{\partial r_D} + \frac{1}{h_D^2}\frac{\partial^2\psi_{mD}}{\partial {z_D}^2}\right) - \lambda_{mf}e^{-2S}\left(\psi_{mD} - \psi_{fD}\right) = \omega_m e^{-2S}\frac{\partial\psi_{mD}}{\partial t_D}. \tag{11}$$

In the initial condition,

$$\psi_{fD}\Big|_{t_D=0} = \psi_{mD}|_{t_D=0} = 0. \tag{12}$$

In the inner boundary condition,

$$\lim_{\varepsilon_D\longrightarrow 0}\left[\lim_{r_D\longrightarrow 0}\int_{z_{wD}-(\varepsilon_D/2)}^{z_{wD}+(\varepsilon_D/2)}\left(\kappa r_D\frac{\partial\psi_{mD}}{\partial r_D} + (1-\kappa)r_D e^{-\gamma_{fD}\psi_{fD}}\frac{\partial\psi_{fD}}{\partial r_D}\right)dz_D\right] = -\frac{1}{2}, |z_D - z_{wD}| \le \frac{\varepsilon_D}{2}. \tag{13}$$

In the outer boundary conditions,

$$\frac{\partial\psi_{mD}}{\partial z_D}\Big|_{z_D=0} = \frac{\partial\psi_{fD}}{\partial z_D}\Big|_{z_D=0} = 0, \tag{14}$$

$$\frac{\partial\psi_{mD}}{\partial z_D}\Big|_{z_D=1} = \frac{\partial\psi_{fD}}{\partial z_D}\Big|_{z_D=1} = 0, \tag{15}$$

$$\lim_{r_D\longrightarrow\infty}\psi_{mD} = \lim_{r_D\longrightarrow\infty}\psi_{fD} = 0. \tag{16}$$

2.3. Solution to the Mathematical Model. It should be noted that equations (10) and (13) are strongly nonlinear with the consideration of the stress sensitivity of fracture permeability. This is because the stress-dependent fracture permeability is a function of the pseudopressure of the fracture. However, the pressure of fracture is an unknown parameter. Therefore, the mathematical model cannot be solved analytically. In this work, the Pedrosa [31] variable substitution and regular perturbation method are firstly deployed to alleviate the nonlinearity. Then, the Laplace transformation and separation of variables are adopted to address the linearized model. Thus, the model can be solved in the Laplace space and the Stehfest and Harald [32] numerical inversion is used to calculate the pressure in real space.

2.3.1. Linearization of the Flow Equation. To linearize the mathematical model, the Pedrosa transformation is employed in this section and given by

$$\psi_{fD}(r_D, t_D)\Big|_{t_D=0} = -\frac{1}{\gamma_{fD}}\ln\left[1 - \gamma_{fD}\eta_{fD}(r_D, t_D)\right], \tag{17}$$

where η_{fD} is an intermediate variable called the perturbation deformation function.

After the Pedrosa transformation, equations (10)–(16) can be rewritten as

$$\kappa\left(\frac{\partial^2\eta_{fD}}{\partial {r_D}^2} + \frac{1}{r_D}\frac{\partial\eta_{fD}}{\partial r_D} + \frac{1}{h_D^2}\frac{\partial^2\eta_{fD}}{\partial {z_D}^2}\right) = e^{-2S}\left[\frac{1}{1-\gamma_{fD}\eta_{fD}}\omega_f\frac{\partial\eta_{fD}}{\partial t_D} + \left(1-\omega_f\right)\frac{\partial\psi_{mD}}{\partial t_D}\right], \tag{18}$$

$$(1-\kappa)\left(\frac{\partial^2\psi_{mD}}{\partial {r_D}^2} + \frac{1}{r_D}\frac{\partial\psi_{mD}}{\partial r_D} + \frac{1}{h_D^2}\frac{\partial^2\psi_{mD}}{\partial {z_D}^2}\right) = e^{-2S}\left\{\left(1-\omega_f\right)\frac{\partial\psi_{mD}}{\partial t_D} + \lambda_{mf}\left[\frac{1}{\gamma_{fD}}\ln\left(1-\gamma_{fD}\eta_{fD}\right) - \psi_{mD}\right]\right\}, \tag{19}$$

$$\eta_{fD}(r_D, t_D)\Big|_{t_D=0} = \psi_{mD}(r_D, t_D)|_{t_D=0} = 0, \tag{20}$$

$$\lim_{\varepsilon_D \longrightarrow 0}\left[\lim_{r_D \longrightarrow 0}\int_{z_{wD}-(\varepsilon_D/2)}^{z_{wD}+(\varepsilon_D/2)}\left((1-\kappa)r_D\frac{\partial \psi_{mD}}{\partial r_D} + \kappa r_D\frac{\partial \eta_{fD}}{\partial r_D}\right)dz_D\right] = -\frac{1}{2}, |z_D - z_{wD}| \le \frac{\varepsilon_D}{2}, \tag{21}$$

$$\left.\frac{\partial \eta_{fD}}{\partial z_D}\right|_{z_D=1} = \left.\frac{\partial \psi_{mD}}{\partial z_D}\right|_{z_D=1} = 0, \tag{22}$$

$$\left.\frac{\partial \eta_{fD}}{\partial z_D}\right|_{z_D=0} = \left.\frac{\partial \psi_{mD}}{\partial z_D}\right|_{z_D=0} = 0, \tag{23}$$

$$\lim_{r_D \longrightarrow \infty} \psi_{mD} = \lim_{r_D \longrightarrow \infty} \eta_{fD} = 0. \tag{24}$$

According to the regular perturbation theory, equations (18)–(24) can be simplified as

$$\kappa\left(\frac{\partial^2 \eta_{fD0}}{\partial {r_D}^2} + \frac{1}{r_D}\frac{\partial \eta_{fD0}}{\partial r_D} + \frac{1}{h_D^2}\frac{\partial^2 \eta_{fD0}}{\partial {z_D}^2}\right) = \left[\omega_f e^{-2S}\frac{\partial \eta_{fD0}}{\partial t_D} + \lambda_{mf} e^{-2S}\left(\eta_{fD0} - \psi_{mD}\right)\right], \tag{25}$$

$$(1-\kappa)\left(\frac{\partial^2 \psi_{mD}}{\partial {r_D}^2} + \frac{1}{r_D}\frac{\partial \psi_{mD}}{\partial r_D} + \frac{1}{h_D^2}\frac{\partial^2 \psi_{mD}}{\partial {z_D}^2}\right) = \left(1-\omega_f\right)e^{-2S}\frac{\partial \psi_{mD}}{\partial t_D} + \lambda_{mf} e^{-2S}\left(\eta_{fD0} - \psi_{mD}\right), \tag{26}$$

$$\eta_{fD0}(r_D, t_D)\Big|_{t_D=0} = \psi_{mD}(r_D, t_D)|_{t_D=0} = 0, \tag{27}$$

$$\lim_{\varepsilon_D \longrightarrow 0}\left[\lim_{r_D \longrightarrow 0}\int_{z_{wD}-(\varepsilon_D/2)}^{z_{wD}+(\varepsilon_D/2)}\left((1-\kappa)r_D\frac{\partial \psi_{mD}}{\partial r_D} + \kappa r_D\frac{\partial \eta_{fD0}}{\partial r_D}\right)dz_D\right] = -\frac{1}{2}, |z_D - z_{wD}| \le \frac{\varepsilon_D}{2}, \tag{28}$$

$$\left.\frac{\partial \eta_{fD0}}{\partial z_D}\right|_{z_D=1} = \left.\frac{\partial \psi_{mD}}{\partial z_D}\right|_{z_D=1} = 0, \tag{29}$$

$$\left.\frac{\partial \eta_{fD0}}{\partial z_D}\right|_{z_D=0} = \left.\frac{\partial \psi_{mD}}{\partial z_D}\right|_{z_D=0} = 0, \tag{30}$$

$$\lim_{r_D \longrightarrow \infty} \psi_{mD} = \lim_{r_D \longrightarrow \infty} \eta_{fD0} = 0. \tag{31}$$

2.3.2. Solution of the Proposed Model. To derive the analytical solution of the model, the mathematical model is translated into the Laplace domain with respect to t_D:

$$L\left[\eta_{fD}(r_D, t_D)\right] = \bar{\eta}_{fD}(r_D, u) = \int_0^{+\infty} \eta_{fD}(r_D, t_D)e^{-ut_D}dt_D, \tag{32}$$

$$L[\psi_{mD}(r_D, t_D)] = \bar{\psi}_{mD}(r_D, u) = \int_0^{+\infty} \psi_{mD}(r_D, t_D)e^{-ut_D}dt_D, \tag{33}$$

where u is the Laplace transform variable.

With equations (32) and (33) and taking the Laplace transform of equations (25)–(31), one can obtain the dimensionless mathematical model in the Laplace space:

For the fracture system,

$$\frac{\partial^2 \bar{\eta}_{fD}}{\partial {r_D}^2} + \frac{1}{r_D}\frac{\partial \bar{\eta}_{fD}}{\partial r_D} + \frac{1}{h_D^2}\frac{\partial^2 \bar{\eta}_{fD}}{\partial {z_D}^2} + \frac{A_1}{\kappa}\bar{\eta}_{fD} + \frac{A_2}{\kappa}\bar{\psi}_{mD} = 0. \tag{34}$$

For the matrix system,

$$\frac{\partial^2 \bar{\psi}_{mD}}{\partial {r_D}^2} + \frac{1}{r_D}\frac{\partial \bar{\psi}_{mD}}{\partial r_D} + \frac{1}{h_D^2}\frac{\partial^2 \bar{\psi}_{mD}}{\partial {z_D}^2} + \frac{A_2}{1-\kappa}\bar{\eta}_{fD} + \frac{A_3}{1-\kappa}\bar{\psi}_{mD} = 0, \tag{35}$$

where $A_1 = -(\lambda_{mf} + u\omega_f)e^{-2S}$, $A_2 = \lambda_{mf}e^{-2S}$, and $A_3 = -[\lambda_{mf} + u(1-\omega_f)]e^{-2S}$.

In the inner boundary condition,

$$\lim_{\varepsilon_D \longrightarrow 0}\left[\lim_{r_D \longrightarrow 0}\int_{z_{wD}-(\varepsilon_D/2)}^{z_{wD}+(\varepsilon_D/2)}\left((1-\kappa)r_D\frac{\partial \bar{\psi}_{mD}}{\partial r_D} + \kappa r_D\frac{\partial \bar{\eta}_{fD0}}{\partial r_D}\right)dz_D\right] = -\frac{1}{2u}, |z_D - z_{wD}| \le \frac{\varepsilon_D}{2}. \tag{36}$$

In the outer boundary conditions,

$$\left.\frac{\partial \bar{\psi}_{mD}}{\partial z_D}\right|_{z_D=0} = \left.\frac{\partial \bar{\eta}_{fD0}}{\partial z_D}\right|_{z_D=0} = 0, \tag{37}$$

$$\left.\frac{\partial \bar{\psi}_{mD}}{\partial z_D}\right|_{z_D=1} = \left.\frac{\partial \bar{\eta}_{fD0}}{\partial z_D}\right|_{z_D=1} = 0, \tag{38}$$

$$\lim_{r_D \longrightarrow \infty} \bar{\psi}_{mD} = \lim_{r_D \longrightarrow \infty} \bar{\eta}_{fD0} = 0. \tag{39}$$

This section uses the separation of variables to solve the dual-porosity and dual-permeability modeling of a horizontal well in a naturally fractured reservoir. With the separation of variables, the dimensionless pseudopressure in the Laplace space can be separated by [25]

$$\bar{\eta}_{jD} = \bar{R}_j(r_D)\bar{Z}_j(z_D), \quad j = m, f. \tag{40}$$

Substituting equation (40) into equations (34) and (35), one can obtain

$$\frac{h_{\mathrm{D}}^2\left(\bar{R}_{\mathrm{j}}'' + (1/r_{\mathrm{D}})\bar{R}_{\mathrm{j}}' - \sigma\bar{R}_{\mathrm{j}}\right)}{\bar{R}_{\mathrm{j}}} = -\frac{\bar{Z}_{\mathrm{j}}''}{\bar{Z}_{\mathrm{j}}} = \lambda. \tag{41}$$

According to equation (41), the fluid flow in the horizontal direction can be written as

$$\bar{R}_{\mathrm{j}}'' + \frac{1}{r_{\mathrm{D}}}\bar{R}_{\mathrm{j}}' - \xi\bar{R}_{\mathrm{j}} = 0, \tag{42}$$

$$\xi = \sigma + \frac{\lambda}{h_D^2}. \tag{43}$$

And the fluid flow in the vertical direction is

$$\bar{Z}_j'' + \lambda\bar{Z}_j = 0. \tag{44}$$

Without consideration of the flow in the z-direction and taking equation (42) into equations (34) and (35), we have

$$\frac{\partial^2\bar{R}_{fD}}{\partial {r_D}^2} + \frac{1}{r_D}\frac{\partial\bar{R}_{fD}}{\partial r_D} + \frac{A_1}{\kappa}\bar{R}_{fD} + \frac{A_2}{\kappa}\bar{R}_{mD} = 0, \tag{45}$$

$$\frac{\partial^2\bar{R}_{mD}}{\partial {r_D}^2} + \frac{1}{r_D}\frac{\partial\bar{R}_{mD}}{\partial r_D} + \frac{A_2}{(1-\kappa)}\bar{R}_{fD} + \frac{A_3}{(1-\kappa)}\bar{R}_{mD} = 0. \tag{46}$$

Under the infinite external boundary of side, the solutions of equations (45) and (46) can be expressed by

$$\bar{R}_f = A_f K_0\left(\sqrt{\sigma}r_D\right), \tag{47}$$

$$\bar{R}_m = A_m K_0\left(\sqrt{\sigma}r_D\right). \tag{48}$$

Substituting equations (47) and (48) into (45) and (46), we have

$$\sigma K_0\left(\sqrt{\sigma}r_D\right)A_f + \frac{A_1}{\kappa}K_0\left(\sqrt{\sigma}r_D\right)A_f + \frac{A_2}{\kappa}K_0\left(\sqrt{\sigma}r_D\right)A_m = 0, \tag{49}$$

$$\sigma K_0\left(\sqrt{\sigma}r_D\right)A_m + \frac{A_2}{1-\kappa}K_0\left(\sqrt{\sigma}r_D\right)A_f + \frac{A_3}{1-\kappa}K_0\left(\sqrt{\sigma}r_D\right)A_m = 0. \tag{50}$$

Because the modeling must have solutions, the coefficients A_m and A_f cannot be zero, so the term σ in equation (50) can be given by

$$\sigma = \frac{-[\kappa A_3 + (1-\kappa)A_1] \pm \sqrt{[\kappa A_3 + (1-\kappa)A_1]^2 - 4\kappa(1-\kappa)\left(A_1A_3 - A_2^2\right)}}{2\kappa(1-\kappa)}. \tag{51}$$

With equation (49)–(51), the general solutions of equations (45) and (46) can be expressed by

$$\bar{R}_f = A_{f,1}K_0(\sqrt{\sigma_1}r_D) + A_{f,2}K_0(\sqrt{\sigma_2}r_D), \tag{52}$$

$$\bar{R}_m = A_{m,1}K_0(\sqrt{\sigma_1}r_D) + A_{m,2}K_0(\sqrt{\sigma_2}r_D), \tag{53}$$

$$\begin{aligned} A_{m,1} &= a_1A_{f,1}, \\ A_{m,2} &= a_2A_{f,2}, \end{aligned} \tag{54}$$

$$\begin{aligned} a_1 &= -\frac{\kappa\sigma_1 + A_1}{A_2}, \\ a_2 &= -\frac{\kappa\sigma_2 + A_1}{A_2}. \end{aligned} \tag{55}$$

Considering the fluid flow in the z-direction, the general solutions of equations (52) and (53) can be given as

$$\bar{R}_f = A_{f,1}K_0\left(\sqrt{\xi_1}r_D\right) + A_{f,2}K_0\left(\sqrt{\xi_2}r_D\right), \tag{56}$$

$$R_m = a_1A_{f,1}K_0\left(\sqrt{\xi_1}r_D\right) + a_2A_{f,2}K_0\left(\sqrt{\xi_2}r_D\right), \tag{57}$$

$$\xi_1 = \sigma_1 + \frac{\lambda}{h_D^2}, \xi_2 = \sigma_2 + \frac{\lambda}{h_D^2}. \tag{58}$$

Combined with the boundary conditions, the terms $A_{f,1}$ and $A_{f,2}$ in equation (56) are

$$\begin{aligned} A_{f,2} &= \frac{1}{u}\frac{(1-a_1)K_0\left(\sqrt{\xi_1}\right)}{[\kappa + (1-\kappa)a_2](1-a_1)K_0\left(\sqrt{\xi_1}\right) - [\kappa + (1-\kappa)a_1](1-a_2)K_0\left(\sqrt{\xi_2}\right)}, \\ A_{f,1} &= \frac{1}{[\kappa + (1-\kappa)a_1]u} - \frac{\kappa + (1-\kappa)a_2}{\kappa + (1-\kappa)a_1}A_{f,2}. \end{aligned} \tag{59}$$

The general solution of equation (44) can be expressed by

$$\bar{Z}_j = C\cos\left(\sqrt{\lambda}z_D\right) + D\sin\left(\sqrt{\lambda}z_D\right). \tag{60}$$

Substituting equation (60) into equations (37) and (38), we have

$$\begin{aligned} &D = 0, \lambda = \lambda_n = (n\pi)^2, \quad n = 0, 1, 2, \cdots, \\ &C = \frac{1}{2}\cos\left(\sqrt{\lambda_n}z_{wD}\right), \lambda_n = (n\pi)^2, \quad n = 0, 1, 2, \cdots, \end{aligned} \tag{61}$$

so the solution in the vertical direction is

$$\bar{Z}_j = \frac{1}{2}\cos\left(\sqrt{\lambda}z_{wD}\right)\cos\left(\sqrt{\lambda}z_D\right). \tag{62}$$

Combined with equations (56), (57), and (62), the pressure solution for a three-dimensional volumetric source can be obtained and expressed by

$$\bar{\eta}_{fD} = \sum_{n=0}^{\infty}\bar{R}_{fn}\cdot\bar{Z}_{fn}. \tag{63}$$

According to the superposition principle, the dimensionless pressure in the Laplace space for constant-rate production can be obtained by integrating equation (63) along with the direction of horizontal wellbore.

$$\bar{\eta}_{sD} = \sum_{n=0}^{\infty} \int_{-L/2/r_w}^{L/2/r_w} \bar{R}_{fn} dx_D \cdot \bar{Z}_w. \tag{64}$$

Equation (64) is the dimensionless pseudopressure solution expression considering the skin effect. The wellbore storage effect can be incorporated in the abovementioned solution using Duhamel's principle [25], and the bottom-hole pressure solution is

$$\bar{\eta}_{wD} = \frac{\bar{\eta}_{sD}}{1 + C_D u^2 \bar{\eta}_{sD}}. \tag{65}$$

$\bar{\eta}_{wD}$ in equation (65) is the dimensionless pressure solution in the Laplace space, and in real space, the dimensionless pressure η_{wD} can be obtained using Stehfest numerical inversion [32]. After that, utilizing the inverse transformation of equation (66), the bottom-hole pressure response for a horizontal well incorporating the stress-dependent permeability of fracture system can be obtained:

$$\psi_{wD}(r_D, t_D) = -\frac{1}{\gamma_{fD}} \ln\left[1 - \gamma_{fD}\eta_{wD}(r_D, t_D)\right]. \tag{66}$$

3. New-Type Curves

In this work, a novel semi-analytical model is presented to examine the combined effects of dual-permeability flow behavior and stress-dependent fracture permeability on the transient pressure response of a horizontal well in a naturally fractured gas reservoir. A series of new transient pressure dynamic curves are drawn to observe different flow regimes based on the solution of the proposed model. The differences between the proposed model and traditional models are discussed, and the effects of some critical parameters on transient pressure response are also analyzed with the proposed model. Furthermore, it provides an efficient method for field engineers and related research and further to interpret pressure signals with accurate matching results and more reasonable interpreted parameters. After that, the effects of some critical parameters, including the dimensionless permeability modulus, the storability ratio of fracture, interporosity flow factor of matrix system into fracture system, and skin factor, on the characteristics of the type curves are examined and analyzed.

3.1. Flow Regime Identification. Figure 3 depicts the standard-type curves of wellbore pressure responses for a horizontal well located at a naturally fractured gas reservoir considering dual-permeability flow and stress-dependent fracture permeability. Basic data used to generate the type curves are listed in Table 2. An entire transient flow process is clearly shown, and the following six main flow stages can be recognized:

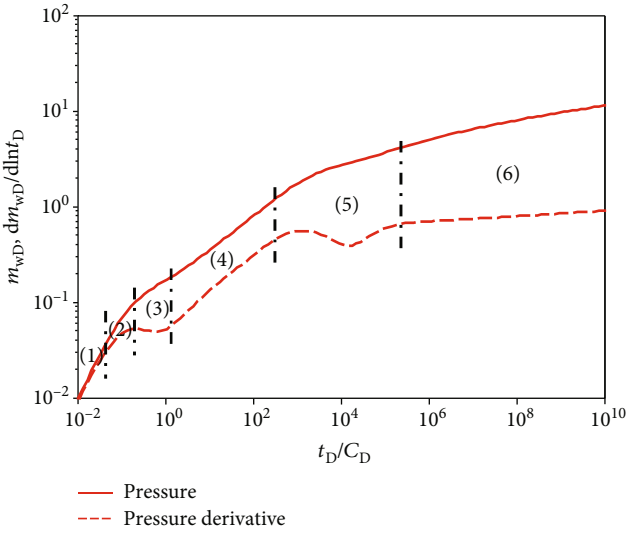

Figure 3: The transient responses with the log-log plot.

Table 2: Parameters used for model validation.

Parameters	Symbol	Value
Dimensionless wellbore storage coefficient	C_D	1×10^{-4}
Skin factor	S	0.1
Dimensionless reservoir thickness	h_D	400
Dimensionless horizontal section position	z_{wD}	0.5
Dimensionless pseudopermeability modulus	γ_{fD}	0.08
The permeability ratio of the fracture system to the sum of the fracture and matrix system	κ	0.9
Capacitance coefficient of the fracture	ω_f	0.05
Interporosity flow factor of the matrix system into the fracture system	λ_{mf}	0.01

(1) Pure wellbore storage stage: this period is characterized by a slope of 1 on the pressure and pressure derivative curves and governed by the wellbore storage coefficient, C

(2) Skin effect transition stage: the pressure derivative curve exhibits like a "hump." The peak of the "hump" is dominated by the skin factor, S

(3) Early radial flow stage: this period is present whenever the wellbore storage coefficient, C, and the horizontal wellbore length, L, are suitable. During this period, the pressure derivative curve is a horizontal line with a value of "$1/(4L_D)$"

(4) Early linear flow stage: it can be identified by a half-slope trend on the pressure derivative curve. During this period, gas flows linearly from the formation to natural fractures

(5) Interporosity flow stage from the matrix system to the fracture system: this process is characterized by a concave in the pressure derivative curve. The

concave shape is controlled by the storability ratio of fracture, ω_f, and the interporosity flow coefficient from the matrix system to the fracture system, λ_{mf}

(6) External boundary response stage: during this period, the pressures in the matrix and fracture systems reach a dynamic balance state. This period is marked by a slope of 0.5 on the pressure derivative curve without considering stress-dependent fracture permeability. However, the pressure derivative curve is no longer a horizontal line with a value of "0.5" but exhibits an upward tendency due to the effect of stress-dependent fracture permeability

3.2. Comparisons with the Traditional Models. So far, few attempts have been made to quantify the combined effects of dual-permeability flow behavior and stress-dependent fracture permeability on the transient pressure behavior of a horizontal well in fractured gas reservoirs. The main difference between the proposed and traditional models [25, 26] is that the dual-permeability flow behavior and stress-dependent fracture permeability are all incorporated in the new model. In this section, we simultaneously simulated the pressure response of both the proposed and conventional models using the same group of formation and well parameters in Table 2.

Figure 4 shows the comparison results of transient responses for the new model with the solution presented by Nie et al. [25]. The main difference between the two models is that stress-dependent fracture permeability is not considered in the model of Nie et al. [25]. As shown in Figure 4, fracture permeability stress sensitivity is found to significantly affect the middle stream flow period and the late-time pseudoradial flow period. There exist obvious differences during late-time pseudoradial flow period. The dimensionless pressure derivative curve exhibits a horizontal line with a value of 0.5 in the model of Nie et al. [25]; however, the derivative curve is no longer horizontal but bends upward in the new model. In addition, the location of the dimensionless pressure and pressure derivative curves during the middle stream flow period is higher in our model. This is because an additional pressure drop will be required to maintain a constant flow rate when the stress-sensitivity effect is taken into account.

We also compared the proposed model with the solution of a single-permeability model [26] based on the same reservoir properties and fracture parameters. The stress-dependent fracture permeability is considered both in two models. As can be seen in Figure 5, the combined effects of dual-permeability flow behavior and stress-dependent fracture permeability play a significant role in the early radial flow stage, the early linear flow stage, and the interporosity flow stage of the matrix system to the fracture system. Dimensionless pressure of the proposed model is lower than that of the single-permeability model [26] during the three flow periods. Besides, the concave in the pressure derivative curve of the dual-permeability model is shallower than that of single-permeability model. This is because the single-permeability model assumes that the fracture system is the only flow pathway directly connected with wellbore; however, the fluid supply from the matrix system to the wellbore is not considered. The dual-permeability flow behavior will accelerate energy supplement in the matrix during production compared with the single-permeability model.

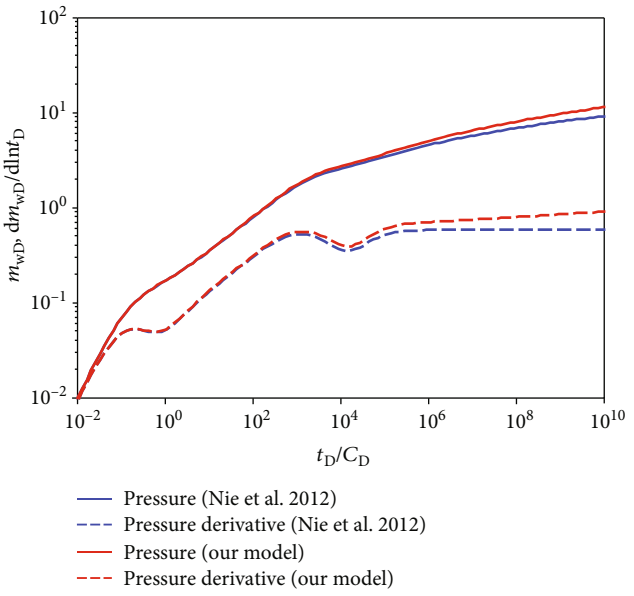

Figure 4: Comparison of the results of the proposed model with that of Nie et al. [25].

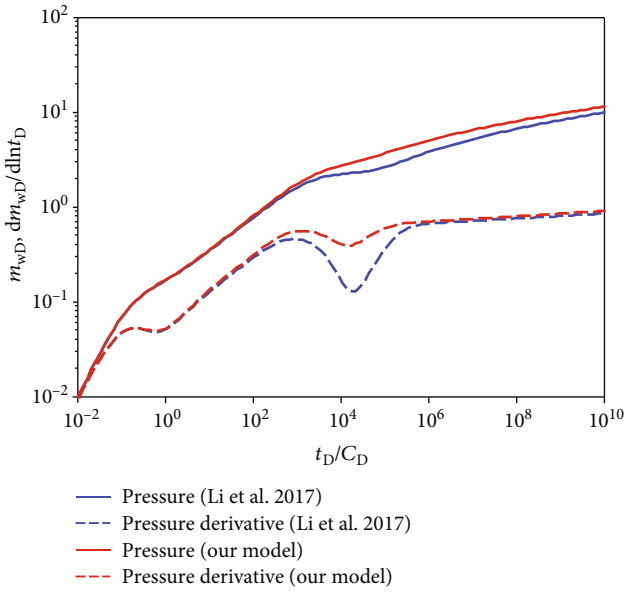

Figure 5: Comparison of the results of the proposed model with that of Li et al. [26].

3.3. Sensitivity Analysis. Based on the proposed model, the influences of stress sensitivity of fracture permeability, storativity ratio of the fracture, interporosity flow factor, and skin factor on pressure response are discussed. Except for the parameters analyzed, other parameters are the same and are shown in Table 2.

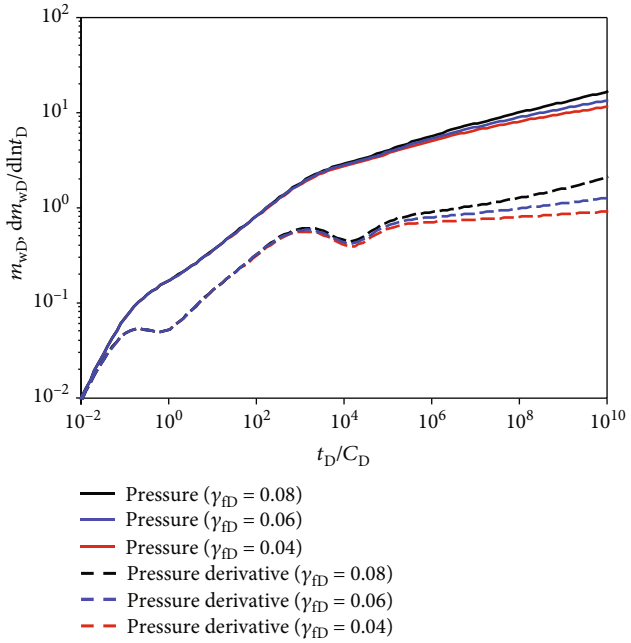

Figure 6: Effect of dimensionless permeability modulus, γ_{fD}, on type curves.

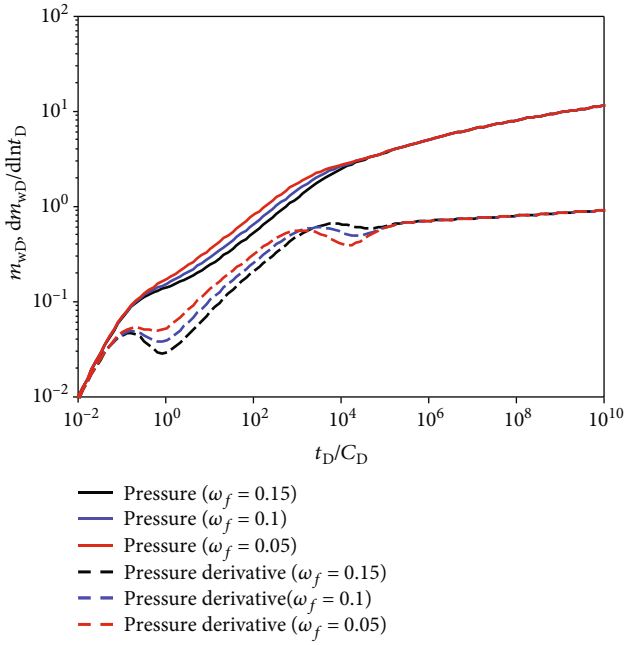

Figure 7: Effect of the storability ratio of the fracture, ω_f, on type curves.

3.3.1. Effect of the Permeability Modulus of the Fracture. The stress-sensitivity effect can be determined with the dimensionless permeability modulus, γ_{fD}. Figure 6 shows the pressure and pressure derivative curves for $\gamma_{fD} = 0.04$, 0.06, and 0.08. As stated, with increasing the value of γ_{fD}, the slope of the derivative curves increases during the intermediate and late time period. This is because the pressure drop increases as the dimensionless permeability modulus increases and fluid flow will be difficult and more gas is left in the reservoir. The stress sensitivity reflects the damage of permeability, and a larger dimensionless permeability modulus will increase the damage of permeability. Consequently, the permeability stress sensitivity of the fracture decreases the cumulative production. So, it is believed that reasonable producing pressure differential is excellent for reducing the negative effect of stress sensitivity on gas productivity in the development of fractured gas reservoirs.

3.3.2. Effect of the Storability Ratio of the Fracture. The effect of the storability ratio of the fracture, ω_f, on transient behavior is shown in Figure 7. As shown in Figure 7, the storability ratio of the fracture not only determines the duration and the depth of the concave but also has a significant effect on the early flow regimes (early radial and early linear flow stage). It can be clearly observed that the larger the ω_f is, the deeper and wider the concave in dimensionless pressure derivative curve. In addition, the dimensionless pressure curve becomes higher with the increase of the storability ratio of the fracture. This is because the storativity ratio of fracture reflects the relative capacity of fluid stored in the fracture system; a smaller storability ratio of the fracture is the response of relative abundant reserves in the matrix system. The pressure drop should increase to maintain the constant production rate when increasing the storability ratio of the fracture.

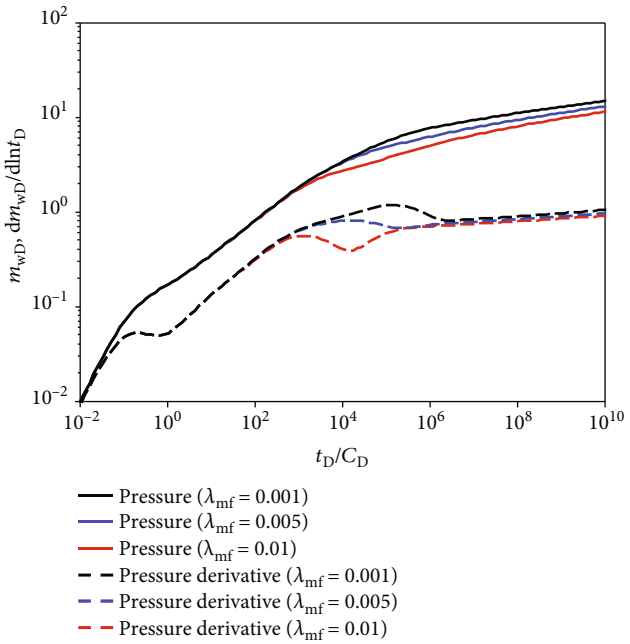

Figure 8: Effect of the interporosity flow factor, λ_{mf}, on type curves.

3.3.3. Effect of the Interporosity Flow Factor. The effect of the interporosity flow factor of the matrix system to the fracture system, λ_{mf}, on pressure response is shown in Figure 8. According to the definition of the interporosity flow factor,

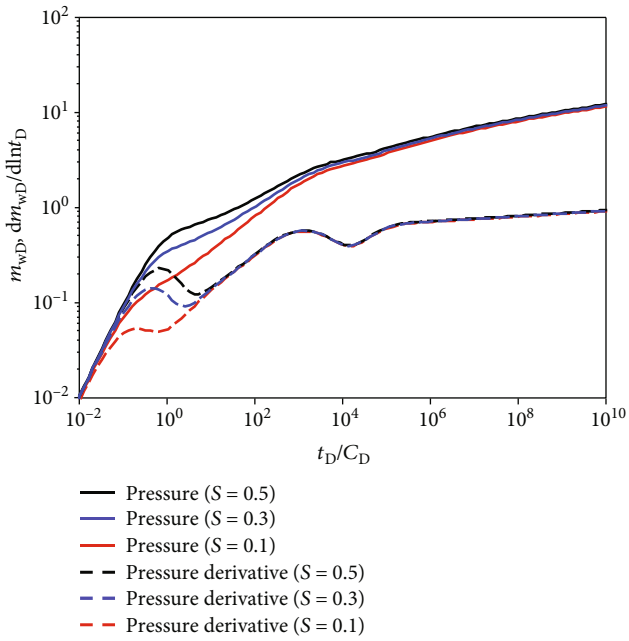

Figure 9: Effect of skin factor, S, on type curves.

the λ_{mf} represents the starting time of the flow exchange from the matrix system to the fracture system. The larger the λ_{mf} is, the earlier the time of the interporosity flow period is. Besides, the late-time pseudoradial flow period would be masked if the λ_{mf} is large enough.

3.3.4. Effect of the Skin Factor. The effect of the skin factor, S, on pressure response is shown in Figure 9. As shown in Figure 9, skin factor plays a significant role in the early transient flow period. A larger skin factor leads to a higher location of dimensionless pressure and pressure derivative curves. This is because the incremental value of the skin factor results in the increasing additional filtration resistance and the skin effect transition period will last longer. The larger the skin factor is, the slower the pressure wave propagates to the external boundary and the larger the pressure drop is.

4. Conclusions

This paper provided a semianalytical model to investigate the combined effects of dual-permeability flow behavior and stress-dependent fracture permeability on the transient pressure response for a horizontal well in a naturally fractured gas reservoir. The main conclusions of this work are as follows:

(i) A horizontal production well in a naturally fractured gas reservoir with consideration of stress sensitivity effect may exhibit six flow stages: pure wellbore storage stage, skin effect transition stage, early radial flow stage, early linear flow stage, interporosity flow stage, and external boundary response stage

(ii) The stress-dependent fracture permeability imposes effects on the intermediate flow period and the late-time pseudoradial flow period; the existence of dual-permeability flow behavior can make the stress sensitivity effect more significant

(iii) The storability ratio of the fracture, ω_f, mainly affects the duration and the depth of the concave, and a larger ω_f leads to a deeper and wider concave in dimensionless pressure derivative curve. In addition, the storability ratio plays a significant role in the early radial flow stage and early linear flow stage. The interporosity flow factor, λ_{mf}, mainly affects the starting time of the flow exchange from the matrix to the fracture. The larger the value of λ_{mf}, the earlier the occurrence of the interporosity flow period

(iv) The proposed model is suitable for various naturally fractured gas reservoirs and can interpret pressure signals with accurate matching results and more reasonable interpreted parameters

Data Availability

The data used to support the findings of this study are included within the article.

Conflicts of Interest

The authors declare that they have no conflicts of interest.

Acknowledgments

The authors acknowledge that this study was partially funded by the 2021 Innovation and Entrepreneurship Training Projects for College Students in Shanxi Province (no. S202110719144).

References

[1] Y. Wu, L. Cheng, S. Fang, S. Huang, and P. Jia, "A green element method-based discrete fracture model for simulation of the transient flow in heterogeneous fractured porous media," *Advances in Water Resources*, vol. 136, p. 103489, 2020.

[2] P. Jia, L. Cheng, S. Huang, and Y. Wu, "A semi-analytical model for the flow behavior of naturally fractured formations with multi-scale fracture networks," *Journal of Hydrology*, vol. 537, pp. 208–220, 2016.

[3] X. Tian, L. Cheng, R. Cao et al., "A new approach to calculate permeability stress sensitivity in tight sandstone oil reservoirs considering micro-pore-throat structure," *Journal of Petroleum Science and Engineering*, vol. 133, pp. 576–588, 2015.

[4] G. E. Barenblatt, I. P. Zheltov, and I. N. Kochina, "Basic concepts in the theory of seepage of homogeneous liquids in fissured rocks [strata]," *Journal of Applied Mathematics and Mechanics*, vol. 24, no. 5, pp. 1286–1303, 1960.

[5] J. E. Warren and P. J. Root, "The behavior of naturally fractured reservoirs," *SPE Journal*, vol. 3, no. 3, pp. 245–255, 1963.

[6] H. Kazemi, M. S. Seth, and G. W. Thomas, "The interpretation of interference tests in naturally fractured reservoirs with uniform fracture distribution," *SPE Journal*, vol. 9, no. 4, pp. 463–472, 1969.

[7] A. O. De Swaan, "Analytic solutions for determining naturally fractured reservoir properties by well testing," *SPE Journal*, vol. 16, no. 3, pp. 117–122, 1976.

[8] R. Raghavan and C. U. Ohaeri, "Unsteady flow to a well produced at constant pressure in a fractured reservoir," in *SPE California regional meeting*, Bakersfield, California, 1981SPE paper no. SPE-9902-MS.

[9] K. V. Serra, A. C. Reynolds, and R. Raghavan, "New pressure transient analysis methods for naturally fractured reservoirs (includes associated papers 12940 and 13014)," *Journal of Petroleum Technology*, vol. 35, no. 12, pp. 2271–2283, 1983.

[10] Y. Jalali and I. Ershaghi, "Pressure transient analysis of heterogeneous naturally fractured reservoirs," in *SPE California regional meeting*, Ventura, California, 1987SPE paper no. SPE 16341-MS.

[11] Y. Wu and K. Pruess, "A multiple-porosity method for simulation of naturally fractured petroleum reservoirs," *SPE Reservoir Engineering*, vol. 3, no. 1, pp. 327–336, 1988.

[12] T. D. Bui, D. D. Mamora, and W. J. Lee, "Transient pressure analysis for partially penetrating wells in naturally fractured reservoirs," in *SPE rocky mountain regional/low permeability reservoirs symposium and exhibition*, Denver, Colorado, 2000SPE paper no. SPE 60289-MS.

[13] Y. Wu, H. Liu, and G. S. Bodvarsson, "A triple-continuum approach for modeling flow and transport processes in fractured rock," *Journal of Contaminant Hydrology*, vol. 73, no. 1-4, pp. 145–179, 2004.

[14] F. Kuchuk, D. Biryukov, and T. Fitzpatrick, "Fractured-reservoir modeling and interpretation," *SPE Journal*, vol. 20, no. 5, pp. 983–1004, 2015.

[15] S. Wang, L. Cheng, S. Huang et al., "A semi-analytical method for modeling two-phase flow behavior in fractured carbonate oil reservoirs," *Journal of Energy Resources Technology*, vol. 141, no. 7, pp. 072902.1–072902.11, 2019.

[16] B. X. Hu and H. Huang, "Stochastic analysis of reactive solute transport in heterogeneous, fractured porous media: a dual-permeability approach," *Transport in Porous Media*, vol. 48, no. 1, pp. 1–39, 2002.

[17] T. M. Al-Shaalan, L. S. K. Fung, and A. H. Dogru, "A scalable massively parallel dual-porosity dual-permeability simulator for fractured reservoirs with super-k permeability," in *SPE annual technical conference and exhibition*, Denver, Colorado, 2003SPE paper no. SPE 84371-MS.

[18] A. P. G. Van Heel, P. M. Boerrigter, and J. J. Van Dorp, "Thermal and hydraulic matrix-fracture interaction in dual-permeability simulation," *SPE Reservoir Evaluation and Engineering*, vol. 11, no. 4, pp. 735–749, 2008.

[19] L. Jiang, T. Liu, and D. Yang, "A semianalytical model for predicting transient pressure behavior of a hydraulically fractured horizontal well in a naturally fractured reservoir with non-darcy flow and stress-sensitive permeability effects," *SPE Journal*, vol. 24, no. 3, pp. 1322–1341, 2019.

[20] P. Yu, D. Dempsey, and R. Archer, "Techno-economic feasibility of enhanced geothermal systems (EGS) with partially bridging multi-stage fractures for district heating applications," *Energy Conversion and Management*, vol. 257, p. 115405, 2022.

[21] V. Celis, R. Silva, M. Ramones, J. Guerra, and G. da Prat, "A new model for pressure transient analysis in stress sensitive naturally fractured reservoirs," *SPE Advanced Technology*, vol. 2, no. 1, pp. 126–135, 1994.

[22] E. Ozkan, R. Raghavan, and S. D. Joshi, "Horizontal-well pressure analysis," *SPE Formation Evaluation*, vol. 4, no. 4, pp. 567–575, 1989.

[23] E. J. Kuchuk, P. A. Goode, D. J. Wilkinson, and R. K. M. Thambynayagam, "Pressure-transient behavior of horizontal wells with and without gas cap or aquifer," *SPE Formation Evaluation*, vol. 6, no. 1, pp. 86–94, 1991.

[24] A. Hashemi, L. M. Nicolas, and A. C. Gringarten, "Well-test analysis of horizontal wells in gas/condensate reservoirs," *SPE Reservoir Evaluation and Engineering*, vol. 9, no. 1, pp. 86–99, 2006.

[25] R. Nie, Y. Meng, Y. Jia, F. X. Zhang, X. T. Yang, and X. N. Niu, "Dual porosity and dual permeability modeling of horizontal well in naturally fractured reservoir," *Transport in Porous Media*, vol. 92, no. 1, pp. 213–235, 2012.

[26] X. Li, L. Cao, C. Luo, B. Zhang, J. Q. Zhang, and X. H. Tan, "Characteristics of transient production rate performance of horizontal well in fractured tight gas reservoirs with stress-sensitivity effect," *Journal of Petroleum Science and Engineering*, vol. 158, pp. 92–106, 2017.

[27] S. Wang, L. Cheng, Y. Xue et al., "A semi-analytical method for simulating two-phase flow performance of horizontal volatile oil wells in fractured carbonate reservoirs," *Energies*, vol. 11, p. 10, 2018.

[28] Z. Sun, B. Huang, Y. Li, H. Lin, S. Shi, and W. Yu, "Nanoconfined methane flow behavior through realistic organic shale matrix under displacement pressure: a molecular simulation investigation," *Journal of Petroleum Exploration and Production Technologies*, vol. 12, no. 4, 2022.

[29] P. Yu, D. Dempsey, and R. Archer, "A three-dimensional coupled thermo-hydro-mechanical numerical model with partially bridging multi-stage contact fractures in horizontal-well enhanced geothermal system," *International Journal of Rock Mechanics and Mining Sciences*, vol. 143, article 104787, 2021.

[30] Z. Sun, S. Wang, H. Xiong, K. Wu, and J. Shi, "Optimal nanocone geometry for water flow," *AIChE Journal*, vol. 68, no. 3, article e17543, 2022.

[31] O. A. Pedrosa, "Pressure transient response in stress-sensitive formations," in *SPE California regional meeting*, Oakland, California, 1986SPE paper no. SPE-15115-MS.

[32] Stehfest and Harald, "Algorithm 368: numerical inversion of Laplace transforms [D5]," *Communications of the ACM*, vol. 13, no. 1, pp. 47–49, 1970.

[33] F. Kuchuk and Biryukov, "Pressure-transient behavior of continuously and discretely fractured reservoirs," *SPE Reservoir Evaluation and Engineering*, vol. 17, no. 1, pp. 82–97, 2014.

Hindawi
Geofluids
Volume 2022, Article ID 4358328, 11 pages
https://doi.org/10.1155/2022/4358328

Research Article

Effect of Pore Geometry on Nanoconfined Bulk-Gas Flow Behavior

Yi Zhang

College of Biology and Agriculture (College of Food Science and Technology), Zunyi Normal University, 563006, China

Correspondence should be addressed to Yi Zhang; sciyiyi@126.com

Received 15 March 2022; Revised 1 April 2022; Accepted 7 April 2022; Published 27 April 2022

Academic Editor: Zheng Sun

In order to improve energy consumption structure in Guizhou province, China, the efficient development of shale gas becomes more and more important. However, the theoretical understanding, towards microscopic gas flow mechanism, is still weak and insufficient. Although many models have been established, one part of them fails to cover all flow mechanisms, and the other part contains several fitting parameters. Moreover, nanopores can be divided into circular pore and slit pore in accordance with pore geometry. For cylindrical nanopores, by fully comparing with the existed models, a new bulk-gas transport model is proposed by weight superposition of slip flow and Knudsen diffusion, in which weight factors are obtained by Wu's model and Knudsen's model, respectively. For slit pores, an analytical equation for bulk-gas flow is proposed as well, which is free of any fitting parameters. The reliability of the proposed models has been clarified. The impacts of reservoir pressure, pore scale, and gas flow mechanism on bulk-gas flow behavior in process of shale gas development are analyzed. It is found that gas transport capacity of slit nanopores is significantly higher than that of cylindrical nanopores at the same pore scale. For slit nanopores, the larger the aspect ratio, the stronger bulk-gas transmission capacity. As the established models are free of fitting parameters and can be applied into the entire Kn range with sufficient accuracy, the research will greatly benefit shale gas development.

1. Introduction

In Guizhou province, China, shale gas is an emerging unconventional natural gas resource, and its development has the potential to reduce local coal combustion. Unlike conventional oil/gas reservoirs, pore size in shale rock is fairly small, falling in the nanoscale, which leads to the inapplicability of the traditional Navier-Stocks equation to describe gas flow behavior. Gas transmission characteristics in nanopores have attracted more and more attention [1, 2]. Karacan and Siriwardane et al. reported that the diameter of matrix pores is less than 10 nm, several times molecular diameter [3, 4]. Howard shows that the pore radius of Frio shale falls in the 5~15 nm range [5]. Nelson experimentally measured that the minimum pore radius in shale is about 5 nm and the maximum pore radius is about 100 nm [6]. In nanoscale, the gas velocity on the pore wall is no longer zero, and the classical Navier-Stokes equation cannot describe the bulk-gas transmission capacity [7–9]. Establishment of a model, suitable for characterizing the gas transmission characteristics in nanopores, will greatly enhance the prediction accuracy of shale gas production performance.

Up to now, the methods, used to describe the bulk-gas transport capacity in nanopores, can be divided into two categories, including molecular simulation as well as analytical equation. Molecular simulation mainly includes lattice Boltzmann [10], direct Monte Carlo [11, 12], and molecular dynamic simulation [13, 14]. MD method calculates the position, energy, and state of each molecules across the whole simulation time, which can accurately simulate the gas transmission characteristics in nanopores. While a single simulation case requires huge computing resources, moreover the simulation timespan is very short, usually less than nanosecond, which fails to meet the realistic physical process in shale [15–17]. In contrast, the analytical model has the advantages of simple calculation and strong practicability, and it can analyze the characteristics of bulk-gas

transmission in extreme cases. It may reveal phenomena that are difficult to be simulated by molecular simulation and experiment. Meanwhile, its deficiency is the limited scope of application. Although many analytical models have been established, some of them do not cover all flow mechanisms, the other part contains several fitting parameters, which often have a great impact on the accuracy of the model.

In 1937, Adzumi studied the flow characteristics of gas in capillary by a large number of experiments and proposed that the determination of fluid flow mechanism depends on Knudsen number. Based on this, the flow mechanism is divided into viscous flow, transition flow, and Knudsen diffusion and developed a full-Kn model by weight superposition of viscous flow and Knudsen diffusion. Unfortunately, Adzumi did not give the specific expression of the weight factor [18–20]. Liu et al. [21] gave the specific expression of the weight factor, but the established bulk-gas transmission model is limited to the case when the Knudsen number is less than 1. Ertekin et al. [22] refer to the existing concept of weight factor to couple Knudsen diffusion and Fick diffusion, but the weight factor will not change with Knudsen number, which quite conflicts with simulation results and experimental data. Azom and Javadpour and Singh and Javadpour [23, 24] linearly added slippage flow and Knudsen diffusion and obtained the full Knudsen number transmission model, but it contains a fitting parameter. Based on the basic theory proposed by Adzumi, Agulera et al. [25] give the weight coefficient, but it also contains three fitting parameters. Beskok and Karniadakis [26] corrected the slippage flow by introducing the molecular sparsity coefficient and extended the formula to the full Knudsen range, but the model contains three fitting parameters. The model proposed by Wu and Xiangfang [27] is based on Beskok's model and takes the intermolecular collision frequency and the collision frequency between molecules and wall as the weight coefficient, including three fitting parameters. Rahmanian et al. [28] referred to the empirical coefficient proposed by Agulera and gave a gas transport model suitable for nanopores with different cross sections, while it includes three fitting parameters. Comparing the established models with the molecular simulation results, it is found that most of the models suffer low accuracy, especially for the slippage flow and transition flow stage.

Because the minerals, forming shale rock, are different in chemical composition, lattice structure, particle size, and petrophysical properties, as a result, the type and size of the formed intergranular, interlayer, and intergranular pores are also different [29–31]. In this paper, the nanopores in the reservoir are simplified into two types, including cylindrical pores and slit pores. As for circular pores, by fully comparing the existed bulk-gas transport models and analyzing their advantages and disadvantages [14, 32], the weight factors of molecular free diffusion and slippage flow are derived, respectively, by referring to Knudsen's model and Wu's model. For slit nanopores, based on the proposed model for cylindrical nanopores, an analytical model of bulk-gas transmission is established for the first time by modifying the corresponding weight factor coefficients. The established bulk-gas transport models do not contain fitting parameters and are suitable for the full Knudsen number range. On this basis, the effects of pore morphology, pore scale, and reservoir pressure on gas bulk phase transmission capacity are studied, and the variation characteristics of bulk-gas transmission capacity in different development stages of shale gas are quantitatively analyzed.

2. Nanoconfined Bulk-Gas Flow Mechanism with Different Pore Geometry

Knudsen number is defined as the ratio of the free path of gas molecules to representative pore size of porous media, characterizing the rarefaction effect of gas [33]. Then, based on the Knudsen number, Schaaf divides the bulk-gas transport mechanism into four basic types [34], namely, continuous flow, slippage flow, transition flow, and Knudsen diffusion. Among them, continuous flow, slippage flow, and Knudsen diffusion had formed a relatively complete theoretical system after years of research. However, accurate description upon the characteristics of transition flow is still challenging.

$$Kn = \frac{\lambda}{d}, \tag{1}$$

where λ is the average free path of gas molecules, m; d is the pore diameter, m.

Taking methane as an example, the molecular effective radius is 0.4 nm. The variation relationship of the average molecular free path with reservoir pressure and temperature is given below.

$$\lambda = \frac{k_B T}{\sqrt{2}\pi\delta_m^2 p}, \tag{2}$$

where δ_m is the effective radius of gas molecules, m; K_B is the Boltzmann constant. Average molecular free path increases with the increase of temperature, but the trend is not sensitive and only plays a slight role when pressure is lower than 1 MPa. The change of pressure has a great influence on this value, and the molecular average free path will gradually increase with the decrease of pressure, and the increasing range will become larger. For specific scale reservoir pores, the reservoir temperature can be regarded as a fixed value, but the decrease of reservoir pressure will increase the Knudsen number rapidly, leading to the variation of gas flow mechanism. Therefore, a single flow mechanism equation is not suitable for unconventional gas reservoir development. Moreover, the pore types of nanopores are complex, and the study of nanopores alone cannot meet the actual needs. It is urgent to establish a high-precision cross-scale gas bulk transport equation suitable for different cross-sections. Next, bulk-gas transport equations of circular tube holes and slit holes in different Knudsen number ranges are introduced.

2.1. Cylindrical Nanopore. When $Kn < 0.001$, the gas nanopore transport mechanism is continuous flow, and the intermolecular collision dominates the transport process. At this time, the flow characteristics can be characterized by the nonslip Navier-Stokes equation [35].

$$J_{yc} = -\frac{r^2 p}{8\mu_g RT}\frac{dp}{dl}, \tag{3}$$

where J_{yc} represents the continuous flow transmission capacity, mol/(m^2·s); r is the pore radius of porous medium, m; p is the fluid flow pressure, Pa; μ_g is the gas viscosity, Pa·s; R is the general gas constant, J/(mol·K); T is the temperature of the fluid, K; and l is the distance in the gas flow direction, m.

When the Knudsen number is between 0.001 and 0.1, the gas nanopore transmission mechanism is slippage flow, the collision frequency between gas molecules and wall increases gradually, and the nonslippage condition breaks down. Then, it is found that satisfactory results can be obtained by modifying the slip boundary conditions [36–46].

$$J_{ys} = -\frac{r^2 p}{8\mu_g RT}\left(1 + \frac{4Kn}{1 - bKn}\right)\frac{dp}{dl}. \tag{4}$$

Among them, J_{ys} characterizing the slippage flow transmission capacity of gas circular tube hole, mol/(m^2·s); b is the gas slippage constant. When the value is 0, it represents the first-order slippage condition, and when the value is -1, it represents the second-order slippage condition. Moreover, according to a large number of molecular simulation and experimental data, the fitting effect of the second-order slippage condition is obviously better than that of the first-order, so the expression of nanopore phase transport of gas slippage flow can be simplified as follows:

$$J_{ys} = -\frac{r^2 p}{8\mu_g RT}\left(1 + \frac{4Kn}{1 + Kn}\right)\frac{dp}{dl}. \tag{5}$$

When the Knudsen number is greater than 10, the transmission mechanism of gas nanopores is Knudsen diffusion, the collision frequency between gas molecules continues to decline, and the collision frequency between molecules and wall dominates the transmission process, which can be expressed by Knudsen equation [16, 26, 27].

$$J_{yk} = -\frac{d}{3}\sqrt{\frac{8}{\boldsymbol{\pi RTM}}}\frac{dp}{dl}. \tag{6}$$

In view of the dominant collision between gas molecules and wall, the influence of wall roughness on gas diffusion must be considered. The coarser the wall, the weaker the gas diffusion ability. The specific relationship can be characterized by the following formula [17, 27].

$$J_{yk} = -\frac{d}{3}\delta^{D_f - 2}\sqrt{\frac{8}{\boldsymbol{\pi RTM}}}\frac{dp}{dl}, \tag{7}$$

where δ is the ratio of molecular diameter to local pore diameter, dimensionless; D_f is the fractal dimension of pore wall, dimensionless. When the fractal dimension is 2, it represents a smooth wall and has no effect on the gas transmission capacity; when the fractal dimension is 3, it represents a rough wall.

2.2. Slit Nanopores. In order to facilitate the investigation of pore morphology on gas transmission capacity, the aspect ratio is defined here (AR*)*.

$$\mathrm{AR} = \frac{w}{h}, \tag{8}$$

where w is the width of slit hole, m; h is the height of slit hole, m.

When the Knudsen number is less than 0.001, the flow velocity of gas molecules on the wall is zero, which is a continuous flow. The specific expression can be seen from Hagen Poiseuille [47].

$$J_{xc} = C(\mathrm{AR})\frac{wh^3}{12\mu}\frac{p}{RT}\frac{dp}{dl}, \tag{9}$$

where J_{xc} is the characterization of gas slippage flow transport capacity in slit holes, mol/s; $C(\mathrm{AR})$ is the continuous flow correction coefficient of slit holes with different aspect ratios, dimensionless [26, 48].

$$C(\mathrm{AR}) = 1 - \frac{192}{\mathrm{AR}\pi^5}\sum_{i=1,3,5\cdots}^{\infty}\frac{\tanh\left(\boldsymbol{i\pi AR}/2\right)}{i^5}. \tag{10}$$

When the Knudsen number is between 0.001 and 0.1, the collision between gas and wall cannot be ignored. After a large number of molecular simulation and experimental results, for the slippage flow, the second-order slippage boundary condition is more reasonable than the first-order boundary slippage condition. At this time, the expression of gas slippage flow is provided.

$$J_{xs} = C(\mathrm{AR})\frac{wh^3}{12\mu}\frac{p}{RT}\left(1 + \frac{6Kn}{1 + Kn}\right)\frac{dp}{dl}, \tag{11}$$

where J_{xs} represents the gas slippage flow transmission capacity of slit hole, mol/s.

When the Knudsen number is greater than 10, the transmission mechanism of gas slit hole is Knudsen diffusion, and the collision frequency between molecules and wall dominates the transmission process. Considering the influence of cross-section shape, the Knudsen diffusion transmission capacity of gas bulk phase in slit hole can be expressed [26].

$$\begin{aligned} J_{xk} &= B(\mathrm{AR})\frac{wh^2}{\sqrt{2RTM}}\frac{dp}{dl}, \\ B(\mathrm{AR}) &= \left[\mathrm{AR}^2\ln\left(\frac{1}{\mathrm{AR}} + \sqrt{1 + \frac{1}{\mathrm{AR}^2}}\right)\right. \\ &\quad \left. + \mathrm{AR}\ln\left(\mathrm{AR} + \sqrt{1 + \mathrm{AR}^2}\right) - \frac{\left(\mathrm{AR}^2 + 1\right)^{1.5}}{3} + \frac{1 + \mathrm{AR}^3}{3}\right], \end{aligned} \tag{12}$$

where $B(\mathrm{AR})$ is the Knudsen diffusion correction coefficient of slit holes with different aspect ratios, dimensionless. It can be seen from the expression that this value is only affected by the aspect ratio.

3. Model Establishment and Verification

3.1. Cylindrical Nanopores. Comprehensive analysis of the comparison results between existing models and molecular simulation shows that the majority of existing models are quite different from molecular simulation results, and only Wu's model and Knudsen's model perform well. Among them, the calculation results of Wu's model are consistent with the molecular simulation data in the slippage flow domain, but there are large errors in the transition flow stage, which cannot accurately describe the gas bulk phase transmission capacity of the transition flow. Knudsen's model is consistent with the molecular simulation results at high Knudsen number stage, but it will overestimate the bulk phase transport capacity of slipstream gas. Referring to Wu's model which can accurately describe the slippage flow and Knudsen's model which can accurately describe the stage of high Knudsen number, the weight factors of slippage flow and Knudsen diffusion are obtained, respectively. Coupling the mentioned two mechanisms, a nanoscale bulk-gas transport model in cylindrical pores, suitable for all Knudsen number, is obtained. The corresponding expression is given below.

$$
\begin{aligned}
J_{ya} &= \frac{1}{1+5Kn} J_{ys} + \frac{Kn+2.507}{Kn+3.095} J_{yk},\\
\frac{J_{ya}}{J_{yk}} &= \frac{3\pi}{128\delta^{D_f-2}Kn}\left(1+\frac{4Kn}{1+Kn}\right)\frac{1}{1+5Kn} + \frac{Kn+2.507}{Kn+3.095},\\
\frac{J_{ya}}{J_{yc}} &= \left(1+\frac{4Kn}{1+Kn}\right)\frac{1}{1+5Kn} + \frac{\delta^{D_f-2}(Kn+2.507)Kn}{Kn+3.095}\frac{128}{3\pi}.
\end{aligned}
\tag{13}
$$

The proposed bulk-gas transport model without fitting parameters can accurately describe the characteristics of each flow mechanism. When the Knudsen number is extremely small, it will degenerate into a continuous flow equation according to formula (4), which is much greater than that at low Knudsen number, so formula (29) will degenerate into a continuous flow equation at low Knudsen number. When the Knudsen number is maximum, it can be directly reduced to Knudsen diffusion equation according to formula (29). When the flow mechanism is slippage flow and transition flow, it can be verified by comparing the calculated values of the model in this paper with the molecular simulation results. The specific comparison results are shown in Figures 1 and 2.

Through the analysis of Figures 1 and 2, it can be seen that the nanopore phase transport model proposed in this paper can always maintain very high accuracy within the whole Knudsen range. Only when the Knudsen number is near 1, the gas transport capacity is slightly underestimated, but its accuracy is still higher than that of Knudsen model. So far, the reliability of the proposed bulk phase transport model without fitting parameters for all Knudsen numbers has been verified, and its high-precision characteristics are shown by comparison with Wu model and Knudsen model.

3.2. Slit Nanopores. Based on the proposed nonfitting parameter nanotube bulk phase transport model and referring to its basic form of weight factor, the slip flow equation and Knudsen diffusion equation applicable to slit hole are coupled, that is, formula (10) and formula (11), and the nonfitting parameter slit hole bulk phase transport model is established. The specific expression is as follows:

$$
\begin{aligned}
J_{xa} &= \frac{1}{1+6Kn} J_{xs} + \frac{Kn+2.45}{Kn+3.6} J_{xk},\\
\frac{J_{xa}}{J_{xk}} &= \frac{C(\mathrm{AR})}{6Kn}\left(1+\frac{6Kn}{1+Kn}\right)\frac{1}{1+6Kn} + \frac{Kn+2.45}{Kn+3.6}B(\mathrm{AR}),\\
\frac{J_{xa}}{J_{xc}} &= \left(1+\frac{6Kn}{1+Kn}\right)\frac{C(\mathrm{AR})}{1+6Kn} + B(\mathrm{AR})\frac{Kn+2.45}{Kn+3.6}6Kn.
\end{aligned}
\tag{14}
$$

Similarly, when the Knudsen number is extremely high, the slit hole model, i.e., formula (32), can be reduced to Knudsen diffusion equation, and when the Knudsen number is extremely small, the model can be reduced to continuity equation. In order to verify the accuracy of the proposed nonfitting parameter model for the transmission capacity of different slit holes and its reliability in the stage of slippage flow and transition flow, the gas bulk phase transmission capacity of different aspect ratios (1, 2, and 4) in different Knudsen number ranges is calculated by the model, and the results are compared with the molecular simulation data [32].

By analyzing the comparison results of Figures 3 and 4, it can be seen that the calculation results of the volume phase transmission capacity of the slit pore model proposed in this paper for different forms of pores within the whole Knudsen range are always highly consistent with the molecular simulation data. At low Knudsen number, only when the aspect ratio is 2, there is a slight difference. At high Knudsen number, calculation results for the transmission capacity of different pore shape can always be consistent with the molecular simulation data. Therefore, the reliability and high-precision characteristics of the slit pore model are verified by comparison with the molecular simulation.

So far, the fitting parameter free circular hole model and slit hole model suitable for the whole Knudsen number range have been established for the first time, and their reliability and accuracy have been verified by comparing with molecular simulation results and existing models. Because the established circular hole and slit hole models do not contain fitting parameters and are suitable for the full Knudsen number with high accuracy, they show the practicability and simplicity that other models do not have. Next, the proposed model is used to study the effects of pore morphology (cylindrical nanopores and slit nanopores), pore scale, and reservoir pressure on gas bulk phase transmission capacity in

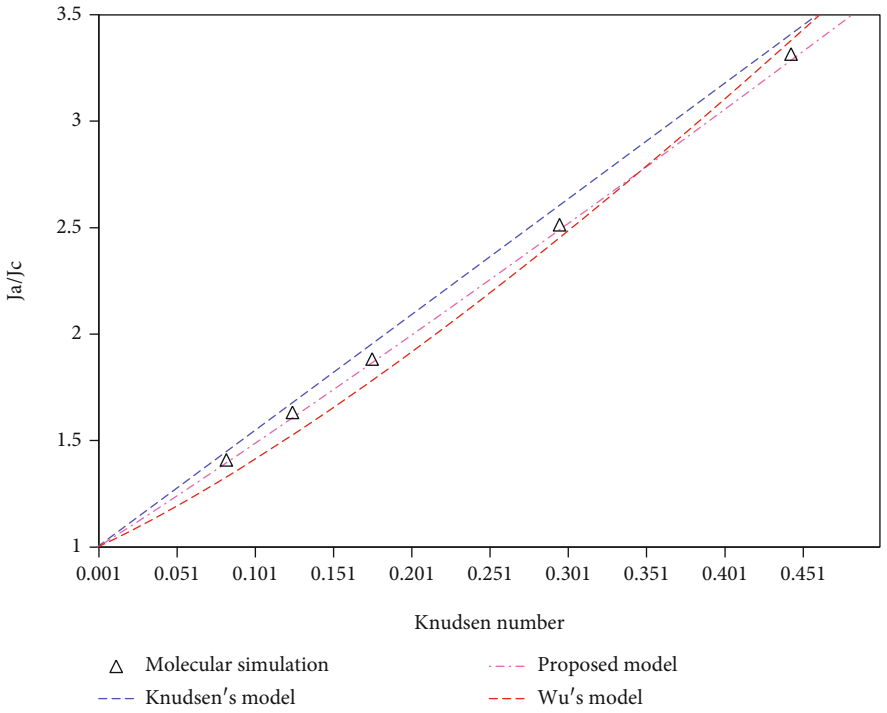

Figure 1: Comparison between proposed model and molecular simulation with low Kn.

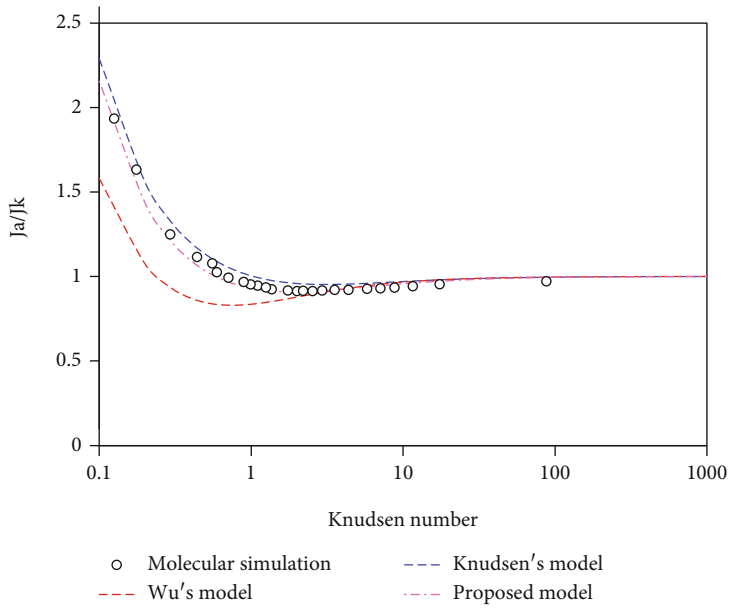

Figure 2: Comparison between proposed model and molecular simulation with high Kn.

the process of gas reservoir development, and the transmission contribution of each transmission mechanism is quantitatively analyzed.

4. Results and Discussion

In the conventional reservoir, because it does not contain a large number of nanopores and the formation pressure is high, the reservoir flow mechanism will not change in the whole life production cycle of the gas well, and it is always continuous flow. In this case, the bulk phase transmission capacity is close to a constant. However, for coal and shale reservoirs with diverse nanopores, with the development, the reservoir pressure continues to decrease, and different production stages often correspond to different transmission types, so the nanopore phase transmission capacity will change greatly. Studying the gas transmission capacity of reservoirs in different production stages is helpful to formulate a reasonable gas production scheme and provide constructive suggestions for the formulation of gas reservoir development scheme. Assuming that the

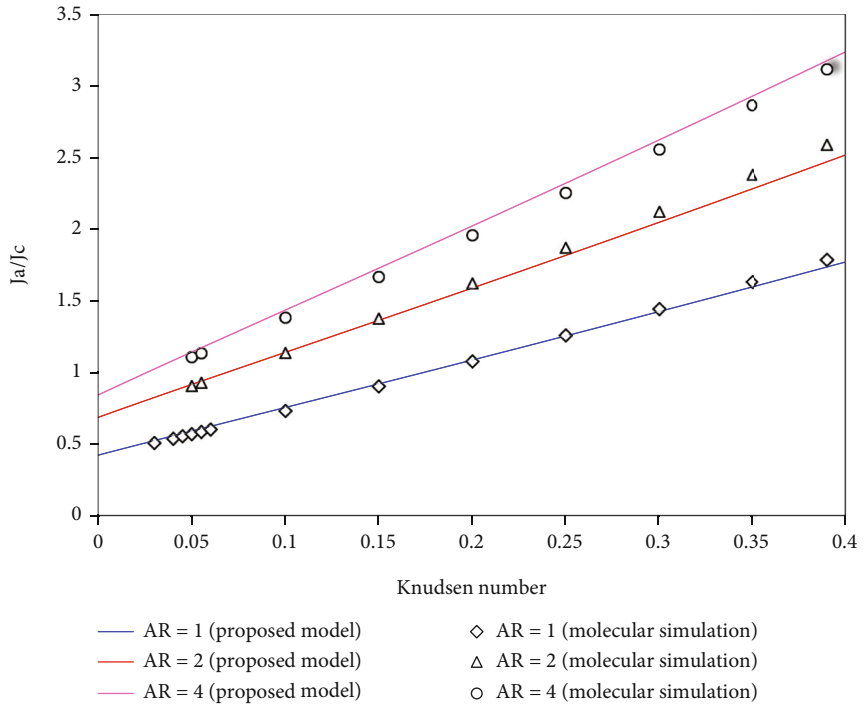

Figure 3: Comparison between proposed model and molecular simulation with low Kn.

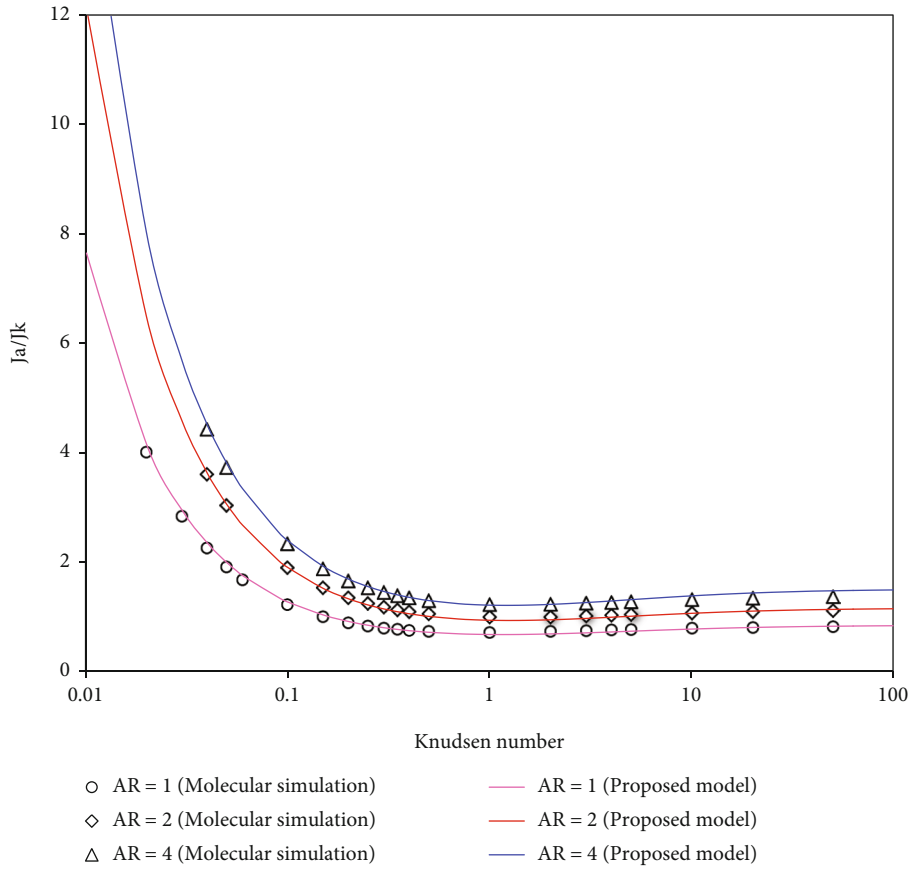

Figure 4: Comparison between proposed model and molecular simulation with high Kn.

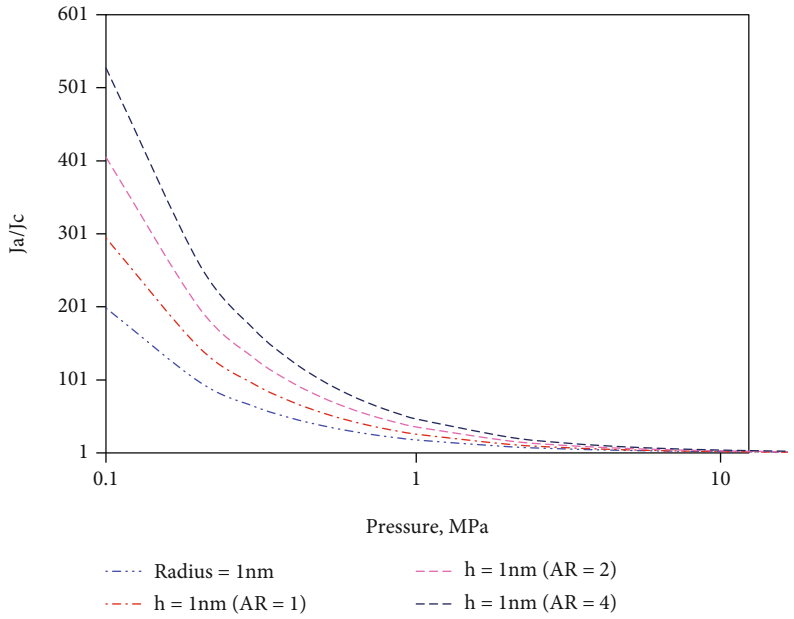

Figure 5: Gas transport capacity versus pressure with different cross-section shapes.

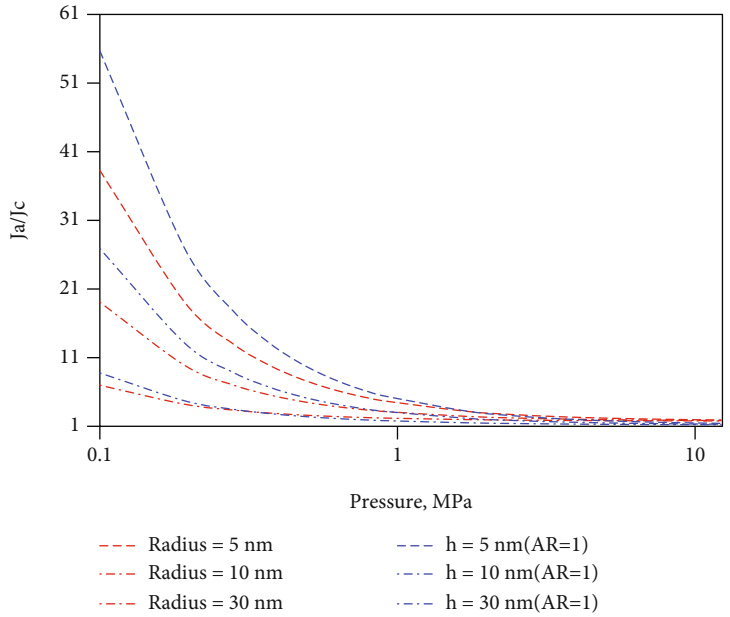

Figure 6: Effect of pore size on gas transport capacity.

reservoir temperature is 323 K, and taking methane as an example, the gas bulk phase transmission capacity in pores with different scales (1~50 nm) is calculated and analyzed, respectively. In view of the characterization of the continuous flow transmission capacity, which remains unchanged under the total Knudsen number, the change of nanopore transmission capacity with pressure is described by the change relationship with reservoir pressure.

According to the analysis of Figure 5, for the specific pore scale, the bulk-gas transport capacity shows an upward trend with the decrease of reservoir pressure. When the reservoir pressure is greater than 1 MPa, the bulk-gas transmission capacity of all pores increases slowly. When the reservoir pressure is less than 1 MPa, the bulk phase transmission capacity of pores increases rapidly, and the growth range increases with the decrease of pressure. For different forms of pores, at the same scale, the transmission capacity of slit nanopores is significantly higher than that of cylindrical nanopores, and transmission capacity of slit nanopores will increase with the increase of aspect ratio. In Figure 6, it can be seen that whether for circular pores or slit pores, under the same reservoir pressure, their bulk phase transmission capacity increases with the decrease of scale, and the growth range increases with the decrease of scale. It can also be seen from Figure 6 that although the transmission capacity of slit holes is stronger than that of cylindrical

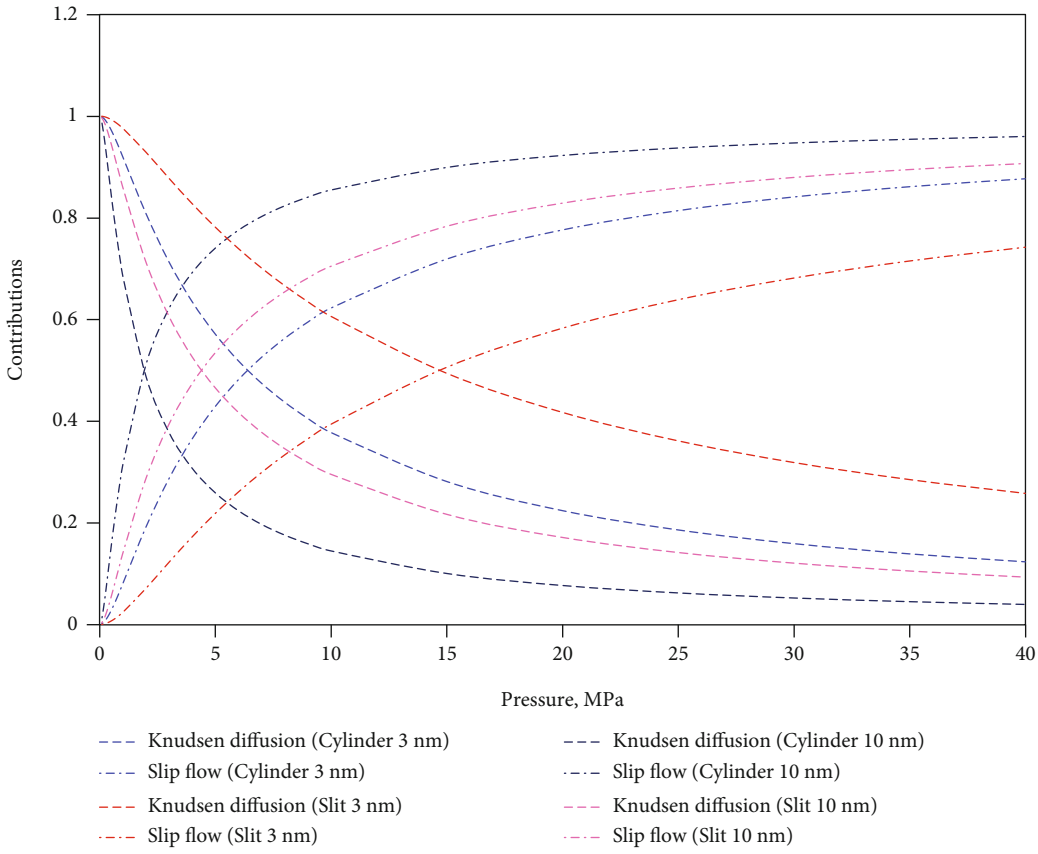

Figure 7: Contribution of different gas transport mechanisms.

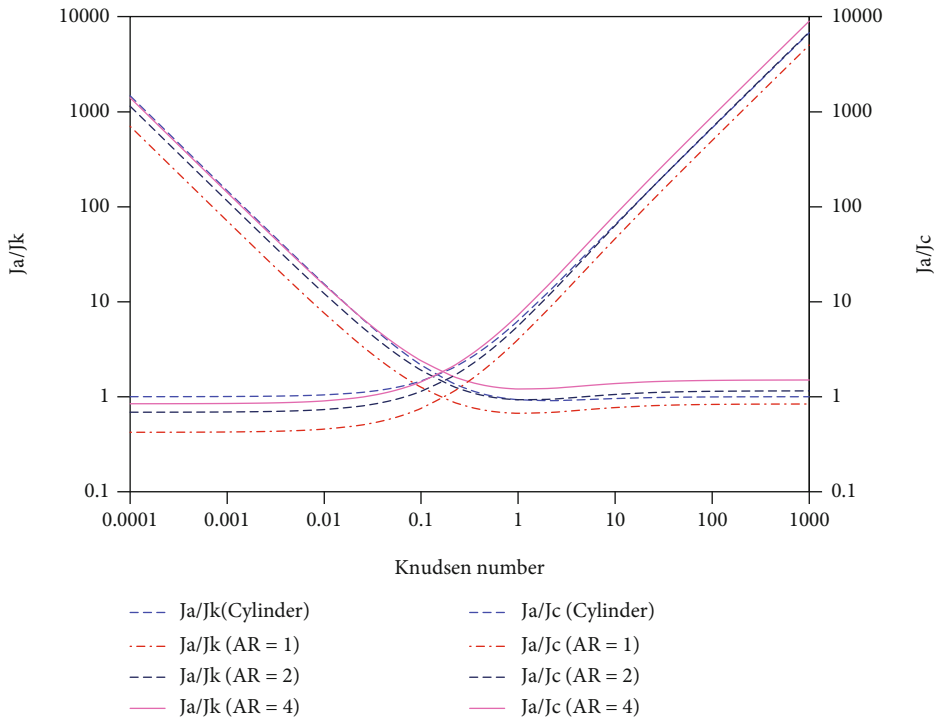

Figure 8: The bulk-gas transport capacity with different Kn values.

nanopores at the same pore size, both differences will gradually become narrow with the increase of pore scale. Therefore, when the pore size in the reservoir is greater than 30 nm, the bulk phase transmission capacity of circular pore and slit pore is basically the same. When the pore size in the reservoir is less than 30 nm, we should focus on the influence of pore morphology on the transmission capacity.

The models, suitable for cylindrical nanopores and slit nanopores, proposed in this paper are obtained by giving the expression of weight factor and coupling slippage flow and Knudsen diffusion. With the development of shale gas, the reservoir pressure decreases continuously, and the contribution of slippage flow and Knudsen diffusion to the overall transmission capacity will change. Here, the contribution factors of slippage flow and Knudsen diffusion to gas bulk phase transmission capacity are defined as follows.

$$F_{yk} = \frac{1}{(1/1 + 5Kn)(Kn + 3.095/Kn + 2.507)J_{ys}/J_{yk} + 1},$$

$$F_{ys} = \frac{1}{1 + (1 + 5Kn)(Kn + 2.507/Kn + 3.09)J_{yk}/J_{ys}},$$

$$F_{xk} = \frac{1}{(1/1 + 6Kn)(Kn + 3.6/Kn + 2.45)J_{xs}/J_{xk} + 1},$$

$$F_{xs} = \frac{1}{1 + (1 + 6Kn)(Kn + 2.45/Kn + 3.6)J_{xk}/J_{xs}}. \quad (15)$$

It can be seen from Figure 7 that for pores of the same size and shape, with the increase of reservoir pressure, contribution of slippage flow gradually increases and the contribution of Knudsen diffusion gradually decreases. This is because the increase of pressure reduces the molecular average free path and Knudsen number, and the flow mechanism in pores changes from Knudsen diffusion to slippage flow. For the pores with the same size and different shapes, with the development, the contribution of Knudsen diffusion in the slit nanopores is always higher than that in the circular nanopores. For the same shape and different pore-scale pores, the analysis shows that the contribution of slippage flow in large-scale pores is higher than that in small pores. Through the analysis of Figure 7, it can also be seen that for the nanoscale pores analyzed in the figure, when the reservoir pressure is higher than 10 MPa, the transmission contribution of each transmission mechanism changes slowly, while when the reservoir pressure is lower than 10 MPa, the transmission mechanism changes sharply. It shows that in the actual gas reservoir production process, due to the concept of pressure drop funnel, there is a large pressure difference between the near well zone and the far well zone. The near well area is mainly affected by Knudsen diffusion, and the far well area is mainly affected by slippage flow mechanism.

Through the established models, the bulk phase transmission capacity of different forms of pores in the whole Knudsen number range is analyzed. It can be seen from the comparison in Figure 8 that for slit nanopores, the larger the aspect ratio of pores, the stronger the bulk phase transmission capacity. The transmission capacity of slit nanopores with AR = 4 is about 1.23 and 2 times that of slit nanopores with AR = 2 and AR = 1 in the whole Knudsen range. For the transmission capacity in cylindrical nanopores, when the Knudsen number is less than 0.1, its transmission capacity is higher than all slit nanopores. When the Knudsen number is between 0.1~10, the transmission capacity in cylindrical nanopores is lower than the slit hole transmission capacity of AR = 4. When the Knudsen number is greater than 10, the transmission capacity in cylindrical nanopores is lower than that in slit nanopores of AR = 2 and only higher than the slit hole with AR = 1.

5. Conclusions

(1) By fully comparing and analyzing the existing models and molecular simulation results, it is found that Wu's model has high accuracy in the slippage flow stage, and Knudsen's model is consistent with the molecular simulation results in the high Knudsen number stage. Using Wu's model and Knudsen's model for reference, the weight factors of slippage flow and Knudsen diffusion are obtained, respectively. The two mechanisms are coupled to obtain the nonfitting parameter bulk-gas transport model. According to the model for cylindrical nanopores, corresponding weight factors are modified to obtain the nonfitting parameter for slit nanopores

(2) Under the same reservoir pressure, the bulk-gas transmission capacity of cylindrical nanopores and slit nanopores increases with the decrease of pore size. For different forms of pores, at the same scale, the transmission capacity of slit nanopores is significantly higher than that of cylindrical nanopores, and the transmission capacity of slit nanopores will increase with the increase of aspect ratio, but the difference between the two will gradually narrow with the increase of pore size. When the pore size in the reservoir is greater than 30 nm, bulk-gas transmission capacity of cylindrical and slit nanopores is basically the same

(3) For slit nanopores, the larger the aspect ratio of pores, the stronger the bulk-gas transmission capacity. The transmission capacity of slit nanopores with AR = 4 is about 1.23 and 2 times that of slit pores with AR = 2 and AR = 1 in the whole Knudsen number range. For transmission capacity in cylindrical nanopores, when the Knudsen number is less than 0.1, its transmission capacity is higher than all slit nanopores analyzed in the calculation case. When Knudsen number is between 0.1~10, transmission capacity in cylindrical nanopores is lower than the slit nanopores of AR = 4. When Knudsen number is greater than 10, transmission capacity in cylindrical nanopores is lower than that of slit nanopores of AR = 2 and only higher than the slit nanopores with AR = 1

Data Availability

Data is available on request.

Ethical Approval

On behalf of all the coauthors, the corresponding author states that there are no ethical statements contained in the manuscripts.

Conflicts of Interest

The author declares that there is no conflict of interest regarding the publication of this paper.

Acknowledgments

The research acknowledges the financial support of the Zunyi Normal University (BS- [2019]-20).

References

[1] C. Rühl and J. Giljum, "BP global energy outlook 2030," *Voprosy Ekonomiki*, no. 5, pp. 109–128, 2013.

[2] M. Yoshimune, T. Yamamoto, M. Nakaiwa, and K. Haraya, "Preparation of highly mesoporous carbon membranes via a sol-gel process using resorcinol and formaldehyde," *Carbon*, vol. 46, no. 7, pp. 1031–1036, 2008.

[3] C. Özgen Karacan, "Heterogeneous sorption and swelling in a confined and stressed coal during CO_2 injection," *Energy & Fuels: An American Chemical Society Journal*, vol. 17, no. 6, pp. 1595–1608, 2003.

[4] H. Siriwardane, I. Haljasmaa, and R. Mclendon, "Influence of carbon dioxide on coal permeability determined by pressure transient methods," *International Journal of Coal Geology*, vol. 77, no. 1–2, pp. 109–118, 2009.

[5] J. J. Howard, "Porosimetry measurement of shale fabric and its relationship to illite/smectite diagenesis," *Clays and Clay Minerals*, vol. 39, no. 4, pp. 355–361, 1991.

[6] P. H. Nelson, "Pore-throat sizes in sandstones, tight sandstones, and shales," *AAPG Bulletin*, vol. 93, no. 3, pp. 329–340, 2009.

[7] C. Cercignani and A. Daneri, "Flow of a rarefied gas between two parallel plates," *Journal of Applied Physics*, vol. 34, no. 12, pp. 3509–3513, 1963.

[8] S. Roy, R. Raju, H. F. Chuang, B. A. Cruden, and M. Meyyappan, "Modeling gas flow through microchannels and nanopores," *Journal of Applied Physics*, vol. 93, no. 8, pp. 4870–4879, 2003.

[9] K. Wu, Z. Chen, and H. Wang, *A Model for Real Gas Transfer in Nanopores of Shale Gas Reservoirs*, EUROPEC, Madrid, Spain, 2015.

[10] E. Piekos and K. Breuer, "DSMC modeling of micromechanical devices," in *30th Thermophysics Conference*, 1995.

[11] G. A. Bird, *Molecular Gas Dynamics and the Direct Simulation of Gas Flows*, , location is USA, 1998Clarendon Press, Oxford, 1998.

[12] M. L. Hudson and T. J. Bartel, *DSMC Simulation of Thermal Transpiration and Accommodation Pump*, Rarefied Gas Dynamics, 1999.

[13] D. C. Rapaport, *The Art of Molecular Dynamics Simulation*, Cambridge University Press, 2011.

[14] S. K. Loyalka and S. A. Hamoodi, "Poiseuille flow of a rarefied gas in a cylindrical tube: solution of linearized Boltzmann equation," *Physics of Fluids A: Fluid Dynamics*, vol. 2, no. 11, pp. 2061–2065, 1990.

[15] F. Javadpour, D. Fisher, and M. Unsworth, "Nanoscale gas flow in shale gas sediments," *Journal of Canadian Petroleum Technology*, vol. 46, no. 10, pp. 55–61, 2007.

[16] F. Javadpour, "Nanopores and apparent permeability of gas flow in mudrocks (shales and siltstone)," *Journal of Canadian Petroleum Technology*, vol. 48, no. 8, pp. 16–21, 2009.

[17] Z. Sun, B. Huang, Y. Li, H. Lin, S. Shi, and W. Yu, "Nanoconfined methane flow behavior through realistic organic shale matrix under displacement pressure: a molecular simulation investigation," *Journal of Petroleum Exploration and Production Technology*, vol. 12, no. 4, pp. 1193–1201, 2022.

[18] H. Adzumi, "Studies on the flow of gaseous mixtures through capillaries. I the viscosity of binary gaseous mixtures," *Bulletin of the Chemical Society of Japan*, vol. 12, no. 5, pp. 199–226, 1937.

[19] H. Adzumi, "Studies on the flow of gaseous mixtures through capillaries. II. The molecular flow of gaseous mixtures," *Bulletin of the Chemical Society of Japan*, vol. 12, no. 6, pp. 285–291, 1937.

[20] H. Adzumi, "Studies on the flow of gaseous mixtures through capillaries. III. The flow of gaseous mixtures at medium pressures," *Bulletin of the Chemical Society of Japan*, vol. 12, no. 6, pp. 292–303, 1937.

[21] Q. Liu, P. Shen, and P. Yang, *Pore scale network modelling of gas slippage in tight porous media*, Fluid Flow & Transport in Porous Media Mathematical & Numerical Treatment, 2002.

[22] K. G. R. Ertekin and F. C. Schwerer, "Dynamic gas slippage: a unique dual-mechanism approach to the flow of gas in tight formations," *SPE Formation Evaluation*, vol. 1, no. 1, pp. 43–52, 1986.

[23] P. N. Azom and F. Javadpour, "Dual-continuum modeling of shale and Tight Gas Reservoirs," in SPE Annual Technical Conference and Exhibition, San Antonio, Texas, USA, 2012.

[24] H. Singh, F. Javadpour, A. Ettehadtavakkol, and H. Darabi, "Nonempirical apparent permeability of shale," *SPE Reservoir Evaluation & Engineering*, vol. 17, no. 3, pp. 414–424, 2014.

[25] R. F. Aguilera, J. F. Ramirez, and C. E. Ortega, *A Variable Shape Distribution (VSD) Model for Characterization of Pore Throat Apertures and Drill Cuttings in Tight and Shale Reservoirs*, 2012.

[26] A. Beskok and G. E. Karniadakis, "Report: a model for flows in channels, pipes, and DUCTS at micro and NANO scales," *Nanoscale and Microscale Thermophysical Engineering*, vol. 3, no. 1, pp. 43–77, 1999.

[27] W. Keliu and L. Xiangfang, "Real gas transport through nanopores of shale gas reservoirs," *China Science: Science and technology*, vol. 46, no. 1, pp. 68–78, 2016.

[28] M. R. R. Shahri, R. Aguilera, and A. Kantzas, "A new unified diffusion-viscous flow model based on pore level studies of tight gas formations," *SPE Journal*, vol. 18, no. 1, pp. 38–49, 2012.

[29] J. Liming, Q. Junli, and X. Yanqing, "SEM micropore characteristics and methane adsorption of common clay minerals," *Journal of Petroleum*, vol. 33, no. 2, pp. 249–256, 2012.

[30] R. Aringhieri, "Nanoporosity characteristics of some natural clay minerals and soils," *Clays and Clay Minerals*, vol. 52, no. 6, pp. 700–704, 2004.

[31] D. J. K. Ross and R. M. Bustin, "The importance of shale composition and pore structure upon gas storage potential of shale gas reservoirs," *Marine and Petroleum Geology*, vol. 26, no. 6, pp. 916–927, 2009.

[32] S. Takata and H. Funagane, "Poiseuille and thermal transpiration flows of a highly rarefied gas: over-concentration in the velocity distribution function," *Journal of Fluid Mechanics*, vol. 669, no. 1, pp. 242–259, 2011.

[33] M. Knudsen, "Die Gesetze der Molekularströmung und der inneren Reibungsströmung der Gase durch Röhren," *Annalen der Physik*, vol. 333, no. 1, pp. 75–130, 1909.

[34] S. A. Schaaf and P. L. Chambré, *Flow of Rarefied Gases*, Princeton University Press, 1961.

[35] J.-G. Choi, D. D. Do, and H. D. Do, "Surface diffusion of adsorbed molecules in porous media: monolayer, multilayer, and capillary condensation regimes," *Industrial & Engineering Chemistry Research*, vol. 40, no. 19, pp. 4005–4031, 2001.

[36] E. H. Kennard, *Kinetic theory of gases*McGraw-Hill, New York, 1st ed edition.

[37] W. A. Ebert and E. M. Sparrow, "Slip flow in rectangular and annular Ducts," *Journal of Fluids Engineering*, vol. 87, no. 4, pp. 1018–1024, 1965.

[38] H. Deng, G. Sheng, H. Zhao et al., "Integrated optimization of fracture parameters for subdivision cutting fractured horizontal wells in shale oil reservoirs," *Journal of Petroleum Science and Engineering*, vol. 212, p. 110205, 2022.

[39] A. K. Sreekanth, "Slip flow through long circular tubes," in *Proceedings of the 6th international symposium on rarefied gas dynamic*, pp. 667–680, 1969.

[40] G. Sheng, Y. Su, and W. Wang, "A new fractal approach for describing induced-fracture porosity/permeability/ compressibility in stimulated unconventional reservoirs," *Journal of Petroleum Science and Engineering*, vol. 179, pp. 855–866, 2019.

[41] S. Chapman and T. G. Cowling, *The Mathematical Theory of Non-uniform Gases*, Cambrige University Press, Cambrige, 1952.

[42] G. E. Karniadakis and A. Bekok, *Microflows: Fundamentals and Simulation*, Springer, Berlin Heidelberg New York, 2002.

[43] Z. Sun, B. Huang, K. Wu et al., "Nanoconfined methane density over pressure and temperature: wettability effect," *Journal of Natural Gas Science and Engineering*, vol. 99, article 104426, 2022.

[44] Y. Mitsuya, "Modified Reynolds equation for ultra-thin film gas lubrication using 1.5Order slip-flow model and considering surface accommodation coefficient," *Transactions of the Japan Society of Mechanical Engineers C*, vol. 115, no. 2, pp. 289–294, 1993.

[45] J. Maurer, P. Tabeling, P. Joseph, and H. Willaime, "Second-order slip laws in microchannels for helium and nitrogen," *Physics of Fluids*, vol. 15, no. 9, pp. 2613–2621, 2003.

[46] Z. Sun, B. Huang, Y. Liu et al., "Gas-phase production equation for CBM reservoirs: interaction between hydraulic fracturing and coal orthotropic feature," *Journal of Petroleum Science and Engineering*, vol. 213, article 110428, 2022.

[47] Z. Sun, S. Wang, H. Xiong, K. Wu, and J. Shi, "Optimal nanocone geometry for water flow," *AICHE Journal*, vol. 68, no. 3, article e17543, 2022.

[48] S. S. Antman, J. E. Marsden, and L. Sirovich, *Microflows and Nanoflows*, Springer, 2005.

Hindawi
Geofluids
Volume 2022, Article ID 9944867, 10 pages
https://doi.org/10.1155/2022/9944867

Research Article

Nanoconfined Bulk-Gas Transport Behavior over a Wide Range of Knudsen Number

Yi Zhang

College of Biology and Agriculture (College of Food Science and Technology), Zunyi Normal University, 563006, China

Correspondence should be addressed to Yi Zhang; sciyiyi@126.com

Received 9 March 2022; Revised 30 March 2022; Accepted 6 April 2022; Published 27 April 2022

Academic Editor: Zheng Sun

Shale matrix, located at Guizhou Province, is rich in nanopores, and gas slippage takes place during shale gas development, resulting in inapplicability of the classical Navier-Stokes equation. Investigation of gas transmission mechanism in nanoscale is helpful to reach a clear understanding of shale gas production performance. On the basis of the Knudsen number, the gas flow mechanism is divided into continuous flow, slippage flow, transition flow, and Knudsen diffusion. Notably, the accurate characterization of transition flow is still challenging up to date. Although there are many established models, they either fail to cover all the flow mechanisms or contain many fitting parameters, the determination of which requires a large number of experimental and molecular simulation data, limiting application of the existing models. Therefore, establishment of bulk-gas transport model over a wide range of Knudsen number without fitting parameters is urgent. First of all, existed theoretical models are compared, and the advantages and disadvantages of previous contributions are analyzed. Weight factors of Knudsen diffusion and slippage flow are obtained, respectively, according to Knudsen's model and Wu's model. Then, a model, free of empirical coefficients, is proposed. After that, effects of pore size, reservoir pressure, and temperature on transmission capacity are investigated. As the proposed model does not contain fitting parameters and remains high accuracy over a wide range of Knudsen number, it shares broad application potential, like shale gas production prediction, reserve estimation in Guizhou Province.

1. Introduction

With decline of global reserves of conventional oil and gas resources, as one of the potential alternative energy resources, shale gas development is the frontier and hotspot [1, 2]. In Guizhou Province, shale gas development will be great help to reduce coal emission and enhance local economic level. However, the corresponding development technology, equipment, and theory are still weak, especially the understanding of pore diffusion mechanism in shale matrix, which makes it difficult to predict shale gas production performance [3]. In view of great difference of gas transport mechanism at different pore scales, it is necessary to elaborate the pore size range in shale gas reservoirs. Fu et al. believe that the pore size in coal matrix is less than 100 nm [4]. Meanwhile, Özgen Karacan [5] and Siriwardane et al. [6] indicated that pore diameter of coal matrix is less than 10 nm. The shale porosity is fairly small, and the permeability falls into the nano-Darcy level. Howard [7] reported that the pore radius in shale ranges from 5 to 15 nm. Katsube [8] found that pore radius of shale, with buried depth of 4400~4500 m, is mainly between 2.7 and 11.5 nm. Reed et al. [9] and Wang and Reed [10] believed that pore radius of shale matrix is between 5 and 1000 nm, and Nelson [11] measured that the minimum pore radius of shale is about 5 nm. As a result, the abundant existence of nanopores in shale is demonstrated.

At nanoscale, fluid slippage takes place, resulting in the inapplicability of classical Navier-Stokes equation [12]. According to the range of Knudsen number, gas flow mechanism is generally divided into continuous flow, slippage flow, transition flow, and Knudsen diffusion. In detail, intermolecular collision dominates continuous flow, while molecule-wall collision dominates the Knudsen diffusion. Because both flow mechanisms are relatively simple, mature theories have been formed at home and abroad [13–15].

With the decrease of pressure or the shrinkage of flow channel, the collision frequency between gas molecules and wall increases gradually, and the gas flow mechanism changes from the continuous flow to slippage flow [15]. Aiming at the characterization method of gas nanopore slippage flow mechanism, Maxwell [16] proposed the first-order boundary condition to modify the Navier-Stokes equation. When $Kn < 0.1$, the proposed equation fits well with the experimental results. Utilizing the first-order boundary condition, Kennard [17], Ebert and Sparrow [18], and Spiga [19] analyzed the characteristics of gas slippage flow in nanopores with different pore geometry. When $Kn > 0.1$, there is a great difference between the experimental observations and the first-order condition, indicating that the first-order boundary conditions are not enough to describe the gas slippage effect [20, 21]. Many scholars successively put forward second-order boundary conditions, hoping that the modified equation can be applied to higher Kn. However, considering the second-order boundary conditions will make the form of the modified equation complex. Finally, the analytical solution can accurately characterize its flow characteristics, and its application range perfectly covers the whole slippage flow [22–27]. The accurate description of transition flow is not only a difficulty at home and abroad but also a key problem to be solved in establishing a bulk-gas transport model covering entire Kn range. Molecular simulation is generally used to study the mechanism of transition flow [28–31]. However, despite the rapid development of computer technology, molecular simulation is still limited by time-consuming calculation, and it cannot be applied to the field.

Adzumi studied the flow characteristics of gas in capillary through a large number of experiments and proposed that the determination of fluid flow mechanism depends on Knudsen number. With the use of weight factor, Adzumi coupled viscous flow and Knudsen diffusion to characterize gas flow behavior in the entire Kn range for the first time. Unfortunately, Adzumi failed to elaborate the expression of the weight factor [32–34]. Liu [35] gave the specific expression of the weight factor on this basis, but the established bulk phase transmission model is only limited to the case when the Kn is less than 1. Liu et al. [36] utilized the weight factor to couple Knudsen diffusion and Fick diffusion, but the weight factor proposed by Liu et al. will not change with Kn. Javadpour [37–39] combined slippage flow and Knudsen diffusion linearly, but it contains an empirical coefficient. Based on the basic theory proposed by Adzumi, Aguilera et al. [40] gave the corresponding weight coefficient expression, but it contains three empirical coefficients. Beskok [32] corrected the slippage flow by introducing the gas rarefaction coefficient and extended the formula to the full Kn range, but it contains three empirical coefficients. The model proposed by Wu [15] weight superposition between slippage flow and Knudsen diffusion, however includes three empirical coefficients. Based on continuous flow and Knudsen diffusion, Rahmanian [41] proposed a bulk-gas transport model, which is suitable for nanopores with different cross-sections, and it includes three empirical coefficients. Notably, the determination of the weight coefficients requires a large number of accurate molecular simulation and experimental data, which seriously limits the application of the existing models in the development of shale gas in Guizhou Province. As a result, it is urgent to establish a universal bulk-gas transport model, which is free of empirical parameters.

2. Bulk-Gas Transport Mechanism

Knudsen number is defined as the ratio of the average free path of gas molecules to the scale of flowing medium, characterizing gas rarefaction [42]. Then, based on the Kn, Schaaf and Chambré divide the bulk transport mechanism of nanoporous gas into four basic types, namely, continuous flow, slippage flow, transition flow, and Knudsen diffusion [43]. Among them, it is still challenging to accurately describe the characteristics of transition flow.

$$Kn = \frac{\lambda}{d}, \tag{1}$$

where λ is the average free path of gas molecules, m, and d is the pore diameter of porous medium, m.

When $Kn < 0.001$, the gas transport mechanism is continuous flow, and the intermolecular collision dominates the transport process. At this point, the flow characteristics can be characterized by the nonslip Navier-Stokes equation. According to the Hagen-Poiseuille equation [15],

$$J_c = -\frac{r^2 p}{8\mu_g RT}\frac{dp}{dl}, \tag{2}$$

where J_c represents the flow capacity of continuum flow mechanism, mol/(m^2·s); r is the pore radius, m; p is the fluid flow pressure, Pa; μ_g is the gas viscosity, Pa·s; R is universal gas constant, J/(mol·K); T is the temperature, K; and l is the distance in the gas flow direction, m.

When the Kn is between 0.001 and 0.1, the gas nanopore transmission mechanism is slippage flow, the collision frequency between gas molecules and wall increases gradually, and the nonslippage condition of continuous flow breaks down. After decades of research at home and abroad, it is found that satisfactory results can be obtained by modifying the slip boundary conditions [44, 45].

$$J_s = -\frac{r^2 p}{8\mu_g RT}\left(1 + \frac{4Kn}{1 - bKn}\right)\frac{dp}{dl}, \tag{3}$$

where J_s is the transport capacity of gas slippage flow, mol/(m^2·s), and b is the gas slippage constant. When b is 0, it represents the first-order slippage condition, and when the value is -1, it represents the second-order slippage condition. Moreover, according to a large number of molecular simulation and experimental data, the fitting effect of the second-

order slippage condition is obviously better than that of the first-order, so the expression of nanopore phase transport of gas slippage flow can be simplified.

$$J_s = -\frac{r^2 p}{8\mu_g RT}\left(1 + \frac{4Kn}{1+Kn}\right)\frac{dp}{dl}. \tag{4}$$

When the Knudsen number is greater than 10, the transmission mechanism of gas nanopores is Knudsen diffusion, the collision frequency between gas molecules continues to decline, and the collision frequency between molecules and wall dominates the transmission process, which can be expressed by Knudsen equation [37, 39].

$$J_k = -\frac{d}{3}\sqrt{\frac{8}{\pi RTM}}\frac{dp}{dl}. \tag{5}$$

In view of the dominant collision between gas molecules and wall in this transmission mechanism, the influence of wall roughness on gas diffusion must be considered. The coarser the wall, the weaker the gas diffusion ability. The relationship can be characterized by the following formula [15, 43].

$$J_k = -\frac{d}{3}\delta^{D_f-2}\sqrt{\frac{8}{\pi RTM}}\frac{dp}{dl}, \tag{6}$$

where δ is the ratio of molecular diameter to local pore diameter, dimensionless, and D_f is the fractal dimension of pore wall, dimensionless. When the fractal dimension is 2, it represents a smooth wall and has no effect on the gas transmission capacity. When the fractal dimension is 3, it represents a rough wall.

3. Evaluation of Existing Gas Bulk Transport Models

3.1. Previous Contributions. Knudsen had proposed the bulk-gas transport model in the field of vacuum science, and it was widely used to describe the characteristics of transition flow and molecular free diffusion. However, using this model will overestimate the transport capacity of slippage flow, and Knudsen model contains two fitting parameters. In order to facilitate the comparison between the models in the following, the existing models are dimensionless [42]. The accuracy of the model at high Knudsen number is analyzed by the ratio of all Knudsen bulk phase model to Knudsen diffusion (J_a/J_k), and the accuracy of the model at low Knudsen number is analyzed by the ratio of all Knudsen bulk phase model to continuous flow (J_a/J_c). For Knudsen model,

$$\frac{J_{ak}}{J_k} = \frac{3\pi}{64Kn} + \frac{1 + 2.507(1/Kn)}{1 + 3.095(1/Kn)}, \tag{7}$$

$$\frac{J_{ak}}{J_c} = 1 + \frac{64Kn}{3\pi}\left(\frac{2.507}{3.095}\right). \tag{8}$$

In the above formula, J_{ak} characterize the gas transmission capacity proposed by Knudsen under the whole Kn range, mol/(m^2·s).

Adzumi studied the flow characteristics of mixed gas in capillary through a large number of experiments and proposed the use of weight factor to couple viscous flow and Knudsen diffusion to characterize full Knudsen flow for the first time [33–35]. It is proposed that the weight factor slowly increases from 0.7 to 1 with the decrease of pressure. When the pressure decreases to a very low level, the value is 1. At this time, molecular free diffusion is the main transmission form. Unfortunately, Adzumi did not give the specific expression of the weight factor.

$$J_{aa} = J_c + \varepsilon J_k. \tag{9}$$

In the above formula, J_{aa} characterize the gas transmission capacity proposed by Adzumi for the whole Knudsen number, mol/(m^2·s), and ε is the weight factor, dimensionless.

Beskok [32] modified the slippage flow by introducing the molecular rarefaction coefficient and extended the formula to the full Kn range. It can achieve good match with the molecular simulation data and experimental results, but it contains two empirical coefficients.

$$J_{ab} = -\frac{r^2 p}{8\mu RT}(1 + \alpha Kn)\left(1 + \frac{4Kn}{1 - bKn}\right)\frac{dp}{dl}, \tag{10}$$

$$\frac{J_{ab}}{J_k} = \frac{3\pi}{64Kn}(1 + \alpha Kn)\left(1 + \frac{4Kn}{1 - bKn}\right), \tag{11}$$

$$\frac{J_{ab}}{J_c} = (1 + \alpha Kn)\left(1 + \frac{4Kn}{1 - bKn}\right), \tag{12}$$

$$\alpha = \alpha_0 \frac{2}{\pi}\tan^{-1}\left(\alpha_1 Kn^{\beta}\right). \tag{13}$$

In the above formula, J_{ab} characterize the gas transmission capacity proposed by Beskok for the total Knudsen number, mol/(m^2·s); α is the gas rarefaction coefficient and increases with the increase of Kn. In this paper, α is 4 and β is 0.4. Figure 1 shows the variation curve of the gas sparsity coefficient with Knudsen number when α takes 1.19 and 1.358, respectively. Gas rarefaction coefficient increases slowly with the increase of Kn. When the Kn rises to a very high level, the coefficient remains basically unchanged. Moreover, for Beskok model, different fitting parameters will have a great impact on the calculation results, and the fitting parameters often need to be determined through a large number of experimental and molecular simulation data, which limits the practicability of the model.

Liu et al. [36] applied the concept of Adzumi weight factor, namely, formula (10), to simulate the gas slippage effect in porous media. Liu et al. believed that the thickness of slippage layer in different nanopores was different and used the

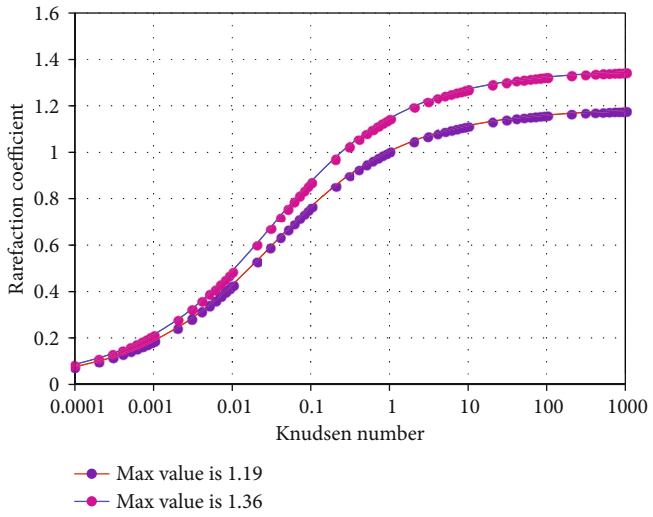

Figure 1: Gas rarefaction coefficient with different empirical factors.

weight factor to characterize the proportion of slippage layer in the flow channel.

$$\varepsilon = 4Kn - 4Kn^2, \tag{14}$$

$$\frac{J_{al}}{J_k} = \frac{3\pi}{128Kn} + 4Kn - 4Kn^2, \tag{15}$$

$$\frac{J_{al}}{J_c} = 1 + \left(4Kn - 4Kn^2\right)\frac{128Kn}{3\pi}. \tag{16}$$

In the above formula, J_{al} characterize the gas transmission capacity proposed by Liu et al. for the whole Knudsen number, mol/(m^2·s).

Javadpour [37] corrected the influence of slippage phenomenon on continuous flow transmission capacity through dimensionless coefficient proposed by Brown [46, 47] according to slippage flow and Knudsen diffusion and added them linearly to describe the transmission characteristics of gas in shale nanopores. Subsequently, Azom [38] and Darabi [48], respectively, considered the influence of real gas effect and wall roughness on the basis of the Javadpour's model. Since both Azom's and Darabi's model are based on Javadpour's model, only Javadpour's model and molecular simulation data need to be compared here.

$$\begin{aligned} J_{aj} &= FJ_c + J_k, \\ F &= 1 + \left(\frac{8\pi RT}{M}\right)^{0.5}\frac{\mu}{\mathrm{Pr}}\left(\frac{2}{\omega} - 1\right), \\ \frac{J_{aj}}{J_k} &= \left[1 + 8Kn\left(\frac{2}{\omega} - 1\right)\right]\frac{3\pi}{128Kn} + 1, \\ \frac{J_{aj}}{J_c} &= 1 + 8Kn\left(\frac{2}{\omega} - 1\right) + \frac{128Kn}{3\pi}. \end{aligned} \tag{17}$$

In the above formula, J_{aj} characterize the gas transmission capacity proposed by Javadpour, mol/(m^2·s); F is the tangential increment coefficient of gas molecular momentum, which represents the ratio of molecular viscous collision to mirror collision. This value varies from 0 to 1. Meanwhile, its determination depends on wall roughness, gas type, temperature, pressure, and many experimental results [49]. Dimensionless parameter F is always greater than 1, and when the bulk flow mechanism becomes continuous flow and slippage flow, the parameter maintains small. While flow mechanism becomes transition flow and Knudsen diffusion, the parameter increases with the increasing Kn.

Based on Adzumi's weight factor idea, Rahmanian [41] proposed the corresponding weight factor, coupled continuous flow and molecular diffusion, and established a bulk-gas transport model covering entire Kn range, but the model contains three fitting parameters.

$$\begin{aligned} J_{ar} &= (1 - \varepsilon)J_c + \varepsilon J_k, \\ \varepsilon &= C_A\left[1 - \exp\left(\frac{-Kn}{Knvisc}\right)\right]^S. \end{aligned} \tag{18}$$

In the above formula, J_{ar} characterizes the gas transmission capacity proposed by Rahmanian for the total Knudsen number, mol/(m^2·s). It is the critical Knudsen number, indicating that the slippage flow of the conveyor is transformed into molecular free diffusion, and both are fitting parameters. For nanoround holes, the corresponding fitting parameters C_A are K_{nvisc} 2.2, 0.3, and 5.

$$\begin{aligned} \frac{J_{ar}}{J_k} &= \left[1 - C_A\left(1 - \exp\left(\frac{-Kn}{Knvisc}\right)\right)^S\right]\frac{3\pi}{128Kn} \\ &\quad + C_A\left(1 - \exp\left(\frac{-Kn}{Knvisc}\right)\right)^S, \end{aligned}$$

$$\begin{aligned} \frac{J_{ar}}{J_c} &= 1 - C_A\left(1 - \exp\left(\frac{-Kn}{Knvisc}\right)\right)^S \\ &\quad + C_A\left(1 - \exp\left(\frac{-Kn}{Knvisc}\right)\right)^S\frac{128Kn}{3\pi}. \end{aligned} \tag{19}$$

Based on slippage flow and Knudsen diffusion, Wu [15] proposed a model to weight superposition the above two mechanisms, in which ratio of intermolecular collision frequency and collision frequency between molecule and pore wall are set as the weight factor for slip flow mechanism and Knudsen diffusion, respectively. Formula for slip flow, proposed by Beskok, is utilized by Wu; therefore, the model proposed by Wu also contains three fitting parameters.

$$\varepsilon = \frac{Kn}{1 + Kn}, \tag{20}$$

$$\frac{J_{aw}}{J_k} = \frac{3\pi}{128\delta^{D_f-2}Kn}\left(1+\frac{4Kn}{1-bKn}\right)\frac{(1+\alpha Kn)}{1+Kn}+\frac{Kn}{1+Kn}, \tag{21}$$

$$\frac{J_{aw}}{J_c} = \left(1+\frac{4Kn}{1-bKn}\right)\frac{(1+\alpha Kn)}{1+Kn}+\frac{\delta^{D_f-2}Kn^2}{1+Kn}\frac{128}{3\pi}. \tag{22}$$

In the above formula, J_{aw} characterizes the gas transmission capacity proposed by Wu for the whole Knudsen number, mol/(m^2·s); α is the gas rarefaction coefficient.

3.2. Evaluation. In order to analyze the accuracy of each model, the calculated values of each model are compared with the results of molecular simulation [50]. The accuracy of the model at high Knudsen number is analyzed by the ratio of total Knudsen bulk phase model to Knudsen diffusion (J_a/J_k), and the accuracy of the model at low Knudsen number is analyzed by the ratio of total Knudsen bulk phase model to continuous flow (J_a/J_c). For the bulk-gas transmission of nanotubes under the full Kn range, the values of fitting parameters in the above model are shown in Table 1.

According to Figure 2, when Knudsen number is between 0.001 and 0.01, the ratio of existing bulk-gas transport model to continuous flow is close to 1, indicating that the bulk-gas transport capacity can be characterized by continuous flow equation when Knudsen number is low. As the Knudsen number continues to increase, the value continues to rise, showing the characteristics that slippage contributes to the transmission capacity. Among them, Javadpour's model rises the fastest and has the largest gap with the molecular simulation results, overestimating the bulk phase transmission capacity. Liu's model is consistent with the molecular simulation results when the Knudsen number is less than 0.1. When the Knudsen number is greater than 0.1, the calculated value of the model is higher than the molecular simulation results, indicating that Liu's model can characterize the characteristics of continuous flow and slippage flow but overestimate the transmission capacity of transition flow. The predicted value of Rahmanian's model underestimates the bulk-gas transmission capacity when the Knudsen number is less than 0.6 and overestimates the gas bulk phase transmission capacity when the Knudsen number is greater than 0.6. The trend of Knudsen's, Beskok's, and Wu's models is consistent with the molecular simulation results fairly well. Among them, Knudsen model slightly overestimates the bulk-gas transmission capacity. In Wu's model, when the Knudsen number is less than 0.3, the calculated value is slightly lower than the molecular simulation result, and when the Knudsen number is greater than 0.3, the calculated value is slightly higher than the molecular simulation result. Beskok's model performs best at low Knudsen number, and the error between Beskok's model and molecular simulation results is always the smallest.

According to Figure 3, due to the unreasonable expression of the weight factor of Liu's model, when Knudsen number is greater than 1, the weight factor is negative, so its predicted value cannot represent gas transmission capacity under high Knudsen number. Javadpour's and Raminian's model overestimates the bulk-gas transmission capacity by 2.2 times and 1.9 times at high Knudsen number. Knudsen's, Beskok's, and Wu's models fit well with the molecular simulation results. When Knudsen number is less than 10, the calculated value of Knudsen's model is slightly higher than the molecular simulation results, and the calculated value of Wu's model is lower than the molecular simulation results with a large error. When Knudsen number is greater than 10, the calculated results of the two models almost coincide and are slightly higher than the molecular simulation results. Beskok's model still performs best under high Knudsen number. When Kn is less than 1, the calculated value is slightly lower than that of molecular simulation. Comprehensive analysis of the comparison results between existing models and molecular simulation shows that Beskok's model shares the highest accuracy. However, the model contains three fitting parameters, which further highlights the necessity of establishing bulk-gas transmission model without fitting parameters. Comparing the establishment methods of the Beskok's model and Wu's model, it can be demonstrated that Beskok extends the slippage flow equation to the total Knudsen number by introducing gas sparsity effect, while Wu's model used the weight factor to

Table 1: The fitting parameters used in the calculation.

Fitting parameters	Numerical value	Fitting parameters	Numerical value
$\alpha_{0(Beskok)}$	1.358	C_A	2.2
α	4	K_{nvisc}	0.3
β	0.4	S	5
ω	0.8	$\alpha_{0(Wu)}$	1.19
δ	0.5	D_f	2.6

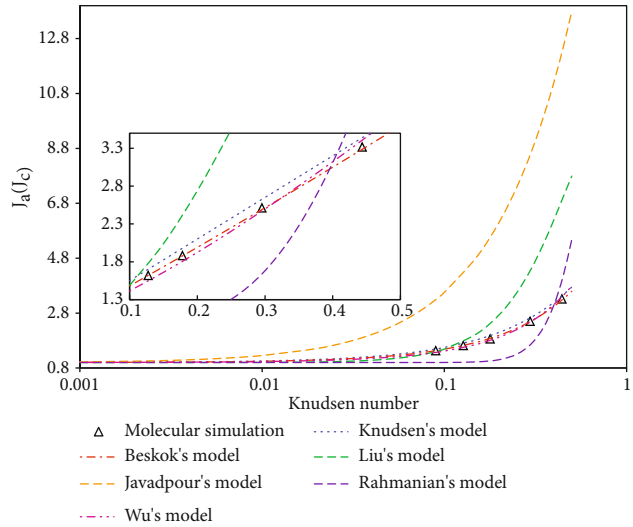

Figure 2: Comparison of existing models and molecular simulation results under low Kn.

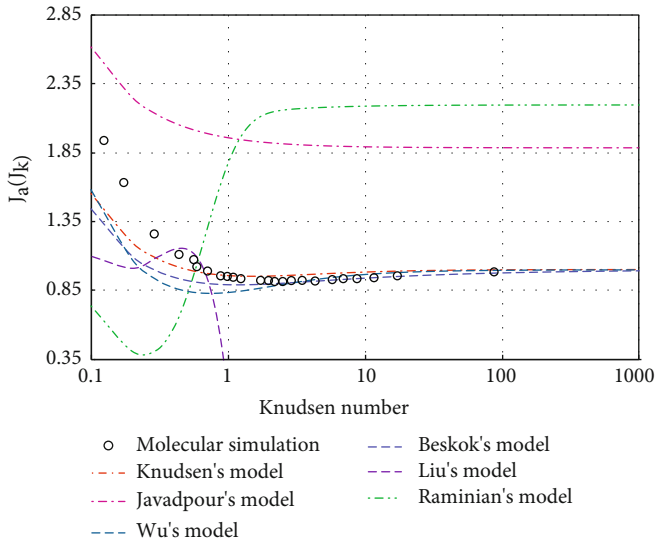

Figure 3: Comparison of existing models and molecular simulation results under high Kn.

couple the slippage flow and molecular diffusion. For Wu's model, the adopted slippage flow mechanism includes fitting parameters, eventually leading to establishment of the model relying on the fitting parameters. However, this kind of method is suitable for establishing the bulk-gas transmission model without fitting parameters.

4. Establishment of Bulk-Gas Transport Model

Through the comparison of the above models, it can be seen that there are four kinds of bulk-gas transmission models using the concept of weight factor. Among them, the weight factor of Liu's model is negative when the Knudsen number is greater than 1, which is obviously unreasonable. Javadpour's model and Raminian's model used weight factors to couple continuous flow and Knudsen diffusion. Because the gas slippage effect is not covered by their flow mechanism, these two models need to use weight factors with fitting parameters. Moreover, through the comparison, the errors of the two models are large, indicating that their weight factors are unreasonable. Wu's model couples slippage flow and Knudsen diffusion, and slippage flow contains the fitting parameters of Beskok's model. When Knudsen number is between 0.1 and 10, that is, transition flow, there is a large error between the calculated value of the model and molecular simulation, but its weight factor does not contain fitting parameters, and the model can accurately describe the characteristics of slippage flow. Therefore, formula (22) can be used to determine the weight factor of slippage flow in the proposed model in this article.

Knudsen's model is widely used in vacuum science and can accurately describe transition flow and molecular diffusion, which can also be obtained from the comparison in the previous section. Therefore, formula (8) can be used to determine the weight factor of Knudsen diffusion in the new model. Based on Wu's model and Knudsen's model, the weight factors of slippage flow and Knudsen diffusion

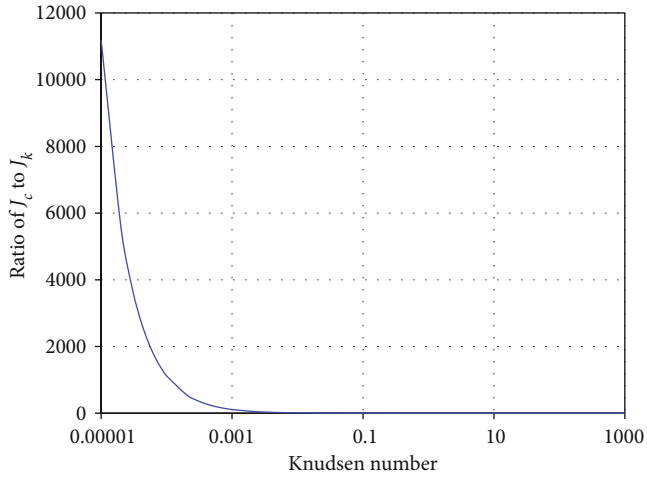

Figure 4: Ratio of continuous flow and Knudsen diffusion with different Kn.

are determined by referring to their expressions, respectively. Smooth nanopore surface is assumed; thus, the wall fractal dimension is 2.

$$J_{as} = \frac{1}{1+5Kn} J_s + \frac{Kn+2.507}{Kn+3.095} J_k, \tag{23}$$

$$\frac{J_{as}}{J_k} = \frac{3\pi}{128\delta^{D_f-2}Kn}\left(1+\frac{4Kn}{1+Kn}\right)\frac{1}{1+5Kn} + \frac{Kn+2.507}{Kn+3.095}, \tag{24}$$

$$\frac{J_{as}}{J_c} = \left(1+\frac{4Kn}{1+Kn}\right)\frac{1}{1+5Kn} + \frac{\delta^{D_f-2}(Kn+2.507)Kn}{Kn+3.095}\frac{128}{3\pi}. \tag{25}$$

In the above formula, J_{as} characterizes the gas transmission capacity proposed in this paper for the full Knudsen number, mol/(m^2·s).

$$\frac{J_c}{J_k} = \frac{3\pi}{128\delta^{D_f-2}Kn}. \tag{26}$$

The bulk-gas transport model without fitting parameters, proposed in this paper, can accurately describe the characteristics of each flow mechanism under entire Kn range. When the Knudsen number is very small, it can be seen from formula (3) that J_S will degenerate to J_C. It can be seen from Figure 4 that J_C is much greater than J_K; then, formula (24) will degenerate into a continuous flow equation at low Knudsen number. When Knudsen number is maximum, according to formula (24), J_{as} directly degenerates into Knudsen diffusion equation. When the flow mechanism is slippage flow and transition flow, it can be verified by comparing the calculated values of the model with the molecular simulation results and (J_a/J_C) and (J_a/J_K), respectively. The specific comparison results are shown in Figure 5. The analysis shows that the model can reach an excellent match with molecular simulation results, which shows that the proposed model can still be perfectly applicable in the slippage flow and transition flow. To sum up, the established nonfitting parameter bulk-gas transport model can accurately describe all flow mechanisms under the full Knudsen number, and its reliability has been verified. Because the model does not contain fitting parameters, it can be directly used to evaluate the gas transmission capacity under different reservoir conditions, demonstrating its simplicity and practicability.

5. Bulk-Gas Phase Transport Capacity during Shale Gas Development

In the development of oil and gas resources, the most important evaluation parameter of reservoir quality is permeability, which represents the gas transmission capacity. In conventional reservoirs, due to the absence of a large number of nanopores and high formation pressure, the general flow mechanism is continuous flow. In this case, the bulk phase transmission capacity is close to a constant. However, for unconventional reservoirs with massive nanopores, the gas transmission mechanism is generally slippage flow and transition flow, and its bulk phase transmission capacity depends on the formation pressure, temperature, and the corresponding pore scale, in which the temperature has little effect on the transmission capacity. In view of the continuous decrease of reservoir pressure in the development process, it is necessary to focus on the analysis of bulk-gas transmission capacity of different pore scales under different reservoir pressure conditions. In the following analysis, the gas is pure methane, and the reservoir temperature is set to 313 k.

It can be seen from Figure 6 that in the process of gas reservoir exploitation, the bulk-gas transmission capacity of different nanopores keeps an upward trend with the decrease of reservoir pressure, and the rising range is closely related to

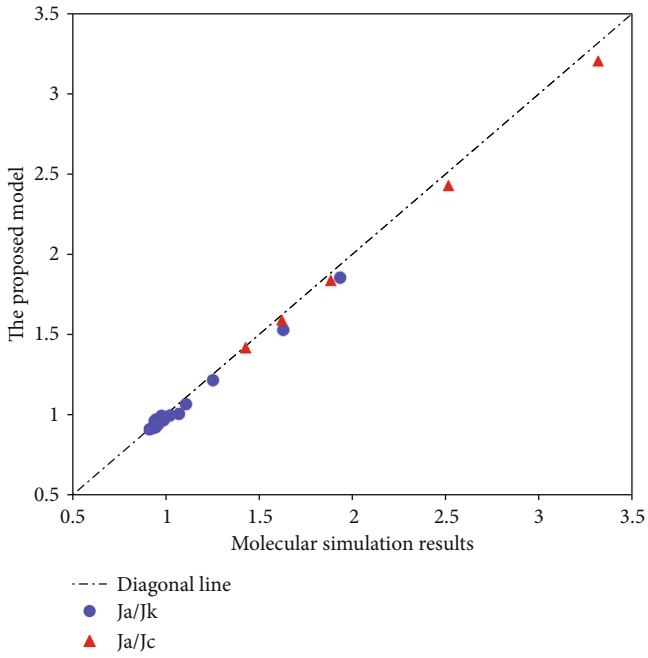

Figure 5: The comparison between proposed model and molecular simulation results.

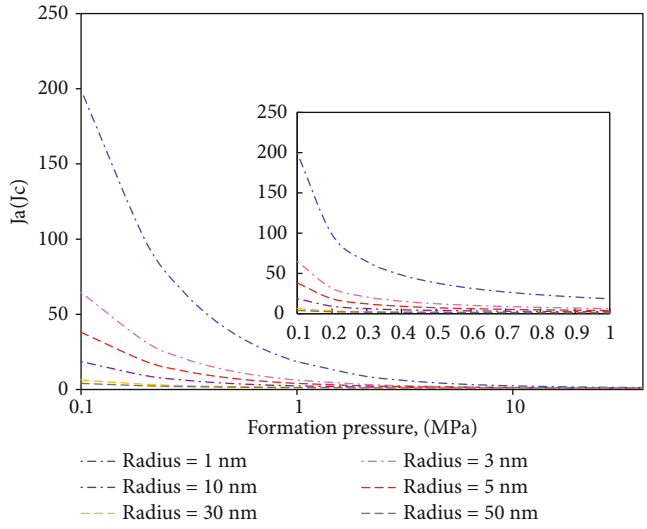

Figure 6: Gas transport capacity in different nanopores during the production process.

the pore scale. The smaller the pore radius is, the faster the bulk-gas transmission capacity is improved. When the local formation pressure is greater than 10 MPa, the bulk-gas transmission capacity can be characterized by continuous flow equation. When the pressure is between 1 and 10 MPa, the transmission capacity of nanopores with different scales increases slowly with the decrease of pressure. When the pressure is less than 1 MPa, the transmission capacity increases rapidly. For 1 nm pores, the transmission capacity is about 200 times that of continuous flow, and for 3 nm and 5 nm pores, it is about 60 times and 40 times. Once

the pore size exceeds 30 nm, its bulk phase transmission capacity is not sensitive to the change of reservoir pressure, and lifting range is no more than 6 times compared with continuous flow.

In view of the small variation range of pore transmission capacity greater than 30 nm with pressure, the transmission characteristics of pores above 30 nm will not be analyzed next. For the same pores, the contribution of slippage flow and Knudsen diffusion mechanism to the overall transmission capacity is different with the decrease of pressure. In this paper, the contribution factors of Knudsen diffusion and continuous flow to the overall transmission capacity of nanopores are defined as follows.

$$F_{ks} = \frac{1}{(1/1 + 5Kn)(Kn + 3.095/Kn + 2.507)(J_s/J_k) + 1},$$
$$F_{ss} = \frac{1}{1 + (1 + 5Kn)(Kn + 2.507/Kn + 3.095)J_k/J_s}. \quad (27)$$

The relationship between them and reservoir pressure is shown in Figure 7. When the reservoir pressure is between 10 and 40 MPa, the bulk-gas transmission greater than 3 nm is mainly contributed by slippage flow, but with the decrease of pressure, the contribution of slippage flow gradually decreases and the contribution of Knudsen diffusion gradually increases. When the reservoir pressure is less than 10 MPa, the contribution of slippage flow to pores larger than 3 nm decreases rapidly, and the contribution of Knudsen diffusion increases rapidly. When the pressure is 0.1 MPa, the bulk-gas transmission characteristics of such pores can be completely characterized by Knudsen diffusion. For pores with a radius of 1 nm, the contribution of each transport mechanism to the overall bulk phase transport capacity varies approximately linearly with the pressure, and when the reservoir pressure is 40 MPa, the contribution of Knudsen diffusion (0.31) is significantly higher than that of pores with a radius of 3 nm and above (0.12 and 0.08), indicating that the nanoscale bulk phase transport capacity and transport type are highly sensitive to the pore radius.

The transport characteristics of nanopores at full Knudsen number can be analyzed by the ratio of the established nonfitting parameter full Knudsen number bulk phase transport model to continuous flow and Knudsen diffusion. As shown in Figure 8, when the Knudsen number is extremely small, the value of (J_{as}/J_c) approaches 1, indicating that the continuous flow can be used to describe the flow characteristics of this stage. When Knudsen number is extremely large, value of (J_{as}/J_k) approaches 1. At this time, Knudsen diffusion can characterize the transmission characteristics. These are consistent with the existing understanding, which verifies the reliability of this model to a certain extent. According to the mechanism of slippage flow and transition flow, which are generally concerned, it can be seen from Figure 8 that the model in this paper also has high accuracy, so it can be used to analyze the flow characteristics in these two states. According to the analysis of Figure 8, (J_{as}/J_c) increases linearly with the increase of Knudsen number.

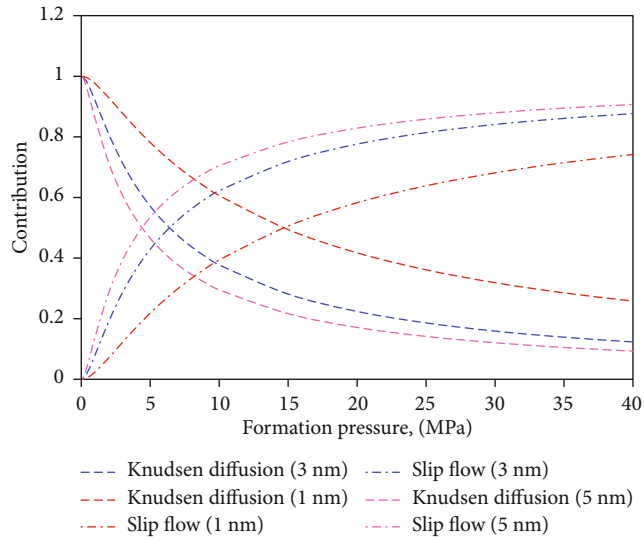

Figure 7: Contribution of different transport mechanisms during the production process.

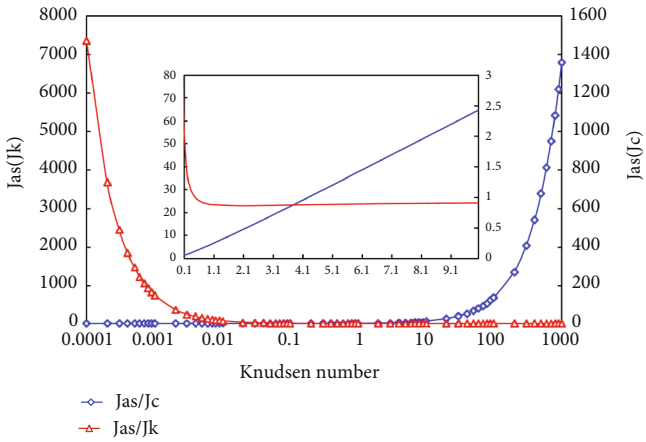

Figure 8: The bulk-gas transport capacity curve with different Knudsen number.

When the Knudsen number is less than 1, (J_{as}/J_k) decreases rapidly with the increase of Knudsen number. When the Knudsen number is greater than 1, the value no longer decreases and approaches 1. When the Knudsen number is greater than 10, the value is stable at 1. This shows that the change law of bulk phase transmission capacity changes in the transition flow stage, and the Knudsen number of 1 is the critical point of the change law.

6. Conclusions

(1) By comparing and analyzing previous models and molecular simulation data, it is found that Liu's model cannot characterize gas transmission capacity when Kn is greater than 1. Models, established by Javadpour and Raminian, overestimate the bulk-gas transmission capacity under high Kn. The Knudsen, Beskok, and Wu models can reach a favorable

match. When Kn is less than 10, the calculated results of Knudsen model are slightly higher than that of molecular simulation. Also, the calculated data of Wu's model underestimates the bulk-gas transmission capacity

(2) An analytical model of full Knudsen number gas bulk transport without fitting parameters is established for the first time. The model is suitable for accurately describing all flow mechanisms for the entire Kn range, and its reliability is verified by comparison with molecular simulation. Because the model does not contain fitting parameters, it can be directly used to evaluate the gas transmission capacity and field data processing under different reservoir conditions, which reflects its simplicity and strong practicability

(3) With the decrease of reservoir pressure, the transmission capacity of bulk-gas keeps an upward trend, and the rising range is closely related to the pore scale. The smaller the pore radius is, the faster the transmission capacity of bulk-gas is improved. In the process of gas reservoir exploitation, with the decrease of reservoir pressure, the contribution of slippage flow gradually decreases and the contribution of Knudsen diffusion gradually increases. By further analyzing the variation characteristics of bulk-gas transmission capacity in the transition flow, it is found that the Kn of 1 is the critical point of bulk-gas transmission capacity changing to Knudsen diffusion

Data Availability

Data are available on request.

Ethical Approval

On behalf of all the coauthors, the corresponding author states that there are no ethical statements contained in the manuscripts.

Conflicts of Interest

The authors declare that there is no conflict of interest regarding the publication of this paper.

Acknowledgments

The research acknowledges the financial support of Zunyi Normal University (BS-[2019]-20).

References

[1] C. Ruehl and J. Giljum, "BP energy outlook 2030," *Energy*, vol. 2030, no. 2, 2011.

[2] M. Yoshimune, T. Yamamoto, M. Nakaiwa, and K. Haraya, "Preparation of highly mesoporous carbon membranes via a sol–gel process using resorcinol and formaldehyde," *Carbon*, vol. 46, no. 7, pp. 1031–1036, 2008.

[3] Z. Sun, B. Huang, Y. Liu et al., "Gas-phase production equation for CBM reservoirs: interaction between hydraulic fracturing and coal orthotropic feature," *Journal of Petroleum Science and Engineering*, vol. 213, p. 110428, 2022.

[4] F. Xuehai, Q. Yong, and W. Chongtao, *Coalbed Methane Geology*, China University of mining and Technology Press, Xuzhou, 2003.

[5] C. Özgen Karacan, "Heterogeneous sorption and swelling in a confined and stressed coal during CO_2 injection," *Energy & Fuels An American Chemical Society Journal*, vol. 17, no. 6, pp. 1595–1608, 2003.

[6] H. Siriwardane, I. Haljasmaa, R. McLendon, G. Irdi, Y. Soong, and G. Bromhal, "Influence of carbon dioxide on coal permeability determined by pressure transient methods," *International Journal of Coal Geology*, vol. 77, no. 1–2, pp. 109–118, 2009.

[7] J. J. Howard, "Porosimetry measurement of shale fabric and its relationship to illite/smectite diagenesis," *Clays & Clay Minerals*, vol. 39, no. 4, pp. 355–361, 1991.

[8] T. J. Katsube, "Statistical analysis of pore-size distribution data of tight shales from the Scotian Shelf," *Current Research, Part E. Geological Survey of Canada, Paper*, vol. 92, 1992.

[9] R. M. Reed, R. G. Loucks, and D. M. Jarvie, "Nanopores in the Mississippian Barnett shale: distribution morphology, and possible genesis," *Gas Shales of North America*, vol. 39, 2007.

[10] F. P. Wang and R. M. Reed, "Pore networks and fluid flow in gas shales//Society of Petroleum Engineers," *SPE Paper*, no. - article 124253, 2009.

[11] P. H. Nelson, "Pore-throat sizes in sandstones, tight sandstones, and shales," *AAPG Bulletin*, vol. 93, no. 3, pp. 329–340, 2009.

[12] C. Cercignani and A. Daneri, "Flow of a rarefied gas between two parallel plates," *Journal of Applied Physics*, vol. 34, no. 12, pp. 3509–3513, 1963.

[13] Z. Sun, B. Huang, K. Wu et al., "Nanoconfined methane density over pressure and temperature: wettability effect," *Journal of Natural Gas Science and Engineering*, vol. 99, p. 104426, 2022.

[14] G. Sheng, Y. Su, and W. Wang, "A new fractal approach for describing induced-fracture porosity/permeability/compressibility in stimulated unconventional reservoirs," *Journal of Petroleum Science and Engineering*, vol. 179, pp. 855–866, 2019.

[15] W. Keliu, L. Xiangfang, and C. Zhangxin, "Real gas transport through nanopores of shale gas reservoirs," *China Science: Science and technology*, vol. 46, no. 1, pp. 68–78, 2016.

[16] J. C. Maxwell, "On stresses in rarefied gases arising from inequalities of temperature," *Proceedings of the Royal Society of London*, vol. 27, pp. 304–308, 1878.

[17] E. H. Kennard, *Kinetic Theory of Gases*, vol. 483, McGraw-hill, New York, 1938.

[18] W. A. Ebert and E. M. Sparrow, "Slip flow in rectangular and annular ducts," *Journal of Fluids Engineering*, vol. 87, no. 4, pp. 1018–1024, 1965.

[19] G. L. M. M. Spiga, "Slip flow in rectangular microtubes," *Nanoscale and Microscale Thermophysical Engineering*, vol. 2, no. 4, pp. 273–282, 1998.

[20] A. K. Sreekanth, "Slip flow through long circular tubes," *Rarefied gas dynamics*, vol. 1, pp. 667–680, 1969.

[21] E. S. Piekos and K. S. Breuer, "Numerical modeling of micromechanical devices using the direct simulation Monte Carlo

method," *Journal of Fluids Engineering*, vol. 118, no. 3, pp. 464–469, 1996.

[22] S. Chapman and T. G. Cowling, *The Mathematical Theory of Non-uniform Gases*, Cambrige University Press, Cambrige, 1952.

[23] G. E. Karniadakis and A. Bekok, *Microflows: Fundamentals and Simulation*, Springer, Berlin Heidelberg New York, 2002.

[24] R. G. Deissler, "An analysis of second-order slip flow and temperature-jump boundary conditions for rarefied gases," *International Journal of Heat & Mass Transfer*, vol. 7, no. 6, pp. 681–694, 1964.

[25] Y. Mitsuya, "Modified Reynolds equation for ultra-thin film gas lubrication using 1.5order slip-flow model and considering surface accommodation coefficient," *Transactions of the Japan Society of Mechanical Engineers C*, vol. 115, no. 2, pp. 289–294, 1993.

[26] J. Maurer, P. Tabeling, P. Joseph, and H. Willaime, "Second-order slip laws in microchannels for helium and nitrogen," *Physics of Fluids*, vol. 15, no. 9, pp. 2613–2621, 2003.

[27] S. Colin and P. L. R. Caen, "Validation of a second-order slip flow model in rectangular microchannels," *Heat Transfer Engineering*, vol. 25, no. 3, pp. 23–30, 2004.

[28] G. A. Bird, *Molecular Gas Dynamics and the Direct Simulation of Gas Flows*, Clarendon Press, Oxford, 1998.

[29] M. L. Hudson and T. J. Bartel, *DSMC Simulation of Thermal Transpiration and Accomodation Pumps (No. SAND-98-2015C; CONF-980765-)*, Sandia National Lab.(SNL-NM), Albuquerque, NM (United States), 1998.

[30] J. C. Harley, Y. Huang, H. H. Bau, and J. N. Zemel, "Gas flow in micro-channels," *Journal of Fluid Mechanics*, vol. 284, no. 284, pp. 257–274, 1995.

[31] S. Chen and G. D. Doolen, "Lattice Boltzmann method for fluid flows," *Fluid Mechanics*, vol. 30, no. 1, pp. 329–364, 1998.

[32] A. Beskok and G. E. Karniadakis, "Report: a model for flows in channels, pipes, and ducts at micro and nano scales," *Nanoscale and Microscale Thermophysical Engineering*, vol. 3, no. 1, pp. 43–77, 1999.

[33] H. Adzumi, "Studies on the flow of gaseous mixtures through capillaries. I The viscosity of binary gaseous mixtures," *Bulletin of the Chemical Society of Japan*, vol. 12, no. 5, pp. 199–226, 1937.

[34] H. Adzumi, "Studies on the flow of gaseous mixtures through capillaries. II. The molecular flow of gaseous mixtures," *Bulletin of the Chemical Society of Japan*, vol. 12, no. 6, pp. 285–291, 1937.

[35] H. Adzumi, "Studies on the flow of gaseous mixtures through capillaries. III. The flow of gaseous mixtures at medium pressures," *Bulletin of the Chemical Society of Japan*, vol. 12, no. 6, pp. 292–303, 1937.

[36] Q. Liu, P. Shen, and P. Yang, "Pore scale network modelling of gas slippage in tight porous media," *Fluid Flow and Transport in Porous Media: Mathematical and Numerical Treatment*, vol. 295, pp. 367–375, 2002.

[37] F. Javadpour, "Nanopores and apparent permeability of gas flow in mudrocks (shales and siltstone)," *Journal of Canadian Petroleum Technology*, vol. 48, no. 8, pp. 16–21, 2009.

[38] P. N. Azom and F. Javadpour, "Dual-continuum modeling of shale and tight gas reservoirs," in *SPE annual technical conference and exhibition*, San Antonio, Texas, USA, 2012.

[39] H. Singh, F. Javadpour, A. Ettehadtavakkol, and H. Darabi, "Nonempirical apparent permeability of shale," *SPE Reservoir Evaluation & Engineering*, vol. 17, no. 3, pp. 414–424, 2014.

[40] R. F. Aguilera, J. F. Ramirez, and C. E. Ortega, "A variable shape distribution (VSD) model for characterization of pore throat apertures and drill cuttings in tight and shale reservoirs," in *SPE Asia Pacific Oil and Gas Conference and Exhibition*, Perth, Australia, 2012.

[41] M. R. R. Shahri, R. Aguilera, and A. Kantzas, "A new unified diffusion-viscous flow model based on pore level studies of tight gas formations," *SPE Journal*, vol. 18, no. 1, pp. 38–49, 2012.

[42] M. Knudsen, "Die Gesetze der Molekularströmung und der inneren Reibungsströmung der Gase durch Röhren," *Annalen der Physik*, vol. 333, no. 1, pp. 75–130, 1909.

[43] S. A. Schaaf and P. L. Chambré, *Flow of Rarefied Gases*, Princeton University Press, 1961.

[44] Z. Sun, B. Huang, Y. Li, H. Lin, S. Shi, and W. Yu, "Nanoconfined methane flow behavior through realistic organic shale matrix under displacement pressure: a molecular simulation investigation," *Journal of Petroleum Exploration and Production Technology*, vol. 12, no. 4, pp. 1193–1201, 2022.

[45] Z. Sun, S. Wang, H. Xiong, K. Wu, and J. Shi, "Optimal nanocone geometry for water flow," *AICHE Journal*, vol. 68, no. 3, p. 17543, 2022.

[46] B. D. Eldridge and L. F. Brown, "The effect of cross sectional pore shape on Knudsen diffusion in porous materials," *AICHE Journal*, vol. 22, no. 5, pp. 942–944, 1976.

[47] S. L. Matson and J. A. Quinn, "Knudsen diffusion through noncircular pores: textbook errors," *AICHE Journal*, vol. 23, no. 5, pp. 768–770, 1977.

[48] A. Ettehad, F. Javadpour, and K. Sepehrnoori, "Gas flow in ultra-tight shale strata," *Journal of Fluid Mechanics*, vol. 710, no. 12, pp. 641–658, 2012.

[49] H. W. de Regt, "The Scientific Letters and Papers of James Clerk Maxwell," *Journal of China Coal Society*, vol. II, pp. 1862–1873, 1996.

[50] S. K. Loyalka and S. A. Hamoodi, "Poiseuille flow of a rarefied gas in a cylindrical tube: solution of linearized Boltzmann equation," *Physics of Fluids A Fluid Dynamics*, vol. 2, no. 11, pp. 2061–2065, 1990.

Hindawi
Geofluids
Volume 2022, Article ID 8706365, 12 pages
https://doi.org/10.1155/2022/8706365

Research Article

Numerical Simulation of Seepage-Heat-Solid Coupling of Gas Seepage in Prepumped Boreholes under Electrothermal High Temperature Field

Xionggang Xie,[1] **Jin Yang**,[1] **XiangYing Luo**,[1] **and Jianjun Ren**[2]

[1]*Institute of Mining, Guizhou University, Guiyang 550025, China*
[2]*College of Physics and Engineering, Xingyi Normal University for Nationalities, Xingyi 562400, China*

Correspondence should be addressed to Xionggang Xie; 414922360@qq.com

Received 21 January 2022; Revised 18 February 2022; Accepted 26 February 2022; Published 6 April 2022

Academic Editor: Yu Pang

In order to verify the law of coal bed gas desorption and permeability under electrothermal high-temperature field, by establishing the mathematical model of gas seepage-heat-solid coupling, and taking gas drainage working face in Guizhou as an engineering example, the characteristics of the high-temperature field of coal under different heating hole temperatures are simulated. The COMSOL software is used to simulate the high-temperature field characteristics, thermal damage, and permeability of coal under different heating hole temperatures. The numerical simulation results show the following:(1) the influence trend of a high-temperature field on coal thermal damage and permeability is consistent, when the heating temperature is higher than 600°C, the thermal damage and permeability of coal seam change suddenly and increase with the increase of temperature. (2) When the temperature of a heating hole is 200-800°C, the gas permeability in the damaged area increases with the increase of temperature. When the heating temperature is greater than 600°C, the radial and axial permeability around the heating hole will increase. (3) Compared with the experimental data obtained by the existing researchers, the simulation results of coal permeability under the electric heating high-temperature field have a high consistency with the experimental results of Junrong and others.

1. Introduction

Most of Chinese coal resources are mined by underground mining. With the extension of the mine to the deep, the number of outburst mines increases, and the disaster of the original outburst mines increases [1, 2]. In order to increase coal seam gas permeability and improve gas drainage effect [3, 4], according to the influence of coal seam temperature, domestic scholars such as Yang [5], Wang et al. [6], Zhiqiang et al. [7], and Zhiwei [8] [9, 10] have studied the relationship between coal seam gas adsorption and desorption and high temperature. In 2009, Yang [11] and others [12, 13] measured the permeability and desorption flow rate of coalbed methane under the influence of temperature by using a triaxial adsorption desorption apparatus, and the experiment proved that the increase of coal temperature can enhance the permeability and desorption flow rate of coalbed methane. In 2012, Liu [14] et al., Wang et al. [15], and Dandan [16] studied the relationship between permeability and temperature of coal rock within 200°C through heating experiment and showed that permeability of coal rock with initial permeability within 0.5 mD could be significantly increased to more than 15 mD after heating treatment, and uneven deformation in coal rock caused microcracks under thermal stress. In 2015, Zhiwei et al. and others [17] established the thermian-fluid-solid coupling mathematical model and three-dimensional numerical simulation of dual porous media and showed that the change of temperature field had a great impact on the change of permeability. After the completion of high-temperature fracturing steam, the permeability of coal seam increased by about 13 times than the original gas.

At present, mineral insulated heating cable (referred to as "heating cable") has been used in petrochemical industry, heating and thermal insulation, ice melting and snow melting,

agricultural soil heating, combustion preheating device, and other fields. It is composed of a temperature controller and a heating cable. After the heating cable is powered on, it is heated slowly, and the temperature of the heated body is controlled at the set temperature by using a professional temperature controller. When the heated body absorbs heat, the temperature rises to reach the required working temperature. The temperature sensor and supporting temperature controller can accurately control the heating temperature. When the temperature reaches the set value, the temperature controller will automatically disconnect the power supply of the heating cable and stop heating the heating cable. When the temperature is lower than the set value, the thermostat turns on the power supply of the heating cable, and the heating cable starts heating. In 2005, Yanfeng et al. [18], Wu et al. [19], and others carried out the snow melting and ice melting experiment of heating cable road by using the concrete specimen of heating cable asphalt layer, studied the snow melting and ice melting mechanism of heating cable pavement, and studied the pavement high temperature field by using the finite element analysis method. In 2007, Shuyuan [20] established the cable heating snow melting model by using the heating cable snow melting experiment on the airport runway. In 2013, Hou and Xu [21], respectively, used asphalt concrete road and cement concrete road to test the relationship between heating speed and heating power and carried out experiments for arranging reinforcement mesh heating experiments. In 2015, Dengchun et al. [22] conducted the deicing experiment of heating cable with highway bridge specimens and studied the freezing and melting process of heating cable under two different spacing. In 2016, Xiaogang et al. [23] designed the isothermal Mi electric heat tracing method experiment for the whole line of the old hot spring electric heat tracing pipeline in Tanggula Mountain, Qinghai, controlled the operation and stop of the heat tracing system, and successfully limited the oil temperature to 40-43°C. In 2016, Nan et al. [24] carried out the research on soil thermal conductivity, described the mode and type of heat transmission in soil, and analyzed various influencing factors of soil thermal conductivity.

To sum up, the factors affecting the medium heat transfer effect mainly include heat conductivity, heat diffusion coefficient, specific heat capacity, and other parameters [25, 26]. The thermal conductivity of the medium determines the distribution of the temperature field in the steady-state heat transfer process, and the specific heat capacity of the medium can only affect the time of the temperature field established by the medium heat conduction. The heating cable conducts heat through the medium in the melting of ice and snow and soil insulation, and the heat is transmitted to the soil particle solid in the asphalt concrete layer and soil through heat conduction, so as to establish a temperature field on its surface and to achieve the effect of snow melting, ice melting, and soil heating. Therefore, the thermal conductivity of coal is the most important parameter affecting and determining the temperature field distribution of coal. Soil and coal belong to low thermal conductivity media. The temperature field has been successfully established in the above soil engineering examples. By increasing the temperature of heating cable, increasing coal moisture [27], and reducing the control range of heating cable, the required electrothermal high temperature field can be established in the outburst coal seam of mine gas drainage face.

2. Characteristics of Gas Bearing Coal under High Temperature Field

2.1. Adsorption Characteristics of High Temperature Coal to Gas. Coal is a porous medium with developed pore system, and more than 90% of gas exists in the micropores of coal matrix. Due to the changes of temperature and pressure, the gas molecules adsorbed in the micropores of coal overcome gravity, leave the inner surface of coal and enter the free state. The adsorption capacity of coal is closely related to temperature. Under the influence of the heating source, a temperature field with a spherical temperature from high to low is formed in the coal body, and a temperature difference is formed between adjacent coals. The gas molecules in the coal body absorb heat and expand, and the kinetic energy increases. The higher the temperature, the greater the gas pressure. Due to the existence of temperature difference, the gas adsorbed by adjacent media will form a pressure difference, which will increase the gas flow and release the adsorbed gas of coal seam. It is generally believed that the adsorption capacity of coal decreases with the increase of temperature, which changes in a negative exponential law.

2.2. Damage Characteristics of Coal under High Temperature Field. Based on the research results of Zhu et al. [28] and others, this paper establishes a thermal damage model based on the elastic mechanic method. It is assumed that each point in the coal and rock body satisfies the generalized Hooke's law. If the coal deformation caused by gas absorption and desorption, temperature and gas pressure change, the constitutive relationship does not change, and the damage effect of coal and rock mass can be described by weakening the corresponding parameters.

3. Thermal-Fluid-Solid Coupling Mathematical Model

3.1. Equation of Stress Field. Based on the assumption of linear elasticity, the constitutive equation of stress and strain of coal containing gas is established, which can describe the function relationship between the strain and effective stress of coal. Under isotropic and linear assumptions, the total strain of coal containing gas includes the sum of linear adsorption expansion strain caused by gas adsorption, linear thermal expansion strain caused by coal temperature rise, coal compression strain caused by gas pressure increase, in situ stress strain, and other factors. According to the total strain of coal, the constitutive equation of THM coupling is

$$\sigma' = 2G\varepsilon + \frac{\nu}{1+\nu}\Theta' - 2G, \left[\frac{\beta}{3}\Delta T - \frac{K_Y}{3}\Delta p + \frac{\varepsilon_L p}{P_L + p}\exp\left(-\frac{c_2\Delta T}{1+c_1 p}\right)\right], \quad (1)$$

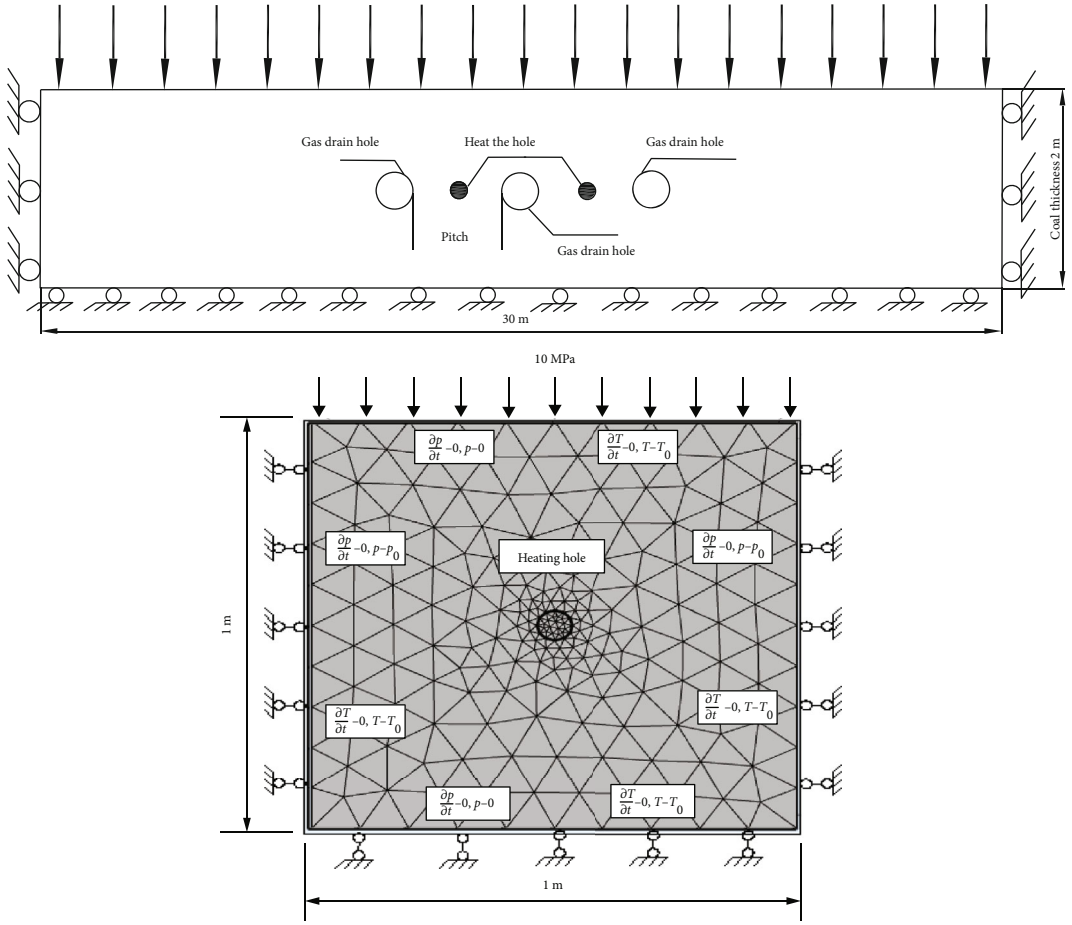

Figure 1: Calculation model of coal seam damage under thermal-fluid-solid coupling.

Table 1: Basic parameters of numerical simulation.

Gas dynamic viscosity coefficient/μ_0	1.087×10^{-5} Pa·s	Density of coal/ρ_c	1.35×10^3 kg/m^3
Initial porosity of coal seam/φ_0	0.045	Gas volume strain constant/ε_L	0.02295
Elastic modulus of coal/E	4×10^9 Pa	Ordinary gas constant/R	8.3143 J/(Mol°C)
Poisson's ratio of coal/υ	0.32	Initial permeability/k_0	1×10^{-15} m^2
Initial gas pressure/p_0	1 MPa	Volumetric thermal expansion coefficient of coal/β	0.116×10^{-3}°C^{-1}
Initial temperature/T_0	20°C	Specific heat capacity of coal skeleton/C_s	1350 J/(kg°C)
Langmuir pressure correction factor/c_1	710 Pa^{-1}	Specific heat capacity of gas/C_g	2160 J/(kg°C)
Langmuir volume correction factor/c_2	0.021°C^{-1}	Thermal conductivity of coal/η	0.443 W/(m°C)
Langmuir pressure constant/P_L	4.109×10^6 Pa	Gas density under standard state/ρga	0.716 kg/m^3
Langmuir volume constant/V_L	0.0477 m^3/kg	Coefficient of thermal expansion of coal	1×10^{-5}/°C

where G is the Ramet coefficient, ε is the total strain, ν is Poisson's ratio, $\Theta' = \sigma_1 + \sigma_2 + \sigma_3 + 3\alpha p$, β is the volumetric thermal expansion coefficient, °C^{-1}, Δp is coal seam gas pressure, Mpa, ΔT is temperature change, °C^{-1}, K_Y is volume compressibility, MPa^{-1}, c_1 is the Langmuir pressure correction coefficient, p^{-1}, c_2 is the Langmuir volume correction coefficient, °C^{-1}, ε_L is Langmuir adsorption strain constant, and P_L is the Langmuir pressure adsorption constant, MP^{-1}.

The tensor form of the constitutive equation can be further deduced from the above equation:

$$Gu_{i,jj} + \frac{G}{1-2\nu} u_{j,ji} + \alpha p_{,i} - K\beta\Delta T_{,i} - K\varepsilon_s\delta_{ij} + F_i = 0. \quad (2)$$

3.2. Seepage Field Equation. The flow process of gas in coal conforms to Darcy's law. Assuming that gravity effect is ignored, the seepage velocity is

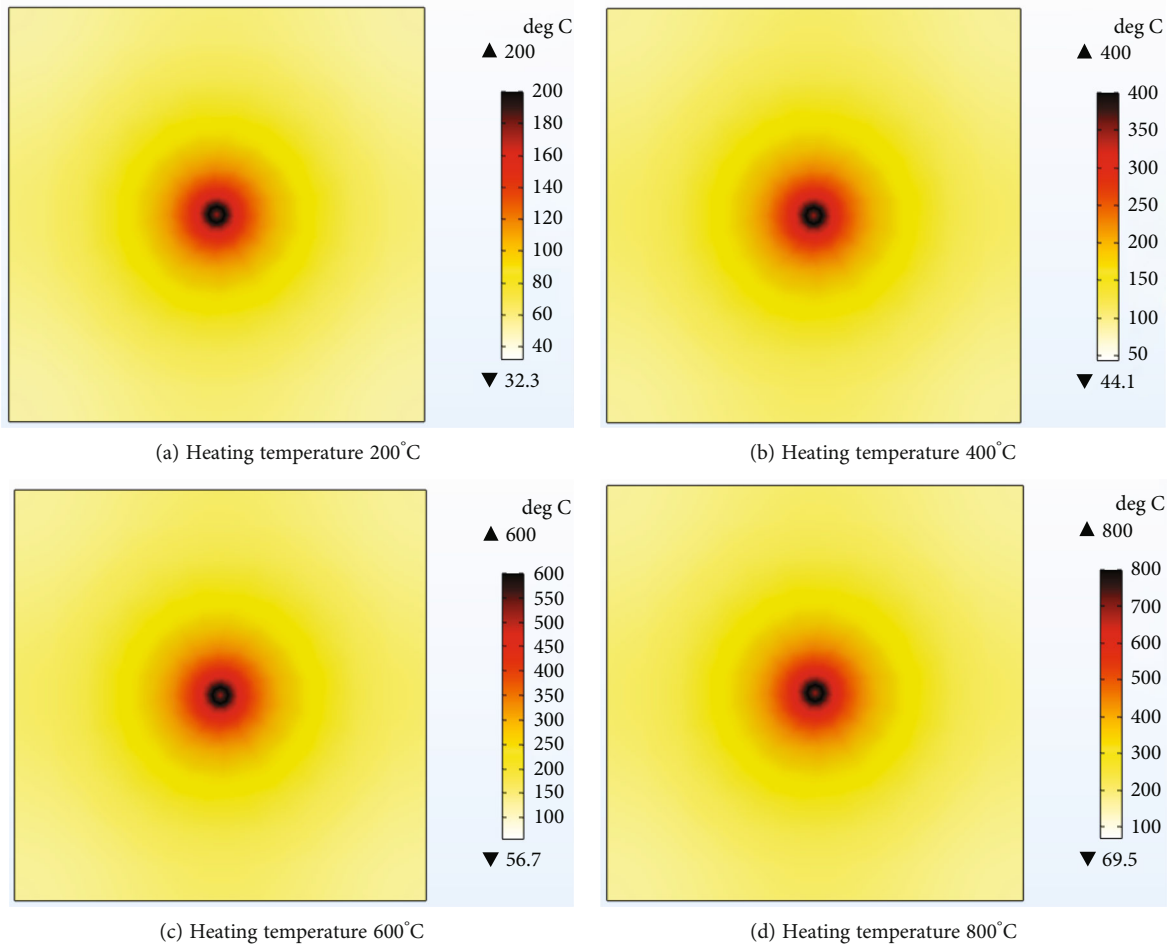

(a) Heating temperature 200°C

(b) Heating temperature 400°C

(c) Heating temperature 600°C

(d) Heating temperature 800°C

Figure 2: Temperature field distribution under different heating temperatures.

$$q = -\frac{k}{\mu}\nabla p, \tag{3}$$

where k is the seepage rate of coal body, m^2, and μ is kinematic viscosity, Pa·s, P is the pressure gradient, Pa/M.

Assuming that the gas is an ideal gas, and the gas content equation conforms to the modified Langmuir equation and the real gas state equation, the gas content per unit volume is

$$Q = \frac{M_g p}{RT}\varphi + (1-\varphi)\rho_{ga}\rho_c \frac{V_L p}{P_L + p}\exp\left(-\frac{c_2 \Delta T}{1 + c_1 p}\right), \tag{4}$$

where Mg value is 16, R value is 8314 $m^2/(s^2\ K)$, ρ GA is the gas density in standard state, kg/m^3, ρ_C is the coal density, kg/m^3, and VL is the Langmuir volume constant, m^3/kg.

The gas flow equation in coal is

$$\frac{\partial Q}{\partial t} + \nabla\left(\rho_g q\right) = 0. \tag{5}$$

Substitute Equation (3) and (4) into Equation (5) to obtain the equation of coal seam gas seepage field:

$$\frac{\partial}{\partial t}\left\{\frac{M_g p}{RT}\varphi + (1-\varphi)\rho_{ga}\rho_c \frac{\varepsilon_L p}{P_L + p}\exp\left(-\frac{c_2(T - T_0)}{1 + c_1 p}\right)\right\} - \nabla\left(\frac{M_g p}{RT}\frac{k}{\mu}\nabla p\right) = 0. \tag{6}$$

3.3. Temperature Field Equation. According to field observation and experiments, it is a complex nonisothermal process that temperature affects gas flow in coal seam.

If the thermal filtration effect is ignored, the influence of temperature on coal includes thermal diffusion and thermal convection. According to the law of energy conservation, the control equation of coupled temperature field of coal containing gas [29] can be deduced as follows:

$$\left[\varphi\rho_g C_p + (1-\varphi)\rho_c C_{p,p}\right]\frac{\partial T}{\partial t} - \rho_g C_p\left(\frac{k}{\mu}\nabla p\right)\nabla T + \nabla\left\{\left[\varphi\eta + (1-\varphi)\eta_p\right]\nabla T\right\} = Q, \tag{7}$$

where (ρC_p), eff, ηeff, p, and η_p are effective specific heat capacity, thermal conductivity coefficient, skeleton constant pressure heat capacity, and skeleton thermal conductivity coefficient of coal body, respectively. C_p and η are the constant pressure heat capacity and thermal conductivity

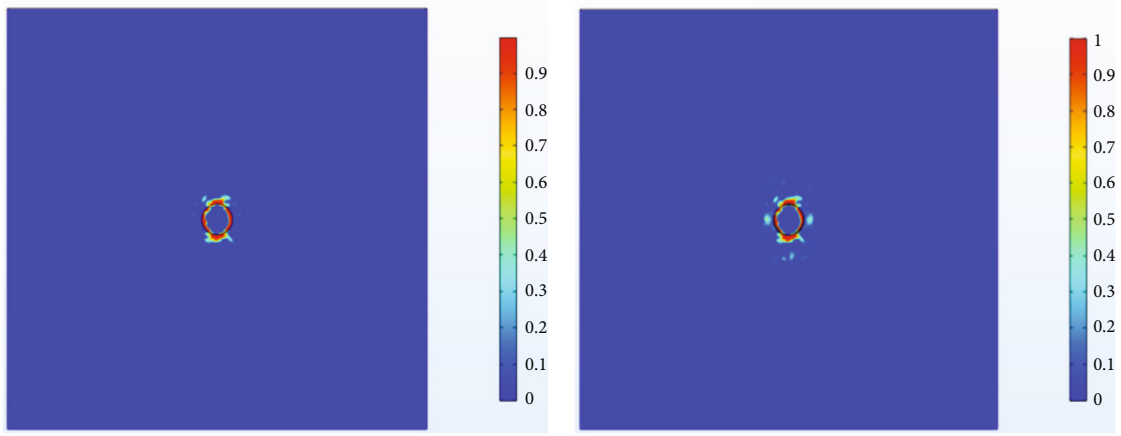

(a) Damage effect at heating temperature of 200°C

(b) Damage effect at heating temperature of 400°C

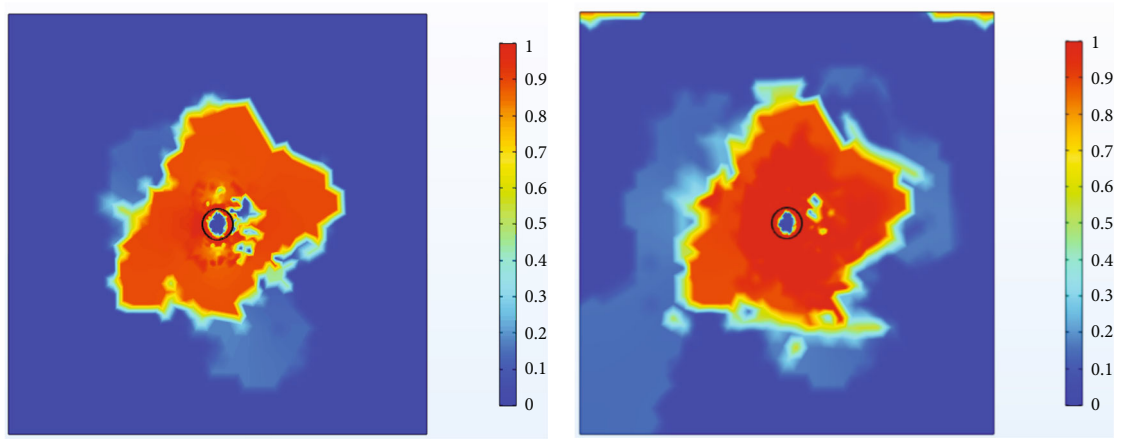

(c) Damage effect at heating temperature of 600°C

(d) Damage effect at heating temperature of 800°C

Figure 3: Damage effect of coal body under different heating temperatures.

coefficient of gas, respectively. H is the unit heat transfer, and Q is the heat source term.

4. Porosity and Permeability Model

4.1. Porosity Coupling Model. Porosity is an important parameter representing the porosity development degree of coal, and its value is affected by three parameters (temperature, gas pressure, and strain in the stress field). Meanwhile, porosity also affects the changes of the three parameters. Thus, the equation of coal porosity [30] can be analyzed as follows:

$$\varphi = 1 - \frac{1-\varphi_0}{1+e}, \left\{1 + \beta\Delta T - K_Y \Delta p + \frac{\varepsilon_L}{1-\varphi_0}\left[\frac{p}{P_L+p}\exp\left(-\frac{c_2\Delta T}{1+c_1 p}\right) - \frac{p_0}{P_L+p}\right]\right\}. \tag{8}$$

Since $e \ll \varphi 0$, it can be taken as $e = 0$, and the above equation can be simplified as

$$\varphi = \varphi_0 - (1-\varphi_0), \left\{\beta\Delta T - K_Y \Delta p + \frac{\varepsilon_L}{1-\varphi_0}\left[\frac{p}{P_L+p}\exp\left(-\frac{c_2\Delta T}{1+c_1 p}\right) - \frac{p_0}{P_L+p}\right]\right\}. \tag{9}$$

4.2. Permeability Coupling Model. Permeability is a physical parameter to measure the permeability effect of gas in coal seam. According to literature, permeability is affected by the porosity of coal seam. If porosity is large, permeability is high; otherwise, permeability is small. In the actual mining process, the pores near the wall are not evenly distributed, and the gas flow rate is greater than zero; so, Darcy's law is no longer applicable. Therefore, the Klinkenberg gas permeability calculation model considering slippage effect is adopted in the coal seam permeability model in this paper:

$$k = k_0\left(\frac{\varphi}{\varphi_0}\right)^3\left(1 + \frac{b}{p}\right). \tag{10}$$

Substituting Equation (9) into Equation (10), the equation

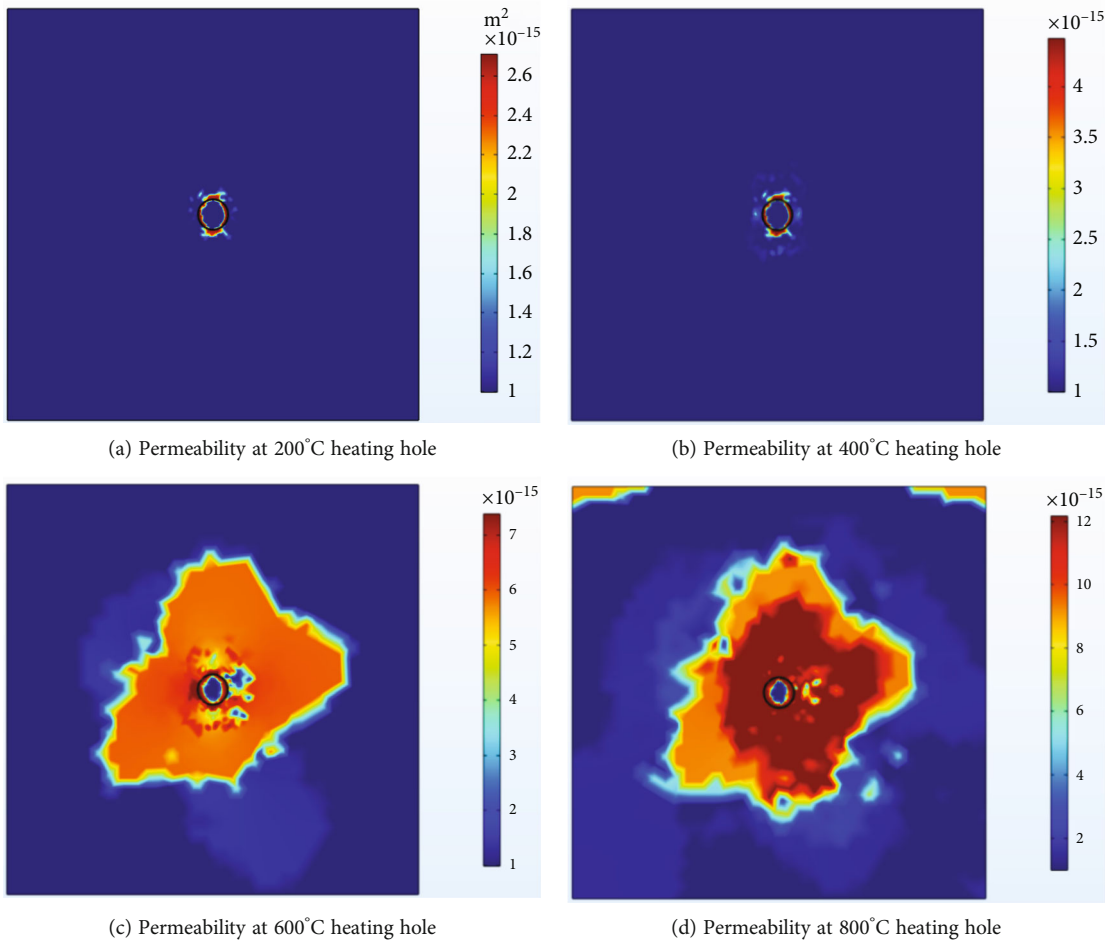

(a) Permeability at 200°C heating hole

(b) Permeability at 400°C heating hole

(c) Permeability at 600°C heating hole

(d) Permeability at 800°C heating hole

Figure 4: Coal body permeability under different heating temperatures.

can be obtained:

$$k = k_0 \left\{ 1 - \frac{1-\varphi_0}{\varphi_0} \left\{ \beta \Delta T - K_Y \Delta p + \frac{\varepsilon_L}{1-\varphi_0} \left[\frac{p}{P_L + p} \exp\left(-\frac{c_2 \Delta T}{1 + c_1 p} \right) - \frac{p_0}{P_L + p} \right] \right\} \right\}^3 \left(1 + \frac{b}{p} \right). \tag{11}$$

5. Simulation of Coal Seam Damage Zone under Thermal Fluid Solid Coupling Condition

The control equation of stress field is obtained by combining geometric equation, equilibrium differential equation, and coal constitutive equation; The gas content equation and Darcy's law are introduced into the gas flow equation to obtain the gas seepage field equation. According to the law of gas heat transfer in porous media and coal skeleton heat convection, heat diffusion, and heat radiation, the heat transfer equation of coal temperature field obtained by energy conservation is used. A thermal-fluid-solid coupling mathematical model and a dynamic change model of porosity and permeability of coal seam were established considering the damage effect and the influence of temperature on coal physical parameters. The COMSOL multiphysic multi physical field coupling simulation software is selected to establish the model. In this paper, the transportation roadway and return air roadway of M6 coal face of a mine in Guizhou Province are simulated as the research object. After the experimental steps are completed, the air inlet ends of the two roadways are sealed to isolate the experimental site from other sites, avoid relevant hidden dangers caused by coal heating, and ensure the safety of personnel and facilities. The model layout is shown in Figure 1. Set the thermal fluid solid coupling model as a two-dimensional model, take the heating hole as the center, heat the coal in a certain range through heat conduction, numerically simulate the characteristics of coal electrothermal high temperature field under the thermal fluid solid coupling condition (as shown in Figure 1), and establish a 1 m × 1 m × 1 m cube model with a radius of 0.02 m that is arranged in the middle of the model to represent the heating hole.

5.1. Model Parameter Setting. In order to ensure the accuracy of the model calculation, the gas drainage working face of a mine in Guizhou Province is selected as the numerical model. The K15 coal seam of the mine is 1.8-2.2 m thick, the spacing

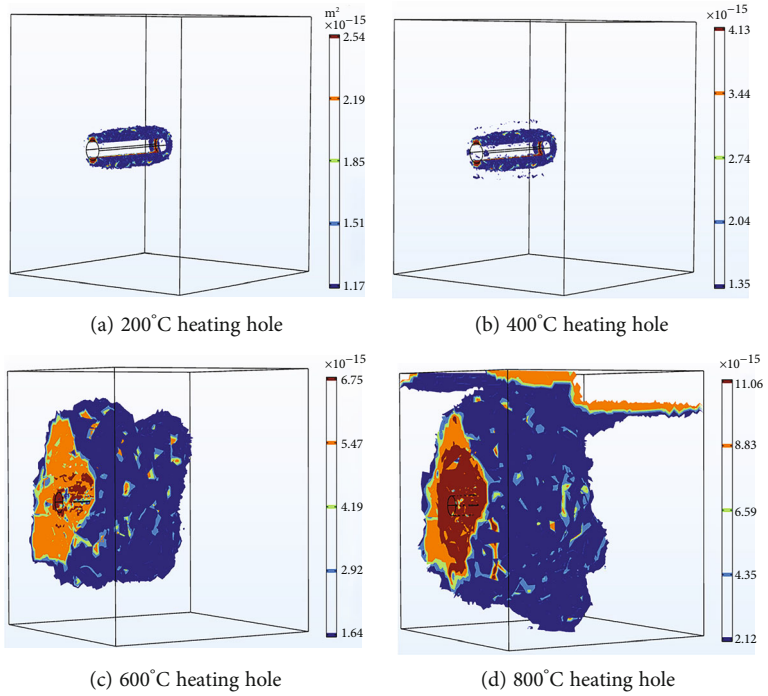

(a) 200°C heating hole (b) 400°C heating hole

(c) 600°C heating hole (d) 800°C heating hole

Figure 5: Isosurface map of coal permeability at different heating temperatures.

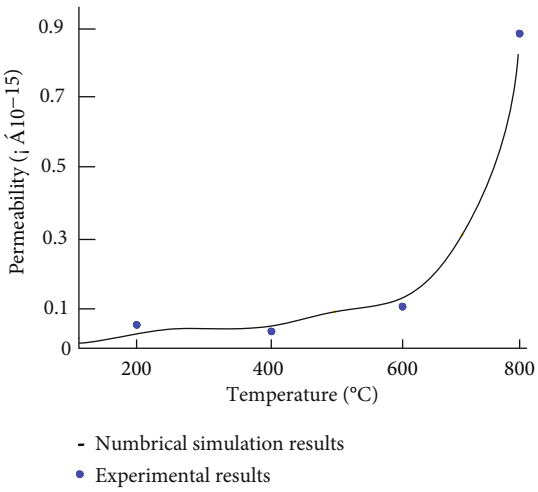

Figure 6: Coal penetration value at different temperatures.

of gas drainage holes is 3 M, and the inclination of the coal seam is 15~20°. A heating hole is arranged between each two drainage holes. Through relevant experiments and calculations, the basic parameters of numerical simulation of K15 coal seam are shown in Table 1.

5.2. Boundary Condition. In order to accurately reflect the coupling relationship of temperature field, stress field, and seepage field, except the upper boundary, other boundaries are set as fixed constraints. Boundary conditions of stress field: the pressure in the vertical direction is set to 10 MPa, as shown in Figure 1. The displacement of the left and right boundaries in the horizontal direction and the upper and lower boundaries in the vertical direction is 0. Boundary conditions of seepage field: set the gas pressure at the left boundary of coal seam as the initial pressure, the right boundary as the atmospheric pressure, and other boundary pressures as 0. Boundary conditions of temperature field: set the heating hole temperature as $T = Tb$. In this paper, the heating temperatures TB in the numerical simulation process are 200°C, 400°C, 600°C, and 800°C, respectively, and it is assumed that there is no heat transfer at the coal seam boundary.

5.3. Analysis of Numerical Simulation Results

5.3.1. Distribution Law of High Temperature Field. The effect of coal heat conduction was observed by setting different temperatures (200°C, 400°C, 600°C, and 800°C). The heating cable heats the gas bearing coal in the heating hole. The numerical simulation results of the temperature field after heating for a period of time are shown in Figure 2.

It can be seen from Figure 2 that with the heating hole as the center, the heat diffuses around with a circle with radius r, gradually forming a stable temperature field, which affects a certain amount of gas bearing coal. When the heating temperature is 200°C, it can be seen from Figure 2(a) that the minimum temperature of coal is 32.3°C. When the heating hole temperature is increased to 600°C, it can be seen from Figure 2(d) that the minimum temperature of coal is 69.5°C, and the minimum temperature of the latter is more than twice that of the former, indicating that with the increase of heating temperature, the overall temperature of coal increases, and the heat conduction effect is better.

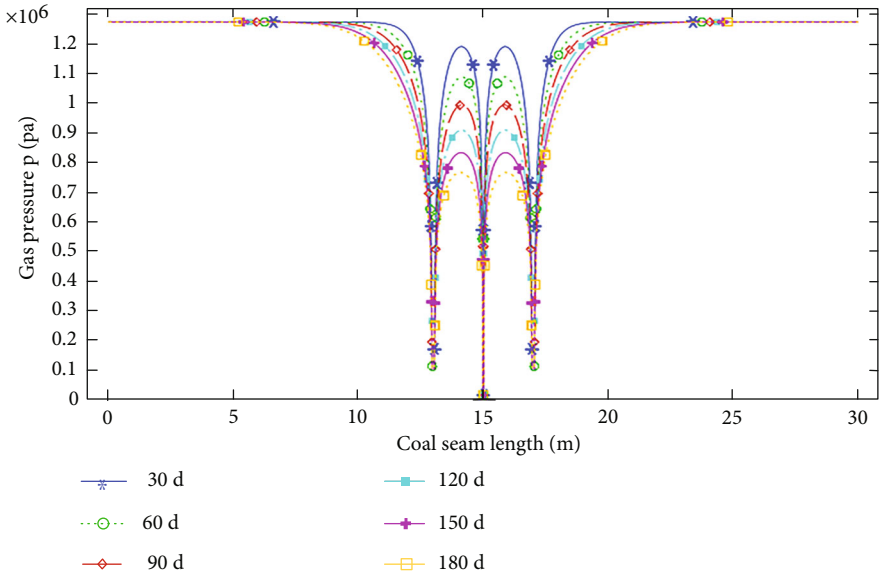

(a) 200°C heating temperature

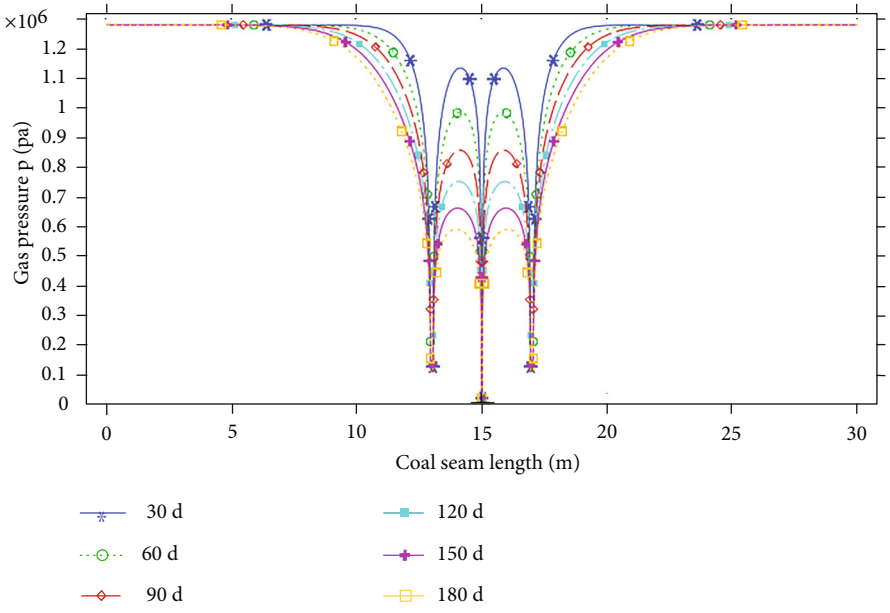

(b) 400°C heating temperature

Figure 7: Continued.

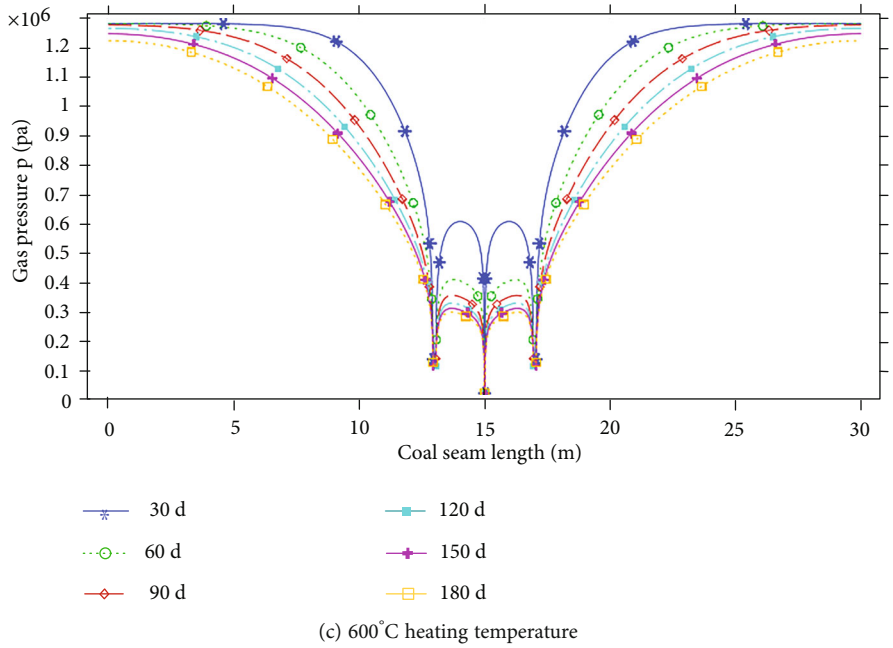

(c) 600°C heating temperature

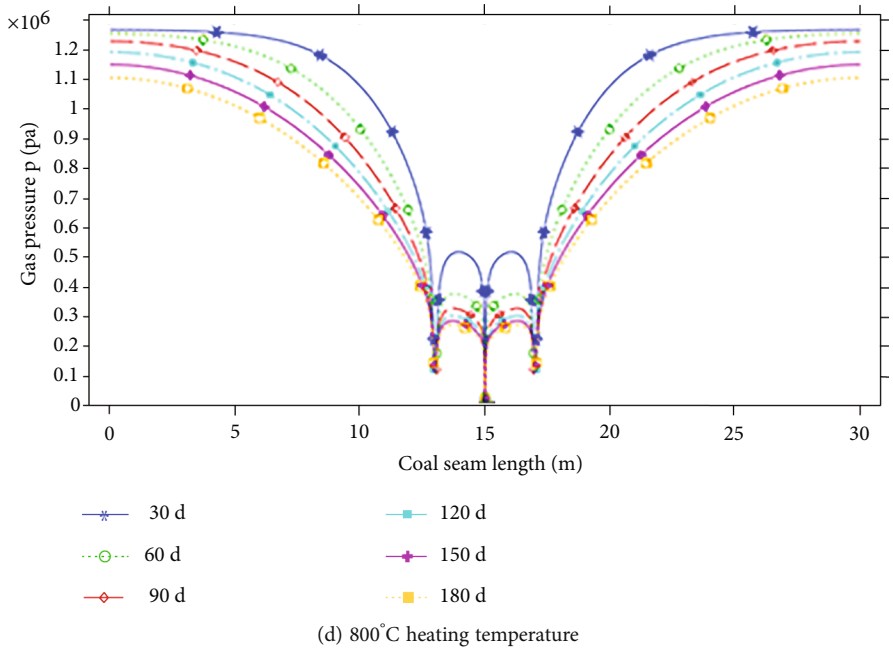

(d) 800°C heating temperature

Figure 7: Pressure distribution of 180 d gas drainage under different heating temperatures.

5.3.2. Temperature Field and Thermal Damage Effect of Coal. In the process of heating coal by heating cable, too high temperature will lead to thermal expansion deformation of coal and then thermal damage. In order to study the influence of temperature on thermal damage of coal, the following numerical simulation research is carried out in this paper. The thermal damage results are shown in Figure 3.

It can be seen from Figures 3(a) and 3(b) that the temperature of the heating hole is 200°C, and only a small part of the coal is damaged, mainly in the up and down directions. When the temperature rises to 400°C, the damage of the coal is slightly greater than that of the heating hole, which is 200°C, but the action range is also small. It can be seen from Figures 3(c) and 3(d) that when the temperature of the heating hole rises to 600°C, a large area of red appears around the hole; that is, the damage area of the coal body suddenly changes, the shape of the damage area is approximately circular, and the influence range of the damage area is 0.2 ~ 0.3 m. As the temperature rises to 800°C, the damage range expands. The scope of influence is extended to the upper left and right corners of the model.

The analysis shows that when the temperature of the heating hole is high, the temperature causes the thermal expansion stress of the gas bearing coal body to be greater than the overburden pressure in the limited space.

Combined with the influence of fixed boundary constraints, tensile failure and shear failure occur around the heating hole, showing the damage effects of Figures 3(c) and 3(d).

5.3.3. Temperature Field and Coal Permeability. Based on the above research, the permeability is affected by temperature parameters. In order to observe the change of permeability under different temperature conditions, this paper simulates the change law of coal seam permeability when the heating temperature is 200°C, 400°C, 600°C, and 800°C, respectively. The simulation results are shown in Figure 4.

The simulation effect of temperature field on coal seam permeability is shown in Figure 4. It can be seen from Figures 4(a) and 4(b) that the temperature of the heating hole is 200°C, and the coal permeability increases in a very small range around the hole, which is not obvious. When the temperature of the heating hole increases to 400°C, the permeability value also increases, and the increased area is slightly larger than the area at 200°C, which is the same as the distribution law of thermal damage. It can be seen from Figures 4(c) and 4(d) that as the temperature of the heating hole rises above 600°C, the permeability area and permeability value of the coal seam increase sharply compared with 400°C. When the temperature of the heating hole reaches 800°C, the permeability value increases by 11 times. It can be seen from the four diagrams that the influence of temperature field on permeability is similar to the damage trend of coal body.

In order to further illustrate the promoting effect of electrothermal high temperature field on permeability of coal body, this paper analyzed the model stereograph and obtained permeability isosurface Figure 5 of numerical simulation model under different heating temperatures.

It can be seen from Figure 5 that when the temperature of the heating hole is 200°C, 400°C, 600°C, and 800°C, the permeability of coal seam increases by 2.5 times, 4.1 times, 6.7 times, and 11 times, respectively. The permeability improvement area is very small at 200°C and 400°C, but it increases significantly at 600°C and 800°C. In Figures 5(a) and 5(b), when the temperature of the heating hole is below 400°C, the permeability increase around the heating hole mainly occurs in the upper and lower directions around the heating hole, and the influence range is small. In Figures 5(a) and 5(b), when the temperature of the heating hole is 600°C and 800°C, the permeability increases not only along the direction of the heating hole but also along the direction of the heating hole. However, the permeability increases along the direction of the heating hole that is significantly higher than that along the direction of the heating hole.

In order to verify the accuracy of the above numerical simulation, the simulation results are compared with the experimental data of Junrong et al. [31]. The results are shown in Figure 6:

According to Figure 6, the numerical simulation results are consistent with the experimental results of Junrong and others. When the coal temperature is 200°C, 400°C, 600°C, and 800°C, the gas permeability of the experimental coal of Junrong and others increases by 0.8 times, 0.9 times, 4.5 times, and 15 times, respectively, while the gas permeability of the numerical simulation coal in this paper increases by 0.5 times,2.1 times,6.7 times, and 11 times, respectively, and there is a small difference between the two groups of data, which may be due to slight errors in the process of numerical simulation. Therefore, the numerical simulation results are in good agreement with the experimental results of Junrong et al.

6. Temperature Field and Gas Extraction Effect in Working Face

The beneficial effect of temperature field on coal face drainage was revealed by analyzing the variation law of gas pressure under different heating temperatures (200°C, 400°C, 600°C, and 800°C). The gas pressure distribution on the horizontal midline of the coal seam for 180 days under different heating temperatures was numerically simulated (as shown in Figure 7).

It can be seen from Figure 7 that when the influence range of 180 d extraction under the action of heating hole is expressed by gas pressure, the effective radius of extraction hole at 200°C, 400°C, 600°C, and 800°C is 2.2 m, 2.6 m, 4.9 m, and 6.1 m, respectively, increasing by 18.2%, 88.5%, and 24.5%, respectively. When the temperature of the heating hole is 600°C, the influence range of extraction increases dramatically.

7. Conclusion

(1) In the heating process of electrothermal high-temperature field, the heating hole is the center, and the heat diffuses around the circle with radius r, gradually forming a stable temperature field. When the heating temperature increases, the overall temperature of coal increases

(2) With the increase of temperature, the damage area of coal body increases, and the gas permeability of coal seam increases. When the temperature of the heating hole is 200°C, 400°C, 600°C, and 800°C, the permeability of coal seam in the damaged area increases 2.5 times, 4.1 times, 6.7 times, and 11 times, respectively. When the temperature of the heating hole is below 400°C, the permeability increase around the heating hole mainly occurs in the upper and lower directions around the heating hole, and the influence range is small. When the temperature of the heating hole is 600°C and 800°C, the permeability increases not only along the heating aperture but also along the heating aperture

(3) Based on the experimental data of Junrong [20] and others, the simulation results of coal permeability under electrothermal high temperature field are compared, which proves that the numerical simulation results are reliable

(4) The influence range of heating hole depends on the heat conduction coefficient of coal skeleton and gas. The higher the heat conduction coefficient is, the larger the influence range of heating hole is, and the gas extraction has little influence on the temperature field. According to the thermal expansion

characteristics of low stress outburst coal seam in mine, an effective way to increase gas permeability by heating the coal seam is determined

Data Availability

The data that support the findings of this study are available from the corresponding author upon reasonable request.

Conflicts of Interest

The authors declare that they have no conflicts of interest.

Acknowledgments

This work was supported by the Natural Science Foundation of China (No. 51864009 and No. 52164016), the Youth Science and Technology Talent Growth Project of Guizhou Provincial Department of Education (grant No. Ky [2018] 414), the Key Project of Natural Science of Guizhou Education Department (Guizhou Education Science (2011) 034), and the Science and Technology Department Joint Fund Project of Guizhou Province, China (grant No. LH [2017] 7036).

References

[1] Y. Liang, "Strategic thinking of co-mining of deep coal and gas in my country," *Journal of China Coal Society*, vol. 41, no. 1, pp. 1–6, 2016.

[2] Y. Zhou, H. Li, J. Huang et al., "Influence of coal deformation on the Knudsen number of gas flow in coal seams," *Energy*, vol. 233, p. 121161, 2021.

[3] National Coal Mine Safety Supervision Bureau, *Countermeasure for the Development of Coal Mine Gas Disaster Prevention Technology (2014)*, State Administration of Safety Supervision, Beijing, 2014.

[4] H. Ji, Y. Mao, and H. Su, "Effects of organic micromolecules in bituminous coal on its microscopic pore characteristics," *Fuel*, vol. 262, p. 116529, 2020.

[5] T. Yang, *Experimental Research and Mechanism Analysis of Temperature Change during Coal Gas Absorption and Desorption*, China University of Mining and Technology (Beijing), Beijing, 2014.

[6] C. Wang, *Experimental Study on Adsorption Gas Migration in Deep Coal Samples under Temperature-Pressure Coupling*, China University of Mining and Technology (Beijing), Beijing, 2011.

[7] L. Zhiqiang, X. Xuefu, and L. Qingming, "Experimental study on coal permeability under different temperature and stress conditions," *Journal of China University of Mining & Technology*, vol. 38, no. 4, pp. 523–527, 2009.

[8] L. Zhiwei, *Research on Low Permeability Coalbed Gas Heat Injection Mining and Its Permeability Law*, Taiyuan University of Technology, Taiyuan, 2015.

[9] T. Cai, Z. Feng, Y. L. Jiang, D. Zhao, D. Zhou, and X. Q. Zhang, "Seepage evolution in coal creep under different temperatures and different stresses," *Chinese Journal of Rock Mechanics and Engineering*, vol. 37, Supplement 2, pp. 3898–3904, 2018.

[10] D. Jiahui, "Experimental study on influence of multiple factors on coal permeability," *Coal Technology*, vol. 39, no. 6, pp. 122–125, 2020.

[11] X. Yang, R. Changzai, and Z. Yongli, "Thermal-fluid-solid coupling mathematical model and numerical simulation of low-permeability coalbed methane injection mining," *Journal of China Coal Society*, vol. 38, no. 6, pp. 1044–1049, 2013.

[12] X. Tongqiang, W. Youpai, Z. Fubao et al., "The stress-seepage-temperature multi-process coupling test system for coal and rock mass," *Journal of China University of Mining & Technology*, vol. 50, no. 2, pp. 205–213, 2021.

[13] L. I. Baolin and W. Guoying, "Numerical simulation of thermal-fluid-solid coupling of the flow dominance of coal under different temperature conditions," *Coal Science and Technology*, vol. 48, no. 11, pp. 141–146, 2020.

[14] L. Hao, C. Jihua, X. Changbo, W. Jijun, and C. Yu, "Mechanism of heat treatment increasing permeability of coal rock," *Oil Drilling & Production Technology*, vol. 34, no. 4, pp. 96–99, 2012.

[15] G. Wang, Q. Xiangjie, J. Chenghao, and Z. Zhen-yu, "Simulations of temperature effects on seepage and deformation of coal microstructure in 3D CT reconstructions," *Rock and Soil Mechanics*, vol. 41, no. 5, pp. 1750–1760, 2020.

[16] Z. Dandan, "Effect analysis of temperature on seepage characteristics between moulded coal and raw coal," *Safety in Coal Mines*, vol. 49, no. 4, pp. 152–155, 2018.

[17] Y. Yuliang, J. Jinhu, L. Chuang et al., "Creep properties and constitutive relation of anthracite under temperature-stress coupling," *Safety in Coal Mine*, vol. 51, no. 5, pp. 61–65, 2020.

[18] L. Yanfeng, W. Haiqin, W. Guanming, L. Junmei, and H. Longshu, "Experimental study of heating cables used to melt snow and ice on pavement," *Journal of Beijing University of Technology*, vol. 33, no. 3, pp. 217–219, 2006.

[19] H. Wu, *Technical Research on Heating Cable Used to Melt Snow and Ice on Road Surface*, Beijing University of Technology, Beijing, 2005.

[20] G. Shuyuan, *Numerical Analysis of Snow Melting in Cable Heating System*, Shanghai Jiao Tong University, 2008.

[21] G. Xu, *Pavement Surface Physical Deicing and Snow Technology Research Based on Built-in Electric Heating*, Harbin, Harbin Institute of Technology, 2013.

[22] Z. Dengchun, Z. Zhaohong, Y. Jiangya, Y. Tongsen, L. Kongqing, and C. Yazhou, "Experimental study on the deicing system of highway bridge heating cables," *Science and Technology of China Safety Production*, vol. 11, no. 11, pp. 90–95, 2015.

[23] Z. Xiaogang, Z. Yi, and Z. Jianyu, "Optimized design and application of MI electric heat tracing in oil pipeline," *Oil and Gas Storage and Transportation*, vol. 35, no. 8, pp. 833–835, 2016.

[24] Z. Nan, X. Shengquan, H. Xinyu, and W. Zhaoyu, "Research status and prospect of soil thermal conductivity and model," *Rock and Soil Mechanics*, vol. 37, no. 6, pp. 1550–1661, 2016.

[25] W. Yinhua and J. Wang, "Application of soil heating system in vegetable pot seedling," *Agricultural Development and Equipment*, vol. 9, pp. 60-61, 2014.

[26] L. Yujing, "Heating cable and its application in civil building," *Shanxi Architecture*, vol. 35, no. 25, pp. 203-204, 2009.

[27] J. Ma, *Research on the Characteristics of Pressure Relief and Gas Migration in the Mining of Protective Layer under a Single High Gas Thick Coal Seam*, Henan University of Science and Technology, Jiaozuo, 2016.

[28] Z. Wancheng, W. Chenhui, T. Jun, Y. Tianhong, and T. Chunan, "Thermal-fluid-force coupling model and its

application during rock damage," *Rock and Soil Mechanics*, vol. 30, no. 12, pp. 3851–3857, 2009.

[29] W. Chenhui, *Coal and Rock Damage Model and Its Application under the Condition of Thermal Fluid-Solid Coupling*, Northeastern University, Shenyang, 2012.

[30] X. Weijing, W. Xiaojun, L. Shichao, Y. Zhengxing, H. Guangli, and Y. Qi, "Deformation characteristics analysis of rock triaxial compression process under the action of seepage pressure," *China Safety Production Science and Technology*, vol. 13, no. 12, pp. 38–42, 2017.

[31] L. Junrong, Q. Jishun, and X. Wu, "Experimental study on the influence of temperature on rock permeability," *Journal of the University of Petroleum (Natural Science Edition)*, vol. 25, no. 4, pp. 51–54, 2001.

Hindawi
Geofluids
Volume 2022, Article ID 1263893, 16 pages
https://doi.org/10.1155/2022/1263893

Research Article

Structural Formation, Evolution, and Genetic Mechanisms of Fault in Controlling Hydrocarbon Migration of Unconventional Rocks: A Case Study of Zhuangnan Fault

Jing Wang,[1] Yongwei Guo,[1] Youwei Cui,[2] Ke Sun,[3] and Huili Chu[1]

[1]*Department of Petroleum Engineering, Hebei Petroleum University of Technology, Chengde 067000, China*
[2]*The Fifth Gas Production Plant of Changqing Oilfield Company, Xi'an 710018, China*
[3]*Sinopec Petroleum Exploration and Production Research Institute, Beijing 100083, China*

Correspondence should be addressed to Yongwei Guo; hebeishiyougyw@sina.com

Received 9 January 2022; Revised 6 February 2022; Accepted 14 February 2022; Published 6 April 2022

Academic Editor: Tao Zhang

Zhuangnan fault zone was affiliated with Gubei subsag of the Zhanhua sag in Jiyang Depression, Bohai gulf basin. Zhuangnan fault zone has two functions as the main east-west strike-slip accommodation structure. That is, on the one hand, Zhuangnan fault zone inherited the rules of development of regional tectonic. On the other hand, the present structure framework of Zhanhua sag was reconstructed by Zhuangnan fault zone. In the study, there are four main seismic reflectors: T0, T1, T2, and T6. They are the basis for researching the planar and vertical features of Zhuangnan fault zone. The structural formation, evolution, and genetic mechanisms of Zhuangnan fault zone are studied from three aspects of geometry, kinematics, and dynamics. In geometry, by the closure interpretation of 43 south-north interpretation sections and 24 east-west interpretation sections, the result indicates that Zhuangnan fault zone has its special regularity and characteristic which has three-piece planar characterization (eastern part, middle part, and western part). Three types of plane combination forms are determined: arched, linear, and "S" curved type. The plane combination structure styles of the Zhuangnan fault zone mainly include feather row, horsetail, grid, diagonal, and parallel style. These planar structural features play an important role in indicating the fault zoning of Zhuangnan fault zone. Based on the plane and section structural styles of Zhuangnan fault zone and the analysis of dynamic evolution, it is found that Zhuangnan fault zone has a succession relationship between deep and shallow fault systems. From tectonic evolution and regional dynamic point of view, this paper discusses the activity law of the Zhuangnan fault zone and the boundary faults on the east and west sides of Jiyang Depression, which are Changdi fault, Wuhaozhuang fault, and Chengnan fault, respectively. This study provides a new and more reasonable explanation for the unique structural characteristics of Zhuangnan fault zone and further confirms the important role and regulation mechanism of Zhuangnan fault zone.

1. Introduction

In recent years, the fine characterization of tectonic features and the relationship between fault evolution in the evolution of the rift basin have been the focus of the research work of scholars at home and abroad [1–3]. Faults are relatively developed in the eastern part of Jiyang Depression. The faults are generally developed in east-west, north-east, and northwest strikes. Zhuangnan fault zone is a secondary structural belt of Zhanhua sag in Jiyang Depression [2, 4, 5]. It is an important readjust fault zone which fault strike is EW. There are also a group of faults which fault strike is SN, among which Changdi fault, Wuhaozhuang fault, and Chengnan fault are the main boundary faults of Zhanhua sag. The strike-slip structural patterns, active rates, and time of these faults have been studied extensively [6–8]. These faults have an important influence on the accumulation process in this area. Therefore, researchers have paid much attention to the formation age, tectonic properties, and dynamic mechanism of faults in this area. It is generally

believed that the fault assemblage of Zhuangnan fault zone communicates the connection between the lower source rock and the upper reservoir. As an important hydrocarbon transport channel, it creates favorable conditions for hydrocarbon accumulation in the upper Ng and Ed Formations [6, 9, 10].

However, due to the complex secondary structure and fault effect of the strike-slip adjustment fault zone, there are still many problems in Zhuangnan fault zone that need further study [11]. The geometric characteristics of Zhuangnan fault zone need to be carefully described [9]. The inheritance characteristics and details of Zhuangnan fault zone need further analysis [10]. As for the formation mechanism of Zhuangnan fault zone, especially the adjustment mechanism between Zhuangnan fault zone and boundary faults, what kind of dynamic factors are still needed to be studied?

In this paper, the geometric characteristics, tectonic evolution, and adjustment mechanism of Zhuangnan fault zone are studied using the latest 3D seismic data of Zhuangnan fault zone in Jiyang Depression which are carefully interpreted and combined with a high-resolution coherency analysis technique. In addition, the formation mechanism of the NS-trending strike-slip faults and the EW-trending strike-slip adjustment fault zone in the east of Jiyang Depression, represented by Zhuangnan fault zone and its boundary faults (Changdi fault, Wuhaozhuang fault, and Chengnan fault), is further analyzed.

2. Regional Geological Outline

Zhuangnan fault zone is a secondary structural belt of Zhanhua sag in Jiyang Depression. Zhuangnan fault zone was composed of a nearly west-east strike listric normal fault and the subfaults derived from the main fault. Zhuangnan fault zone is bordered by Chengdong fault on the west and the Wuhaozhuang fault and Changdi fault on the east (Figure 1). Four oilfields were developed in Zhuangnan fault zone, which were Zhuangxi oilfield, Wuhaozhuang oilfield, Changdi oilfield, and Laohekou oilfield. Those oilfields consist of many oil-bearing strata, which are distributed in the Archaeozoic, Palaeozoic, and Mesozoic and included some reservoirs buried deeply [7, 12–15]. Paleozoic buried hill reservoir is the most important oil pool types in Zhuangxi oilfield. Major exploration targets of Wuhaozhuang oilfield, Changdi oilfield, and Laohekou oilfield are reservoirs in the Cenozoic (Steven 1999) [3, 16].

All four oilfields are the typical complicated fault-block oilfields in east China. They have more styles and more complex forming causation types. At present, Zhuangxi oilfield relies mainly on structure reservoir; Wuhaozhuang oilfield is dominated in composite structure-lithology reservoir [4, 17] (Shamik 2010). Changdi oilfield is complicated by many faults and belongs to anticline reservoir having multilayer of sands, which is divided into two tectonic types: Paleozoic buried hill structure and Mesozoic draping structure. The main accumulation model of Laohekou oilfield in upper Guantao formation is the lithologic oil and gas pools [5, 6, 8, 18].

3. Structure Types

Applying three-dimensional seismic data, geological data, and logging data, we analyze and describe the structural feature and fracture feature of Zhuangnan fault zone. Geoframe 4.3 seismic interpretation software has been applied to seismic layer labeling and making synthetic seismogram, coherent data analysis, and seismic explanation [8, 19, 20], by making synthetic seismic records of well data of test wells, a fine horizon calibration for the target strata. By accurately interpreting with a 3D coherence analysis and seismic section in plain, section, and space, the geometry characteristics of Zhuangnan fault zone have preliminarily been understood. The application of coherent data volume to interpret fault blocks in complex fault block areas is a very effective tool [9, 13, 14, 21] (Alissa 2009). The time slice of a coherent data body can unveil the direction of the Zhuangnan fault zone generally, the configurations of faults in both areal and vertical directions, and guidance-find the secondary fracture. Considering most of the faults in Zhuangnan fault zone are nearly west-east strike, the east-west interpretation section should be the one that supplements a focus on the south-north interpretation section (Feng 2013).

3.1. Vertical Fault Assemblage. The closure of intersecting geophysical information has been an important problem in geophysical data interpretation. By the closure interpretation of 43 south-north interpretation sections and 24 east-west interpretation sections, the article summarized fault growth in Zhuangnan fault zone below. Zhuangnan fault zone had developed on the tectonic background of Zhuangnan buried hill. The fault zone has the characteristic of plastic uplifting by reason of the spreading function and antithetic drag of the main faults in Zhuangnan fault zone. The study found that Zhuangnan fault zone had the characteristics of more active faults developed on both sides of the fault zone than the middle part of the fault zone. And the faults were concentrated developed in the north of the area.

From that, we divided Zhuangnan fault zone into three parts: western part (line: 1371-1450), middle part (line: 1450-1650), and eastern part (line: 1650-1791).

Western part: the evolution of Zhuangnan fault zone experiences three stages. With four listric faults trending NEE, dipping S developed of early evolution, those faults are arranged in equivalence and parallelism. Fault styles are mainly step faults. Those faults have long fault displacement, which can cut the overlying formations and basement strata.

In the median period of development, four secondary fractures dipping north were developed. Those faults ending on the listric faults dipping S are located on the southernmost part of the four listric faults.

Those secondary fractures are arranged in equivalence and parallelism. Fault styles are mainly step faults. The median period subordinate structure fault and the early main faults display a "y" character form fault array in profile. Fault styles are mainly graben and step fault. Those secondary fractures also have long fault displacement, which mainly cut the overlying formations.

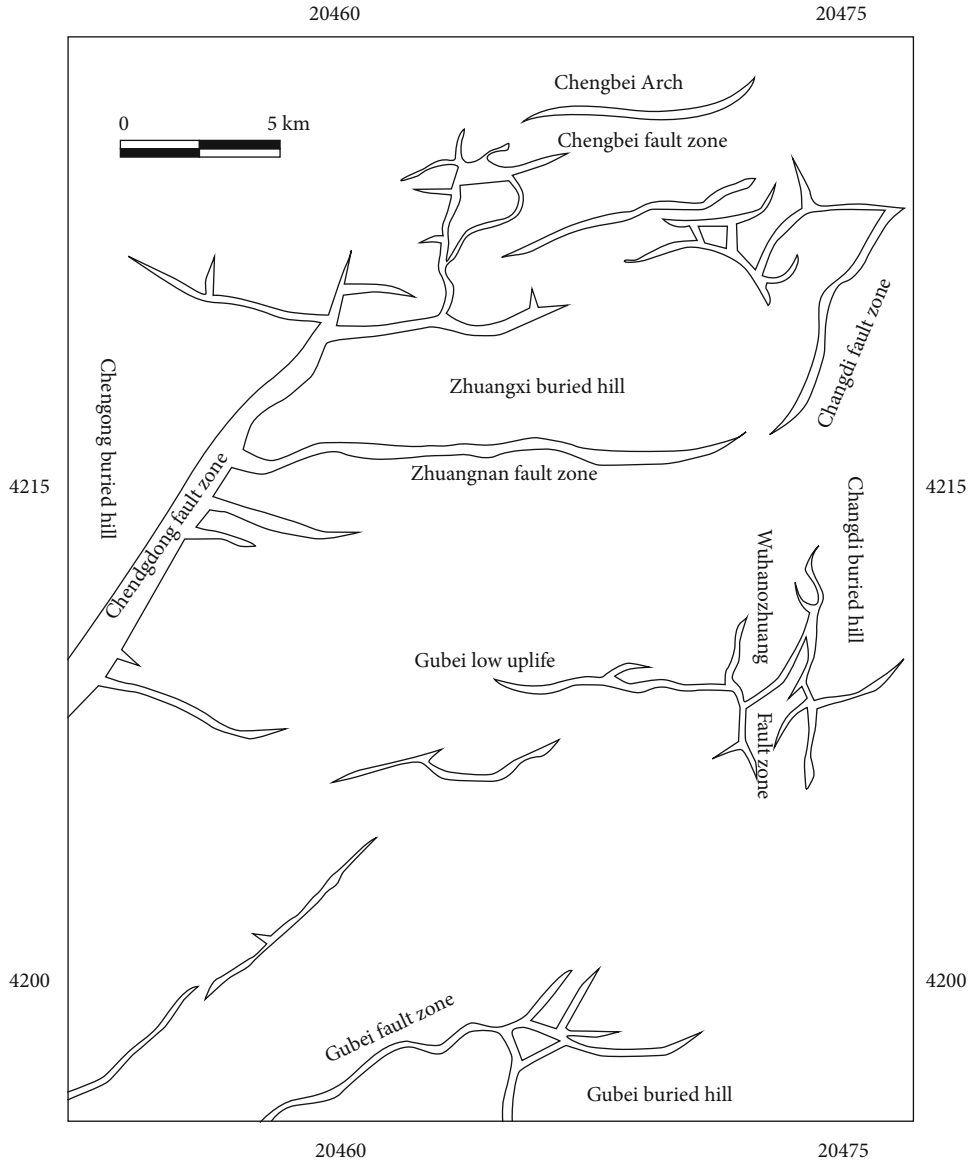

Figure 1: Structural position of Zhuangnan fault zone.

The late development faults grow on the four secondary fractures of median period development, which displayed an "anti-y" character form fault array with median development faults in profile. The late development faults have short fault displacement, which only cut the shallow formation (Figure 2 and Table 1).

Middle part: most early development faults gradually cease their activity, which only cut the basement strata. The activity of Zhuangnan fault is always persisted. Zhuangnan fault becomes the most important fault dipping S which section shape is listric. The gradient of Zhuangnan fault slackens from the top down. Zhuangnan fault cuts the basement strata. The subsidiary shear fractures complicate the overlying formations. The major "y" character form fault array in the studied area was composed of Zhuangnan fault and one secondary fracture in dipping N. Three stages of secondary fracture evolved between them. The combinations of the faults of different phases are "y" character form and "anti-y" character form. Overall, the middle part of the structure possesses the characteristic of faults in the overlying formations which are more complex than that in the basement strata (Table 2).

Eastern part: the eastern part is the activity of early development fault enhancement. Three-fifths of early development faults cut the overlying formations and basement strata, and two-fifths of early development faults cut the basement strata, which do not cut the overlying formations. Four secondary fractures dipping north were developed in Cenozoic strata. There is a strong symbiotic relationship between the main faults of F1, F3, and F5 and the secondary fault of F2. F2 fault was cut by F1 fault, displaying "y" character form fault array in profile with F1 and F3 faults. F4 fault was the late development fault, displaying "y" character form with main faults (Table 3).

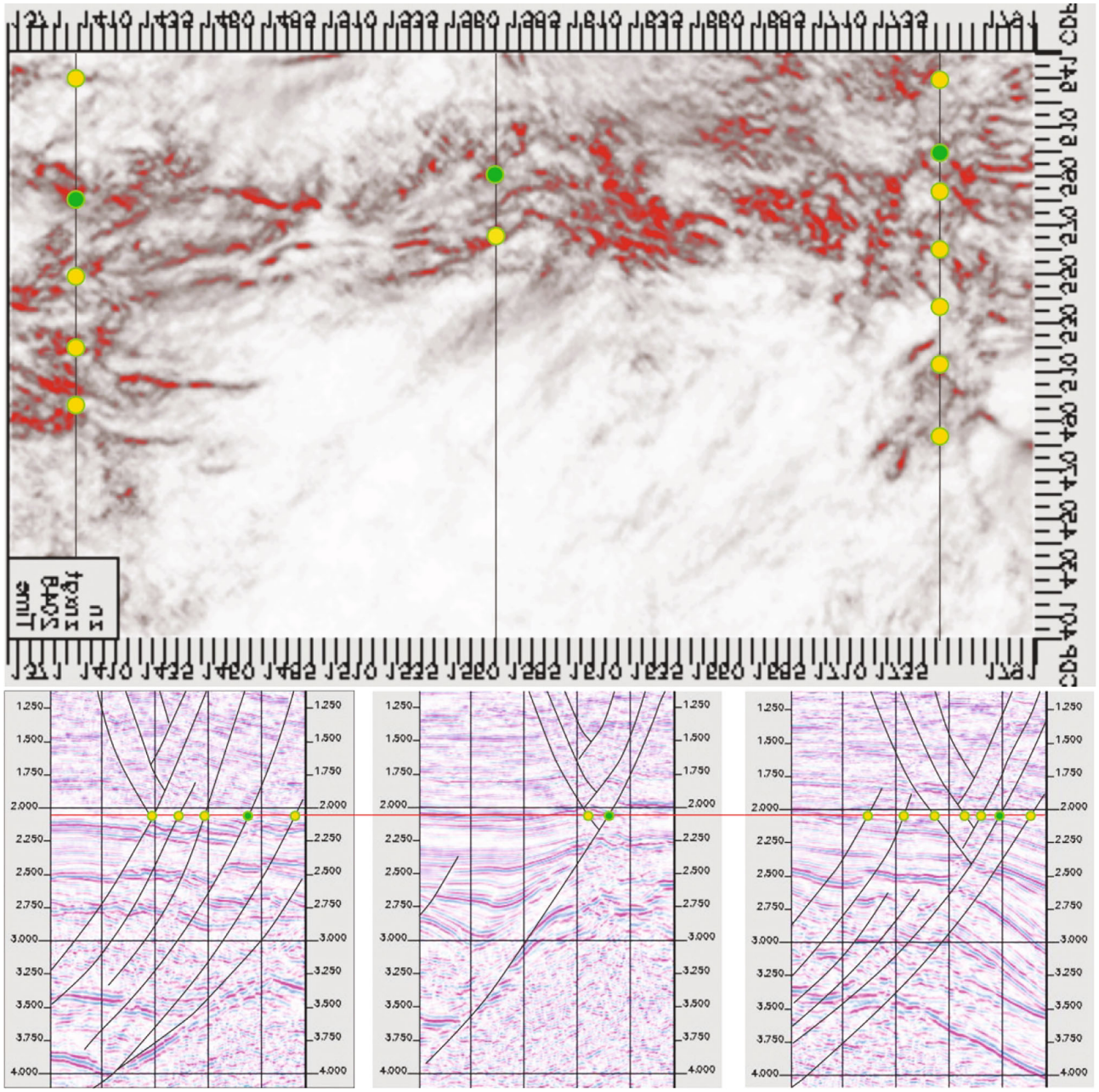

Figure 2: Fault interpretation on coherent slice and seismic time slices.

Table 1: Major fault elements of the western part.

Fault	Fault strike	Dip directions	Fault dip	Fault displacement (m)	Extended length (km)	Section shape
F1	NEE	S	35-70	500	>8	Listric
F2	NEE	N	45-60	200-300	4	Platelike
F3	EW	S	40-50	300-400	>8	Listric
F7	NWW	S	40-50	100-200	3	Listric
F8	NEE	S	45-60	100-200	2.5	Platelike
F9	NEE	N	45-60	100-200	2.5	Platelike
F10	NEE	N	40-50	100	2	Platelike

Table 2: Major fault elements of the middle part.

Fault	Fault strike	Dip directions	Fault dip	Fault displacement (m)	Extended length (km)	Section shape
F1	EW	S	35-70	500	>8	Listric
F2	EW	N	45-60	200-300	4	Platelike
F3	EW	S	40-50	300-400	5	Platelike
F4	NWW	N	40-50	100-200	3	Platelike
F6	EW	N	45-60	100-200	5	Platelike

Table 3: Major fault elements of the eastern part.

Fault	Fault strike	Dip directions	Fault dip	Fault displacement (m)	Extended length (km)	Section shape
F1	NEE	S	35-70	500	>8	Listric
F2	NWW	N	45-60	200-300	4	Platelike
F3	NWW	S	40-50	100-200	>8	Platelike
F5	NEE	S	45-60	100-200	>8	Listric

3.2. Characteristics of Plane Faults and Plane Fault Combination. By tracking the four selected main seismic reflection horizons T6, T2, T1, and T0, the interpretation of plane faults in the main horizons of the study area is finally completed, combined with the explanation of the section fracture and the fracture characteristics displayed in the coherent body slices along the layer. The characteristics of plane fracture combination of main horizons, such as T6, T2, T1, and T0, are shown in Figure 3.

3.2.1. T0 Reflector. The morphologies of the three main fracture planes are mainly arched bending. The fault strikes nearly east-west and arches upwards northward in the middle of the fault zone. The relationship of the plane combinations is a parallel arrangement. The secondary faults strike nearly northwest-west, and most of them are linear, and some of them are curved. The strikes between the secondary faults are nearly parallel, and they are obliquely intersecting with the main faults, which mostly occur in the bending deformation parts of the main faults. The overall fracture pattern of the T0 reflector is shown as a grid-like combination (Figure 3).

3.2.2. T1 Reflector. Fractures gradually decreased in the middle part, and the main fracture form was still arched. The secondary faults that are opposite to the main fault have the same overall trend as the main fault, which is a parallel combination. There are secondary faults on both sides of the fault zone, and secondary small faults develop at the eastern end of the antithetic fault, which intersect with a small angle and parallel to the Zhuangnan fault. There are many small south-dipping faults in the south of the antithetic fault, all of which have the same trend as the Zhuangnan fault, which are linear and parallel combinations. In the western part of the fault zone, there exist six secondary faults with curved shapes and the same trend. The two small faults in the southernmost area extend shorter, and the two faults have an echelon-like arrangement. The T1 reflector fault system appears as a parallel combination mode as a whole (Figure 4).

3.2.3. T2 Reflector. The width of the main fault, the Zhuangnan fault, gets obviously wider than that of the overlying reflectors T0 and T1, which reflects the slowing downtrend of the slope of the fault zone, and its profile shape turns into a shovel shape. The strike is nearly east-west, and the central part bends northward. The volume of the secondary faults becomes smaller, and the extension length is shortened. They mostly occur in the east and west of the fault zone and parallel to the main fault. There are three secondary faults in the northern part of the main fault, which are not continuous with each other and tend to be in en echelon arrangement. The southern faults are scattered, and two northeast-trending faults in the west are arranged in parallel with a northeast-trending fault in the east. Two secondary faults in the lower part develop in the central-southern and southeastern part of the fault zone, which strike NWW and are arranged in parallel. The secondary fractures of the T2 reflector and the main fault are in parallel combinations. The development positions of the secondary faults are scattered, and the strikes are not all the same: some are en echelon combinations, and some are parallel-type combinations (Figure 5).

3.2.4. T6 Reflector. The fault width of the main fault becomes wider, indicating that the slope of the fault continues to decrease, and the shovel shape of the profile becomes more prominent. The combined relationship between the Zhuangnan fault of the main fault and the secondary fault is more complicated. The western region is mainly a parallel combination mode. The small southern fault end adjacent to the main fault has developed secondary faults, showing the characteristics of stress release at the fault end. A fault, which is derived between the eastern part of the fault zone and the north part of the leading fault, intersects with the main fault at a small angle, gradually extends westward, and parallels to the main fault. Two south-dipping faults have also developed in the north, and their strikes are consistent with the main fault. A secondary fault is derived from the extension direction of the curved part in the middle of the main fault, and a number of divergent small faults develop at the end.

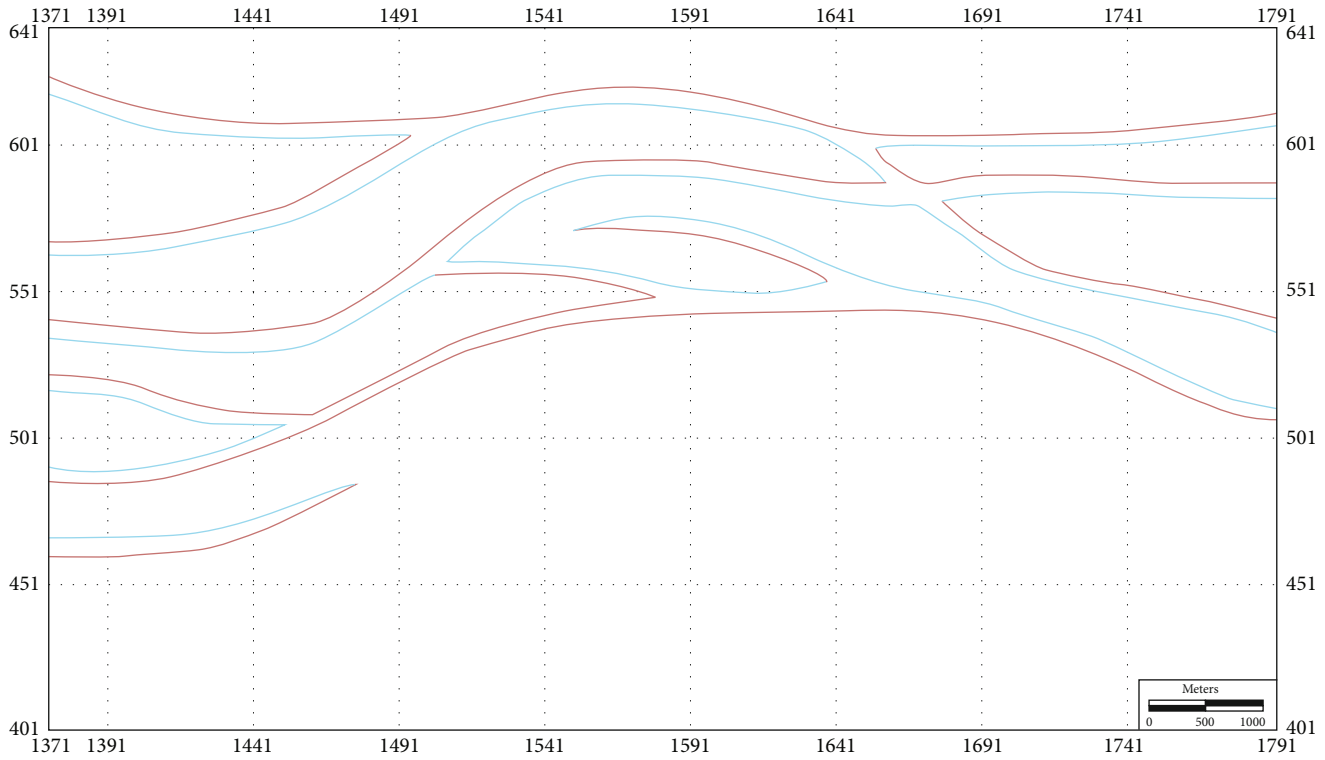

Figure 3: T0 reflector plane fracture system.

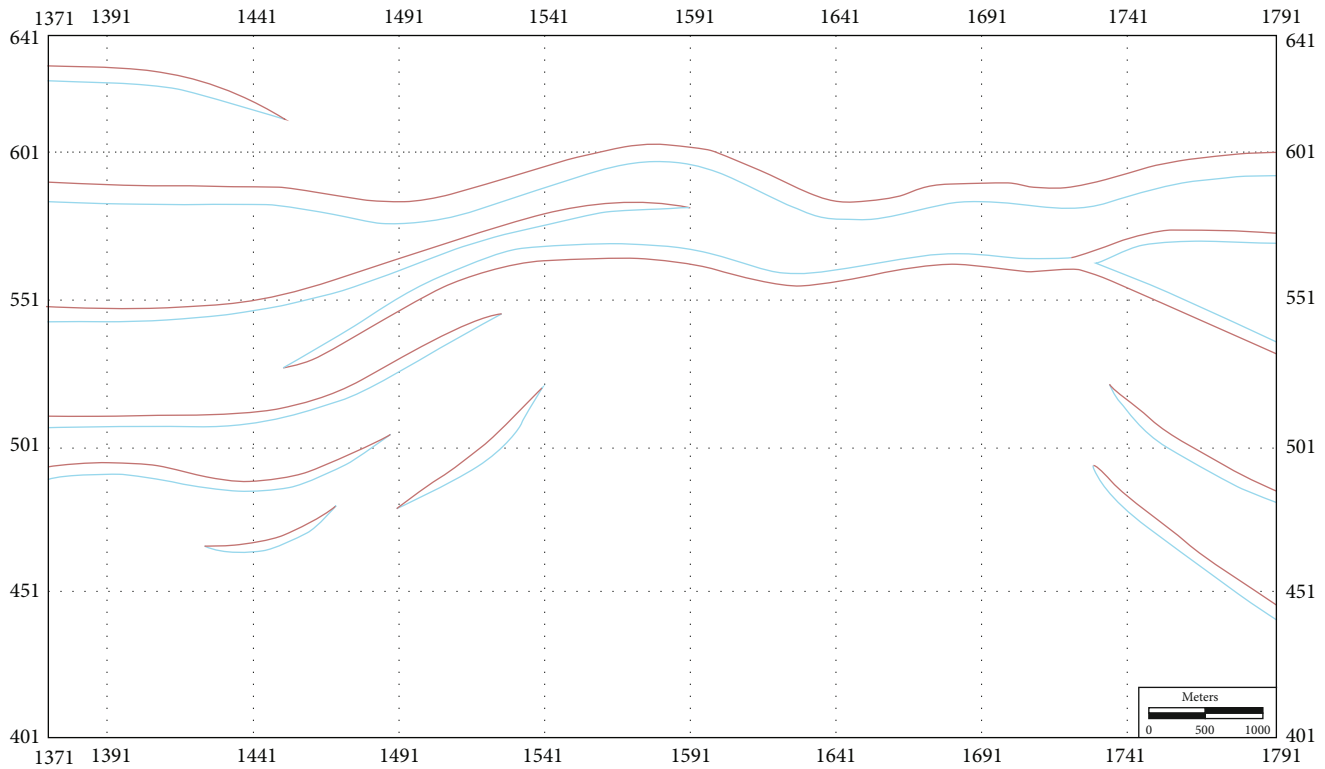

Figure 4: T1 reflector plane fracture system.

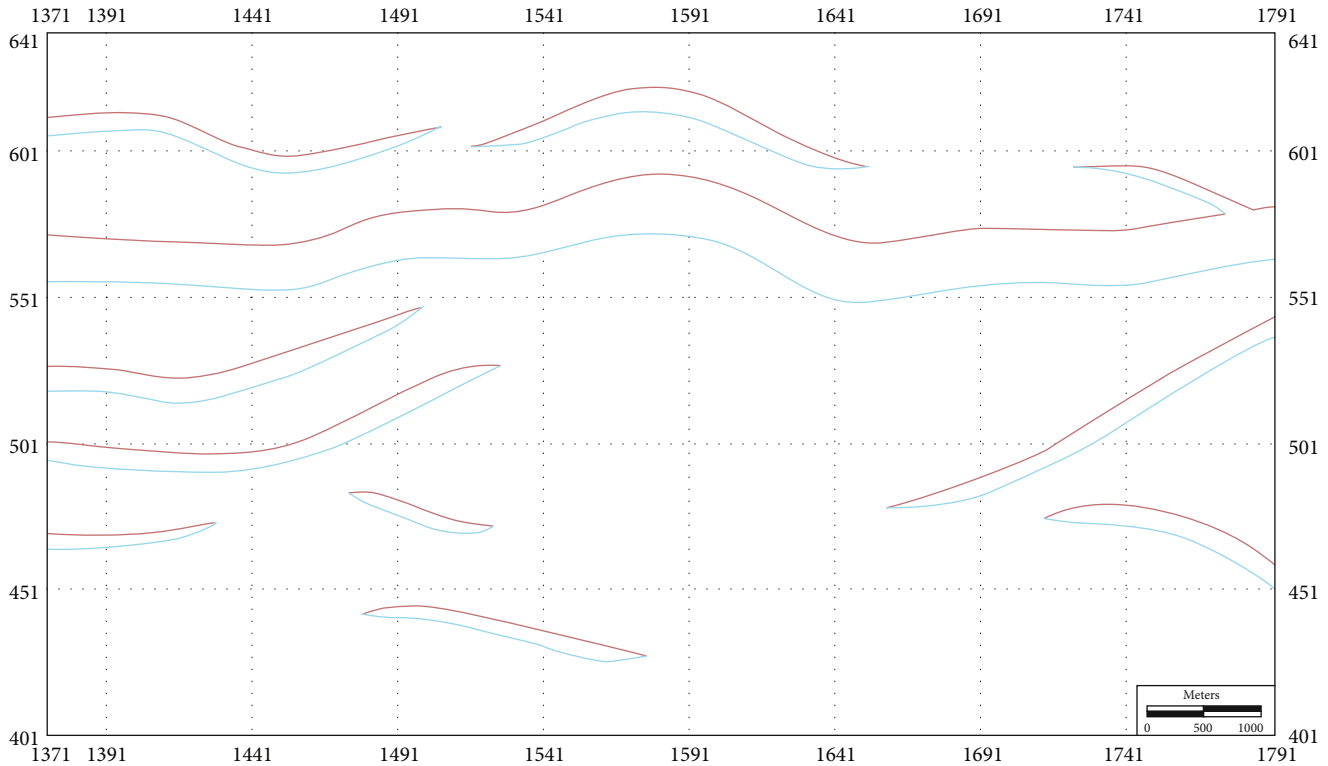

Figure 5: T2 reflector plane fracture system.

On the east side of the extension fault, there exist two secondary faults arranged in parallel with the main fault; on the west side of the extension fault, there are two NEE inclined secondary faults. The T6 reflector layer appears as a parallel combination mode as a whole, and there is a combination mode in the Chinese character "enter" at the tail end of both the main fault and the secondary fault (Figure 6).

After research, the characteristics of the main fault and the secondary fault are summarized as follows:

The characteristics of the main fault: the main fault is the Zhuangnan fault (F1). The Zhuangnan fault, the southern boundary fault of the Zhuangxi buried hill, controls the Meso-Cenozoic sedimentary, plays a role in connecting the tertiary oil source and the buried hill reservoir, and is of great significance to the accumulation of the Zhuangxi buried hill. From the data collected and processed, it is observed that the fault displacement from top to bottom in the study area gradually grows. According to the observation of the extension of the fault from the seismic profiles, the shovel shape of the fault in the Zhuangnan buried hill site has gradually steepened, which may be one reason for the increase in the fault displacement. However, in the upper part of the fault zone, there are multiple secondary faults, and the fault tendency is basically the same. There are three main faults in the same direction (F3, F5, and F7) associated with the Zhuangnan fault. In the seismic profiles, the four faults are equally spaced and arranged in parallel. The F3 fault has a longer extension distance, which is parallel to the Zhuangnan fault. The F5 fault develops in the eastern and western sections of the Zhuangnan fault zone, but its western side intersects with the antithetic fault F2, and the eastern section intersects with F3, the same direction fault. The F7 fault develops in the west wing of the Zhuangnan fault zone with a shorter extension distance and intersects with the main fault. Compared with the development of faults in other depth ranges, the three main faults mostly concentrate on the eastern and western edges of the Zhuangnan fault zone, and the central parts do not develop or only extend to the basement fault, and some of the faults do not cut through the overlying strata.

Characteristics of secondary faults: in summary of the characteristics of the seismic reflection profiles of each segment of the faults, the most important antithetic secondary fault is the F2 fault. The antithetic secondary faults mainly develop on the top reflector of Ed3, which can cut through the Guantao formation. When it comes to the shallow part, the amount of secondary faults gradually becomes larger and divergent. The cross-sectional characteristics of the secondary faults such as F2, F4, and F6 are shown as a step-like combination. In the plane combinations, the F4 and F6 faults extend for a short distance, and they intersect in a plume shape along the bending tangent of the F2 fault. The combination relationship between the secondary fault and the main fault is mainly the "y" shape combination and the reverse "y" shape combination; the plane combinations mainly include parallel stepped combination and grid-like interweaving (Figure 7).

By analyzing the combined patterns in space of Zhuangnan fault zone, the morphology of the Zhuangnan fault zone is characterized by gentle at the bottom and steep at the top, showing the characteristics of listric fault. The lower flat area

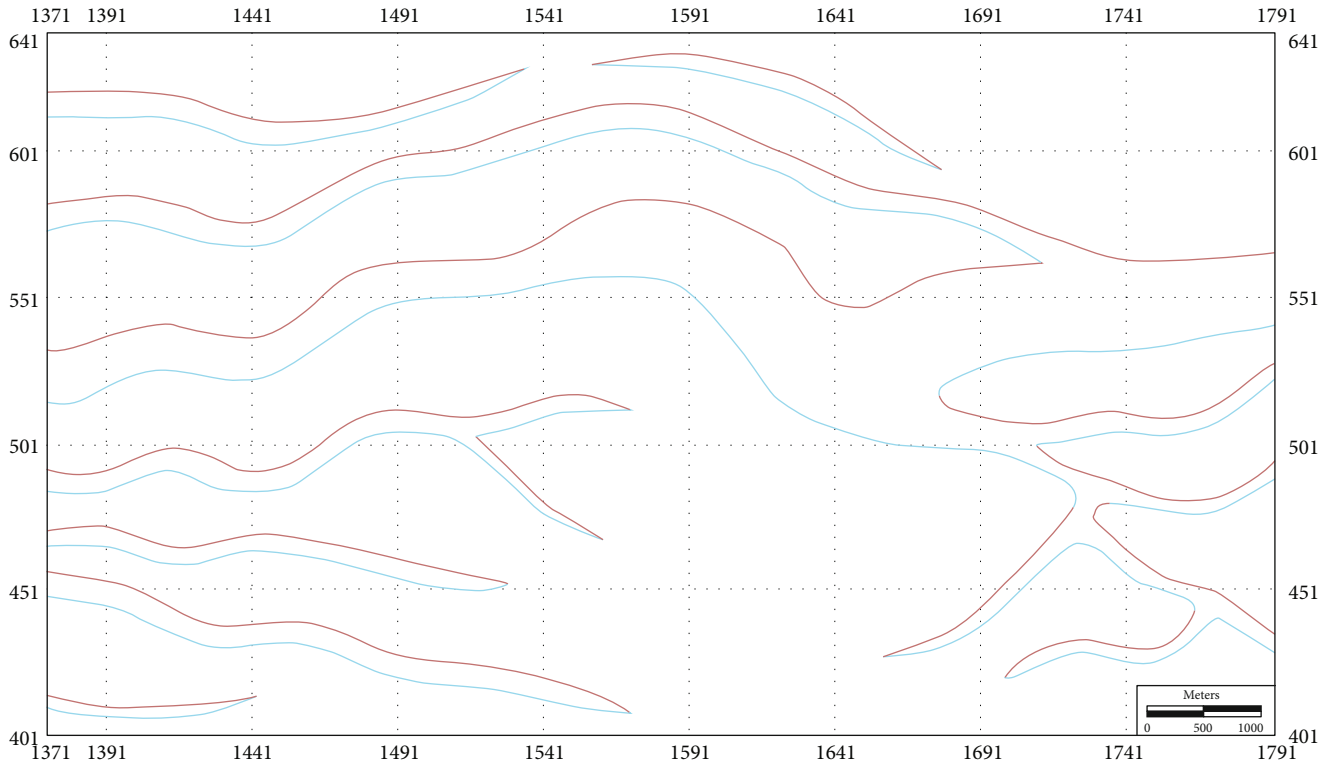

Figure 6: T6 reflector plane fracture system.

of the listric fault has experienced strike-slip shear. Secondary faults located in shallow layers are more developed, which is the result of equilibrium stress release. The plane combination structure styles are as follows: feather row, horsetail, grid, and diagonal. The Zhuangnan fault zone had the characteristics of more active faults developed on both west and east parts of the fault zone than the middle part of the fault zone. The faults developed in the middle part line up in parallel. This feature indicates that the Zhuangnan fault zone is greatly influenced by the adjacent faults on both sides and gradually extends to the middle part of the fault zone, so the middle part of the Zhuangnan fault zone has relatively little influence.

3.3. Structural Style Research. American geologists Harding et al. (1979) and Lowell (1985) did systematic studies on structural styles and believe that structural styles refer to the overall characteristics of related structures with close ties in section morphology, plane distribution, arrangement, and stress mechanism and are a combination of structural deformation under the same stress environment, which is an organic combination of multiple related structures.

According to the morphology of the faults and the combination modes, the following five structural styles under the action of stress are summarized: extensional structural style, extension-strike-slip structural style, strike-slip structural style, extrusion-strike-slip structural style, and extrusion structural style. According to the main fault properties, geometric forms, and combination styles of the Zhuangnan fault zone, it is believed that there are two structural styles in the Zhuangnan fault zone: extensional structural styles.

There are two main types of morphology for the Zhuangnan fault section: plate type (flat type) and shovel type. The main fault section of Zhuangnan is shovel type—-the slope of the upper fault is steeper, and the lower part is slower. Other secondary and associated main faults are all planar. With the gradual increase in the degree of fault evolution, the fault plane generally evolves from the plate type to the shovel type and then to the sloping type. Affected by the characteristics of the near east-west trend of the Zhuangnan fault zone, the combination modes of the profile, mainly stepped fault combination and y-shaped fault combination, can be well observed in the north-south line profile of the Zhuangnan fault zone. The y-shaped fault is mainly composed of the Zhuangnan main fault and its southern secondary faults, which reflect the combined type of growth faults. Under the influence of the extension of the Zhuangnan fault, the hanging wall flexed. Stratum combination styles mainly include graben combination and step combination.

In the plane structure style, the Zhuangnan fault zone mainly strikes in EW direction, and the fault zone generally bends northward in the central area. Its plane geometry is generally arched, and the local forms mainly include linear, arc, and "S" curved type. Through the study of structural characteristics, it is concluded that the Zhuangnan fault zone has the structural characteristics of east and west segmentation. This feature is of great significance to the study of dynamic mechanisms, and it is very likely to represent the different stages of fracture reformation on both sides. The arched bending shape in the middle of the Zhuangnan fault zone is very special, which further reflects the difference in stress caused by the development of faults on both sides of

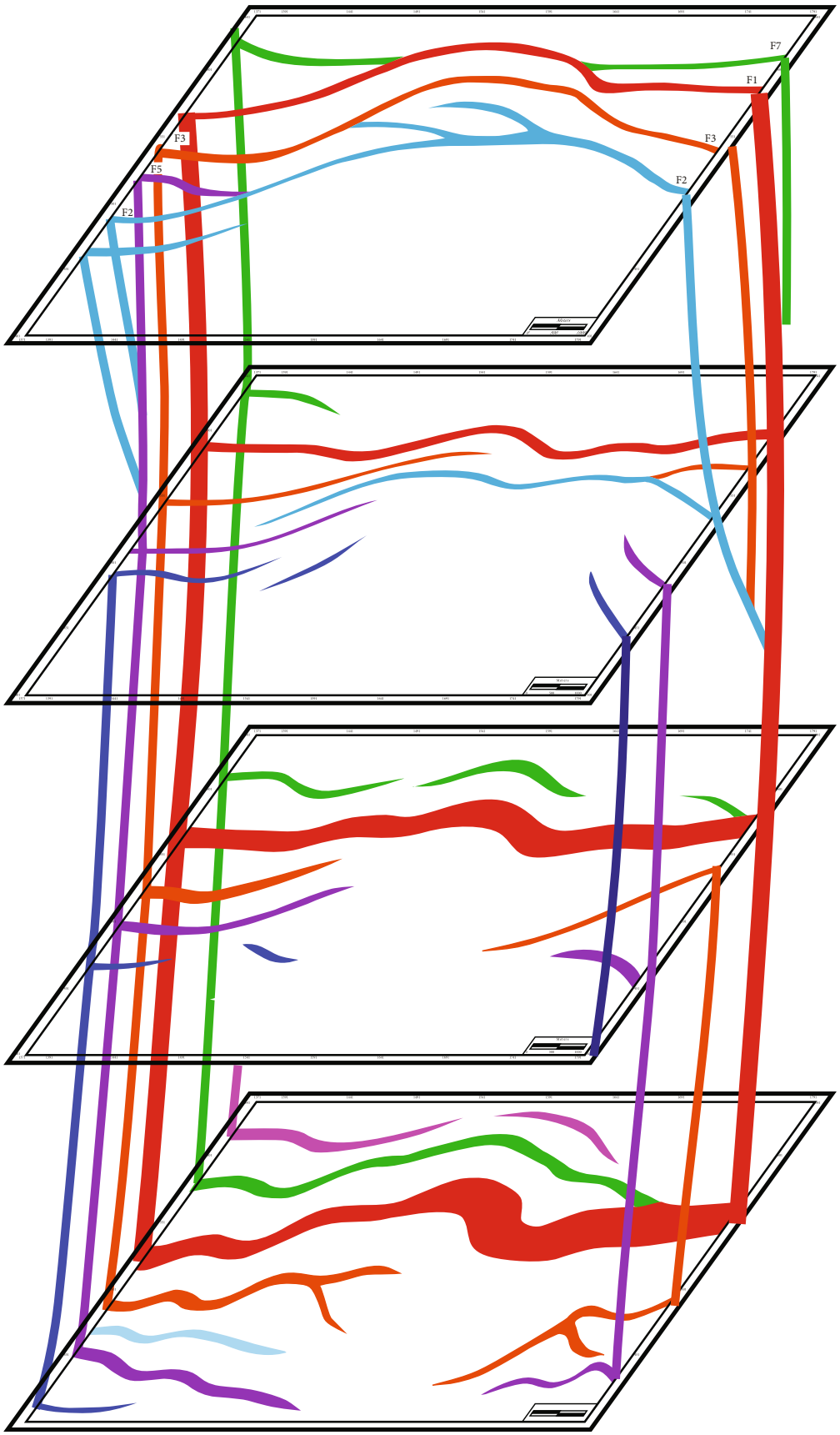

Figure 7: Combined patterns in space of Zhuangnan fault zone.

the east and west and is balanced by the bending deformation of the middle of the fault. This arched shape is an important structural phenomenon that adjusts the structural balance.

The plane combination structure styles of the Zhuangnan fault zone mainly include feather row, horsetail, grid, diagonal, and parallel style (Figure 8). Among them, the first three combined styles mainly appear in secondary fractures. Actually, the parallel combination mode and the oblique combination mode are the most important. The parallel combination model not only appears in secondary faults but also exists in the combination of the main secondary faults and the Zhuangnan main fault.Main faults through the Zhuangnan fault zone have a horizontally stretching distance. They are arranged parallel to each other and have arches bending in the middle part. There are also have the feather row combination which can reflect the strike-slip characteristics. The secondary faults and induced structures are located at the end of the main fault, and the plane combination structure styles are feather row, horsetail, grid, and diagonal (Figure 9). These combination structure characteristics are also an important basis for dividing Zhuangnan fault zone into three parts.

3.4. Planar Fault Assemblage. Three breaking with near E-W strike through the Zhuangnan fault zone have a horizontally stretching distance. They are arranged parallel to each other and have arches bending in the middle part.

Zhuangnan fault (F1) is the most important fault as the southern boundary fault of Zhuangxi buried hill and is also an important oil-controlling fault. From the collection and processing of data, the cause of Zhuangnan fault throw increasing from bottom to top was identified. It is because the dip directions of Zhuangnan fault are steeper above Zhuangxi buried hill.

Four synthetic faults are associated with Zhuangnan fault. They are F2, F3, F9, and F10. They are arranged parallel to each other and evenly spaced. In those four faults, F2 and F3 faults have a longer horizontally stretching distance than F9 and F10 faults. F9 and F10 faults are mainly distributed in the west area of the Zhuangnan fault zone.

Except for the associated faults, many secondary fractures derived from F1 fault and F2 fault were developed. The secondary fractures derived from F1 fault extended along the tangent to the bend deformation occurring on the middle part of Zhuangnan fault zone (F5 tangent to the main fault along the east and F7 tangent to the main fault along the west). And the "入" Chinese character form fault array was shaped with Zhuangnan fault. Three secondary fractures derived from F2 fault are developed between F2 and F3. They are arranged in echelon to each other and evenly spaced. The secondary fractures join with the F2 fault in bipenniform. The order of these secondary fractures is F6 to F4 and then F8 from east to west (Figure 2).

Two sets of faults provide the condition of shelter for hydrocarbon accumulation. The "入" Chinese character form fault array promoted formation of fault screened structure types of favorable traps from the hydrocarbon accumulation perspective. A large structural trap from the south of F2 fault is made up of buried hill draping structural belt and a sealing fault cutting the draping anticline (Figure 10).

The analysis of the geometrical characteristics of Zhuangnan fault zone leads out the following rule: the structural pattern of Zhuangnan fault zone is normal fault assemblage. Zhuangnan fault zone has two main section structure patterns, stair-step shape structure pattern and composite "y" character form structure pattern. Parallel is the main plane structure pattern; the bipenniform structure pattern characterized by strike-slip is the important supplement plane structure pattern. The evolution of Zhuangnan fault zone is under the extensional and shear stress field environment.

We need an in-depth study of geological evolution and dynamics of Zhuangnan fault zone on the basis of geometrical characteristic study.

4. Tectonic Evolution and Regional Dynamics

Through the structural interpretation and analysis of the section, the structural style of the Zhuangnan fault zone is discussed: the fault type of the Zhuangnan fault zone is mainly a combination of normal faults, and the structural style of the section is mainly a combination of stepped faults and "y"-shaped faults. The plane structure is mainly parallel, and there are also diagonal combinations that can reflect the characteristics of strike-slip. The main stress characteristics of the overall structural style are tensile stress and shear stress. As a result of the experience of superposition and reformation of multiperiod tectonic movements, the structural style of the Zhuangnan fault zone is complicated. The Zhuangnan fault zone has experienced three stages of tectonic movement and two stages of tectonic transformation. The three phases of tectonic movement are Indosinian movement, Yanshan movement, and Himalayan movement. The two tectonic transition stages are Late Indosinian-Early Yanshan, corresponding to the Middle Triassic-Jurassic-Early Cretaceous, the stress field transforms from compression to extension; Late Yanshan-Early Himalayan geology chronologically corresponds to the Late Cretaceous-Paleo-Modern, the stress field transforms from left-handed stress to right-handed stress [46-51]. When the tectonic transition periods of the two fault zones are compared, certain inheritance and transformation characteristics can be found between the two. It is of important guiding significance for the study of the formation mechanism of the Zhuangnan fault zone to make full use of this feature.

The study of regional dynamic mechanism helps to get a clear understanding of the evolution background of the Zhuangnan fault zone, which is of great significance for our accurate understanding of the structural characteristics of the Zhuangnan fault zone, which are always inherited and innovative. In the study of the structural characteristics of the Zhuangnan fault zone, it is shown that the Zhuangnan fault zone has the characteristics of a three-segment distribution in the east, middle, and west segments. The east and west segments have similar fracture characteristics and are more complex than the middle segment. These features all reflect its important characteristics as a regulating fault,

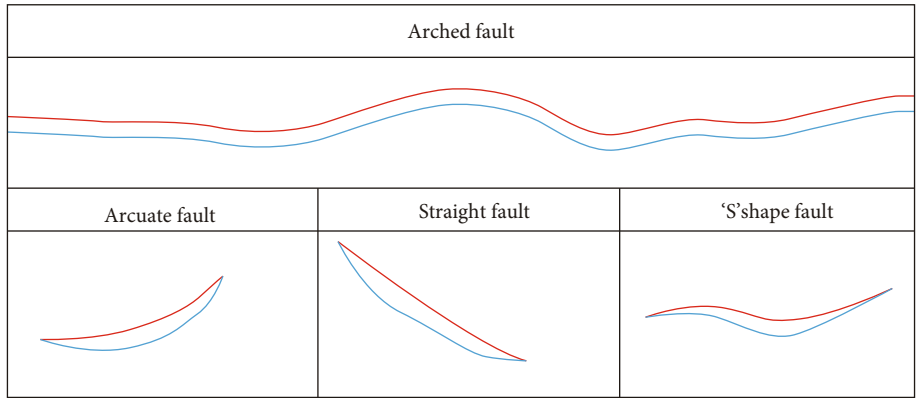

Figure 8: Four types of plane faults in Zhuangnan fault zone.

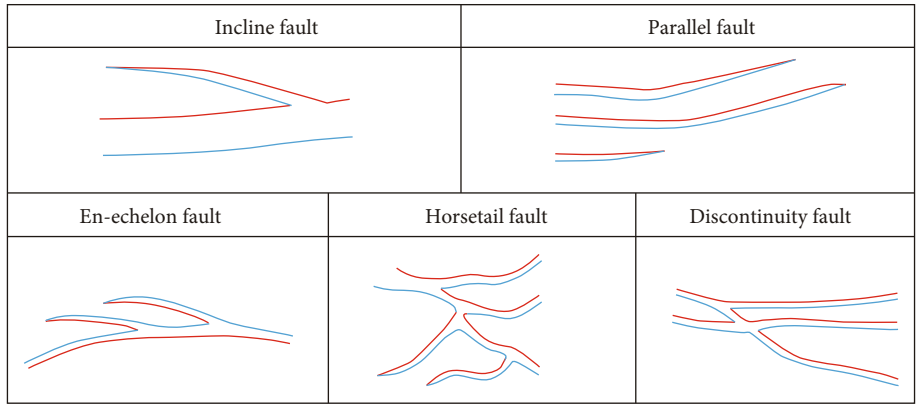

Figure 9: Five types of plane combination structure in Zhuangnan fault zone.

which is significantly affected by the main faults on the east and west sides and has a noteworthy reforming effect on the faults on both sides.

First, calculating and analyzing the activity of the main faults on the east and west sides of the Zhuangnan fault zone contribute to the study of the inheritance relationship between faults. The west side of the Zhuangnan fault zone is mainly the NNE-trending Chengdong fault, and the two main faults on the west side are the NEE-trending fault, the Changdi fault, and the NW-trending fault, the No. 5 pile fault.

Zhuangnan fault zone is an important west-east strike structural belt of Zhanhua sag. The geological evolution and dynamics of it are closely related to the evolution and dynamics of Zhanhua sag. The activities of Tan-Lu fault zone have a significant impact on the east of Zhanhua sag.

The extending direction of faults in Zhuangnan fault zone is consistent with the strike of major faults of the western branches of Tan-Lu fault zone and Lai-xi fault. The strike-slip structural style occurs vertically as echelon faults in the east of Zhuanghua sag like Changdi fault, Gudong fault, and Kendong fault and faults in the west like Chengdong fault, Yidong fault, and Yinan fault. Fault strike is NNE or nearly NE. Those faults controlled the distribution of Meso-Cenozoic strata and the development of the tectonic. Zhuangnan fault zone is located between Changdi fault and Chongdong fault. Fault strike is EW. Zhuangnan fault zone is the accommodation zone with other faults which strike is EW, nearly NE, and NW in Zhuanghua sag. Zhuangnan fault zone has the characteristics of longer horizontally stretching distance, large fault throw, and long active time whose active lives covered the period from Mesozoic to Neogene, which controls the sedimentation, tectonic evolution, and oil-gas accumulation in Zhuanhua sag. Geological evolution and dynamics of Zhuangnan fault zone are closely related to the activity of the three boundary faults (Chengdong fault, Changdi fault, and Wuhaozhuang fault).

Zhuangnan fault zone reached Chengdong fault in western Zhanhua sag and joined Changdi fault in eastern Zhanhua sag. Wuhaozhuang fault developed on the southeast part of Zhuangnan fault zone (Figure 11).

In the structural pattern of Zhanhua sag, Wuhaozhuang fault, Guxi fault, and Luoxi fault which fault strike is NW are arranged in echelon to the left row from north to south. These features clearly reflect the left-lateral strike-slip character of Tan-Lu fault zone in the Early Mesozoic. Kendong fault, Changdi fault, and Gudong fault which fault strike is NNE are arranged in echelon to the right row from north to south, reflecting the right-lateral strike-slip character of Tan-Lu fault zone in the Late Mesozoic. The stress system converted from left-lateral strike-slip to right-lateral strike-slip during the Mesozoic. The changes of stress in different

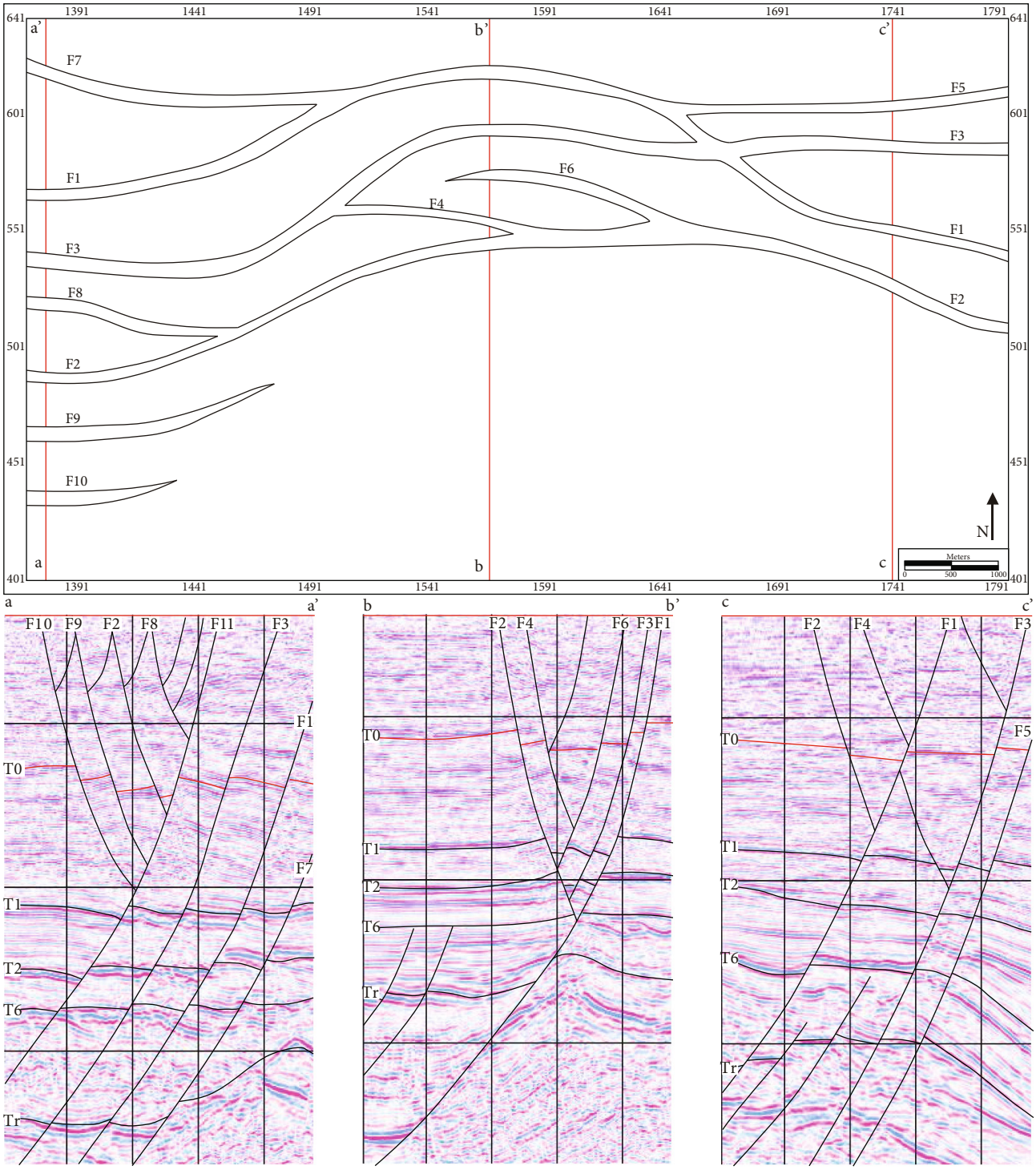

Figure 10: Fault combination styles in plain and section of T0 reflection horizon.

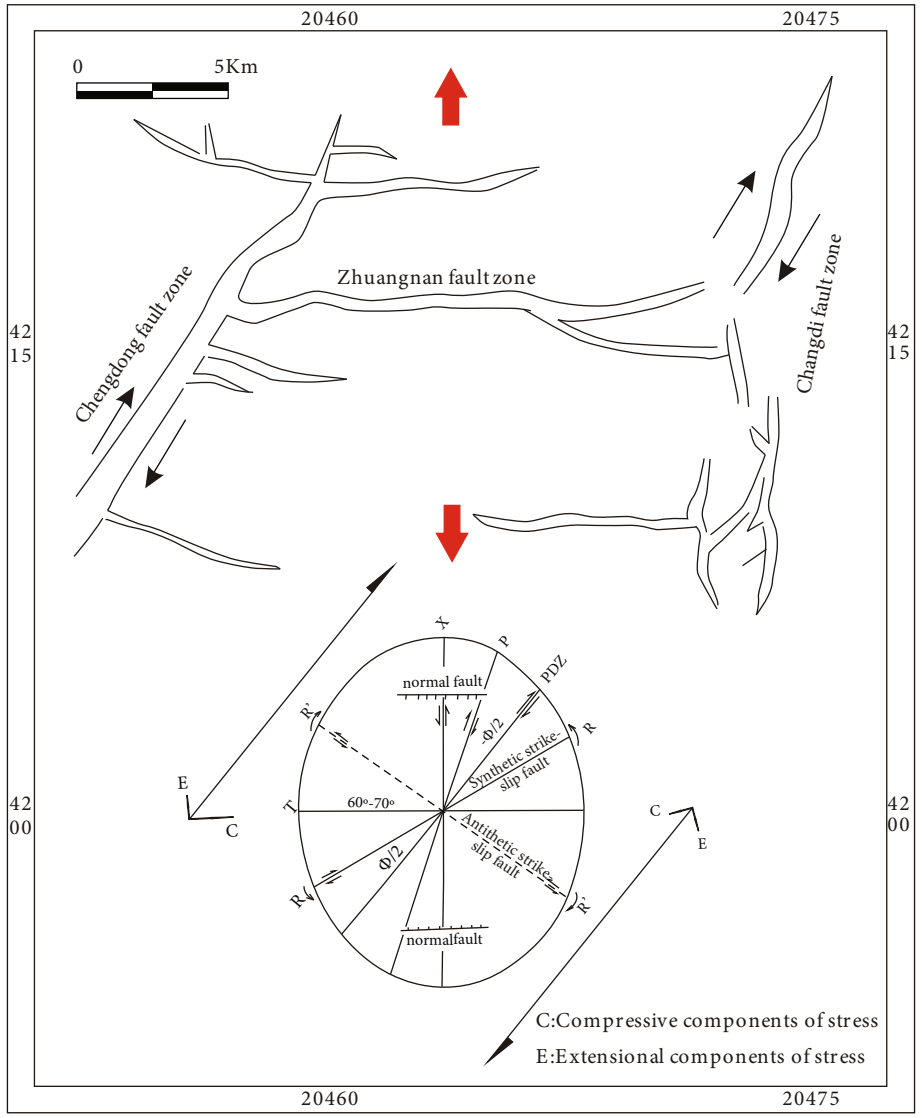

Figure 11: Tectonic stress field of Zhuangnan fault zone.

geologic periods created complex superimposed structures and form the present fracture systems in Zhuangnan fault zone.

5. Geological Evolution and Dynamics of Zhuangnan Fault Zone

Based on the analysis of the tectonic evolution and regional dynamic background, the geological evolution and dynamics of Zhuangnan fault zone in Zhanhua sag need further discussion and clarification.

The geometry characteristics of Zhuangnan fault zone were systematically investigated, and the results indicated that Zhuangnan fault zone has three-piece planar characterization (eastern part, middle part, and western part). The structural feature of the eastern part and western part is more complex than the middle part.

The east and west parts of the Zhuangnan fault zone are affected by different faults, and their activity is different. The faults in the middle part are the difference of fracture activity intensity between the two ends of the balance; bending deformation occurs, forming a special adjustment structure. The special arched and curved structure of the Zhuangnan fault zone reflects the process of the stress gradually transferring to the interior in the eastern and western sections.

First, it is aimed at the definitude inheritance relationship of faults in Zhuangnan fault zone by analyzing and calculating the activity of main faults developed in the eastern part and the western part.

West Zhuangnan fault zone reached Chengdong fault which fault strike is NNE. Data from moving velocity of both faults show that the activity of Zhuangnan fault was consistent with Chengdong fault.

There were two peak-activity periods of the two faults. They were the sedimentary period of the third member of Shahejie Formation and the sedimentary period of the first member of Shahejie Formation. The first peak-activity period of Zhuangnan fault zone was a bit later than Chengdong fault. The second peak-activity period of the two faults is quite satisfactory.

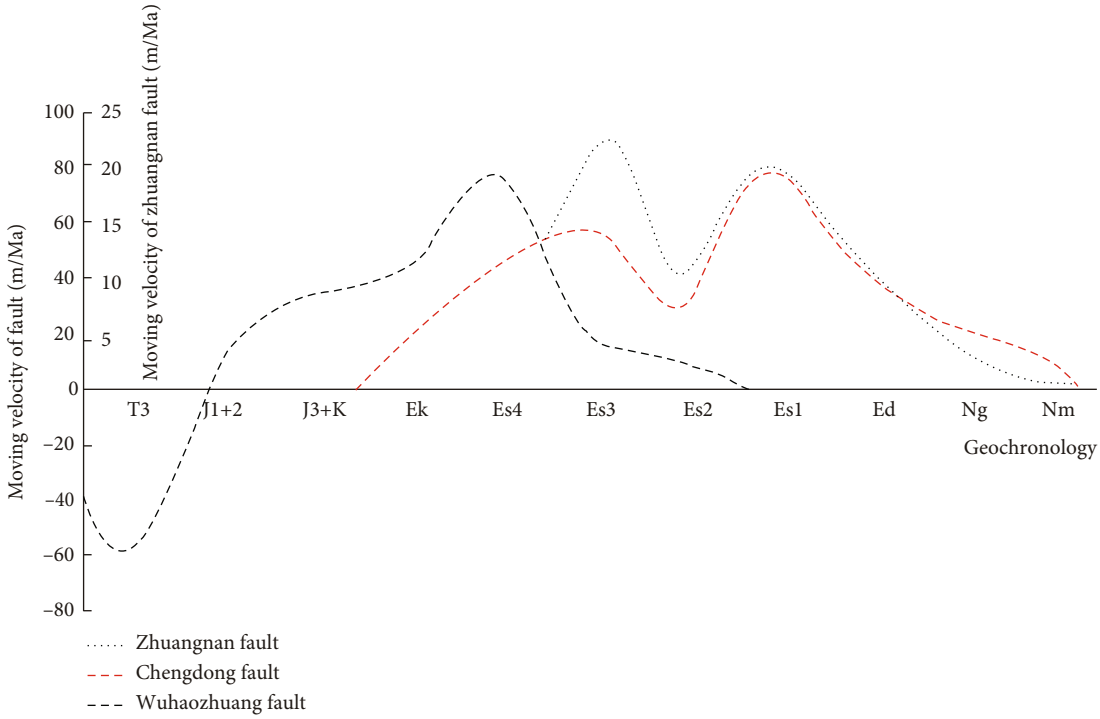

Figure 12: Activity of Zhuangnan fault, Chengnan fault, and Wuhaozhuang fault.

The active time of Chengdong fault is longer than that of Zhuangnan fault since the Late Cretaceous Period to the sedimentary period of Minghuazhen Formation. The active time of Zhuangnan fault is since the middle sedimentary period of the fourth member of Shahejie Formation to the sedimentary period of Minghuazhen Formation. When the active time of Chengdong fault reaches the first peak, Zhuangnan fault has started to develop.

From the sedimentary period of the third member of Shahejie Formation, the moving velocity of both faults is quite satisfactory. These indicate that the activity of Chengdong fault is the most important direct factor in the activity of West Zhuangnan fault zone. Meanwhile, Zhuangnan fault plays a great role in the reconstruction of Chengdong fault.

East Zhuangnan fault zone reached two faults, Changdi fault which fault strike is NNE and Wuhaozhuang fault which fault strike is NW, respectively.

The activity of the two main eastern boundary faults of Zhuangnan fault zone is Changdi fault and Wuhaozhuang fault. The Changdi fault and Wuhaozhuang fault strike nearly south-north. Changdi fault is a representative strike-slip fault zone in the east of Jiyang Depression, which included deep and shallow fault systems. The deep fault system is the main body of Changdi fault. The shallow fault system consisted of NS-trending left-order en echelon faults (Figure 12).

Branching faults developed in the east wall of Changdi fault, which showed the "入" Chinese character form shape combined with the main fault, which was caused by the difference of boundary conditions during horizontal twisting. The eastern part of Zhuangnan fault zone connects with the west side of Changti fault, and the west side of Changti fault develops a fault terrace, which cuts with the east-west strike faults. The Zhuangnan fault developed gradually from east to middle, which is accompanied by intense fault activity. Zhuangnan fault zone as the main east-west strike-slip accommodation structure plays an important regulating role. Therefore, the activity of the Changdi fault plays an important role in controlling the structural development of the Zhuangnan fault zone

The activity characteristics of Wuhaozhuang fault who has long-term activity controls the development of the tectonic framework of Zhuangnan fault zone. From the fourth member of Shahejie Formation to the third member of Shahejie Formation, the activity of Zhuangnan fault was really just started and gradually increased. However, activities of Wuhaozhuang fault have come to the last stage, and large-scale fault activities stop. The structure activity of East Zhuangnan fault zone has been less affected by Wuhaozhuang fault (Figure 4).

Our knowledge of the fault properties of Changdi fault has some disagreements among the experts. At present, the unified understanding of Changdi fault reached is primarily the regional structure evolution. Changdi fault is located in the west Tanlu strike-slip fault zone. Affected and controlled by the strike-slip fault zone, faults are developed. The formation of Changdi fault experienced a complex evolutionary process. Changdi fault is still prominently featured in the characters of strike-slip and extrusion structure despite being reconstructed by NS extension in Cenozoic. The eastern segment of Changdi fault exhibits a complex structure composed of several branches, shaping the "入" Chinese character form fault array with Changdi fault. Structures differ greatly in features between the two sides of Changdi fault.

The western segment of Changdi fault was cut into a series of complex fault noses and fault blocks which fractures are faulted steps on the section by faults of EW fault strike. The differences in trend and margin condition are the main reasons for the different actions in structural belts. Zhuangnan fault zone plays a vital role in balancing the differences of margin condition as the main E-W strike-slip accommodation structure. In turn, Changdi fault makes important effects on the fault evolution of East Zhuangnan fault zone.

6. Conclusions

This paper focuses on the structural formation, evolution, and genetic mechanisms of Zhuangnan fault zone in controlling hydrocarbon migration of unconventional rocks. From three aspects of geometry, kinematics, and dynamics in conclusion, below is a summary of what we learned through this study.

(1) Zhuangnan fault zone has two functions as the main E-W strike-slip accommodation structure. That is, on the one hand, Zhuangnan fault zone inherited the rules of development of regional tectonic. On the other hand, the present structure framework of Zhanhua sag was reconstructed by Zhuangnan fault zone

(2) In geometry, the cross-sectional fracture forms of the Zhuangnan fault zone are mainly shovel type (Zhuangnan main fault) and plate type, generating four types of combination—"y" type combination, compound "y" type combination, stepped combination, and horst combination. The plane fracture forms include arched bending (Zhuangnan main fault), straight, curved, and "S" curved. The plane combination styles mainly include feather row, horsetail, grid, diagonal, and parallel

(3) Zhuangnan fault zone has a three-stage distribution structure on the plane: the eastern and western sections have a large number of faults, and the spreading range is large; the middle section has a small number of faults, and the development position is concentrated. The structure characteristic of the east and west parts of Zhuangnan fault zone is more complex than the structure characteristic of the middle part of Zhuangnan fault zone

(4) Based on the plane and section structural styles of Zhuangnan fault zone and the analysis of dynamic evolution, it is found that Zhuangnan fault zone has a law of inheritance development and evolution between deep and shallow fault systems. In space, it has the bottom-up characteristics of complex-simple-complex evolution

(5) Through the tectonic evolution and dynamic research of regional and Zhuangnan fault zone, it was found that Zhuangnan fault zone is manipulated by the activity of the three main boundary faults of Zhanhua sag (Changdi fault, Wuhaozhuang fault, and Chengdong fault). The offsets of the three boundary faults gradually decrease into the accommodation zone, so the tectonic framework of Middle Zhuangnan fault zone has been less affected by boundary faults. Zhuangnan fault is the only fault in dipping S which cut the overlying formations and basement strata. The arch bending in the middle part of Zhuangnan fault zone is to balance the significant differences between the activity intensity of the two main boundary faults of Zhanhua sag

Data Availability

There is no data to support the findings of this study.

Conflicts of Interest

The authors declare that they have no known competing financial interests or personal relationships that could have appeared to influence the work reported in this paper.

References

[1] T. Harding and J. D. Lowell, "Structural styles, their plate-tectonic habitats, and hydrocarbon traps in petroleum provinces," *AAPG bulletin*, vol. 63, no. 7, pp. 1016–1058, 1979.

[2] J. D. Lowell, "Structural Styles in Petroleum Exploration," *OGCI Publications, Tulsa*, vol. 1985, pp. 1–43, 1985.

[3] W. He and Z. Liu, "Numerical simulation of formation damage by drilling fluid in low permeability sandstone reservoirs," *Journal of Petroleum Exploration and Production*, vol. 11, no. 4, pp. 1865–1871, 2021.

[4] Y. Wang, "Geological characteristics of hydrocarbon migration along a strike fault: a case study of Shaojia Fault, Zhanhua Sag, Jiyang Depression," *Petroleum Geology & Experiment*, vol. 40, no. 5, pp. 684–690, 2018.

[5] T. Zhang, F. Javadpour, Y. Yin, and X. Li, "Upscaling water flow in composite nanoporous shale matrix using lattice Boltzmann method," *Water Resources Research*, vol. 56, article e2019WR026007, 2020.

[6] D. Dong, L. Qiu, Y. Ma et al., "Control of tectonics on sedimentation of sandstone and process of sediment filling in multi-fault lacustrine basins: a case study on the Eocene in eastern Zhanhua Sag, Jiyang Depression in Bohai Bay Basin," *Oil and Gas Geology*, vol. 39, pp. 653–663, 2018.

[7] X. Liu, Y. Zhuang, L. Liang, and J. Xiong, "Investigation on the influence of water-shale interaction on stress sensitivity of organic-rich shale," *Geofluids*, vol. 2019, Article ID 2598727, 13 pages, 2019.

[8] X. Luo, "Structural evolution and 'golden zones' of hydrocarbon exploration distibution in Gubei sub-sag," *Petroleum Geology and Engineering*, vol. 33, no. 2, pp. 1–5, 2019.

[9] G. Chen, Z. Qin, G. Zhang, and T. Li, "Characteristics and mechanical analysis of the collapsed accumulation body in the underground fault fracture zone," *Energy Sources Part A Recovery Utilization and Environmental Effects*, vol. 3, pp. 1–22, 2019.

[10] L. Yang, H. Tang, and D. Wang, "Structural styles and mechanism of oblique rifting: take Zhanhua Sag in Jiyang Depression for example," *Geological Review*, vol. 67, no. Supp. 1, pp. 129-130, 2021.

[11] A. A. Henza, M. O. Withjack, and R. W. Schlische, "Normal-fault development during two phases of non-coaxial extension: an experimental study," *Journal of Structural Geology*, vol. 32, no. 11, pp. 1656–1667, 2009.

[12] Y. Meng, X. Li, M. Jiang, D. Feng, T. Zhang, and Z. Zhang, "Experimental research on three dimensional flow characteristics of multiple horizontal fractures utilizing an innovative experiment apparatus," *Arabian Journal of Geosciences*, vol. 11, no. 10, p. 243, 2018.

[13] N. S. Qiu, X. G. Su, Z. Y. Li et al., "The Cenoaoic tectonothermal evolution of depressions along both sides of mid-segment of Tancheng-Lujiang Fault Zone, East China," *Chinese Journal of Geophysics*, vol. 50, no. 5, pp. 1479–1507, 2007.

[14] N. S. Qiu, X. G. Su, Z. Y. Li et al., "The Cenozoic tectonothermal evolution of depressions along both sides of mid-segment of Tancheng-Lujiang Fault Zone, East China," *Chinese Journal of Geophysics*, vol. 50, no. 5, pp. 1309–1320, 2007.

[15] B.-T. Shan, "Geometry of border faults and their control effect on oil and gas accumulation in Tyang Depression," *Special Oil and Gas Reservoirs*, vol. 14, no. 1, p. 19, 2007.

[16] G. Schreurs, R. Hanni, and P. Vock, "Analogue modelling of transfer zones in fold and thrust belts: a 4-D analysis//Schellart W P and Passchier C. Analogue modelling of large-scale tectonic processes," *Journal of the Virtual Ex-plorer*, vol. 7, pp. 43–49, 2002.

[17] B. Xia, X. X. Huang, Z. R. Cai, H. Y. Jia, B. F. Lu, and R. Wang, "Relationship between tectonics and hydrocarbon reservoirs from Indo-Chinese epoch to stage of Yanshan in Jiyang Depression," *Natural Gas Geoscience*, vol. 18, no. 6, pp. 832–837, 2007.

[18] P. L. Li, *The Oil and Gas Geology and Their Exploration in the Terreatrial Faciea Rift-Subaidence Basing (in Chinese)*, Beijing Petroleum Industry Press, 2003.

[19] J. B. Liu, D. J. Yuan, Z. M. Song, B. Li, Y. W. Qu, and J. G. Ren, "Analysis of Cenozoic tectonic evolution and IIS dynamic background of the Jiyang depression," *Geology and Resources*, vol. 26, no. 4, pp. 346–352, 2017.

[20] L. Zhang, Z. P. Wu, W. Li, X. Wu, and H. Jia, "Research on the extensional transfer structures in the Jiyang depression," *Geotectonica et Metallogenia*, vol. 36, no. 2, pp. 24–31, 2012.

[21] H. G. Lao and Q. H. Cheng, "The tectonic evolution of lateral transitional zone in southern Jiyang depression and its hydrocarbon accumulation," *Geological Review*, vol. 58, no. 5, pp. 893–900, 2012.

Hindawi
Geofluids
Volume 2022, Article ID 9539999, 12 pages
https://doi.org/10.1155/2022/9539999

Research Article

Preparation of Oil-Based Foam Gel with Nano-SiO_2 as Foam Stabilizer and Evaluation of Its Performance as a Plugging Agent for Fractured Shale

Daqi Li,[1,2] Fan Li,[1,2] Song Deng,[1,3] Jinhua Liu,[1,2] Yahong Huang,[1,3] and Shuo Yang[1,3]

[1]*Key Laboratory of Shale Oil & Gas Enrichment Mechanism and Effective Development, Beijing 100083, China*
[2]*Sinopec Research Institute of Petroleum Engineering, Beijing 100020, China*
[3]*School of Petroleum Engineering, Changzhou University, Changzhou 213164, China*

Correspondence should be addressed to Song Deng; dengsong@cczu.edu.cn

Received 3 January 2022; Revised 17 February 2022; Accepted 28 February 2022; Published 27 March 2022

Academic Editor: Tao Zhang

The development of natural fracture will lead to lost circulation, which will be likely to cause economic losses and reduce drilling efficiency. In order to solve this problem, an oil-based pressure-bearing foam gel plugging agent for fractured shale was developed. The basic components such as foaming agent, foam stabilizer, and cross-linking agent were optimized and compounded, and the basic formula of the oil-based foam gel system was 0.6%DSFA foaming agent + 0.3%BPMO foaming agent + 0.5%EPDM + 1.5% SBS + 0.05%rigid cross – linking agent (DB) + 0.02%modified SiO_2 nanoparticles. Then, the performance of the oil-based foam gel plugging agent was evaluated through core plugging experiments, and the results showed that the prepared plugging agent had good stability and plugging performance with a plugging rate of about 90%.

1. Introduction

In recent years, as conventional crude oil reserves gradually decrease, the unconventional resources are gaining high demand [1]. Therefore, the shale resources including shale gas, shale oil, and oil shale have attracted attention worldwide [2]. However, during the drilling of shale reservoirs, due to the relatively developed natural fractures of the shale, the problem of lost circulation is serious [3]. Lost circulation refers to the phenomenon that a large amount of drilling fluid leaks into the formation during the drilling process. It is easy to induce wellbore instability and wellbore collapse, blowout, stuck drilling, and other drilling accidents, causing a lot of economic losses and reducing drilling efficiency. This problem deserves much attention in on-site operation, and the use of foam plugging agent is a new and low-cost plugging method [4–9].

The conventional foam plugging agents use water phase as continuous medium. Due to the high density of base fluid, the degree of reduction of system density is limited by objective conditions, especially in some high-pressure well sections that the plugging agent stability is easily affected. Moreover, shale hydration and expansion are likely to occur in low-pressure reservoirs with strong water sensitivity, and the use of water-based foam plugging agents in the oil layer will cause reservoir damage [10, 11]. In addition, conventional foam plugging agents are subject to formation factors, which will shorten their validity period and affect the application of this technology [12].

Polymer gel plugging agent is also one of the most widely used chemical plugging agents in oilfield plugging. It has the advantages of low cost, simple process, and good plugging effect. Foam gel plugging agent combines the advantages of foam plugging agent and gel plugging agent, which uses gel as the continuous phase and gas as the dispersed phase. It is composed of base liquid, polymer components, foaming agents, foam stabilizers, cross-linking agents, etc. The foam gel plugging agent is prepared by dissolving the foaming agent in a polymer solution of polymer and adding a cross-linking agent. The plugging agent preferentially enters the formation with high water saturation, and the foam with liquid as the dispersion medium is first generated in the

formation, and then, the polymer interacts with the cross-linking agent to form a gel. The properties of foam gel are very special. The system exhibits foam behavior before the cross-linking reaction and bulk gel behavior after the cross-linking reaction. Compared with oil-based foam, its continuous external phase is gel; compared with gel, it contains a large amount of uniformly distributed gas in the gel. Therefore, it can not only overcome the shortcomings of general oil-based foams that are easy to burst but also can overcome the shortcomings of poor gel diffusion performance [13–19].

At present, there are many researches on water-based foam gel plugging agents. However, due to the high cost of using oil as the continuous phase and the need to consider factors such as temperature resistance and pressure-bearing capacity, research on oil-based foam gel plugging agents is still lacking. In this paper, the oil-based foam gel plugging agent is studied in order to solve the problem of fractured shale leakage, and a preparation method of oil-based foam gel plugging agent is proposed. The plugging effect, pressure-bearing capacity, and temperature resistance capacity of the prepared loss plugging agent were evaluated.

2. Experimental Materials and Methods

2.1. Experiment Material. The materials used in the experiment were as follows: oil base fluid: diesel and kerosene; foaming agents: sorbitan monostearate (Span 60), sorbitan oleate dehydrated (Span 80), octadecyl trimethyl ammonium bromide (CTMAB), propylene glycol monooleate (BPMO), and DSFA (provided by Beijing Hanqian Technology Co., Ltd.); foam stabilizers: modified SiO_2 nanoparticles, styrene-isoprene-styrene block copolymer (SIS), ethylene-propylene-nonconjugated diene terpolymer (EPDM), and styrene-butadiene block copolymer (SBS); cross-linking agent: diethanolamine (DEA), rigid cross-linking agent (DB), and divinylbenzene (DVB); and shale core (diameter 25 mm and length 50 mm).

2.2. Experimental Methods and Procedures

2.2.1. Foaming Ability and Stability of Foam. The Waring blender method (the device is shown in Figure 1) is the most convenient way to evaluate the performance of foam. The specific method is as follows:

According to different mass concentrations (0.3%, 0.6%, 0.9%, and 1.2%), 5 kinds of foaming agents were foamed in 50 mL oil base liquid at 20°C without adding other substances. The Waring blender was used to stir at a high speed of 8000 r/min for 1 minute, and the stirred foaming agent solution was poured into a 500 mL large graduated cylinder. The initial volume of the foam was read immediately and was recorded as the foaming volume.

A stopwatch was used to measure the time required for the volume of the foam to decay by half and recorded it as the half-life. The comprehensive foaming index (F_q) was used to compare the foaming ability of different foaming agents, and the foaming agent with better foaming effect was screened out.

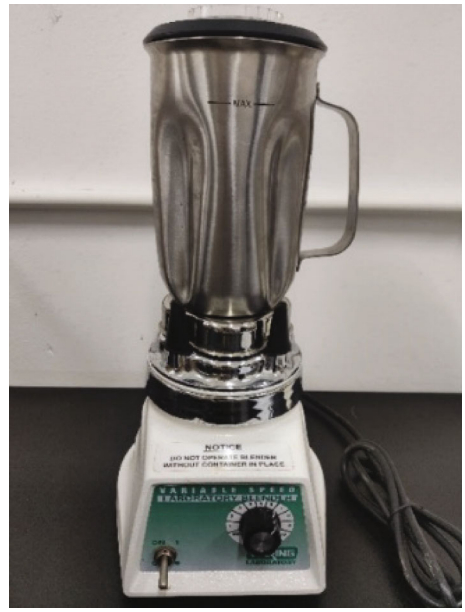

Figure 1: Waring blender.

$$F_q = \frac{3}{4} V_0 t_{1/2}. \quad (1)$$

In the formula, V_0 is the initial foaming volume, $t_{1/2}$ is the half-life of foaming liquid, and the experimental data is recorded in the table below.

2.2.2. Optimization of Foam Stabilizer. Despite of the good foaming capacity of a single foaming agent, its half-life is short; thus, the oil-soluble foam stabilizer was added, which can enhance the intermolecular adsorption strength through the synergistic effect between molecules and greatly improve the foam stability [20, 21].

The principles for screening oil-based foam stabilizers were as follows: (1) It can make the oil base fluid have proper viscosity. (2) The polarity is similar to the foaming agent (nonpolar) to enhance the synergistic effect and promote the interaction of molecules. (3) It is better for the molecule to have multiple nonpolar points to increase the strength of the mask. (4) It is also best to reduce the surface tension of the foam system. In accordance with the screening principle of foam stabilizers, a large number of foam stabilizers were investigated and finally selected: styrene-isoprene-styrene block copolymer (SIS), ethylene-propylene-nonconjugated diene terpolymer (EPDM), and styrene-butadiene block copolymer (SBS).

In addition, many scholars have found that nanoparticles can improve the stability of foam [22–25]. But the unmodified SiO_2 nanoparticles have a large specific surface area and have a tendency to agglomerate, so they have a tendency to precipitate at the bottom, especially for low-viscosity systems, which affects the application of silica. Therefore, the general silica needs to be chemically modified to improve its dispersion stability. For this reason, we used siloxane containing epoxy groups to modify the silica and then used the reactivity of amine groups with epoxy groups

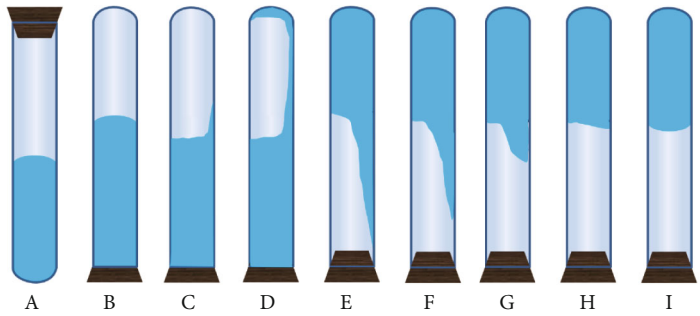

Figure 2: Schematic diagram of gel strength rating.

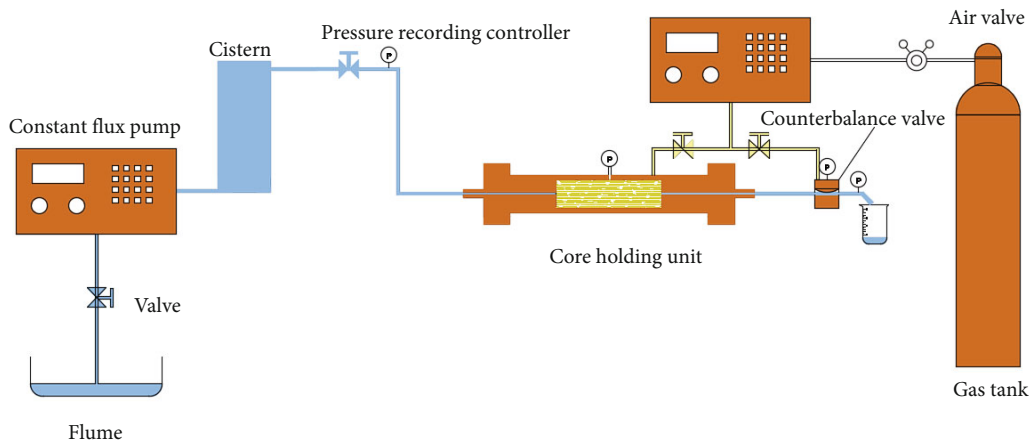

Figure 3: Diagram of the experimental device for core plugging.

for further modification. The amine group and epoxy were modified for the second time, so that the silica surface had long carbon chain functional groups with low surface energy, which can improve the dispersion stability of silica in oily systems.

In this paper, the optimized oil-based foaming agent system was added to 50 mL oil-based liquid, and SIS, EPDM, and SBS (1.0%, 2.0%, and 3.0%) were added in the solution. Its foaming volume and half-life were measured. Low concentration-modified SiO_2 nanoparticles were added into the optimized foam stabilizer system, and its foam stabilizer performance was determined.

2.2.3. Optimization of Gel System. As there is no standard for the evaluation method of gel-forming performance, the empirical method for evaluating gel strength in Figure 2 was used. When the gel strength is D to E, a small amount of gel can slowly flow to the other end when it is turned over, and most of it (greater than 15%) has no fluidity. At 80°C, simulated formation water or distilled water was used to prepare foam gel systems of different formulations, and the gel-forming properties of the system were examined. When the foam gel strength reaches D to E level, the configuration was completed.

The amount of cross-linking agent added will affect the strength of the gel and the gel time. If the amount of cross-linking agent is too high, the degree of cross-linking is too large, which will cause the stretching and rotation of the

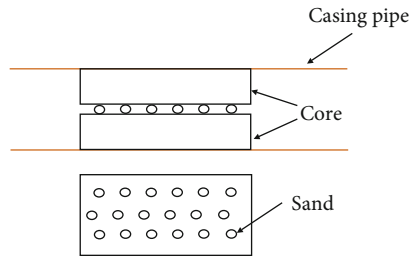

Figure 4: Spatial situation diagram of particle size distribution in the core.

gel molecules to be restricted, and the structure of the gel is likely to be destroyed under the action of external force. When the amount of cross-linking agent added is too low, the various reactive monomers cannot undergo sufficient cross-linking reaction, and the spatial network formed will be large, the elasticity of the product will decrease, and the impact resistance will decrease. The performance of DEA, DB, and DVB three cross-linking agents at different dosages was compared.

2.2.4. Preparation of Oil-Based Foam Gel System. The base fluid of oil-based foam gel must meet the requirements of environmental protection and reservoir protection, and at the same time, it must be economical. Therefore, diesel and kerosene were initially selected as the base fluid. Mix

Table 1: Experimental parameters.

Experiment number	Inflow velocity (mL/s)	Temperature (°C)	Annulus pressure (MPa)	Sand diameter (mm)	Whether to add plugging agent	Core diameter/length(mm)	Porosity (%)	Permeability ($10^{-3}\mu$ m^2)
1	1	80	6	0.850	No	25/50	6.2	1.790
2	1	80	6	0.850	Yes	25/50	6.2	1.790
3	2	80	7	0.850	No	25/50	5.4	0.981
4	2	80	7	0.850	Yes	25/50	5.4	0.981
5	1	80	6	0.425	No	25/50	4.8	0.869
6	1	80	6	0.425	Yes	25/50	4.8	0.869
7	2	80	7	0.425	No	25/50	4.6	0.808
8	2	80	7	0.425	Yes	25/50	4.6	0.808
9	1	80	6	0.180	No	25/50	4.4	0.782
10	1	80	6	0.180	Yes	25/50	4.4	0.782
11	2	80	7	0.180	No	25/50	4.2	0.691
12	2	80	7	0.180	Yes	25/50	4.2	0.691

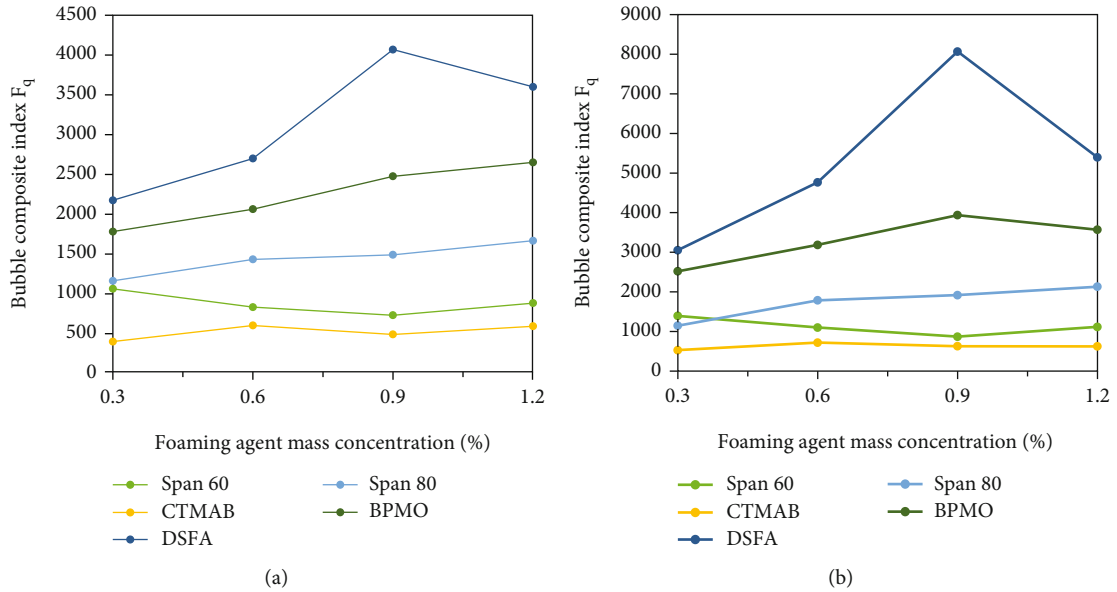

Figure 5: The foaming performance of different foaming agents in kerosene (a) and diesel (b).

700 mL diesel (or kerosene) with 300 mL water, add 2% emulsifier, add 2 g sodium carbonate and 40 g sodium bentonite, and stir at 8000 r/min for 20 min to obtain water-in-oil emulsion. Then, we add the appropriate amount of foaming agent, foam stabilizer, and cross-linking agent to the base fluid, and the mixture was poured into the Waring blender. The mixture was mechanically agitated at 8000 rpm for 1 min in the Waring blender, and then, the resulting foam was poured into a sealed cylinder and placed in an oven at 80°C until a foam gel formed.

2.2.5. Core Plugging Experiment. In order to meet the actual requirements of the site, we need an oil-based foam gel plugging agent with a pressure-bearing capacity of 6 MPa or more. In order to determine the plugging performance under this pressure, we have developed a comparative experiment plan. The experimental device diagram is shown in Figure 3. The overall experimental process was to take white sand and place it in the middle of the core to simulate cracks and put the core into the core holder. The foam gel plugging agent was added on the left side of the core, the drilling fluid was replaced with groundwater, and the plugging agent was driven into the core fractures. The flow rate of groundwater flowing into the annulus of the core, annulus pressure, and core back pressure parameters were set. A graduated cylinder was placed at the exit, and the amount of drilling fluid lost during this time period was recorded. For comparison, we did not add a plugging agent in the comparison experiment to test the leakage of drilling fluid through different degrees of fractures in a certain period of time. Sand particle size was used to simulate different permeability, and spatial situation diagram of particle size distribution in the core is shown in Figure 4. The specific experimental parameters are shown in Table 1:

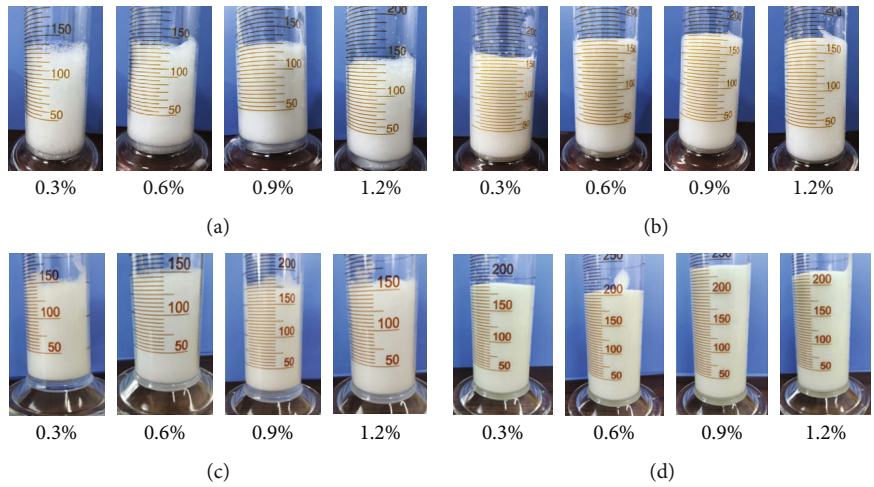

Figure 6: (a) Foaming situation of different mass concentrations of BPMO in kerosene. (d) Foaming situation of different mass concentrations of BPMO in diesel. (c) Foaming situation of different mass concentrations of DSFA in kerosene. (d) Foaming situation of different mass concentrations of DSFA in diesel.

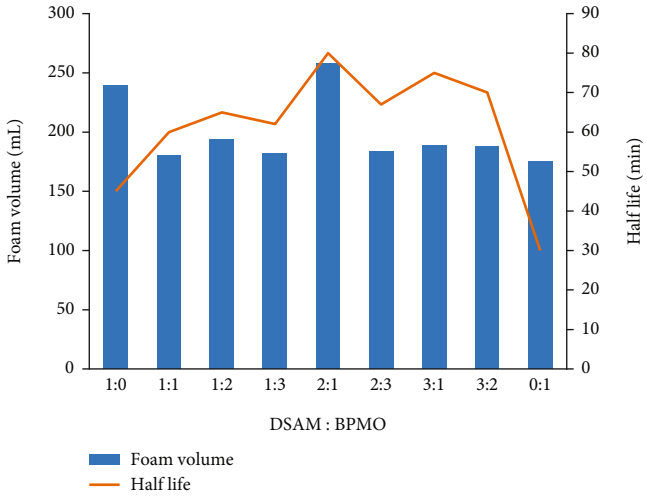

Figure 7: The foaming performance of the compound system of DSFA and BPMO in different proportions.

The following formula was used to express the blocking rate:

$$\text{plugging efficiency} = \frac{(\text{water loss volume} - \text{lost circulation material volume})}{\text{water loss volume}} \cdot 100\%. \quad (2)$$

3. Results and Discussions

3.1. Optimization of Oil-Based Foaming Agent System. Foaming agent is a surfactant that can increase the gas-liquid ratio of the foam gel and increase the stability of the foam [18]. The foaming ability of five foaming agents, sorbitan monostearate (Span 60), sorbitan oleate (Span 80), octadecyl trimethyl ammonium bromide (CTMAB), propylene glycol monooleate (BPMO), and DSFA, were evaluated.

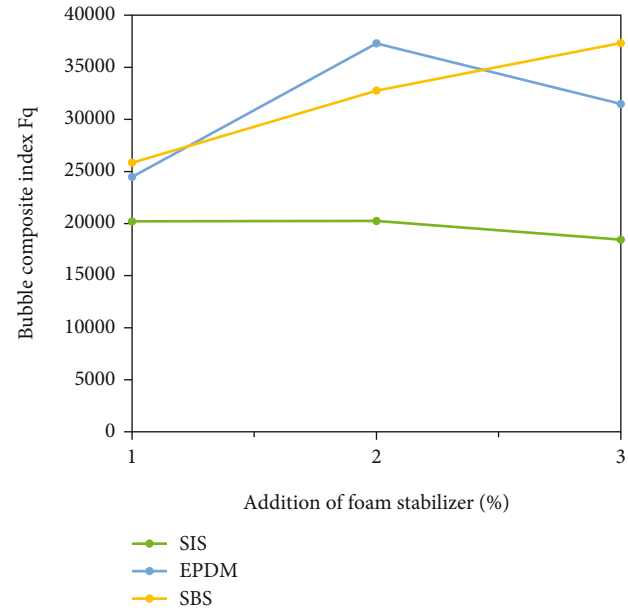

Figure 8: Foam stabilization performance of different oil-based foam stabilizers.

As shown in Figure 5, DSFA and propylene glycol monooleate (BPMO) have better foaming performance. And when diesel is used as the base fluid, the foaming agent has better foaming performance.

Figure 6 shows the foaming of BPMO blowing agent and DSFA blowing agent in kerosene-based fluid and diesel-based fluid. It can be seen that when diesel is used as the base fluid, the foam is denser.

Propylene glycol monooleate (BPMO) and DSFA were combined in pairs, and the sum of the mass concentration (0.3%, 0.6%, 0.9%, and 1.2%) and the foaming agent addition ratio (1 : 0, 1 : 1, 1 : 2, 1 : 3, 2 : 1, 2 : 3, 3 : 1, 3 : 2, and 0 : 1) was changed, foaming in diesel base. The foaming ability and foaming performance of the compound system were

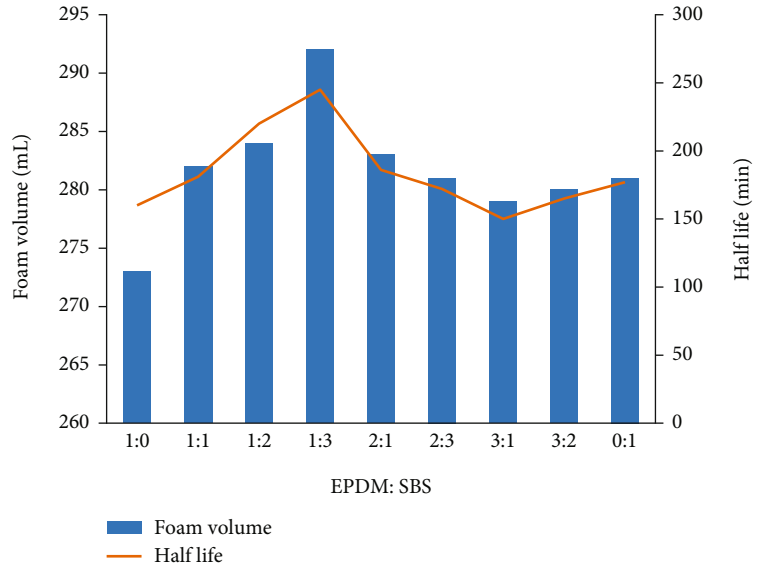

Figure 9: Foam stabilization performance of the mixed system of EPDM and SBS in different proportions.

evaluated, the best compound ratio was determined, and it was compared with a single foaming agent.

The foaming performance of DSFA and BPMO with different compounding ratios is different. With the increase of the mass concentration, the foaming performance of the compound system with different ratios has been improved, but when the mass concentration is greater than 0.9%, the foaming performance shows a slight change, indicating that increasing the foaming agent concentration can improve the foaming performance. The best foaming mass concentration is 0.9%. Comparing the foaming performance of different ratios, it can be seen that the foaming performance is best when DSFA/BPMO = 2 : 1. When the mass concentration is 0.9%, the foaming volume can reach up to 258 mL, the half-life can reach 80 s, and the comprehensive foam value can reach 15480. Therefore, if DSFA is compounded with BPMO, the best compounding ratio is DSFA/BPMO = 2 : 1 , and the best compounding mass concentration is 0.9%. The experimental data with a mass concentration of 0.9% was analyzed, as shown in Figure 7. It can also be clearly seen from Figure 6 that the optimal ratio of DSFA and BPMO is 2 : 1.

3.2. Optimization of Foam Stabilizer System

3.2.1. Selection of Optimum Foam Stabilizer. In this section, the foam stabilizing performance of several oil-based foam stabilizers was evaluated. The data is recorded in Figure 8. It can be seen from the table that EPDM and SBS can significantly increase the half-life of the foam.

The optimized foam stabilizers were tried to mix and use. The foam stabilizer system at different ratios (1 : 0, 1 : 1, 1 : 2, 1 : 3, 2 : 1, 2 : 3, 3 : 1, 3 : 2, and 0 : 1) and different mass concentrations (1.0%, 2.0%, and 3.0%) was investigated, and the best compound ratio was determined. According to the experimental data, the optimal mass concentration is 2.0%. The experimental data with a mass concentration of 2% was analyzed. And the results are shown in Figure 9. The best ratio of EPDM/SBS is determined as 1 : 3.

3.2.2. Optimization of Modified Nanosilica Concentration. The adsorption of modified nanosilica particles on the oil-gas interface can significantly improve the mechanical strength of the interface film and reduce the occurrence of bubble merging (as shown in Figure 10). The particles dispersed in the bubble liquid film can slow down the liquid film drainage speed and increase the stability of the foam.

The foam stabilization performance of different concentrations (0.016%, 0.018%, 0.02%, 0.022%, 0.04%, and 0.026%) of modified nanosilica was evaluated. The tracker automatic interface rheometer was used to study the gas-liquid interface properties of the system and to measure the surface tension of the sample after adding modified nanosilica particles. The surface tension of the sample after adding different mass concentrations of modified SiO_2 nanoparticles is shown in Figure 11. After adding modified nanosilica particles, the surface tension is greatly reduced. When the dosage is 0.02%, it drops to a minimum of 16.0mN/m and continues to increase the dosage and the change is not obvious. The foam stability is obviously improved after adding modified SiO_2 nanoparticles.

3.3. Optimization of Cross-Linking Agent. 200 mL of foam system solution with simulated formation water was prepared, and 0.05% diethanolamine (DEA), rigid cross-linking agent (DB), and divinylbenzene (DVB) were used as cross-linking agents. Waring high-speed stirring was used. The samples were stirred uniformly for 3 min with a Waring stirrer and aged at 80°C for 24 h. The foaming volume and half-life of the foam gel system were investigated.

The cross-linking agent was added to the basic formula at 0%, 1%, 2%, and 3% of the volume of the base liquid. The experimental results are shown in Table 2.

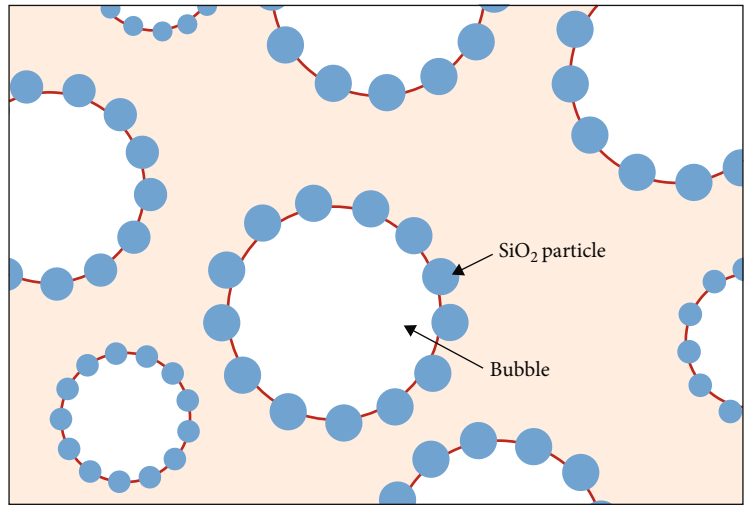

Figure 10: Schematic diagram of stable bubbles of SiO_2 nanoparticles.

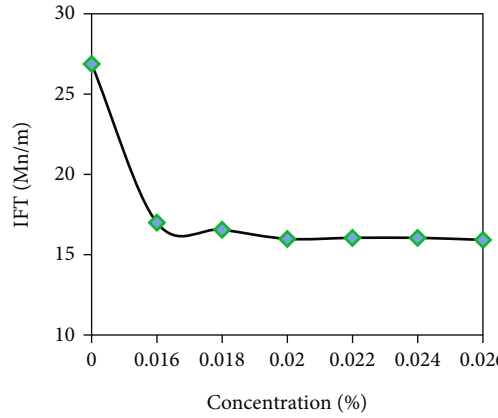

Figure 11: Surface tension of the sample after adding different mass concentrations of SiO_2 nanoparticles.

From the experimental results, it can be seen that when the amount of cross-linking agent DEA is too small, the cross-linking reaction between the monomers cannot be fully carried out, and no solid-like gel is formed. With the increase of DEA addition, the strength of the gel was improved, but after exceeding a certain amount, the strength of the gel changed less. On the other hand, the time to form the gel gradually decreased with the increase of cross-linking agent addition. This is due to the fact that the cross-linking point, which plays a bridging role, increases with the increase of the addition amount, which accelerates the polymerization cross-linking reaction.

The cross-linking agent DB was added to the base formulation at 1%, 2%, 3%, and 4% of the base volume, and the experimental results are shown in Table 3. Table 4 shows the performance of the cross-linking agent DVB.

It can be seen from the above experimental results that the cross-linking agent DB forms a gel system, and compared with other gel systems, the gel formation time is faster, the initial viscosity is controllable, the final set viscosity is large, and the stability is good. So the cross-linking agent DB was chosen as the cross-linking agent.

Table 2: The influence of cross-linking agent DEA on gel.

The amount of cross-linking agent DEA	0	1%	2%	3%
Gel formation time (min)	—	78	49	67
Strength of the gel	A	B	C	C

Table 3: The influence of cross-linking agent DB on gel.

The amount of cross-linking agent DB	1%	2%	3%	4%
Gel formation time (min)	72	67	50	50
Strength of the gel	B	C	D	D

Table 4: The influence of cross-linking agent DVB on gel.

The amount of cross-linking agent DVB	1%	2%	3%	4%
Gel formation time (min)	82	75	63	64
Strength of the gel	B	C	D	D

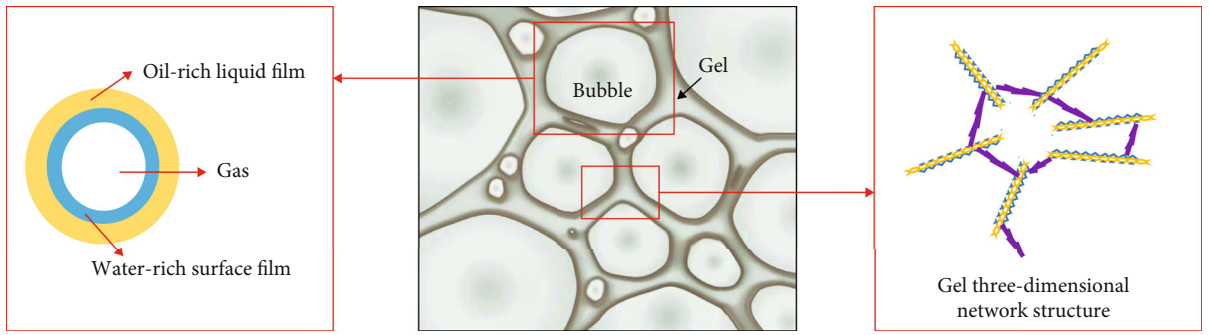

Figure 12: Schematic diagram of oil-based foam gel structure.

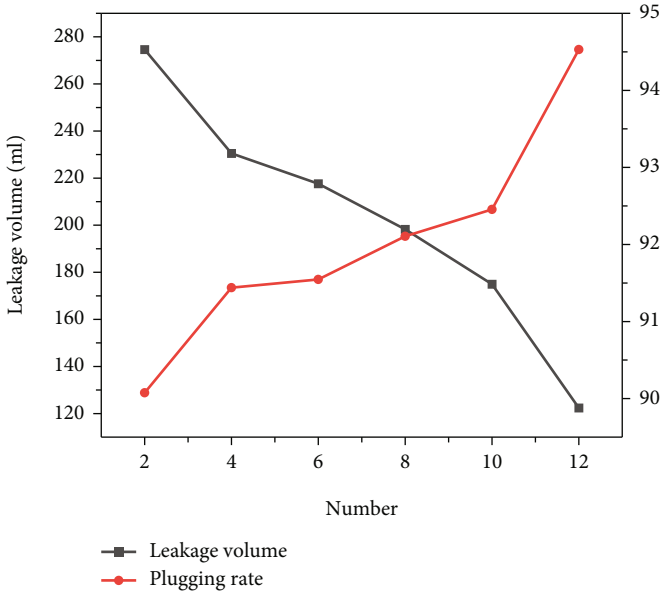

Figure 13: Change of plugging agent performance.

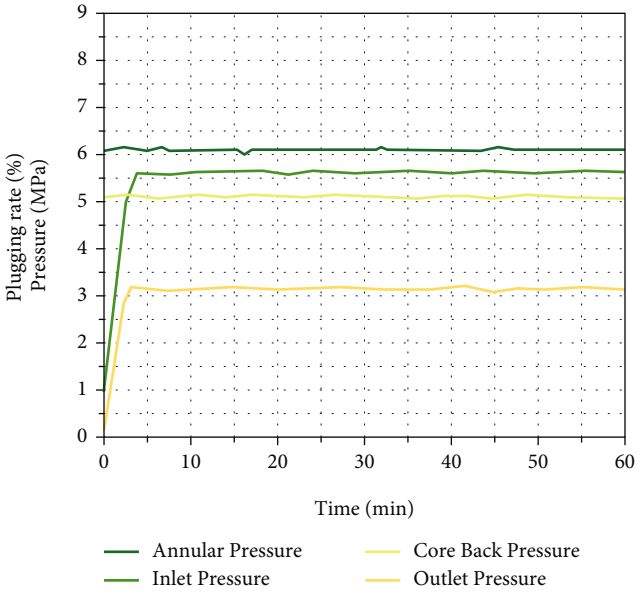

Figure 14: Experiment 3 plugging pressure change.

Therefore, the basic formula to determine the oil-based foam gel system was as follows: 0.6%DSFA foaming agent + 0.3%BPMO foaming agent + 0.5%EPDM + 1.5%SBS + 0.05%crosslinking agent DB + 0.02%modified SiO_2 nanoparticles.

3.4. Analysis of Plugging Mechanism. The structure of the oil-based foam gel is shown in Figure 12. The formation process is that the base liquid forms under the action of the oil-based foaming agent, and the liquid in the foam wall gradually turns into gel under the action of additives and finally forms a mixed system of solid gel and gas. Foam gel has the characteristics of foam before gelling, at which time the viscosity is relatively low. The large-flow foam gel has good fluidity and diffusibility before gelation, so it can spread quickly and eventually wrap the shale cracks. After gelation, the viscosity gradually increases, and it has the characteristics of gel, thereby greatly improving the plugging performance. In addition, the use of oil-based foam gel does not cause shale hydration.

3.5. Performance Evaluation of Plugging Agent

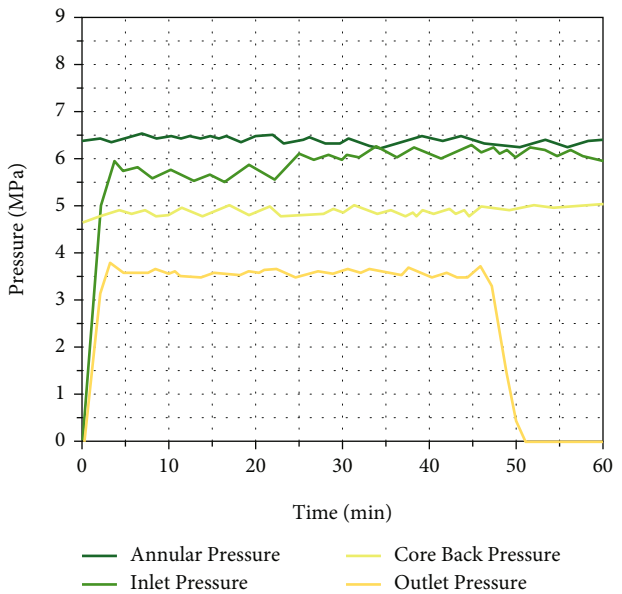

Figure 15: Experiment 4 plugging pressure change.

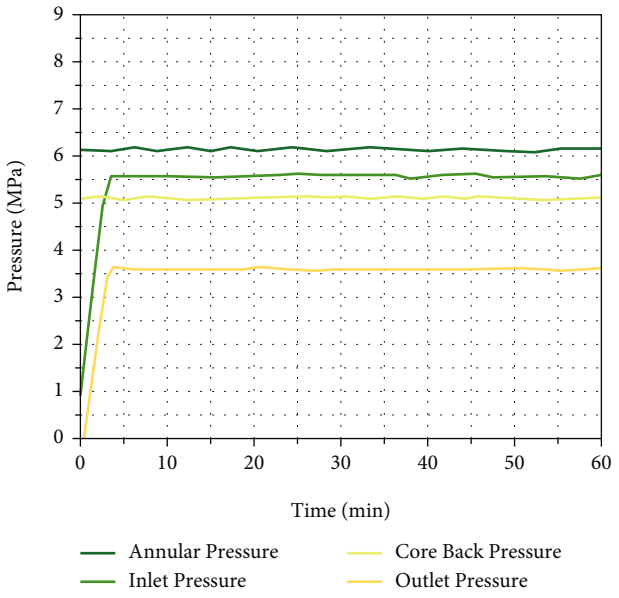

Figure 16: Experiment 7 plugging pressure change.

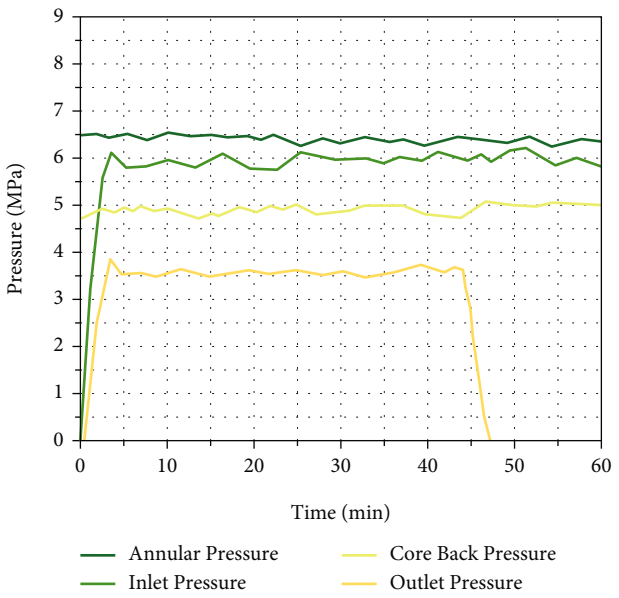

Figure 17: Experiment 8 plugging pressure change.

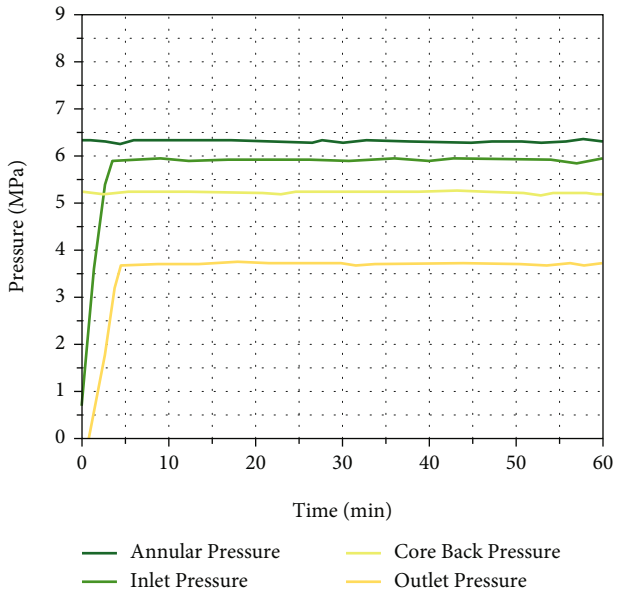

Figure 18: Experiment 11 plugging pressure change.

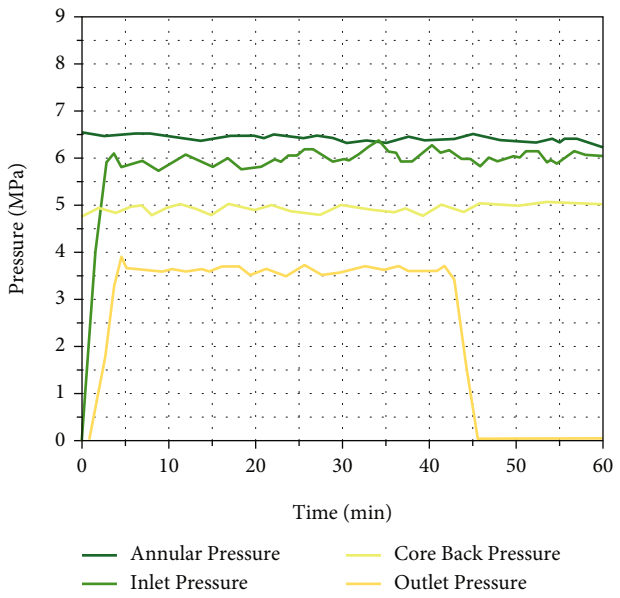

Figure 19: Experiment 12 plugging pressure change.

3.5.1. Core Plugging Experiment. The results of the core plugging experiment are shown in Figure 13. Figure 13 selects the leakage and plugging rate data with a pressure of 6 MPa. It is not difficult to see that under the condition of constant pressure, as the particle size of the sand decreases, its leakage gradually decreases, and the corresponding plugging rate is gradually increasing.

Select experiment 3, 4, 7, 8, 11, and 12 with a pressure of about 6 MPa and observe the pressure changes, as shown in Figures 14–19. Figures 14, 16, and 18 are graphs showing the pressure change trends of water passing through fractures in the cores with different particle sizes. As the sand size gets smaller and smaller, the annulus pressure begins to increase, but the increasing trend is not obvious. Similarly, the outlet pressure also increases with the increase of the sand size.

Comparing Figure 14 with Figure 15, the pressure fluctuation trend of Figure 15 is greater than that of Figure 14. Comparing the various pressures, the annulus pressure in experiment 4 is obviously greater than that in experiment 3. The annulus pressure, core back pressure, and inlet pressure in experiment 4 all have an upward trend, while experiment 3 tends to be stable. This can be understood as follows: the viscosity of the plugging agent is relatively large, and the inflow of drilling fluid is organized when the core is plugged, thereby increasing the pressure. When the pressure gradually increases, it can reflect that the plugging agent starts to work. These changes can also be seen in the pressure

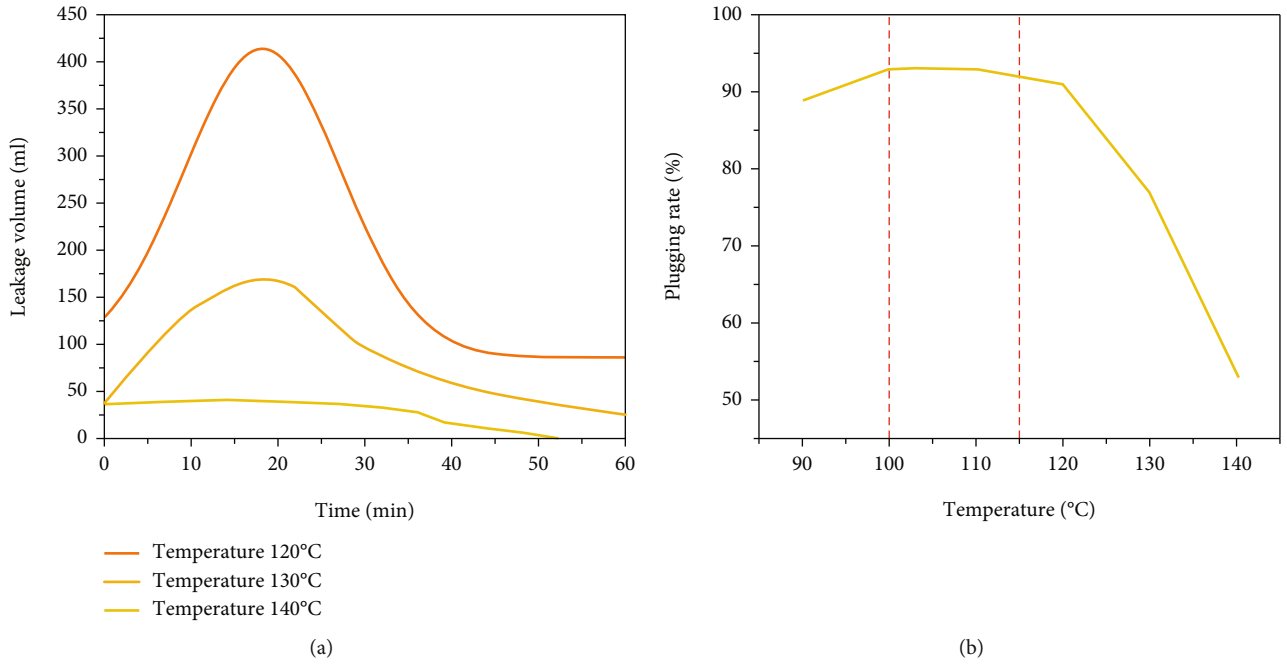

Figure 20: (a) The change in leakage over time at different temperatures. (b) The plugging rate of the plugging agent at different temperatures.

diagrams of experiment 7 and experiment 8 and experiment 11 and experiment 12.

As shown in Figure 15, the inlet pressure at the beginning of the experiment showed a linear upward trend, and at about 2 minutes, it began to gradually stabilize, showing signs of a slow rise. Because of the increase in inlet pressure, the annulus pressure rises, exceeding the set value of 6 MPa and hovering around 6.5 MPa. We mainly observe the changes in outlet pressure and back pressure. The outlet pressure is 0 at the beginning of the laboratory, and until 1 min later, the drilling fluid drives the plugging agent into the core and flows out from the pores of the core. The inflection point appeared at 45 min, and the inlet pressure began to decrease linearly at 45-50 min. Then, observe the core back pressure, the fluctuation range began to decrease at 45-50 minutes, until the beginning of 50 minutes, and the core back pressure gradually stabilized. The corresponding outlet pressure starts to be 0 at 51 min, indicating that the plugging agent starts to work at this time. The inlet pressure rises slowly as a whole.

In Figure 17, the overall pressure changes in the experiment are not much different from those in Figure 15. However, at 45 min, the outlet pressure appeared an inflection point until the outlet pressure at 47 min was 0, indicating that the plugging agent had begun to plug the core. This situation can be attributed to the fact that when the cracks are smaller, the starting time of the plugging agent will be shortened. In Figure 19, the inflection point of the outlet pressure appears at 42 minutes, and the pressure drop is at 45 minutes when the pressure drops to zero. The plugging time of the plugging agent changes with the size of the crack.

Combining the above experimental phenomena, we can find that when the gap of the crack is smaller, the plugging efficiency of the plugging agent is higher, and the plugging time is shorter. The overall plugging rate is above 89%, indicating that the plugging effect of the plugging agent is more prominent. In the field, we can increase the gel composition of the plugging agent accordingly, which can shorten the action time of the plugging agent.

3.5.2. The Influence of Temperature on the Performance of the Plugging Agent. Temperature has a certain effect on the performance of the plugging agent. The experimental temperature was changed to test the plugging performance of the plugging agent at different temperatures. Figure 20(a) shows the change in leakage over time at different temperatures, and Figure 20(b) shows the plugging rate of the plugging agent at different temperatures.

It can be seen from Figure 20(a) that when the temperature is 130°C and 140°C, as time increases, the amount of leakage increases significantly. When the temperature is 120°C, the leakage change is small. It can be seen from Figure 20(b) that when the temperature increases to 100-115°C, the plugging rate is higher. When the temperature exceeds 120°C, the plugging rate gradually decreases. Therefore, the best operating temperature range of this oil-based foam gel plugging agent is 100-115°C.

4. Conclusion

(1) In order to solve the leakage problem of fractured shale, an oil-based pressure-bearing foam gel plugging agent was developed through laboratory experiments. The foaming agent, foam stabilizer, crosslinking agent, and other components were optimized, and the optimal addition amount and compounding ratio were determined. The basic formula of the oil-based foam gel system was determined:

0.6%DSFA foaming agent + 0.3%BPMO foaming agent + 0.5%EPDM + 1.5%SBS + 0.05%crosslinking agent DB + 0.02%modified SiO_2 nanoparticles

(2) The oil-based foam gel plugging mechanism was analyzed. The properties of oil-based foam gel before gelation are similar to foam, and it is easy to spread and wrap cracks. The gel formed after gelation has good stability and blocking properties, and the oil-based foam gel will not cause shale hydration and expansion

(3) Then, a core plugging experiment device was designed, and the oil-based pressure-bearing foam plugging agent was evaluated for its plugging performance. Results of the study showed that the prepared plugging agent had good stability and plugging performance with a plugging rate of about 90% and the plugging agent still has a good plugging rate under the pressure of 6 MPa

Data Availability

The data used to support the findings of this study are included within the article.

Conflicts of Interest

The authors declare that they have no conflicts of interest.

Acknowledgments

This work was supported by the Open Fund of State Key Laboratory of Shale Oil and Gas Enrichment Mechanisms and Effective Development [grant number 20-YYGZ-KF-GC-01] and the National Natural Science Foundation of China (NSFC) [grant number U19B6003-05].

References

[1] Z. Wu, H. Liu, X. Wang, and Z. Zhang, "Emulsification and improved oil recovery with viscosity reducer during steam injection process for heavy oil," *Journal of Industrial and Engineering Chemistry*, vol. 61, pp. 348–355, 2018.

[2] B. Zhang, B. Shan, Y. Zhao, and L. Zhang, "Review of formation and gas characteristics in shale gas reservoirs," *Energies*, vol. 13, no. 20, pp. 5427–5450, 2020.

[3] X. Zhai, H. Chen, Y. Lou, and H. Wu, "Prediction and control model of shale induced fracture leakage pressure," *Journal of Petroleum Science and Engineering*, vol. 198, p. 108186, 2021.

[4] Y. Luo, M. Chen, D. Liu, Y. Jin, M. Du, and J. Hou, "Technology and applications of foam drilling fluid in fractured and complex formations," *Petroleum Science and Technology*, vol. 30, no. 16, pp. 1747–1754, 2012.

[5] Z. Wang, "The status and development direction of plugging technology for complex formation lost circu lation," *Sino-Global Energy*, vol. 19, no. 1, pp. 39–48, 2014.

[6] R. Sweatman, R. Faul, and C. Ballew, "New solutions for subsalt-well lost circulation and optimized primary cementing," *Society of Petroleum. Engineers*, 1999.

[7] T. N. Ivanova and I. Żabińska, "Modern methods of elimination of lost circulation in directional wells," *Management Systems in Production Engineering*, vol. 29, no. 1, pp. 65–74, 2021.

[8] J. Sun, Y. Bai, R. Cheng et al., "Research progress and prospect of plugging technologies for fractured formation with severe lost circulation," *Petroleum Exploration and Development*, vol. 48, no. 3, pp. 732–743, 2021.

[9] Z. Wu, H. Liu, Z. Pang, C. Wu, and M. Gao, "Pore-scale experiment on blocking characteristics and EOR mechanisms of nitrogen foam for heavy oil: a 2D visualized study," *Energy and Fuels*, vol. 30, no. 11, pp. 9106–9113, 2016.

[10] J. Luo, Z. Wang, and X. Deng, "Application of oil-based drilling fluid in the Tazhong Shuntuogole block," *West China Exploration Engineering*, vol. 32, no. 6, pp. 47–51, 2020.

[11] H. Sun, J. Luo, F. Yang, N. Qin, M. Yao, and X. Gao, "Research and application of oil-based foam underbalanced drilling technology in Shengbei area," *Natural Gas Exploration and Development*, vol. 38, no. 1, pp. 68–72, 2015.

[12] Y. Li, C. Dai, Y. Wu, and R. Wang, "A new type of gelled foam plugging agent with resistance to temperature, salt and dilution," *IOP Conference Series: Earth and Environmental Science*, vol. 565, no. 1, p. 5, 2020.

[13] M. M. Almajid and A. R. Kovscek, "Pore-level mechanics of foam generation and coalescence in the presence of oil," *Advances in Colloid and Interface Science*, vol. 233, pp. 65–82, 2016.

[14] B. Huang, W. Zhang, Q. Zhou, C. Fu, and S. He, "Preparation and experimental study of a low-initial-viscosity gel plugging agent," *ACS Omega*, vol. 5, no. 25, pp. 15715–15727, 2020.

[15] S. N. Tan, D. Fornasiero, R. Sedev, and J. Ralston, "The role of surfactant structure on foam behaviour," *Colloids & Surfaces A Physicochemical & Engineering Aspects*, vol. 263, no. 1-3, pp. 233–238, 2005.

[16] J. Xue, Z. Zhang, Y. Wang, and W. Zhou, "Lab research on foam gel profile plugging agent," *Liaoning Chemical Industry*, vol. 9, pp. 921-922, 2012.

[17] B. Wang, J. Sun, K. Lv, F. Shen, and Y. Bai, "Effects of a crosslinking agent on a supramolecular gel to control lost circulation," *New Journal of Chemistry*, vol. 45, no. 16, pp. 7089–7095, 2021.

[18] H. Jia, S. Chen, and Z. Zhou, "Strength-enhanced nanocomposite foamed gel as a temporary wellbore plugging fluid: formulation design and working performance," *Journal of Dispersion Science and Technology*, vol. 42, no. 8, pp. 1249–1258, 2021.

[19] W. Liu, J. Guo, W. Li, L. Jv, and B. Li, "The development and application of a microsphere gel composite plugging agents," *Petroleum Drilling Techniques*, vol. 44, pp. 34–39, 2016.

[20] Y. Zhang, Z. Chang, W. Luo, S. G. W. Li, and J. An, "Effect of starch particles on foam stability and dilational viscoelasticity of aqueous-foam," *Chinese Journal of Chemical Engineering*, vol. 23, no. 1, pp. 276–280, 2015.

[21] A. Verma, G. Chauhan, and K. Ojha, "Characterization of α-olefin sulfonate foam in presence of cosurfactants: stability, foamability and drainage kinetic study," *Journal of Molecular Liquids*, vol. 264, pp. 458–469, 2018.

[22] Z. Yousef, M. Almobarky, and D. S. Schechter, "Enhancing the stability of foam by the use of nanoparticles," *Energy & Fuels*, vol. 31, no. 10, pp. 10620–10627, 2017.

[23] A. J. Worthen, S. L. Bryant, C. Huh, and K. P. Johnston, "Carbon dioxide-in-water foams stabilized with nanoparticles and

surfactant acting in synergy," *AICHE Journal*, vol. 59, no. 9, pp. 3490–3501, 2013.

[24] R. Singh and K. K. Mohanty, "Synergistic Stabilization of Foams by a Mixture of Nanoparticles and Surfactants,," in *SPE Improved Oil Recovery Symposium*, Tulsa, OK, USA, 2014.

[25] T. S. Horozov, "Foams and foam films stabilised by solid particles," *Current Opinion in Colloid & Interface Science*, vol. 13, no. 3, pp. 134–140, 2008.

Hindawi
Geofluids
Volume 2022, Article ID 7151851, 9 pages
https://doi.org/10.1155/2022/7151851

Research Article

Mechanism of Coal Seam Permeability Enhancement and Gas Outburst Prevention under Hydraulic Fracturing Technology

Xinhua Wu,[1] **Tao Zhu**,[1] **Yufei Liu**,[1] **Guoyu Zhang**,[1] **Guanghui Zheng**,[1] **and Fengnian Wang**[2]

[1]*Tiandi Huatai Ming Management Co. Ltd., Beijing 10083, China*
[2]*State Key Laboratory for Geomechanics and Deep Underground Engineering, China University of Mining and Technology (Beijing), Beijing 100083, China*

Correspondence should be addressed to Fengnian Wang; wangfn_bj@163.com

Received 15 January 2022; Revised 28 February 2022; Accepted 7 March 2022; Published 22 March 2022

Academic Editor: Zheng Sun

In view of the high gas pressure and low permeability of deep coal seam, it is difficult to control gas, which affects the safety production of coal mine. The technical scheme of hydraulic fracturing to improve the permeability of coal seam is put forward, and the gas drainage technology is used to control the gas emission of coal seam. The fracturing effect under different water pressure, different gradient fracturing times, and in situ stress is analyzed by using 3DEC (3-Dimensional Distinct Element Code) discrete element software. The simulation analysis and field verification results show that the coal seam gas pressure increases linearly with the buried depth. In situ stress characteristics and hydraulic strength are the key factors affecting the effect of hydraulic fracturing. The fracturing radius increases with the increase of flow. When the construction pressure of hydraulic fracturing test is 18 MPa, the distance between fracturing hole and drainage hole is 8.5 m. The actual measurement shows that after hydraulic fracturing and gas drainage, the maximum gas emission is reduced by 51%, and the average gas emission is reduced by 58%.

1. Introduction

China's coal reserves rank high in the world, and most of the coal seams are buried underground. As one of the main hazard sources in underground coal face mining, gas seriously threatens the production safety of fully mechanized coal face and the personal safety of operators and then restricts the coal mining efficiency. With the deep mining of coal mines in China, the in situ stress, gas pressure, and gas content increase, the coal seam is soft, and the air permeability decreases, which leads to the difficulty of gas drainage and the increase of outburst risk.

For coal mine gas control and related rock mechanic problems, many experts have carried out relevant research. For example, Li et al. [1] use pulse hydraulic fracturing technology to prevent coal mine gas disasters. The results show that the pressure change in the process of pulse hydraulic fracturing reflects the expansion of fractures and conducive to the expansion of fractures under the action of pulse pressure. The initial pressure during pulse hydraulic fracturing is negatively correlated with water volume and fracturing time. Li et al. [2] proposed the combination of surface and underground natural gas exploitation methods to realize joint exploitation; second, joint mining is realized by drilling up and down coal seams and along coal seams; third, the goal of joint mining of coal and coalbed methane. Wang et al. [3] established a three-dimensional gas drainage project and studied and verified the effect of soft rock protective layer in mining technology practice. You et al. [4] proposed an innovative and practical coal

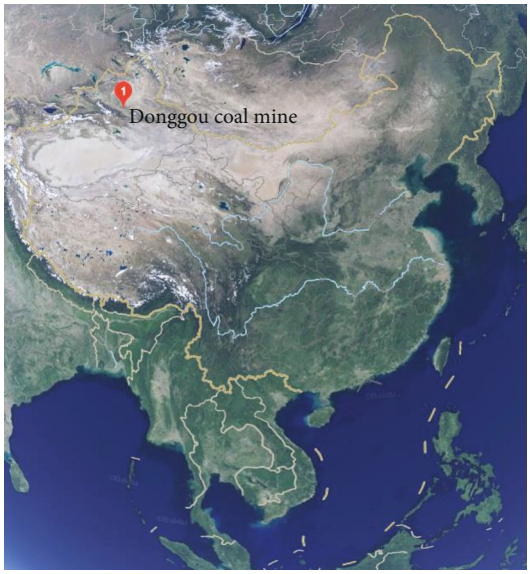

(a) Study target location

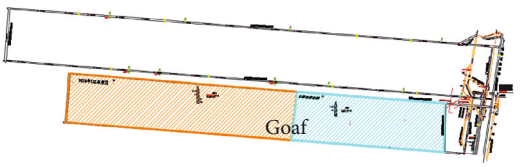

(b) Layout characteristics of working face

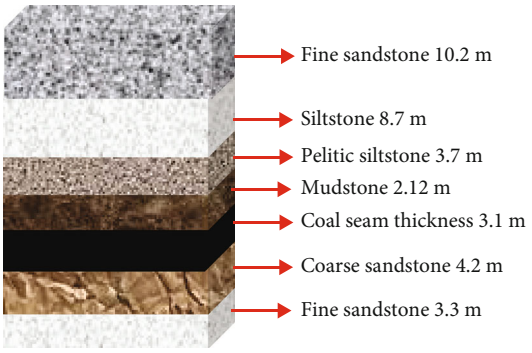

(c) Lithologic histogram

Figure 1: Research target location and project overview.

mine gas risk assessment method to provide help for the prevention and control of coal mine gas accidents. Si et al. [5] established a constitutive equation of coal considering the closed pore effect. On this basis, the gas migration model of closed pore coal seam is established, including gas diffusion model between closed pore and open pore and fracture gas seepage model. Jun et al. [6] used high-pressure water jet slotting to release the gas pressure in the coal seam, increase the permeability of the coal body, improve the gas drainage efficiency, and eliminate the risk of outburst. Aguado and Nicieza [7] proposed that high-pressure water injection and mining protective coal seam methods can improve safety.

Song et al. [8] summarized and analyzed the latest technologies for controlling gas explosion. Guo et al. [9] analyzed the influence of faults on gas occurrence, and the research shows that the complexity of faults increases the difficulty of mine gas prevention and control and seriously threatens mine safety. Gao et al. [10] analyzed the influence of mining rate on in situ stress, which is also an important factor affecting gas emission. Lin et al. [11] proposed a cross hole hydraulic slotting technology for preventing and controlling coal and gas outburst disasters in coal roadway excavation. Zhou et al. [12] combined the

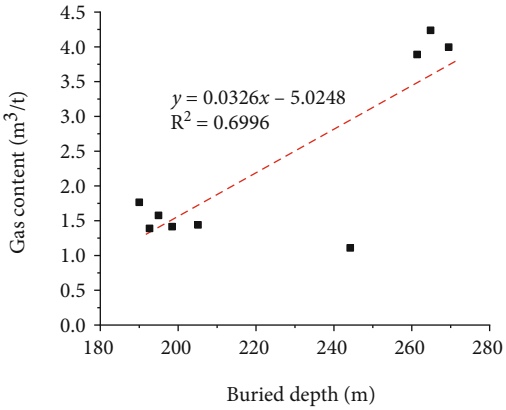

Figure 2: Regression trend line between gas content and coal seam buried depth.

stress balance equation and gas transport equation and simulated and calculated the distribution laws of displacement, stress, and gas pressure in solid on the basis of numerical simulation. Huang et al. [13] proposed measures to prevent and control gas explosion accidents by using fault tree analysis method. Mingzhong et al. [14] evaluated the deep buried in situ stress evaluation method. Gao et al. [15] studied the spatial propagation law of gas explosion in goaf of coal mine. Li and Hua [16] considered that gas release can also release rock mass strain energy. Cui et al. [17, 18] analyzed the influencing factors of hydraulic fracturing.

In recent years, gas casualties have occurred frequently. For example, 44 people died in the gas explosion accident in Xiaojiawan coal mine; gas outburst accident in Dengfeng coal mine killed 5 people; gas explosion in Dashan coal mine killed 12 people. According to the current research status and the actual engineering geological characteristics of the target mine, this paper plans to use the method of hydraulic fracturing for gas drainage. Through numerical simulation, DFN is used to model the fracture field, and the effects of fracturing time, water pressure, and in situ stress on the fracturing effect are analyzed. Finally, the appropriate construction method is selected for engineering test research.

2. Engineering Background

2.1. Engineering Geology. Donggou coal mine is located in China, Xinjiang, and 56 km south of Hutubi County, as shown Figure 1. The administrative division is under the jurisdiction of Shiti Township, Hutubi County. The minable coal seams in Donggou coal mine are B_1, B_2, B_3, B_4^1, and B_4^2, and the fault structure in the mining area is relatively developed. Controlled by the regional monoclinal structure, the mine field is generally a monoclinal structure gently inclined to the north, with a dip of 10°-25° and inclination of 10°-15°. The strata in the mining area from old to new are Qianxia Formation (c2qx) of Middle Carboniferous, Xiaoquangou group (T2~3xq) of Middle Upper Triassic, Badaowan Formation (j1b) and Sangonghe Formation (j1s) of Lower Jurassic, Xishanyao Formation (J2x) and Toutunhe Formation (j2t) of Middle Jurassic, Qigu Formation (J3q) and Kalaza Formation (J3k) of Upper Jurassic, and the first subgroup of Tugulu Formation of Lower Cretaceous (k1tga). Xishanyao Formation of Middle Jurassic is the main coal bearing formation in the mining area.

The target working face studied in this paper is located in $B4^2$ coal seam, with buried depth of 136.38~50.24 m, thickness of 1.67~5.23 m, and average of 3.13 m. The recoverable thickness is 1.67~3.77 m, the average recoverable thickness is 2.95 m, the standard deviation of thickness is 0.93, and the coefficient of variation is 29%. The lithology of the roof is fine sandstone, siltstone, argillaceous siltstone, and mudstone, and the lithology of the floor is coarse sandstone, fine sandstone, siltstone, argillaceous siltstone, and carbonaceous mudstone.

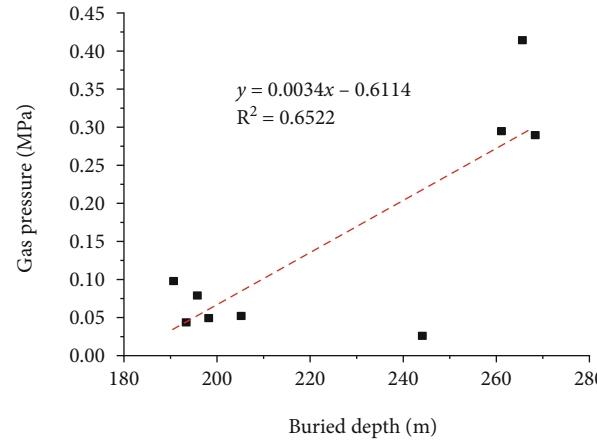

Figure 3: Regression trend line between gas pressure and coal seam buried depth.

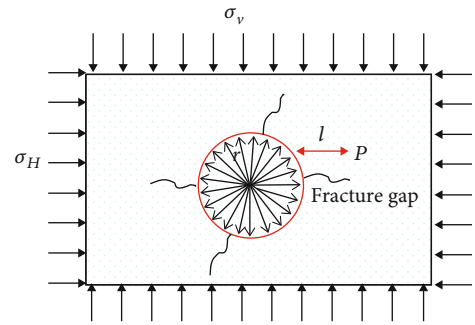

Figure 4: Mechanical model of crack initiation under hydraulic fracturing.

2.2. Gas Distribution and Emission Characteristics. The roof and floor of $B4^2$ coal seam are mudstone and carbonaceous mudstone with poor permeability, which is beneficial to the preservation of coal seam gas. In addition, the fractures within the mine range are not very developed, so the gas connectivity of each coal seam is relatively poor. The measured results show that with the increase of coal seam burial depth, the proportion of methane increases and the gas content increases. As shown in Figure 2, it shows the gas content under different burial depths. The results show that the gas content is about 1.2 m^3/t when the burial depth is 190 m. Under the burial depth of 270 m, the gas content is as high as 4 m^3/t, the burial depth increases by 1.42 times, and the gas content increases by 3.33 times.

According to the results in Figure 3, the gas pressure gradient of B_4^2 coal seam with buried depth is 0.34 m^3/t/km. Based on the analysis of gas emission law of transportation roadway, return air roadway, and working face, the measured value of gas emission from transportation roadway of working face is 5.9 m^3/min. The measured value of gas emission from transportation roadway is 4.28 m^3/min. During the mining of the working face, the gas emission reaches 15 m^3/min.

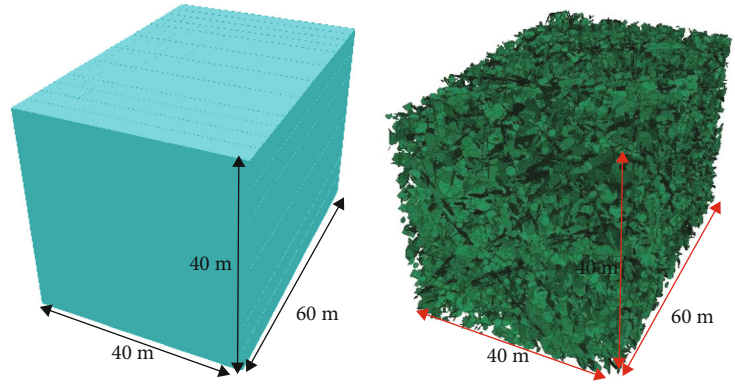

(a) Calculate model size (b) DFN model

Figure 5: Numerical calculation discrete element model.

Table 1: Basic physical and mechanical parameters of coal and rock.

Compressive strength/ MPa	Tensile strength/ MPa	Elastic modulus/ GPa	Poisson's ratio	Internal friction angle/ (°)	Friction coefficient	Density/ (kg/m^3)
10.12	2.18	2.49	0.28	35.22	0.734	1289

3. Hydraulic Fracturing Mechanism and Numerical Calculation Model

3.1. Mechanism of Increasing Coal Seam Permeability under Hydraulic Fracturing. Hydraulic fracturing started from oil and gas exploitation and is gradually applied to coal seam gas drainage. There are primary microfractures and pore structures in the coal body, but these structures are closed under the action of high ground stress, and the permeability channel is not fully open, resulting in internal gas accumulation. After high-pressure water is injected into the borehole, the stress on the borehole wall is concentrated and the primary fractures begin to expand and open. With the continuous fracturing, the fracture further expands around, thus increasing the permeability of gas flow. Figure 4 shows the schematic diagram of hydraulic fracturing. Formula (1) represents the stress at any point around the borehole [19, 20].

$$\begin{bmatrix} \sigma_t = \dfrac{\sigma_v + \sigma_H}{2}\left(1 - \dfrac{R^2}{r^2}\right) + \dfrac{\sigma_v - \sigma_H}{2}\left(1 + \dfrac{3R^4}{r^4} - \dfrac{4R^2}{r^2}\right)\cos 2\theta \\ \sigma_\theta = \dfrac{\sigma_v + \sigma_H}{2}\left(1 + \dfrac{R^2}{r^2}\right) - \dfrac{\sigma_v - \sigma_H}{2}\left(1 + \dfrac{3R^4}{r^4}\right)\cos 2\theta \\ \tau_{r\theta} = -\dfrac{\sigma_v - \sigma_H}{2}\left(1 - \dfrac{3R^4}{r^4} + \dfrac{2R^2}{r^2}\right)\sin 2\theta \end{bmatrix}. \tag{1}$$

Assuming that the water pressure is p, the stress load will be caused to the unit body around the hole wall. The stress caused by the water pressure is shown in

$$\sigma_r{}^p = p, \tag{2}$$

$$\sigma_\theta{}^p = -p. \tag{3}$$

When the stress $\sigma_\theta{}^p$ caused by water pressure is greater than or equal to σ_θ, cracks will occur around the hole wall. In conclusion, the characteristics of in situ stress and hydraulic strength are the key factors affecting the effect of hydraulic fracturing.

3.2. Numerical Calculation Model and Results. The three-dimensional discrete element numerical simulation software 3DEC is used to establish the numerical calculation model. The size of the model is set as $40 * 40 * 60$ m, the vertical stress is the weight of the overburden, and the lateral pressure coefficient is 1.3. The model uses DFN (discrete fracture network) for initial fracture division [21, 22], as shown in Figure 5. Assuming that the model medium has elastic brittle mechanical properties, its failure process belongs to elastic damage theory, and the physical and mechanical parameters of coal are shown in Table 1. The damage of the medium element of the model conforms to the maximum tensile strength and Mohr Coulomb criterion. In the numerical calculation, the model block adopts Mohr Coulomb criterion, and the joint adopts Coulomb slip criterion. Based on the coupling theory of pore and seepage, the coupling equation of stress joint seepage is introduced.

In the process of seepage flowing in the fracture grid, the seepage affects the rock mass stress distribution through the normal seepage force and tangential drag applied to the fracture wall, and the damage caused by stress redistribution reacts on the fracture seepage. The effect

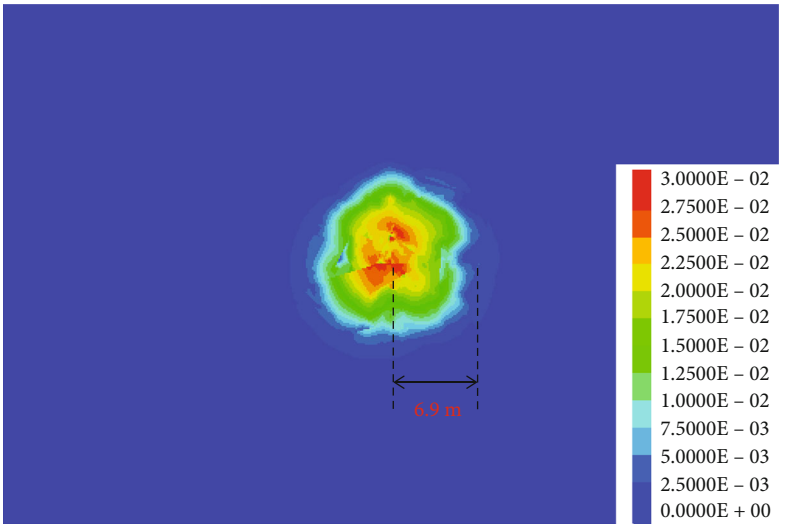

(a) Hydraulic fracturing time 250 s

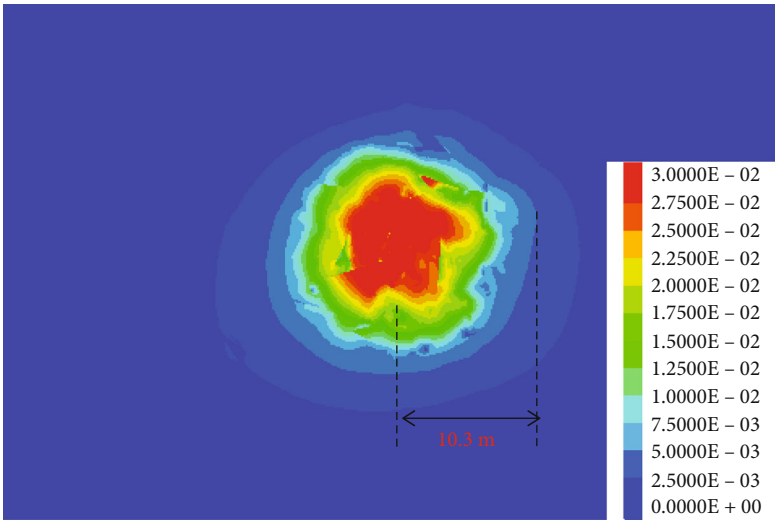

(b) Hydraulic fracturing time 350 s

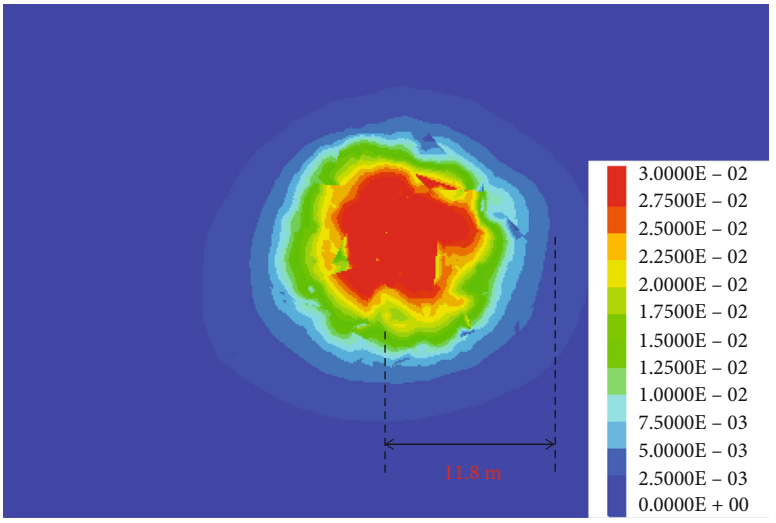

(c) Hydraulic fracturing time 450 s

Figure 6: Continued.

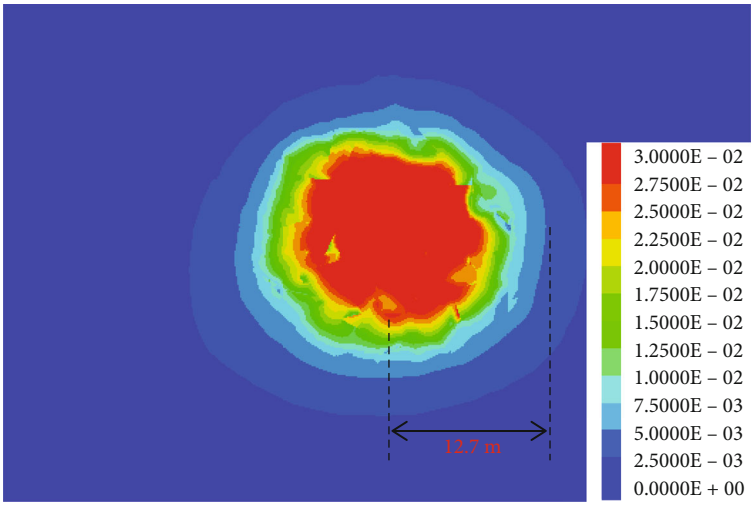

(d) Hydraulic fracturing time 650 s

Figure 6: Characteristics of fracturing radius under different fracturing time (10 m^3/h).

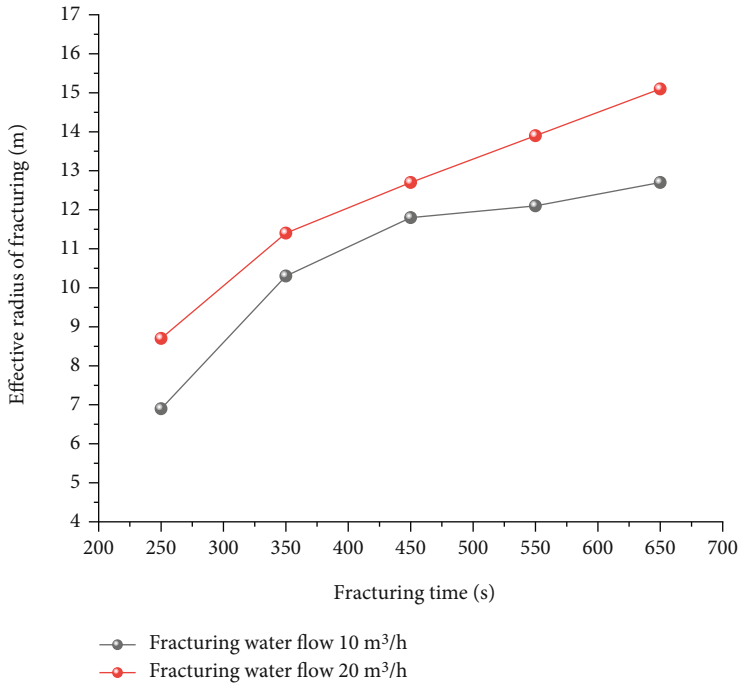

Figure 7: Relationship between effective fracturing radius and fracturing time.

of stress on seepage can be expressed by cubic law, such as formulas (4)–(5).

$$q_f = \frac{\gamma(b_0 + \Delta b)^3}{12\mu} J, \tag{4}$$

$$\Delta b = f(\sigma). \tag{5}$$

The influence of seepage on stress can be determined by the equivalent load of seepage force on the fracture surface at the node, as shown in

$$F_i = \frac{l}{6}\left(2p_i + p_j\right); F_j = \frac{l}{6}\left(p_i + 2p_j\right); T_i = \frac{b_0}{4}\left(p_i - p_j\right); T_j = \frac{b_0}{4}\left(p_j - p_i\right). \tag{6}$$

In the formula, γ, μ represents the unit weight and dynamic viscosity coefficient of water, respectively. b_0 is the initial opening of the crack. Δb is the variable of crack opening under stress. p_i, p_j is the seepage hydrostatic pressure at both ends of the fracture. l is fracture aperture. F_i, F_j is the normal equivalent nodal force. T_i, T_j is the tangential equivalent nodal force. Fracturing time is the key factor affecting the effective radius of hydraulic fracturing, as shown in Figure 6, which shows that the joint fissure opening increases with the increase of water injection time.

Fracturing time is the key factor affecting the effective radius of hydraulic fracturing, as shown in Figure 6, which shows that the joint fissure opening increases with the increase of water injection time. When the grouting flow is 10 m^3/h, the grouting duration is 250 s, 350 s, 450 s, and 650 s, respectively, and the effective radius of fracturing is 6.9 m, 10.3 m, 11.8 m, and 12.7 m, respectively.

As shown in Figure 7, it shows the relationship between effective fracturing radius and fracturing time under different flow. According to the data, the fracturing radius increases with the increase of flow. At the same time, the fracturing radius is greatly affected by the fracturing time in the early stage and then slows down.

Initial in situ stress field is also an important factor affecting hydraulic fracturing. In order to better analyze the initiation pressure under different stress levels, numerical calculation is carried out. Fix the maximum horizontal principal stress as 11.5 MPa and the vertical stress as 11.5 MPa, 13.0 MPa, 14.4 MPa, and 17.3 MPa. The ratio of vertical stress to horizontal stress is 1.0, 1.1, 1.25, and 1.5, respectively.

As shown in Figure 8, when the vertical stress is 11.5 MPa, the cracking pressure is 15.8 MPa, and the instability pressure of tunnel wall is 22.1 MPa. When the vertical stress is 13 MPa, the cracking pressure is 14.3 MPa, and the instability pressure of tunnel wall is 19.6 MPa. When the vertical stress is 14.4 MPa, the cracking pressure is 13.2 MPa, and the instability pressure of tunnel wall is 18.2 MPa.

When the vertical stress is 17.3 MPa, the cracking pressure is 9.9 MPa, and the instability pressure of tunnel wall is 17.7 MPa. The increase of vertical stress leads to the increase of tensile stress at the top of the borehole, which makes the crack easier to expand.

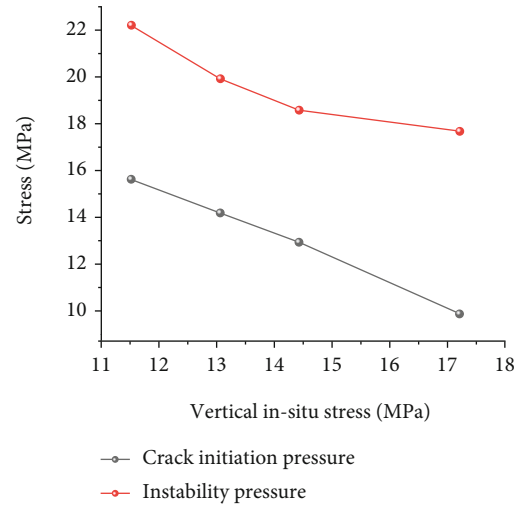

Figure 8: Effect of vertical stress on hydraulic fracturing.

4. Application of Hydraulic Fracturing Technology

The technical equipment of hydraulic fracturing is mainly composed of power supply system, water supply system, and fracturing system. The fracturing system is mainly composed of high-pressure water injection pump, water tank, high-pressure fracturing pipe, special hole sealer for hydraulic fracturing, and monitoring system. XRB2B emulsion pump is selected as the core equipment water injection pump, with rated pressure of 20 MPa and flow of 80 L/min. The hole sealer is selected, with applicable hole diameter of 40~50 mm, maximum expansion diameter of 70 mm, and pressure resistance of 30 MPa under working state. The gas extraction pump station is equipped with two sets of high and low negative pressure systems. The model of high negative pressure extraction pump is 2BE4620-2BY4. The model of low negative pressure extraction pump is 2BE4520-2BY4, one for use and one for standby.

According to the gas occurrence of the coal seam and the roadway layout of the working face, hydraulic fracturing boreholes and gas drainage boreholes are, respectively, arranged in the return air roadway. The spacing between the fracturing hole and the pumping hole is 8.5 m. The pumping hole is 18 m longer than the fracturing hole. It takes 65 min from the start of water injection to the maximum water pressure, and the total water injection time is about 260 min. The construction pressure of this hydraulic fracturing test is determined to be 18 MPa. The drilling arrangement is shown in Figure 9.

After 12 hours of fracturing, drain water from each fracturing hole and extraction hole. When the water flow is small and there is high concentration gas, connect the extraction hole and fracturing hole into the underground gas extraction system at the same time. In order to record the gas emission parameters of the hydraulic fracturing effect, the gas emission of adjacent working faces without fracturing is compared.

Figure 10 shows the change trend of gas emission in the roadway with time during the mining process of the working face after gas drainage. The black curve indicates that gas drainage is carried out directly without hydraulic fracturing and the gas emission characteristics in the mining process of the working face.

The red curve indicates the gas emission characteristics in the mining process of the working face after hydraulic fracturing and gas drainage. Without hydraulic fracturing, the maximum gas emission is 10.5 m^3/min, and the average value is 9.2 m^3/min. After hydraulic fracturing, the maximum gas emission is 5.1 m^3/min, and the average value is 3.8 m^3/min. The maximum value is reduced by 51%, and the average value is reduced by 58%.

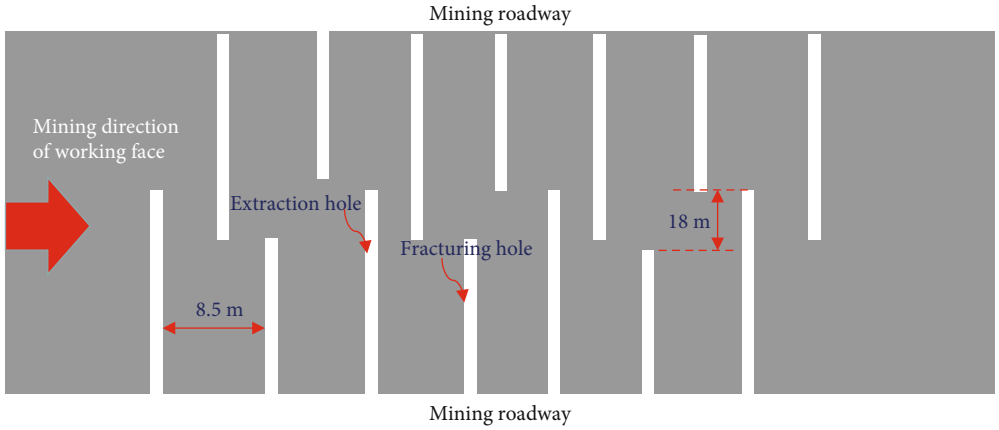

Figure 9: Layout of pumping and pressure relief boreholes in working face.

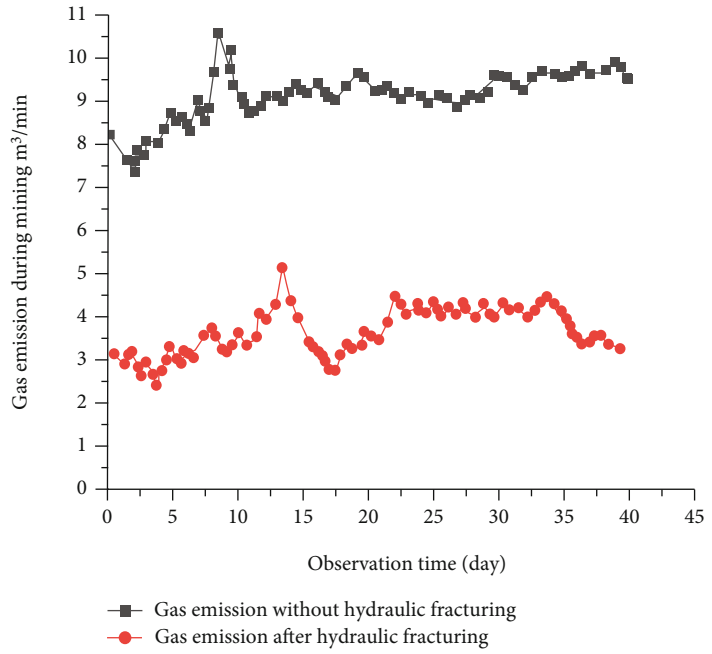

Figure 10: Effect of hydraulic fracturing on gas emission from coal face.

5. Conclusion

Based on the severe situation of coal mine gas outburst, this paper carried out the research on hydraulic fracturing gas discharge. Through engineering investigation, numerical calculation, and field application, the influence of key parameters such as in situ stress, liquid injection pressure, and pressure injection time on fracture effect is analyzed, which is finally applied to engineering practice.

(1) The variation gradient of gas pressure in B_4^2 coal seam with buried depth is 0.34 m^3/t/km. The characteristics of in situ stress and hydraulic strength are the key factors affecting the effect of hydraulic fracturing

(2) Use DFN (discrete fracture network) for initial fracture division; based on the pore seepage coupling theory, the stress joint seepage coupling equation is introduced. The results show that under the working condition of 10 m^3/h, the grouting duration is 250 s, 350 s, 450 s, and 650 s, respectively, and the effective fracturing radius is 6.9 m, 10.3 m, 11.8 m, and 12.7 m, respectively. The fracturing radius is greatly affected by the fracturing time in the early stage, which varies with the fracturing time slow down after. The increase of vertical stress leads to the increase of tensile stress at the top of the borehole, which makes the crack easier to expand

(3) According to the field measurement, the construction pressure of hydraulic fracturing test is 18 MPa, the spacing between fracturing hole and extraction hole is 8.5 m, and the extraction hole is 18 m longer than the fracturing hole, which can meet the needs of field engineering. After hydraulic fracturing and gas drainage, the maximum gas emission is reduced by 51% and the average value is reduced by 58%.

Data Availability

The data used to support the findings of the study are available within the article.

Conflicts of Interest

The authors declare that they have no conflicts of interest.

Acknowledgments

This work was financially supported by the Tiandi Huatai Independent Science and Technology Innovation Fund Project (nos. TDHTKY2021005 and TDHTKY2021009) and the Science and Technology Innovation and Entrepreneurship Fund Project of Tiandi Technology Co., Ltd. (no. 2020-TD-MS007).

References

[1] Q. Li, B. Lin, and C. Zhai, "A new technique for preventing and controlling coal and gas outburst hazard with pulse hydraulic fracturing: a case study in Yuwu coal mine, China," *Natural Hazards*, vol. 75, no. 3, pp. 2931–2946, 2015.

[2] H. Li, J. Ma, Z. Wang, W. Wang, and Y. Liu, "A gas outburst prevention and control strategy for single thick coal seams with high outburst risk: a case study of Hudi coal mine in Qinshui Basin," *Energy Science & Engineering*, vol. 8, no. 7, pp. 2471–2491, 2020.

[3] L. Wang, Z. Lu, D. Chen et al., "Safe strategy for coal and gas outburst prevention in deep-and-thick coal seams using a soft rock protective layer mining," *Safety Science*, vol. 129, article 104800, 2020.

[4] M. You, S. Li, D. Li, and S. Xu, "Applications of artificial intelligence for coal mine gas risk assessment," *Safety Science*, vol. 143, article 105420, 2021.

[5] L. Si, Z. Li, M. Kizil, Z. Chen, Y. Yang, and S. Ji, "The influence of closed pores on the gas transport and its application in coal mine gas extraction," *Fuel*, vol. 254, article 115605, 2019.

[6] X. Jun, L. Yunpei, Z. Quanle, L. Lei, and L. Xuelong, "Elimination of coal and gas outburst risk of low-permeability coal seam using high-pressure water jet slotting technology: a case study in Shihuatian coal mine in Guizhou Province, China," *Energy Science & Engineering*, vol. 7, no. 4, pp. 1394–1404, 2019.

[7] M. B. D. Aguado and C. G. Nicieza, "Control and prevention of gas outbursts in coal mines, Riosa-Olloniego coalfield, Spain," *International Journal of Coal Geology*, vol. 69, no. 4, pp. 253–266, 2007.

[8] W. Song, J. Cheng, and W. Wang, "Underground mine gas explosion accidents and prevention techniques–an overview," *Archives of Mining Sciences*, vol. 66, no. 2, 2021.

[9] P. Guo, Y. Cheng, K. Jin, and Y. Liu, "The impact of faults on the occurrence of coal bed methane in Renlou coal mine, Huaibei coalfield, China," *Journal of Natural Gas Science and Engineering*, vol. 17, pp. 151–158, 2014.

[10] M. Gao, J. Xie, Y. Gao et al., "Mechanical behavior of coal under different mining rates: a case study from laboratory experiments to field testing," *International Journal of Mining Science and Technology*, vol. 31, no. 5, pp. 825–841, 2021.

[11] B. Lin, F. Yan, C. Zhu et al., "Cross-borehole hydraulic slotting technique for preventing and controlling coal and gas outbursts during coal roadway excavation," *Journal of Natural Gas Science and Engineering*, vol. 26, pp. 518–525, 2015.

[12] A. Zhou, K. Wang, L. Li, and C. Wang, "A roadway driving technique for preventing coal and gas outbursts in deep coal mines," *Environmental Earth Sciences*, vol. 76, no. 6, p. 236, 2017.

[13] H. Huang, M. I. Wan, and D. Y. Yin, "Research on analysis and prevention of coal mine gas explosion accident based on FAT," *Journal of Mechanical Engineering Research and Developments*, vol. 39, no. 1, pp. 234–238, 2016.

[14] G. Mingzhong, H. Haichun, X. Shouning et al., "Discing behavior and mechanism of cores extracted from Songke-2 well at depths below 4,500 m," *International Journal of Rock Mechanics and Mining Sciences*, vol. 149, article 104976, 2022.

[15] K. Gao, S. Li, R. Han et al., "Study on the propagation law of gas explosion in the space based on the goaf characteristic of coal mine," *Safety Science*, vol. 127, article 104693, 2020.

[16] X. Z. Li and A. Z. Hua, "Prediction and prevention of sandstone-gas outbursts in coal mines," *International Journal of Rock Mechanics and Mining Sciences*, vol. 43, no. 1, pp. 2–18, 2006.

[17] G. Cui, W. Wang, B. Dou et al., "Geothermal energy exploitation and power generation via a single vertical well combined with hydraulic fracturing," *Journal of Energy Engineering*, vol. 148, no. 1, p. 4021058, 2022.

[18] G. Cui, L. Yang, J. Fang, Z. Qiu, Y. Wang, and S. Ren, "Geochemical reactions and their influence on petrophysical properties of ultra-low permeability oil reservoirs during water and CO_2 flooding," *Journal of Petroleum Science and Engineering*, vol. 203, article 108672, 2021.

[19] Y. Lu, Z. Ge, F. Yang, B. Xia, and J. Tang, "Progress on the hydraulic measures for grid slotting and fracking to enhance coal seam permeability," *International Journal of Mining Science and Technology*, vol. 27, no. 5, pp. 867–871, 2017.

[20] W. Wang, X. Li, B. Lin, and C. Zhai, "Pulsating hydraulic fracturing technology in low permeability coal seams," *International Journal of Mining Science and Technology*, vol. 25, no. 4, pp. 681–685, 2015.

[21] C. Zhu, X. Xu, X. Wang et al., "Experimental investigation on nonlinear flow anisotropy behavior in fracture media," *Geofluids*, vol. 2019, Article ID 5874849, 9 pages, 2019.

[22] G. Li, Y. Hu, S. Tian, M. weibin, and H. L. Huang, "Analysis of deformation control mechanism of prestressed anchor on jointed soft rock in large cross-section tunnel," *Bulletin of Engineering Geology and the Environment*, vol. 80, no. 12, pp. 9089–9103, 2021.

Hindawi
Geofluids
Volume 2022, Article ID 8318819, 10 pages
https://doi.org/10.1155/2022/8318819

Research Article

Characteristics and Research Direction of Triassic in the South Yellow Sea Basin, China

Kong Weijun,[1] **Su Shuzhen**,[1] **Zhang Jianning**,[1] **Shi Guoji**,[1] **Huang Yao**,[1] **Zhu Kui**,[1] **and Chen Qinghua**[2]

[1]*Production Department, Corporation Jiangsu Oilfield Sub-Company, SINOPEC, Yangzhou, Jiangsu 225200, China*
[2]*School of Geosciences, China University of Petroleum, Qingdao, Shandong 266580, China*

Correspondence should be addressed to Kong Weijun; kongweijun_2021@126.com

Received 9 January 2022; Revised 25 February 2022; Accepted 26 February 2022; Published 17 March 2022

Academic Editor: Zheng Sun

To advance oil and gas exploration in the South Yellow Sea Basin, characteristics of Triassic, including its correlation with regional strata, distribution, lithology characteristics, and karst development characteristics, are studied by geological mapping. Results show that there exist Zhouchongcun Formation and Qinglong Formation in the Triassic. Zhouchongcun Formation corresponds to Dongma Formation in the lower Yangtze Region, Badong Formation in the middle Yangtze Region, and Lekoupo Formation in the upper Yangtze region. The upper Qinglong Formation corresponds to the Nanlinghu Formation and Longshan Formation in Xiyanzi district, and Jialingjiang Formation in the middle and upper Yangtze region. Its lithology is limestone, intercalated with marl, mudstone, and argillaceous siltstone. The lower Qinglong Formation corresponds to the Yinkeng Formation at the lower Yangtze group. The lower Qinglong group has the complex lithologic characteristics, which can be divided into six categories from top to bottom, including limestone weathering crust layer, limestone, marl with mudstone, mudstone with limestone, marl with limestone, and mudstone interbedding limestone and mudstone. Karst phenomenon is well developed in the lower Qinglong Formation, and the thickness of weathering crust, revealed by cz35-2-1 well, reaches 60.5 m. Triassic in the South Yellow Sea Basin is mainly distributed in the central uplift and southern depression, showing the regional differences in distribution. Karstification is probably the main reason for this significant difference. Identification of karst phenomenon and stratigraphic division method towards Triassic drilling coring are two important directions of Triassic study in the South Yellow Sea Basin.

1. Introduction

Triassic system was founded by von Alberti, a German geologist in 1834 [1–3], according to the characteristics of three sets of stratigraphic units in southern Germany and other parts of Europe [4, 5]. According to the international chronostratigraphic table (2020) [6–9], the limit of Triassic geological age ranges from 251.902 ma~201.3 ma. Triassic is widely distributed in the world and in China [10], for example, the Tarim Basin, Ordos Basin, and Junggar Basin in northern China, western Guizhou, Eastern Yunnan, and western Yunnan. Moreover, there are also well-developed Triassic systems in northern Tibet, such as the Zhehala group in the middle of the Bangong Lake-Nujiang junction zone [6]. Triassic is one of the most important geological periods in the process of tectonic evolution in China [4]. Volcanic events and biological extinction in the early Triassic Indian stage have always been the focus of many researchers [11–13]. The Triassic system is rich in mineral resources, such as the enrichment of minerals in the Triassic System on both banks of the middle and lower reaches of the Yangtze River [5]. Xujiahe Formation of Upper Triassic, Leikoupo Formation of Middle Triassic, Jialingjiang Formation, and Feixianguan Formation of Lower Triassic are developed in Triassic in the Sichuan Basin. Recently, major oil and gas reservoirs are discovered in the Triassic in Sichuan Basin [12, 13], including Puguang, Yuanba, Moxi, and other (large) gas fields. Triassic carbonate rocks are the reservoir rock type of these (large) gas fields. The South Yellow Sea Basin has a promising broad oil and gas exploration

prospect, and the Triassic carbonate rock is suitable for the formation of oil and gas reservoir. It is of great significance to make a major breakthrough in oil and gas exploration in the South Yellow Sea Basin as soon as possible and carry out in-depth research on Triassic in the basin. From the perspective of oil and gas exploration, this paper studies the characteristics of Triassic in the South Yellow Sea Basin of China, including lithologic characteristics, karst development characteristics, relevant correlation with regional strata, and distribution characteristics.

2. Overview of the Study Area

The South Yellow Sea Basin is located at the Yangtze fault block area (Figure 1). According to the trough platform theory, it belongs to the Yangtze quasiplatform. The Yangtze quasiplatform is further divided into the upper, middle and lower Yangtze areas, and the South Ring Basin is located at the lower Yangtze area.

The South Yellow Sea Basin can be divided into three major internal structural units, including the northern depression (Yantai depression), central uplift (Laoshan uplift), and southern depression (Qingdao depression). The Subei Basin is adjacent to the South Yellow Sea Basin. In fact, the southern depression of the South Yellow Sea Basin can be regarded as the marine extension of the Subei Basin.

The South Yellow Sea Basin has developed for a long time. The caprock deposition began in the Sinian period, and many sets of extremely thick carbonate rock strata developed, such as Sinian Cambrian, Middle Carboniferous Lower Permian, and lower Triassic carbonate rock strata. Indianan movement is the most important tectonic activity, experienced by the Yangtze fault block area, which makes the Yangtze fault block area transform from large-scale marine basin to small continental basin.

As depicted in Figure 2, the South Yellow Sea Basin covers a large area of about 300,000 square kilometers, with a geographical range of 32°~34° N as well as 120°~124°. It has a wide exploration area, few exploration wells have been drilled, and the degree of exploration is low.

3. Triassic Characteristics

The Triassic in the South Yellow Sea Basin includes Zhoucun Formation and Qinglong Formation, and Qinglong Formation can be further divided into the upper Qinglong Formation and lower Qinglong Formation. Characteristics of Triassic in the South Yellow Sea Basin, as discussed below, include lithologic characteristics, karst phenomenon, stratigraphic regional correlation, and distribution.

3.1. Correlation with Regional Strata. The lower Yangtze region can be divided into five stratigraphic divisions (Figure 3), including Xianning-Anqing-Nanjing division, Jiuhuashan-Wuxi-Nantong division, Changsha-Nanchang division, Duchang-Dongzhi division, Wuyuan-Huangshan division, and Huaiyushan-Tianmu Mountain layer division [15]. Notably, only the limestone of the lower Triassic Qinglong Formation can be seen in Duchang-Dongzhi division, and only the upper Triassic Sanqiutian Formation and the upper Triassic Tianmu mountain layer division can be seen in Wuyuan-Huangshan division and Huaiyushan-Tianmu layer division. The Permian-Jurassic Duojiang formation is characterized by coarse clastic rock series. Xianning-Anqing-Nanjing, Jiuhuashan-Wuxi-Nantong, and Changsha-Nanchang zones are the major areas, where carbonate rocks developed in the lower Triassic.

According to Figure 3, the South Yellow Sea (southern depression) belongs to the Northeast seaward extension of Xianning-Anqing-Nanjing zone. It is urgent to investigate the characteristics of Triassic in the South Yellow Sea Basin (southern depression) and fully understand the research results of Triassic stratigraphic division. In order to achieve comprehensive knowledge, it is necessary to systematically sort out the problems related to Triassic strata.

Triassic system is located at Anhui Province. Bounded by Mountain-Zhangbaling denudation area, it is divided into the North type and the South type. The Triassic System on both sides of the Yangtze River and southern Anhui belongs to the southern type and belongs to the Xianning-Anqing-Nanjing stratigraphic division (Figure 3), respectively [15–17]. The stratigraphic groups, including Xiaoliangting Formation, Tashan Formation, Nanlinghu Formation, Fenshuiling Formation, Longtoushan Formation, Hujiawu Formation, Chenjiawu Formation, Yueshan Formation, Tongtoujian Formation, Lalijian Formation, Yinkeng Formation, Helongshan Formation, and Wutian Formation, Wuzhishan Formation, have been found at early times.

The traditionally utilized stratigraphic division scheme, in terms of Triassic, is lower Triassic Yinkeng Formation, Helongshan Formation, Middle Triassic Biandanshan Formation, Upper Triassic Yueshan Formation, Tongtoujian Formation, and Lalijian Formation. The scheme is later altered as the lower Triassic Yinkeng Formation, Helongshan Formation, Nanlinghu Formation, Yueshan Formation, Tongtoujian Formation, and Upper Triassic Lalijian Formation.

According to the results of the regional survey team of Anhui Bureau of Geology and mineral resources (1987) [1], the standard profile and main lithological characteristics of the Yinkeng Formation, Helongshan Formation, Nanlinghu Formation, Yueshan Formation, Tongtoujian Formation, and Lalijian Formation in the lower Yangtze subregion are as follows.

The Yinkeng Formation and Longshan Formation were created by Guichi stratigraphic research team of Anhui Province in 1965. The standard zone is located at Guichi county. The lithology of Yinkeng Formation is yellow green and grayish green calcareous mudstone, interbedded with dark gray thin to medium thick limestone, and argillaceous limestone. The thickness of the upper limestone falls in the range of 83~286 m. Lithology of Helongshan Formation is mainly light gray banded limestone, intercalated with a small amount of yellow green calcareous shale, and thin limestone, with a thickness of 21-235 m. Nanlinghu Formation was founded by Wang Changyi in 1964. The standard section is located at Nanlinghu, Nanling County. Its lithology is characterized by thin to medium thick limestone in the lower part, purplish red or yellow green nodular limestone

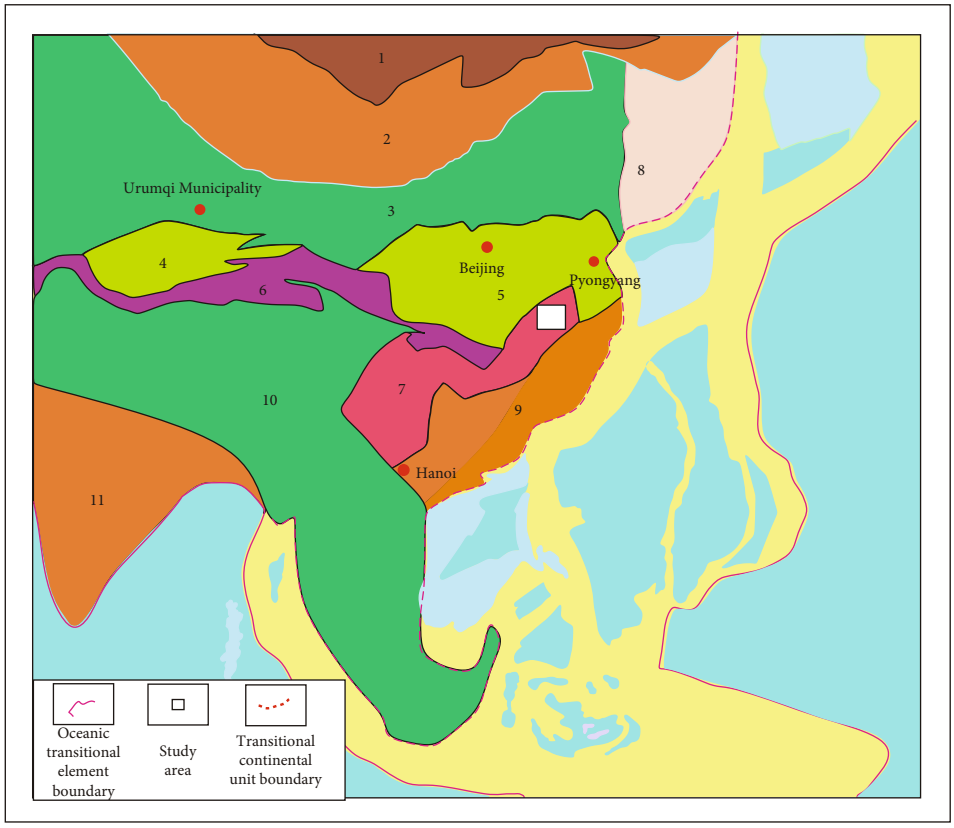

Figure 1: Tectonic location of the South Yellow Sea Basin.

in the bottom, and cyan gray medium thick dense limestone in the upper part, mixed with thin soft wrinkled limestone. The East Maanshan Formation was found by Wang Guixiang in 1979. The standard section is located at Yueshan, Huaining County. The lower part is mainly dolomite, and the upper part is mainly salt soluble breccia. It is generally 110-200 m thick and can reach more than 675 m in the end. The lower part of Yueshan Formation contains Middle Triassic Badong fauna fossils, which are similar to the Zhouchongcun Formation in Ningzhen mountains. The Yueshan Formation, Tongtoujian Formation, and Lalijian Formation were named by Huaining 326 team in 1966. The standard profile of Yueshan Formation is in Yueshan, Huaining County. The main lithology is grayish white and grayish green siltstone and silty shale, intercalated with bluish gray dolomitic limestone and its convex mirror. The Yueshan Formation is only found in Wuhu-Anqing stratigraphic community. Standard section of Tongtoujian Formation is located at Tongtoujian near the Yueshan mountain, Huaining County. The main lithology is purplish red siltstone and silty mudstone mixed with fine sandstone, with a thickness of about 1735 m. The distribution of Tongtoujian Formation is limited, which is only found in Wuhu-Anqing stratigraphic community. This formation is rich in bivalve fossils, and its characteristics are similar to those of the lower part of Huangmaqing Formation in Jiangsu Province.

The standard section of Lalijian Formation is located at Lalijian near Yueshan mountain, Huaining County. It is mainly gray to gray black sandstone, siltstone, sandy shale, and gray black carbonaceous or carbonaceous shale, intercalated with unstable coal seams, with a thickness of 18-75 m. The distribution of this group is limited, and the surface is rarely exposed.

Zhu and Wang (1992) [18] summarized the division scheme of the Early Triassic in Jiangsu and Anhui, and the other three division schemes reflect the current division and correlation relationship. The lithologic characteristics of the lower Triassic in Jiangsu and Anhui may change in different regions. From top to bottom, the main petrological characteristics of the lower Triassic in Ningzhen area are vermicular limestone nodular limestone mudstone, and shale with thin limestone. The main lithological characteristics of the lower Triassic in the area are limestone, thin limestone, and large wormhole limestone, mixed with a small

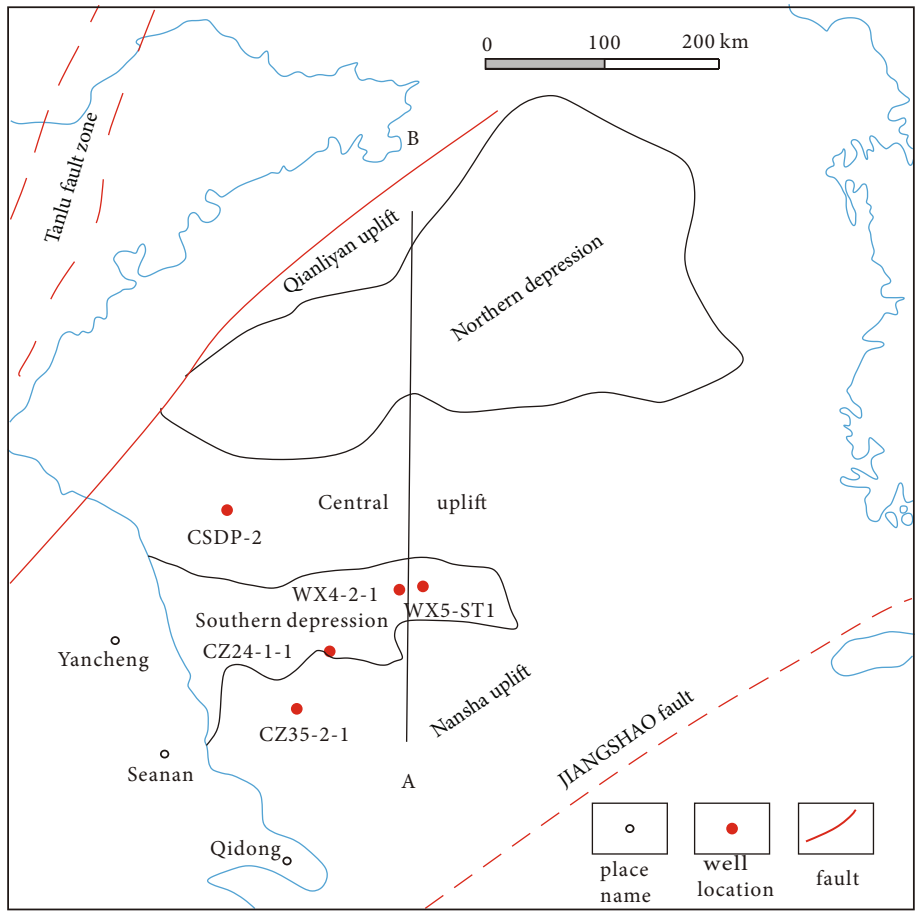

Figure 2: Plane distribution of Triassic wells drilled in the South Yellow Sea Basin [14].

amount of nodular limestone-thin limestone. The change of lithology reflects the different paleogeographic environment. The appearance of oolite limestone and gravelly limestone reflects that its sedimentary environment has the characteristics of marginal facies.

The Huangmaqing Formation, belonging to Middle Triassic Latin stage to the Late Triassic Kani stage, is a set of continental clastic rock, dominated by purplish red in the middle and lower reaches of the Yangtze River [18]. There are large areas of exposed areas on both north and south sides (Figure 4). Various phenomena show that after entering the late Middle Triassic, the large set of limestone of Qinglong Formation of Lower Triassic and evaporite series of Zhouchongcun Formation of Middle Triassic are in an environment of extensive denudation and weathering leaching, which is conducive to the karst phenomenon.

In short, many researchers have carried out the comparative study of Triassic between different units in the Yangtze paraplatform [10, 15, 20]. The Qinglong Formation in the lower Yangtze region corresponds to the Daye Formation in the middle Yangtze region. The upper Qinglong Formation, including Nanlinghu Formation and Helongshan Formation, in the lower Yangtze region corresponds to the Jialingjiang Formation in the middle and upper Yangtze region, and the lower Qinglong Formation in lower Yangtze region corresponds to Feixianguan Formation in middle and upper Yangtze region.

3.2. Lithologic Characteristics. The main lithological characteristics of Shangqinglong Formation are limestone mixed with marl, mudstone, and shale. Main lithological characteristics of Shangqinglong Formation are limestone, mixed with mudstone. The main characteristics of Shangqinglong Formation are interbedding of limestone and marl, limestone mixed with marl, mudstone, and argillaceous siltstone. These wells reveal a common feature of Shangqinglong Formation, demonstrating that the limestone is generally mixed with mudstone, even shale, as well as siltstone.

The main lithological characteristics of Xiaqinglong Formation are limestone weathering shell (well section 1185.5-1246 m, thickness 60.5 m), limestone, marl, and mudstone (well section 1246-1327 m, thickness 81 m), large limestone section (well section 1327-1676 m, thickness 349 m), mudstone mixed with limestone and marl (well section 1676-1779 m, thickness 103 m), limestone and mudstone interbedding (1779-2036.5 m well section, 257.5 m thick), and mudstone mixed with limestone (2036.5-2077 m well section, 40.5 M thick). The lithology of Xiaqinglong Formation, encountered by csdp-2 well, is characterized by limestone mixed with mudstone, mudstone, and

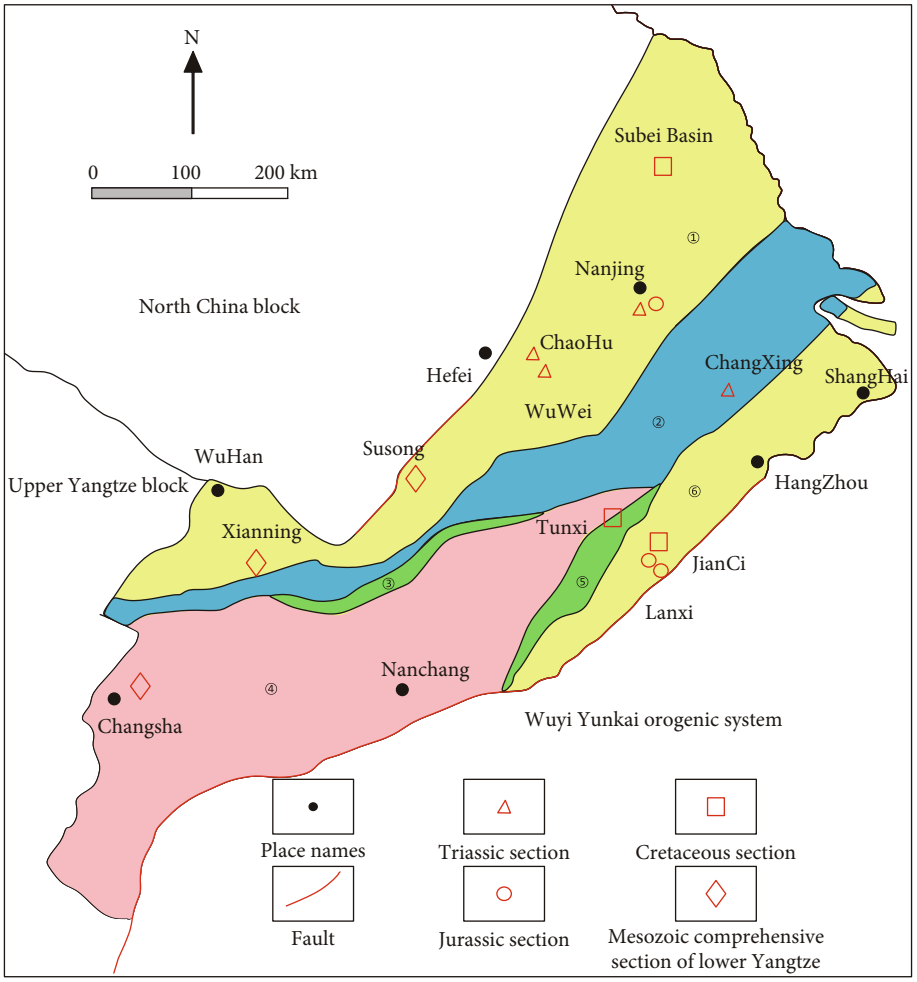

Figure 3: Stratigraphic map of lower Yangtze region [15].

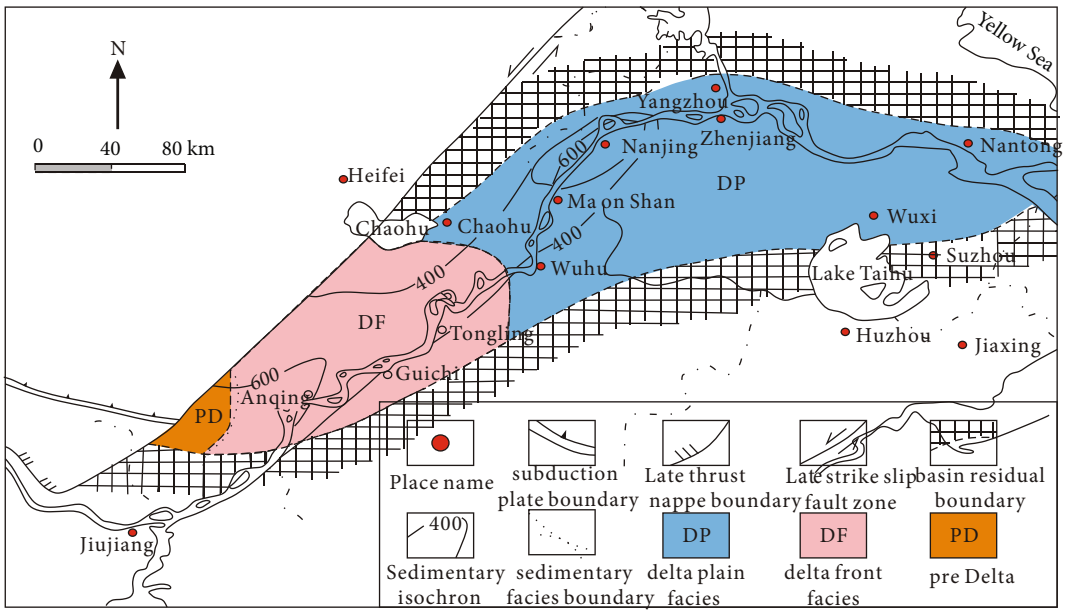

Figure 4: Sedimentary facies of Huangmaqing Formation in Jiangsu and Anhui [19].

dolomite. It should be emphasized that the lithology characteristics of the lower Qinglong Formation, revealed by three wells drilled in the South Yellow Sea Basin, are very different.

3.3. Karst Development Characteristics. The Well wx5-st1 reveals that the lithology of Zhouchongcun Formation is karst breccia, belonging to developed karst phenomenon, and the thickness of karst breccia is 70 m. Well cz35-2-1 reveals that the of Xiaqinglong Formation, ranging from well section 1185.5-1246 m, is gray white, light gray, and gray limestone weathering crust section. Two of the five wells, drilled in Triassic revealed karst phenomenon, indicate that the drilling rate of karst phenomenon is still very high. The thickness of karst interval, revealed by well cz35-2-1, is beyond 60 m, indicating that the influence depth of karstification is relatively large.

As for carbonate areas with obvious karst phenomena, there exist many argillaceous fillings in underground solution gaps and caves through weathering and leaching, and many silty fillings, formed by groundwater, can be seen. For the study of karst phenomena, the identification of karst filling is very important, especially cave filling. Cave fillings have different classifications. Loucks (1999) divided cave fillings into crack breccia, mixed breccia, and cave sedimentary fillings [21]. Xiao et al. (2003) divided cave sediments and deposits into three categories [22], including the flowing mechanical deposits, chemical deposits, and gravity collapse deposits. Specifically, flowing mechanical deposits can be divided into transportable conglomerate facies deposits and transportable sandstone deposits, the latter including fine sandstone, siltstone, and mudstone. For carbonate rock areas with significant karst, large influence depth, and serious sand mud filling, drilling coring is required. The fine sandstone, siltstone, and mudstone encountered can be characterized as interlayer of carbonate rock. In the previous studies focusing on the karst phenomenon of Ordovician carbonate rocks in outcrop area and Tahe oilfield, Tarim Basin, there are many examples in this research scope [23–25]. However, in the previous achievements and understanding of the characteristics of Triassic in the South Yellow Sea Basin [26, 27], these phenomena are basically not involved.

3.4. Distribution Characteristics. Among the five Triassic wells (cz24-1-1, cz35-2-1, wx4-2-1, wx5-st1, and csdp-2), only one well (wx5-st1) encountered Zhouchongcun Formation, only three wells (cz24-1-1, wx4-2-1, and wx5-st1) encountered Qinglong Formation, and only three wells (cz35-2-1, wx5-st1, and csdp-2) encountered Shangqinglong Formation. And the Zhoucun Formation, Shangqinglong Formation, and Xiaqinglong Formation are locally distributed.

According to the three-point scheme of the South Yellow Sea Basin (Northern depression, central uplift, and southern depression), the Triassic is mainly distributed in the central uplift and southern depression, showing significant regional differences in distribution (Figures 5 and 6). The regional comparison results show that the lithology of the Triassic in the South Yellow Sea Basin, revealed by drilling, is significantly different from that in the region. In southern depression of the South Yellow Sea Basin, the Triassic is seriously cut by faults, showing the distribution characteristics of blocks. Relevant studies show that (Figure 6) the residual thickness of Triassic in the southern depression of the South Yellow Sea Basin exceeds 1250 m [14, 28, 29].

4. Discussion

Well wx5-st1 encountered Zhouchongcun Formation at 1340–1410 m, with a thickness of 70 m. The lithology is calcareous breccia, with a particle size of 20-30 mm [25]. Regionally, the main lithology of Zhouchongcun Formation is gypsum breccia, including small insect trace limestone and dolomite. In terms of Genesis, karst breccia and gypsum breccia are also very different. Therefore, the lithology of Zhoucun Formation, drilled in the South Yellow Sea Basin, is very different from that of the regional standard section. The main lithology of Nanlinghu Formation is characterized by thin to medium thick limestone in the lower part, purplish red or yellow green nodular limestone in the bottom, and green gray medium thick dense limestone in the upper part. The main lithology of Helongshan Formation is light gray banded limestone, mixed with a small amount of yellow green calcareous shale and thin limestone, with a thickness of 21-235 m.

It can be seen from the comparison that the main characteristics of Shangqinglong Formation, reflected by wells cz24-1-1, wx24-2-1, and wx5-st1, are quite different from the regional lithological characteristics. This difference is mainly reflected in the widespread existence of mudstone interlayer in all wells, and some wells (well wx5-st1) also have argillaceous siltstone interlayer. In the lower Yangtze region, the lower Qinglong Formation corresponds to the Yinkeng Formation. On the standard section, the lithology of Yinkeng Formation is yellow green and grayish green calcareous mudstone interbedded with dark gray thin to medium thick limestone and argillaceous limestone. According to comparison, the main lithologic characteristics of Xiaqinglong Formation, reflected by well cz35-2-1, are very different from those of the region. First, the thickness of Yinkeng Formation on the standard profile is only 83-286 m, while the thickness of cz35-2-1 well is 891.5 m. Second, a large set of limestone, with a thickness of 56 m, was encountered when drilling well cz35-2-1, which is a typical lithology of Shangqinglong Formation.

In short, mudstone intercalation generally appears in the upper part of Qinglong Formation in wells, drilled in Qinglong Formation. These phenomena may be the result of primitive sedimentation or late karst. A large set of carbonate rocks and karst phenomena are widely developed in the lower Triassic in the Yangtze paraplatform, for example, large-scale karst cave group developed in Longwanggang, Hunan Province, the large-scale karst cave group developed in Yixing, Jiangsu Province, and the large-scale karst cave group developed in Xingguo, Anhui Province. Many karst caves are also distributed in the vicinity of the cave. The important karst caves include Dashan rock (cave), Huimao Cave, Rhinoceros cave, Tianhe cave, and Guanyin cave. These karst caves form a large karst cave group. In terms

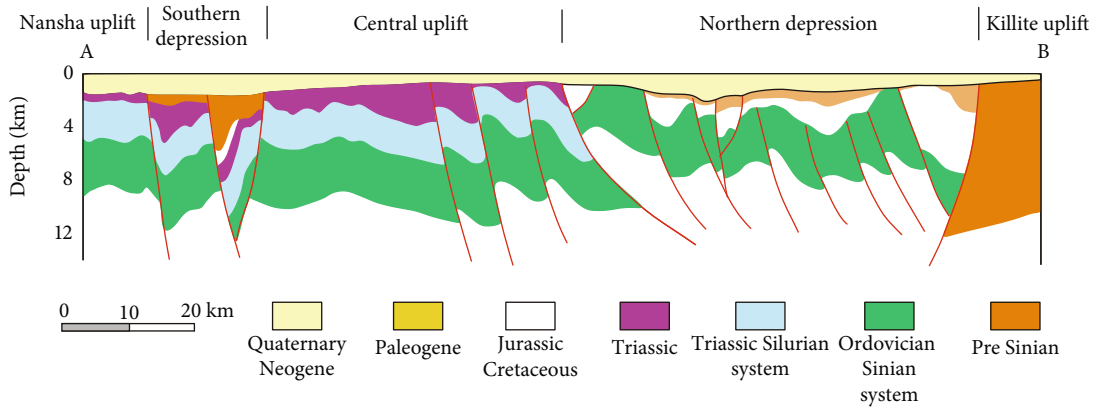

Figure 5: Profile distribution of Triassic in the South Yellow Sea Basin [14].

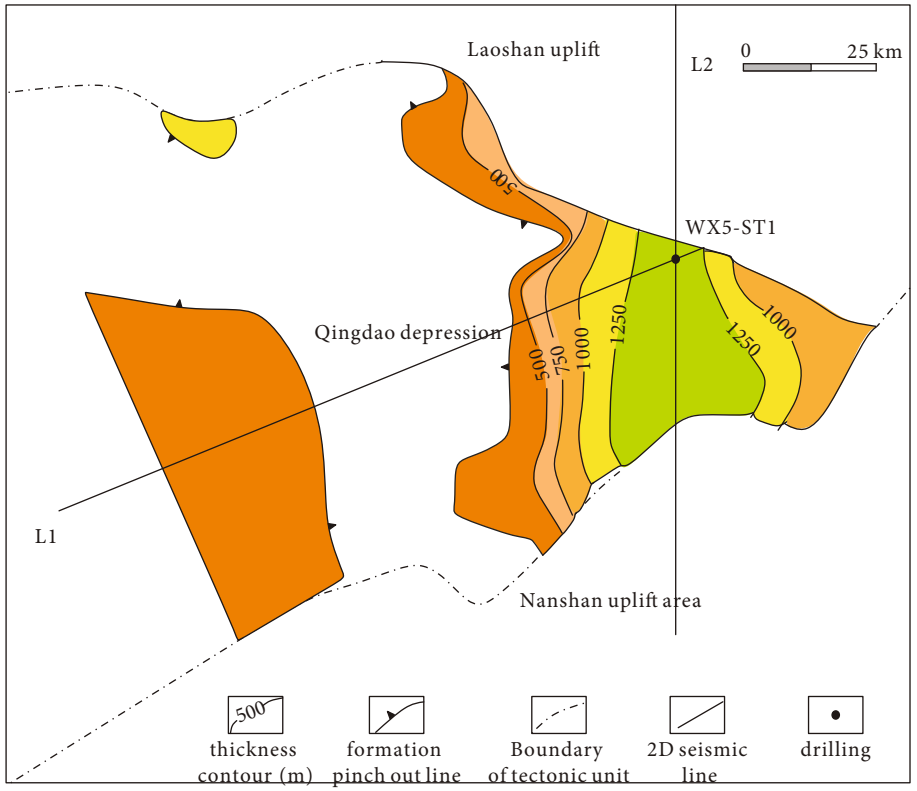

Figure 6: Triassic residual thickness and its distribution in the southern depression of the South Yellow Sea Basin [14].

of Longwang cave and its large-scale karst caves nearby, the area, where these holes are located, is about 14 km^2.

There are abundant karst phenomena in Longwang cave (Figure 7). Fractures in the cave are well developed [28, 29]. It is found that the development of fractures has a positive correlation with the development degree of karst. The development degree of karst phenomena in different locations is different. At the fault or fracture turning point, medium and large stalactites are less developed.

Karst caves are densely developed in Yixing, Jiangsu Province. The soluble rock series in the area are carbonate rocks, and faults are very developed, including NW, NW, NE, and NE direction. The developed large-scale karst caves include Shanjuan cave, Zhanggong cave, Yuquan cave, Linggu cave, Muli cave, and Xishi cave (Figure 8). Among them, Shanjuan cave, Lyon cave in France, and Han cave in Belgium are known as the three wonders of the world. Large-scale karst caves are mainly developed in areas where large-scale carbonate rocks of Qinglong Formation of lower Triassic are exposed, such as Shanjuan cave, Zhanggong cave, Yuquan cave, and Linggu cave.

As mentioned earlier, for carbonate rock areas with significant karstification, sand mud filling, the fine sandstone, siltstone, and mudstone drilled in the drilling coring can

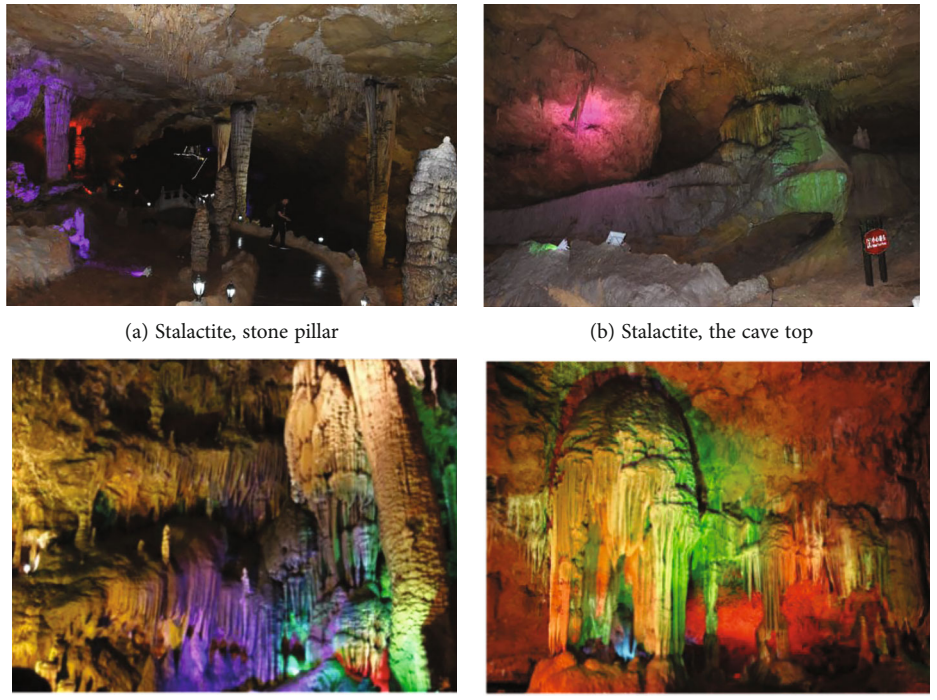

(a) Stalactite, stone pillar

(b) Stalactite, the cave top

(c) Stalactites, pillars and waterfalls

(d) Stalactites

Figure 7: Karst morphological types and characteristics in Longwang cave.

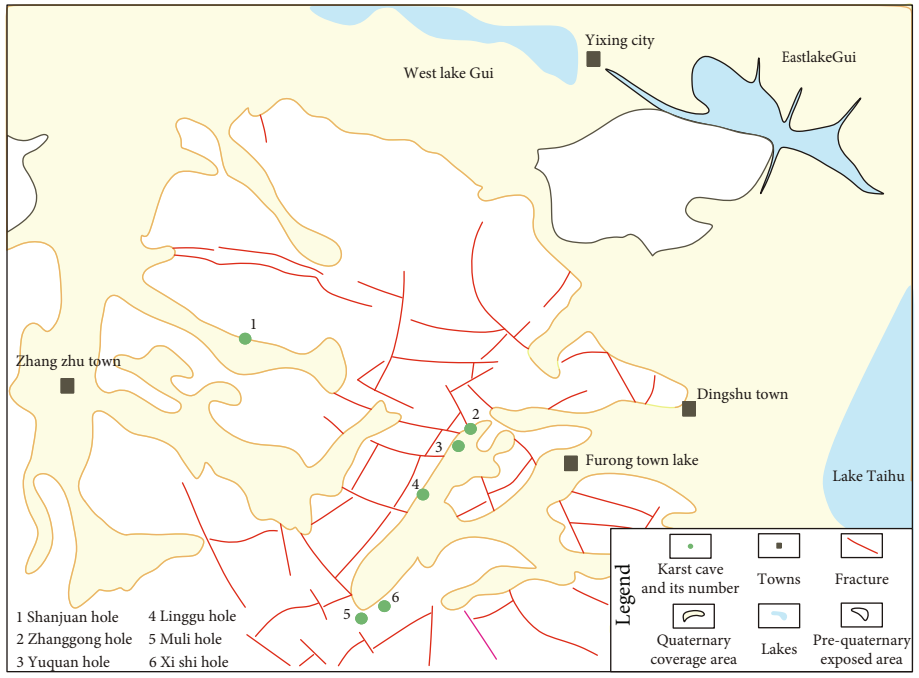

Figure 8: Distribution diagram of large karst caves in Yixing, Jiangsu.

be characterized as interlayer of carbonate rock. Tahe oilfield in Tarim Basin is a world-famous large oilfield; the Ordovician Karst carbonate rock series is the main reservoir. This set of carbonate rock series is distributed on the long-term uplift, with significant karst development, and the depth of karst zone can reach more than 250 m. At least two cave filling intervals are developed in well section 5548–5553 m of well T403 in block 4 of Tahe oilfield. Among them, one section is distributed in well section 5539.5-5548.5 m. The other section is distributed at 5505.5-5539.5 m. In a large set of

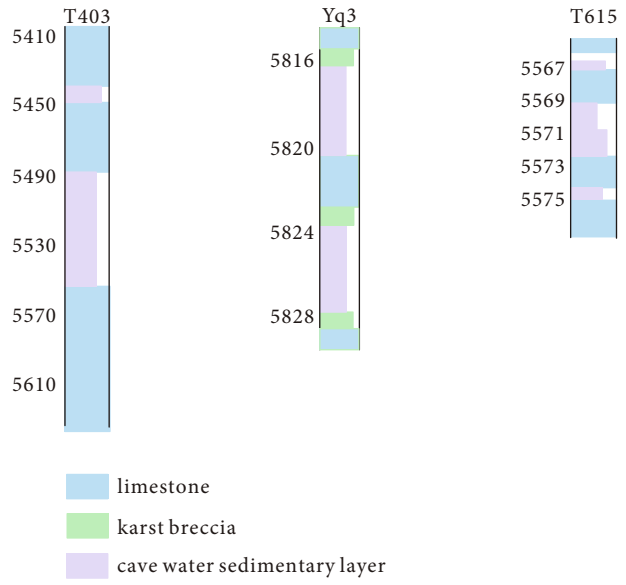

Figure 9: Karst filling in well section 4929.00-4980.78 m of yq3 well in Yuqi Area of Tahe Oilfield.

carbonate formations, these cave filling deposits appear in the form of interlayer (Figure 9(a)). Three cave filling intervals also appear in well t615 in block 6 of Tahe oilfield in well section 5560~5580 m (Figure 9(b)); it is characterized by interlayer in Ordovician carbonate rocks. In the well section 4929.00-4980.78 m of yq3 well in Yuqi area of Tahe oilfield, there are two large karst filling layers, which are characterized by large thickness, and the Ordovician carbonate rocks are characterized by interlayer (Figure 9(c)).

In the carbonate rock distribution area with strong karstification, great influence depth, serious sand mud filling, and the lithology can change greatly due to the transformation of karstification, from a large set of carbonate rocks to intercalated with clastic rocks. This change in lithology will increase difficulties in stratigraphic division and lead to wrong stratigraphic division results. This problem is very prominent for the upper and lower Qinglong Formation of Triassic in the South Yellow Sea Basin. The study is of great significance for carbonate reservoir evaluation.

5. Conclusions

(1) The lithological characteristics of Triassic groups in the South Yellow Sea Basin are significantly different from those in the region. The lithology of Zhouchongcun Formation in the South Yellow Sea Basin, revealed by drilling, is karst breccia, which is characterized by gypsum breccia and dolomite. The lithology of Shangqinglong Formation in the South Yellow Sea Basin revealed by drilling is limestone mixed with marl, mudstone, and argillaceous siltstone. Lithological characteristics of this formation area are mudstone, mudstone, and marl interbedding. The limestone, intercalated with syngenetic breccia, is developed in some areas

(2) The Triassic karst in the South Yellow Sea Basin is developed, the thickness of karst breccia of Zhouchongcun Formation is up to 70 m, and the thickness of weathered crust of Xiaqinglong Formation is up to 60.5 m. Triassic strata in the South Yellow Sea Basin are locally distributed, mainly in the central uplift, and southern depression of the South Yellow Sea Basin

(3) The lithologic characteristics of the upper and lower Qinglong Formation revealed by drilling in the South Yellow Sea Basin may be the result of karstification transformation. In-depth study of the genesis and formation period of its lithologic characteristics is not only a karstification problem in carbonate rock area but also a very important stratigraphic division and correlation problem

Data Availability

Data are available on request.

Ethical Approval

On behalf of all the co-authors, the corresponding author states that there are no ethical statements contained in the manuscripts.

Conflicts of Interest

The authors declare that there is no conflict of interest regarding the publication of this paper.

Acknowledgments

The authors acknowledge the SINOPEC for the permission to publish this work.

References

[1] Team, R.G.S. and Bureau of Geology and Mineral Resources of Anhui Province, *The Stratigraphy of Anhui Province, Volume of Ordovician*, Anhui Science and Technology Publishing House, Hefei, 1989.

[2] C. Laixing, X. Guolin, W. Huiqing et al., "Multistage accumulation of Mesozoic Paleozoic marine oil and gas in the central uplift of the South Yellow Sea Basin - exploration enlightenment from csdp-2 well," *Journal of Jilin University (Earth Science Edition)*, vol. 51, no. 2, pp. 307–324, 2021.

[3] C. Chuzhen, "New understanding of some Triassic stratigraphic ages in southern China," *Geological Review*, vol. 6, no. 3, pp. 231248-231249, 1960.

[4] C. Jianwen, G. Jianming, L. Gang, L. Huijun, Y. Yong, and Z. Yuxi, "The marine Mesozoic Paleozoic oil and gas resources in the South Yellow Sea basin are huge," *Marine Geological Frontier*, vol. 32, no. 1, pp. 1–7, 2016.

[5] C. Yixiu and Y. Dan, "Research progress on the genesis of stratabound sulfide deposits in Tongling ore concentration area of the metallogenic belt in the middle and lower reaches of the Yangtze River," *Deposit Geology*, vol. 40, no. 1, pp. 128–142, 2021.

[6] C. Yulu, Z. Kuanzhong, L. Guanqing, N. Ciren, Z. Shouren, and C. Guorong, "Discovery and significance of angular unconformity of Upper Triassic Quehala group in underlying rock series in the middle of Bangonghu Nujiang junction zone," *Geological bulletin*, vol. 24, no. 7, pp. 621–624, 2005.

[7] C. Zongqing, "On natural gas exploration in Feixianguan Formation of Lower Triassic in Sichuan Basin," *Journal of Petroleum*, vol. 28, no. 50, pp. 12–19, 2007.

[8] H. Yan, "Early and Middle Triassic foraminifera in Jiangsu and Anhui," *Journal of Micro Paleontology*, vol. 5, no. 1, pp. 85–92, 1988.

[9] L. Junqing, *Sedimentary Characteristics and Environmental Significance of Late Early Triassic along the Yangtze River in Anhui Province*, Hefei University of technology, Hefei, 2013.

[10] Q. Zhanfeng, *Fine Study on Sequence Stratigraphy and Reservoir of Feixianguanzu in Puguang Gas Field, Eastern Sichuan*, Chengdu University of technology, Chengdu, 2008.

[11] Bureau of Geology and mineral resources of Jiangsu Province, *Regional Geology of Jiangsu Province and Shanghai*, Geological Publishing House, Beijing, 1984.

[12] M. Lihua, Z. Jianhua, and L. Weibing, "Sequence stratigraphic framework and reservoir development characteristics of Puguang gas field," *Fault- Block Oil & Gas Field*, vol. 17, no. 3, pp. 312–315, 2010.

[13] Z. Sun, B. Huang, K. Wu et al., "Nanoconfined methane density over pressure and temperature: wettability effect," *Journal of Natural Gas Science and Engineering*, vol. 99, article 104426, 2022.

[14] T. Jinnan, C. Daoliang, L. Lei et al., "Triassic comprehensive stratigraphy and time frame in China," *Chinese Science: Earth Science*, vol. 49, no. 1, pp. 194–226, 2019.

[15] N. T. Lin, D. H. Gao, J. Sun, L. Wei, and J. Peng, "Seismic attributes and geological significance of Permian and Triassic in Qingdao depression, South Yellow Sea Basin," *Journal of Petroleum*, vol. 33, no. 6, pp. 987–995, 2012.

[16] Z. Zhang, W. He, Y. Wei, X. Ke, and M. S. Luo, "Evolution of Mesozoic sedimentary basins in the lower Yangtze," *Earth Science Journal of China University of Geosciences*, vol. 39, no. 8, pp. 1017–1034, 2014.

[17] W. Weihong and D. Hongliang, "Study on sedimentary facies of Triassic Qinglong formation in lower Yangtze region," *Complex Oil and Gas Reservoir*, vol. 2, no. 3, pp. 5–10, 2009.

[18] Z. Hongfa and W. Shuyi, "Genesis of Triassic nodular limestone and vermicular limestone in southern Jiangsu and southern Anhui," *Petroleum Experimental Geology*, vol. 14, no. 4, pp. 453–460, 1992.

[19] Y. Wenzhe, Y. Zhizheng, and B. Zhongqi, "A large river delta sedimentary system - on the sedimentary environment of HUANGMAQING formation of middle upper Triassic in Jiangsu and Anhui," *Acta Geo Sinica*, vol. 20, no. 3, pp. 309–317, 1999.

[20] Z. Yinguo and L. Jie, "Characteristics of Permian Triassic sedimentary system and its sedimentary evolution in the South Yellow Sea Basin," *Journal of Jilin University (Earth Science Edition)*, vol. 44, no. 5, pp. 1406–1418, 2014.

[21] R. G. Loucks, "Paleocave carbonate reservoirs; origins, burial-depth modifications, spatial complexity, and reservoir implications," *AAPG Bulletin*, vol. 11, no. 83, pp. 1795–1834, 1999.

[22] X. Yuru, H. Fengyu, and S. Yimei, "Study on the characteristics of ancient cave type carbonate reservoir - taking the Ordovician ancient cave in Tahe oilfield as an example," *Petroleum and Natural Gas Geology*, vol. 24, no. 1, 2003.

[23] Z. Sun, B. Huang, Y. Li, H. Lin, S. Shi, and W. Yu, "Nanoconfined methane flow behavior through realistic organic shale matrix under displacement pressure: a molecular simulation investigation," *Journal of Petroleum Exploration and Production Technology*, 2021.

[24] Z. Sun, S. Wang, H. Xiong, K. Wu, and J. Shi, "Optimal nanocone geometry for water flow," *AICHE Journal*, vol. 2022, no. 68, article e17543, 2021.

[25] Z. Yucheng, C. Qinghua, S. Ke et al., "Distribution characteristics and development model of karst in Hunan," *Journal of China University of Petroleum (NATURAL SCIENCE EDITION)*, vol. 44, no. 4, pp. 163–173, 2020.

[26] Y. Yanqiu, *Distribution of Upper Permian Lower Triassic in Southern Yellow Sea and Significance of Oil and Gas Exploration*, Jilin University, Changchun, 2004.

[27] P. Yu, D. Dempsey, and R. Archer, "A three-dimensional coupled thermo-hydro-mechanical numerical model with partially bridging multi-stage contact fractures in horizontal-well enhanced geothermal system," *International Journal of Rock Mechanics and Mining Sciences*, vol. 143, article 104787, 2021.

[28] Z. Tao, *Study on the Formation and Maintenance of Ordovician Karst Reservoir in Akekule Uplift*, China University of Geosciences (Beijing), Tarim Basin. Beijing, 2012.

[29] J. Qiang, T. Fei, L. Xinbian, and K. Xun, "Collapse and filling characteristics of Ordovician paleorunoff karst zone in Tahe oilfield," *Oil and Gas Geology*, vol. 36, no. 5, pp. 729–735, 2015.

Hindawi
Geofluids
Volume 2022, Article ID 3910586, 11 pages
https://doi.org/10.1155/2022/3910586

Research Article

Characteristics of Middle-Lower Ordovician Ultradeeply Buried Carbonate Reservoirs in Shunbei Area, Tarim Basin—A Case Study from Well SHBP1

Xiao Chongyang,[1,2,3] Zhao Rui,[4] Fu Heng,[1,2] Huang Cheng,[3] Han Jun,[3] and Lin bo[3]

[1]*College of Energy, Chengdu University of Technology, 610059, China*
[2]*State Key Laboratory of Oil and Gas Reservoir Geology and Exploration, Chengdu, Sichuan 610059, China*
[3]*Northwest Oilfield Branch Company, SINOPEC, Urumqi 830011, China*
[4]*Petroleum Exploration and Production Research Institute, SINOPEC, Beijing 100083, China*

Correspondence should be addressed to Fu Heng; doublesun_show@163.com

Received 9 January 2022; Revised 14 February 2022; Accepted 16 February 2022; Published 15 March 2022

Academic Editor: Zheng Sun

Fracture-pore complexes, located at fault zones of Darriwilian carbonates, are the main exploration targets in the Shunbei area, Tarim Basin. This article focuses on the carbonate characteristics in the Lower Ordovician of Well ShunbeiPeng1 (SHBP1), the carbonate is sandwiched by two trending NW-SE deep-seated, strike-slip faults in the Shuntuoguole uplift. Based on detailed core investigation and careful petrographic examination, two main reservoir types, denoting microquartz and dolomite, are recognized. The former is mainly constrained in the lower part of the sampled core and gradually evolves to the latter with progressively decreases of silica. Integrated isotopic geochemistry (C, O, and Sr) and fluid inclusion microthermometry suggest that the fluids are hydrothermal origin and migrate along deep-seated strike-slip faults, forming favorable carbonate reservoirs. The fault-controlled hydrothermal reservoirs, characterized by the strong amplitude in the seismic profile, would be the most promising exploration area in deeply buried carbonates in the Tarim Basin, particularly in the Shuntuoguole area.

1. Introduction

The lower Paleozoic carbonate rocks, located at the Tarim Basin, contain abundant oil and gas resources and are the main targets for hydrocarbon exploration in the future [1, 2–6]. However, the characteristics, mechanism, and distribution of the promising carbonate reservoirs have not been clearly understood, probably due to the ultradeeply burial and multiple intensive tectonic alterations. As a result, it is urgent to perform investigations to reveal the inherent characteristics of ultradeeply buried carbonate reservoirs in Tarim Basin.

Shunbei area, located in the Shuntuoguole low uplift, is characterized with low exploration position. Notably, from the purpose of hydrocarbon exploration in Shunbei area, fault zone is the main target area [7–11]. Since the successive breakthrough of the Shunbei No. 1 Fault and subsequent No. 5, No. 7 Faults demonstrated the abundant distribution of fault-controlled carbonate reservoirs in the Middle Ordovician carbonates [12–16]. In light of abnormal beaded reflectors, the high-quality reservoirs may exist in the deep-buried geological layers, ranging from Florian to Dapingian successions [9, 17, 18]. However, these reservoirs have not yet been detailed studied, due to the scarcity of the drilling core dataset. Therefore, this article aims at determining the characteristics of the deep-burial carbonate reservoirs, and their relationships to the tectonic activity as well as evolution, and documents the main influential factors of these deep-burial carbonate reservoirs finally. In order to reach the goals, in this article, a systematic petrographic and geochemical study of Well SHBP1, located at the Lower Ordovician Yingshan Formation of the Middle Ordovician, is carried out, proving siliceous is of secondary metasomatism origin. The above observations further indicate that transformation

is important for the siliceous fluid reservoirs in this block. Till now, current investigation, upon Shunbei Yingshan Formation, is greatly limited as a result of low exploration and well coring data, therefore it is hard to judge the siliceous metasomatism of reservoirs, its function to transform the spatial distribution characteristics, and its scale. Accordingly, the study of the core of Well SHBP1 will be an important way to clarify the nature and source of siliceous fluid and serves as the prediction tool of the development characteristics, genesis, and main controlling factors of the fracture hydrothermal-controlled carbonate reservoir. This research will provide reference for future oil and gas exploration of deep-buried carbonate reservoirs.

2. Geological Setting

Shunbei area is located in the north of the Shuntuoguole low uplift, falling in the conjunction between the Awati faulted depression, Manjiaer depression, and Shaya uplift. The Shuntuoguole uplift formed in the middle Caledonian and underwent multiple tectonic activities, such as the Hercynian and Indo-china, forming the nowadays framework. A series of deep-seated and strike-slip faults, which intersect the strata from the crystalline basement through the Upper Ordovician Yijianfang Formation, are present in the Shuntuoguole uplift [7, 8, 19, 20]. The Cambrian-Lower Ordovician in the Shunbei area is dominated by huge thick carbonate rocks, and then, the craton disappeared. In the late Hercynian period, the northern Tianshan Ocean and the southern Tettis Ocean closed orogeny, and the Tarim block became the southern margin of the Eurasian continent, and the Marine sediments were dominated by the continental littoral shallow lake and fluvial facies. Under the control of oblique and rotating stress fields, generated by the multistage activities of the two paleo-uplifts in Tazhong and Tabei, a series of intraplate strike-slip fault zones, sharing a good matching relationship with regional tectonic events, formed in the Shuntuoguole area (Figure 1). Multistage fault zones, with NE and NW directions and large strike-slip features, are developed in the area, which cut down through the Cambrian to the basement and disappeared in the Upper Ordovician mudstone or Yijianfang Formation plastic formation [7, 8]. Notably, the vertical structure has upright or flower-like shape. Moreover, analysis results from multiple wells indicate the desirable reservoir-forming conditions in Shunbei area, and the fault zone is the main favorable area for hydrocarbon enrichment.

Well SHBP1 is sandwiched between No. 5 and No. 7 strike-slip fault zone, trending NW-SE direction, meanwhile it has negative flower structure and conjugates the NE-trending strike-slip faults in the Xayar uplift (Figure 1). In the block, there are different positions of deficiency in the middle and upper Silurian series, middle and lower Devonian series, upper Carboniferous series, lower and upper Permian series, Jurassic series, upper Cretaceous series, and Paleogene Kugelman formation, while the rest of strata are fully developed. In the block, the Ordovician strata are fully developed, including the lower series Penglaiba formation, the middle series Yingshan formation, the middle series Tongyi Jianfang formation, the upper series Qierbak formation, Lianglitage formation, and Sangtamu formation. Among them, the Tongjianfang formation and the Yingshan formation in the Ordovician system are the main target strata, and the Penglaiba formation-Yingshan formation developed NE concealed faults, and the reservoir type is fracture-cavity type.

3. Methods

The samples, for cathodoluminescence (CL) analysis, were processed by twin polishing, then pasted with epoxies, and tested with the help of CL8200 MK5 cathodoluminescence apparatus. The working conditions were set as high pressure at 8 ~ 10 kV, electric current at 0.4 ~ 0.6 mA, and vacuum degree at 13~7 Pa.

As for scanning electron microscope (SEM) analysis, fresh core samples were put in a 50°C oven for four hours at first and then coated with gold membrane. At room temperature, the samples were observed, using a Quanta 200 scanning electron microscope with frequency of 50 HZ and resolution of 30 nm.

In situ C-O isotope analysis was conducted on sections with thickness ranging from 50 to 100 μm, using laser Raman ablation on a Thermo Fisher MAT253 mass spectrometer. Specifically, the laser spot diameter is 200 μm, and GBW4405 and 811 standards are adopted for parallel analysis, with a resolution of ±0.22% for both $\delta^{13}C$ and $\delta^{18}O$ measurement.

Sr isotopic analysis was carried out on a Finnigan MAT-253 Triton TI mass spectrometer with an error of 0.002%. The samples for fluid inclusion analysis were prepared into 0.1 mm sections by twin polishing operation, and a Leica DM4500P microscope was employed for mineral observation. During a Linkam TS1400XY type cooling/heating stage, homogenization and freezing-point temperatures were measured, the resolutions can reach 2°C and 0.5 (±5%)°C, respectively.

3.1. Petrography Characteristics. The cores, sampling at the vicinity of the lower boundary of Yingshan Formation from Well SHBP1, which is the only cored individual well in study area, are badly damaged. The color of the whole rock is gray to white gray. From the bottom to the top, two units could be subdivided based on detailed core investigation as well as microscopic examination.

The lower unit, with color from light to gray, has a high content of silica with minor black quartz crystals (Figure 2(a)). The content of silica gradually decreases downwards, whereas the calcareous increases (Figure 2(b)). From a microscopic perspective, two distinctive quartz textures are recognized, suggesting the matrix and cement quartz (Figures 2(c) and 2(d)). The matrix quartz is mainly composed of microcrystalline quartz (Figures 2(e) and 2(f)) and chalcedony. The former is very small (<5 ~ 20 μm) with equigranularity structure, whereas the latter is fibrous and/or radial with cryptocrystalline texture. In contrast, the quartz cements commonly consist of coarse to very coarse crystalline (20~2000 μm), and its shape varies from blade to columnar

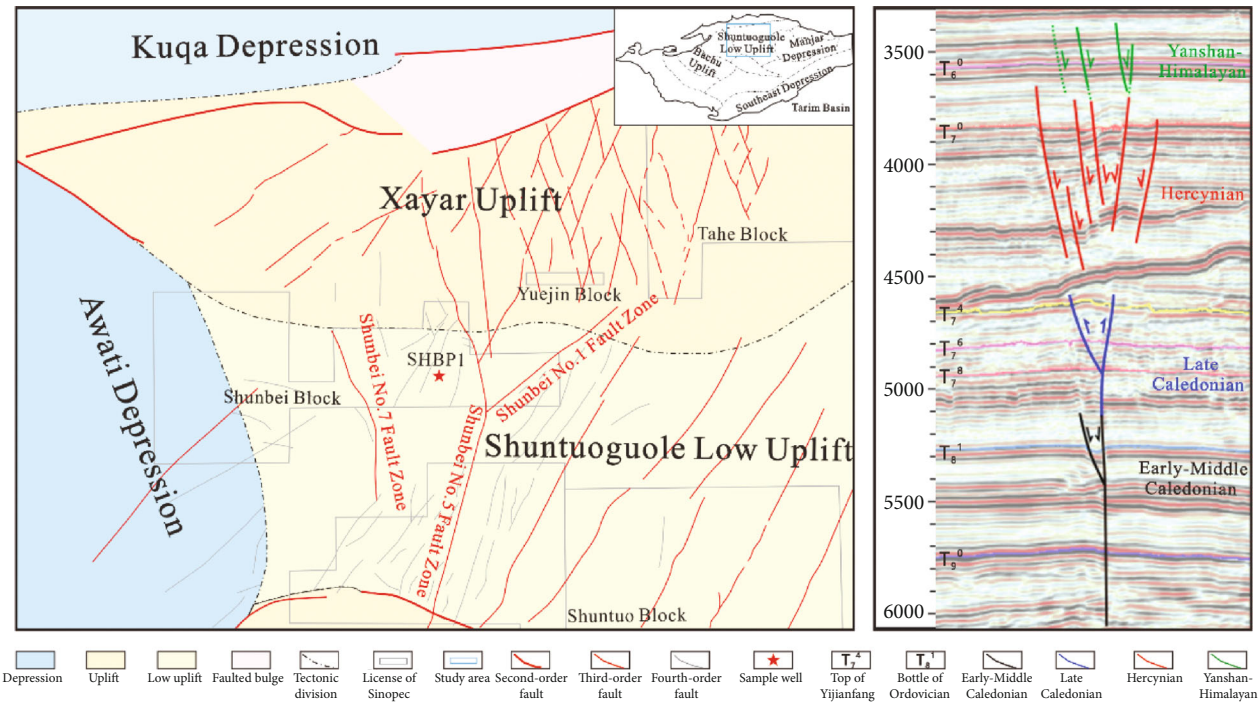

Figure 1: Tectonic location of Shunbei area in Tarim Basin.

forms (Figure 2(c)). In addition, crystals occur as fracture infills with mosaic texture and become coarsening from the rim towards the center (Figure 2(d)).

The upper interval is mainly composed of dolomite, which is gray to light gray (Figures 3(a) and 3(b)). The existence of relict breccias can be observed locally (Figure 3(a)). Pore spaces, produced by dissolution, pervasively occur along the fractures and are partially filled by coarse calcite cements or organic materials (Figures 3(a) and 3(b)). With the utilization of the microscope, the size of dolomite crystals ranges from 5 to 20 μm, characterized by euhedral to subhedral crystals with planar to rectilinear crystal surfaces. Also, it is evident that some dolomite crystals are subject to mild corrosion. Intercrystallite pores are pervasively present and partially occluded by microquartz mineral (Figures 3(c) and 3(d)). Dolomites near fissures are broken into honeycomb pores, while fissures or caves are filled with megacrystal calcite (Figures 3(e) and 3(f)). To current knowledge, core characteristics indicate the typical fluid reforming traces. In this work, efforts have been made to identify the role of fluid in reforming reservoirs by geochemical means.

4. Results

4.1. C-O Isotope Characteristics. The limestones, collected from the Yingshan Formation, Shuntuoguole area, have $\delta^{13}C$ values from -1.25‰ to -1.08‰ VPDB and $\delta^{18}O$ from -7.95‰ to -7.42‰ VPDB. Calcite veins in the limestone have $\delta^{13}C$ values from -2.21‰ to -2.06‰ VPDB and $\delta^{18}O$ from -12.24‰ to -12.08‰ VPDB. Dolomite in Well SHBP1 has $\delta^{13}C$and $\delta^{18}O$ values of -2.14‰ and -7.78‰, respectively. Calcite fillings have $\delta^{13}C$ values from -3.2‰ to -2.6‰ VPDB (average -2.71‰) and $\delta^{18}O$ values from 18.6‰ to 15.4‰ VPDB (average -16.525‰) (Figure 4).

4.2. Sr Isotope Characteristics. The micrite in Yingshan Formation of Shunbei area has a narrow range of $^{87}Sr/^{86}Sr$ ratio, varying from 0.708750 to 0.708792, which is basically consistent with the previously reported ratio of micrite in this area ($^{87}Sr/^{86}Sr$: 0.708899) (Li, Acta Petrolei Sinica). The pack stones yield $^{87}Sr/^{86}Sr$ ratios of 0.70881 to 0.708914, with an average of 0.70885, which is generally consistent with the isotopic ratio of Middle Ordovician age (0.7087~0.7089) [21–23]. Late-stage calcite fillings in fissures have $^{87}Sr/^{86}Sr$ ratios (0.709805~0.710201), greatly higher than those of limestones (Figure 5).

4.3. Fluid Inclusion Microthermometry. Inclusions in dolomite have diameters mostly of <10 μm; therefore, relevant work cannot be conducted. However, massive two-phase inclusions are developed in megacrystal calcite cement, and vapor-liquid two-phase saline inclusions mostly take place in the oriented bands. These inclusions are colorless under transmission light, and they have little typical secondary evolution, with sizes falling in the range of 3 ~ 15 μm, the average value is 8 μm. The minimum homogenization temperature is 124°C, and the maximum temperature exceeds the tolerance of the measuring instrument; thus, homogenization could not be achieved. All the measured temperatures are beyond 230°C. According to inclusion quantity, the average temperature was set slightly higher than 160°C, and the measured main homogenization temperatures were controlled in the 150~160°C or>200°C intervals (Figure 6). The freezing-point temperatures vary from -22.1°C to -8.9°C with an average of -10.9°C. According to the formula

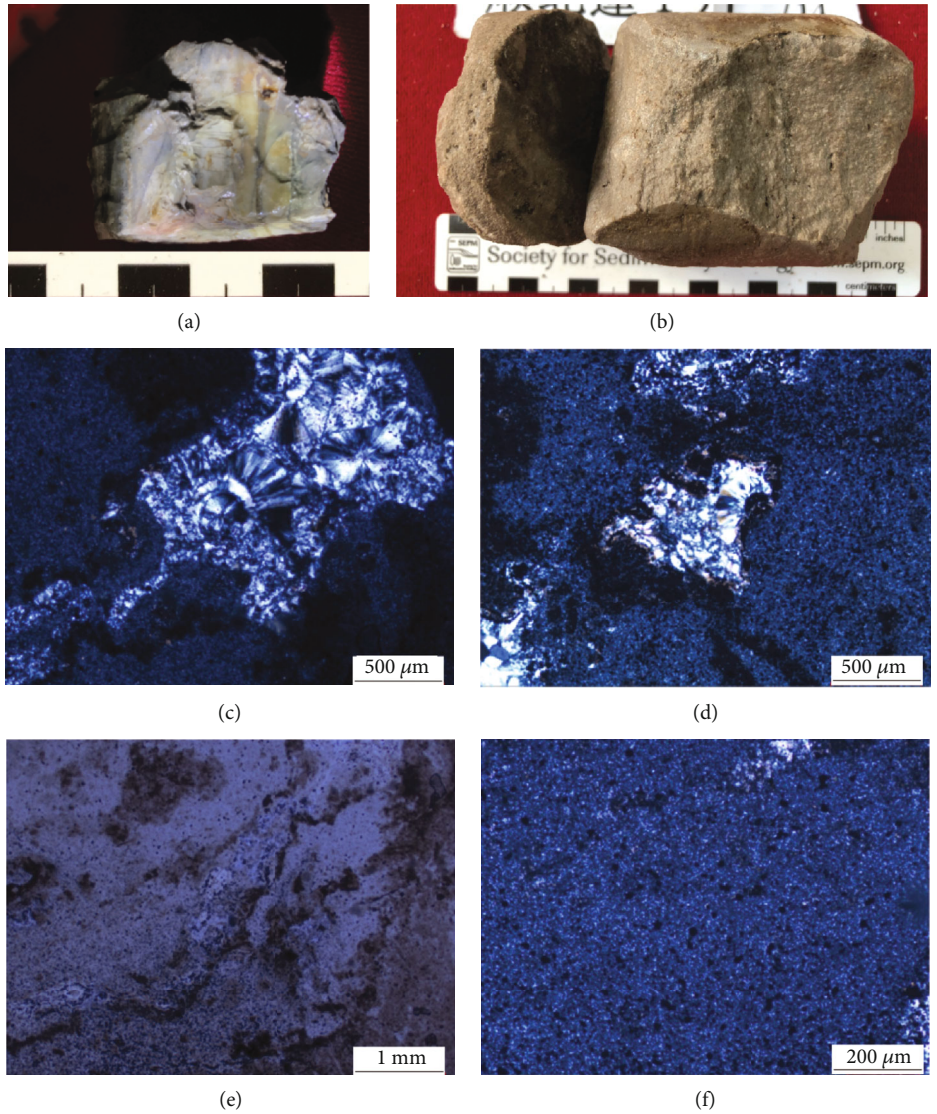

Figure 2: The lower unit characteristics of Well SHBP1. Microscopic/petrographic characteristics of samples in the lower core: (a) Light gray siliceous rock. Silicification develops along fractures, layered siliceous bands, and pyrite, 8455.71-8455.73 m; (b) Light gray siliceous rock. Silica is mainly cryptocrystalline, quartz crystal growth, and residual filling along the fracture wall can be seen on the fracture surface, 8455.73-8455.77 m; (c) Qtz is present as the subhedral quartz crystal, which developed a few pores. Quartz fills the fractures, chalcedony is filled in the fractured-cavity, as observed in microscopic photo of XPL, 8455.74 m; (d) Silicified rock with crystalloblastic texture is composed of microcrystalline quartz and granular quartz, with large intercrystallite pores and reprecipitated calcite cement, 8455.73 m, XPL; (e) Siliceous rocks. It is dominated by microcrystalline quartzite, which consists of microcrystalline quartz and granular quartz with crystalloblastic texture, 8455.72 m, PPL; (f) Siliceous rocks. Partially magnified slice of E, microcrystalline quartz, 8455.72 m, XPL.

[24], the salinities were calculated, ranging from 15.2 to 17.9 wt% NaCl equivalent, with an average of 16.2 wt% NaCl equivalent. In compliance with the definition of fluid inclusion combination [25, 26], it is believed that there are two groups of inclusions. Other than that, considering the temperature difference exceeds 30°C, the hydrothermal fluids may exist.

5. Discussions

According to the aforementioned results, the development characteristics of reservoirs can be summarized. At first, pores are formed along with high-angle fractures and fractured breccias. Then, the reservoir space is composed of dilatant pore-caves along fissures, dolomite intercrystallite (corrosion) pores, and autogenic quartz intercrystallite pores. Aside from that, reservoir development mechanism can be summarized as the interface-controlled faulting-hydrothermal activity. The four main evidences are as follows:

(1) From the macroscopic view, observation of core indicates the fading thermal color along fissures. Moreover, with the help of a microscope, it can be

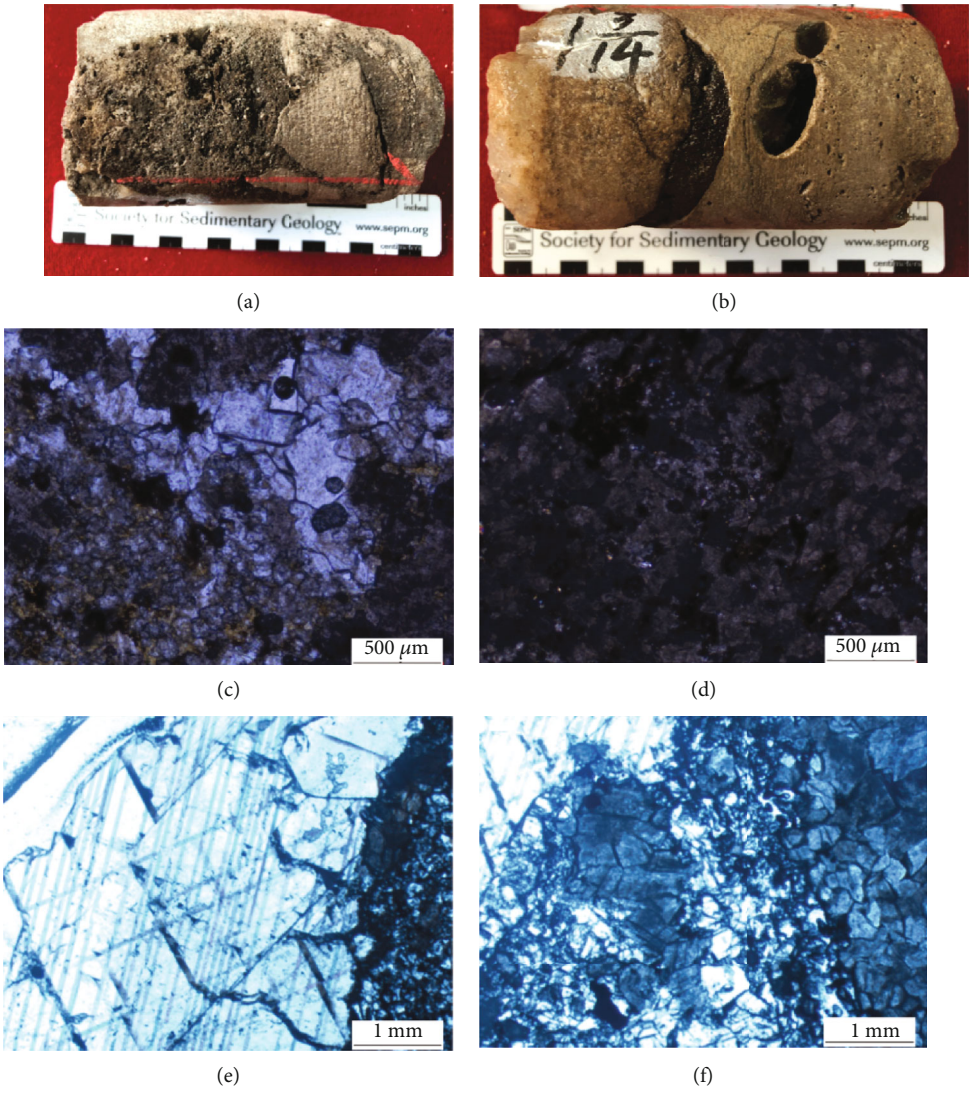

(a) (b) (c) (d) (e) (f)

Figure 3: The upper unit characteristics of Well SHBP 1. Microscopic/petrographic characteristics of samples in the upper unit: (a) Gray siliceous dolomite. The dissolution of dolomite and matrix breccia can be found in the fracture, and the dissolution is filled with siliceous and calcite cement, 8453.72-8453.82 m; (b) Fine-medium crystal dolomite. Corrosion pores, 20-50 mm in diameter, are filled with calcite and siliceous parts. There are directional distribution characteristics in the pores, and honeycomb dissolution can be found along the cracks, 8451.12-8451.24 m; (c) Microscopic photo of (a) quartz grains in the intercrystallite of honeycomb dolomite develops the secondary calcite, 8453.74 m, PPL; (d) Siliceous fine-monocrystalline dolomite. Suture Wire Cut Dolomite, 8452.14 m, PPL; (e and f) Powder-fine dolomite. Honeycomb structure, edge of siliceous, and giant crystal calcite, 8450.02 m, PPL.

observed that thermal catacaustic phenomena appear in corrosion pore, and where quartz replacement happens. Thermal color fading is a phenomenon that the rock turns locally or totally shallow (even to white) in color, generally along fissures. This is mainly induced by thermal fluids, activating along fissures and reacting with the surface rocks [27, 28]. Thermal color fading is common in Ordovician carbonate rocks in Tazhong area and mainly displays dark-gray or gray. In addition, thermal color fading is observable in the Silurian sandstone near fissures. Thermal color fading is generally small scaled and merely within several centimeters of two sides of a fissure. As for the case of cores of Well SHBP1, dolomites around fissures experience thermal color fading, and most of them (protolith) are not altered and their color remains grayish white. The alteration only occurs near fissures, and the after-alteration color turns into shallow gray to white

Under thermal activity, a special thermal catacaustic phenomenon is discovered in Silurian sandstones of the Tahe oil/gas field [28]. For lots of sandstone grains, there is one or multiple irregular networked fissures, which are mostly isotropic. Fissures among different grains are generally discontinuous. If the fracturing activity is caused by oriented external force, fissures shall show certain orientation and continuity. The thermal catacaustic phenomenon in sandstone grains is caused by the thermal process, as pressure decreases, hydrothermal fluids swelled rapidly in

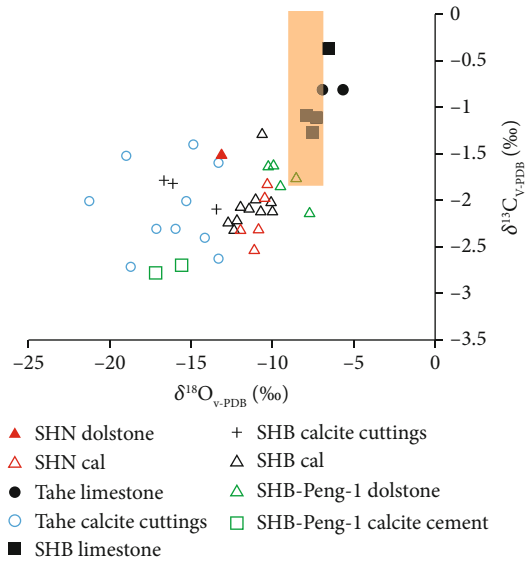

Figure 4: C-O isotopic characteristics.

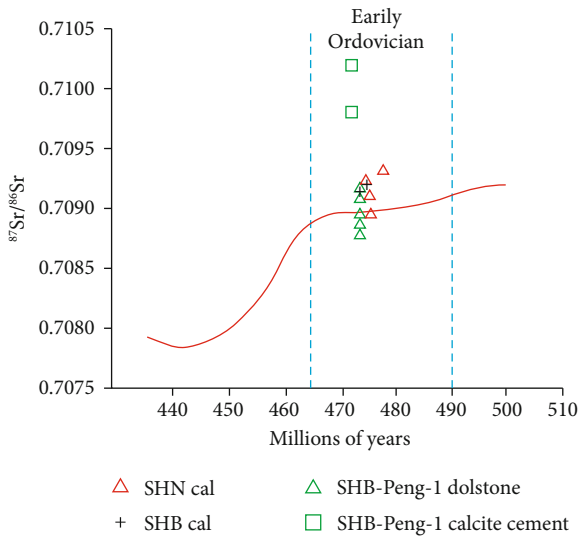

Figure 5: Sr isotopic characteristics.

volume or boiled [29–31]. Honeycomb dissolution pores, observed in Well SHBP1, under a microscope show very similar thermal catacaustic phenomena, fine-crystalline dolomites are densely developed in networked microfissures and filled with automorphic microcrystalline quartz, meanwhile the fissures do not have superior orientation.

(2) A typical hydrothermal mineral assemblage was discovered, denoting the quartz+zeolite. Zeolite is chiefly filled in vesicles and fissures in intermediate–basic volcanic lava, as well as intergranular fissures in volcaniclastic rocks. Zeolite accounts for 5 ~ 32% of the total rock volume, with an average of 18% [32]. Zeolite is generally white, shallow gray, and shallow red. Under a polarizing microscope, zeolite generally occurs as flaky, platy, or needle-like aggregates and displays low negative protuberance. In addition, the crystal surfaces are clear and characterized by gray to white interference colors or a fairly small extinction angle. SEM analysis shows that they occur as columnar or platy-columnar autogenic crystals, with size spanning from 15 to 30 μm. Interpenetration twins are observable, mostly occurring as aggregates filling in pores

On the basis of SEM image observation and spectrum analysis, zeolite occurs in places where honeycomb dissolution pore is developed (Figure 4), with a content of <1%. In the samples here, two shapes of zeolite are observable: (1) the first shape has a high percentage, and the zeolite occurs as aggregates and its outline is close to a rhomb, mainly composed of Ca, Al, and Si; and (2) the second shape is regular and similar to the orthorhombic system of plagioclase, mainly composed of Ca, Al, Si, and O with minor Mg and K. Composition of zeolite is $CaAl_2Si_4O_{12}.6H_2O$, and it is a typical product of high-temperature dolomite, reacting with Si-rich fluid under an alkaline environment.

According to theoretical calculation results (Figure 7), dolomite can react with Si-bearing fluids at 150°C, forming talc [33, 34]. Experimental results of dolomite vs. Si-rich fluids show that dolomite can react with Si-bearing fluids, forming CO_2. Within this experimental temperature range, the solubility of calcite is higher than that of dolomite at the same temperature. According to the aforementioned study, dolomite and calcite can react with Si-bearing fluids at 100~200°C, forming CO_2 and Mg/Ca silicates and calcium metasilicate, including talc, zeolite, and other minerals. Besides, in the closed (dolomite–quartz–clay) mineral–water–CO_2 system, clay minerals (smectite) can transform into illite/smectite mixed-layer minerals in alkaline condition.

(3) The measured C-O isotopic values, varying from -1.5 to 0.5‰, are similar with concurrent marine limestone. Additionally, it is discovered that their $\delta^{13}C_{V\text{-}PDB}$ characteristics of the matrix and secondary calcite are different [16, 35, 36], and $\delta^{18}O_{V\text{-}PDB}$ characteristics of the matrix and calcite veins were different from those of seawater at the same time. Carbon isotope is comparatively stable, the C isotope range for surrounding rock of Well SHBP1 is lower than <-1‰ of coeval sea water and higher than <-1‰ of secondary calcite, typical negative bias affected by organic carbon is not discovered. The genesis may be the influence, exerted by high temperature or freshwater. The $\delta^{18}O_{V\text{-}PDB}$ values of the buried dolomites are more negative than those of seawater and marine cements, and more negative than those of contemporaneous dolomites. O isotope shows typical negative bias. Given that $\delta^{13}C$ has proved that organic carbon is lacking, $\delta^{18}O$ of Well SHBP1 shows more typical negative bias characteristics than that of Shunnan area. From the C-O isotope intersection diagram, it can be demonstrated that the quasi-identical formation causes of the dolomite in Well SHBP1 and secondary calcite, further inferring that this characteristic is more affected by

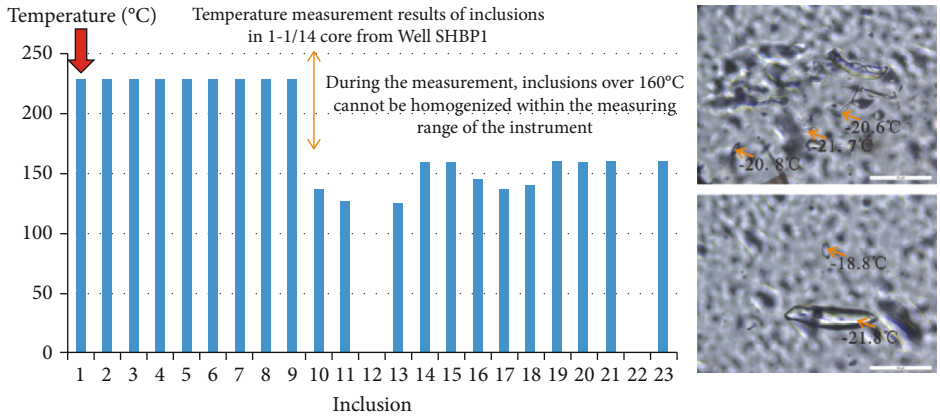

Figure 6: Inclusion temperature characteristics.

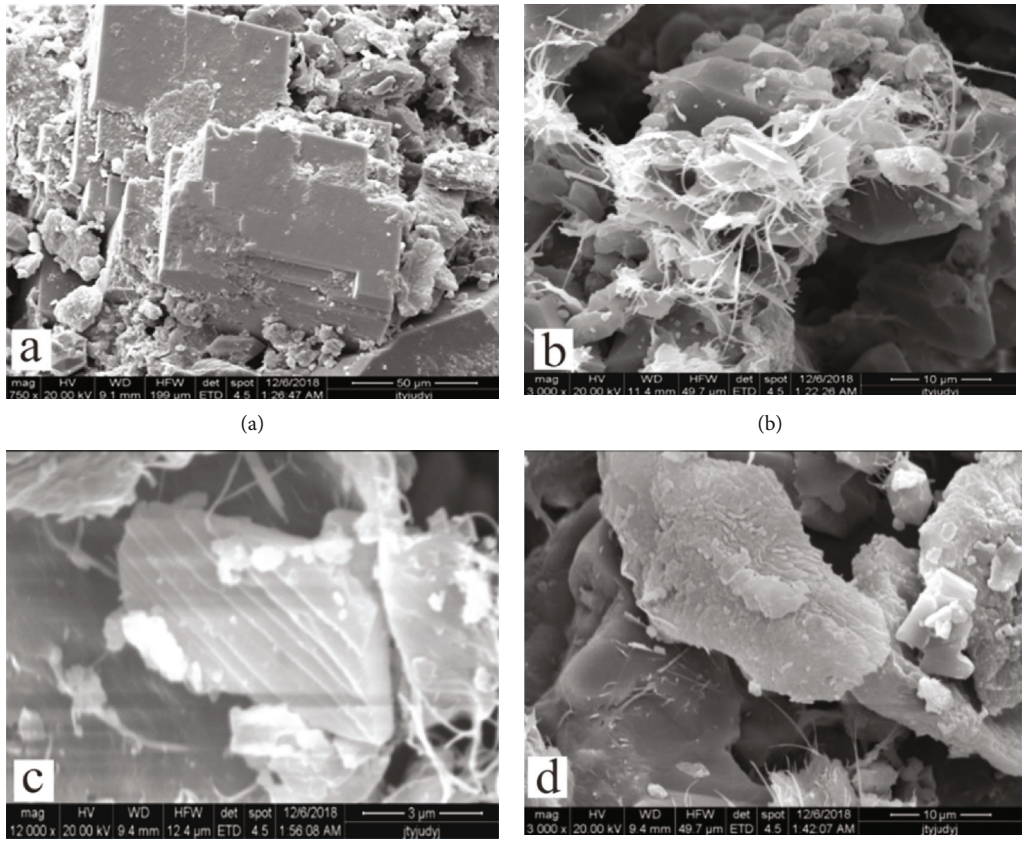

(a) (b) (c) (d)

Figure 7: Characteristics under SEM analysis.

high-temperature fluids and freshwater carbonates, formed by early-stage atmospheric freshwater. *Sr* isotopic characteristics show that bedrock samples from Shunbei area have similar $^{87}Sr/^{86}Sr$ ratio, compared with coeval sea water. In the early Ordovician, the $^{87}Sr/^{87}Sr$ ratio of global seawater ranges from 0.7087 to 0.7092, with an average of 0.7090 [36], and $^{87}Sr/^{86}Sr$ of seawater in the middle Ordovician ranges from 0.70870 to 0.70890. The $^{87}Sr/^{86}Sr$ ratio of the most of the dolomites is generally slightly higher than that of the early-middle Ordovician seawater. $^{87}Sr/^{86}Sr$ ratio indicates the injection of exogenous fluids, but two calcite samples have $^{87}Sr/^{86}Sr$ ratio greatly higher than that of coeval sea water. This phenomenon may be affected by crust-derived Sr, given that C-O isotope analysis shows very

limited atmospheric freshwater characteristics. It is believed that seepage flow poses weak influences on *Sr* isotope. According to the lower formation features, it is inferred that the *Sr* isotopic characteristics are affected by globally widespread lower Cambrian black shale and siliceous rock [37, 38]. Comprehension of C-O isotope characteristics indicate that they are affected by hydrothermal solution

Evidence for the existence of hydrothermal fluids is inclusion temperature measurement. According to the core depth of Well SHBP1 (8450.00~8455.77 m), the ground temperature of the cored location is supposed to be 160°C. Temperature measurement of sparry calcite cement, filled in fissures–caves, indicates that the homogenization temperatures mostly exceed 160°C, and homogenization cannot achieve 230°C evenly. This suggests that the fluid temperature, when corroded magnesium calcium carbonates reprecipitate and form calcium carbonate, is higher by 5°C than that of surface rocks, after siliceous fluid reacting with dolomite. This agrees with the standard of hydrothermal fluid. Therefore, diagenetic, reforming at this position, can be determined to be faulting–hydrothermal fluid reforming.

In fact, similar phenomena are not rare in the middle–lower Ordovician strata of the Tarim Basin. By means of observation, spectrum measurement, formation water Sr isotopic assay of massive rock thin sections from the reservoir interval of the Ordovician, and analysis of fault attributes, the activity characteristics of hydrothermal corrosion fluids and the control on high-quality reservoirs were investigated in-depth. The study implies that hydrothermal minerals are chiefly developed along with fault-associated structural corrosion fissures and pores/caves. Faults are the main pathway for hydrothermal fluid migration and the main controlling factor for forming high-quality reservoirs. Homogenization temperatures, H-O isotopes, and REE composition of fluid inclusions imply that quartz in the lower Paleozoic carbonate rocks was formed by magmatic-hydrothermal fluids. Furthermore, when quartz was precipitated from magma-hydrothermal fluid, carbonate reservoirs were suffered from obvious corrosion. Li (2015) shows hydrothermal alteration and metasomatic silification phenomena in the Ordovician Yingshan Formation and cored interval of Shunnan Well, located at Tarim Basin, and corrosion fissures/caves, loose siliceous limestone/siliceous rock, hydrothermal veins, and coarse quartz clusters are widely developed. Geochemical analyses of core samples indicate that hydrothermal fluids display mixing signatures. The heat was sourced from magmatism, and formation water provided the main fluids, forming medium–low temperature, high-salinity silicified hydrothermal fluids.

As mentioned above, structure-controlled hydrothermal corrosion mainly occurs inside the fractured zone of a strike-slip fault. Due to the seismic wave disturbance, induced by formation fracturing/fault detachment, strong amplitude or "bead-like" strong reflection usually occurs in where fault hydrothermal activity takes place. Inside rock formations, due to fracturing or subsequent hydrofracturing, aroused by thermal brine fluid charging, abundant fissures and breccias are formed in carbonate formations, and wide matrix metasomatic silification happens, enhancing dolomite (or limestone) porosity (molar volume replacement effect). Recharging of episodic thermal brine fluids may dissolve dolomite or limestone, forming drusy caves which are partially filled by megacrystal calcite. If hydrothermal dissolution is strong enough, local collapse of rock formations can occur, thus aggravating the sink of rock formation. Accordingly, hydrothermal dissolution is called as hydrothermal karstification by some scholars [39]. Compared to carbonate wall rocks, these positions usually have more pores, caves, and fissures, while after late-stage fluid reforming, they can turn into potential high-quality reservoirs (Figure 7). Notably, the strong-amplitude abnormal reflector has the width of ~200 m in Shuntuoguole area, and this strong-amplitude reflector can be well recognized by 3D seismic sections, transecting its axis.

In Shunbei oil/gas fields, the geometrical morphology of faults can be drawn according to seismic data amplitude and coherence volume analysis, while porosity and its space variation, inside strong amplitude anomalous bodies, can be precisely depicted by the comprehensive analysis of seismic attributes and logging data. In turn, they can constrain the scope of faulting–hydrothermal action, providing us a more sensible and objective understanding on the reservoir development features. Although multiple methods, including C-O isotope measure, Sr isotope, as well as fluid inclusion analysis, have been applied in this article, the research still suffers some deficiencies. First of all, there are little drilling cores for deep-burial carbonate reservoirs in Tarim Basin. As we know, comprehensive geological knowledge for a specific area roots in the abundant cores, which can provide massive information for analysis. In this article, the majority of the characteristics learn from the case of Well SHBP1, which may result in fairly great uncertainty. Other than that, it is really hard to examine the reliability of the conclusions, summarized on the basis of the experimental data, theoretical analysis, and observations. Finally, applicability activity of the research efforts to the realistic field is still lacking. In light of the above limitations, the authors will continue this research in the future.

6. Conclusions

(1) Based on the detailed core investigation and petrographic examination, two units, including the lower microquartz interval and upper dolomite interval, could be further categorized for the whole core samples. The intense diagenesis of SHBP1 Well was greatly constrained along with the vicinity of faults and/or fractures, indicating the distinctive characteristic of tectonic-controlled hydrothermal alteration

(2) The deep-seated strike-slip faults in the Shunbei area could have provided preferential conduits for hydrothermal fluids migrating upward to the shallow burial carbonates, resulting in intensive dissolution and subsequent cementation. Therefore, fault-controlled hydrothermal reservoirs, characterized

by the strong amplitude in the seismic profile, are widely distribute in the interior of Yingshan Formation

(3) This study provides a useful explanation of tectonic-controlled hydrothermal alteration, which could be helpful to make the exploration strategy, aiming at finding favorable carbonate reservoirs in deeply buried carbonates in the Tarim Basin, particularly in the Shuntuoguole area

Data Availability

Data available on request.

Ethical Approval

On behalf of all the coauthors, the corresponding author states that there are no ethical statements contained in the manuscripts.

Conflicts of Interest

The authors declared no potential conflicts of interest with respect to the research, authorship, an/or publication of this article.

Acknowledgments

We sincerely thank Professor Liu from Peking University and Dr. You from Sinopec Petroleum Exploration and Production Research Institute for their help in the experimental data. The first author acknowledges the Projects of Science and Technology Department of Sinopec (P21033-3) for supporting a part of this work. The research was also supported by NSFC Basic Research Program on Deep Petroleum Resource Accumulation and Key Engineering Technologies (No. U19B6003-02).

References

[1] G. R. Davies and L. B. Smith, "Structurally controlled hydrothermal dolomite reservoir facies: an overview," *AAPG Bulletin*, vol. 90, no. 11, pp. 1641–1690, 2006.

[2] F. J. Lucia, C. Kerans, and J. W. Jennings, "Carbonate reservoir characterization 2007: an integrated approach," *Journal of Petroleum Technology*, vol. 55, no. 6, pp. 70–72, 2003.

[3] S. F. Dong, D. Z. Chen, X. Q. Zhou, Y. Qian, M. Tian, and H. Qing, "Tectonically driven dolomitization of Cambrian to Lower Ordovician carbonates of the Quruqtagh area, northeastern flank of Tarim Basin, north-west China," *Sedimentology*, vol. 64, no. 4, pp. 1079–1106, 2017.

[4] F. Z. Jiao, "Significance of oil and gas exploration in NE strike-slip fault belts in Shuntuoguole area of Tarim Basin," *Oil & Gas Geology*, vol. 38, no. 5, pp. 831–839, 2017.

[5] Y. S. Ma, Z. L. He, P. R. Zhao et al., "A new progress in formation mechanism of deep and ultra-deep carbonate reservoir," *Acta Petrolei Sinica*, vol. 40, no. 12, pp. 1415–1425, 2019.

[6] G. Y. Zhu, X. W. Liu, H. J. Yang et al., "Genesis and distribution of hydrogen sulfide in deep heavy oil of the Halahatang area in the Tarim basin, China," *Journal of Natural Gas Geoscience*, vol. 2, no. 1, pp. 57–71, 2017.

[7] S. Deng, H. Li, Z. Zhang, J. Zhang, and X. Yang, "Structural characterization of intracratonic strike-slip faults in the central Tarim Basin," *AAPG Bulletin*, vol. 103, no. 1, pp. 109–137, 2019.

[8] S. Deng, H. L. Li, Z. P. Zhang, X. Wu, and J. B. Zhang, "Characteristics of differential activities in major strike-slip fault zones and their control on hydrocarbon enrichment in Shunbei area and its surroundings, Tarim Basin," *Oil & Gas Geology*, vol. 39, no. 5, pp. 878–888, 2018.

[9] X. Y. Han, S. Deng, L. J. Tang, and Z. Cao, "Geometry, kinematics and displacement characteristics of strike-slip faults in the northern slope of Tazhong uplift in Tarim Basin: a study based on 3D seismic data," *Marine and Petroleum Geology*, vol. 88, pp. 410–427, 2017.

[10] Y. T. Li, L. X. Qi, and S. N. Zhang, "Characteristics and development mode of the Middle and Lower Ordovician fault-karst reservoir in Shunbei area,Tarim Basin," *Acta Petrolei Sinica*, vol. 40, no. 12, pp. 1470–1484, 2019.

[11] H. B. Qiu, T. Yin, Z. C. Cao et al., "Strike-slip fault and Ordovician petroleum exploration in northern slope of Tazhong Uplift, Tarim Basin," *Marine Origin Petroleum Geology*, vol. 22, no. 4, pp. 44–52, 2017.

[12] Y. Liu, N. Qiu, H. Li, A. Ma, J. Chang, and J. Jia, "Terrestrial heat flow and crustal thermal structure in the northern slope of Tazhong uplift in Tarim Basin," *Geothermics*, vol. 83, p. 101709, 2020.

[13] K. Shang, "Reservoir space characterization and classification of the ultra-deep limestone reservoirs in the northern slope of Central Tarim Basin," *Special Oil & Gas Reservoirs*, vol. 25, no. 5, pp. 65–70, 2018.

[14] K. Shang, N. Guo, and Z. C. Cao, "Main controlling factors of reservoir in Ordovician Yijianfang Formation on the northern slope of middle Tarim Basin," *Marine Origin Petroleum Geology*, vol. 22, no. 1, pp. 39–46, 2017.

[15] D. You, Z. Cao, M. Xu, Y. Qian, S. Wang, and X. Wang, "Genetic mechanism of multi-type dolomite reservoirs in Ordovician Yingshan Formation,Tarim Basin," *Oil & Gas Geology*, vol. 41, no. 1, pp. 92–100, 2020.

[16] D. H. You, J. Han, W. X. Hu et al., "Characteristics and formation mechanisms of silicified carbonate reservoirs in well SN4 of the Tarim Basin," *Energy Exploration & Exploitation*, vol. 36, no. 4, pp. 820–849, 2018.

[17] D. Wei, Z. Gao, C. Zhang, T. Fan, and J. S. Tsau, "Characterization of the deeply buried microporous limestone: case study from the Shunnan area, Tarim Basin, NW China," *Geological Journal*, vol. 55, no. 2, pp. 4920–4935, 2019.

[18] Z. Chai, Z. H. Chen, H. Liu et al., "Light hydrocarbons and diamondoids of light oils in deep reservoirs of Shuntuoguole Low Uplift, Tarim Basin: implication for the evaluation on thermal maturity, secondary alteration and source characteristics," *Marine and Petroleum Geology*, vol. 117, p. 104388, 2020.

[19] Z. Sun, B. Huang, Y. Li, H. Lin, S. Shi, and W. Yu, "Nanoconfined methane flow behavior through realistic organic shale matrix under displacement pressure: a molecular simulation investigation," *Journal of Petroleum Exploration and Production Technology*, 2021.

[20] Z. Sun, S. Wang, H. Xiong, K. Wu, and J. Shi, "Optimal nanocone geometry for water flow," *AICHE Journal*, vol. 68, no. 3, p. e17543, 2021.

[21] R. E. Denison, R. B. Koepnick, W. H. Burke, and E. A. Hetherington, "Construction of the Cambrian and Ordovician seawater $^{87}Sr/^{86}Sr$ curve," *Chemical Geology*, vol. 152, no. 3-4, pp. 325–340, 1998.

[22] L. Hecht, R. Freiberger, H. A. Gilg, G. Grundmann, and Y. A. Kostitsyn, "Rare earth element and isotope characteristics of hydrothermal carbonates: genetic implications for dolomite-hosted talc mineralization at Gopfersgrun," *Chemical Geology*, vol. 155, no. 1-2, pp. 115–130, 1999.

[23] H. R. Qing, C. R. Barnes, D. Buhl, and J. Veizer, "The strontium isotopic composition of Ordovician and Silurian brachiopods and conodonts: relationships to geological events and implications for coeval seawater," *Geochimica et Cosmochimica Acta*, vol. 62, no. 10, pp. 1721–1733, 1998.

[24] R. J. Bodnar, "Revised equation and table for determining the freezing point depression of H_2O-NaCl solutions," *Geochimica et Cosmochimica Acta*, vol. 57, no. 3, pp. 683-684, 1993.

[25] G. X. Chi and H. Z. Lu, "Validation and representation of fluid inclusion microthermometric data using the fluid inclusion assemblage (FIA) concept," *Acta Petrologica Sinica*, vol. 24, no. 9, pp. 1945–1953, 2008.

[26] R. H. Goldstein and T. J. Reynolds, "Systematics of fluid inclusions in diagenetic minerals," *SEPM Short Course*, vol. 31, 1994.

[27] Z. Sun, B. Huang, K. Wu et al., "Nanoconfined methane density over pressure and temperature: wettability effect," *Journal of Natural Gas Science and Engineering*, vol. 99, p. 104426, 2022.

[28] D. Y. Zhu, Z. J. Jin, W. X. Hu, and X. F. Zhang, "Effects of deep fluid on carbonates reservoir in Tarim Basin," *Geological Review*, vol. 54, no. 3, pp. 348–354, 2008.

[29] J. Michel, "Hydrothermal breccias in vein-type ore deposits: a review of mechanisms, morphology and size distribution," *Ore Geology Reviews*, vol. 12, no. 3, pp. 111–134, 1997.

[30] W. J. Phillips, "Hydraulic fracturing and mineralization," *Journal of the Geological Society*, vol. 128, no. 4, pp. 337–359, 1972.

[31] H. Westphal, G. P. Eberli, L. B. Smith, G. M. Grammer, and J. Kislak, "Reservoir characterization of the Mississippian Madison formation, Wind River basin, Wyoming," *AAPG Bulletin*, vol. 88, no. 4, pp. 405–432, 2011.

[32] H. Liang, "Formation and distribution of zeolite in volcanic rock and its effect on reserviors in Santanhu Basin," *Acta Sedimentologica Sinica*, vol. 29, no. 3, pp. 537–543, 2011.

[33] M. B. Holness, "Fluid flow paths and mechanisms of fluid infiltration in carbonates during contact metamorphism: the Beinn an Dubhaich aureole, Skye," *Journal of Metamorphic Geology*, vol. 15, no. 1, pp. 59–70, 1997.

[34] F. Tornos and B. F. Spiro, "The geology and isotope geochemistry of the talc deposits of Puebla de Lillo (Cantabrian Zone, Northern Spain)," *Economic Geology*, vol. 95, no. 6, pp. 1277–1296, 2000.

[35] S. J. Huang, "Carbonate Diagenesis," *Geological Publishing House*, pp. 54–63, 2011.

[36] J. Veizer, D. Ala, K. Azmy et al., "87Sr/86Sr, δ13C and δ18O evolution of Phanerozoic seawater," *Chemical Geology*, vol. 161, no. 1-3, pp. 59–88, 1999.

[37] D. M. Banerjee, M. Schidlowski, F. Siebert, and M. D. Brasier, "Geochemical changes across the Proterozoic-Cambrian transition in the Durmala phosphorite mine section, Mussoorie Hills, Garhwal Himalaya, India," *Palaeogeography Palaeoclimatology Palaeoecology*, vol. 132, no. 1-4, pp. 183–194, 1997.

[38] S. Jiang, J. Yang, H. Ling et al., "Extreme enrichment of polymetallic Ni-Mo-PGE-Au in Lower Cambrian black shales of South China: an Os isotope and PGE geochemical investigation," *Palaeogeography Palaeoclimatology Palaeoecology*, vol. 254, no. 1-2, pp. 217–228, 2007.

[39] D. Z. Chen, "Structure-controlled hydrothermal dolomitization and hydrothermal dolomite reservoirs," *Oil & Gas Geology*, vol. 29, no. 5, pp. 614–622, 2008.

[40] B. U. Haq and S. R. Schutter, "A Chronology of Paleozoic sea-level changes," *Science*, vol. 322, no. 5898, pp. 64–68, 2008.

[41] O. Catuneanu, W. E. Galloway, C. G. S. C. Kendall et al., "Sequence stratigraphy: methodology and nomenclature," *Newsletters on Stratigraphy*, vol. 44, no. 3, pp. 173–245, 2011.

[42] B. Cheng, H. Liu, Z. C. Cao, X. Wu, and Z. Chen, "Origin of deep oil accumulations in carbonate reservoirs within the north Tarim Basin: insights from molecular and isotopic compositions," *Organic Geochemistry*, vol. 139, article 103931, 15 pages, 2020.

[43] R. L. Folk and J. S. Pittman, "Length-slow chalcedony: a new testament for vanished evaporites," *Journal of Sedimentary Research*, vol. 41, pp. 1045–1058, 1971.

[44] F. H. Jiang, "The study of micro pore characteristics on different depth soft soil consolidation by mercury intrusion porosimetry," *Science Technology and Engineering*, vol. 11, no. 31, pp. 7701–7706, 2011.

[45] L. Bing, Z. Rui, K. Qiangfu et al., "An Ordovician carbonate reservoir in strike-slip structures producing form fault-associated fracture systems, 3D seismic region of Northern Shun 8 block," *Carbonates and Evaporites*, vol. 34, no. 3, pp. 545–556, 2019.

[46] M. D. Li, "Thermodynamic discussion on dolomite serpentinization and talcification," *Journal of Mineralogy and Petrology*, vol. 4, pp. 100–104, 1991.

[47] L. Chunyan, L. Changsong, W. Yi, and W. Maobing, "Burial dissolution of Ordovician granule limestone in the Tahe oilfield of the Tarim Basin, NW China, and its geological significance," *Acta Geologica Sinica*, vol. 82, no. 3, pp. 520–529, 2008.

[48] Z. Lu, Y. Li, N. Ye et al., "Fluid inclusions record hydrocarbon charge history in the Shunbei Area, Tarim Basin NW China," *Geofluids*, vol. 2020, Article ID 8847247, 15 pages, 2020.

[49] N. Xinfeng, S. Anjiang, P. Wenqing et al., "Geological modeling of excellent fracture-vug carbonate reservoirs: a case study of the Ordovician in the northern slope of Tazhong palaeouplift and the southern area of Tabei slope, Tarim Basin, NW China," *Petroleum Exploration and Development*, vol. 40, no. 4, pp. 414–422, 2013.

[50] R. Esposito, R. Klebesz, O. Bartoli et al., "Application of the Linkam TS1400XY heating stage to melt inclusion studies," *Central European Journal of Geosciences*, vol. 4, no. 2, pp. 208–218, 2012.

[51] W. Xiaolin, W. Ye, H. Wenxuan et al., "Experimental studies on the interactions between dolomite and SiO2-rich fluids: implications for the formation of carbonate reservoirs," *Geological Review*, vol. 63, no. 6, pp. 1639–1652, 2017.

[52] T. F. Xia, S. L. Chen, and S. J. Li, "Effects of water chemistry on microcracking and compressive strength of granite," *International Journal of Rock Mechanics and Mining Sciences*, vol. 38, no. 4, pp. 557–568, 2001.

[53] Z. Chaojun, J. Chengzao, L. Benliang, L. Xiuyu, and L. Yunxiang, "Ancient karsts and hydrocarbon accumulation in the middle and western parts of the North Tarim uplift, NW China," *Petroleum Exploration and Development*, vol. 37, no. 3, pp. 263–269, 2010.

[54] Z. Jiahui, Z. Rui, W. Yasheng, L. Tianjia, C. Xuemin, and G. Kunzhang, "The origin and distribution of Ordovician Yingshan dolomite on the northern slope of Tazhong area in Tarim Basin," *Carbonates and Evaporites*, vol. 34, no. 3, pp. 507–523, 2019.

Hindawi
Geofluids
Volume 2022, Article ID 2420869, 15 pages
https://doi.org/10.1155/2022/2420869

Research Article

Molecular Simulation of CH_4 Nanoscale Behavior and Enhanced Gas Recovery in Organic-Rich Shale

Yang Li,[1] **Lize Lu**,[1] **Jingyi Zhu**,[2] **Zhaozhong Yang**,[3] **Jianhua Qu**,[4] **Heng Xue**,[4] **and Jingyun Ouyang**[4]

[1]*China ZhenHua Oil Co., Ltd., China*
[2]*College of Chemistry and Chemical Engineering, Southwest Petroleum University, China*
[3]*State Key Laboratory of Oil and Gas Reservoir Geology and Exploitation, Southwest Petroleum University, China*
[4]*Chengdu North Petroleum Exploration and Development Technology Co., Ltd., China*

Correspondence should be addressed to Yang Li; xiaolong_0_@126.com

Received 18 January 2022; Accepted 18 February 2022; Published 7 March 2022

Academic Editor: Zheng Sun

Occurrence and transport are two important nanoscale behaviors in the exploitation of shale gas. Nanopores in a realistic shale organic matrix are composed of kerogen molecules, which will have a great impact on surface-gas interactions and gas nanoconfined behavior. Although there are previous studies, the physics of gas transport through shale systems remains ambiguous. In this work, cylindrical nanopore models representing different pore sizes and organic-rich shale were constructed. By applying the molecular dynamics simulation method, the occurrence characteristics and transport characteristics of CH_4 in the nanopores of organic-rich shale were studied. At last, the process of the adsorbed CH_4 displaced by CO_2 and N_2 in shale nanopores at the subsurface condition was explored. This work can provide a better understanding of gas nanoscale behavior in shale systems and assist the future design of the CO_2 sequestration and enhanced gas recovery technique.

1. Introduction

Shale gas is one of the most promising alternative resources to conventional natural gas resources, and the development of shale gas is of strategic importance to energy security. However, the special reservoir conditions and seepage characteristics of shale gas determine the characteristics of rapid natural decline and low natural production capacity of gas reservoirs. Current shale gas reservoirs are mostly developed in a depletion drive, and the recovery rate is generally low. Unlike conventional oil and gas reservoirs, shale gas reservoirs have a complex pore structure and large size range. Typically, shale pores are classified into three categories according to the International Union of Pure and Applied Chemistry (IUPAC): micropores (<2 nm), mesopores (2-50 nm), and macropores (>50 nm) [1, 2]. Zhang et al. [3] studied the microscopic characteristics of shale pore structures, and they noted that 95.6% of shale pores are nanopores, making it difficult to visualize the microscopic flow behavior of CH_4.

Shale gas mainly consists of free gas in pores and fractures, adsorbed gas in clay surfaces and organic pores, and dissolved gas in the liquid phase [4–6]. The adsorbed gas content is considerable, which can account for 20%-85% of the total volume of shale gas [7]. Previous studies have shown that most of the adsorbed gas is mainly occurred in the organic matter nanopores of shale [8], and the adsorbed gas content is positively correlated with the organic carbon content of shale [9]. Kerogen is a dispersed organic matter in shale, although it only accounts for a small proportion of the shale volume, but due to the large specific surface area and strong affinity for gas molecules, kerogen becomes the main space for shale adsorbed gas [10].

In recent years, the method of gas injection to displace CH_4 is usually used in engineering to enhance the extraction efficiency [11]. Among them, CO_2 injection in shale gas

reservoirs not only can sequester CO_2 and reduce the greenhouse effect but also can promote CH_4 desorption and improve CH_4 recovery rate, which has received wide attention in recent years. Therefore, the study of shale gas microflow behavior using kerogen as an adsorbent is an important guideline for enhanced shale gas recovery technology.

Thanks to the advantages of molecular dynamics (MD) method at scale, they have been widely used in unconventional oil and gas extraction research, such as shale oil, shale gas, combustible ice, and coalbed methane (CBM) [12, 13]. It is because MD are based on classical mechanics and quantum mechanics method that can effectively reveal the link between structure and properties as well as understand the interactions between physicochemical systems. The pore structure of organic matter in shale is complex and dispersed in inorganic matter, which is difficult to be separated from shale while keeping its pore structure unbroken. The organic matter pores are mainly distributed at the nanoscale, and the pore throat channel size is comparable to the molecular mean free range, which makes it difficult for experimental methods to characterize the dynamic behavior of shale gas in these pore channels. Therefore, MD have become a powerful tool to study the structure and properties of shale at the nanoscale, and the MD method can have a greater advantage in studying the interaction between kerogen and fluids [14].

In molecular simulation calculations, two main ways are currently used to study the interaction between shale and gases; one is to select kerogen molecules as a representative to replace the structure of shale organic matter; the other research method is to use graphene sheets or carbon nanotubes to replace the carbon skeleton in shale for fluid adsorption and transport properties. Yiannourakou et al. [15] on the basis of experimental techniques established the molecular fragment of mature kerogen, and the predicted CH_4 adsorption isotherm of the obtained microporous material was in good agreement with the experimental data. Collell et al. [16] replaced the molecular structure of kerogen with aromatic hydrocarbon molecular groups and obtained the structure of shale organic matter with a density of 1.24 g/cm^3 by MD method. Wang et al. [17] investigated the effect of graphite flakes on the adsorption and transport of CH_4 molecules using the Monte Carlo method. The adsorption behavior of pores composed of graphite showed that pores with sizes in the range of 1-50 nm were the main pores for shale gas adsorption, and the adsorption showed a multilayer trend as the pressure increased subject to intermolecular interactions. Kazemi et al. [18, 19] reported that in slit-like organic nanopores of 2 nm, as the pressure gradient increased from 1.8 kPa·nm^{-1} to 17.65 kPa·nm^{-1}, the shale gas flux increased from 4498 to 37244 kg·m^{-2}·s^{-1}. The contribution of adsorbed molecules could exceed 50%, and with increasing pore size, the adsorption of 10 nm slit organic pores decreased to less than 40%. Cao et al. [20] and Noorian et al. [21] similarly investigated the experimentally observed slip phenomenon through molecular simulations, showing that the slip length was related not only to the Knudsen number but also to the surface roughness. Ungerer et al. [10] proposed six different types of molecular models of low to high maturity keregon that exhibit thermodynamic properties consistent with trends in the literature. These structures are widely used in studies of competing adsorption processes of CO_2/CH_4 and transport characteristics of mixed fluids [22, 23]. Slit organic pores can also be constructed from these structures for analysis of fluid flow processes [24]. These results show that MD simulation is an effective method to compensate for the shortcomings of experimental methods in characterizing the dynamical processes in the structure of kerogen at nanoscale [10]. The effects of pore size distribution, pore throat size, pore roughness, and pore network connectivity on shale gas transportation can also be effectively investigated by MD [25–27].

Through experimental analysis, it is found that the pore channels in shale organic matter are extremely irregular and the pore surface is very heterogeneous, and it has been found that the roughness of the pore surface has a large effect on both the flow rate and state of shale gas. However, so far, the studies have mainly focused on the fluid interaction with the simplified model, which differs significantly from the realistic pore model. In addition, the research on gas injection for CH_4 displacement has mainly focused on CBM, and there are fewer studies for the special geological conditions of shale reservoir. There are also more factors affecting the effect of displacement, such as injection gas type, injection rate, and injection pressure and formation pressure, and the influence law of these main parameters on displacement is not very clear. Therefore, the fluid displacement and transport processes in shale organic matter nanopores are not well understood. The physical models constructed in this work embody the complex amorphous structure and strong inhomogeneous surface properties within the shale pores, which can be accurately characterized nanoconfined CH_4 flow behavior in realistic shale organic matter. The aim of this paper is to investigate the flow characteristic laws of shale gas at the microscopic scale and to study the gas injection displacement thus helping to select reasonable parameters and improve the extraction efficiency, both of which are essential to guide the development of shale gas reservoirs.

2. Models and Methodology

2.1. Construction of Nanopore Structure Model. Although simulations can be performed based on simplified models equivalent to shale organic nanopores, simulations of gas microscopic behavior using realistic shale organic nanopore models are more necessary because the chemical composition, pore structure, and surface roughness of kerogen matrix have essential effect on the gas microscopic behavior in shale organic nanopores. Based on the investigation of the pore genesis and development characteristics of shale, it is found that the organic pores inside real shale are generally circlelike based on massive scanning electron microscopy microscopic images of shale samples [28–30].

One of the nanopore structure model construction method is kerogen molecule randomly placed into a simulation cell with periodic boundaries, and then, a shale matrix model with microporous characteristics was established by the MD method under an isothermal-isobaric ensemble with a constant number of molecules. It should be noted that the

shale organic nanopore structure model established by this method has complex basic properties, such as pore size distribution, morphological characteristics, topological characteristics, and surface roughness. All of these factors together lead to the corresponding gas microscopic behavior results. If the shale organic nanopore model is used directly to study the gas microscopic behavior under nanoconfined conditions, the specific effects of each factor need to be determined and quantified. To solve this problem, this paper generalizes the shale organic nanopores into capillary bundles, and the capillary bundle pore model assumes that the microscopic pores of porous media are composed of capillary bundles with different radius parallel to each other. It is a good solution to draw a single capillary and use it as single shale organic nanopore for the study of gas microscopic behavior.

The most straightforward method to generate nanopores in organic solids is to remove the atoms in the target region [16]. This method results in accurate pore size and smooth pore surface after removing the solid atoms from the nanopore, but it also exposes a major problem in that the molecular topology and the charge distribution of the nanopore surface are disrupted. Collell et al. [16] proposed a method for inserting repulsive dummy atoms during the model construction, forming spherical nanopores with a radius of about 1 nm. This method compensates for the shortcomings of the atom removal method, however, it is not possible to form nanopores with other geometries such as slit pore or cylindrical pore, and it is also difficult to form pores with large radius. Based on Collell's work, Zhou et al. [31] proposed an MD-based cutter atom pore generation method. This method can construct nanopores of arbitrary shape and size, and the constructed nanopores have a reasonable physical meaning of porous matrix. Therefore, this paper chooses to use the cutter atom method to construct the nanopore structure model of shale organic matter.

As aforementioned, the kerogern molecule is carbon-based macromolecule representing shale organic matter, besides that, some representative kerogen molecular models had proposed by a recent review work [32]. Based on the different element ratios of kerogen with different maturation and burial histories, Bousige et al. [33] divided kerogen into four main types: type-I kerogen, type-II kerogen, type-III kerogen, and type-IV kerogen. As shale reservoirs are basically not generated by type-IV kerogen [34], therefore, in this work, we utilized three typical types (I, II, and III) of kerogen molecules to represent authentic shale organic matter with different thermal maturity [10]. The chemical formula for type-I kerogen is $C_{251}H_{385}O_{13}N_7S_3$, type-II kerogen is $C_{252}H_{294}O_{24}N_6S_3$, and type-III kerogen is $C_{233}H_{204}O_{27}N_4$; the molecular structures of kerogen molecules are present in Figure 1.

First, modeling the single-nanopore structure of shale organic matrix needs to determine the number of molecules required for different models. After determining the number of kerogen molecules, the kerogen molecules were randomly placed into the simulation cell with fixed cutter atoms, which were composed of carbon atoms forming a clipping region and located at the center of the simulation cell, as the initial state of the shale organic matrix skeleton. Then, a series of MD simulations were performed for the whole system to make the configuration relax. During the relaxation process, the cutter atoms remained fixed and the kerogen molecules were continuously compressed and cannot enter the clipping region, thus forming a nanopore surrounded by kerogen molecules.

Finally, the cutter atoms were removed and the solid shale organic nanopores with the desired pore size and kerogen type were constructed by the above process. The pore size can be controlled by adjusting the volume of the clipping area formed by the cutter atoms. The process of constructing a nanopore with the target kerogen type and pore size is illustrated in Figure 2.

2.2. Simulation Details. In this work, the MD of the microoccurrence behavior of CH_4 was performed using the large-scale atomic/molecular massively parallel simulator (LAMMPS) from Sandia National Laboratories, USA [35]. The force field was chosen the all-atomic pcff+ force field developed by the Materials Design team[15], which uses the LJ 9-6 potential to describe dispersion-repulsion interactions and uses point charges to describe Coulomb interactions, classical bond stretching, bending, and torsion terms. Periodic boundary conditions were applied in the x, y, and z directions. The relaxation process was carried out by a series of heating and cooling MD simulations; the specific steps are listed in Table 1.

During the simulations, the cut-off distance set by the van der Waals force was 12 Å for short-range interactions, and long-range electrostatic interactions were calculated using the particle-particle-particle-mesh (PPPM) method with an accuracy set to 1×10^{-4}. The Wäldmann-Hagler mixing rule was implemented to describe the different atomic interactions [36]. The time step of the MD simulations was set to 1 fs for the microcanonical ensemble and 1 $\times 10^{-1}$ fs for the isothermal-isobaric ensemble, where constant temperature and constant pressure were achieved by coupling to the atomic velocity and unit dimension, respectively. The constant temperature was applied to the translational degrees of freedom of the atoms, and the Nosé-Hoover algorithm was used to control the temperature of the system [37]. The constant pressure was isotropically coupled to the entire volume of the simulated cell without changing its geometry [38]. To control the temperature and pressure, the damping coefficients were set to 100 and 1000 fs, respectively, and the equations of motion were calculated using the velocity Verlet method. After the relaxation process, the cutter atoms were removed and the configuration was followed by a short time MD equilibrium simulation under the canonical ensemble, which was used to reduce the possible stress concentration on the surface of the pore wall.

After obtaining the structure model of the shale organic nanopore with the desired pore size and kerogen type, the gas microoccurrence behavior within the nanoconfined space will be simulated by applying the equilibrium molecular dynamics (EMD) simulation method. Using the cylindrical nanopore model as a flow channel, the dynamic

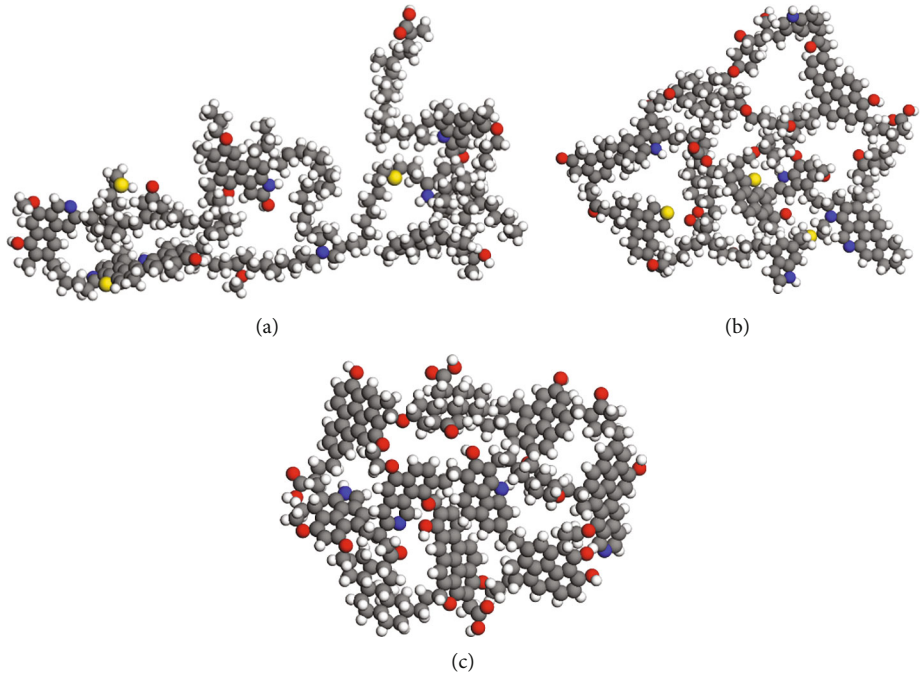

Figure 1: The kerogen molecular model of different types. (a) The type-I kerogen $C_{251}H_{385}O_{13}N_7S_3$; (b) the type-II kerogen $C_{252}H_{294}O_{24}N_6S_3$; (c) the type-III kerogen $C_{233}H_{204}O_{27}N_4$. Color atom correspondence: gray for C, white for H, red for O, blue for N, and yellow for S.

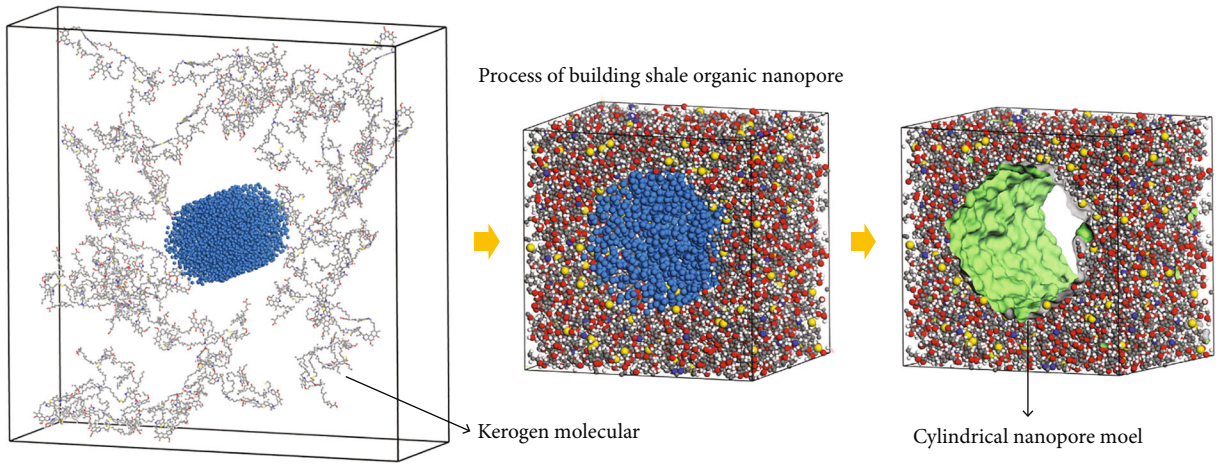

Figure 2: Schematic diagram of shale organic nanopore construction process.

Table 1: MD simulation steps for constructing shale organic nanopores.

Ensemble	Pressure (MPa)	Temperature (K)	Simulation time (ns)
NVT	-	1000	3.0
NPT	60	1000	6.0
NPT	60	700	6.0
NPT	60	400	6.0
NVT	-	338	3.0

characteristics of CH_4 transport in shale nanopores were revealed by applying nonequilibrium molecular dynamics (NEMD) simulation method. At last, the MD simulation method was used to explore the process of the adsorbed CH_4 displaced by CO_2 and N_2 in shale organic nanopores at the subsurface condition.

3. Results and Discussion

3.1. CH_4 Distribution. In this section, through Grand Canonical Monte Carlo (GCMC) and EMD simulation of CH_4 molecules in shale organic nanopores, the distribution of CH_4 in shale organic nanopores of different pore sizes and kerogen types under different pressure conditions were

obtained. At the same time, the model was validated, and the CH_4 distribution characteristics in the nanoconfined pores were analyzed. For shale reservoir, which is a multicomponent, heterogeneous porous medium, high temperature, and high pressure system [39–41], CH_4 adsorption in in situ reservoir is particularly complex, which has become the bottleneck of shale gas occurrence mechanism research. To reveal the occurrence and transport characteristics of CH_4, the influence of temperature and pressure at the subsurface condition will be evaluated in our simulation work.

First, a certain number of CH_4 molecules were put into the established nanopore space, and then, the system was simulated 3~10 ns under the canonical ensemble to make the system reach the equilibrium state, to obtain the stable pore pressure. Regarding the number of CH_4 molecules put in, based on the ideal gas equation of state, the number of molecules in the shale organic nanopore space under the target pore pressure is preliminarily calculated. Then, it was adjusted based on the results of the EMD simulation, and finally, the final number of molecules by the average pressure of the CH_4 molecules in the system was determined. The equilibrium pressure parameters obtained by the nanopore models of different pore sizes and kerogen types under different numbers of CH_4 molecules are shown in Table 2.

As can be seen from Table 2, a total of 27 simulation schemes with different kerogen types, pressures, and pore sizes were set up to study the distribution state of CH_4 in the nanopores. After EMD simulations, the CH_4 density distribution of all schemes is displayed in the form of 2D cloud maps in Figures 3–5. In order to facilitate the comparison of the CH_4 distribution states under different conditions, the maximum value of the color scale of all density distribution maps was set to 0.5 g/cm^3.

It is obvious from the CH_4 density distribution maps that the distribution of CH_4 within the shale organic nanopores is heterogeneous and does not exactly follow the central symmetric, which is quite different from the previous simulation result using a simplified model based on graphene. Due to the strong chemical heterogeneity of the kerogen matrix, the nanopores have different chemical structures at different positions on the pore surface, which further indicates that the interaction strength of CH_4 on the surface of the nanopores is different. Therefore, CH_4 will accumulate on surfaces with high-energy adsorption sites. In contrast, on some weak-energy adsorption sites, the adsorption capacity is weak and the accumulation of CH_4 will not occur. The complex surface properties are based on the inherent physical properties of kerogen molecules to construct shale organic nanopores, which is the necessary reason to explain the three-dimensional heterogeneous distribution of CH_4 in shale organic nanopores. This is the critical point distinguishing the findings of this paper and other existing studies, and also, the proof of the claim that the physical model constructed in this paper shares the most similarity with the realistic shale organic matrix.

In addition to observing the heterogeneous distribution of CH_4 within the shale organic nanopores, it can also be clearly seen that there is high-density region near the nanopore wall and the bulk region inside the nanopores. CH_4 not only adheres to the surface of shale organic nanopore, but also there is a small portion of CH_4 which enters the kerogen matrix and stays there.

Table 2: The basic parameters of CH_4 EMD simulation under nanoconfined conditions.

Kerogen type	Pore diameter (nm)	CH_4 molecular number	Pressure (MPa)
Type-I	1	75	9.8
		125	19.8
		190	50.2
	2	110	10.2
		215	20.5
		270	51.3
	4	520	9.5
		800	19.7
		1300	52.1
Type-II	1	80	10.2
		110	20.3
		190	49.8
	2	120	10.0
		220	19.9
		290	51.9
	4	530	9.9
		810	19.6
		1200	50.5
Type-III	1	85	9.2
		120	21.3
		180	51.8
	2	120	10.6
		210	20.9
		280	50.9
	4	510	9.5
		800	19.9
		1300	50.2

As illustrated in the density distribution of CH_4 inside shale organic nanopores, there is no clear boundary near the surface of the nanopores established by kerogen molecules compared to that established by graphene-based nanopores. It can also be analyzed from Figures 3–5 that the overall density of CH_4 inside the nanopore increases with increasing pore pressure, both the near-surface region and the central bulk region. Notably, due to the inherent surface composition of the shale organic nanopore, distinct peak density sites can be found in specific nanopores, and the relative position of the peak density remains constant. In addition, only one main density peak can be observed in the shale organic nanopores, which implies that the adsorption behavior of CH_4 within the shale organic nanopores is monolayer adsorption. It can be used as evidence of the application of monolayer adsorption theory to shale. Moreover, the thickness of the CH_4 high-density region in the nanopores is almost the same regardless of the kerogen type,

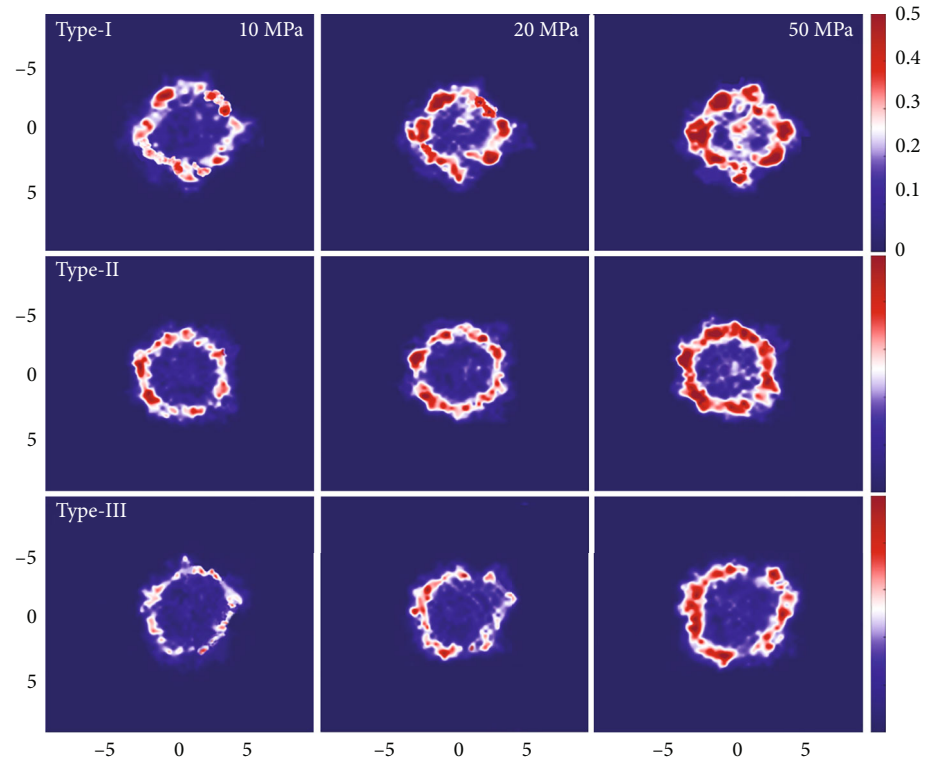

Figure 3: CH_4 density distribution in 1 nm shale organic nanopore under different pressure conditions.

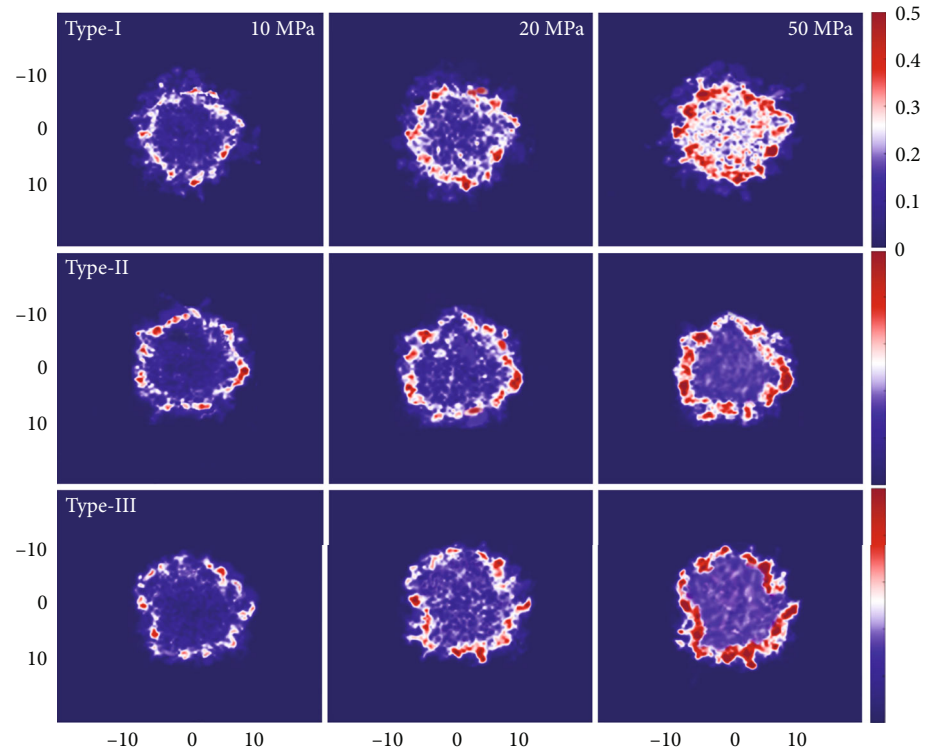

Figure 4: CH_4 density distribution in 2 nm shale organic nanopore under different pressure conditions.

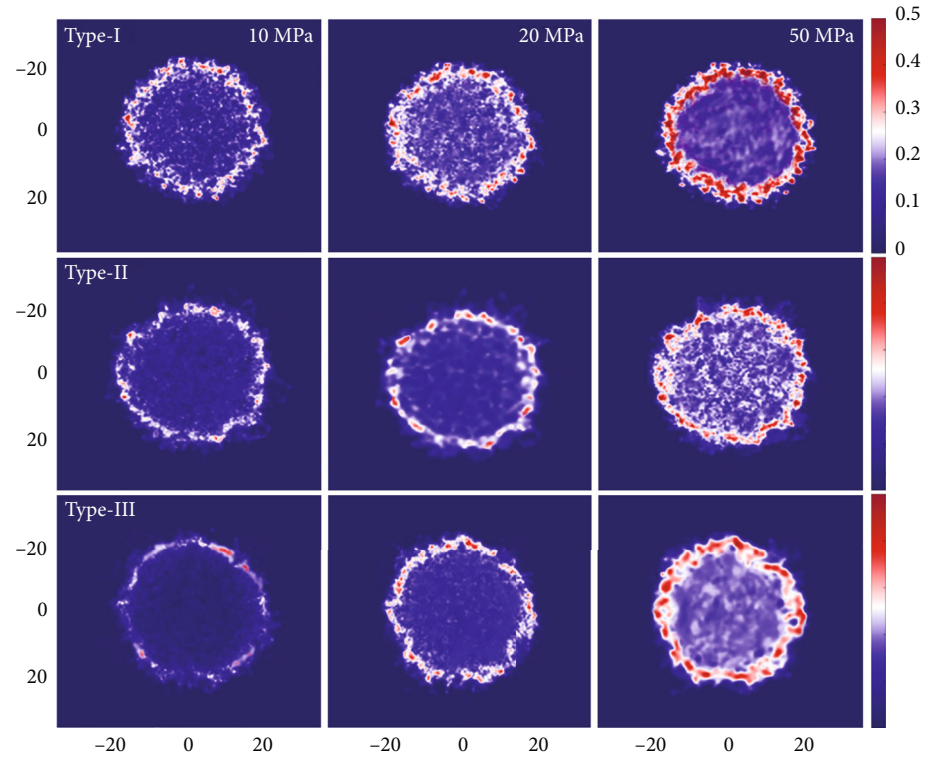

Figure 5: CH_4 density distribution in 4 nm shale organic nanopore under different pressure conditions.

pore pressure, and pore size. This further suggests that the proportion of high-density region in small nanopores will be higher than that in large nanopores, which has an important influence on the average density in the nanopores.

In order to further validate the model, the shale organic nanopores with the same pore size, different kerogen types, and pressure conditions were selected following, and the bulk-region density simulation results will be compared with the National Institute of Standards and Technology (NIST) database to prove the accuracy of the simulation method and model in this study.

As can be observed in Figure 6(a), the density of CH_4 molecules in the bulk region (4 nm pore diameter) collected by EMD simulation can achieve excellent agreement with the NIST data. Based on the above content, it is shown that the molecular simulation conducted in this study successfully described the distribution characteristics of CH_4 in the shale organic nanopores. It further shows that the force field parameter assignment on each particle in the simulation system was correct. Therefore, it can reflect the accuracy of the simulation method and model of this research to a certain extent.

From the above analysis and other recently simulation work [42, 43], it can be observed that the peak density in the high-density region is related to the pore size, while the bulk-region density is not affected by the pore size but mainly by the temperature and pressure to which the molecules within the nanopore were subjected. Therefore, the adsorption layer affects the average density within the nanopore. Moreover, the density distribution is a key factor affecting the fluid flow capacity from a microscopic point of view and the gas production performance of a gas well from a macroscopic point of view. Therefore, it is worthwhile to further analyze the density characteristics under the effect of adsorption within the nanopore

The average density (ρ_{ave}) inside the nanopore divides the bulk-region density (ρ_{bulk}) within the nanopore defined as the density ratio (R_{dens}), which is described as follows:

$$R_{dens} = \frac{\rho_{ave}}{\rho_{bulk}}. \quad (1)$$

The relationship between the density ratio and pressure of the type-II kerogen models with different pore sizes was analyzed, and the results are shown in Figure 6(b).

It can be seen from Figure 6(b) that the density ratio varies roughly from 1.16 to 4.69 and under the same pressure condition increases as the pore size decreases. This can be explained by the fact that the thickness of the high-density adsorption region does not vary with the pore size, so that the proportion of high-density region in small-sized nanopores is higher than that in large-sized nanopores, thus leading to an increase in the average density with decreasing pore size. It can also be seen in Figure 6(b) that the density ratio of the same pore size decreases with increasing pressure and the magnitude of the change gradually decreases. Thus, the contribution of the high-density adsorption region dominates under low-pressure conditions, while this contribution gradually becomes weaker under high-pressure conditions.

Considering that kerogen type also has an effect on the adsorption capacity, the variation relationship between

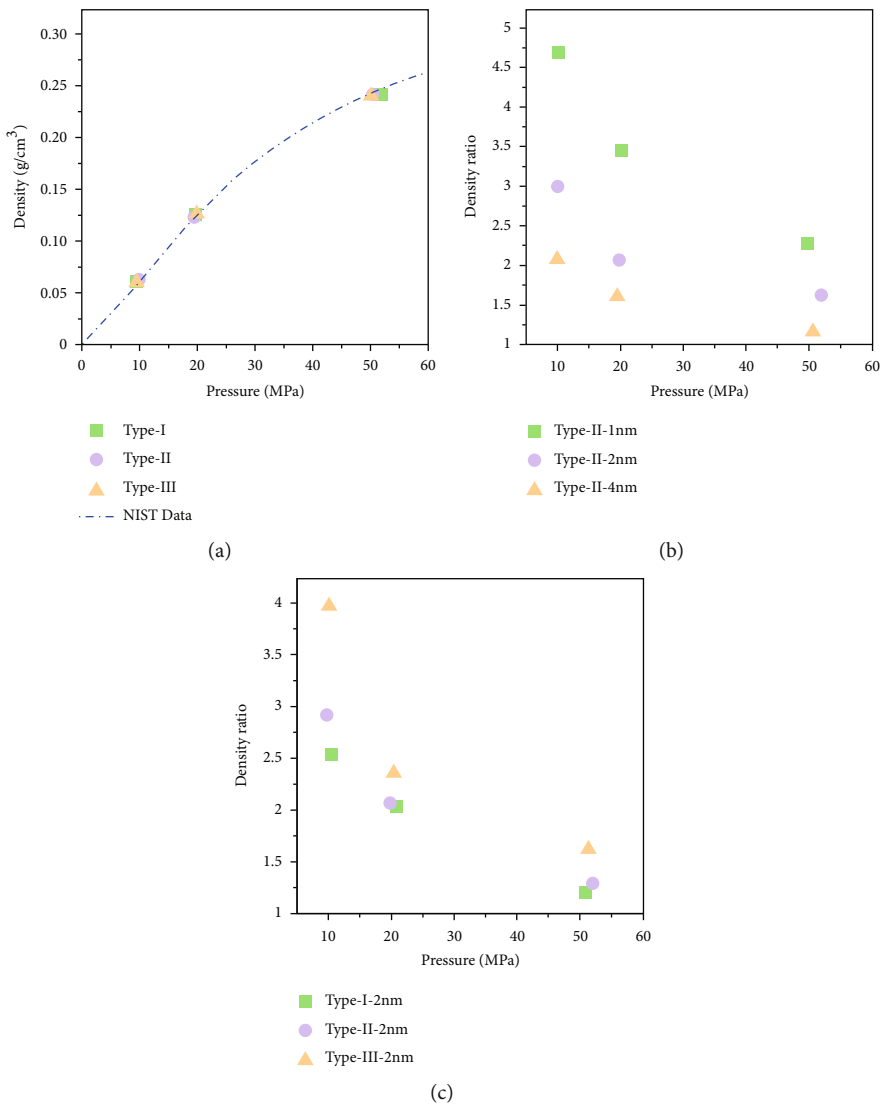

FIGURE 6: Comparison of CH_4 density simulation results. (a) CH_4 bulk density simulation results vs. NIST data, (b) density ratio vs. pressure with the same kerogen type, and (c) density ratio vs. pressure with the same pore size.

density ratio and pressure was analyzed for the three kerogen type models with the same pore size (2 nm), and the results are shown in Figure 6(c). It can be observed that the density ratio of the same kerogen type decreases with the increase of pressure. Besides, at a certain pressure, the density ratios show an increasing trend with the increase of maturity, in the order of high- to low-maturity kerogen. This phenomenon is related to the adsorption capacity of different kerogen type, and the high-maturity kerogen nanopores have a strong adsorption capacity, which means that at a certain pressure, compared with other kerogen type, the density peak formed by the adsorption layer will be higher.

3.2. CH_4 Transport Characteristic. To study the flow pattern of CH_4 within the nanopore, we used external force non-equilibrium molecular dynamics (EF-NEMD) simulations to deviate the occurrence system from equilibrium[44]. The specific procedure is that, based on the equilibrium state configuration obtained from EMD simulations, a force of constant magnitude is applied to the CH_4 molecules inside the pore, which leads to NEMD simulations and makes the system enter the steady state. The force value was set so that the acceleration of each molecule was kept at 10^{-4} to 10^{-3} nm/ps^2 to ensure a linear response. Due to the additional force on the gas, a certain pressure drop (ΔP) is generated in the flow direction, which can be calculated from

$$\Delta P = \frac{N_G \times F_E}{A_{cross}}, \tag{2}$$

where N_G, F_E, and A_{cross} denote the number of molecules applying external force, the external force, and the nanopore cross-sectional area.

It should be noted that the fluid flow rate during the NEMD simulation refers to the center-of-mass motion of each fluid atom, and considering the degrees of freedom in the direction of fluid flow leads to an excessive calculated

fluid temperature. Therefore, it is more reasonable to consider only the degrees of freedom perpendicular to the direction of the driving force when calculating the fluid temperature in this thermostatic way. Once the flow regime within the shale nanopores reaches a steady state, the fluid flux (J_z) can be obtained by measuring the average density ($\bar{\rho}$) and average flow velocity ($\bar{v}$) of the regime in the steady state, where $J_Z = \bar{\rho} \cdot \bar{v}$.

In order to present the NEMD simulation results in detail and to further analyze the transport characteristics of CH_4 molecules within the nanopores, the velocity distribution of CH_4 molecules in shale organic nanopores under different conditions was analyzed below using control variates method. Figure 7 show the results of the velocity distribution of CH_4 transport within type-I, type-II, and type-III kerogen nanopores with different pore pressures (10, 20, and 50 MPa), pore size (1, 2, and 4 nm), pressure drop (0.25, 0.75, and 1.25 MPa), and ambient temperature (308, 338, and 368 K). In addition, in order to control the single variable in different tests, the physical parameters of the benchmark one are 20 MPa (pore pressure), 2 nm (pore size), 0.75 MPa (pressure drop), and 338 K (ambient temperature).

It can be seen that the variation of velocity distribution with different tests is essentially the same within the shale nanopore model for different kerogen types. For the impact of pore pressure (Figures 7(a), 7(e), and 7(i)), when the pressure was 50 MPa, the shape of the velocity distribution curves is a parabolic shape with nonslip boundaries. As the pore pressure decreases, the velocity profiles within the different shale nanopores show a common feature, the generation of a slip boundary. When the pressure was 20 MPa, the shape of the velocity distribution curve in the nanopore is close to the classical parabolic shape and the velocity peak at the pore wall disappears, but the velocity inflection points in the adsorption layer region and the central region of the pore can still be seen. Since different shale organic nanopores at different pore pressures have similar velocity distribution characteristics, the velocities at different pore pressures were normalized using type-II kerogen shale organic nanopore as an example (Figure 8(a)), and the normalized velocity values were obtained based on the average velocities at different pressures within the pore.

As can be seen from Figure 8(a), the velocity distribution within the shale nanopores can be divided into three regions. The first region ($Np\text{-}_{wall}$) is adjacent to the shale nanopore wall, where gas atoms are strongly repelled by the solid wall and almost no atoms or velocities appear; the second region ($Np\text{-}_{adsorbed}$) is around the adsorption layer where complex phenomena exist, the slip velocity decreases with increasing pore pressure and disappears at high pressures, and the velocity values are reduced at the potential well where density peaks exist compared to the other regions; the third region ($Np\text{-}_{bulk}$) is the central bulk phase region of the nanopore, where the transport behavior mainly follows the classical parabolic pattern, but with different curvatures due to the rarefaction effect in the nanopores[45].

It can be concluded that the CH_4 molecules in the adsorption layer exhibit completely different transport characteristics compared to the bulk phase region in the center of the nanopore. This is mainly due to the different density distributions of the adsorbed layer and the bulk phase region within the shale nanopores leading to their different velocity distributions. As an example to illustrate the results of the density distribution curve of type-II kerogen (Figure 8(b)), when the pressure was low (10 MPa), the low peak at the nanopore wall in the density profile indicates that the adsorption and nanospatial confinement of the nanopore wall were weak, and fewer CH_4 molecules were adsorbed on the nanopore surface, so it corresponds to Figure 8(a), which the transport velocity is higher near the nanopore wall. As the pore pressure increases, the density of CH_4 molecules increases within the nanopore, and the difference in density between the $Np\text{-}_{adsorbed}$ region and the $Np\text{-}_{bulk}$ region decreases. When the pressure reached 50 MPa, due to the strong confinement effect in the shale nanopores under high pressure conditions, the velocity profile showing a nonslip boundary feature. That can be elaborated as the pressure increases; the main kinetic behavior of CH_4 molecules in shale nanopores changes from collisions between gas molecules and nanopore wall to gas intermolecular collisions, which leads to significant differences in gas transport characteristics at different pressures.

Figures 7(b), 7(f), and 7(j) show the results of the velocity distribution under the influence of different pressure drop. It can be seen that the velocity distribution within the shale nanopore is positively correlated with the pressure drop. The approximate parabolic shape of the simulated CH_4 velocity profile obtained in the center of the nanopore again indicates the presence of viscous flow during the transport of supercritical state CH_4 within the shale nanopore. Furthermore, by observing closely at the different velocity profile values, especially in the $Np\text{-}_{bulk}$ region, it can be found a near-linear relationship between pressure drop and the velocity values. When the velocity values about 0.17 Å/ps at 1.25 MPa pressure drop are 1.7 times larger than ~0.1 Å/ps at 0.75 MPa pressure drop and are 5 times larger than ~0.03 Å/ps at 0.25 MPa pressure drop.

Moreover, the results of the velocity distribution of CH_4 molecules under the influence of different pore sizes are analyzed in Figures 7(c), 7(g), and 7(k). It can be clearly seen that the velocity profile of CH_4 molecules within the shale nanopores is highly dependent on the pore size, with higher values of flow velocity for larger pore sizes. And further comparative analysis will reveal that the velocity profile shows a nonlinear relationship with pore size, as exemplified by the type-II kerogen (Figure 7(g)), where the maximum velocity in the central region of the nanopore (~0.27 Å/ps) is about 2.7 times higher for the 4 nm pore size condition than for the 2 nm pore size case (~0.1 Å/ps) and 6.75 times (~0.04 Å/ps) for the 1 nm pore size case. This illustrates the large effect of pore size on the gas flow capacity within shale nanopores, where several-fold differences in pore size can lead to flow rate differences of almost more than an order of magnitude. This is consistent with continuous flow theory (Poiseuille's law), where the gas flow rate within the channel is proportional to the square of the channel size and the

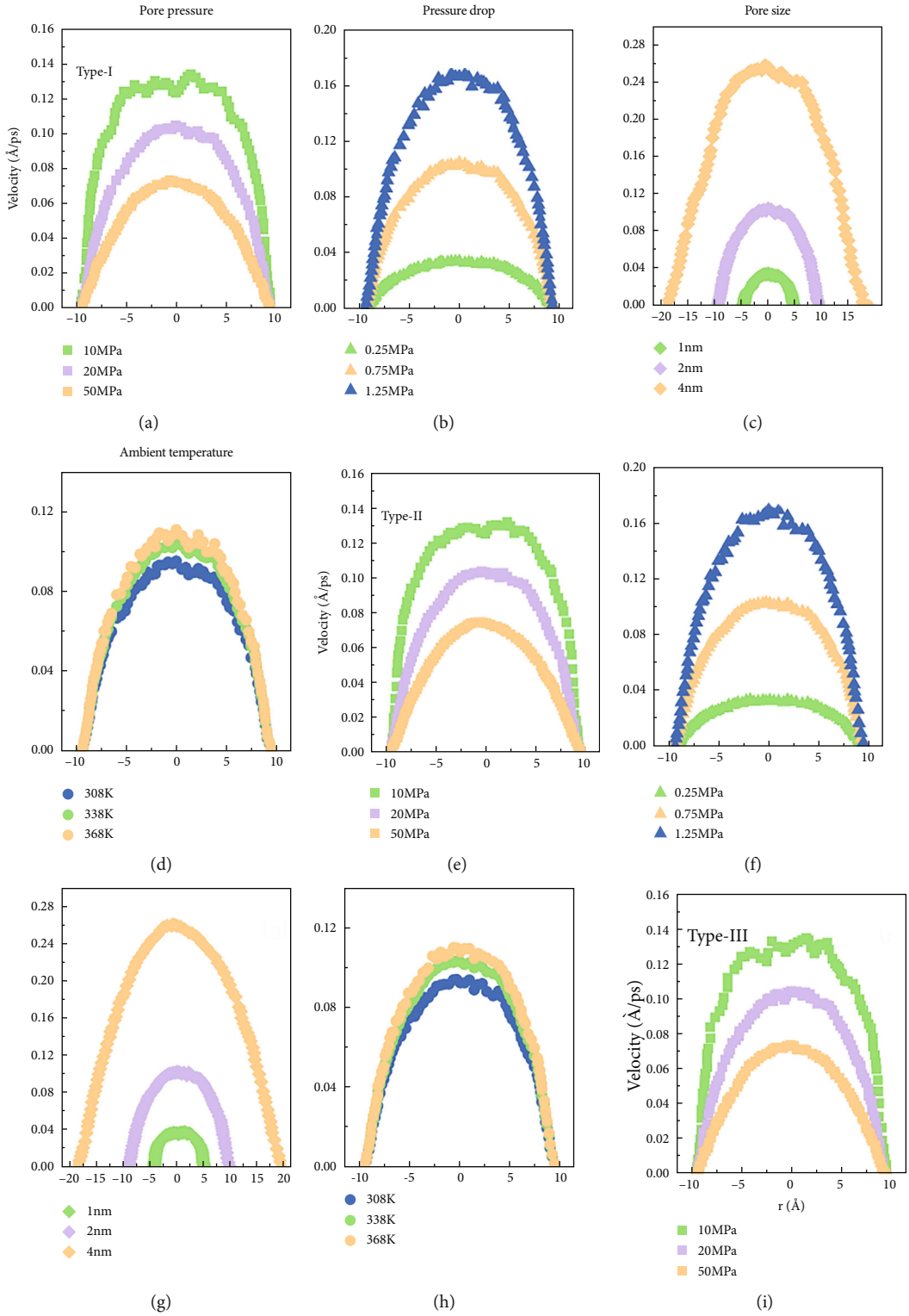

Figure 7: Continued.

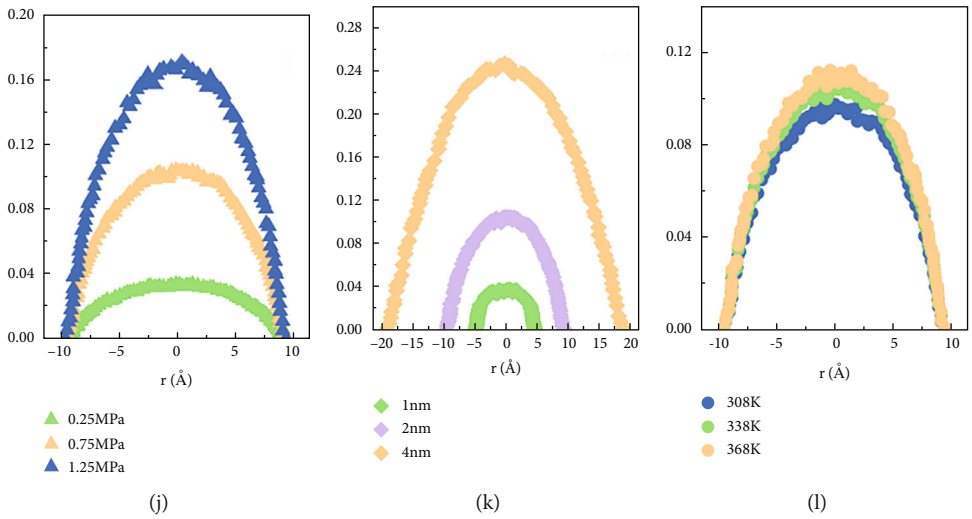

Figure 7: Velocity distribution of CH_4 in shale organic nanopores under different conditions. Type I: (a–d), Type II: (e–h), Type III: (i–l). Pore pressure (a, e, and i), pressure drop (b, f, and j), pore size (c, g, and k), and ambient temperature (d, h, and l).

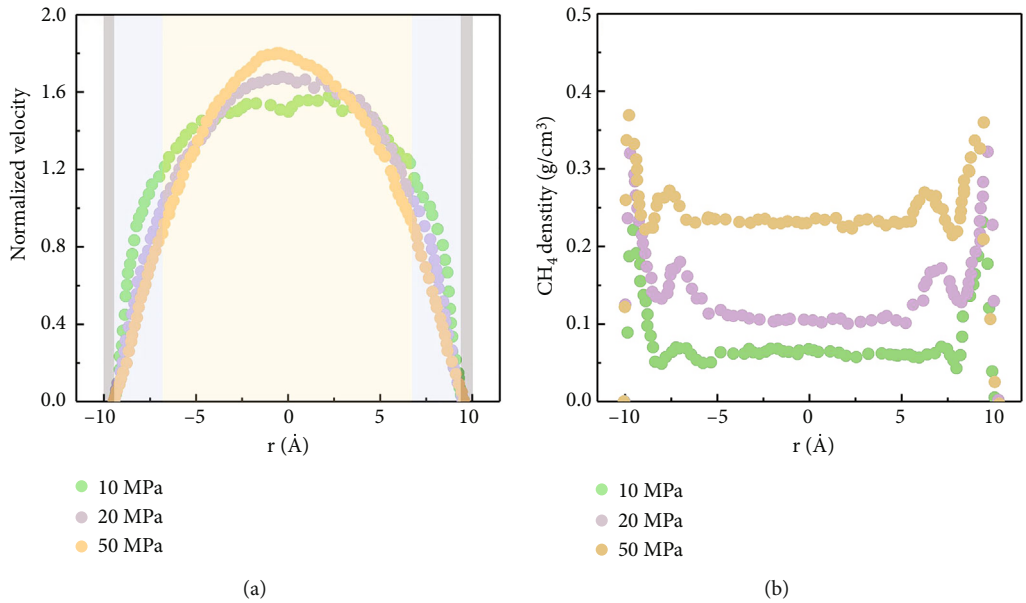

Figure 8: Normalized velocity and CH_4 density distribution in the nanopores of type-II kerogen under different pore pressures.

underlying mechanisms were revealed by previous research results [46, 47].

Finally, the simulation results of CH_4 molecular velocity distribution within the shale nanopores at different ambient temperatures were compared. From the velocity distribution of CH_4 molecules within shale nanopores in Figures 7(d), 7(h), and 7(l), for the effect of ambient temperature, it can be found that the difference between velocity distributions under different ambient temperature conditions is small, indicating that the increase in temperature mainly accelerates the thermal movement of molecules and has little enhancement for the velocity in the transport direction. Therefore, the transport capacity of the gas can be roughly considered to be the same under different shale reservoir temperature conditions.

In summary, the above analysis of the transport simulation results illustrates that the transport pattern of CH_4 in shale nanopores is complex and different from the behavior in homogeneous carbon nanotubes or graphene nanochannels. The nonhomogeneous nanopore walls result in velocity profiles that are not symmetrically distributed, and the chemical structures of different kerogen types alter the interaction between CH_4 and shale nanopore surface, which affects the molecular transport velocity. Conventional understanding ignores the shale gas transport pattern with adsorption, which may underestimate the gas permeability in shale reservoirs. In a future research work, we will compare the MD results with the classical theoretical model values and then develop a new model for the apparent permeability of gas in shale organic nanopore, trying to

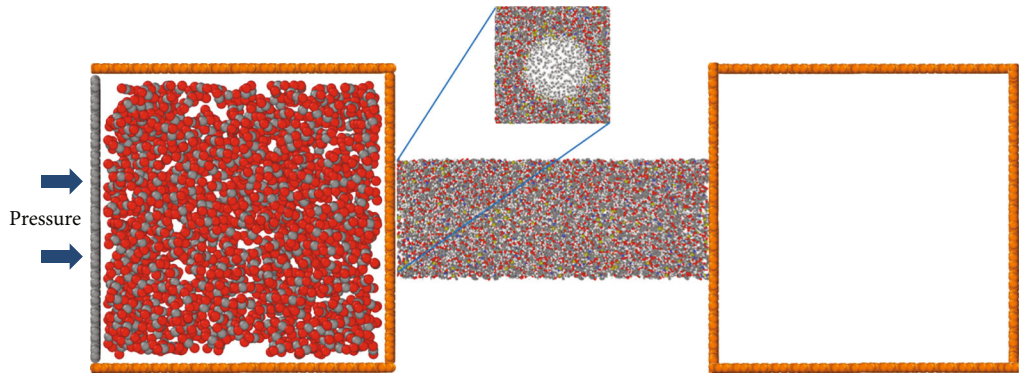

Figure 9: Molecular model of CH_4 displacement by injection gas. The gray wall at the left-hand side represents piston to maintain the injection pressure in box. The injection gas is either CO_2 or N_2 and in the schematic diagram is CO_2.

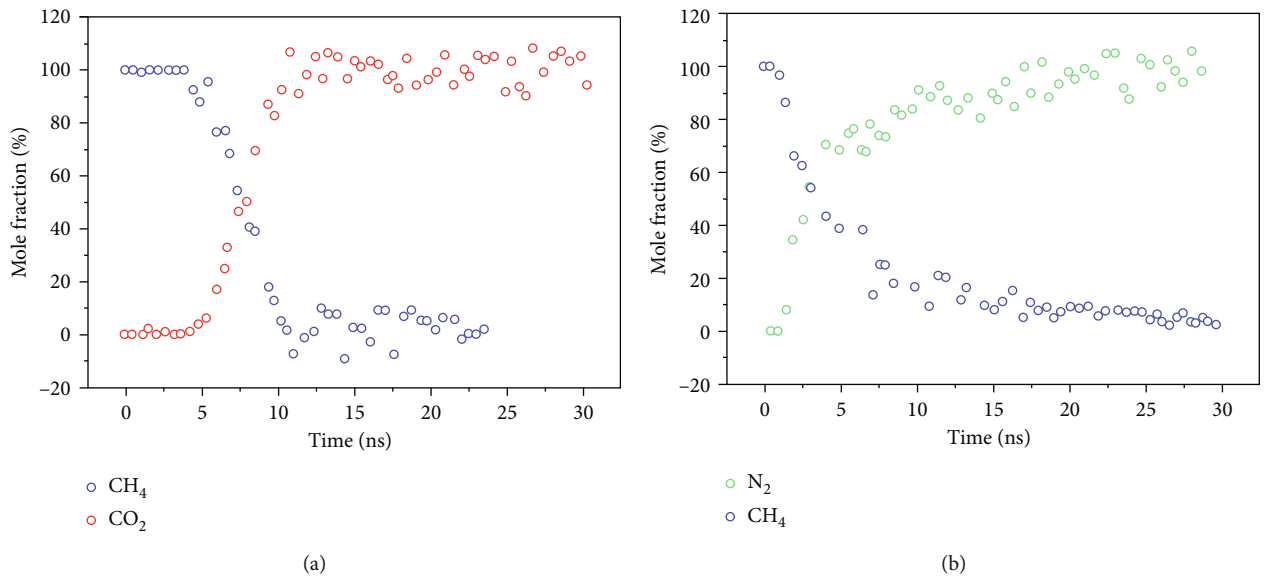

Figure 10: Displacement gas composition recorded from the MD as a function of displacement time. (a) CO_2 displacing CH_4; (b) N_2 displacing CH_4.

applicate our simulation work to real shale matrices with multiscale complex pore networks.

3.3. Displacement of the Adsorbed CH_4. To improve the recovery of adsorbed CH_4, gas injection displacement is an efficient method. According to the research investigation, the commonly chosen injection gas in enhanced gas recovery engineering is CO_2 and N_2 [48–50]. Compared to CH_4, CO_2 has a higher adsorption capacity and shale matrix has strong surface heterogeneity, in which the oxygen-containing functional groups on the surface of shale nanopore enhance the displacement of CO_2 to CH_4. Not only that, CO_2 can be sequestered in the shale formation by means of gas injection. In addition to CO_2, N_2 is also a common choice for gas injection. According to Dalton's partial pressure law, with the injection of N_2, the partial pressure of CH_4 will decrease. Besides, N_2 has many advantages, such as being abundant, readily available, and nontoxic and noncorrosive.

This section focuses on the displacement of adsorbed CH_4 by the injection gas, which is still implemented using a MD method and with the help of the LAMMPS open source program. The model schematic diagram is shown in Figure 9; the injection gas is either CO_2 or N_2. In the initial state, both boxes were not connected to the shale organic nanopores. The injection gas was equilibrated in the left box while the CH_4 was adsorbed in the nanopore. In this section, the selected working condition is that the injection gas pressure is 12 MPa while the adsorbed CH_4 pressure is 10 MPa. In addition, the temperature of the whole system was controlled using a Nosé-Hoover thermostat at 338 K. Subsequently, create the entrance between the boxes and nanopore, and dig a hole (remove atoms) in the wall between the nanopore and the boxes on both sides, which is the size of the cross section of the nanopore. Then, the injected gas entered the nanopore for the displacement under the pressure difference. In subsequent simulations, the content of each component of the output gas in the

right-hand box was counted to analyze the displacement mechanism and process.

The process of CH_4 displacement by CO_2 and N_2 was studied comparatively. Figure 10 gives a graph of the variation in the concentration of each component of the output gas after the displacement of CH_4 by CO_2 and N_2. When CO_2 was injected, the mole fraction change curve shows a trend of long breakthrough time and sharp front, as shown in Figure 10(a). Since CO_2 tends to adsorb on the shale nanopore surface, the amount of CO_2 in the bulk state is less and its passage through the nanopore was slower. When the injected gas comes in contact with the adsorbed CH_4, a front was formed. When CO_2 breaks through the nanopore space, the concentration of output CH_4 rapidly decreases to zero. This also indicates a sharper CO_2 front within the nanopore space. On the contrary, when N_2 was injected, the mole fraction change curve shows a trend of short breakthrough time and a flat front, as shown in Figure 10(b). Since N_2 has a weaker adsorption capacity, it can pass through the nanopore faster and accelerate CH_4 desorption earlier. Even though N_2 has already broken through the nanopore, CH_4 continues to be produced. When enough N_2 was injected, the concentration of output CH_4 gradually tends to zero. These findings suggest that both CO_2 and N_2 can efficiently displace the adsorbed CH_4. The above simulation results are consistent with the experimental results of related literature, which once again validates the accuracy of the simulation method.

4. Conclusion

Three shale organic nanopore models of different maturity were established based on real kerogen molecules. The GCMC, EMD, and NEMD simulation methods were used to study the microbehavior of CH_4 under nanoscale conditions. First, the CH_4 occurrence characteristics in shale organic nanopores were analyzed through obtaining the density distribution under different pressure conditions. Moreover, the transport characteristic was elaborated through the velocity distribution of CH_4 molecules in shale organic nanopores under different conditions using control variates method. Lastly, the displacement of adsorbed CH_4 by the injection gas was investigated by simulating the process of CH_4 displacement by CO_2 and N_2 comparatively. The following specific conclusions were as follows:

(1) CH_4 is mainly adsorbed as a monolayer in shale organic nanopores; in the occurrence of gas within the nanopores, there are high-density adsorption layer region and bulk phase region; density ratios are negatively correlated with both pressure and pore size; the reduction of the pore size will help to improve the gas storage capacity in the nanopores

(2) The velocity distribution of CH_4 within the shale organic nanopore can be divided into three regions; the flow velocity is positively correlated with pressure drop, pore size, and ambient temperature and negatively correlated with pore pressure; the rapid flow of CH_4 is more favorable at lower pore pressures, at higher pressure drop or in larger pore size

(3) Both CO_2 and N_2 can effectively displace the adsorbed CH_4; it is found that when CO_2 was injected, the breakthrough time is long and the front is sharp and when N_2 was injected, the breakthrough time is short and the front is flat

Data Availability

Most of the data used to support the findings of this study are available within the article; the code of LAMMPS used during the study are available from the corresponding author by request.

Conflicts of Interest

The authors declare that they have no conflicts of interest.

Acknowledgments

The research was financially supported by the Sichuan Science and Technology Program (2020JDJQ0059) and the China Postdoctoral Science Foundation (2021M700113).

References

[1] M. Zou, C. Wei, M. Zhang, J. Shen, Y. Chen, and Y. Qi, "Classifying coal pores and estimating reservoir parameters by nuclear magnetic resonance and mercury intrusion porosimetry," *Energy & Fuels*, vol. 27, no. 7, pp. 3699–3708, 2013.

[2] J. Rouquerol, D. Avnir, C. W. Fairbridge et al., "Physical chemistry division commission on colloid and surface chemistry, subcommittee on characterization of porous solids: recommendations for the characterization of porous solids," *Pure and Applied Chemistry*, vol. 66, no. 8, pp. 1739–1758, 1994.

[3] Q. Zhang, R. Liu, Z. Pang, W. Lin, W. Bai, and H. Wang, "Characterization of microscopic pore structures in Lower Silurian black shale ($S_1$1), southeastern Chongqing, China," *Marine and Petroleum Geology*, vol. 71, pp. 250–259, 2016.

[4] R. J. Ambrose, R. C. Hartman, M. Diaz-Campos, I. Y. Akkutlu, and C. H. Sondergeld, "New pore-scale considerations for shale gas in place calculations," in *SPE Unconventional Gas Conference*, Pittsburgh, Pennsylvania, USA, 2010.

[5] R. C. Hartman, R. J. Ambrose, I. Y. Akkutlu, and C. R. Clarkson, "Shale gas-in-place calculations part II-multi component gas adsorption effects," in *North American Unconventional Gas Conference and Exhibition*, The Woodlands. Texas, USA, 2011.

[6] R. J. Ambrose, R. C. Hartman, M. Diaz-Campos, I. Y. Akkutlu, and C. H. Sondergeld, "Shale gas-in-place calculations part I: new pore-scale considerations," *SPE Journal*, vol. 17, no. 1, pp. 219–229, 2012.

[7] J. B. Curtis, "Fractured shale-gas systems," *AAPG bulletin*, vol. 86, no. 11, pp. 1921–1938, 2002.

[8] W. A. Xiaoqi, Z. Zengqiang, J. Xu et al., "Molecular simulation of CO_2/CH_4 competitive adsorption in organic matter pores in shale under certain geological conditions," *Petroleum Exploration and Development*, vol. 43, no. 5, pp. 841–848, 2016.

[9] F. Yang, Z. Ning, R. Zhang, H. Zhao, and B. M. Krooss, "Investigations on the CH_4 sorption capacity of marine shales from Sichuan Basin, China," *International Journal of Coal Geology*, vol. 146, pp. 104–117, 2015.

[10] P. Ungerer, J. Collell, and M. Yiannourakou, "Molecular modeling of the volumetric and thermodynamic properties of kerogen: influence of organic type and maturity," *Energy Fuel.*, vol. 29, no. 1, pp. 91–105, 2015.

[11] G. Wei, W. Xiong, G. Shusheng, H. Zhiming, L. Honglin, and Y. Rongze, "Impact of temperature on the isothermal adsorption/desorption characteristics of shale gas," *Petroleum Exploration and Development*, vol. 40, no. 4, pp. 514–519, 2013.

[12] T. Wu, Q. Xue, X. Li et al., "Extraction of kerogen from oil shale with supercritical carbondioxide: molecular dynamics simulations," *Journal of Supercritical Fluids the*, vol. 107, pp. 499–506, 2016.

[13] Z. Sun, S. Wang, H. Xiong, K. Wu, and J. Shi, "Optimal nanocone geometry for water flow," *AIChE Journal*, vol. 68, no. 3, article e17543, 2021.

[14] J. H. Xiang, F. G. Zeng, H. Z. Liang, B. Li, and X. X. Song, "Molecular simulation of the $CH_4/CO_2/H_2O$ adsorption onto the molecular structure of coal," *Science China Earth Sciences*, vol. 57, pp. 1749–1759, 2014.

[15] M. Yiannourakou, P. Ungerer, B. Leblanc et al., "Molecular simulation of adsorption in microporous materials," *Oil & Gas Science and Technology*, vol. 68, no. 6, pp. 977–994, 2013.

[16] J. Collell, G. Galliero, F. Gouth et al., "Molecular simulation and modelisation of CH_4/ethane mixtures adsorption onto a microporous molecular model of kerogen under typical reservoir conditions," *Microporous and Mesoporous Materials*, vol. 197, pp. 194–203, 2014.

[17] S. Wang, Q. Feng, F. Javadpour, T. Xia, and Z. Li, "Oil adsorption in shale nanopores and its effect on recoverable oil-in-place," *International Journal of Coal Geology*, vol. 147-148, pp. 9–24, 2015.

[18] M. Kazemi and A. Takbiri-Borujeni, "Non-equilibrium molecular dynamics simulation of gas flow in organic nanochannels," *Journal of Natural Gas Science and Engineering*, vol. 33, pp. 1087–1094, 2016.

[19] M. Kazemi and A. Takbiri-Borujeni, "Flow of gases in organic nanoscale channels: a boundary-driven molecular simulation study," *Energy & Fuels*, vol. 30, no. 10, pp. 8156–8163, 2016.

[20] B. Y. Cao, M. Chen, and Z. Y. Guo, "Effect of surface roughness on gas flow in microchannels bymolecular dynamics simulation," *International Journal of Engineering Science*, vol. 44, no. 13-14, pp. 927–937, 2006.

[21] H. Noorian, D. Toghraie, and A. R. Azimian, "The effects of surface roughness geometry of flow undergoing Poiseuille flow by molecular dynamics simulation," *Heat and Mass Transfer*, vol. 50, no. 1, pp. 95–104, 2014.

[22] D. R. Katti, H. B. Upadhyay, and K. S. Katti, "Molecular interactions of kerogen moieties with Na-montmorillonite: an experimental and modeling study," *Fuel*, vol. 130, pp. 34–45, 2014.

[23] S. Rui and M. Cui, "Molecular simulation on competitive adsorption mechanism of CH_4/CO_2 on shale kerogen," *Arabian Journal of Geosciences*, vol. 11, no. 15, p. 403, 2018.

[24] F. Perez and D. Devegowda, "Spatial distribution of reservoir fluids in mature kerogen using molecular simulations," *Fuel*, vol. 235, pp. 448–459, 2019.

[25] M. F. Castez, E. A. Winograd, and V. M. Sanchez, "CH_4 flow through organic-rich nanopores: the key role of atomic-scale roughness," *The Journal of Physical Chemistry C*, vol. 121, no. 51, pp. 28527–28536, 2017.

[26] Y. Pang, M. Y. Soliman, H. Deng, and X. Xie, "Experimental and analytical investigation of adsorption effects on shale gas transport in organic nanopores," *Fuel*, vol. 199, pp. 272–288, 2017.

[27] L. Huang, Z. Ning, Q. Wang et al., "Molecular simulation of adsorption behaviors of methane, carbon dioxide and their mixtures on kerogen: effect of kerogen maturity and moisture content," *Fuel*, vol. 211, pp. 159–172, 2018.

[28] S. Wang, X. Yao, Q. Feng et al., "Molecular insights into carbon dioxide enhanced multi-component shale gas recovery and its sequestration in realistic kerogen," *Chemical Engineering Journal*, vol. 425, article 130292, 2021.

[29] Z. Sun, X. Li, W. Liu, T. Zhang, M. He, and H. Nasrabadi, "Molecular dynamics of methane flow behavior through realistic organic nanopores under geologic shale condition: pore size and kerogen types," *Chemical Engineering Journal*, vol. 398, article 124341, 2020.

[30] S. Wang, Y. Liang, Q. Feng, and F. Javadpour, "Sticky layers affect oil transport through the nanopores of realistic shale kerogen," *Fuel*, vol. 310, no. Part C, article 122480, 2022.

[31] B. Zhou, R. Xu, and P. Jiang, "Novel molecular simulation process design of adsorption in realistic shale kerogen spherical pores," *Fuel*, vol. 180, pp. 718–726, 2016.

[32] H. Yu, H. Y. Xu, J. C. Fan, Y. B. Zhu, F. C. Wang, and H. A. Wu, "Transport of shale gas in microporous/nanoporous media: molecular to pore-scale simulations," *Energy & Fuels*, vol. 35, no. 2, pp. 911–943, 2021.

[33] C. Bousige, C. M. Ghimbeu, C. Vix-Guterl et al., "Realistic molecular model of kerogen's nanostructure," *Nature materials*, vol. 15, no. 5, pp. 576–582, 2016.

[34] J. A. Donadelli, A. Canneva, G. Erra, and A. Calvo, "XPS direct analysis on shale rocks: correlation with kerogen type and maturity," *Fuel*, vol. 257, article 116004, 2019.

[35] S. Plimpton, "Fast parallel algorithms for short-range molecular dynamics," *Journal of Computational Physics*, vol. 117, no. 1, pp. 1–19, 1995.

[36] M. Waldman and A. T. Hagler, "New combining rules for rare gas van der Waals parameters," *Journal of Computational Chemistry*, vol. 14, no. 9, pp. 1077–1084, 1993.

[37] W. G. Hoover, "Canonical dynamics: equilibrium phase-space distributions," *Physical review A*, vol. 31, no. 3, pp. 1695–1697, 1985.

[38] G. J. Martyna, D. J. Tobias, and M. L. Klein, "Constant pressure molecular dynamics algorithms," *Journal of Chemical Physics*, vol. 101, no. 5, 1994.

[39] C. Zou, Q. Zhao, L. Cong et al., "Development progress, potential and prospect of shale gas in China," *Natural Gas Industry*, vol. 41, no. 1, pp. 1–14, 2021.

[40] A. R. Bhandari, P. B. Flemings, and R. Hofmann, "The dependence of shale permeability on confining stress and pore pressure," *Journal of Natural Gas Science and Engineering*, vol. 92, article 104008, 2021.

[41] H. Yu, J. Chen, Y. B. Zhu, F. C. Wang, and H. A. Wu, "Multiscale transport mechanism of shale gas in micro/nano-pores," *International Journal of Heat and Mass Transfer*, vol. 111, pp. 1172–1180, 2017.

[42] Z. Sun, B. Huang, Y. Li, H. Lin, S. Shi, and W. Yu, "Nanoconfined methane flow behavior through realistic organic shale matrix under displacement pressure: a molecular simulation investigation," *Journal of Petroleum Exploration and Production Technology*, pp. 1–9, 2021.

[43] S. Wang, Q. Feng, F. Javadpour, M. Zha, and R. Cui, "Multiscale modeling of gas transport in shale matrix: an integrated study of molecular dynamics and rigid-pore-network model," *SPE Journal*, vol. 25, no. 3, pp. 1416–1442, 2020.

[44] H. Frentrup, C. Avendaño, M. Horsch, A. Salih, and E. A. Müller, "Transport diffusivities of fluids in nanopores by non-equilibrium molecular dynamics simulation," *Molecular Simulation*, vol. 38, no. 7, pp. 540–553, 2012.

[45] A. Beskok and G. E. Karniadakis, "Report: a model for flows in channels, pipes, and ducts at micro and nano scales," *Microscale thermophysical engineering*, vol. 3, no. 1, pp. 43–77, 1999.

[46] H. Yu, H. Xu, J. Fan, F. Wang, and H. Wu, "Roughness factor-dependent transport characteristic of shale gas through amorphous kerogen nanopores," *The Journal of Physical Chemistry C*, vol. 124, no. 23, pp. 12752–12765, 2020.

[47] H. Yu, H. Y. Xu, J. Xia, J. C. Fan, F. C. Wang, and H. A. Wu, "Nanoconfined transport characteristic of methane in organic shale nanopores: the applicability of the continuous model," *Energy & Fuels*, vol. 34, no. 8, pp. 9552–9562, 2020.

[48] X. Du, M. Gu, Z. Liu, Y. Zhao, F. Sun, and T. Wu, "Enhanced shale gas recovery by the injections of CO_2, N_2 and CO_2/N_2 mixture gases," *Energy & Fuels*, vol. 33, no. 6, pp. 5091–5101, 2019.

[49] S. A. Jikich, D. H. Smith, W. N. Sams, and G. S. Bromhal, "Enhanced gas recovery (EGR) with CO_2 sequestration: a simulation study of effects of injection strategy and operational parameters," in *SPE Eastern Regional/AAPG Eastern Section Joint Meeting*, Pittsburgh, PA, U.S.A, 2003.

[50] A. Bahadori, *Fundamentals of Enhanced Oil and Gas Recovery from Conventional and Unconventional Reservoirs*, Gulf Professional Publishing, 2018.

Hindawi
Geofluids
Volume 2022, Article ID 6193082, 11 pages
https://doi.org/10.1155/2022/6193082

Research Article

Experimental Study on the Oil Recovery Performance of CO_2 Huff-and-Puff Process in Fractured Tight Oil Reservoirs

Kun Qian,[1] **Yu Huang**,[2] **Yanfeng He**,[1] **Xiangji Dou**,[1] **and Xiaojun Wu**[1]

[1]*School of Petroleum Engineering, Changzhou University, Changzhou 213164, China*
[2]*Oil and Gas Production Engineering Service Center, Sinopec East China Oil and Gas Company, Taizhou, Jiangsu 225300, China*

Correspondence should be addressed to Kun Qian; qiankun@cczu.edu.cn

Received 14 January 2022; Accepted 11 February 2022; Published 2 March 2022

Academic Editor: Zheng Sun

In order to investigate energy supply capacity and oil production contribution of near-fracture and fracture-free zone in fractured tight oil reservoirs, a series of CO_2 huff-and-puff tests were designed and carried out in different experimental conditions. A fracture-matrix long-core system was established to simulate the near-fracture zone and matrix zone of tight oil reservoirs. The NMR technique was utilized to identify the microscopic remaining oil of certain core samples. The effects of fracture length, soaking time, depressurization method, and asphaltene precipitation on the oil recovery performance of CO_2 huff-and-puff process were evaluated, respectively. The results indicated that the dissolution and diffusion range of the injected CO_2 can be apparently increased from both macro and micro aspects through increasing the length or density of the fractures and extending the soaking time; and, during puff period, the slow depressurization method has better recovery effect on near-fracture zone, while the step depressurization method has better recovery effect on distal fracture-free matrix. After CO_2 huff-and-puff process, the oil recovery of the medium pores near fracture could be close to oil recovery of the large pores, which is higher than 60%. But, in the distal matrix, the oil recovery of the medium pores was only a little higher than depletion development. The remaining oil of medium pores in distal fracture-free matrix still has great potential to be developed after CO_2 huff-and-puff process.

1. Introduction

Tight oil has huge exploration and development potential [1] and the development of tight oil has become the key factor to the stable production of crude oil in China [2, 3]. In this study, the target reservoir is a typically tight oil reservoir located in Shanbei area, Northwest China. The average permeability of the formation is about 0.53 mD and the average porosity is only 8.3%. The production of tight oil reservoirs declines rapidly due to the limited supply capacity of the matrix, and the reservoir energy cannot be effectively replenished by conventional water injection due to the narrow pore throat [4, 5].

CO_2 injection has been proven to be an effective method to improve the oil recovery of tight oil reservoirs [6, 7]. Continuous CO_2 flooding, CO_2-WAG injection (water alternating gas injection), and CO_2 huff-and-puff process are commonly used CO_2-EOR (enhance oil recovery) techniques [7]. Due to great heterogeneity of the target tight oil reservoir, the continuous CO_2 flooding and CO_2-WAG injection could result in serious gas channeling and early breakthrough [8]. In consideration of these issues, CO_2 huff-and-puff process seems to be a feasible method to enhance oil recovery from tight oil reservoir.

Abedini and Torabi [9] and Pu et al. [10] investigated the oil recovery mechanisms and performance of the immiscible and miscible CO_2 huff-and-puff process, and it was found that interfacial tension reduction, oil swelling, and extraction of lighter components by CO_2, especially during miscible CO_2 injections, are the main oil recovery mechanisms during CO_2 huff-and-puff process. In comparison with conventional reservoirs, the effect of CO_2 diffusion and nanopore confinement plays a significant role in enhancing oil recovery of tight oil reservoirs [11–15]. Qian et al. [16] illustrated that CO_2 can enter small pores and extract the oil in the smaller and blind pores at higher injection pressure during CO_2 injection through nuclear magnetic resonance (NMR) technique. Zhang et al. [17] found that CO_2

molecular diffusion and capillary pressure lead to 3.8% increase of CO_2 huff-and-puff oil recovery performance in tight oil reservoirs through numerical model. For tight reservoirs with stronger heterogeneity and lower permeability, the CO_2 huff-and-puff technique can obtain higher incremental oil recovery factor on the base of depletion [18]. In addition, the production parameters in tight reservoirs have also been optimized through experimental and numerical simulations [5, 17, 19].

During the CO_2 huff-and-puff process in tight reservoirs, the presence of fractures is conducive to the entry of CO_2 into deep formation and increasing the exposure surface of tight matrix to CO_2 [20]. Wang [8] clarified the conductivity of fractures in tight oil reservoirs by the three-dimensional physical model with staged-fracturing horizontal well. Bai et al. [21] demonstrated that the fracture can increase the oil recovery of near-fracture zone by 14% compared with fracture-free zone. Additionally, fracture can significantly reduce the effect of matrix permeability on oil recovery of tight reservoirs. Also, the fracture filled with CO_2 can enlarge the interaction between CO_2 and the oil in matrix. Sun et al. [22] used the embedded discrete fracture model (EDFM) to conduct simulation of Middle Bakken tight oil reservoir and found that CO_2 diffusion is the most important factor of CO_2 huff-and-puff effectiveness on cumulative oil production.

In order to exploit the transport process of oil from matrix into the CO_2-filled factures system, Hawthorne et al. [20] conducted initial CO_2-exposure experiments and found that the hydrocarbons in very tight Bakken shale sample could be completely achieved with longer exposure time and smaller rock sizes. Further, Eide et al. [23] studied CO_2 diffusion in fractured chalk with X-Ray CT imagine during CO_2 injection process and found that the oil recovery by CO_2 diffusion is about 95% at core scale and the oil recovery by CO_2 diffusion is strongly influenced by system size. Wang demonstrated that when tight sandstone core plug is exposed to CO_2, the concentration-driven diffusion of hydrocarbons caused by CO_2 diffusion is the main mechanism to enhance oil recovery [24]. Wei et al. [25] utilized NMR technique to monitor the oil distribution in the matrix and fracture and indicated that the mass transfer between the matrix and fracture proceeded to increase oil production intensively during the soaking time in the first cycle and contributed less in second and third cycles. In addition, the characteristics of produced oil also indicated that the presence of fracture can increase the CO_2 mass transfer between CO_2 and oil in the matrix [26]. As mentioned, the CO_2 recovery mechanisms and effects on the oil recovery factor in fractured tight oil reservoirs have been widely studied; and the mass transfer between CO_2 and oil in the near-fracture matrix also has been discussed through CT, NMR, and oil composition analysis. However, the near-fracture tight formation was mainly investigated with the single-core samples exposed to CO_2. The energy supply capacity and microscopic remaining oil distribution of fracture-free matrix in fractured tight reservoirs during CO_2 huff-and-puff process need to be further characterized.

In this study, a fracture-matrix long-core system was firstly established to simulate the near-fracture zone and matrix zone of tight oil reservoirs. Then, a series of CO_2 huff-and-puff tests were designed and carried out in different experimental conditions. The NMR technique was utilized to identify the microscopic remaining oil of certain core samples. The effects of fracture length, soaking time, and depressurization method on the oil recovery performance were evaluated, respectively. Additionally, the permeability reduction was measured to determine the formation damage caused by asphaltene precipitation. The results of this study provide a further understanding of energy supply capacity of near-fracture and fracture-free zone during CO_2 huff-and-puff process. Meanwhile, the oil production contribution of different pores in fractured tight oil reservoirs was investigated.

2. Experimental Section

2.1. Fracture-Matrix Long-Core System. During the development process of tight oil reservoirs, the artificial fractures are developed near the well [5]. The fractured cores or matrix cores utilized in physical simulation alone cannot accurately characterize the fractured tight oil reservoirs. Therefore, the artificial fractured cores and matrix cores were combined to establish a fracture-matrix system to simulate fractured oil reservoirs, shown in Figure 1. Squeezing and pressing method was used to generate fractures. The rough wall surface of the fracture was covered with quartz sands. Then, the broken core was recombined and fixed with a heat shrinkable sleeve (Figure 2).

2.2. Materials. In this study, five tight sandstone core samples were collected from Chang 8 reservoir of Changqing Oil Field, China. Among them, core #1 and core #2 were artificially fractured. The properties of cores are listed in Table 1. The cores were composited to establish long core A and long core B with different fracture length (Figure 3).

The original oil sample and brine sample were also collected from Chang 8 reservoir. The density and viscosity of the oil sample were measured to be 843.4 kg/m^3 and 3.37 mPa s at the atmospheric pressure and the reservoir temperature of 61°C. The Gas Chromatography (GC) compositional analysis of the crude oil sample is shown in Figure 4 with Agilent 7890A chromatography. The purity of CO_2 used in this study was equal to 99.99% supplied by Beijing Huayuan Gas Chemical Co., Ltd. The minimum miscible pressure (MMP) between the crude oil and CO_2 was 22.33 MPa with slim-tube tests at reservoir temperature.

The reservoir brine sample was collected from the same formation and cleaned. The reservoir brine has the total dissolved solids (TDS) of 30917.8 mg/L, which was evaluated to be the water type of calcium chloride. The brine viscosity was measured to be 0.43 mPa s at the atmospheric pressure and 61°C.

2.3. Experimental Procedures of CO_2 Huff-and-Puff Tests. The experimental conditions of this study are shown in Table 2 and the experimental flow chart is shown in Figure 5. The general procedure of the CO_2 huff-and-puff tests is briefly described as follows:

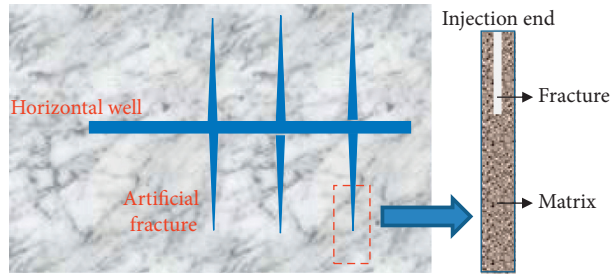

Figure 1: Diagram of fracture-matrix long-core system.

Figure 2: Artificial fractured core.

Table 1: Basic properties of core samples.

Core no.	Type	Length (cm)	Porosity (%)		Permeability (mD)	
			Before fracture	After fracture	Before fracture	After fracture
1	Fracture	5.014	11.86	12.35	1.56	1249.34
2	Fracture	5.776	11.40	11.74	1.94	896.21
3	Matrix	4.876	13.46	—	3.10	—
4	Matrix	5.028	13.61	—	3.02	—
5	Matrix	5.992	12.75	—	2.20	—

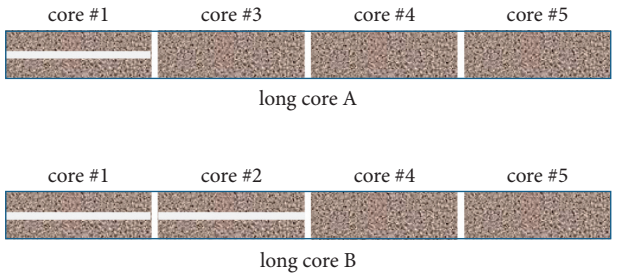

Figure 3: Schematic diagram of long core A and long core B.

(1) Prior to each test, the core plugs were thoroughly cleaned by using a Dean-Stark extractor (SXT-02, Shanghai Ping Xuan Scientific Instrument Co., Ltd.,

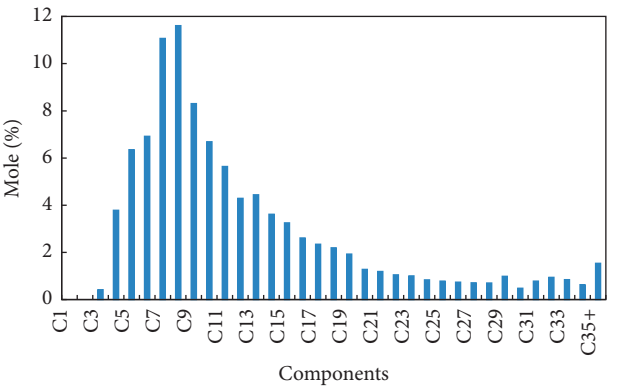

Figure 4: Components of the oil sample under the temperature of 21°C.

Table 2: Conditions of CO_2 huff-and-puff tests at the reservoir temperature of 61°C.

Test number	Long core number	Fracture length (cm)	Initial oil saturation (%)	Soaking time (h)	Pressure-drop method
1	A	5.014	63.25	12	Rapid
2	B	10.790	65.77	12	Rapid
3	A	5.014	65.93	24	Rapid
4	B	10.790	66.07	12	Slow
5	B	10.790	66.29	12	Step

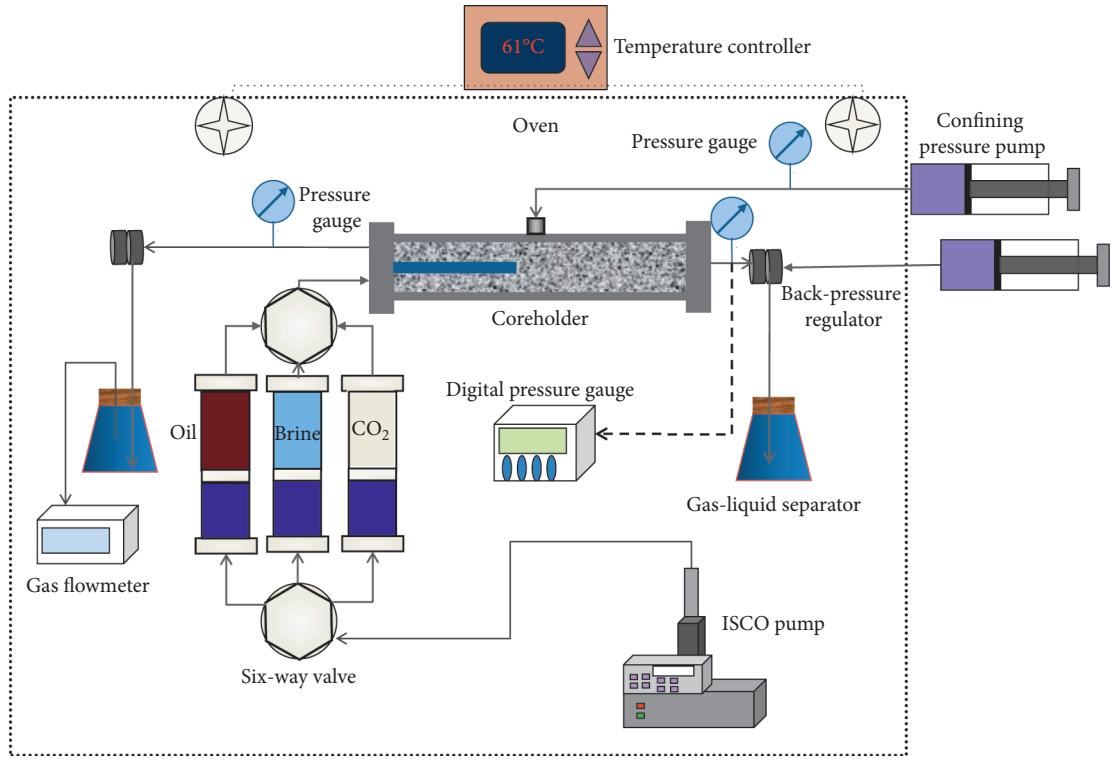

Figure 5: Schematic diagram of the experimental setup used for CO_2 huff-and-puff tests conducted at temperature of 61°C.

China) for 20~30 days. After the core plugs were cleaned and dried at 100°C, the gas permeability and porosity were measured with nitrogen (High-Pressure Gas Permeameter/Porosimeter, Temco, Tulsa, USA).

(2) The target core plugs were placed in core holder and vacuumed for 48 hours. The formation brine prepared with deuterium water was injected at the flow rate of 0.2 cm^3/min to saturate the core plugs, and the saturated cores were moved to NMR apparatus and scanned to make sure the hydrogen signal of the brine is eliminated. Then the core plugs were placed in the long-core holder again and displaced by brine again to ensure complete water saturation.

(3) After that, 3.0 PV of the crude oil was pumped through the core plug at a constant rate of 0.1 cm^3/min until no water was produced to achieve the connate water saturation (S_{wc}) and the initial oil saturation (S_{oi}) at the reservoir temperature of 61°C. The T_2 spectrum of the certain cores was measured again after the core plugs had been saturated with crude oil.

(4) The certain core plugs were placed in the long-core holder in order. The long core was displaced by crude oil again to ensure complete oil saturation. The long-core system was pressurized to the initial formation pressure of 20 MPa with crude oil. Afterwards, the depletion development was conducted to the atmospheric pressure by reducing back pressure.

(5) After depletion development, CO_2 was injected under constant pressure. After the distal end of the core holder reached the desired pressure of 16 MPa, which is the current formation pressure, the pump continued the constant pressure condition for 30 min and the soaking time was adjusted according to the experiment needs. The puff cycle was then started at the injection end of the core holder with

the pressure of atmosphere. These cycles were continued until no considerable oil production was obtained. The injection and production pressure was continuously monitored and recorded. The cumulative produced oil volume was recorded by a video camera and the cumulative volume of the produced gas was measured and recorded by using the gas flow meter.

(6) After the CO_2 huff-and-puff tests, the T_2 spectrum of the certain core samples was measured with NMR apparatus.

(7) Change the experimental conditions and repeat the above experimental steps.

3. Results and Discussion

3.1. Effects of Fracture Length. Long core A and long core B with different fracture length (Figure 3) were established to conduct CO_2 huff-and-puff tests. The oil recovery factors of long core A and long core B during depletion development are 12.62% and 13.43%, respectively. Long core B with longer fracture can obtain higher cumulative oil recovery factor with less huff-and-puff cycles. After the entire huff-and-puff tests, the ultimate recovery factor of long core B is 5.37% higher than that of long core A, which are, respectively, 51.14% and 45.77%, as shown in Figure 6.

Combined with the peak and trough in the T_2 spectrum, the matrix and fracture of the core can be identified in the initial oil-saturated state. The T_2 spectrum was artificially divided into three intervals [16], micro pores (≤5 ms), medium pores (5~100 ms), large pores, and fractures (≥100 ms). As shown in Figure 7, the remaining oil distributions of core #1 after the ultimate huff-and-puff tests with long core A and long core B are similar. But more oil in micro pores of core #1 was obtained in long core A (Figure 7), due to the one more huff-and-puff cycle in long core A. The oil recovery factors of core #1 after tests with long core A and long core B are 68.23% and 67.01%, respectively. In the near-fracture zone, the oil recovery factor of micro pores can be close to 20% and the lower oil recovery limit of pores can be as low as the pore radius corresponding to the T_2 relaxation time of 1 ms (Figure 7).

Core #3 was the matrix core closest to the fracture and core #5 was the furthest matrix core from the fracture in long core A. After huff-and-puff tests with long core A, the ultimate oil recovery factor of core #3 was 44.31% and the ultimate oil recovery factor of core #5 was only 14.79%. Obviously, with the distance from the fracture increasing, the effect of CO_2 huff-and-puff process becomes poorer. When the fracture was extended from long core A to long core B, the oil recovery of core #5 was significantly increased from 14.79% to 28.42%. Figure 8 presents that the increased production mainly comes from medium and large pores corresponding to the T_2 relaxation time more than 5 ms. The lower oil recovery limit of distal matrix can decrease with fracture extending. The extended fracture can not only expand oil drainage range but also improve the mass-transfer efficiency of CO_2. Therefore, higher oil recovery factor could be achieved with less huff-and-puff cycles through increasing the length or density of the fractures.

The distance from the matrix core plug center to the fracture is calculated and listed in Table 3. Figure 9 shows the oil recovery factor of different pores in matrix with different distances to the fracture. The farther away it is from the fracture, the lower the oil recovery is in different pores. As presented in Figure 9, the oil recovery factor of the oil in medium pores has the largest decline. In the near-fracture zone, the oil recovery of the medium pores could be close to the oil recovery of the large pores and fractures (Figure 9), which was higher than 60%. But, in the distal matrix, the cumulative oil recovery of the medium pores was 16.17%, which was only a little higher than oil recovery of depletion development.

In addition to large pores, the oil in medium pores could be the main force to production in Changqing tight oil reservoirs. CO_2 huff-and-puff technique only has a good effect on the oil recovery of near-fracture zone. But the remaining oil of medium pores in distal matrix still has great potential to be developed after CO_2 huff-and-puff process. Adjusting the CO_2 development method and changing the well pattern would be feasible methods to develop remaining oil in matrix [5, 12].

3.2. Effects of Soaking Time. Soaking time is a significant parameter in CO_2 huff-and-puff operation. The CO_2 huff-and-puff experiments with different soaking time were conducted with long core A. Figure 10 presents the difference between cumulative oil recovery factors of each huff-and-puff cycle with different soaking time of 12 h and 24 h. The cumulative recovery factor of soaking for 24 h with 3 cycles is slightly higher than that of soaking for 12 h with 6 cycles. It is beneficial for CO_2 to dissolve and diffuse in the oil with increasing the soaking time, especially for the tight reservoirs. For the same total soaking time of the whole CO_2 huff-and-puff process, longer soaking time with less cycles can have better recovery effect and save development cost. When the huff-and-puff tests continued to operate until no oil was produced, the cumulative recovery factor of soaking for 24 h was 8.42% higher than that of soaking for 12 h.

The remaining oil distribution of fractured core #1 and the distal matrix core #5 after the tests are shown in Figures 11 and 12. Microscopically, longer soaking time can increase the oil recovery factor of micro pores. The oil recovery factors of micro pores of core #1 and core #5 increased by 7.71% and 6.16%, respectively (Table 4). Meanwhile the lower oil recovery limit of pores decreased. The oil in smaller pores could be obtained with longer soaking time (Figures 11 and 12). Macroscopically, longer soaking time can increase CO_2 sweep efficiency. When the soaking time was 12 h, the recovery factor of core #5 was 14.79%. When the soaking time was increased to 24 h, the recovery factor of core #5 increased to 23.71%. Therefore, the dissolution and diffusion range of the injected CO_2 was apparently increased from both macro and micro aspects after extending soaking time.

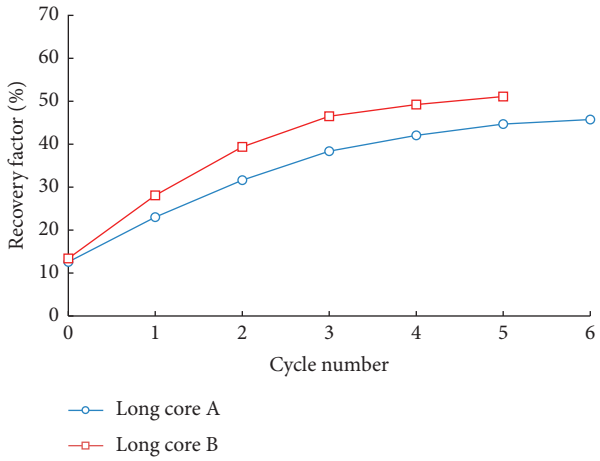

Figure 6: The difference between the cumulative oil recovery factors of long core A and long core B at each huff-and-puff cycle.

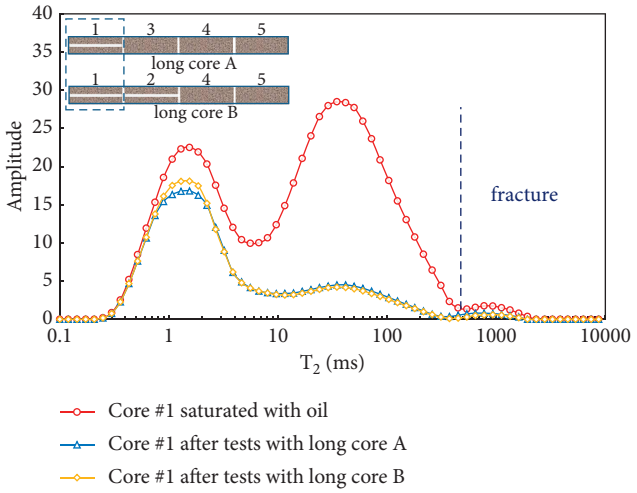

Figure 7: The difference between remaining oil distributions of core #1 after huff-and-puff tests with long core A and long core B.

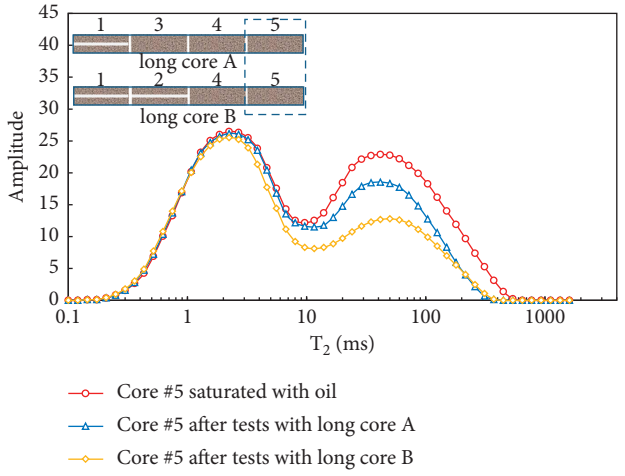

Figure 8: The difference between remaining oil distributions of core #5 after the huff-and-puff process with long core A and long core B.

Table 3: The distance from the core center to the fracture.

Core	The distance to the fracture (cm)	Oil recovery factor (%)
Core #1 in long core A	0	68.23
Core #1 in long core B	0	67.01
Core #3 in long core A	2.996	44.31
Core #5 in long core B	7.390	30.42
Core #5 in long core A	13.382	14.79

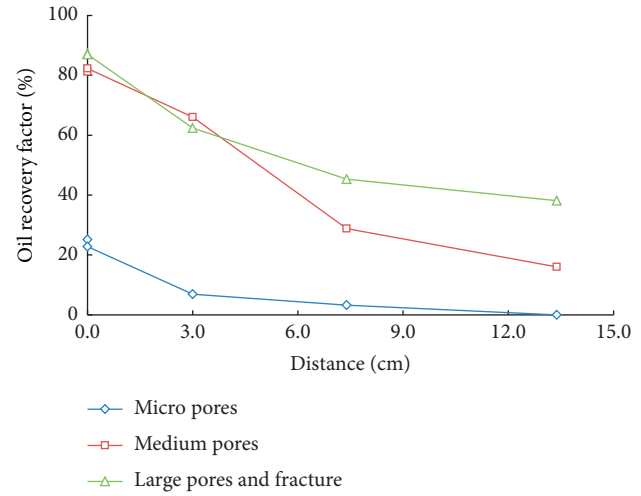

Figure 9: The oil recovery factor of different pores in matrix with different distances to the fracture.

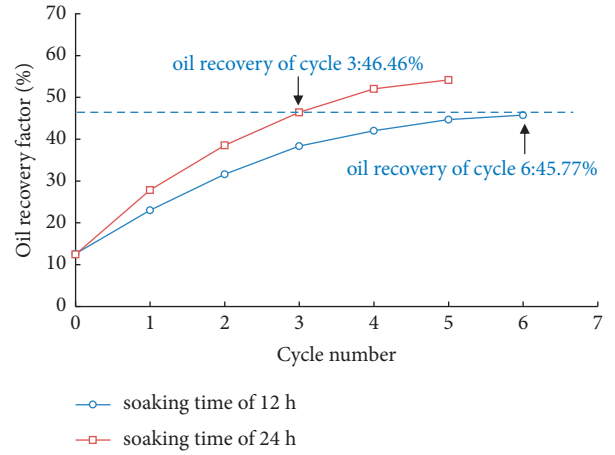

Figure 10: The difference between cumulative oil recovery factors of each huff-and-puff cycle with different soaking time.

3.3. Effects of Depressurization during Puff Period. In the puff period of the first huff-and-puff cycle, three different depressurization methods were performed. Table 5 presents the production status of different depressurization methods, and Figure 13 shows pressure change of distal end during different depressurization process.

According to production dynamics and oil recovery factor changing with time (Figure 14), the production period was divided into three stages:

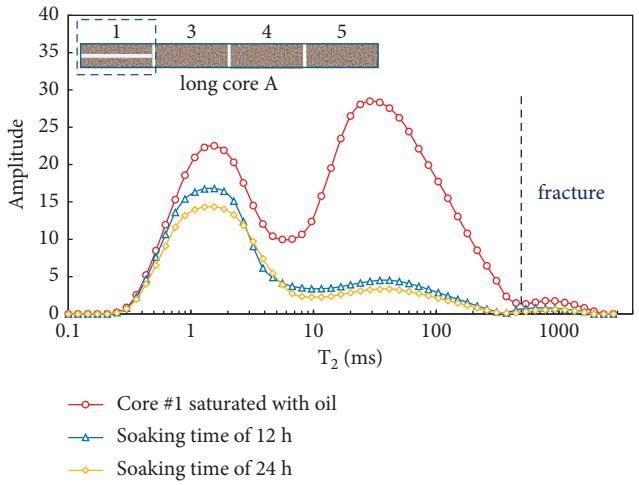

Figure 11: The microscopic remaining oil distribution of fractured core #1 after huff-and-puff tests with different soaking time.

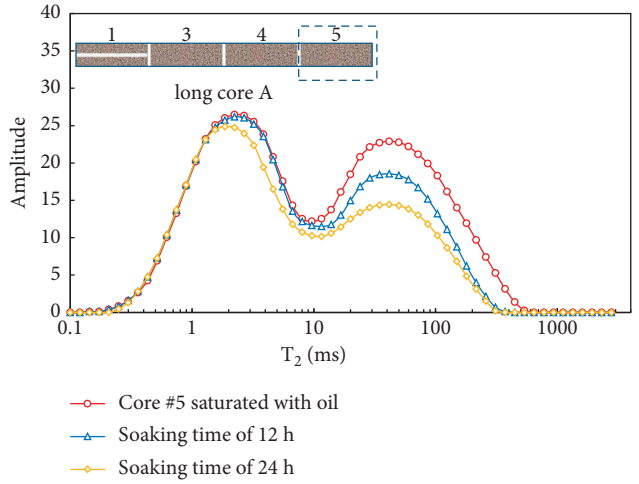

Figure 12: The microscopic remaining oil distribution of matrix core #5 after huff-and-puff tests with different soaking time.

Table 4: The oil recovery factor of different pores after huff-and-puff tests with different soaking time.

Core number	Pore types	Soaking time	
		12 h (%)	24 h (%)
Core #1	Micro pores (≤5 ms)	26.27	33.98
	Medium pores (5~100 ms)	82.12	87.14
	Large pores (≥100 ms)	87.13	90.50
	Total	68.23	70.92
Core #5	Micro pores (≤5 ms)	0.00	6.16
	Medium pores (5~100 ms)	16.00	31.33
	Large pores (≥100 ms)	47.13	59.46
	Total	14.79	23.71

(1) Gas flowback stage: in the huff period, the injected CO_2 preferentially occupied fractures and large pores and then dissolved and diffused into smaller pores [24]. After the soaking period, there was still a large amount of free gas remaining in the large pores and fractures. Therefore, at the beginning of each depressurization process, a large amount of gas was produced with the system pressure decreasing (Figure 13). This period was very short and there was almost no oil output (Figure 14(b)).

(2) Free gas drive stage: after CO_2 flowback, some free CO_2 was still trapped in the near-wellbore area. At the same time, there was also crude oil in the near-wellbore area and fractures. Then the oil was driven and carried out by free CO_2. At this stage, the oil and CO_2 were produced alternately, which was mainly manifested as a large section of gas and a small section of oil. The GOR (gas oil ratio) fluctuated greatly (Figure 15) and the oil production rate was relatively low (Figure 14(b)).

(3) Solution gas drive stage: during the depressurization process, dissolved gas was continuously released. When the oil production rate was significantly increased, the drive mode was changed from free gas drive to solution gas drive. When the solution gas drive proceeded to the final stage, the capacity of energy supply decreased. Solution gas drive stage was the main oil production stage in different depressurization method.

The cumulative oil recovery factor of puff period was influenced by the depressurization method (Figure 14(a)). After first cycle, the oil recovery factor of slow depressurization was 17.24%, which was higher than that of rapid depressurization process by 2.59%. Once the pressure started to drop, the CO_2 bubble began to nucleate. Then, the bubble grew and filled pores with the pressure decreasing [27]. In rapid depressurization process, the nucleated CO_2 bubbles were produced before they became larger to occupy the pore space due to the huge pressure gradient. So the crude oil in the pores could not be driven effectively by the dissolved gas. However, in slow depressurization process, the CO_2 nucleation had more time to grow to fill the pore space [28]. The grown CO_2 bubble can drive the crude oil in the matrix to the fracture and near-wellbore zone. When the CO_2 bubbles increased to a certain size, the narrow pore throat would hinder the mobility of the bubbles due to Jamin effect [29]. As pressure decreased, the gas bubbles could coalesce into a continuous gas phase and migrated. The GOR oscillated down during the first half of solution gas drive stage in the slow depressurization method.

The highest oil recovery factor of the three depressurization methods was step depressurization, which was 18.40%. There was little difference in production times between slow depressurization method and step depressurization method. But the step pressure-drop process can avoid the rapid fracture closure and the compression of pores due to the stress sensibility. So the oil in distal core could be recovered more smoothly. The highest oil recovery factor of step depressurization method illustrates that fracture closure time has great influence on the oil recovery of fractured tight sandstone reservoirs.

Figures 16 and 17 are the microscopic remaining oil distributions of fractured core #2 and distal matrix core #5 after huff-and-puff tests with different depressurization method. After injection, CO_2 preferentially entered the

Table 5: Production status of different depressurization methods.

Depressurization method	Back pressure (MPa) (production pressure)	Production valve (throttle valve)	Oil recovery factor of depletion (%)	Oil recovery factor of first cycle (%)
Rapid	0	50% open	13.43	14.65
Slow	0	10% open	13.29	17.24
Step	16-12-8-4-0	50% open	13.40	18.40

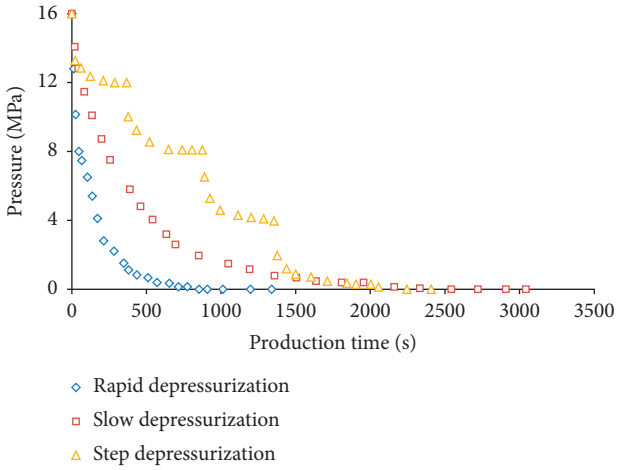

Figure 13: Pressure change of distal end during puff period of the first huff-and-puff cycle with different depressurization method.

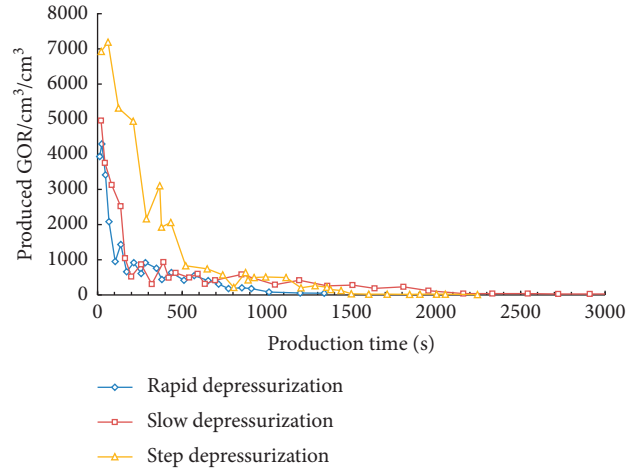

Figure 15: GOR during puff period of the first huff-and-puff cycle with different depressurization method.

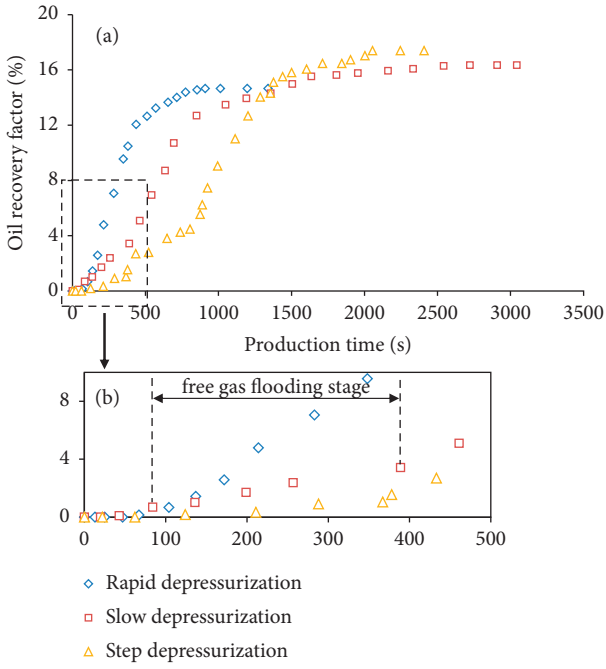

Figure 14: Oil recovery factor during puff period of the first huff-and-puff cycle with different depressurization method.

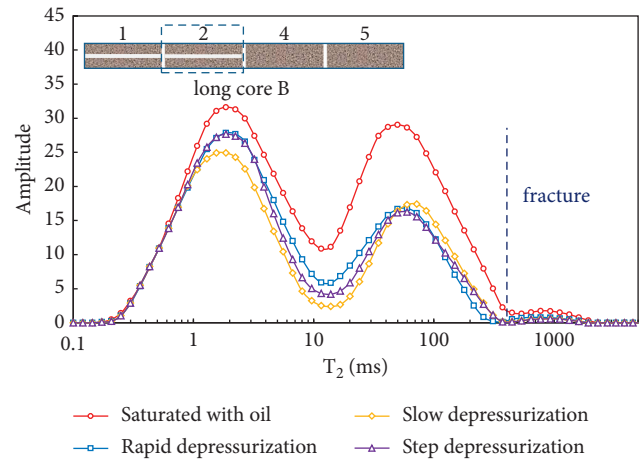

Figure 16: The microscopic remaining oil distribution of fractured core #2 after huff-and-puff tests with different depressurization method.

larger pores, dissolved, and diffused into the oil in micro pores [30]. The existence of fracture increased the dissolution and diffusion of CO_2 into the matrix with expanding the contact range between CO_2 and oil. Thus the oil recovery factor of the fractured core #2 was much higher than that of matrix core #5. Moreover, the oil recovery factor in pores of different sizes was overall higher in in near-fracture zone (Table 6).

In addition, the microscopic remaining oil distribution can also reflect the influence of different depressurization method on oil recovery (Figures 16 and 17). In near-fracture zone, both medium pores and large pores were the main contributors to oil production. The oil recovery factors of medium pores and large pores were around 50% (Table 6). In particular, in the solution gas drive stage of slow depressurization process, the CO_2 nucleation had more time to grow to drive the oil in the pores. Consequently, in fractured core #2, the oil recovery of the micro and medium pores is

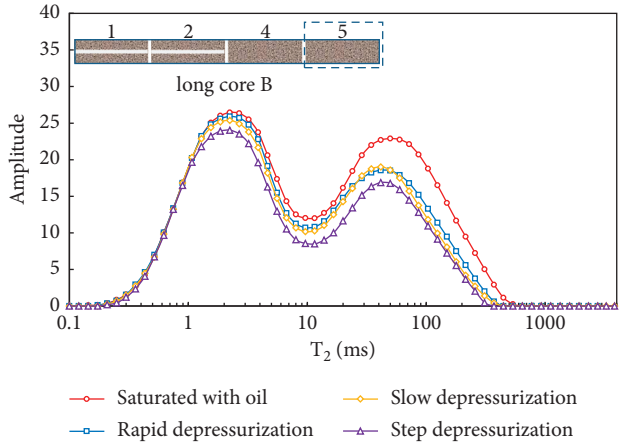

Figure 17: The microscopic remaining oil distribution of matrix core #5 after huff-and-puff tests with different depressurization method.

Table 6: The oil recovery factor of different pores after huff-and-puff tests with different depressurization method.

Pore types	Fractured core #2			Matrix core #5		
	Rapid (%)	Slow (%)	Step (%)	Rapid (%)	Slow (%)	Step (%)
Micro pores (≤5 ms)	11.93	20.50	13.02	2.13	4.76	9.83
Medium pores (5~100 ms)	45.78	55.75	51.35	15.80	17.98	28.94
Large pores (≥100 ms)	60.36	48.07	53.07	38.40	48.81	55.22
Total	36.16	39.37	37.29	18.67	19.17	23.85

higher than rapid and step depressurization methods (Figure 16, Table 6). But the oil recovery of the large pores in slow depressurization was less than the other two methods, because part of the oil from the micro and medium pores was retained in the large pores in the last stage of slow depressurization method with low pressure difference.

In matrix core #5, the microscopic remaining oil distributions of the rapid and slow depressurization methods are much the same (Figure 17 and Table 6). The microscopic remaining oil distribution of the step depressurization method is obviously lower than those of the other two methods, and the oil in smaller pores can be recovered (Figure 17). During the process of step depressurization process, the fracture closure time was postponed, which is conductive to the oil drainage from matrix to fracture.

After the entire huff-and-puff cycles, the oil recovery factors of the huff-and-puff process with rapid, slow, and step depressurization were 51.14%, 53.28%, and 55.54%, respectively. The oil recovery factor of the first huff-and-puff cycle is obviously different, as presented in Figure 18. With cycles proceeding, the remaining oil saturation decreased and the remaining oil viscosity increased [31]. The solubility of CO_2 in the remaining oil was also getting less. The advantage of the slow depressurization method in solution gas drive stage decreased. For this reason, the oil recovery factor of slow depressurization method became closer to that of fast depressurization method in each cycle. As mentioned before, the oil recovery factor of huff-and-puff process with step depressurization process was always higher. Therefore, step depressurization combined with slow pressure drop during puff period in the first two cycles is an effective method to increase the oil recovery factor of the CO_2 huff-and-puff process of tight oil reservoirs. In the later cycles, the depressurization combined with rapid pressure drop can be utilized to save production time.

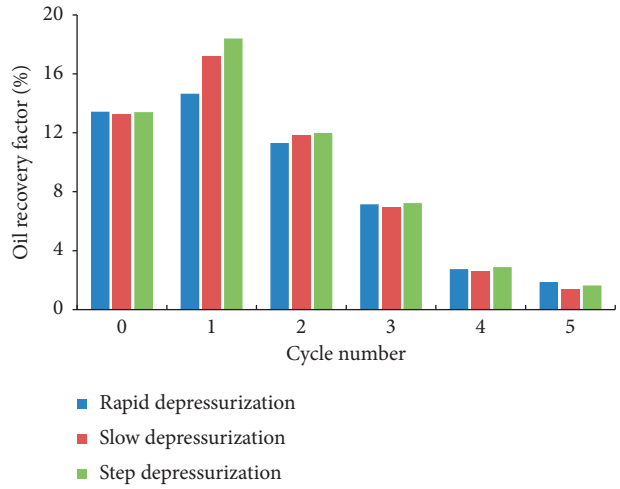

Figure 18: The oil recovery factor of depletion production period and each huff-and-puff cycle with different depressurization method.

3.4. Effects of Asphaltene Precipitation. After the CO_2 huff-and-puff process with long core A of Test 1, the core samples were cleaned by a Soxhlet Extractor with the solvent of petroleum ether which cannot dissolve asphaltene [32]. The percentage of permeability reduction is obtained by comparing the gas permeability of the core before and after CO_2

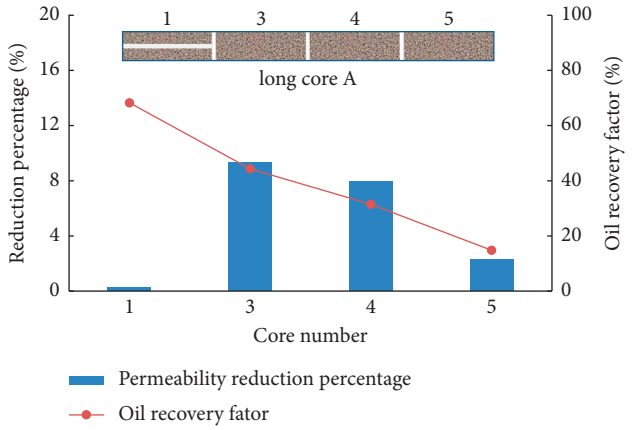

Figure 19: Permeability reduction percentage and oil recovery factor of different cores in long core A.

huff-and-puff tests, which is calculated by the following equation:

$$R_k = \frac{K_{gb-}K_{ga}}{K_{gb}} \times 100\%, \quad (1)$$

where R_k is the permeability reduction percentage of the core sample, %; K_{gb} is the gas permeability of the core sample before CO_2 flooding, mD; K_{ga} is the gas permeability of the core sample after CO_2 flooding, mD.

The injected CO_2 destroys the stable state of the asphaltene-resin system, which leads to the flocculation and precipitation of the asphaltene [9]. In the CO_2 huff-and-puff tests, asphaltene precipitation still occurred [16] and the permeability of the cores decreased after the huff-and-puff tests in tight oil reservoirs. The asphaltene particles were difficult to be transported out because of the small pore throats of the matrix. But the asphaltene precipitation had little effects on the permeability of fractured core #1 with strong flow conductivity. As shown in Figure 19, the permeability reduction percentage has a certain positive correlation with oil recovery factor, except fractured core #1, because, in the CO_2 huff-and-puff process, the higher oil recovery factor indicates the better solubility of CO_2 in oil. The permeability reduction percentages of core #3 and core #4 are 12.20% and 9.93%, respectively, while the permeability reduction percentage of distal core #5 is only 3.64% due to the lowest CO_2 solubility.

4. Conclusions

In this paper, a series of CO_2 huff-and-puff tests were conducted with fractured tight cores from Changqing Oil Field, China. The NMR technique was utilized to analyze the remaining oil of the core plugs. The effects of fracture length, soaking time, depressurization method, and asphaltene precipitation on the oil recovery performance were evaluated. According to the obtained experimental results, the following conclusions have been drawn:

(1) Higher oil recovery factor could be achieved with less huff-and-puff cycles through increasing the length or density of the fractures and extending the soaking time. Moreover, the dissolution and diffusion range of the injected CO_2 could be apparently increased from both macro- and microaspects.

(2) In addition to large pores, the remaining oil of medium pores in distal fracture-free matrix still has great potential to be developed after CO_2 huff-and-puff process. Adjusting the CO_2 development method and changing the well pattern would be feasible methods to develop remaining oil.

(3) Step depressurization combined with slow pressure drop during puff period in the first two cycles is an effective method to increase the oil recovery factor of the CO_2 huff-and-puff process of tight oil reservoirs. In the later cycles, the depressurization combined with rapid pressure drop can be utilized to save production time.

(4) During CO_2 huff-and-puff process, the asphaltene precipitation has little effects on the permeability of the near-fracture zone. But the matrix closer to the injection end has more serious asphaltene precipitation and greater permeability loss than distal matrix.

Data Availability

The data used to support the findings of this study are available from the corresponding author upon request.

Conflicts of Interest

The authors declare that they have no conflicts of interest.

Acknowledgments

This research was supported by the National Natural Science Foundation of China (funding name: Study on the Microscopic Phase Behavior and Migration Mechanism of CO_2 and Multicomponent Alkanes in Shale Dynamical Nanopore) (no. 52004038) and CNPC-CZU Innovation Alliance Funding (funding name: Development of Multi-Component Thermofluid Experimental Equipment and Research on the Mechanism of Multi-Component Thermofluid).

References

[1] N. Zhou, S. Lu, and M. Wang, "Limits and grading evaluation criteria continental basins of China," *Petroleum Exploration and Development*, vol. 48, no. 5, pp. 939–949, 2021.

[2] C. Jia, C. Zou, J. Li, D. Li, and M. Zheng, "Evaluation criteria, major types, characteristics and resource prospects of tight oil in China," *Petroleum Research*, vol. 1, no. 1, pp. 1–9, 2016.

[3] L. Sun, C. Zou, A. Jia et al., "Development characteristics and orientation of tight oil and gas in China," *Petroleum Exploration and Development*, vol. 46, no. 6, pp. 1073–1087, 2019.

[4] Y. Tang, R. Wang, Z. Li, M. Cui, Z. Lun, and Y. Lu, "Experimental study on spontaneous imbibition of CO_2-rich brine in tight oil reservoirs," *Energy & Fuels*, vol. 33, no. 8, pp. 7604–7613, 2019.

[5] P. Zuloaga, W. Yu, J. Miao, and K. Sepehrnoori, "Performance evaluation of CO_2 huff-n-puff and continuous CO_2 injection in tight oil reservoirs," *Energy*, vol. 134, pp. 181–192, 2017.

[6] A. K. Al-Khazraji and M. B. Awang, "Evaluation of miscible CO_2-flooding to improve oil recovery in a clastic heterogeneous reservoir," in *Proceedings of the IADC/SPE Asia Pacific Drilling Technology Conference*, Singapore, August 2016.

[7] Z. Song, Y. Song, Y. Li, B. Bai, K. Song, and J. Hou, "A critical review of CO_2 enhanced oil recovery in tight oil reservoirs of north America and China," *Fuel*, vol. 276, no. 5, Article ID 118006, 2020.

[8] W. Xue-wu, X. Pufu, Y. Zheng-ming, L. Xue-wei, X. Zhi-zeng, and W. Li-qiang, "Laboratory and field-scale parameter optimization of CO_2 huff-n-puff with the staged-fracturing horizontal well in tight oil reservoirs," *Journal of Petroleum Science and Engineering*, vol. 186, Article ID 106703, 2020.

[9] A. Abedini and F. Torabi, "Oil recovery performance of immiscible and miscible CO_2 huff-and-puff processes," *Energy & Fuels*, vol. 28, no. 2, pp. 774–784, 2014.

[10] W. Pu, B. Wei, F. Jin et al., "Experimental investigation of CO_2 huff-n-puff process for enhancing oil recovery in tight reservoirs," *Chemical Engineering Research and Design*, vol. 111, pp. 269–276, 2016.

[11] A. Habibi, M. R. Yassin, H. Dehghanpour, and D. Bryan, "Experimental investigation of CO_2-oil interactions in tight rocks: a montney case study," *Fuel*, vol. 203, pp. 853–867, 2017.

[12] J. J. Sheng and B. L. Herd, "Critical review of field EOR projects in shale and tight reservoirs," *Journal of Petroleum Science and Engineering*, vol. 159, pp. 654–665, 2017.

[13] D. Alfarge, M. Wei, B. Bai, and A. Almansour, "Effect of molecular-diffusion mechanisim on CO_2 huff-n-puff process in shale-oil reservoirs," in *Proceedings of the SPE Kingdom of Saudi Arabia Annual Technical Symposium and Exhibition*, Dammam, Saudi Arabia, April 2017.

[14] Z. Sun, B. Huang, Y. Li, H. Lin, S. Shi, and W. Yu, "Nanoconfined methane flow behavior through realistic organic shale matrix under displacement pressure: a molecular simulation investigation," *Journal of Petroleum Exploration and Production Technology*, vol. 335, pp. 1–9, 2021.

[15] Z. Sun, B. Huang, K. Wu et al., "Nanoconfined methane density over pressure and temperature: wettability effect," *Journal of Natural Gas Science and Engineering*, vol. 99, Article ID 104426, 2022.

[16] K. Qian, S. Yang, H. Dou, Q. Wang, L. Wang, and Y. Huang, "Experimental investigation on microscopic residual oil distribution during CO_2 huff-and-puff process in tight oil reservoirs," *Energies*, vol. 11, no. 10, p. 2843, 2018.

[17] Y. Zhang, W. Yu, Z. Li, and K. Sepehrnoori, "Simulation study of factors affecting CO_2 huff-n-puff process in tight oil reservoirs," *Journal of Petroleum Science and Engineering*, vol. 163, pp. 264–269, 2018.

[18] W. Yu, H. R. Lashgari, K. Wu, and K. Sepehrnoori, "CO_2 injection for enhanced oil recovery in bakken tight oil reservoirs," *Fuel*, vol. 159, pp. 354–363, 2015.

[19] Z. Lei, S. Wu, T. Yu et al., "simulation and optimization of CO_2 huff-n-puff processes in tight oil reservoir: a case study of chang-7 tight oil reservoirs in ordos basin," in *Proceedings of the SPE Asia Pacific Oil and Gas Conference and Exhibition*, Brisbane, Australia, October 2018.

[20] S. B. Hawthorne, C. D. Gorecki, J. A. Sorensen, E. N. Steadman, J. A. Harju, and S. Melzer, "Hydrocarbon mobilization mechanisms from upper, middle, and lower bakken reservoir rocks exposed to CO_2," in *Proceedings of the SPE Unconventional Resources Conference Canada*, Calgary, Canada, November 2013.

[21] H. Bai, Q. Zhang, Z. Li et al., "Effect of fracture on production characteristics and oil distribution during CO_2 huff-n-puff under tight and low-permeability conditions," *Fuel*, vol. 246, pp. 117–125, 2019.

[22] R. Sun, W. Yu, F. Xu, H. Pu, and J. Miao, "Compositional simulation of CO_2 huff-n-puff process in middle bakken tight oil reservoirs with hydraulic fractures," *Fuel*, vol. 236, pp. 1446–1457, 2019.

[23] Ø. Eide, M. A. Fernø, Z. Alcorn, and A. Graue, "Visualization of carbon dioxide enhanced oil recovery by diffusion in fractured chalk," *SPE Journal*, vol. 21, no. 1, pp. 112–120, 2016.

[24] H. Wang, Z. Lun, C. Lv et al., "Nuclear-magnetic-resonance study on mechanisms of oil mobilization in tight sandstone reservoir exposed to carbon dioxide," *SPE Journal*, vol. 23, no. 3, pp. 750–761, 2018.

[25] B. Wei, K. Gao, T. Song et al., "Nuclear-magnetic-resonance monitoring of mass exchange in a low-permeability matrix/fracture model during CO_2 cyclic injection: a mechanistic study," *SPE Journal*, vol. 25, no. 1, pp. 440–450, 2020.

[26] B. Wei, M. Zhong, K. Gao et al., "Oil recovery and compositional change of CO_2 huff-n-puff and continuous injection modes in a variety of dual-permeability tight matrix-fracture models," *Fuel*, vol. 276, Article ID 117939, 2020.

[27] D. S. George, O. Hayat, and A. R. Kovscek, "A microvisual study of solution-gas-drive mechanisms in viscous oils," *Journal of Petroleum Science and Engineering*, vol. 46, no. 1-2, pp. 101–119, 2005.

[28] P. Nguyen, J. W. Carey, H. S. Viswanathan, and M. Porter, "Effectiveness of supercritical-CO_2 and N_2 huff-and-puff methods of enhanced oil recovery in shale fracture networks using microfluidic experiments," *Applied Energy*, vol. 230, pp. 160–174, 2018.

[29] M. Zhang, Q. Sang, H. Gong, Y. Li, and M. Dong, "Effect of depletion rate on solution gas drive in shale," *IOP Conference Series: Earth and Environmental Science*, vol. 108, no. 3, Article ID 032078, 2018.

[30] H. Gao, Y. Liu, Z. Zhang, B. Niu, and H. Li, "Impact of secondary and tertiary floods on microscopic residual oil distribution in medium-to-high permeability cores with NMR technique," *Energy & Fuels*, vol. 29, no. 8, pp. 4721–4729, 2015.

[31] M. Cao and Y. Gu, "Physicochemical characterization of produced oils and gases in immiscible and miscible CO_2 flooding processes," *Energy & Fuels*, vol. 27, no. 1, pp. 440–453, 2013.

[32] E. Y. Sheu, "Petroleum asphaltene properties, characterization, and issues," *Energy & Fuels*, vol. 16, no. 1, pp. 74–82, 2002.